

BIOMIMETIC POLYMERIC PARTICLES FOR BIOMEDICAL THERAPEUTICS

By
Randall A. Meyer

A dissertation submitted to Johns Hopkins University in conformity with the
requirements for the degree of Doctor of Philosophy

Baltimore, MD

August 2018

© 2018 Randall A. Meyer

All Rights Reserved

Abstract

The overall goal of this thesis is to investigate the various applications in which micron and nanometer sized polymeric particles could be synthesized to mimic biological cells and tissues to achieve a therapeutic effect. Particularly, the emphasis of this particle design is on the development of artificial antigen presenting cells (aAPC) for immunotherapy. Although the work in this thesis is varied in nature, this dissertation can be broadly categorized in three aims. In **Aim 1**, the role of shape in the design of aAPC was investigated with respect to use for cancer immunotherapy. An automated process was developed for the generation of anisotropic particles as well as a model system with which to evaluate their therapeutic efficacy in combination with immune checkpoint blockades. These therapeutics were then evaluated in a murine model and non-spherical aAPC were found to outperform spherical aAPC. Furthermore, the core polymeric material was modified to generate much stronger aAPC, with sufficient immunostimulation to engage the endogenous immune cells. In **Aim 2**, the role of surface chemistry was investigated in the design and use of particles for biomimetic drug delivery applications. Particles with biomimetic surface bound lipid membranes were synthesized to mimic the natural biological membrane of a cell. Anisotropic particles were synthesized and coated with naturally derived red blood cell membranes and were found to outperform equivalently coated spherical nanoparticles in various important drug delivery parameters such as pharmacokinetics and cellular uptake and elimination. In **Aim 3**, the role of stimulus response was investigated with respect to particle design. Particles with thermally triggered shape memory effect were synthesized and found to allow for spatiotemporally controlled shape control of spherical and ellipsoidal particles.

In addition, focused ultrasound triggered drug delivery particles were synthesized to enable focal, noninvasive neuromodulation in a rat seizure model. The particle therapeutic systems developed as part of this thesis will have a wide and diverse impact on multiple fields in medicine including immunotherapy, regenerative medicine, and neuromodulation.

Thesis Committee

Jordan J. Green (primary advisor, reader)

Professor, Departments of Biomedical Engineering, Materials Science and Engineering,
Chemical and Biomolecular Engineering, Neurosurgery, Ophthalmology, and Oncology
Johns Hopkins University School of Medicine

Jonathan P. Schneck (reader)

Professor, Departments of Pathology, Medicine, and Oncology
Johns Hopkins University School of Medicine

Kevin J. Yarema

Associate Professor, Department of Biomedical Engineering
Johns Hopkins University School of Medicine

Hai-Quan Mao

Professor, Departments of Materials Science and Engineering, and Biomedical Engineering
Johns Hopkins University

Dedication

I would like to dedicate this thesis to my grandfather Samuel P. Leach, who recently passed away on May 31, 2018. When I was a young child I sent him my report card showing I received a grade average of 98%. He sent me back a card with a thermometer showing the thermometer was at a high level but not quite at the top. He wrote in my card “Great job getting a 98% average, but don’t stop there. Always strive for your best!” Several years later in high school, I received a grade average above 100% due to weighted classes. As usual I sent my grandfather my report card, and he sent me back another card showing the thermometer from the previous card had burst as I had achieved what he was not expecting to be possible! That mentality stayed with me throughout my graduate career and led me through the composition of this thesis. Thanks to my grandfather’s advice, I will always strive for my best and never settle for good enough.



Acknowledgements

The work presented in this thesis would not have been possible without the collaborative effort of several individuals providing support in various capacities. First, I would like to acknowledge my thesis advisor Dr. Jordan J. Green. I could not have asked for better guidance in the preparation of this thesis. As my mentor, he was simultaneously supporting of my research endeavors when problems would arise and willing to allow me sufficient independence to pursue various fruitful research opportunities that otherwise did not conform to my primary project. I thoroughly appreciate all of the knowledge, wisdom, and skills Dr. Green imparted to me during my graduate tenure in the preparation of becoming a professional scientist.

The work presented in this thesis was also predicated on several individuals in the Green Group that I have had the fortunate opportunity to work with during the tenure of my Ph. D. Dr. Joel C Sunshine was my primary graduate student mentor and provided significant guidance in the initial stages of my graduate education that continued through to my final years. I have also had the opportunity to work with several graduate students in the preparation of this thesis including Elana Ben-Akiva, who has been instrumental in the membrane coating work, and Kelly R. Rhodes who has been of great assistance with aAPC materials design and non-invasive neuromodulation. In addition to these individuals, I would like to acknowledge the undergraduate research assistants that have assisted me throughout the preparation of this thesis including Qiuyin Ren, Callie Deng, Daphne E. Schlesinger, Ka Ho Nicholas Cheung, Alison Bartkowski, Jenna Ballard, and Austin Petronack. I would also like to acknowledge the assistance and scientific input of all of the members of the Green Group during my tenure including Dr. Stephany Y.

Tzeng, Dr. Corey J. Bishop, Dr. Ron B. Shmueli, Dr. Kristen L. Kozielski, Dr. Jayoung Kim, Dr. Maziar Mohammadi, Dr. Johan Karlsson, David R. Wilson, Hannah J. Vaughan, and Yuan Rui.

In addition to Dr. Green and the entire Green Group, I have had the fortunate opportunity to collaborate with the laboratory of Dr. Jonathan P. Schneck with regard to development of artificial antigen presenting cells and cancer immunotherapies. Dr. Schneck, although not my primary thesis mentor, has in effect served as my secondary research advisor. He has always shown great enthusiasm and support toward efforts in aAPC parameter modulation with respect to various biomimetic features.

The laboratory of Dr. Schneck has also been instrumental in the completion of this thesis and have been co-authored on several of the publications derived from this work. Specifically I would like to thank Dr. Alyssa K. Kosmides, John W. Hickey, Kent Aje, Dr. Karlo Perica, and Dr. Matthias Oelke for their support in the immunological testing and evaluation of aAPC for cancer immunotherapy.

The work presented in this thesis would not have been possible without the assistance of several other collaborators throughout my tenure in graduate school. Specifically, I would like to acknowledge Dr. Kevin J. Yarema and Dr. Mohit P. Mathew for their work with me on the synthetic lipid membrane particle coating projects. I would also like to acknowledge Dr. Qiongyu Guo, Dr. James B. Spicer and Lauren Olasov for their collaborative efforts on the synthesis and evaluation of the shape memory particles. In addition I would like to thank Dr. Raag Airan for the collaborative efforts and guidance in the pursuit of focused ultrasound triggered drug delivery particles for non-invasive neuromodulation.

I also wish to thank the various sources of funding that were made available to me for financial support during my graduate student tenure. I would like to acknowledge the JHU INBT Cancer Nanotechnology Research Fellowship, the Ruth L. Kirchstein National Research Service Award F31 Fellowship, the Achievement Rewards for College Scientists Fellowship provided by the Jones Group, and the Siebel Scholarship provided by the Siebel Foundation as sources of funding during graduate school. I would also like to acknowledge the National Cancer Institute and the National Institute for Biomedical Imaging and Bioengineering for research support.

I wish to acknowledge several individuals, not involved directly with scientific content of this thesis, but for their support over the years during my training in becoming a professional scientist. I would like to thank Dr. James W. Casey, my undergraduate faculty research advisor, and Dr. Kristine Petesch, my graduate student research advisor for their support and teachings during my undergraduate research tenure. Prior to working with these two individuals I had no research experience and few credentials required for working in a laboratory. They gave me a chance to work in a scientific research environment and I thoroughly appreciate the opportunity.

Finally, I would like to acknowledge all of the incredible support from my family during the tenuous period of graduate school. I would like to thank my mother, Patricia A. Meyer “Memah” for being a wonderful mother to me throughout my life, and more specifically providing the emotional support required to complete this thesis. I would also like thank my father, Randall S. Meyer “Dedah” for being an incredible father to me throughout my life, as well as his scientific contributions to the design of the automated thin film stretcher. I simply could not ask for better parents and words cannot describe

everything they have done for me in my life. I would also like to thank my extended family including my grandparents, aunts, uncles, and cousins for their support during this period of my life.

Finally, I would like to thank one individual who shall remain anonymous and represented by the letters QDM. This individual has also always been there for me and I am incredibly thankful to have him in my life. BQM.

Table of Contents

Abstract	ii
Thesis Committee	iv
Dedication	v
Acknowledgements	vi
List of Tables	xiii
List of Figures	xiv
1. Chapter 1: Introduction	1
1.1 Overview of the Thesis	1
1.2 Specific Aims	3
1.3 Summary of Contributions	5
2. Chapter 2: State of the Art	9
2.1 Overview of the Impact of Shape in Particle Design	9
2.2 Overview of Artificial Antigen Presenting Cell Technology	28
2.3 Overview of the Impact of Surface Properties in Particle Design	50
2.4 Tables	65
2.5 Figures	68
2.6 References	80
3. Chapter 3: An Automated Multidimensional Thin Film Stretching Device for the Generation of Anisotropic Polymer Micro- and Nanoparticles	96
3.1 Introduction	96
3.2 Materials and Methods	99
3.3 Results and Discussion	104
3.4 Conclusions	112
3.5 Figures	113
3.6 References	120
4. Chapter 4: Biodegradable Artificial Antigen Presenting Cells with Anti PD-1 Immunotherapy to Treat Melanoma	124
4.1 Introduction	124
4.2 Materials and Methods	127
4.3 Results and Discussion	135
4.4 Conclusions	148
4.5 Figures	149
4.6 References	154
5. Chapter 5: Biodegradable Nanoellipsoidal Artificial Antigen Presenting Cells for Antigen Specific T-Cell Activation	157
5.1 Introduction	157
5.2 Materials and Methods	159

5.3	Results and Discussion-----	166
5.4	Conclusions-----	174
5.5	Tables-----	176
5.6	Figures-----	177
5.7	References-----	188
6.	Chapter 6: Biomimetic Biodegradable Artificial Antigen Presenting Cells for Enhanced “Off-The-Shelf” Melanoma Immunotherapy-----	191
6.1	Introduction-----	191
6.2	Materials and Methods-----	194
6.3	Results and Discussion-----	197
6.4	Conclusions-----	202
6.5	Figures-----	204
6.6	References-----	212
7.	Chapter 7: Anisotropic Biodegradable Particles Coated with Supported Lipid Bilayers for Spatially Dynamic Protein Presentation-----	215
7.1	Introduction-----	215
7.2	Materials and Methods-----	217
7.3	Results and Discussion-----	224
7.4	Conclusions-----	232
7.5	Figures-----	234
7.6	References-----	247
8.	Chapter 8: Anisotropic Biodegradable Particles Coated with Naturally Derived Red Blood Cell Membranes for Enhanced Drug Delivery-----	251
8.1	Introduction-----	251
8.2	Materials and Methods-----	253
8.3	Results and Discussion-----	260
8.4	Conclusions-----	270
8.5	Figures-----	272
8.6	References-----	283
9.	Chapter 9: Entanglement Based Thermoplastic Shape Memory Polymeric Particles with Photothermal Actuation for Biomedical Applications-----	287
9.1	Introduction-----	287
9.2	Materials and Methods-----	290
9.3	Results and Discussion-----	296
9.4	Conclusions-----	302
9.5	Figures-----	304
9.6	References-----	317
10.	Chapter 10: Noninvasive Targeted Transcranial Neuromodulation via Focused Ultrasound Gated Drug Release from Nanoemulsions-----	320
10.1	Introduction-----	320
10.2	Materials and Methods-----	323

10.3	Results and Discussion-----	330
10.4	Conclusions-----	337
10.5	Figures-----	339
10.6	References-----	345
11.	Chapter 11: Future Directions-----	347
11.1	Introduction-----	347
11.2	Future Directions for Anisotropic aAPC Particles-----	349
11.3	Future Directions for PLGA/PBAE Cationic Polymer Blended Particles-----	352
11.4	Future Directions for Biomimetic Particle Membrane Coating-----	357
11.5	Future Directions for Stimulus Controlled Therapeutics-----	362
11.6	Conclusions-----	368
11.7	Figures-----	370
11.8	References-----	381
Vita	-----	384

List of Tables

Table 2.1: Summary of applications of various anisotropic polymeric nanoparticles

Table 2.2: Examples of the various existing aAPCs and their efficacies.

Table 2.3. Summary of various surface engineering features for immunoengineering.

Table 5.1: Impact of particle stretching on particle surface area.

List of Figures

Figure 2.1: Summary of various particle shapes that can be synthesized with the thin film stretching top-down method.

Figure 2.2: Shape memory applications of anisotropic microparticles.

Figure 2.3: Example of bottom-up strategy for stripped anisotropic polymeric particle synthesis.

Figure 2.4: Synthesis of non-spherical polymeric particles by a microfluidic device.

Figure 2.5: Example of enhanced *in vivo* biodistribution mediated by particle shape.

Figure 2.6: Schematic of the antigen presenting cell/T-Cell interaction.

Figure 2.7: Schematic of the immune synapse that forms between an APC and T-Cell.

Figure 2.8: Various important design criteria for artificial antigen presenting cells.

Figure 2.9: Example of the use of cellular aAPC for long term stimulation of T-Cells.

Figure 2.10: Schematic of the principle of killer aAPC.

Figure 2.11: Schematic of synthetic and naturally derived membrane coated particle systems.

Figure 2.12: Impact of ligand rearrangement on aAPC mediated activation of T-Cells.

Figure 3.1: Schematic of the automated thin film stretcher.

Figure 3.2: Anisotropic particles of various size synthesized by the automated process.

Figure 3.3: Prolate and oblate ellipsoidal particles formed through the automated process.

Figure 3.4: Impact of temperature on the two dimensional stretching of particles.

Figure 3.5: Impact of strain rate on the generation of prolate ellipsoidal particles.

Figure 3.6: Particles encapsulating small molecules can be deformed through thin film stretching,

Figure 3.7: Different biomaterials can be made into anisotropic polymeric microparticles.

Figure 4.1: *In vitro* assessment of biodegradable artificial antigen presenting cell functionality.

Figure 4.2: *In vitro* assessment of aAPC and anti-PD1 Synergy.

Figure 4.3: *In vivo* assessment of micro aAPC pharmacokinetics.

Figure 4.4: *In vivo* synergy of aAPC and anti-PD1 for melanoma treatment.

Figure 4.5: Impact of combination aAPC and anti-PD1 therapy on T-Cell phenotype *in vivo*.

Figure 5.1: *In vitro* characterization of non-spherical nano aAPC.

Figure 5.2: Particle surface protein release rate of non-spherical aAPC.

Figure 5.3: Representative flow cytometry gating for nanoparticle uptake experiments.

Figure 5.4: *In vitro* assessment of non-spherical nano aAPC T-Cell stimulation.

Figure 5.5: Shape dependence of nanoparticle uptake by macrophages and endothelial cells.

Figure 5.6: Viability of macrophages following particle incubation.

Figure 5.7: *In vivo* pharmacokinetics of non-spherical nano aAPC.

Figure 5.8: Dispersion fraction analysis from pharmacokinetic data of non-spherical nano aAPC.

Figure 5.9: Organ distribution of non-spherical nano aAPC.

Figure 5.10: *In vivo* T-Cell stimulation of non-spherical nano aAPC.

Figure 5.11: *In vivo* melanoma tumor treatment mediated by non-spherical nano aAPC.

Figure 6.1: Schematic of the principle of the enhanced aAPC.

Figure 6.2: Chemical drawings of PLGA and PBAEs used to make PLGA/PBAE particles.

Figure 6.3: Schematic of PLGA/PBAE aAPC synthesis strategy.

Figure 6.4: SEM images and size characterization of PLGA/PBAE aAPC.

Figure 6.5: Protein conjugation efficiency of PLGA and PLGA/PBAE aAPC.

Figure 6.6: *In vitro* T-Cell stimulation mediated by PLGA/PBAE aAPC.

Figure 6.7: Evaluation of T-Cell binding to PLGA and PLGA/PBAE aAPC.

Figure 6.8: *In vivo* functional efficacy of PLGA/PBAE based enhanced aAPC.

Figure 7.1: Schematic of anisotropic lipid coated microparticle synthesis.

Figure 7.2: Schematic of anisotropic lipid coated microparticle functionalization.

Figure 7.3: SEM characterization of anisotropic lipid coated microparticles.

Figure 7.4: Confocal image analysis of anisotropic lipid coated microparticles.

Figure 7.5: Viability of macrophages during lipid coated particle uptake experiment.

Figure 7.6: Shape dependent cell uptake of anisotropic lipid coated particles.

Figure 7.7: Fluorescent avidin conjugation efficiency to lipid coated particles.

Figure 7.8: Functionalization of anisotropic lipid coated particles.

Figure 7.9: Analysis of biotinyl molecule adhesion to surface of lipid coated particles.

Figure 7.10: Analysis of lipid coated particle stability in lyophilization.

Figure 7.11: Time course stability of lipid coated particles.

Figure 7.12: Targeted binding of anisotropic lipid coated microparticles.

Figure 7.13: Anisotropic lipid coated particle membrane fluidity.

Figure 8.1: Schematic of coating process for RBC membrane coated particles.

Figure 8.2: SEM and size analysis of RBC membrane coated anisotropic particles.

Figure 8.3: Confocal image analysis of anisotropic RBC membrane coated particles.

Figure 8.4: Stability of anisotropic RBC membrane coated particles in lyophilization.

Figure 8.5: Stability of anisotropic RBC membrane coated particles in time course incubation.

Figure 8.6: Membrane fluidity of anisotropic RBC membrane coated microparticles.

Figure 8.7: *In vitro* characterization of anisotropic RBC membrane coated nanoparticles.

Figure 8.8: Shape and coating dependence on macrophage uptake of RBC membrane coated nanoparticles.

Figure 8.9: *In vivo* pharmacokinetics of anisotropic RBC membrane coated nanoparticles.

Figure 8.10: Organ distribution of anisotropic RBC membrane coated nanoparticles.

Figure 8.11: Biomimetic nanosponge activity of RBC membrane coated anisotropic nanoparticles.

Figure 9.1: Schematic of shape memory principle and analysis of polymeric alignment in anisotropic microparticles.

Figure 9.2: SEM characterization of shape memory microparticles.

Figure 9.3: DSC heating curve of shape memory microparticles.

Figure 9.4: Absorbance spectrum and concentration standard curve of gold nanoparticle in shape memory microparticles.

Figure 9.5: TEM characterization of hydrophobically stabilized gold nanoparticles.

Figure 9.6: TEM images of hydrophobic gold nanoparticles in shape memory microparticles.

Figure 9.7: Shape memory microparticles without encapsulated gold nanoparticles.

Figure 9.8: Bulk heating shape memory effect of polymeric microparticles.

Figure 9.9: Laser triggered shape memory effect of shape memory microparticles.

Figure 9.10: Spatial control of laser triggered shape memory effect of microparticles.

Figure 9.11: Shape memory effect dependent phagocytosis of shape memory microparticles.

Figure 9.12: Time course shape memory effect of microparticles in confocal microscopy.

Figure 9.13: Viability of macrophages incubated with shape memory microparticles.

Figure 10.1: Schematic of focused ultrasound triggered drug release from nanoemulsions.

Figure 10.2: *In vitro* characterization of size and propofol release from nanoemulsions.

Figure 10.3: *In vivo* pharmacokinetic profile of nanoemulsions.

Figure 10.4: *In vivo* functional efficacy of propofol releasing nanoemulsions.

Figure 10.5: Safety profile of nanoemulsions triggered to release propofol.

Figure 11.1: Synthesis of monodisperse anisotropic microparticles.

Figure 11.2: Oblate ellipsoidal aAPC T-Cell stimulation.

Figure 11.3: Regulatory T-Cell induction mediated by PLGA/PBAE aAPC.

Figure 11.4: Natural killer cell activation mediated by PLGA/PBAE aAPC.

Figure 11.5: PBAE transfection based redirection cancer immunotherapy.

Figure 11.6: Platelet membrane coated anisotropic microparticles.

Figure 11.7: Dendritic cell membrane coated polymeric microparticle.

Figure 11.8: Cancer targeting sialic acid analogue clicking lipid-polymeric hybrid nanoparticles.

Figure 11.9: Gold nanorod based photothermal triggered drug release.

Figure 11.10: Doxorubicin release ultrasound triggered release from nanoemulsions.

Figure 11.11: Magnetic polymeric particle superparamagnetism and MRI contrast.

Chapter 1: Introduction

1.1 Overview of Thesis

The work presented in this thesis from the most generalized standpoint possible can be summarized as a dissertation on the design and implementation of therapeutics that are based on micron and nanoscale polymeric particles that possess a particular feature of biomimicry. Specifically, these particle systems were designed to mimic the features of cellular anatomy and physiology that allow cells to perform their natural functions in the body with precision and efficiency. Chapter 2 presents background information on the state of the art for biomimetic therapeutics. Although not a comprehensive investigation into all possible characteristics of a cell that can be mimicked in a particle system, this thesis is focused on the exploration of particle shape (to mimic cell shape), particle surface chemistry (to mimic cell membranes), and particle stimulus response (to mimic cell physiology).

In recent years, particle shape has been found to impact their efficacy as biomedical therapeutics. By designing particles that deviate from the traditional spherical shape, it has been shown therapeutic efficacy can be greatly enhanced. In Chapter 3, a process for the automated generation of ellipsoidal polymeric particles is presented. The primary application that these non-spherical particles has been applied to is in the generation of artificial antigen presenting cells (aAPC), particles that are designed to mimic antigen presenting cells in their interaction with T-Cells to direct the effector function of the latter. Chapter 4 demonstrates how biodegradable polymeric aAPC can be combined with the immune checkpoint blockade to achieve modest therapeutic effect in a murine treatment model. Chapter 5 then incorporates the principle of non-spherical

particles and aAPC to demonstrate enhanced therapeutic efficacy of nanoellipsoidal aAPC in a murine melanoma model. Finally, Chapter 6 summarizes a new direction in the design of aAPC, namely the use of a novel polymeric blend in the synthesis of aAPC.

In addition to shape, biomimetic surface chemistry has been found to be an important factor in the therapeutic efficacy of particle-based therapeutics. Generally, the trend has been found that increasing the biomimicry of the particle surface results in increased biological functionality. This has been accomplished through various mechanisms but one promising strategy has been the synthesis of supported lipid bilayers on the surface of the particle to reproduce the cell membrane, a key cellular component to allow it to interact with the extracellular environment. The work in this thesis along this line of investigation has been to engineer these artificial cell membranes on the surface of the anisotropic ellipsoidal particles. In Chapter 7, synthetic lipids were utilized to create an artificial membrane on the surface. It was found that these particles maintain the properties of cell membranes including lateral membrane fluidity and presentation of ligands for interaction with other cells. In Chapter 8, naturally derived cell membranes from red blood cells (RBC) were used to coat the anisotropic particles. It was found from this work that the RBC membranes synergized with particle shape to enhance particle drug delivery efficacy and pharmacokinetic properties.

The final parameter of biomimicry investigated in this thesis is the capability of particle therapeutics to perform an action in response to a controlled stimulus. Cells in the body have a tremendous capacity to respond to a variety of mechanical, chemical, and electrical cues to perform a variety of functions. Particles can be similarly engineered to respond to an external stimulus that effects a biologically relevant function such as drug

release or thermal ablation. The work in the thesis along this paradigm of biomimicry centers around two particle systems designed to mimic cellular physiology through stimulus response. In Chapter 9, a system for photothermal actuation of particle shape changes is presented and found to influence the interaction of particles with phagocytes similarly to what was presented in previous chapters through shape effects. In Chapter 10, a liquid core particle was developed for the focused ultrasound triggered release of neuromodulatory agents for non-invasive neuromodulation. It was found that the particles were sufficiently potent to silence chemically induced seizures in a rodent model.

Finally, some speculative future directions for these projects are presented in Chapter 11. These are possible and probable projects and uses for the biomimetic therapeutics that are presented in the thesis. These ideas represent the very forefront of biomimetic particle technology and have the potential to revolutionize the landscape of biomedical therapeutics.

1.2 Specific Aims

The following is an outline of the specific aims that served as the benchmarks for completion of this dissertation. Each of the aims corresponds to one of the feature of biomimetic particle therapeutics that were summarized in section 1.1. In Aim 1 the role of particle shape and particle material was investigated with respect to artificial antigen presenting cells and serves as the basis for the work presented in Chapters 3, 4, 5, and 6. In Aim 2, the role of particle surface chemistry was investigated in terms of anisotropic particle cell membrane coating. This work serves as the basis of Chapters 7 and 8. In Aim 3, the role of particle stimulus response is investigated with respect to photothermal

actuation of particle shape change and focused ultrasound triggered drug delivery for noninvasive neuromodulation. The work of this aim serves as the basis of Chapters 9 and 10.

Specific Aim 1. Develop anisotropic polymeric particles of various ellipsoidal shapes and apply these materials to the design of artificial antigen presenting cells (aAPCs) for cancer immunotherapy.

- a. Develop an automated thin film stretching process for the generation of anisotropic polymeric micro- and nanoparticles.
- b. Develop an *in vivo* tumor treatment model for evaluation of aAPC efficacy.
- c. Examine the effect of particle shape in the design and efficacy of micro and nanodimensional aAPCs for antigen specific T-Cell activation.
- d. Develop enhanced artificial antigen presenting cells using polymeric blends and apply to cancer immunotherapy.

Specific Aim 2. Develop supported lipid bilayers (SLBs) from synthetic and naturally derived lipid sources and apply to biomimetic drug delivery.

- a. Develop functionalized supported lipid bilayers from synthetic lipid sources and characterize stability and membrane fluidity.
- b. Develop functionalized supported lipid bilayers from naturally derived cell based lipid sources and characterize potential for biomimetic drug delivery.
- c. Implement anisotropic supported lipid bilayers from naturally derived cell-based lipid sources for enhanced pharmacokinetics and drug delivery.

Specific Aim 3. Synthesize polymeric particles of varying biomimetic materials and investigate potential for drug delivery and immunotherapy.

- a. Develop polymeric micro- and nanoparticles encapsulating hydrophobically stabilized gold nanoparticles for laser triggered shape memory.
- b. Develop ultrasound sensitive particles for spatiotemporally controlled delivery of anesthetic for noninvasive neuromodulation.
- c. Implement ultrasound sensitive particles for spatiotemporally controlled neuromodulation in a rat pharmacokinetic model and a rat seizure model.

1.3 Summary of Contributions

The following is a summary of the major scientific contributions that have been published and presented as a result of the work described in this thesis presented by the chapter in which they correspond to:

Chapter 2:

- **Meyer RA** and Green JJ. Shaping the Future of Nanomedicine: Anisotropy in Polymeric Nanoparticle Design. *Wiley Interdisciplinary Reviews: Nanomedicine and Nanobiotechnology*, 8(2), 2016, 191-207.
- Ben-Akiva E,* **Meyer RA**,* Wilson DR,* and Green JJ. Surface engineering for lymphocyte programming. *Advanced Drug Delivery Reviews*. 114(2017), 2017, 102-115.
- **Meyer RA** and Green JJ. Artificial Antigen Presenting Cells: Biomimetic Strategies for Directing the Immune Response. *Biomaterials in Regenerative Medicine and the Immune System*. Springer International Publishing, 2015, 257-277.

Chapter 3:

- **Meyer RA**, Meyer RS, and Green JJ. An automated multidimensional thin film stretching device for the generation of anisotropic polymeric micro- and nanoparticles. *Journal of Biomedical Materials Research Part A* 103(8), 2015, 2747-2757.
- **Meyer RA**, Meyer RS, Green JJ. An Automated Thin Film Stretching Device for the Generation of Anisotropic Polymeric Micro- and Nanoparticles. *NanoDDS*. 2016.

Chapter 4:

- Kosmides AK,* **Meyer RA**,* Hickey JW, Aje K, Green JJ, and Schneck JP. Biodegradable artificial antigen presenting cells with anti PD-1 immunotherapy to treat melanoma. *Biomaterials*, 118, 2017, 16-26.
- **Meyer RA**, Kosmides AK, Aje K, Schneck JP, and Green JJ. Anti-PD1 and Biodegradable Artificial Antigen Presenting Cell Dual Therapy for Melanoma. *Biomedical Engineering Society Annual Meeting*, 2015.

Chapter 5:

- **Meyer RA**,* Sunshine JC,* Perica K, Kosmides AK, Aje K, Schneck JP, and Green JJ. Biodegradable Nanoellipsoidal Artificial Antigen Presenting Cells for Antigen Specific T-Cell Activation. *Small* 11(13), 2015, 1519-1525. (Featured on the Back Cover)
- **Meyer RA**, Sunshine JC, Perica K, Aje K, Schneck JP, and Green JJ. Biodegradable Nanoellipsoidal Artificial Antigen Presenting Cells for Cancer Immunotherapy. *Biomedical Engineering Society Annual Meeting*, 2014.

Chapter 6:

- **Meyer RA**, Hickey JW, Kosmides AK, Rhodes KR, Bartkowski A, Schneck JP, Green JJ. Biomimetic Biodegradable Artificial Antigen Presenting Cells for Enhanced “Off-The-Shelf” Melanoma Immunotherapy. *Biomedical Engineering Society*. 2017.

Chapter 7:

- **Meyer RA**,* Mathew MP,* Ben-Akiva E, Sunshine JC, Shmueli RS, Ren Q, Yarema KJ, and Green JJ. Anisotropic biodegradable particles coated with supported lipid bilayers for spatially dynamic protein presentation. *Acta Biomaterialia*. 72, 2018, 228-238.
- **Meyer RA**, Mathew MP, Sunshine JC, Shmueli RB, Ren Q, Yarema KJ, and Green JJ. Anisotropic Supported Lipid Bilayers for Spatially Dynamic Surface Protein Presentation. *Society for Biomaterials Annual Meeting*, 2015.

Chapter 8:

- **Meyer RA**, Ben-Akiva E, Cheung Ka Ho, Green JJ. Biomimetic Anisotropic Polymeric Particles with Naturally Derived Cell Membranes for Enhanced Drug Delivery. *Tissue Engineering and Regenerative Medicine Society*. 2016

Chapter 9:

- Guo Q,* Bishop CJ,* **Meyer RA**,* Wilson DR, Olasov L, Schlesinger DE, Mather PT, Spicer JB, Elisseff JH, and Green JJ. Entanglement-Based Thermoplastic Shape Memory Polymeric Particles with Photothermal Actuation for Biomedical Applications, *ACS Applied Materials and Interfaces*, 10(16), 2018, 13333-13341.

- Guo Q, Bishop CJ, **Meyer RA**, Olasov L, Schlesinger DE, Spicer JB, Elisseeff JH, Kumar A, and Green JJ. Development of Light Induced Shape Memory Microparticles for Biomedical Applications. *Biomedical Engineering Society Annual Meeting*, 2015.

Chapter 10:

- Airan RD*, **Meyer RA***, Ellens NK, Rhodes KR, Ren Q, Deng C, Farahani K, Pomper MG, Kadam SD, Green JJ. Focused ultrasound mediated drug delivery from polymeric perfluorocarbon nanoemulsions for noninvasive neuromodulation, *Nano Letters*, 17(2), 2017, 652-659.
- **Meyer RA**, Airan RD, Ellens NK, Farahani K, Pomper MG, Kadam SD, Green JJ. Focused Ultrasound Mediated Drug Delivery from Polymeric Perfluorocarbon Nanoemulsions for Noninvasive Neuromodulation. *Biomedical Engineering Society*, 2016.

Chapter 11:

- **Meyer RA**, and Green JJ. Biodegradable Polymer Iron Oxide Nanocomposites: The Future of Biocompatible Magnetism. *Nanomedicine* 10(23), 2015, 3421-3425.
- **Meyer RA***, Sunshine JC*,* and Green JJ. Biomimetic Particles as Therapeutics. *Trends in Biotechnology* 33(9), 2015, 514-524.

* = Authors contributed equally

Chapter 2: State of the Art

2.1 Overview of the Impact of Shape in Particle Design

2.1.1 Introduction

Polymeric nanoparticles are finding increasing success in nanomedicine applications as both therapeutics and diagnostics. Due to their biocompatibility, their capability to circumvent normal biological barriers to small molecules, and their targeting abilities, polymeric nanoparticles have been shown effective in numerous functions. These applications include most prominently drug delivery vehicles for various types of chemical and biological therapeutics¹⁻⁴ and contrast agents for diagnostic and imaging purposes.⁵⁻⁷ A wide range of fabrication methods exist for polymeric nanoparticles including bulk emulsions,⁸ microfluidics,⁹ and self-assembly.¹⁰ These methods have been successful at synthesizing spherical nanoparticles with advantageous properties including biodegradability, drug release, biological targeting, and evasion of *in vivo* elimination.

One property of nanoparticles that has been investigated extensively in the literature for controlling biological interactions is particle size.¹¹⁻¹³ Nanodimensional polymeric constructs have been synthesized across the full range of 1-1000 nm depending on their desired application. Although particle size has been shown to have a significant

This chapter contains material modified from the following articles previously published as: Meyer RA and Green JG. Shaping the Future of Nanomedicine: Anisotropy in Polymeric Nanoparticle Design. *WIREs: Nanomed. Nanobiotechnol.*, 8(2), 2016, 191-207. Ben-Akiva E, Meyer RA, Wilson DR, and Green JJ. Surface engineering for lymphocyte programming. *Adv. Drug Deliver. Rev.* 114(2017), 2017, 102-115. Meyer RA and Green JJ. Artificial Antigen Presenting Cells: Biomimetic Strategies for Directing the Immune Response. *Biomaterials in Regenerative Medicine and the Immune System*. Springer International Publishing, 2015, 257-277. Meyer RA, Sunshine JC, and Green JJ. Biomimetic Particles as Therapeutics. *Trend. Biotechnol.* 33(9), 2015, 514-524.

effect on properties such as biodistribution and cellular uptake of polymeric nanomedicines, it is not the only parameter that should be considered in the design of a nanotherapeutic or nanodiagnostics. Interest in nanoparticle shape has emerged in the past several years as a novel strategy to control the interface between particles and biological systems and to enhance efficacy of polymeric nanomedicines.¹⁴ Anisotropy and shape specificity in biological interactions have been shown to be a critical parameters at the molecular,¹⁵ cellular,¹⁶ and tissue levels.¹⁷ As such, to enable superior biological interaction between a nanoparticle and its target, the shape of the nanoparticle should be rationally engineered for its biological function. In this review, shape has been considered in a variety of settings including nanoparticle drug delivery, targeting, cellular uptake, biodistribution, immunoengineering, and tissue engineering.

This section describes the state-of-the-art of polymeric anisotropic nanoparticles and summarizes the main fabrication methods and applications of anisotropic nanoparticles in the literature over the past decade. The primary focus of this section is on polymeric nanoparticles and on engineered nanoscale features. While larger, micron scale polymeric particles and inorganic nanoparticles are also of interest, they are beyond the scope of this chapter and a reader is referred to other manuscripts^{18,19} that discuss these circumstances. Future research into the fabrication and application of anisotropic polymeric nanoparticles will provide insight into the benefits of their utilization and optimize their use in nanomedicine.

2.1.2 Fabrication of Anisotropic Nanoparticles and Nanofeatures

Top-Down Methods

Top-down assembly methods are widely applicable and controllable for the fabrication of nanostructures including nonspherical anisotropic particles. Through macroscopic manipulation to environments containing preformed nanoscale objects, a wide variety of particle shapes and morphologies can be produced. The main top-down fabrication methods utilized for the fabrication of anisotropic nanoparticles and creation of nanofeatures include mechanical deformation by thin film stretching, particle replication in non-wetting templates, and micro/nanoscale lithography.

A widely applied method to generate particles of non-spherical shape is the thin film stretching method pioneered by Ho et. al.²⁰ The method consists of synthesizing spherical polymeric nanoparticles and casting them into a thin film of polyvinyl alcohol. The film is then heated above the glass transition temperature of the polymer so that the particles can be easily deformed and the thin film is stretched utilizing a single dimensional mechanical tension application device. Upon cooling, the resulting particles are ellipsoidal in shape and have been demonstrated to have an aspect ratio of 2-5.²⁰ Alternatively, rather than increasing temperature, a solvent can also be used to enable particle deformation within a film. In recent years, this method has been adapted and further developed to produce polymeric micro- and nanoparticles consisting of a wide repertoire of shapes. By translating the method to two dimensions and modifying particle deformation procedures, Champion et. al. demonstrated the capability to generate many different shapes including rods, discs, worms, bullets, barrels, as well as porous morphological variants of these shapes (**Figure 2.1**).²¹

Particles fabricated by thin film stretching method have also been of recent interest for their shape memory properties. Yoo et. al. published a study investigating the

effect of various environmental stimuli on the shape retraction of ellipsoidal PLGA particles,²² rendered anisotropic by the thin film stretching method. The authors demonstrated complete reversion to a spherical form in the presence of liquefying factors including increased temperature, decreased pH, and chemical treatment. In addition, upon incubating shape-switching opsonized microparticles with macrophages, the authors demonstrated that the particle resisted uptake until it assumed a spherical form.²²

Wischke et. al. examined the capability of copolymers composed of polycaprolactone (PCL) and poly(pentadecalactone) (PPDL) to undergo shape programming and reversion.²³ Utilizing the stretching method and taking advantage of the fact that the polymers possessed a “permanent reprogramming” melting temperature and a “temporary reprogramming” melting temperature, the authors were able to induce shape change from oblate ellipsoid to prolate ellipsoid as well as reversion of the ellipsoids to the spherical form (**Figure 2.2**).²³

Another method utilized for the production of nonspherical nanoparticles is the particle replication in non-wetting templates (PRINT) technique. Pioneered by Rolland et. al. this method allows for excellent top-down control over particle morphology.²⁴ The method consists of first synthesizing a silicon mold with nanoscale features by e-beam lithography. From this fabricated template, a photocurable non wetting polymer perfluoropolyether (PFPE) is deposited and solidified to form the mold. The non-wetting nature of the polymer allows for individual, discrete particles to be molded as opposed to a film smear. The authors demonstrated wide versatility of this method through the synthesis of poly (lactic acid), poly(pyrole), and poly(ethylene glycol) (PEG) particles of various shapes including cones, rods, and arrows.²⁴ The method was combined with

mechanical elongation of the PFPE mold to produce rods with a higher aspect ratio as well as disc shaped particles.²⁵ In addition, this procedure has been recently combined with layer by layer spray-on technology to generate biologically active nanoparticles.²⁶

An additional technique that has been investigated extensively in the literature for the fabrication of anisotropic nanoparticles and nanostructures is particle lithography.

Through the use of particle-surface interactions, various methods have been developed to add nanoscale features anisotropically onto micron scale particles. Contact printing has been utilized to induce Janus-like “two faced” anisotropy in micron sized latex particles.²⁷ Micron scale particle lithography has been utilized to add nanoscale anisotropic features to chemically modified polystyrene particles. By immobilizing the particles on a charged glass surface, the authors were able to block the functionalization of a nanoscale region on the surface of the particle. Upon release from the surface, the previously blocked nanoscale region could be further modified.²⁸ Nanoscale patches of gold have also been deposited on tightly packed lattices of microparticles.²⁹ The morphology of these particles is controlled through the crystal structure of the multilayer particle lattices.

In addition to particle lithography, nanoimprint lithography has recently been appropriated for the fabrication of anisotropic polymeric nanoparticles. Direct fabrication of nanorods has also been reported through a procedure in which a nanoetched silicon is utilized as a template to mold a photoresist in order to produce rod shaped particles less than a micron in size.³⁰ This procedure could theoretically be translated to any photocurable polymer and aspect ratio can be regulated by the depth of silicon etching. Nanoimprint lithography has also been applied to synthesize anisotropic

particles made of a crosslinked peptide that can be utilized to encapsulate antibodies and nucleic acids.³¹ The authors demonstrated that these particles could be degraded and release their cargo through the addition of a protease. Thus, there are multiple approaches to successful top-down fabrication of nanoparticles designed to have various anisotropic shapes.

Bottom-Up Methods

Nonspherical nanoparticles have also been synthesized from a variety of directed self-assembly methods. Generally these procedures are more experimental in nature and have not found widespread application due to the difficulty of controlling self-assembly. However, the simplicity of these bottom-up approaches makes them attractive for the synthesis of anisotropic nanoparticles. These methods include block co-polymer aggregation, phase separation by polymerization, and particle core destabilization.

Block copolymers offer the capability to design particle shape at the molecular level. By varying the length and composition of the individual blocks in a block copolymer, anisotropic nonspherical particles can be synthesized by self-assembly. One example of the use of block copolymers in non-spherical particle synthesis was a study published by Jiang et.al. which demonstrated the self-assembly of PEG and polyphosphoaramidate (PPA) block copolymers into long string like micelles in the presence of DNA plasmids.³² The resultant nanoparticles demonstrated an enhanced stability in aqueous media as well as reduced toxicity for *in vivo* applications. Other approaches have yielded better control over the rod-like shape of the particles. Petzetakis et. al. demonstrated the use of enantiomerically pure poly lactide (as opposed to the mixture of D and L enantiomers which is commonly used) in a block copolymer with

polyacrylic acid resulted in the formation of self-assembled cylindrical micelles.³³ The aspect ratio was shown to be a function of the time of self-assembly. Stripped non-spherical particles have been synthesized by block copolymers of polystyrene and poly(2-vinylpyridine) (P2VP) along with a surfactant gold nanoparticle.³⁴ The block copolymer forms an alternating layer structure and this was exploited to produce ellipsoidal particles with stripes by utilizing gold nanoparticles that neutralized the preferential interaction of the polystyrene with the emulsion interface (**Figure 2.3**).

Phase separation emulsions offer the potential to synthesize Janus particles as well as non-spherical anisotropic polymeric particles. Kaewsaneha et. al. demonstrated the production of polymeric nanoparticles with a single magnetic face.³⁵ Starting with an emulsion of styrene, acrylic acid, and oleic acid coated magnetic nanoparticles, the polymerization of the two organics resulted in a polymer matrix that excluded the magnetic nanoparticles, resulting in the uneven distribution on the surface. Emulsions of liquid crystal materials with a polymerizable monomer have enabled the synthesis of non-spherical microparticles with nanocolloids at their poles.³⁶ By taking advantage of the positional preference for surface defects in the liquid crystal, the authors demonstrated a polar arrangement of polystyrene nanoparticles on the surface of the microparticle. In addition, upon removal of the liquid crystal, the polymerized material assumed a non-spherical shape due to the deswelling of the polymer matrix.³⁶ Anisotropic bulging nanoparticles have been reported utilizing the polymerizable nature of surface styrene monomers. Park et. al. demonstrated the formation of dumbbell shaped particles through the initiation of styrene surface polymerization with a core-shell polystyrene/poly(styrene-co-trimethoxysilylpropylacrylate) particle.³⁷ Multibulge

anisotropic particles have also been synthesized with seed particles of poly (vinyl chloride-co-acetoacetoxyethyl methacrylate).³⁸ Induced polymerization of surface adsorbed polystyrene resulted in a bulging morphology of these particles that could be controlled by increasing the concentration of the acetoacetoxyethyl monomer in the seed particle.

Block copolymer nanoparticles have also been investigated for a shape memory effect. Yang et. al. studied the capability of the copolymer poly(9,9dioctylfluorene-co-benzothiadiazole) to achieve a native ellipsoidal shape after bulk synthesis by emulsion.³⁹ Upon heating this liquid crystalline polymer above its nematic transition temperature, it attained a temporary spherical shape. Reversion to ellipsoidal shape was evident upon cooling as well. The stripped ellipsoidal nanoparticles described above³⁴ have also been utilized for a shape memory application. By crosslinking the P2VP layer the authors demonstrated a pH dependent, reversible swelling and deswelling property of the polymer matrix to produce ellipsoidal shapes with different aspect ratios.⁴⁰

Particle core destabilization also offers the bottom-up capability to produce anisotropically shaped particles. By either starting with a hollow core template, or chemically destabilizing the core of a core shell particle, various shapes have been produced. In the case of a hollow particle precursor, liquefaction alone has also been shown to produce particles of red blood cell (RBC) shape. Doshi et. al. demonstrated how hollow polystyrene particles could be heated, thereby inducing a collapse of the particle into an RBC shape.⁴¹ In the same study, RBC shaped particles were shown to be produced from poly (lactic-co- glycolic) acid through solvent based liquefaction. Chemical destabilization of spherical core polystyrene particles has also been shown to

produce rod shaped nanoparticles of bovine serum albumin (BSA) and poly L lysine (PLL).⁴² Zhou et. al. demonstrated that coating a spherical polystyrene template with BSA and PLL followed by solvent based extraction of the polystyrene core resulted in the fracturing of the surface layer and the production rod shaped nanoparticles.⁴²

Microfluidic Methods

Microfluidics technology has revolutionized many fields of research including particle synthesis. Although the majority of microfluidic particle synthesis has been completed on the micron scale (to which the reader is referred to a more comprehensive review⁴³⁻⁴⁵), there has been some research on the synthesis of nanoparticles and nanoscale features utilizing microfluidics technology. The predominant methods that have emerged for the synthesis of nanoscale particles on a microfluidic chip include electrojetting and nanoprecipitation.

Electrojetting has been utilized in a variety of applications and has been used with microfluidics technology to produce Janus particles. Roh et. al. demonstrated the synthesis of biphasic particles that have Janus surface characteristics.⁴⁶ By electrojetting two different solutions adjacent to each other, nanoparticles and microparticles made of dextran were formed with nanoscale features. In addition, this method was utilized with poly acrylic acid to generate nonspherical Janus nanoparticles.⁴⁶ This method was extended to produce micron scale Janus particles encapsulating nanoscale superparamagnetic particles and titanium dioxide particles for imaging.^{47,48} The authors demonstrate localized distribution of these nanoparticles within the larger nano and micron scale structures.

Nanoprecipitation in a microfluidic device has been recently investigated for its capability of fabrication of nonspherical nanoparticles as well as anisotropic micron sized structures with nanoparticulate features. Hasani Sadrabadi et. al. demonstrated direct fabrication of anisotropic polybenzimidazole (PBI) nanoparticles by focused hydrodynamic flow of a solution containing the polymer.⁴⁹ As the solvent exchange took place at the flow interface, nanoparticles precipitated out of the focused flow (**Figure 2.4**). The anisotropy of the particles was controlled by changing the ratio of the inlet focusing flow.⁴⁹ Lan et. al. utilized a similar hydrodynamic focusing scheme to synthesize microparticles with an anisotropic coating of nanoparticles by the use of coinjection of a photocurable phase and a nonphotocurable phase.⁴⁸ By dispersing nanoparticles in the nonphotocurable phase a single face of spherical nanoparticles was formed on the surface.⁴⁸ Another method developed by Suh et. al. demonstrated the capability to induce growth of magnetic nanoparticles on the surface of anisotropically fabricated microparticles synthesized by a stop flow photolithography process.⁵⁰ The shape of the particles could be directed by a photomask and the Janus nature was achieved by a side by side laminar flow of two polymer solutions. Polyethylene glycol (PEG) and poly (acrylic acid) (PAA) were utilized for these studies and the authors demonstrated subsequent growth of magnetic nanoparticles directed by the anionic nature of the PAA.⁵⁰ Nanoprecipitation of particles into micro scale molds has also been utilized for production of anisotropic microstructures. Angly et. al. demonstrated the capability to form densely packed nonspherical arrays of nanoparticles through a selective permeable microfluidic chamber.⁵¹ Water droplets containing PEG and silicon

dioxide coated gold nanoparticles were assembled into lithographically specified superstructures by evaporation of the water phase through convection of dry gas.

2.1.3 Characterization of Anisotropic Nanoparticles

Nonspherical anisotropic microparticles and nanoparticles are routinely characterized by microscopy methods including scanning electron microscopy (SEM), transmission electron microscopy (TEM), atomic force microscopy (AFM), and optical microscopy. Although these procedures work suitably for a thorough characterization of anisotropic nature of these constructs, they typically require substantial preparation and expensive microscopes. As a result there is active research in developing alternative methods of characterizing non-spherical nanoparticles.

Mathaes et. al. made a comparison of different standard methods utilized in particle and cell characterization to detect differences between spherical and non-spherical microparticles and nanoparticles.⁵² These protocols included flow cytometry/coulter counter for microparticles and asymmetrical flow field flow fraction for nanoparticles. The authors were able to detect differences between the spherical and nonspherical of aspect ratio 3-5 microparticles and aspect ratio 4 nanoparticles that were 40 nm in size in each of the assays. In addition, they were able to record characteristic data that could be used to predict the shape of an unknown sample of particles.⁵²

Innovative light scattering methods have also been developed for the characterization of non-spherical nano and microparticles. Wang et. al. utilized predictive dipole modeling of holograms projected by particles scattering a laser beam.⁵³ The resulting approximation method was able to characterize 3D diffusion and rotation of non-spherical microparticles of aspect ratio 2 and size 2 microns. In addition, this

method was utilized to characterize the content and anisotropy of spherical Janus nanoparticles of size 900 nm.⁵³ Methods based on light scattering of gold nanorods at different wavelengths of light⁵⁴ and light scattering detecting differences of electrophoretic mobility of nanorods vs nanospheres⁵⁵ have also been reported.

2.1.4 Biomedical Applications of Anisotropic Nanoparticles

Shape Specific Targeting

Among the most useful properties that have been demonstrated for nonspherical nanoparticles are the inhibition of non-specific cellular uptake leading to enhanced *in vivo* biodistribution⁵⁶ and the increased targeting capabilities due to the higher radius of curvature.¹⁴ These two properties have been investigated extensively in recent years and have been characterized in a wide variety of systems. These characteristics of anisotropic nanoparticles make the technology an attractive platform for biomedical applications (see **Table 2.1**).

Inhibition of non-specific cellular uptake is an important attribute for *in vivo* therapeutics as the reticuloendothelial (RES) system's clearance of nanoparticles prevent the majority of the administered dose from reaching its target. Sharma et. al. investigated the capability of non-spherical micro and nanoparticles to resist cellular uptake by macrophages, the primary cells responsible for RES clearance.⁵⁷ By utilizing confocal microscopy image analysis, their results demonstrated that prolate ellipsoids (AR 2) attached to the cells more efficiently than oblate ellipsoids (AR 2) which in turn attached more efficiently than spheres. However, uptake of prolate ellipsoids was inhibited 50% compared to spheres whereas uptake of oblate ellipsoids was enhanced nearly 300% compared to spheres.⁵⁷ Similar trends were demonstrated with mesenchymal stem cells

(MSCs) and HeLa cells.⁵⁸ It was shown that not only particle shape, but also the aspect ratio of the ellipsoidal particle had an impact on cellular uptake as a particle with an aspect ratio of 4 was internalized at a rate nearly 3-fold higher than an ellipsoid with an aspect ratio of 2.⁵⁸ Orientation of the particle once it is attached to the cell membrane appears to play a role in phagocytosis. Champion et. al. demonstrated that prolate and oblate microellipsoids that attached to cells on their long axis were not phagocytosed as readily as ellipsoidal particles attached on their short axis.⁵⁹ The orientation was shown to be important for “UFO” shaped particles as particles approaching at a 45° angle were not internalized at all compared to particles approaching at 0° and 90° angles.⁵⁹ The work was translated to a theoretical model of shape dependent uptake presented by Dasgupta et. al.⁶⁰ Computation results based on the minimization of free energy of binding and membrane deformation indicated that nanoellipsoids attach on their long axis. The particles must then undergo a transition to attachment on the short axis in order to be internalized completely by a cell.⁶⁰ Particle internalization pathways have also been investigated for anisotropic particles. It has been shown that smaller (150-200 nm) anisotropic cylindrical nanoparticles are taken up by clathrin-mediated endocytosis and caveolae-mediated endocytosis.⁶¹ The importance of which uptake pathway nanoparticles take has been investigated⁶² and can directly impact the efficacy of intracellular therapeutics. Surface density of 5 kDa PEG (PEG_{5K}) has also been shown to be an important factor in the macrophage uptake and cellular biodistribution of anisotropic 320 nm nanoparticle therapeutics.⁶³ Reduced PEGylation surface density (0.028 PEG_{5K}/nm²) resulted in higher macrophage uptake, lower *in vivo* circulation time,

and higher accumulation in the liver compared to higher surface density of PEG_{5K} (0.083 PEG_{5K}/nm²).⁶³

In addition to the altered cellular uptake patterns exhibited by anisotropic particles, shape appears to confer increased specific uptake mediated by stronger avidity of surface bound targeting ligands. Antibody targeting efficacy and specificity was directly demonstrated *in vitro* by Barua et. al.⁶⁴ The authors utilized Trastuzumab (an antibody specific for the human epidermal growth factor receptor HER2) and cell lines that were HER2 + and HER2-. Cell uptake was shown to be increased 1.5-3 fold for nanodimensional prolate and 1.5-2.5 fold for oblate ellipsoids compared to spheres for only the HER2+ cell lines.⁶⁴ Circular disk particles have also been shown to have greater targeted adhesion efficiency than rod-like disk particles under various flow shear rates.⁶⁵ Substantial investigation has also been conducted into the role of size and shape for *in vivo* targeting as well. Muro et. al. demonstrated anti ICAM-1 surface bound discs had 30 fold higher targeting specificity for endothelial cells and longer circulation time than spheres.⁶⁶ However, the spheres were taken up by targeted cells more readily than the discs. Prolate ellipsoids have also been shown to have targeting enhancement over spherical particles. Kolhar et. al. investigated the *in vitro* and *in vivo* accumulation of targeted rods vs. spheres.⁶⁷ The authors found that under flow *in vitro* there was about a 2-fold increase in specific adhesion of rods compared to spheres under shear rates ranging from 15 s⁻¹ to 250 s⁻¹. Similarly there was close to a 2 fold decrease non-specific adhesion of rods compared to spheres at lower shear rates (15 s⁻¹). *In vivo* experiments demonstrated that rods had greater accumulation in the organs they were targeted to compared to spheres. For lung targeted rods, there was a 2 fold increase in accumulation

of rods vs. spheres. For brain targeted rods there was a 7.5 fold increase in the accumulation of rods compared to spheres (**Figure 2.5**).⁶⁷

Drug Delivery

With the added benefits of reduced non-specific cell uptake, longer circulation time *in vivo* and higher specific targeting, anisotropic non-spherical particles have been utilized for a wide variety of applications. One of the most prominent uses for non-spherical nanoparticles in recent years has been for delivery of small molecule drugs such as chemotherapeutics and genetic material such as siRNA. Many of the fabrication methods presented in this review have been extended to produce non-spherical nanoparticles with unique properties that are tailored for specific drug delivery applications.

The PRINT technology has been utilized in multiple applications for non-spherical particle drug delivery. Hasan et. al. demonstrated a novel approach to the delivery of short interfering RNA (siRNA) for gene knockdown.⁶⁸ The authors utilized a modified emulsion technique to encapsulate siRNA in PLGA and then induced biomimicry in their nanoparticle production through the addition of a cationic lipid coat. Although there was no comparison to a spherical particle, the authors demonstrated comparable efficacy to Lipofectamine 2000 for gene delivery to a variety of cell lines. In addition, there was a 60-80% knockdown of KIF11 in prostate cancer cells by the cylindrical particles.⁶⁸ A similar study was published by Xu et. al. utilizing lipid coated PRINT BSA particles with a bio-reducible cross-linker for RNA replicon delivery for vaccination purposes.⁶⁹ There was a 2 fold increase in transfection efficacy observed by the formulated particles compared to the commercially available TransIT reagent. The

authors were also able to demonstrate the utility of this platform as a genetic vaccine through the enhanced delivery of RNA encoding the influenza hemagglutinin gene.⁶⁹

PRINT based PLGA particles have also been utilized in chemotherapeutic applications as well. Chu et. al. demonstrated the favorable pharmacokinetics of a non-spherical PLGA particle loaded with Docetaxel.⁷⁰ There was greater tumor accumulation over the initial time points and lower clearance by spleen and liver of the non-spherical particles compared to the spherical particles. The same group also synthesized PRINT PLGA non-spherical particles with acid sensitive prodrug of Docetaxel to enable higher dosing and antitumor therapeutic effect.⁷¹ The prodrug encapsulated in the particle was shown to be able to be delivered at higher effective doses in the particle to mediate significant antitumor effects in a subcutaneous cancer model, without excess toxicity. The enhanced pharmacokinetic profiles of the non-spherical particle enabled them to remain just as effective as the free chemotherapeutic drug even though they had reduced toxicity.⁷¹

Another class of PRINT based particles utilized in drug delivery carriers have been in RBC mimicking particles for oxygen transport.^{72,73} Although these particles are micron in size (due to the desire to achieve complete biomimicry of the RBC), the studies resulted in important implications for the design of nanoparticle therapeutics to achieve the same goal of oxygen transport. RBC mimicking hydrogels were utilized to conjugate hemoglobin internally without the loss of protein activity.⁷² Also, due to a low elastic modulus, the particles could be sheared at physiologically relevant rates without loss of structures. In addition to the proof of principle, these hydrogel microparticles were utilized to investigate the role of particle modulus in the administration and clearance of

therapeutics.⁷³ By controlling the modulus of the hydrogel microparticles, the authors demonstrated that these therapeutics could avoid entrapment in the lung and elimination in the spleen and liver. Decreasing the modulus by 8 fold also led to a 30 fold increase in circulation time of the particles. Further investigations into how the role of modulus plays into the biodistribution of analogous nanoparticles would be of great interest.

Self-assembled nonspherical particles by block copolymer micelle aggregation have also been utilized for drug delivery applications. As described above, Jiang et. al. pioneered a method to form condensed plasmid-PEG-PPA micelles that demonstrated an enhanced stability for *in vivo* applications.³² A follow up study illustrated that the condensation shape could be controlled by the polarity of the solvent with increasing hydrophobicity corresponding to increased sphericity of the particles.⁷⁴ This study was particularly interesting because the authors were able to achieve enhanced *in vivo* luciferase transfection of hepatic cells by intrabiliary administration of the worm-like nanoparticles compared to the spherical nanoparticles. The worm-like particle was immensely superior to the spherical particle, mediating a 10000 fold increase in luciferase expression of hepatic cells.⁷⁴ Block copolymer nanoparticles of various shapes and sizes have also been successfully applied to drug delivery of chemotherapeutics. Karagoz et. al. demonstrated the capability of rod-like and worm-like micelles of copolymers containing styrene, vinyl benzaldehyde, and oligo (ethylene glycol) methacrylate to encapsulate doxorubicin via conjugation to aldehyde groups in the polymer.⁷⁵ The resulting worm-like and rod-like micelles exhibited greater capability to be taken up by target cells and thus an enhanced ability to deliver the payload of doxorubicin to mediate cellular toxicity. Geng et. al. also published promising results in

the synthesis of filamentous micelles consisting of block copolymers containing PEG-polyethylethylene and PEG-polycaprolactone.⁷⁶ Particles bearing shapes with 4 fold higher length were shown to circulate *in vivo* for 2-3 days longer than micelles with a shorter length and also mediated higher tumor apoptosis than their shorter counterparts.⁷⁶

2.1.5 Conclusions

Non-spherical polymeric nanoparticles hold promise for various biomedical applications. Although shape has been traditionally neglected with respect to polymeric nanoparticle design, in recent years it has come to light as an important parameter. With the advent of many new fabrication methods based on top-down, bottom-up, and microfluidic technologies, our understanding of how to control the shape and anisotropy of polymeric nanoparticles is continuing to expand.

Top-down technologies allow readily translatable methods for applications in the biomedical sciences due to their reliable production of uniformly anisotropic nanoparticles. These methods include thin film stretching of spherical particles, PRINT based lithography, particle lithography, and nanoimprint lithography. Among these methods, the thin film stretching protocol is the easiest and most approachable protocol to produce particles bearing anisotropic shape. Many of the current biomedical applications of anisotropic particles utilize fabrication methods based on the thin film stretching method. However, particles produced by the thin film stretching protocol are limited to prolate/oblate ellipsoidal shape and derivatives thereof. Lithography based techniques such as PRINT and nanoimprint lithography can circumvent this shape limitation, however they are more difficult to implement in practice. As efforts progress to identify

the optimal shaped particle for each biomedical scenario, each of these methods can be utilized for the translatable production of anisotropic particles.

Bottom-up and microfluidic technologies offer the promise of simple platforms to rapidly synthesize large batches of anisotropic nanoparticles. Key methods in this category of fabrication include phase separation emulsion, block copolymer micelle formation, and microfluidic nanoprecipitation. Phase separation emulsion is an approachable method to generate anisotropy on spherical polymeric nanoparticles, however this technology has not been well established for biomedical applications. Block copolymer micelle formation has been utilized to produce particles of different shapes encapsulating various therapeutics and has already shown promise for translation. However, it can be difficult to control the micelle formation as evidenced by the limited repertoire of shapes that can be produced with this method. Microfluidic nanoprecipitation shares similar advantages and disadvantages as block copolymer micelle formation, except translation of anisotropic polymeric nanoparticle produced on microfluidic device to biomedical applications is more limited. Further experimentation into the control of anisotropy in particles fabricated by the bottom up method will be of great interest in the coming years.

Given the existence of these well-established methods for synthesizing non-spherical, anisotropic nanoparticles, there are many applications in fields such as drug delivery, immunoengineering, and tissue engineering, which can benefit immensely from consideration of shape in the design of nanotherapeutics. Due to the increased *in vivo* circulation time and targeted avidity/cell uptake, non-spherical nanoparticles are a versatile, robust platform for drug delivery such as intracellular delivery of genetic

therapeutics and chemotherapeutic drugs. In addition, the increased avidity for ligand targeted nanoparticles make them the ideal candidate for the application of nanomedicine to immunoengineering.

The distinct topological features of anisotropic polymeric nanoparticles can also be utilized in the synthesis of novel tissue engineering scaffolds to better mimic the ECM. Among the numerous applications of nanoparticles in medicine, tissue engineering has become a prominent venue for the utilization of nanofabricated materials.⁷⁷ Although the application of nanoparticles in tissue engineering and regenerative medicine has been numerous,⁷⁸ the impact of anisotropic nanostructures is just coming to be understood for the *ex vivo* induction of various tissues. Non-spherical nanostructures can be key to the development of tissues as nanotopography has been proven to be important for the accurate delivery of ECM cues to cells in the development of tissues.^{79,80} Non-polymeric, non-particulate anisotropic nanostructures such as carbon nanotubes,⁸¹ electrospun fibers,⁸² and hydroxyapatite nanoparticles⁸³ have demonstrated the importance of anisotropic nanotopographical features in tissue scaffold engineering and also highlight the potential impact polymeric particles can have in this discipline.

Although the breadth of applications is vast, we have only begun to understand the benefits that non-spherical and anisotropic nanoparticles can confer compared to traditional spherical particle. Continued investigation into the properties, fabrication methods, and interactions with biological systems will elucidate the true potential of the anisotropic polymeric nanoparticle and make an immense impact in nanomedicine research.

2.2 Overview of Artificial Antigen Presenting Cell Technology

2.2.1 Introduction

Immunotherapy can be broadly defined as modulation of the immune system to achieve a medicinal benefit. Several examples of modern immunotherapies include the use of cytokines for general immune activation in disease such as chronic granulomatous disorder⁸⁴ or the use of immunosuppressive drugs such as steroids in the treatment of autoimmune disorders.⁸⁵ As our understanding of the immune system continues to develop, so does our capability to intervene therapeutically. Over the past few decades there has been a significant increase in new immunotherapies developed to treat a variety of diseases. Among these is the manipulation of autologous antigen presenting cells to achieve a therapeutic effect. Although partly successful in some limited cases such as prostate cancer,⁸⁶ autologous antigen presenting cell-based therapy suffers from several drawbacks such as limited potency due to susceptibility to immune regulation and the high costs and labor involved with cellular therapy.⁸⁷ Therefore, there is an impetus to develop an alternative strategy to achieve the same desired goal of adaptive immune system modulation.

One promising technology is the artificial antigen presenting cell (aAPC) to serve as a biomimetic platform to modulate the adaptive immune system. Artificial antigen presenting cells are synthetic constructs that are designed to recapitulate the natural process of T-Cell activation by biological antigen presenting cells (APCs). Through the presentation of crucial APC signal proteins on a surface, aAPCs are capable of directing a T-Cell response very similar to the natural APC. aAPCs possess certain advantages over autologous biological APCs. Generally, an aAPC is based on a plastic particle that is much easier to produce and maintain, thus making the aAPC technology capable of being

an “off the shelf” therapy.⁸⁷ In addition, aAPCs are not derived from an immune cell progenitor and thus are resistant to the immune suppression that can inhibit the activity of natural APCs. aAPCs have also been proven to be equally or more effective than the autologous APC at immune system stimulation in certain scenarios. Taken together, these traits of the aAPC make it an attractive platform for immunotherapy with applications to treat various diseases such as cancer, infectious disease, and autoimmune disorders.

This section covers the relevant immunobiology as well as several criteria that should be considered in the design of aAPCs, including fully synthetic aAPCs as well as engineered biological cells that function as cellular aAPCs. In addition, the approaches that have been taken to develop the aAPC as well as the broad application of these constructs in various biomedical scenarios are reviewed. Continued development of aAPCs will greatly benefit medicine as an engineered synthetic strategy to control the power of the immune response.

2.2.2 The Natural APC

A strong understanding of the natural APC/T-Cell interaction is required in order to generate the most effective aAPC for antigen specific T-Cell modulation. The following summarizes the basic APC physiology as well as the important aspects of the APC/T-Cell interaction that should be considered in the design of this technology.

The Role of APC in Innate and Adaptive Immunity

Adaptive immune modulation interactions occur primarily through the professional antigen presenting cell. Nearly every cell in the body acts as an “antigen presenting cell” due to their ability to present MHC Class I restricted antigens on the

surface. In addition, B-Cells and cytotoxic T-Cells can present antigens through the MHC Class II surface protein in order to be activated further by helper T-Cells. Despite these capabilities to present antigens on the surface, generally these cell types are subject to effector functions of the immune system and do not heavily impact the course of an immune response. Professional aAPCs have the capabilities to strongly influence the immune system through the presentation of antigens restricted to MHC Class I and Class II as well as companion signals to either activate or suppress the T-Cell response. The two types of cells that have been identified as “professional APC” include dendritic cells and macrophages. Generally dendritic cells are considered the primary APC of the body with specific physiological adaptation for this function.⁸⁸ The dendritic cell will be used in subsequent explanation of APC activity.

APCs have a special function in immunity as the bridge between innate and adaptive immune systems. Immature dendritic cells generally reside in the periphery and continuously screen environmental antigens through rapid macropinocytosis. Although extracellular antigens are generally exclusively presented by MHC Class II molecules (to engage helper CD4+ T Cells), APCs can partake in cross-presentation of these antigens to present them on MHC Class I molecules (to interact with cytotoxic CD8+ T-Cells). DCs are activated into their mature, immunogenic form through encountering a danger signal. This can include pathogen associated molecular patterns (PAMPs), inflammatory cytokines, or previously activated T-Cells. Upon activation, the dendritic cell will halt rapid cellular uptake, upregulate antigen presenting MHC molecules, produce more costimulatory surface signals, and synthesize chemokine homing receptors for lymph node targeted chemotaxis. Upon entering the lymph nodes the dendritic cell will interact

with target T-Cells to activate them to carry out their effector functions.⁸⁹ Activation will also result in a positive feedback loop with macrophages and natural killer cells in the innate immune system through the production of cytokines IL-12 and IFN γ .⁹⁰ In the absence of the correct danger signal, dendritic cells have also been shown to promote tolerance through regulatory T-Cell induction.⁹¹

Signal 1, Signal 2, and Signal 3: APC Communication with a T-Cell

The most important aspect in the design of an aAPC is recapitulation of the signals that a natural APC relays to a T-Cell upon cell contact. These signals are in part mediated by cell surface receptor interactions as well as soluble cytokines. Together, three signals enable tight control of the nature of the immune response. (**Figure 2.6**)

Signal 1 is considered the “Recognition” signal. At the protein level, this signal occurs as the result of the interaction of the T-Cell Receptor (TCR) and the antigen loaded in the MHC complex. This signal is central to the specificity of the immune system as it establishes the identity of target antigen the T-Cell will seek in its subsequent effector function. In addition to the TCR (CD3) signal, the T-Cell differentiation marker (CD-4 for helper T-Cells and CD-8 for cytotoxic T-Cells) participates in the Signal 1 protein machinery. It has been proposed that these co-receptors help to concentrate the MHC protein to permit for continued signaling despite relatively low affinity of the MHC/TCR interaction.⁹²

Signal 2 can be described as the “Outcome” signal. While Signal 1 establishes the identity of the antigen in question, Signal 2 directs the nature of the T-Cell response to the APC/T-Cell binding event. For T-Cell activation, the classic stimulatory pathway is through CD28 on the T-Cell surface.⁹² In addition, 41BB and CD40 on the surface of

T-Cells have been shown to have an activation effect in the context of CD4⁺ T-Cells engaging a CD8⁺ T-Cell to further activate it.⁹³ Other important types of Signal 2 are the ones that induce anergy in target T-Cells. This is important for the establishment of peripheral tolerance for autologous antigens. Some of the proteins on the T-Cell that have been shown to be involved in this suppressive form of Signal 2 include the Fas receptor for apoptosis, CTLA-4 and PD-1 for inhibition of immune activation, as well as the absence of Signal 2 for induction of anergy.⁹⁴

Signal 3 provides additional direction for the T-Cell response and typically consists of soluble cytokines secreted by the APC during T-Cell engagement. Signal 3 has been shown to direct the character of the type of T-Cell response that is elicited upon activation. Generally this signal has been determined to be a product of polarization to one of two types of dendritic cell for the Th1 response or the Th2 response. One of the most well characterized cytokines involved in this process is IL-12 secreted by APCs upon engagement. This has been linked to the development of a Th1 type response, directed towards the elimination of intracellular pathogens. Recently, a fourth potential signal has also been characterized in dendritic cells.⁹⁵ DCs have been shown to induce upregulation of chemokine receptors in T-Cells by the use of Vitamin A and Vitamin D. IL-12 has also been shown to have an effect on the homing capabilities of T-Cells.⁹⁶

The APC/T-Cell Interface

Given the majority of the intercellular signaling that occurs between the APC and the T-Cell occurs at the APC/T-Cell interface, this is a critical factor that must be taken into account in the mimicry of the APC by the aAPC. Typically when a natural APC engages a T-Cell, it has been shown that there is a dynamic rearrangement of surface

proteins involved in immune signaling. The mature complex that forms has been termed the immunological synapse or IS. This synapse has been shown to have a distinct molecular composition with the TCR and the CD28 costimulatory molecule in an inner central supra-molecular activation cluster (cSMAC), integrin-based adhesion molecules such as LFA-3 concentrated outside the cSMAC in the peripheral supra-molecular activation cluster (pSMAC), and actin rich exterior zones termed distal supra-molecular activation clusters (dSMAC) (**Figure 2.7**). The role of the immune synapse in TCR signaling and subsequent acquisition of effector function is not completely understood, but it has been confirmed to play an important role. Although a concentric ring formation is the most well studied, it is not the only formation that the IS can assume.⁹⁷

T-Cell/APC IS formation is a highly specific process that occurs only in the event that the TCR and MHC bound antigen match with appropriate specificity. T-Cells are specialized for high throughput scanning of multiple antigen presenting cells to find a correct match. Such temporary interactions between the T-Cell and the APC are termed immune kinapses. In the event that a T-Cell finds its specific APC partner (as dictated by the time scale of the TCR and MHC-antigen interaction), an immunological synapse forms. Despite the fact that the TCR and costimulatory molecule CD28 are concentrated in the center of the IS, the signaling events are generally not localized to this region. Instead, the TCR and associated costimulatory signals form as microclusters (on the order of 100 nm in size) which quickly travel to the center of the IS propelled by actin polymerization. TCR signaling at this time is characterized by low affinity and rapid signaling events that are sustained as the cluster moves. The TCR signaling is strongest in the dSMAC and weakens as the cluster reaches the cSMAC. The ultimate fate of the

TCR once it reaches the cSMAC is unclear but depending on the antigen, it has been shown to continue signaling, or be eliminated from the surface membrane.⁹⁸

Another important consequence of the IS formation is the polarization of the T-Cell membrane for appropriate effector function. Upon IS formation, the T-Cell will translocate its secretory granules to the portion of the membrane that is engaged with the APC in a region of the cSMAC. For helper T-Cell effector functions, this allows for the localized delivery of stimulatory cytokines and signals to target cells such as B-Cells and other APCs. In the context of killer T-Cells, this relocation to the cSMAC can be very important as it allows for localized release of cytotoxic compounds that are prevented from escaping into the peripheral cell space by the “sealed” regions of the pSMAC. As such, a CD8⁺ cell can be highly selective in the target cell it destroys.⁹⁸

2.2.3 Design Considerations for the aAPC

Given the complex nature of the APC interaction with the T-Cell there are many parameters to consider in the fabrication of aAPCs. Many aAPC characteristics have been engineered and have led to insight into effective biomimicry conditions. These parameters include size and shape of the aAPC, surface proteins for relaying the critical Signal 1 and Signal 2, protein release to mimic Signal 3, and recreation of the IS through the use of a fluidic membrane. (**Figure 2.8**)

Size and Shape of the APC

One of the most important parameters described in the literature for the design of an aAPC is size. Generally it has been considered that the optimal size for an aAPC is at the micron/cellular level. For aAPCs, it has been shown that size can have an important effect on aAPC efficacy.⁹⁹ For *in vitro* efficacy using a PLGA based aAPC, it has been

shown that micron scale aAPCs could induce a 3 fold increase in IL-2 production of CD8⁺ T-Cells for the same protein dose as nano scale aAPCs.¹⁰⁰ However, due to biodistribution considerations, micron sized aAPCs may not be the optimal choice for *in vivo* use. Recently it has been shown that nanodimensional aAPCs can induce nearly a 10 fold increase in IFN γ production upon *in vivo* immunization compared to micron scale aAPCs.¹⁰¹ This was linked to a favorable biodistribution of the nano scale aAPC, in that it demonstrated superior draining to the lymph nodes, the natural site of T-Cell/APC interaction. Continued investigation into the impact of size will be important in the design of the optimal aAPC.

Another important biophysical parameter that has recently come to light in the design of the aAPC is shape. As was described previously, the surface area of contact between the T-Cell and the APC is critical for proper stimulation. Rigid, spherical aAPCs allow for minimal surface area contact with the target T-Cell. However, rod-shaped aAPCs can increase the available area of contact between the aAPC and the T-Cell through the increased radius of curvature of the long axis. This was shown to have a very powerful effect on the activation of CD8⁺ lymphocytes. Spherical and ellipsoidal aAPCs, with the same volume and the same protein on their surfaces, were compared for their capability to induce antigen specific proliferation and the ellipsoidal aAPCs were shown to increase the expansion of CD8⁺ T-Cells by up to 20 fold.¹⁰² In addition, live cell confocal imaging revealed a higher prevalence of aAPC conjugates as well as a preference for the long axis of the aAPC in conjugation. An *in vivo* effect was also seen with the ellipsoidal aAPC mediating stronger tumor immunity compared to the spherical

aAPC.¹⁰² Although traditionally neglected in terms of aAPC design, shape is another important design consideration in the fabrication of aAPCs.

Proteins for Antigen Presentation and Costimulation: Signal 1 and Signal 2

The choice of surface protein and the density at which it is presented have also been shown to be important for aAPC function. For Signal 1, there have been two predominantly used strategies to trigger the T-Cell receptor. The first is the use of an anti-CD3 antibody as a direct trigger for the TCR (CD3). Although this is a simple way to deliver Signal 1 and is used ubiquitously throughout the research community for the study of T-Cell biology, it lacks the antigen specificity that a natural APC possesses. Therefore, this strategy can be used to trigger T-Cells *in vitro*, but *in vivo* there would be the complication of antigen specificity. The second, and more popular for disease based applications of aAPCs, is the direct use of a MHC class I (for CD8+ T-Cells) or MHC class II (for CD4+ cells) loaded with the cognate antigen. Although slightly more complicated than the use of a monoclonal antibody, the added benefit of antigen specificity is absolutely necessary for the use of aAPCs in therapeutic applications.⁸⁷

Recreation of the second signal delivered upon APC engagement is generally accomplished by the use of a monoclonal antibody to directly trigger a costimulatory molecule on the surface of the T-Cell. The most popular targets for Signal 2 are CD28 and 41BB. Although classic aAPCs have focused on the use of anti CD28, 41BB has been shown to effectively stimulate lymphocytes.¹⁰³ More recent advances in aAPC technology have shown that a blend of these two signal protein may be optimal in the design of an aAPC. A 25:75 blend of CD28 and 41BB induced a 3-5 fold greater

expansion of CD8⁺ cells than anti-CD28 or anti-41BB alone.¹⁰⁴ In addition, it was demonstrated that these cells had a strong effector and memory function *in vitro*.

Surface density of the aAPC proteins is another parameter to be considered in the design of an effective aAPC. Recent advances in nanofabrication have allowed for nanometer scale control over surface density and orientation of stimulatory proteins. Utilizing anti-CD3 as a Signal 1, Matic et. al. demonstrated that 1000 proteins/ μm^2 spacing of anti-CD3 proteins was optimal at triggering T-Cell activation as evidenced by increased production of IL-2 and enhanced rates of proliferation (upon the addition of anti-CD28 as a costimulatory signal) compared to 120 and 60 proteins/ μm^2 .¹⁰⁵

Soluble Cytokines and Recreation of Signal 3

Although not critical for aAPC function, the capability to deliver a third signal through soluble cytokines has been of interest in the design of APCs. The strategy to achieve this in biological APCs has been to transfect the cell with a gene to produce a soluble cytokine. Although this is an interesting possibility in the design of engineered biological APCs, it can be difficult to control the amount of the soluble cytokine that is released. Currently, the technology has been limited to use in studying the biology of certain cytokines released during the APC/T-Cell engagement including IL-21 which has been shown to have opposing effects of activation and suppression.¹⁰⁶ The engineering of a third signal into aAPCs can be accomplished through the use of a controlled release system as the core particle. In this manner, the core of the particle can be designed to optimize Signal 3, whereas the particle surface is designed to optimize Signal 1 and Signal 2. Controlled release from the core can be accomplished through the use of a biodegradable polymer such as PLGA. The advantage of the use of Signal 3 in a

biodegradable acellular system is that the rate of delivery can be controlled based on the type of biomaterial. Currently, there has been limited use of a third signal in the design of an acellular aAPC. Steenblock et. al. demonstrated the feasibility of this approach by encapsulation and controlled release of IL-2 in a PLGA-based aAPC.¹⁰⁷ It was shown that there was a 3-4 fold increase in the expansion of T-Cells upon stimulation of encapsulated IL-2 as opposed to exogenous IL-2 due to local concentration release effects. This approach has the potential to lead to much higher local concentrations of soluble cytokines at a T-cell surface than the concentrations that can be achieved through systemic *in vivo* administration.¹⁰⁷

2.2.4 Cellular aAPCs

While the focus of this section is on acellular antigen presenting cells, such as those fabricated from beads or particles, engineered biological cells, or cellular artificial antigen presenting cells, have also been constructed. Cellular aAPCs derived from the genetic modification of existing cell lines remain a popular choice for the modulation of T-Cell activity for therapeutic purposes. (**Table 2.2**) Although cell-based therapies are immensely expensive compared to acellular therapies, many of these cell based strategies have been entered into clinical trials for various diseases. The following is a summary of the key advances in the field of cellular based aAPCs.

K562 Cell Line

The most popular cell line utilized in the design of a cellular aAPC is the K562 human leukemia line.¹⁰⁸ This cell type is frequently used due to the absence of any endogenous MHC molecules on its surface, thus allowing for the expression of only of the chosen MHC for antigen specific cell therapy. In addition, this cell line does not

express any of the costimulatory molecules characteristic of a natural aAPC. This allows for greater control over the type of stimulatory protein that is delivered upon aAPC/T-Cell engagement. They also lack expression of inhibitory molecules that can be used by APCs to suppress the activity of T-Cells. In addition, these cells can easily be genetically modified and have a history of safe use in humans. Taken together, these advantages make the K562 cell line an attractive platform for cellular aAPC development.¹⁰⁸

Several different categories of the K562 cell line based APC have been developed based on the application and immune cell to be targeted. One type of K562 aAPC that has been developed was a cell line to activate CD4⁺ T-Cells. Through transduction of genes encoding the HLA-DR MHC Class II protein as well as the costimulatory signals for CD28, the authors were able to generate a stable aAPC cell line with expression of all desired proteins on the surface.¹⁰⁹ The authors were able induce exogenous antigen presentation through the added transduction of a gene encoding the Fc γ receptor, thus enabling receptor mediated endocytosis. Fold expansion of antigen specific T-Cells was noted to be greater the 1,000 fold over the course of 150 days with repeated stimulation by the cellular aAPCs. In addition, the authors did not note the generation of regulatory T-Cells.¹⁰⁹

The K562 has also been applied to the stimulation of CD8⁺ cytotoxic T-Cells as well as CD4⁺ cells, in numerous applications. One interesting example is the use of a costimulation strategy with both CD28 and 41BB. The authors utilized a K562 cell line genetically modified to express the Fc γ receptor for immobilization of an anti-CD3 and an anti-CD28 antibody.¹¹⁰ The authors then transduced these cells with a gene encoding the 41BB ligand for costimulation. With this strategy, the authors were able to generate

up to 1,000-10,000 fold expansion of CD8⁺ T-Cells over the course of 25 days. The ultimate fold expansion was nearly 100 times greater than the cellular APCs bearing anti-CD3 and anti-CD28 alone.¹¹⁰

Other examples of the use of the K562 cell line have also been reported for different, specific applications. CD19 transduced K562 cells were utilized to stimulate T-Cells with chimeric antigen receptors designed to react specifically to CD19. Through zinc finger nuclease based elimination of the endogenous TCR, the authors were able to generate an APC and companion T-Cell line that could specifically target B cell lymphoma.¹¹¹ A similar strategy was used to generate natural killer cells that exerted a cytotoxic effect on CD19⁺ cells.¹¹² K562 based aAPC were also genetically modified further to secrete the soluble cytokine IL-21 as a Signal 3.¹⁰⁶ Although not used for a biomedical application, the authors were able to use this technology to study the biological effects of this cytokine.

Murine and Drosophilla Based aAPCs

In addition to human based cell systems, other xenogenic systems have been developed using similar transduction strategies. One of the earliest cell based aAPC systems to be utilized for T-Cell expansion was the *Drosophila* based cell line.¹¹³ Using a similar strategy to that of the K562 cells of genetic transduction with a murine MHC molecule class 1 protein, a costimulatory molecule for CD28, and ICAM-1 for integrin based binding to LFA-3 on T-Cells, these *Drosophila* cells were able to mediate expansion of murine CD8⁺ T-Cells. Due to the foreign nature of the cells, the authors also noted a stimulatory effect on B-Cells, which could then be relayed to the CD8⁺ T-Cells.¹¹³

Another alternative to the K562 is the mouse fibroblast line NIH/3T3. These cells were transduced with the genes for an HLA MHC protein and a costimulatory molecule for CD28.¹¹⁴ In addition, these cells were genetically modified to express the ICAM-1 protein for adhesion to the T-Cell through LFA-3. The aAPC was shown to efficiently mediate antigen targeted activation of influenza primary CD8⁺ T-Cells. Compared to the autologous APC, stimulation with this aAPC resulted in a 2 fold increase in the number of CD8⁺ T-Cells derived from peripheral blood. In addition, these cells were able to mediate an antigen specific cytotoxicity against melanoma cells.¹¹⁴

2.2.5 Acellular aAPCs

Despite the broad utility that cellular aAPCs have demonstrated, there are still a number of concerns over their use. Genetic modification of cells has the potential to result in cancerous growth due to the unpredictable nature of the site of insertion into the target genome. In addition, cell based therapies are time consuming and costly to produce. While possessing the advantage of supreme cell mimicry, cellular aAPCs also lack the antigen flexibility that an “off the shelf” particle based system can provide. Switching the type and nature of the protein signal is much simpler, and can be engineered more precisely, using an acellular aAPC system with a defined conjugation chemistry. To that end, numerous acellular aAPCs have been developed and characterized for the activation and suppression of target T-Cell populations.¹¹⁵ (**Table 2.2**)

Polymeric Particle aAPCs

Some of the earliest work in the development of aAPCs was with non-biodegradable polystyrene particles. Immobilization of protein ligands for aAPC

function involved a simple surface adsorption. Polystyrene based aAPCs have been used in antigen specific and antigen non-specific stimulation of T-Cells.¹¹⁶ One example of the use of polystyrene is in the expansion of ovalbumin specific T-Cells. Tham et.al. utilized a polystyrene bead displaying an MHC I molecule loaded with an ovalbumin antigen as well as recombinantly produced B7-1 and B7-2, the natural ligand for CD28 costimulation. *In vitro* stimulation results demonstrated a 3-fold increase of proliferation and IL-2 production of CD8+ T-Cells compared to soluble stimulation proteins.¹¹⁷

Over recent years, emphasis has shifted from non-biodegradable polymers to biodegradable polymers for aAPC construction. These materials have gained popularity in recent years due to their capabilities of controlled degradation and thus predictable elimination from the body. In addition, biodegradable polymeric aAPCs offer the advantage of sustained release of a third soluble signal. Taken together, these advantages have resulted in effective aAPCs for a wide variety of applications.

One of the earliest examples of the biodegradable aAPC was the use of polyglycolic acid microparticles as a platform for APC protein immobilization.¹¹⁸ For the generation of aAPCs, the authors demonstrated a conjugation-free surface adsorption of anti-CD3 and anti-CD28 antibodies. The aAPC was evaluated against a plate coated with these antibodies and was determined to 2-fold more efficient at eliciting T-Cell proliferation. Combining this aAPC with another degradable particle containing GM-CSF, the authors were able to demonstrate *in vivo* efficacy by reduced tumor burden of a fibrosarcoma cancer implantation.¹¹⁸

More recent biodegradable systems have focused on the use of PLGA based particles for aAPC synthesis. Steenblock et. al. developed a PLGA aAPC using both

MHC dimer and anti-CD3 as a Signal 1 and anti-CD28 as a Signal 2.¹⁰⁰ The authors were able to demonstrate a 3-fold production of IL-2 by CD8⁺ T-Cells compared to soluble signal protein. In addition, the study demonstrated the utility of a biodegradable polymer to have sustained release of a third signal, IL-2. Comparing IL-2 released locally by the particle to bulk delivery of IL-2, there was a 2-fold increase in the production of IFN γ by target T-Cells.¹⁰⁰

A major advantage of these biodegradable polymeric systems is the ability to modify particle shape by one of many established protocols. As was described earlier, the impact of aAPC shape on function and T-Cell stimulatory capacity has recently come to light. Combining this approach with the biodegradable polymer based approach of sustained cytokine or chemokine release may result in an even more powerful aAPC which may be useful for clinical applications.

Liposome aAPCs

Liposomes have also been of interest as a platform for aAPC generation. Owing in part to their fluid membranes, a liposome based aAPC has the potential to allow for recreation of the IS during T-Cell signaling. One of the first aAPC platforms involved the use of liposomes reconstituted from cellular membranes.¹¹⁹ While the use of liposomes as aAPCs has not found widespread application for therapeutic application or for the expansion of clinically relevant T-Cells, there are examples of efficacy. One was the use of GM-1 enriched liposomes for clustering of anti-CD3 and anti-CD28 stimulation ligands mediated by neutravidin bound cholera toxin. The authors compared this liposome based aAPC to a rigid bead based aAPC and found close to a 1.5-fold

increase in the expansion of Mart-1 antigen specific T-Cells, with an overall expansion of about 175-fold over the course of 14 days.¹²⁰

Magnetic aAPCs

Another popular choice of materials for construction of aAPCs are paramagnetic materials. Due to the ease of purification and processing, these magnetic particles have found widespread application in the generation of aAPCs. One study published by Oelke et. al. focused on the antigen specific expansion of CD8⁺ T-Cells.¹²¹ The strategy was to couple an HLA MHC Class I loaded with antigen as a Signal 1 and an anti-CD28 molecule as a Signal 2. The authors demonstrated 1,000-fold expansion of specific cells responding to the target antigen. The T-Cells also demonstrated excellent targeted effector activity in a cell lysis assay.¹²¹

One interesting and recent application of magnetic materials is in the induction of TCR clustering by magnetic field driven aggregation of nano aAPC bound to the receptors. Through antibody staining of TCR before and after an applied magnetic field, the authors demonstrated a doubling of cluster size and overall reduction in the number of clusters per T-Cell.¹²² At a maximal dose, these magnetically clustered nano aAPCs were able to mediate a 15-fold antigen specific expansion of target T-Cells compared to the non-clustered nano aAPCs which only mediated a 5-fold expansion of cells over 7 days. *Ex vivo* stimulation of these T-Cells under the influence of the magnetic field also led to a reduced tumor burden and enhanced survival of mice in an adoptive transfer immunotherapy model.¹²²

Other Materials

Another material which has found use in the application of aAPCs are single walled carbon nanotubes (SWNTs). This material has a large surface area that can be used for activation of T-Cells. The authors demonstrated a more than 10-fold production of IL-2 of T-Cells by anti-CD3 loaded onto the surface of these carbon nanotubes vs. free antibody in solution.⁴³ There was also a demonstrated effect of surface area for activation. Through expansion of the available SWNT surface area for activation, the authors were able to demonstrate enhanced activation of T-Cells for a similar dose of protein to fabricate the aAPCs.¹²³

Quantum dots have also been utilized recently for the stimulation of T-Cells. Through the use of MHC Class I protein and anti-CD28 immobilized on the surface of 30 nm quantum dots, the authors of this study were able to demonstrate an antigen specific expansion of T-Cells.¹²⁴ Over the course of 7 days, there was a 15-fold expansion of target T-Cells and no expansion of non-cognate T-Cells. In addition these quantum dot aAPCs mediated an excellent *in vivo* tumor reduction in an adoptive transfer model.¹²⁴

2.2.5 Biomedical Applications of the aAPC

Cancer Immunotherapy

One of the primary applications of aAPCs over the past years has been in the induction and expansion of cytotoxic T-Cells for cancer immunotherapy. Both cellular and acellular aAPCs have been utilized for this purpose. One study that highlights the use of aAPC for this purpose was the application of micron scale latex particles bonded to MHC dimer to serve as a Signal 1 and a blend of anti- CD28, 41BBL, and CD83 as Signal 2.¹²⁵ The bead based system was able to mediate a 250-fold expansion of melanoma CTL from naïve splenocytes. In addition, a strong *in vivo* effect was

demonstrated in both a murine lung metastasis model and a subcutaneous melanoma adoptive transfer model.¹²⁵

Efficacy of aAPCs in the context of cancer immunotherapy has also been shown in the context of human cytotoxic lymphocytes. Butler et. al. demonstrated impressive long term CD8⁺ expansion and functionality of human CD8⁺ T-Cells.¹²⁶ The platform utilized was the K562 cells line transduced to express a human MHC molecule as well as costimulatory molecules for CD28. Similar to previous studies with this cell based aAPC, there was a rapid short term expansion of antigen specific T-Cells (~100,000 fold over 5 weeks).¹²⁶ However, there was impressive long term efficacy noted as well. Over the course of 1.5 years there was more than a 1,000,000 fold expansion of antigen specific T-Cells which were verified to have effector function in a cancer cell lysis assay.¹²⁶ (**Figure 2.9**) Following the successful preclinical studies, this cellular aAPC has been transferred to clinical trials for *ex vivo* expansion of T-Cells for immunotherapy of advanced melanoma.¹⁰⁸

Infectious Disease

Beyond cancer therapy, the aAPC platform has also been investigated in the context of infectious disease. One pathogen which has been investigated extensively for potential treatment by aAPC based immunotherapy is cytomegalovirus (CMV).

Adoptive immunotherapy in the context of CMV has been previously established using autologous APCs.¹²⁷ Despite this clinical efficacy, the need to establish an autologous APC for each patient would render the therapy very expensive. As a result, an aAPC was developed for the expansion of CMV specific CD8⁺ T-Cells. The platform utilized was the murine fibroblast cell line expressing a human based MHC protein. The aAPC was

shown to induce a near 100-fold expansion over 10-14 days of culture with CD8⁺ cells from CMV⁺ human donors.¹²⁸ These T-Cells were also shown to have specific effector function against target cells. In addition, the authors of this study demonstrated the capability to generate memory T-Cells from this population.¹²⁸

aAPC platforms have also been investigated in the context of other viral infections. One of the published examples is the use of aAPCs to treat Epstein-Barr virus (EBV). Lu et. al. utilized a latex bead coated with a human MHC dimer loaded with cognate EBV peptide, as well as anti-CD28 and ICAM-1 as costimulatory molecules and adhesion molecules respectively. The authors demonstrated a selective cytotoxicity against cells pulsed with the target EBV associated antigen.¹²⁹ Another platform which could benefit from the use of aAPCs is human immunodeficiency virus (HIV-1). Clinical benefit has already been established utilizing an autologous APC platform.¹³⁰ Additional research into the use of expanded CD8⁺ T-Cells to treat the active or latent reservoir of HIV infection will likely be of benefit in the coming years.

Autoimmunity and Killer aAPCs

In addition to the stimulation of T-Cells to attack a target disease such as cancer or infection, there has been research devoted to researching how aAPCs can mimic the regulatory function of normal aAPCs through deletion of T-Cells in an antigen specific fashion (**Figure 2.10**). Termed “Killer aAPCs” these particles have been designed from a paramagnetic bead conjugated to MHC dimer to serve as a Signal 1 and anti-Fas as a Signal 2 to mimic the engagement of Fas by the FasL on the APC to induce activated T-Cell apoptosis.¹³¹ This technology has been used in a demonstrative capacity using Mart-1, the melanoma antigen, and CMVpp65, the CMV antigen. Culturing antigen specific

T-Cells with the cognate killer aAPC resulted in more than a 5-fold reduction of the T-Cell population.¹³² This was not observed in non-cognate populations of T-Cells. In addition, this elimination was shown to occur within 30 min of the beginning of coculture.¹³² This technology is promising for autoimmune disorders as several different target antigens have been implicated in diseases such as Type I diabetes, multiple sclerosis, and primary biliary cirrhosis.¹³¹

2.2.6 Conclusion

Artificial antigen presenting cell technology enables the capability for modern science to harness and control the immense power of the mammalian adaptive immune system. Many platforms have been developed for this technology. Cell based aAPCs, including the K562 leukemia cell line and murine fibroblast lines have shown direct and powerful activation of T-Cells in an antigen specific manner. There are several ongoing clinical trials with different cell based aAPCs for various diseases.¹⁰⁸ Acellular, biomaterials-based aAPCs have proven nearly as effective as cell-based aAPCs and have enabled this powerful arm of immunotherapy to be translated to an “off-the-shelf” technology. These aAPCs also enable precise tuning of their physical, chemical, and biological properties. As a result, therapeutic aAPC platforms are becoming more amenable to clinical use. Continued development of both of these platforms will be interesting to follow in the coming years.

One of the key advantages of the aAPC design is its ability to have an impact in any disease that has an immune component. As a result, the aAPC technology has found application in many illnesses for which immune targeted antigens have been identified. Cancer immunotherapy has benefitted greatly from the aAPC due to the capability but

inadequacy of the natural immune response to a cancerous growth. In addition, aAPCs have been developed for several viral infections including EBV and CMV. Despite a focus on aAPCs for T-Cell activation, there has also been work in the development of aAPCs to deplete T-Cells in an antigen specific fashion. This could have an impact for autoimmune diseases and organ transplantation where the current option is systemic immunosuppression.

aAPCs represent a successful biomimicry of the APC in its regular function of immune cell engagement. With a thorough understanding of the function and physiology of APCs, we can engineer more effective aAPCs for a wide variety of applications. Ongoing development of aAPCs for biomedical and therapeutic purposes will greatly benefit human medicine through engineered synthetic control of the natural immune response.

2.3 Overview of Surface Chemistry in Particle Design

2.3.1 Introduction

The field of drug delivery has in many ways focused on the controlled delivery of soluble biomolecules to tissue types of interest and increasingly to targeted cell types. While this mode of delivery covers many categories of therapeutics, including both small molecule drugs and biologics such as peptides, proteins, and nucleic acids, certain types of biologics require presentation from a surface, rather than soluble presentation, for their desired cellular function. Biomimetic materials, in particular, that aim to mimic the physical, chemical, and biological aspects of natural biological materials for cellular engineering, must take into account this feature of surface presentation. As understanding of these natural systems has advanced, investigators have sought to design

artificial systems capable of mimicking and controlling these interactions to shape the cellular response. Moving towards this goal, engineered particle and surface based systems have been designed that can modulate the activity of a variety of cell sub-types *in vitro* and *in vivo* for purposes of therapeutics.

Biological cells are surrounded by highly complex membranes composed of lipid bilayers and glycosylated cell surface proteins, which are highly organized and transmit and receive critical signals that direct normal and abnormal cellular function. Recently, there has been increased attention in taking cues from this biology to design therapeutic particles with greater biomimicry. There are two main approaches towards development of particles that mimic cell surfaces. Bottom-up approaches begin with the molecular components of cellular membranes and specifically add in the desired surface proteins synthetically either by surface functionalization of an intact lipid bilayer or by formulating the proteins with lipid linkers and adding them during a particle coating step. Top-down approaches begin with harvested membranes from biological cells that are directly added to particle cores.

2.3.2 Fabrication of Surface Mimetic Particles for Drug Delivery

Bottom-Up Approaches

A major goal in particle-based drug delivery involves the avoidance of non-specific uptake and rapid clearance from the blood by immune cells such as macrophages. Classical approaches towards this problem involve densely conjugating hydrophilic polymers such polyethylene glycol (PEG) to the particle surface in an effort to minimize interactions with biomolecules and cells based on hydrophobic interactions and charge.^{133,134} One approach to improve on the PEGylated particle model is

identification and use of biological “self” signals. CD47 has recently been identified as perhaps the most potent “self” marker and Rodriguez et. al. developed “self” peptides, computationally derived from human CD47, that optimally bind to the same binding partner as CD47 (CD172a).¹³⁵ These “stealth” self-peptides strongly inhibit nanoparticle uptake by macrophages at far lower densities than are required for effective protection by PEG, requiring only a single CD47 molecule per 60 nm particle.¹³⁵

Cellular membranes are formed from fluid lipid bilayers and present a variety of protein signals in addition to being shielded by a dense glycocalyx. Sengupat et al developed anticancer “nanocells” (NC)¹³⁶ composed of a core PLGA nanoparticle with an encapsulated chemotherapeutic that was surrounded by a peglyated-lipid envelope that trapped an anti-angiogenic agent. This allowed for rapid release of the antiangiogenic agent followed by slower release of the chemotherapeutic, enabling vascular shutdown prior to direct tumor killing. NC showed significant tumor accumulation, tumor growth inhibition, mouse survival, tumor cell apoptosis, and reduced systemic toxicity.

Polymer-supported lipid bilayers (SLBs) have been used for a long time as cell-surface models.¹³⁷⁻¹⁵⁰ Advantages of SLBs over polymer-support free systems such as free standing lipid membranes or liposomes include improved mechanical stability and maintenance of membrane fluidity.^{144,145} They have been developed for phase-transition chromatography^{146,147} as well as isolation of cell membranes on particle surfaces.¹⁴⁸⁻¹⁵⁰ In a biomimetic approach, the Brinker group developed “protocells” with mesoporous silica cores surrounded by fully synthetic lipid bilayers.¹⁵¹⁻¹⁵⁴ These fully synthetic protocells can encapsulate a variety of chemically active drugs and present ligands on the supported lipid bilayer surface, including short peptides and larger antibodies or glycoproteins

(**Figure 2.11A**). This enables presentation of a variety of important biological signals on the cell-like artificial surface, including targeting moieties to enhance specific cell targeting and fusogenic peptides to enhance endosomal escape on the surface of the nanocarrier.¹⁵⁴ Compared to liposomes presenting the same targeting peptides, these protocells show increased membrane fluidity and as a result show enhanced specific binding due to the ability to recruit additional peptides to the particle-cell interface, increasing the multivalency of the interaction.¹⁵⁴

Top-Down Approaches

Rather than synthesizing an artificial membrane out of fully synthetic components, several groups have recently explored the concept of harvesting and purifying biological membranes from cells and then using the purified membrane to coat particles. Red blood cells (RBCs) offer a number of advantages as potential targets for biomimetic therapeutic particles as they have extremely long circulating half-lives, possess a discoidal-shape, and have the flexibility to squeeze through capillaries. Multiple groups have purified RBC membranes and generated RBC vesicles, named resealed erythrocytes, which can then be loaded with a variety of hydrophilic drugs in the same fashion as with synthetic liposomes.¹⁵⁵⁻¹⁵⁷ Challenges with this approach include early removal from the circulation, early drug release for smaller or more lipophilic molecules, and variability with particle fabrication and stability.

Hu et. al.¹⁵⁸ fused RBC vesicles with nanoparticle cores to form RBC membrane camouflaged nanoparticles (**Figure 2.11b**). These RBC membrane camouflaged nanoparticles showed superior *in vivo* half-life compared to PEGylated nanoparticles. The process coats the nanoparticles in a unilamellar fashion, preserves the majority of the

membrane proteins, including CD47, and presents them in a correct-side out orientation.¹⁵⁹ These RBC-coated particles were used as RBC decoys to protect against RBC lysis from pore forming toxins (PFTs).¹⁶⁰ When formulated with PFTs and injected, these particles engender effective immune responses against the PFTs.¹⁶¹

Leukocytes or white blood cells use their cell surface interactions to bind to inflamed endothelium and respond to infection in the tissues. Parodi et. al.¹⁶² encapsulated nanoporous silica nanoparticles with white blood cell (leukocyte) membranes and demonstrated that these “leukolike vectors” (LLVs) recapitulate functions of white blood cells, including avoiding immunological clearance, interacting with endothelial cells, and transporting drugs across a model of inflamed endothelium. In the presence of TNF-alpha, LLVs are transported across an inflamed endothelial barrier 4-fold more efficiently than bare particles, showing the same propensity to cross-inflamed endothelium as biologic leukocytes. These properties allowed doxorubicin-loaded LLVs to show enhanced tumor cell killing with relative protection of the endothelium, delayed liver clearance, and tumor accumulation in mice.

Nanoparticle biomimicry may be extended to other cell types as well through the harvesting of cellular “ghosts” such as from platelets¹⁶³ or mesenchymal stem cells (MSCs).¹⁶⁴ MSCs show intriguing active tumor-targeting properties, and Furman et al. showed that MSC vesicles or nanoghosts loaded with sTRAIL could substantially inhibit prostate tumor growth *in vivo*.¹⁶⁴ Of particular note, this effect was restricted to nanoghosts derived from MSCs, as nanoghosts derived from human smooth muscle cells, which were of similar size and physical properties, showed no therapeutic effect.¹⁶⁴ This type of biomimicry is not restricted to use of purified membranes from healthy cells

alone. Cancer cell membrane coated nanoparticles (CCNPs)¹⁶⁵ have also been produced and are efficiently taken up by dendritic cells and useful as cancer nanovaccines. CCNPs may also show enhanced tumor targeting for direct delivery of anticancer drugs.

2.3.3 Fabrication of Surface Mimetic Particles for Immunoengineering

One of the varied areas of biology where the proper balance of physical, chemical, and biological interactions appears most critical is in the signaling of the immune system. Thus, for the engineering of lymphocytes, surface engineering of biomolecules is key to deliver the proper signals for lymphocyte programming. This section highlights immunoengineering approaches including the components of the necessary chemical and biological signals that engender cellular responses, the required features of the surfaces that best present these signals such as surface fluidity, and the physical properties of the supporting substrate that also modulate lymphocyte behavior (Table 2.3).

Surface Patterning and Fluidity

Interactions between lymphocytes and APCs or soluble antigens are highly complex in spatial arrangement. An immunological synapse (IS) is formed at the interface between lymphocytes and APCs. The IS is characterized by dynamic rearrangements of proteins into specific clusters. Randomly distributed, immobilized proteins cannot recapitulate this organization and clustering.¹⁶⁶ As a result, patterned and fluid surfaces have been engineered to replicate the IS and enhance lymphocyte modulation.

Microfabrication allows for deposition of proteins in a site-specific manner on surfaces at resolutions down to approximately 1 μm to allow for effective pre-clustering

of signal molecules to study lymphocyte activation.¹⁶⁷ Using microfabrication with biotinylated photoresist to pattern anti-CD3 onto a glass substrate, solid focal spots were shown to be more effective for T-Cell activation than annulus shaped protein deposition, demonstrating the importance of receptor clustering for T-Cell activation.¹⁶⁸ This study further concluded that differences in T-Cell activation were due specifically to the shape of the protein deposition spots and not due to density of ligand or surface area of the receptor, which has implications for particle systems that are capable of only displaying a certain surface area to T-Cells based on their geometry.^{102,168}

In contrast to microfabricated surfaces that allow for receptor localization at the micron level, nanoarrays of gold nanoparticles to specifically localize ligands at defined intervals between 35-150 nm have been used to study the importance of inter-receptor spacing for T-Cell activation.¹⁰⁵ Using anti-CD3 conjugated to gold nanoparticles, a spacing of 60 nm was shown to be optimal for maximal threshold stimulation of T-Cells,¹⁰⁵ which has implications for the design of particle-based aAPC systems with surface conjugated ligands where ligand localization is more challenging to define.

The fluidity of proteins on a synthetic surface of a particle is an important component of mimicking the membrane fluidity of a cell. Surface fluidity allows particles to behave in a more biomimetic manner by enabling receptor clustering, which is an important aspect of the physiological interaction between T cells and APCs.

Supported lipid bilayers (SLB) on planar substrates have long been utilized to study receptor interactions between cells, in particular as they enable membrane fluidity and facilitate receptor clustering. Artificial APC surfaces have been engineered to mimic the lateral diffusivity of the IS by coating a support substrate with an SLB containing

Signal 1, Signal 2, and adhesion molecules. SLBs with immobilized ligands separated by chromium strips for precise localization have been used to demonstrate the importance of receptor clustering for T-Cell activation.¹⁶⁹ This study was one of the first to demonstrate the necessity of ligand positioning and fluidity for the formation an immunological synapse required for robust T-Cell activation.¹⁶⁹ SLBs have also been used to study the requirements for TCR triggering, which were found to include surface-anchoring of pMHC, T-Cell surface adhesion, and subsequent ability of the T-Cell to move, suggesting that a fluid aAPC/T-Cell contact area is optimal.¹⁷⁰ Ligand mobility, specifically, has been shown to be an important parameter in modulating T-Cell response.¹⁷¹ SLBs of different lipid compositions were engineered to vary ligand mobility, and those with greater ligand mobility had increased CD3 accumulation at the IS and increased phosphotyrosine (pY) signaling at the TCR microclusters (**Figure 2.12A**).

Knowledge of the importance of membrane fluidity for immunological synapse formation has implications for lymphocyte surface engineering that have been investigated through the use of liposomes with conjugated signal molecules that allow for free movement and clustering of the biomolecules.^{120,172} As planar SLBs are only relevant for *ex vivo* T cell expansion, 3D aAPCs with membrane fluidity have been engineered by incorporating Signal 1, Signal 2, and adhesion molecules into liposomes.^{120,172,173} TCR molecules on T-Cells engaging with liposome-based aAPCs formed clusters over time that co-localized with the aAPCs, suggesting the formation of an IS.¹⁷³ In the first generation of liposome-based aAPCs, the pMHC molecules were randomly distributed throughout the membrane.¹⁷³ However, pre-clustering MHC class II on lipid rafts for highly concentrated spots of signaling molecules has been shown to

increase activation of T-Cells.¹⁷⁴ As a result, liposome-based aAPCs were enhanced by pre-clustering the T-Cell ligands in microdomains on the aAPC surface, which significantly increased antigen-specific T cell stimulation.¹⁷² Microdomains composed of anti-CD3, anti-CD28, and anti-LFA-1 were anchored to GM-1-enriched liposomes by neutravidin bound cholera toxin. This liposome-based aAPC generated almost a 1.5-fold increase in the expansion of T-Cells compared to bead-based aAPCs with immobilized ligands, with an overall expansion of over 150-fold over the course of 14 days. Liposome-based aAPCs allow receptor clustering but are limited by shape, size, and the number of signaling molecules that can interact with the T-Cell. SLBs atop a particle core would allow for control over these parameters, in addition to surface fluidity. Particles coated with lipid bilayers have been successfully engineered for targeted drug delivery applications,^{154,175} and are an interesting approach for next generation aAPCs.

Alternative engineering methods allow for receptor clustering on T-Cells without patterning the particle surface or using a fluid lipid bilayer. One way to accomplish this is through the use of a semi-flexible polymer based on poly(isocyno peptides) conjugated with anti-CD3 and anti-CD28 to allow for receptor clustering, as well as efficient multivalent binding.^{175,176} The polymers were able to activate T-Cells at significantly lower concentrations *in vitro* than rigid spherical poly(lactic-*co*-glycolic acid) (PLGA) counterparts, but their efficacy and biodistribution *in vivo* has yet to be studied.

With the knowledge of receptor clustering necessary for TCR activation, nanoparticle systems capable of self-clustering in response to paramagnetic activation have been designed that allow for larger focal spot formation, with a length scale similar

to that of micron-sized particles.^{124,177} Perica *et al.* engineered paramagnetic iron-dextran nano-aAPC to drive receptor clustering.^{122,124} Under the influence of an external magnetic field, nanoparticles bound to T-Cells aggregate, leading to receptor clustering on the T-Cell and an increase in TCR cluster size (**Figure 2.12B**). T-Cells activated by the nano-aAPC in a magnetic field mediated tumor rejection in a melanoma adoptive immunotherapy model and were more effective in activating naïve T-Cells than nano-aAPC without magnetic field counterparts. In addition, magnetic preclustering of these nano aAPC resulted in 80% long term survival of mice compared to unclustered controls.^{122,124}

Similar to T-Cells, B-Cells form an immunological synapse when engaged with APCs, and receptor clustering is an important component of B-cell activation.^{178,179} Antigen binding to the BCR triggers BCR crosslinking and the formation of microclusters, which initiate downstream signaling that leads to B-Cell activation.^{178,180} BCR/antigen clusters in the cSMAC, while LFA-1/ICAM-1 migrate to the pSMAC.^{179,181} However, unlike T-Cells, adhesion molecules are not required for mature synapse formation if the affinity of BCR-antigen binding is high enough.¹⁷⁹ SLBs and liposomes have been used to recapitulate this spatial organization for B-Cell modulation.

Supported lipid bilayers have been used to study B-Cell activation by membrane-anchored antigen *in vitro*.¹⁷⁹⁻¹⁸⁷ Typically, SLBs contain biotinylated anti-IgM, anti-IgD, or anti-IgG as surrogate antigen tethered to biotinylated lipids with a streptavidin linker.¹⁸⁸ Anti-IgG SLBs with lateral mobility result in enhanced BCR microcluster formation and signaling compared to immobilized IgG, which form small and unstable microclusters that lead to inefficient signaling.¹⁸⁰ Although adhesion molecules are not

required to induce BCR clustering and synapse formation, incorporating ICAM-1 into SLBs can enhance contact formation for lower-avidity antigens.^{179,184}

Although biotinylation is widely used to conjugate IgG to SLBs, it is difficult to control the location of biotin binding on the antibody, which can lead to inaccessibility of the antigen to BCRs, and multiple IgG molecules can bind to one streptavidin molecule.¹⁸⁸ Zhang *et al.* addressed these issues by using a modified D domain from staphylococcal protein A molecule fused with a polyhistidine tag, which binds to nickel-containing SLBs.¹⁸⁸ Protein A binds IgG with high affinity only in the constant region. This technique enhanced lateral mobility compared to tethering IgG with streptavidin. However, this approach cannot be used to target B-Cells expressing IgG BCRs since the linker protein will bind the BCRs. Others have similarly utilized nickel-containing SLBs to conjugate histidine-tagged antigen and adhesion molecules,¹⁸⁹⁻¹⁹² as well as the inhibitory receptor FcγRIIB, which blocks BCR microcluster formation and prevents downstream signaling.¹⁹³

Results using planar lipid bilayers suggest that a liposome-based design for B-Cell therapies may be more effective than particles with immobilized antigen.¹⁹⁴ Researchers have used liposomes presenting peptide antigen to stimulate a B-Cell IgG response by including a costimulatory TLR ligand¹⁹⁴ and to induce tolerance by incorporating the ligand for CD22, an inhibitory co-receptor.¹⁹⁵ Studies have focused to a greater extent on delivering free antigen encapsulated in liposomes to B-Cells.¹⁹⁶ However, given that membrane-anchored antigen stimulates B-Cells more strongly, surface presentation on fluid particles is a promising new direction.¹⁸¹

Surface Rigidity and Mechanical Properties

The effect of substrate stiffness on lymphocyte modulation has been relatively unexplored but has been shown to have an important role in the differentiation and activation of other cell types, such as mesenchymal stem cells (MSCs)¹⁹⁷⁻²⁰⁰ and endothelial cells.²⁰¹⁻²⁰³ For example, Engler *et al.* showed that substrate stiffness alone can drive MSC differentiation fate.¹⁹⁸ A limited number of studies have shown that lymphocyte activation and differentiation may be affected by planar substrate rigidity.²⁰⁴⁻²⁰⁹ This is an interesting area for further investigation of particle-based systems, as particle stiffness is an important component of cellular biomimicry.

It has been shown that mechanical forces can mediate T-Cell signaling, through both the TCR/CD3 complex and the costimulatory receptor, CD28.^{210,211} T-Cells cultured on elastomer pillar arrays presenting CD3 and CD28 activating antibodies generated traction forces on the pillars.²⁰⁴ Traction forces were also generated through the TCR on pillars presenting antigen-loaded MHC. Additionally, inhibition of actin polymerization^{169,170,212} and myosin²¹³ significantly inhibits TCR signaling. This evidence suggests that cytoskeletal and cellular forces play a role in T-Cell activation at the immunological synapse. Optimizing particle rigidity may allow T-Cells to perform mechanosensing during the formation of the immune synapse as they do with biological APCs.

While particle stiffness has not been explored, it has been shown that the rigidity of planar surfaces plays a role in T-Cell activation, proliferation, and differentiation. Kam and colleagues have investigated the effect of substrate stiffness on *ex vivo* T-Cell activation and expansion.^{206,207} Human T-Cells were cultured on PDMS substrates of varying elastic modulus coated with anti-CD3 and anti-CD28, and softer substrates ($E <$

100 kPa) exhibited enhanced polyclonal expansion compared to stiffer substrates ($E > 2$ MPa).²⁰⁶ Specifically, softer substrates yielded a higher level of CD4⁺ and CD8⁺ T-Cell stimulation, as evidenced by increased proliferation and IL-2 production. Additionally, softer substrates generated a greater proportion of IFN- γ producing Th1-differentiated cells. In a different study, mouse T-Cells expanded on polyacrylamide gels of elastic modulus varying from 10 to 200 kPa showed increased IL-2 secretion on stiffer substrates.²⁰⁷ The seemingly opposite trends in the two studies are likely due to the different ranges of elastic moduli tested—the mouse T-Cells were cultured on polyacrylamide gels ranging in elastic modulus from 10 to 200 kPa,²⁰⁷ while the human T-Cell study tested PDMS substrates ranging from 50-100 kPa to >2 MPa.²⁰⁶ Both papers show that the optimal elastic modulus for T-Cell stimulation in the ranges tested is approximately 100 kPa. A different group looked at a larger range of elastic moduli—Jurkat T-Cells were cultured on polyacrylamide gels of elastic modulus (E) ranging from 200 Pa to ~ 6 kPa.²⁰⁵ T-Cell signaling persisted for a longer period of time on softer substrates, but the efficiency of T-Cell activation and expansion on the different substrates needs to be further investigated.

Additional research needs to be performed to determine the effect of surface rigidity of particles, in addition to planar substrates, on T-Cell activation and differentiation. In engineering particle-based aAPCs, mimicking the low compressive modulus of biological APCs may optimize the T-Cell-aAPC interaction. Dendritic cells have been measured to have an elastic modulus of ~ 800 Pa when activated,²¹⁴ so T-Cell activation may be optimal on surfaces with lower elastic moduli. The effect of particle stiffness on T-Cells needs to be explored to better understand the mechanics of

lymphocyte signaling and to optimize particle therapies designed to modulate lymphocytes.

There has been a limited amount of research on the effect of substrate stiffness on B-Cell stimulation. Unlike T-Cells, B-Cells encounter antigen *in vivo* on substrates of varying stiffness—for example, B-Cells sense antigen on the surface of stiff viral capsids, on the membranes of infected host cells, and in soluble form. Liu and colleagues found that B-Cells cultured on antigen-coated polyacrylamide gels of elastic moduli varying from 2.6 to 22.1 kPa were more strongly activated and were better able to perform antigen affinity discrimination on the stiffest substrate.²⁰⁸ B-Cells were even more efficiently activated on a PDMS surface with an elastic modulus of 1100 kPa compared to a 20 kPa substrate, as measured by formation of the immune synapse.²⁰⁹ However, the softer substrate showed enhanced B-Cell expansion and antibody response. Further evaluation with a larger number of substrate elastic moduli is necessary. Nonetheless, these studies suggest that B-Cells perform mechanosensing and that optimizing particle rigidity based on the desired response could be beneficial for therapies designed to modulate B-Cells, such as particle-based vaccines and B-Cell lymphoma treatments.

2.3.4 Conclusion

In this section, current approaches at extending the therapeutic efficacy of nanoparticle and microparticle systems were discussed in the context of designing the particles to be more biomimetic. Bio-inspired design of nanoparticles enables long circulation times and stealth interaction with off-target molecules and cells and simultaneous high affinity interactions with target cells. Such biomimetic particles can encapsulate and release soluble small molecules and proteins extracellularly or

intracellularly and can also present biological molecules in specific orientations to trigger cell signaling of target cells.

Recent advances in the field of immunoengineering have enabled the development of technologies designed to activate and deactivate lymphocytes, including T-Cells and B-Cells. Researchers have attempted to recapitulate the complex spatial arrangement of proteins and membrane reorganization that occurs during the formation of the immunological synapse by engineering surfaces with patterned proteins and surface fluidity. While these features have all been individually implemented, in the future, enhanced biological factors, surface diffusivity, surface area, and mechanical properties will likely be combined to create highly effective advanced biomimetic materials for immunotherapy.

These approaches can be used to combat many diseases, including treating cancer in new ways including through nanoparticle-based vaccines and construction of artificial antigen presenting cells. The future of particle-based therapeutics involves learning from natural biological systems and designing the needed physical, chemical, and biological parameters to emulate them. Such biomimetic therapeutic particles have a promising outlook to benefit human health.

2.5 Tables

Table 2.1: Summary of applications of various anisotropic polymeric nanoparticles

Method	Application	Material*	Size	Shape**	Result	Ref
Thin Film Stretching	Inhibition of macrophage uptake	PS	500 nm – 4 μ m	Prolate ellipsoid (AR 2), Oblate ellipsoid (AR 2)	Prolate ellipsoids attached 4 times more, oblate ellipsoids phagocytosed 3 fold more than spheres.	⁵⁷
	Inhibition of MSC/HeLa uptake	PS	100 nm	Prolate ellipsoid (AR 2-4)	AR 2 particles taken up 2-5 times more than AR 4 particles	⁵⁸
	Enhanced antibody specificity	PS	200 nm	Prolate/oblate ellipsoid (AR 3),	Targeted prolate ellipsoid particles taken up 3 times more than spheres	⁶⁴
	Endothelial targeting	PS	100 nm - 10 μ m	Oblate ellipsoid (AR 3)	30 fold organ specificity of targeted ellipsoids vs. spheres	⁶⁵
	<i>In vivo</i> brain and lung targeting	PS	200 nm	Prolate ellipsoid (AR 3)	Targeted ellipsoids accumulated 2 fold more in lung and 7.5 fold more in brain compared to sphere	⁶⁷
	Artificial antigen presenting cells	PLGA	4.5 μ m	Prolate ellipsoid (AR 2-7)	20 fold increase in antigen specific proliferation by ellipsoid aAPC compared to spherical.	¹⁰²
Particle Replication in Non-Wetting Templates (PRINT)	siRNA delivery	PLGA	320 nm	Rod shaped (AR 4)	60-80% knockdown of KIF11 in cancer cells over 72 hrs.	⁶⁸
	RNA replicon delivery	BSA	1 μ m	Cylindrical	2 fold increase in target protein expression over Trans IT	⁶⁹
	Docetaxel delivery	PLGA	320 nm	Cylindrical (AR 4)	Reduced tumor size and toxicity vs free drug	⁷¹
Self-Assembly	Plasmid delivery	PEG-PPA	40-70 nm	Rod like (AR 3)	10000 fold increase of <i>in vivo</i> expression of target gene by rods compared to spheres	⁷⁴
	Doxorubicin delivery	POEGMA-P(ST-co-VBA)	20-200 nm	Rod and worm shaped	7 fold increase of cancer cell killing of worms over spheres	⁷⁵
	Enhanced biodistribution	PEG-PEE/PCL	1-8 μ m	Worm shaped	2 fold increase in circulation time for 4 fold increase in AR**	⁷⁶

* PS = polystyrene, PLGA = poly(lactic-co-glycolic acid), BSA = bovine serum albumin, PPA = polyphosphoramidate. POEGMA-P(ST-co-VBA) = poly[oligo(ethyleneglycol) methacrylate]-block-[poly(styrene)-co-poly(vinyl benzaldehyde)]. PEE = polyethylethylene. PCL = polycaprolactone. ** AR = aspect ratio

Table 2.2: Examples of the various existing aAPCs and their efficacies.

Type	Material*	Size	Signal 1	Signal 2	Efficacy	Ref
Cellular	K562 cells	10-20 μ m	HLA MHC Class II	B7-1	1000 fold expansion of CD4+ T-Cells.	¹⁰⁹
	K562 cells	10-20 μ m	HLA MHC Class I	B7-1	1,000,000 fold expansion of CD8+ T-Cells over 1.5 years.	¹²⁶
	K562 cells	10-20 μ m	Anti-CD3	Anti-CD28/41BB-L	1000-10000 fold expansion of CD8+ T-Cells.	¹¹⁰
	NIH/3T3 murine fibroblasts	18 μ m	HLA MHC Class I	B7-1	2 fold greater CD8+ expansion compared to autologous APC.	¹¹⁴
	NIH/3T3 murine fibroblasts	18 μ m	HLA MHC Class I	B7-1	100 fold expansion of CMV CD8+ T-Cells over 14 days.	¹²⁸
Acellular	PS	5 μ m	K ^b MHC Class I	B7-1/B7-2	3 fold secretion of IL-2 compared to soluble protein.	¹¹⁷
	PS	6 μ m	HLA MHC Class I	Blend of Anti-CD28/ Anti 41BB	5 fold increase of CD8+ T-Cells of blended Signal 2 compared to individual Signal 2.	¹⁰⁴
	PGA	7 μ m	Anti-CD3	Anti-CD28	2 fold greater CD8+ T-Cell expansion compared to plate bound ligand.	¹¹⁸
	PLGA encapsulating IL-2	6 μ m	Anti-CD3	Anti-CD28	3 fold greater secretion of IL-2 by T-Cells compared to soluble signal.	¹⁰⁷
	Non-Spherical PLGA	4-5 μ m	D ^b MHC Class I IgG dimer	Anti-CD28	20 fold greater of expansion of CD8+ T-Cells of ellipsoidal compared to spherical particles.	¹⁰²
	Liposomes	60 nm	Anti-CD3	Anti-CD28	175 fold expansion of CD8+ T-Cells over 14 days.	⁹⁷
	Magnetic Dynal® Beads	4.5 μ m	HLA MHC Class I	Anti-CD28	1000 fold expansion of antigen specific CD8+ T-Cells.	¹²¹
	Magnetic Dynal® Beads	4.5 μ m	HLA MHC Class I	Anti-Fas	5 fold reduction in antigen specific CD8+ T-Cells.	¹³²
	SWNT Bundles	5-10 nm tubes/100 μ m bundles	Anti-CD3	None	10 fold increase in secretion of IL-2 compared to soluble antibody.	¹²³
	QDs	30 nm	D ^b MHC Class I	Anti-CD28	15 fold expansion of CD8+ T-Cells over 7 days.	¹²⁴

*PS = Polystyrene, PGA = Poly glycolic acid, PLGA = Poly(lactic-co-glycolic acid), SWNT = Single walled carbon nanotubes, QDs = Quantum Dots

Table 2.3. Summary of various surface engineering features for immunoengineering.

Lymphocyte Target	Surface Feature ¹	Material ²	Signal Protein ³	Result	Ref
T-Cells	MHC Dimer for antigen specific activation	Dynal® microbead	S1: MHC Dimer + S2: Anti-CD28	Micro-aAPC gave 10 ⁶ expansion <i>ex vivo</i> over two months of tumor specific T-Cells	121
	Paracrine delivery of IL-2	PLGA	S1: Anti-CD3 + S2: Anti-CD28	Enhanced CD8+ expansion with IL-2 delivery	107
	Ellipsoidal shape – micron scale	PLGA	S1: MHC Dimer + S2: Anti-CD28	20-fold increase in T-Cell proliferation in ellipsoidal aAPC compared to spherical	102
	Ellipsoidal shape – nano scale	PLGA	S1: MHC Dimer + S2: Anti-CD28	3-fold stronger <i>in vivo</i> induction of T-Cells by ellipsoidal aAPC compared to spherical aAPC	215
	MHC Dimer with FasL	Dynal® microbead	S1: MHC Dimer + S2: FasL	Killer aAPC induced T-Cell apoptosis with both high efficacy and specificity	132
	SLB with variable ligand mobility	DMPC and DPPC	S1: Anti-CD3	T-Cell activation and IS formation preferentially induced by more fluid membranes	171
	Paramagnetic nanoparticle	Iron-dextran	S1: MHC Dimer + S2: Anti-CD28	5.5-fold increase in T cell expansion with magnetic clustering of nano aAPC compared to non-clustered nano aAPC	122
	Planar substrate with variable rigidity	PDMS	S1: Anti-CD3 + S2: Anti-CD28	4-fold increase in T cell expansion on softest substrate compared to stiffest substrate.	206
B-Cells	Patterned antigen with surface fluidity	Liposome	Trimeric HIV-1 spikes	B-Cell activation against HIV-1 antigen <i>ex vivo</i>	216
	Combine B-Cell and CD4+ T-Cell stimulation	Copolymer	OVA antigen + B-Cell epitope	Enhanced activation of B-Cells in combination with CD4+ cells	217
	Planar substrate with variable rigidity	Polyacrylamide	Anti-IgM	Enhanced B-Cell activation on stiffer substrates	208
NK Cells	Membrane bound IL-15	K562 cells	sIL-15 + 4-1BBL	<i>Ex vivo</i> expansion of NK cells	218
	Membrane bound IL-15 and IL-21	K562 cells	sIL-15 + sIL-21	Enhanced NK cell stimulation with both IL-15 and IL-21	219

2.6 Figures

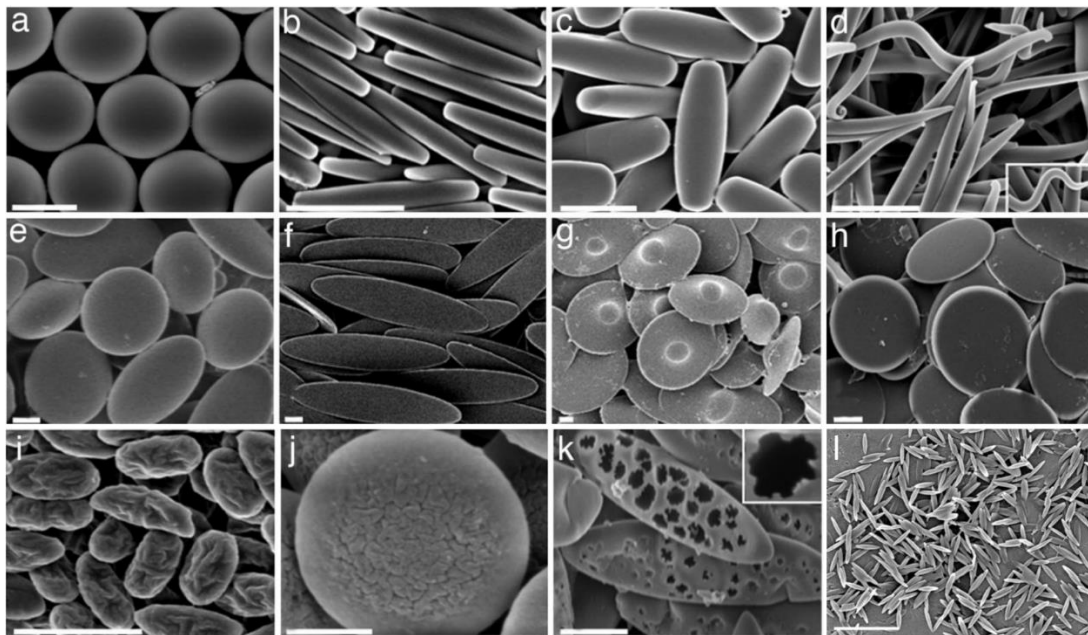


Figure 2.1: A wide repertoire of particle shapes can be produced with the thin film stretching method. (a) Spherical, (b) rectangular disk, (c) prolate ellipsoidal, (d) worm-like, (e) oblate ellipsoidal, (f) prolate ellipsoidal disk, (g) UFO-like, (h) flattened circular disk, (i) wrinkled prolate ellipsoidal, (j) wrinkled oblate ellipsoidal, and (k) porous prolate ellipsoidal particles can all be synthesized by liquefaction in a thin film and mechanical stretching. The technology is also translatable to the (l) nanoscale as the size of the particle is determined by bulk spherical particle synthesis. Scale bars are 2 μm . Adapted with permission from ref 21.

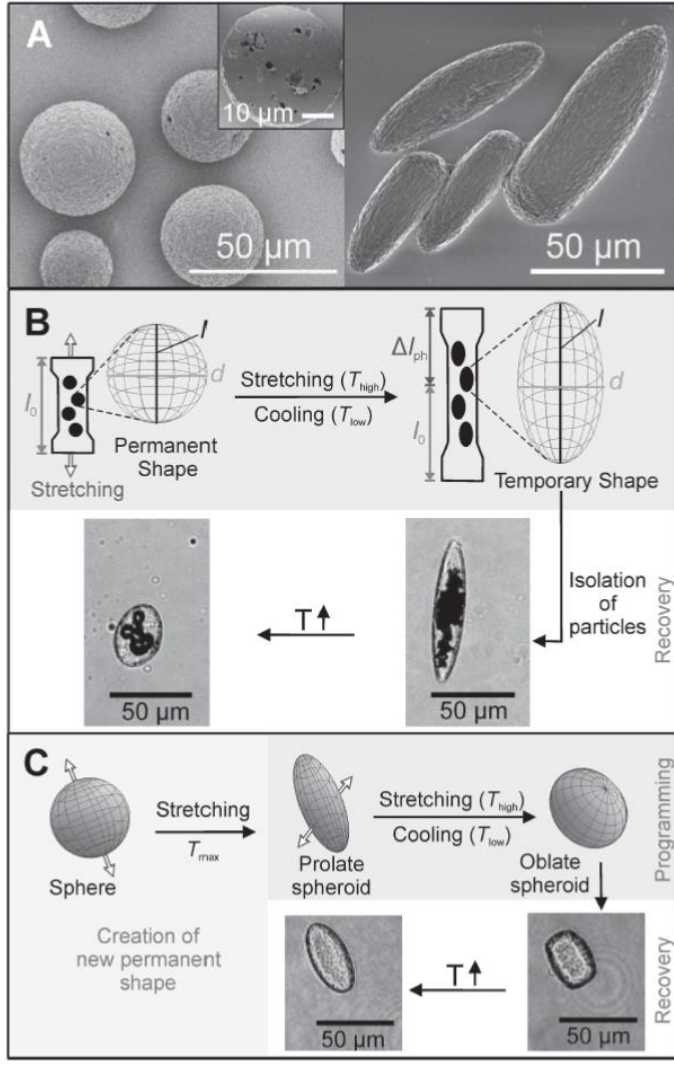


Figure 2.2: Shape memory and reprogramming applications are one application of nanoparticles produced from block copolymers. (a) Non spherical and spherical microparticles utilized as an example to explain the procedure of shape reprogramming. (b) Schematic of temporary shape reprogramming process utilized. Particles are stretched to a non-spherical shape at the “temporary reprogramming” temperature and upon heating the particles reassume their spherical shape. (c) Schematic of permanent reprogramming and shape memory reversion to ellipsoidal particles. Spherical particles are first stretched to prolate ellipsoids at the “permanent reprogramming” temperature, followed by stretching to oblate ellipsoids at the “temporary reprogramming” temperature. Upon heating, the oblate ellipsoid assumes the permanently programmed prolate ellipsoid shape. Similar trends were seen with nanoparticles in the study. Adapted with permission from ref 23.

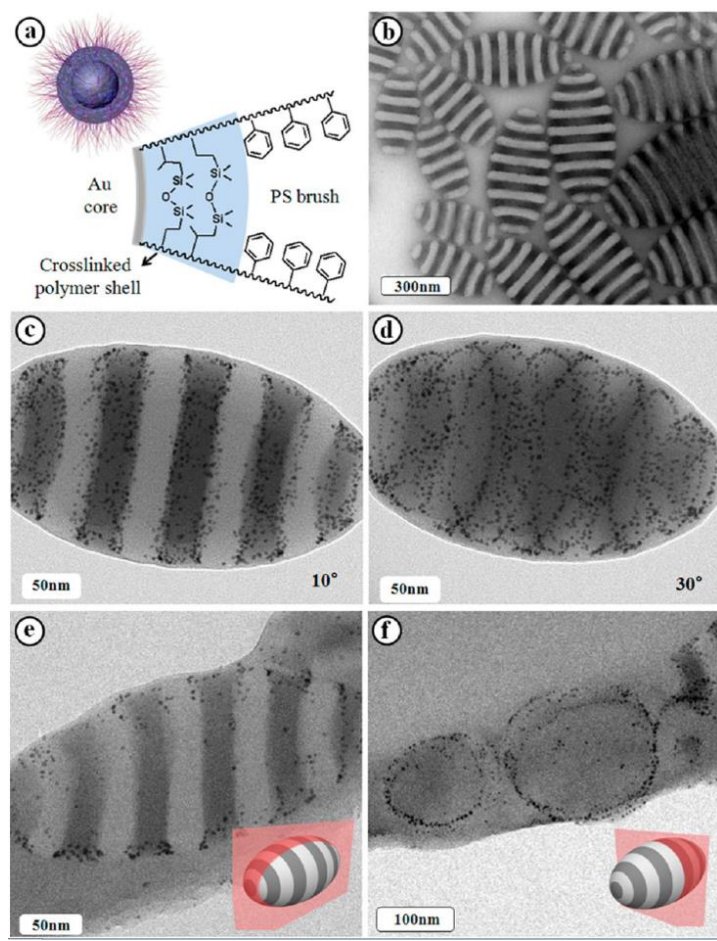


Figure 2.3: Nonspherical stripped nanoparticles can be synthesized from the gold nanoparticle based surfactant dissolution of a layer block copolymer. (a) The main driving force behind the formation of this particle from a layered spherical particle is the administration of a smaller gold nanoparticle with a crosslinked polymer shell and polystyrene on the surface. (b) Stripped ellipsoidal nanoparticles can be formed through this emulsion based bottom up process. (c) and (d) Zoomed in and rotated TEM micrographs of the particle demonstrate how the gold acts as a surfactant for only one of the two polymer layers. (e) and (f) Cross-sections of the particle at different orientations illustrate the localization of the gold nanoparticle surfactant to the outside of the stripped ellipsoidal nanoparticle. Adapted with permission from ref 34.

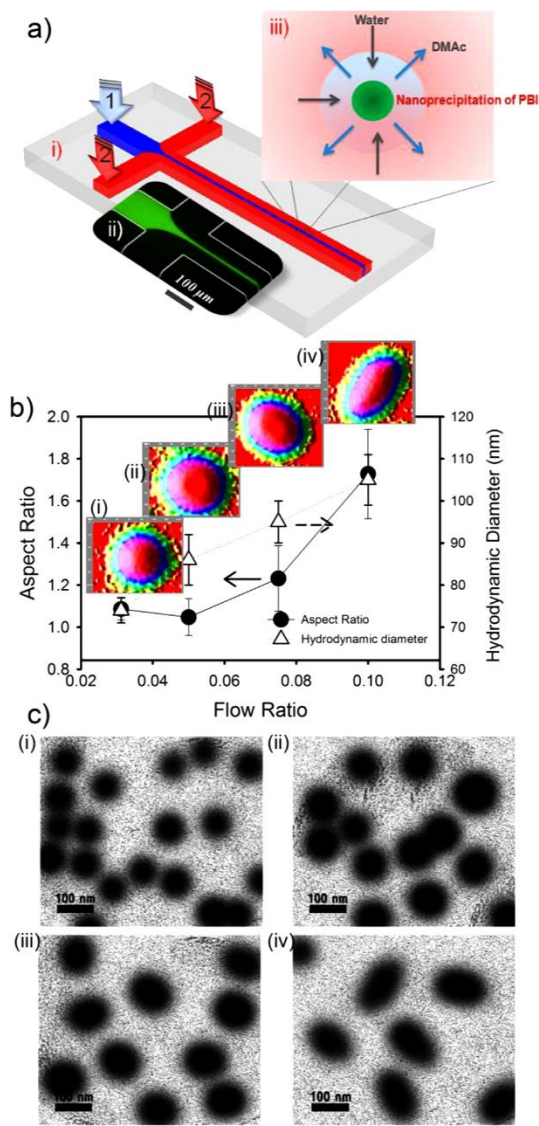


Figure 2.4: Nonspherical polymeric nanoparticles can be synthesized by nanoprecipitation of polymer in a focus flow microfluidic device. (a) A solution of polymer is injected into the inlet along with two other flanking streams to focus polymer solution. Subsequent solvent exchange results in the nanoprecipitation of particles. (b) By controlling the ratio of focus solution flow and polymer solution flow, the aspect ratio and size of the nanoparticles can be tuned as desired. (c) TEM images of particles produced with increasing flow ratios of the two inlet solutions. Non-spherical particles of nanoscale size are successfully produced by this method. Adapted with permission from ref 47.

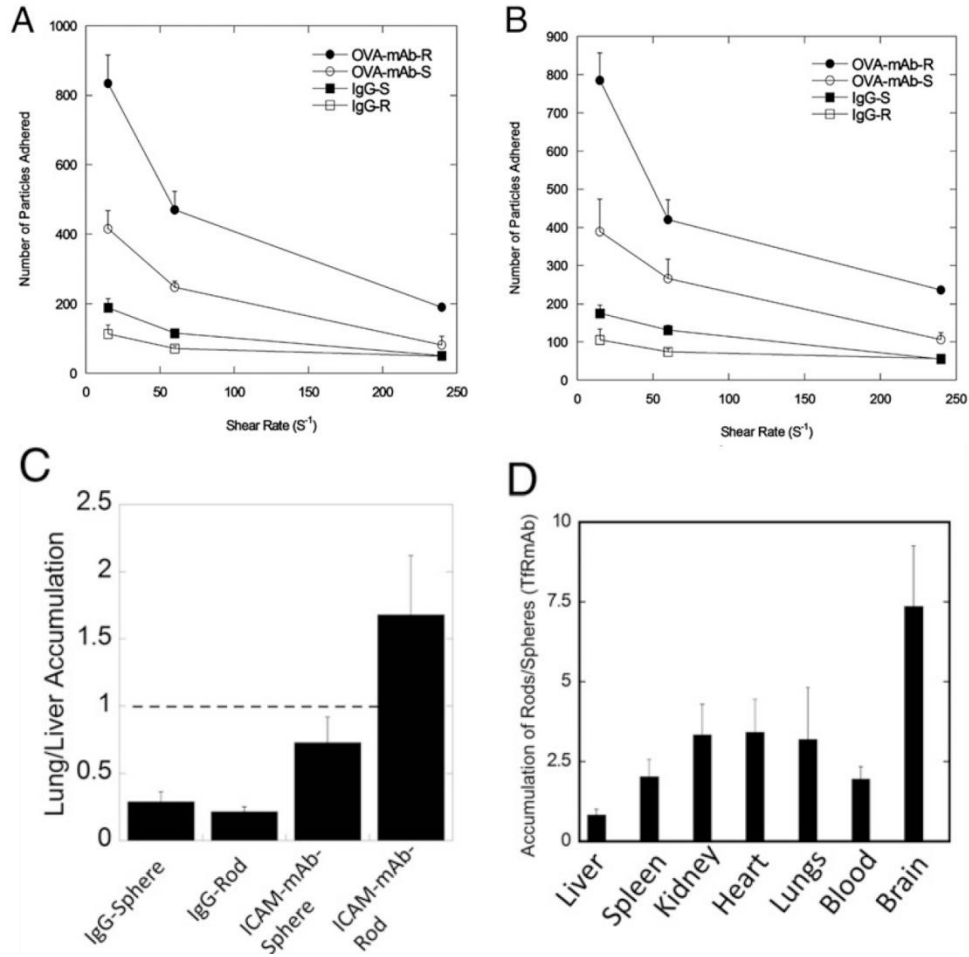


Figure 2.5: Non-spherical particles mediate better specific adhesion under flow and enable enhanced *in vivo* targeting. (a) Number of particles adhered at the inlet of a microfluidic device of targeted (OVA-mAb) and nontargeted (IgG) rods (R) and spheres (S) under different shear rates. (b) Number of particles attached at the bifurcation of the device to simulate the bifurcation of a blood vessel. Increased specific adhesion and decreased non-specific adhesion are evident for rods vs. spheres. (c) Increased accumulation of ICAM targeted rods in the liver compared to spheres measured by lung to liver accumulation ratio. (d) Increased ratio of rod shaped transferrin receptor targeted particle to equivalent spherical particle accumulation in the brain indicates enhanced *in vivo* targeting capabilities of rods compared to spheres. Adapted with permission from ref 67.

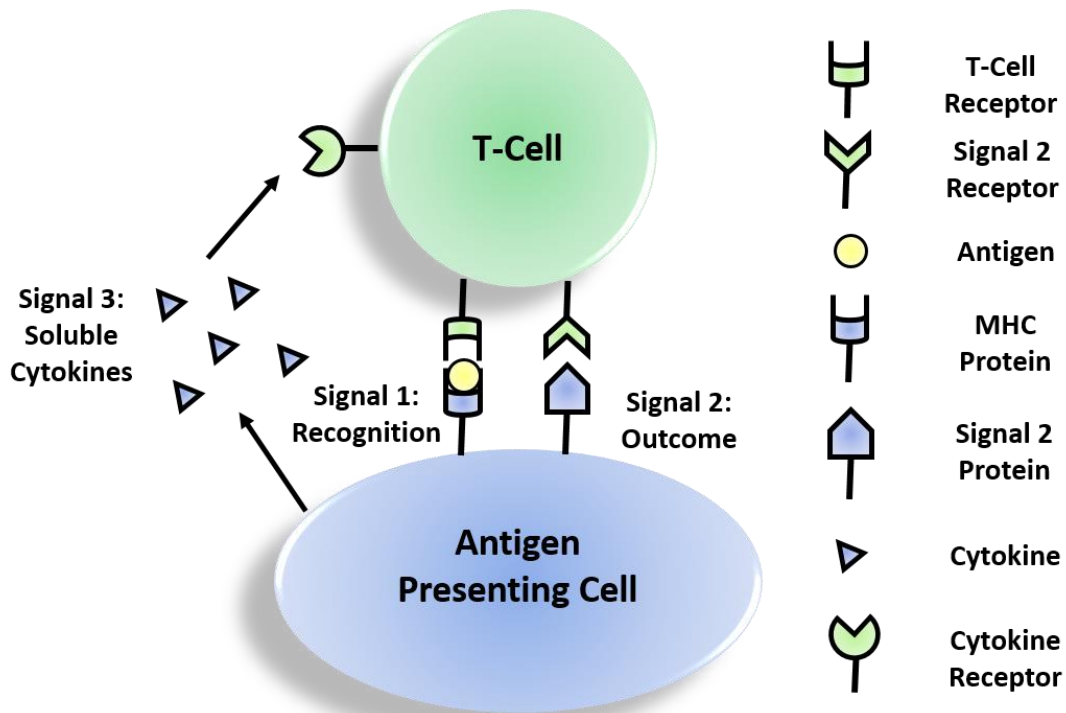


Figure 2.6: The natural APC relays several signals to T-Cells to decide the fate of the interaction. Signal 1 is what is used in APC/T-Cell recognition and ensures antigen specificity in the APC's effect on the immune system. Typically it is mediated by the surface bound TCR on the T-Cell and the antigen bound to the MHC on the surface of the antigen presenting cell. Signal 2 determines the overall outcome of the interaction. This can be used to activate the T-Cell to proliferate and target the antigen in question, become anergic or apathetic to the antigen presented, or differentiate into a regulatory T-Cell to actively suppress an immune response to that antigen. Signal 2 is mediated by a variety of surface bound proteins. Signal 3 consists of soluble cytokines released by the T-Cell during the interaction and provides further direction for the nature of the T-Cell response.

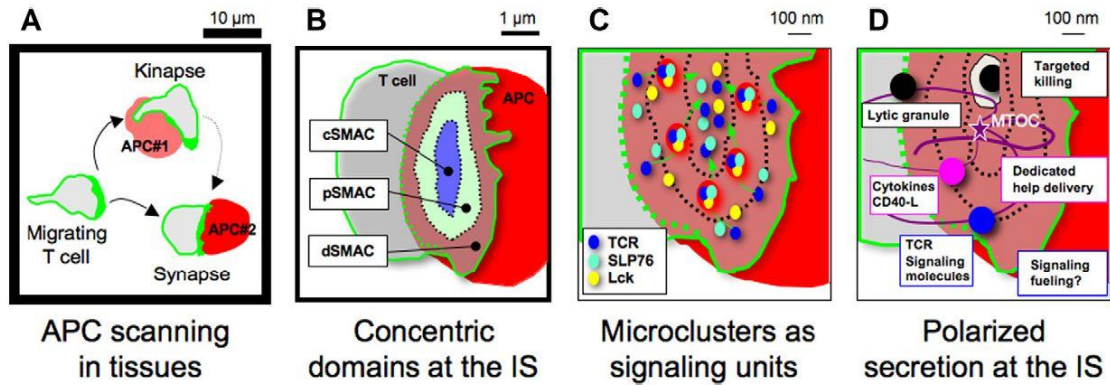


Figure 2.7: The natural APC/T-Cell interaction is a dynamic process at the cellular and molecular level. (A) Natural T-Cells will rapidly scan through multiple antigen presenting cells through the formation of immune kinapses. If there is sufficient compatibility between the T-Cell and the APC, the two cells will form a much tighter interaction termed the immunological synapse. (B) The immunological synapse consist of three concentric domains of surface receptor termed the cSMAC, dSMAC, and pSMAC. (C) Productive T-Cell signaling begins as microclusters of TCRs and various signaling proteins form in the dSMAC, bind to the APC, and are transported to the cSMAC where signaling ends. (D) After interaction with an APC, the T-Cell will polarize its secretory vesicles to the site of the IS formation to allow for either targeted killing or targeted delivery of helper cytokines. Adapted with permission from ref 98.

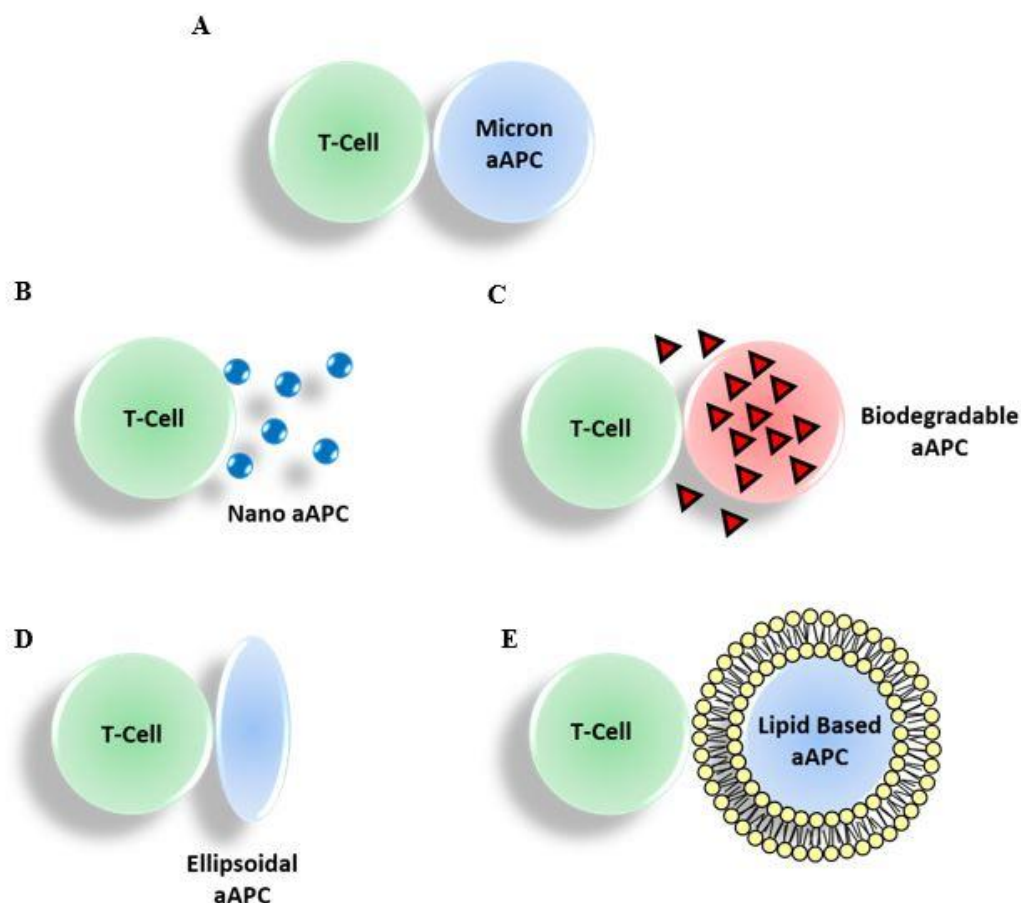


Figure 2.8: Various parameters have been considered in the design of an optimal aAPC. (A) The classic aAPC consists of a micron scale artificial bead bound to surface proteins to serve as Signal 1 and Signal 2. (B) Newer aAPC designs have focused on the use of nanoparticles as a scaffold for immune protein immobilization. Although not as efficient as microparticles at stimulating T-Cells, the nano aAPC has the added benefit of more favorable *in vivo* properties such as biodistribution. (C) Classic aAPC platforms utilized spherical microparticles whereas new data suggests that a non-spherical shape such as an ellipsoid is preferable due to the higher radius of curvature for aAPC interaction. (D) Biodegradable aAPCs can be used to enable local delivery of costimulatory cytokines and Signal 3. (E) New aAPC designs can enable the dynamic rearrangement of surface proteins through the use of lipid based aAPCs either with liposomes or supported lipid bilayers.

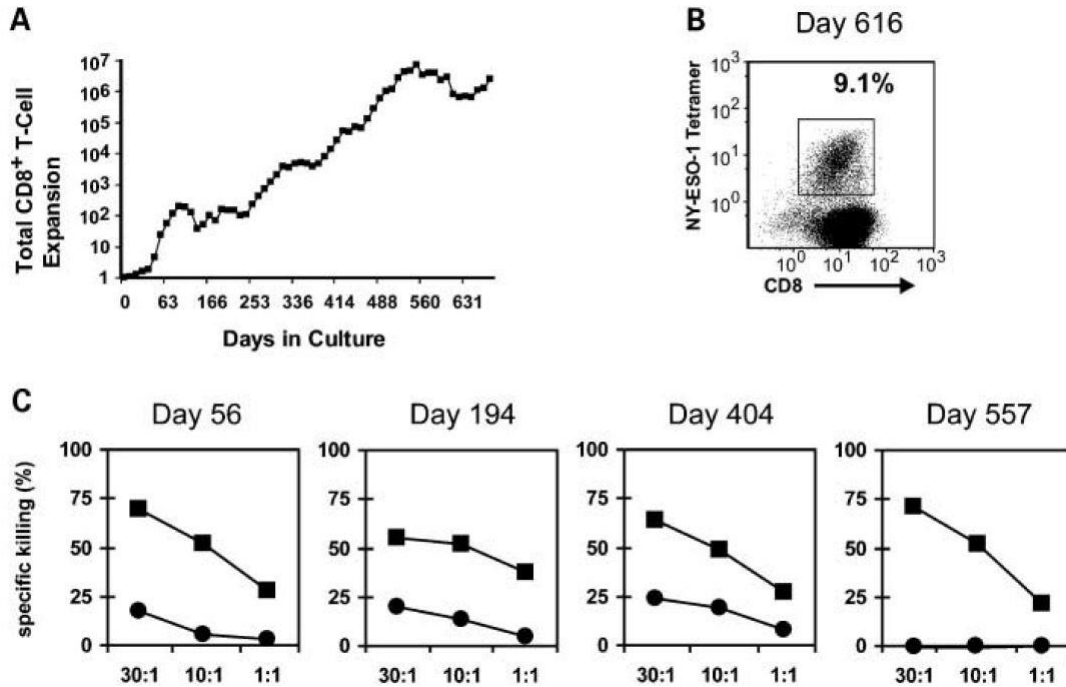


Figure 2.9: Cellular aAPCs have demonstrated the potential to generate long lasting, anti-tumor T-Cell responses. (A) Human CD8⁺ T-Cells were stimulated with the K532 aAPC cell line over the course of nearly 2 years and proliferation was noted to be more than 1,000,000 fold over this time period. (B) MHC tetramer staining demonstrates an antigen specific enrichment of T-Cells directed toward human cancer antigen NY-ESO-1. (C) T-Cell effector function was evaluated over the 2 year stimulation period and expanded T-Cells were able to maintain their antigen targeted killing effector function during the entire time of stimulation. Adapted with permission from ref 126.

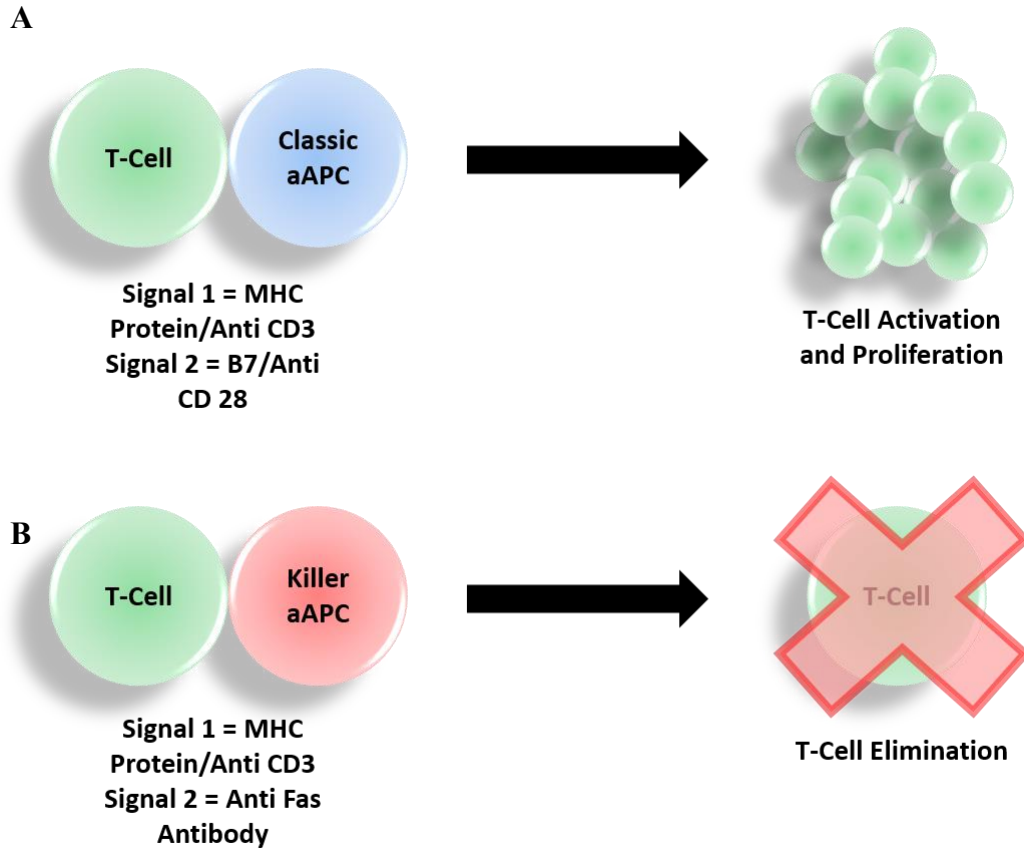


Figure 2.10: aAPCs can be applied to modulate many aspects of the immune system similar to natural APCs. (A) Traditional aAPCs incorporate recognition Signal 1 proteins as well as costimulatory Signal 2 molecules such as recombinant B7 or anti-CD28. The result is T-Cell activation and proliferation. (B) aAPCs can also be used to down regulate the immune response. By maintaining the same Signal 1 proteins, and changing the Signal 2 protein to be an apoptosis inducing ligand, aAPCs can be used to deplete T-Cells in an antigen specific/non-specific manner.

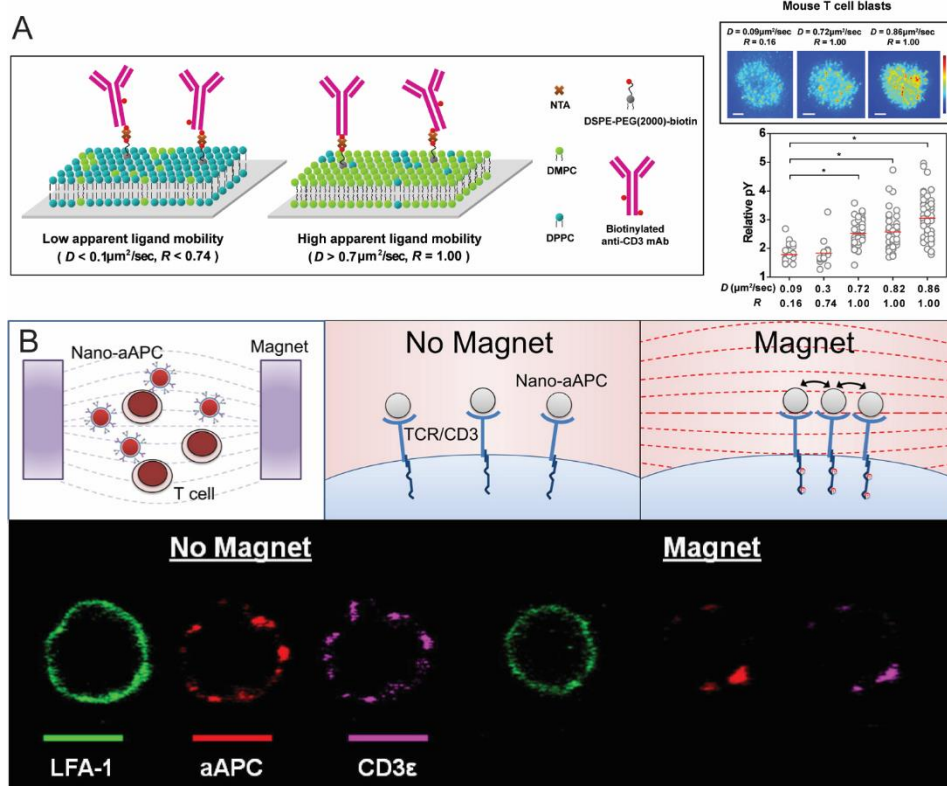


Figure 2.12. Receptor clustering is critical for T cell activation. (A) Supported lipid bilayers conjugated with biotinylated anti-CD3 mAb via NTA (neutravidin) were synthesized with different compositions of DMPC (1,2-dimyristoyl-sn-glycero-3-phosphocholine) and DPPC (1,2-dipalmitoyl-sn-glycero-3-phosphocholine) to produce ligand mobility. SLBs with a higher diffusion coefficient (D), which corresponds to greater ligand mobility, induced higher levels of TCR signaling. Adapted with permission from ref 171 (B) Paramagnetic nano-aAPC induce clustering of the TCR/CD3 complex on T cells under the influence of a magnetic field. Adapted with permission from ref 122.

2.7 References

1. Farokhzad, O.C. Langer, R. Nanomedicine: developing smarter therapeutic and diagnostic modalities. *Adv. Drug Deliver. Rev.* 2006;58(14):1456-9.
2. Cheng, R., Meng, F., Deng, C., Klok, H.-A. Zhong, Z. Dual and multi-stimuli responsive polymeric nanoparticles for programmed site-specific drug delivery. *Biomaterials* 2013;34(14):3647-57.
3. Brannon-Peppas, L. Blanchette, J.O. Nanoparticle and targeted systems for cancer therapy. *Adv. Drug Deliver. Rev.* 2012;64:206-12.
4. Colson, Y.L. Grinstaff, M.W. Biologically responsive polymeric nanoparticles for drug delivery. *Adv. Mater.* 2012;24(28):3878-86.
5. Shokeen, M., Pressly, E.D., Hagooly, A., Zheleznyak, A., Ramos, N., Fiamengo, A.L., Welch, M.J., Hawker, C.J. Anderson, C.J. Evaluation of multivalent, functional polymeric nanoparticles for imaging applications. *ACS Nano* 2011;5(2):738-47.
6. Vollrath, A., Schubert, S. Schubert, U.S. Fluorescence imaging of cancer tissue based on metal-free polymeric nanoparticles—a review. *J. Mater. Chem. B* 2013;1(15):1994-2007.
7. Choi, K.Y., Liu, G., Lee, S. Chen, X. Theranostic nanoplatforms for simultaneous cancer imaging and therapy: current approaches and future perspectives. *Nanoscale* 2012;4(2):330-42.
8. Rao, J.P. Geckeler, K.E. Polymer nanoparticles: preparation techniques and size-control parameters. *Prog. Polym. Sci.* 2011;36(7):887-913.
9. Bally, F., Garg, D.K., Serra, C.A., Hoarau, Y., Anton, N., Brochon, C., Parida, D., Vandamme, T. Hadziioannou, G. Improved size-tunable preparation of polymeric nanoparticles by microfluidic nanoprecipitation. *Polymer* 2012;53(22):5045-51.
10. Chen, S., Cheng, S.X. Zhuo, R.X. Self-Assembly Strategy for the Preparation of Polymer-Based Nanoparticles for Drug and Gene Delivery. *Macromol. Biosci.* 2011;11(5):576-89.
11. Lerch, S., Dass, M., Musyanovych, A., Landfester, K. Mailänder, V. Polymeric nanoparticles of different sizes overcome the cell membrane barrier. *Eur. J. Pharm. Biopharm.* 2013;84(2):265-74.
12. Walkey, C.D., Olsen, J.B., Guo, H., Emili, A. Chan, W.C. Nanoparticle size and surface chemistry determine serum protein adsorption and macrophage uptake. *J. Am. Chem. Soc.* 2012;134(4):2139-47.
13. Kulkarni, S.A. Feng, S.-S. Effects of particle size and surface modification on cellular uptake and biodistribution of polymeric nanoparticles for drug delivery. *Pharm. Res.* 2013;30(10):2512-22.
14. Tao, L., Hu, W., Liu, Y., Huang, G., Sumer, B.D. Gao, J. Shape-specific polymeric nanomedicine: emerging opportunities and challenges. *Exp. Biol. Med. (Maywood)* 2011;236(1):20-9.
15. Falchi, F., Caporuscio, F. Recanatini, M. Structure-based design of small-molecule protein–protein interaction modulators: the story so far. *Future Med. Chem.* 2014;6(3):343-57.
16. Fletcher, D.A. Mullins, R.D. Cell mechanics and the cytoskeleton. *Nature* 2010;463(7280):485.

17. Bidan, C.M., Kommareddy, K.P., Rumpler, M., Kollmannsberger, P., Fratzl, P. Dunlop, J.W. Geometry as a factor for tissue growth: towards shape optimization of tissue engineering scaffolds. *Adv. Healthcare Mater.* 2013;2(1):186-94.
18. Champion, J.A., Katare, Y.K. Mitragotri, S. Particle shape: a new design parameter for micro-and nanoscale drug delivery carriers. *J. Control. Release* 2007;121(1-2):3-9.
19. Murphy, C.J., Sau, T.K., Gole, A.M., Orendorff, C.J., Gao, J., Gou, L., Hunyadi, S.E. Li, T. Anisotropic metal nanoparticles: synthesis, assembly, and optical applications. *J. Phys. Chem. B* 2005;109:13857-70.
20. Ho, C., Keller, A., Odell, J. Ottewill, R. Preparation of monodisperse ellipsoidal polystyrene particles. *Colloid Polym. Sci.* 1993;271(5):469-79.
21. Champion, J.A., Katare, Y.K. Mitragotri, S. Making polymeric micro-and nanoparticles of complex shapes. *Proc. Natl. Acad. Sci. U. S. A.* 2007;104(29):11901-4.
22. Yoo, J.-W. Mitragotri, S. Polymer particles that switch shape in response to a stimulus. *Proc. Natl. Acad. Sci. U. S. A.* 2010;107(25):11205-10.
23. Wischke, C., Schossig, M. Lendlein, A. Shape-Memory Effect of Micro-/Nanoparticles from Thermoplastic Multiblock Copolymers. *Small* 2014;10(1):83-7.
24. Rolland, J.P., Maynor, B.W., Euliss, L.E., Exner, A.E., Denison, G.M. DeSimone, J.M. Direct fabrication and harvesting of monodisperse, shape-specific nanobiomaterials. *J. Am. Chem. Soc.* 2005;127(28):10096-100.
25. Wang, Y., Merkel, T.J., Chen, K., Fromen, C.A., Betts, D.E. DeSimone, J.M. Generation of a library of particles having controlled sizes and shapes via the mechanical elongation of master templates. *Langmuir* 2010;27(2):524-8.
26. Morton, S.W., Herlihy, K.P., Shopsowitz, K.E., Deng, Z.J., Chu, K.S., Bowerman, C.J., DeSimone, J.M. Hammond, P.T. Scalable Manufacture of Built-to-Order Nanomedicine: Spray-Assisted Layer-by-Layer Functionalization of PRINT Nanoparticles. *Adv. Mater.* 2013;25(34):4707-13.
27. Cayre, O., Paunov, V.N. Velev, O.D. Fabrication of dipolar colloid particles by microcontact printing. *Chem. Comm.* 2003;18):2296-7.
28. Snyder, C.E., Yake, A.M., Feick, J.D. Velegol, D. Nanoscale functionalization and site-specific assembly of colloids by particle lithography. *Langmuir* 2005;21(11):4813-5.
29. Zhang, G., Wang, D. Möhwald, H. Patterning microsphere surfaces by templating colloidal crystals. *Nano Lett.* 2005;5(1):143-6.
30. Buyukserin, F., Aryal, M., Gao, J. Hu, W. Fabrication of polymeric nanorods using bilayer nanoimprint lithography. *Small* 2009;5(14):1632-6.
31. Glangchai, L.C., Caldorera-Moore, M., Shi, L. Roy, K. Nanoimprint lithography based fabrication of shape-specific, enzymatically-triggered smart nanoparticles. *J. Control. Release* 2008;125(3):263-72.
32. Jiang, X., Leong, D., Ren, Y., Li, Z., Torbenson, M.S. Mao, H.-Q. String-like micellar nanoparticles formed by complexation of PEG-b-PPA and plasmid DNA and their transfection efficiency. *Pharm. Res.* 2011;28(6):1317-27.

33. Petzetakis, N., Dove, A.P. O'Reilly, R.K. Cylindrical micelles from the living crystallization-driven self-assembly of poly (lactide)-containing block copolymers. *Chem. Sci.* 2011;2(5):955-60.
34. Jang, S.G., Audus, D.J., Klinger, D., Krogstad, D.V., Kim, B.J., Cameron, A., Kim, S.-W., Delaney, K.T., Hur, S.-M. Killops, K.L. Striped, ellipsoidal particles by controlled assembly of diblock copolymers. *J. Am. Chem. Soc.* 2013;135(17):6649-57.
35. Kaewsaneha, C., Tangboriboonrat, P., Polpanich, D., Eissa, M. Elaissari, A. Anisotropic janus magnetic polymeric nanoparticles prepared via miniemulsion polymerization. *J. Polym. Sci. Part A: Polym. Chem.* 2013;51(22):4779-85.
36. Mondiot, F.d.r., Wang, X., de Pablo, J.J. Abbott, N.L. Liquid crystal-based emulsions for synthesis of spherical and non-spherical particles with chemical patches. *J. Am. Chem. Soc.* 2013;135(27):9972-5.
37. Park, J.-G., Forster, J.D. Dufresne, E.R. High-yield synthesis of monodisperse dumbbell-shaped polymer nanoparticles. *J. Am. Chem. Soc.* 2010;132(17):5960-1.
38. Niu, Q., Pan, M., Yuan, J., Liu, X., Wang, X. Yu, H. Anisotropic Nanoparticles with Controllable Morphologies from Non-Cross-Linked Seeded Emulsion Polymerization. *Macromol. Rapid Comm.* 2013;34(17):1363-7.
39. Yang, Z., Huck, W.T., Clarke, S.M., Tajbakhsh, A.R. Terentjev, E.M. Shape-memory nanoparticles from inherently non-spherical polymer colloids. *Nature materials* 2005;4(6):486.
40. Klinger, D., Wang, C.X., Connal, L.A., Audus, D.J., Jang, S.G., Kraemer, S., Killops, K.L., Fredrickson, G.H., Kramer, E.J. Hawker, C.J. A Facile Synthesis of Dynamic, Shape-Changing Polymer Particles. *Angew. Chemie Int. Ed.* 2014;53(27):7018-22.
41. Doshi, N., Zahr, A.S., Bhaskar, S., Lahann, J. Mitragotri, S. Red blood cell-mimicking synthetic biomaterial particles. *Proc. Natl. Acad. Sci. U. S. A.* 2009;106(51):21495-9.
42. Zhou, Z., Anselmo, A.C. Mitragotri, S. Synthesis of Protein-Based, Rod-Shaped Particles from Spherical Templates using Layer-by-Layer Assembly. *Adv. Mater.* 2013;25(19):2723-7.
43. Shum, H.C., Abate, A.R., Lee, D., Studart, A.R., Wang, B., Chen, C.H., Thiele, J., Shah, R.K., Krummel, A. Weitz, D.A. Droplet microfluidics for fabrication of non-spherical particles. *Macromol. Rapid Comm.* 2010;31(2):108-18.
44. Luo, G., Du, L., Wang, Y., Lu, Y. Xu, J. Controllable preparation of particles with microfluidics. *Particuology* 2011;9(6):545-58.
45. Yang, S., Guo, F., Kiraly, B., Mao, X., Lu, M., Leong, K.W. Huang, T.J. Microfluidic synthesis of multifunctional Janus particles for biomedical applications. *Lab Chip* 2012;12(12):2097-102.
46. Roh, K.-H., Martin, D.C. Lahann, J. Biphasic Janus particles with nanoscale anisotropy. *Nat. Mater.* 2005;4(10):759.
47. Hwang, S., Roh, K.-H., Lim, D.W., Wang, G., Uher, C. Lahann, J. Anisotropic hybrid particles based on electrohydrodynamic co-jetting of nanoparticle suspensions. *Phys. Chem. Chem. Phys.* 2010;12(38):11894-9.

48. Lan, W., Li, S., Xu, J. Luo, G. A one-step microfluidic approach for controllable preparation of nanoparticle-coated patchy microparticles. *Microfluid. Nanofluid.* 2012;13(3):491-8.
49. Hasani-Sadrabadi, M.M., Majedi, F.S., VanDersarl, J.J., Dashtimoghadam, E., Ghaffarian, S.R., Bertsch, A., Moaddel, H. Renaud, P. Morphological tuning of polymeric nanoparticles via microfluidic platform for fuel cell applications. *J. Am. Chem. Soc.* 2012;134(46):18904-7.
50. Suh, S.K., Yuet, K., Hwang, D.K., Bong, K.W., Doyle, P.S. Hatton, T.A. Synthesis of nonspherical superparamagnetic particles: in situ coprecipitation of magnetic nanoparticles in microgels prepared by stop-flow lithography. *J. Am. Chem. Soc.* 2012;134(17):7337-43.
51. Angly, J., Iazzolino, A., Salmon, J.-B., Leng, J., Chandran, S.P., Ponsinet, V., Désert, A., Le Beulze, A.I., Mornet, S.p. Tr guer-Delapierre, M. Microfluidic-induced growth and shape-up of three-dimensional extended arrays of densely packed nanoparticles. *ACS Nano* 2013;7(8):6465-77.
52. Mathaes, R., Winter, G., Engert, J. Besheer, A. Application of different analytical methods for the characterization of non-spherical micro-and nanoparticles. *Int. J. Pharm.* 2013;453(2):620-9.
53. Wang, A., Dimiduk, T.G., Fung, J., Razavi, S., Kretzschmar, I., Chaudhary, K. Manoharan, V.N. Using the discrete dipole approximation and holographic microscopy to measure rotational dynamics of non-spherical colloidal particles. *J. Quant. Spectrosc. Radiat. Transfer* 2014;146(499-509).
54. Zhang, B., Lan, T., Huang, X., Dong, C. Ren, J. Sensitive single particle method for characterizing rapid rotational and translational diffusion and aspect ratio of anisotropic nanoparticles and its application in immunoassays. *Anal. Chem.* 2013;85(20):9433-8.
55. Li, M., You, R., Mulholland, G.W. Zachariah, M.R. Development of a pulsed-field differential mobility analyzer: a method for measuring shape parameters for nonspherical particles. *Aerosol Sci. Tech.* 2014;48(1):22-30.
56. Toy, R., Peiris, P.M., Ghaghada, K.B. Karathanasis, E. Shaping cancer nanomedicine: the effect of particle shape on the in vivo journey of nanoparticles. *Nanomedicine* 2014;9(1):121-34.
57. Sharma, G., Valenta, D.T., Altman, Y., Harvey, S., Xie, H., Mitragotri, S. Smith, J.W. Polymer particle shape independently influences binding and internalization by macrophages. *J. Control. Rel.* 2010;147(3):408-12.
58. Florez, L., Herrmann, C., Cramer, J.M., Hauser, C.P., Koynov, K., Landfester, K., Crespy, D. Mailänder, V. How shape influences uptake: interactions of anisotropic polymer nanoparticles and human mesenchymal stem cells. *Small* 2012;8(14):2222-30.
59. Champion, J.A. Mitragotri, S. Role of target geometry in phagocytosis. *Proc. Natl. Acad. Sci. U. S. A.* 2006;103(13):4930-4.
60. Dasgupta, S., Auth, T. Gompper, G. Shape and orientation matter for the cellular uptake of nonspherical particles. *Nano Lett.* 2014;14(2):687-93.
61. Gratton, S.E., Ropp, P.A., Pohlhaus, P.D., Luft, J.C., Madden, V.J., Napier, M.E. DeSimone, J.M. The effect of particle design on cellular internalization pathways. *Proc. Natl. Acad. Sci. U. S. A.* 2008;105(33):11613-8.

62. Kim, J., Sunshine, J.C. Green J.J. Differential polymer structure tunes mechanism of cellular uptake and transfection routes of poly (β -amino ester) polyplexes in human breast cancer cells. *Bioconjugate Chem.* 2013;25(1):43-51.
63. Perry, J.L., Reuter, K.G., Kai, M.P., Herlihy, K.P., Jones, S.W., Luft, J.C., Napier, M., Bear, J.E. DeSimone, J.M. PEGylated PRINT nanoparticles: the impact of PEG density on protein binding, macrophage association, biodistribution, and pharmacokinetics. *Nano Lett.* 2012;12(10):5304-10.
64. Barua, S., Yoo, J.-W., Kolhar, P., Wakankar, A., Gokarn, Y.R. Mitragotri, S. Particle shape enhances specificity of antibody-displaying nanoparticles. *Proc. Natl. Acad. Sci. U. S. A.* 2013;110(9):3270-5.
65. Adriani, G., de Tullio, M.D., Ferrari, M., Hussain, F., Pascazio, G., Liu, X. Decuzzi, P. The preferential targeting of the diseased microvasculature by disk-like particles. *Biomaterials* 2012;33(22):5504-13.
66. Muro, S., Garnacho, C., Champion, J.A., Leferovich, J., Gajewski, C., Schuchman, E.H., Mitragotri, S. Muzykantov, V.R. Control of endothelial targeting and intracellular delivery of therapeutic enzymes by modulating the size and shape of ICAM-1-targeted carriers. *Mol. Ther.* 2008;16(8):1450-8.
67. Kolhar, P., Anselmo, A.C., Gupta, V., Pant, K., Prabhakarparandian, B., Ruoslahti, E. Mitragotri, S. Using shape effects to target antibody-coated nanoparticles to lung and brain endothelium. *Proc. Natl. Acad. Sci. U. S. A.* 2013;110(26):10753-8.
68. Hasan, W., Chu, K., Gullapalli, A., Dunn, S.S., Enlow, E.M., Luft, J.C., Tian, S., Napier, M.E., Pohlhaus, P.D. Rolland, J.P. Delivery of multiple siRNAs using lipid-coated PLGA nanoparticles for treatment of prostate cancer. *Nano Lett.* 2011;12(1):287-92.
69. Xu, J., Luft, J.C., Yi, X., Tian, S., Owens, G., Wang, J., Johnson, A., Berglund, P., Smith, J. Napier, M.E. RNA replicon delivery via lipid-complexed PRINT protein particles. *Mol. Pharm.* 2013;10(9):3366-74.
70. Chu, K.S., Hasan, W., Rawal, S., Walsh, M.D., Enlow, E.M., Luft, J.C., Bridges, A.S., Kuijter, J.L., Napier, M.E. Zamboni, W.C. Plasma, tumor and tissue pharmacokinetics of Docetaxel delivered via nanoparticles of different sizes and shapes in mice bearing SKOV-3 human ovarian carcinoma xenograft. *Nanomedicine* 2013;9(5):686-93.
71. Chu, K.S., Finnis, M.C., Schorzman, A.N., Kuijter, J.L., Luft, J.C., Bowerman, C.J., Napier, M.E., Haroon, Z.A., Zamboni, W.C. DeSimone, J.M. Particle replication in nonwetting templates nanoparticles with tumor selective alkyl silyl ether docetaxel prodrug reduces toxicity. *Nano Lett.* 2014;14(3):1472-6.
72. Chen, K., Merkel, T.J., Pandya, A., Napier, M.E., Luft, J.C., Daniel, W., Sheiko, S. DeSimone, J.M. Low modulus biomimetic microgel particles with high loading of hemoglobin. *Biomacromolecules* 2012;13(9):2748-59.
73. Merkel, T.J., Jones, S.W., Herlihy, K.P., Kersey, F.R., Shields, A.R., Napier, M., Luft, J.C., Wu, H., Zamboni, W.C. Wang, A.Z. Using mechanobiological mimicry of red blood cells to extend circulation times of hydrogel microparticles. *Proc. Natl. Acad. Sci. U. S. A.* 2011;108(2):586-91.

74. Jiang, X., Qu, W., Pan, D., Ren, Y., Williford, J.M., Cui, H., Luijten, E. Mao, H.Q. Plasmid-templated shape control of condensed DNA–block copolymer nanoparticles. *Adv. Mater.* 2013;25(2):227-32.
75. Karagoz, B., Esser, L., Duong, H.T., Basuki, J.S., Boyer, C. Davis, T.P. Polymerization-Induced Self-Assembly (PISA)–control over the morphology of nanoparticles for drug delivery applications. *Polym. Chem.* 2014;5(2):350-5.
76. Geng, Y., Dalhaimer, P., Cai, S., Tsai, R., Tewari, M., Minko, T. Discher, D.E. Shape effects of filaments versus spherical particles in flow and drug delivery. *Nat. Nanotechnol.* 2007;2(4):249.
77. Dvir, T., Timko, B.P., Kohane, D.S. Langer, R. Nanotechnological strategies for engineering complex tissues. *Nat. Nanotechnol.* 2011;6(1):13.
78. Zhang, S. Uludağ, H. Nanoparticulate systems for growth factor delivery. *Pharm. Res.* 2009;26(7):1561.
79. Kim, H.N., Jiao, A., Hwang, N.S., Kim, M.S., Kim, D.-H. Suh, K.-Y. Nanotopography-guided tissue engineering and regenerative medicine. *Adv. Drug Deliver. Rev.* 2013;65(4):536-58.
80. Kim, E.-S., Ahn, E.H., Dvir, T. Kim, D.-H. Emerging nanotechnology approaches in tissue engineering and regenerative medicine. *Int. J. Nanomed.* 2014;9(Suppl 1):1.
81. Hopley, E.L., Salmasi, S., Kalaskar, D.M. Seifalian, A.M. Carbon nanotubes leading the way forward in new generation 3D tissue engineering. *Biotechnol. Adv.* 2014;32(5):1000-14.
82. Rim, N.G., Shin, C.S. Shin, H. Current approaches to electrospun nanofibers for tissue engineering. *Biomed. Mater.* 2013;8(1):014102.
83. Roohani-Esfahani, S.-I., Nouri-Khorasani, S., Lu, Z., Appleyard, R. Zreiqat, H. The influence hydroxyapatite nanoparticle shape and size on the properties of biphasic calcium phosphate scaffolds coated with hydroxyapatite–PCL composites. *Biomaterials* 2010;31(21):5498-509.
84. Delsing, C.E., Gresnigt, M.S., Leentjens, J., Preijers, F., Frager, F.A., Kox, M., Monneret, G., Venet, F., Bleeker-Rovers, C.P. van de Veerdonk, F.L. Interferon-gamma as adjunctive immunotherapy for invasive fungal infections: a case series. *BMC Infect. Dis.* 2014;14(1):166.
85. Lodhi, S., Lamb, K. Meier-Kriesche, H. Solid Organ Allograft Survival Improvement in the United States: The Long-Term Does Not Mirror the Dramatic Short-Term Success. *Am. J. Transplant.* 2011;11(6):1226-35.
86. Cheever, M.A. Higano, C.S. PROVENGE (Sipuleucel-T) in prostate cancer: the first FDA-approved therapeutic cancer vaccine. *Clin. Cancer Res.* 2011;17(11):3520-6.
87. Oelke, M., Krueger, C., Giuntoli II, R.L. Schneck, J.P. Artificial antigen-presenting cells: artificial solutions for real diseases. *Trend. Mol. Med.* 2005;11(9):412-20.
88. Knight, S.C. Stagg, A.J. Antigen-presenting cell types. *Curr. Opin. Immunol.* 1993;5(3):374-82.
89. Rossi, M. Young, J.W. Human dendritic cells: potent antigen-presenting cells at the crossroads of innate and adaptive immunity. *J. Immunol.* 2005;175(3):1373-81.

90. Ohteki, T. Koyasu, S. Role of antigen-presenting cells in innate immune system. *Arch. Immunol. Ther. Ex.* 2001;49(S47-S52).
91. Adalid-Peralta, L., Fragoso, G., Fleury, A. Sciutto, E. Mechanisms underlying the induction of regulatory T cells and its relevance in the adaptive immune response in parasitic infections. *Int. J. Biol. Sci.* 2011;7(9):1412.
92. Gascoigne, N.R. Zal, T. Molecular interactions at the T cell–antigen-presenting cell interface. *Curr. Opin. Immunol.* 2004;16(1):114-9.
93. Capece, D., Verzella, D., Fischietti, M., Zazzeroni, F. Alesse, E. Targeting costimulatory molecules to improve antitumor immunity. *Biomed. Res. Int.* 2012;2012
94. Von Bubnoff, D., De La Salle, H., Wessendorf, J., Koch, S., Hanau, D. Bieber, T. Antigen-presenting cells and tolerance induction. *Allergy* 2002;57(1):2-8.
95. Kaliński, P., Hilken, C.M., Wierenga, E.A. Kapsenberg, M.L. T-cell priming by type-1 and type-2 polarized dendritic cells: the concept of a third signal. *Immunol. Today* 1999;20(12):561-7.
96. Kalinski, P. Dendritic cells in immunotherapy of established cancer: Roles of signals 1, 2, 3 and 4. *Curr. Opin. Infect. Dis.* 2009;10(6):526.
97. Alarcón, B., Mestre, D. Martínez-Martín, N. The immunological synapse: a cause or consequence of T-cell receptor triggering? *Immunology* 2011;133(4):420-5.
98. Valitutti, S., Coombs, D. Dupré, L. The space and time frames of T cell activation at the immunological synapse. *FEBS Lett.* 2010;584(24):4851-7.
99. Mescher, M. Surface contact requirements for activation of cytotoxic T lymphocytes. *J. Immunol.* 1992;149(7):2402-5.
100. Steenblock, E.R. Fahmy, T.M. A comprehensive platform for ex vivo T-cell expansion based on biodegradable polymeric artificial antigen-presenting cells. *Mol. Ther.* 2008;16(4):765-72.
101. Fifi, T., Gamvrellis, A., Crimeen-Irwin, B., Pietersz, G.A., Li, J., Mottram, P.L., McKenzie, I.F. Plebanski, M. Size-dependent immunogenicity: therapeutic and protective properties of nano-vaccines against tumors. *J. Immunol.* 2004;173(5):3148-54.
102. Sunshine, J.C., Perica, K., Schneck, J.P. Green, J.J. Particle shape dependence of CD8+ T cell activation by artificial antigen presenting cells. *Biomaterials* 2014;35(1):269-77.
103. Chacon, J.A., Wu, R.C., Sukhumalchandra, P., Molldrem, J.J., Sarnaik, A., Pilon-Thomas, S., Weber, J., Hwu, P. Radvanyi, L. Co-stimulation through 4-1BB/CD137 improves the expansion and function of CD8+ melanoma tumor-infiltrating lymphocytes for adoptive T-cell therapy. *PloS One* 2013;8(4):e60031.
104. Rudolf, D., Silberzahn, T., Walter, S., Maurer, D., Engelhard, J., Wernet, D., Bühring, H.-J., Jung, G., Kwon, B.S. Rammensee, H.-G. Potent costimulation of human CD8 T cells by anti-4-1BB and anti-CD28 on synthetic artificial antigen presenting cells. *Cancer Immunol. Immun.* 2008;57(2):175-83.
105. Matic, J., Deeg, J., Scheffold, A., Goldstein, I. Spatz, J.P. Fine tuning and efficient T cell activation with stimulatory aCD3 nanoarrays. *Nano Lett.* 2013;13(11):5090-7.
106. Ansén, S., Butler, M.O., Berezovskaya, A., Murray, A.P., Stevenson, K., Nadler, L.M. Hirano, N. Dissociation of its opposing immunologic effects is critical for

- the optimization of antitumor CD8⁺ T-cell responses induced by interleukin 21. *Clin. Cancer Res.* 2008;14(19):6125-36.
107. Steenblock, E.R., Fadel, T., Labowsky, M., Pober, J.S. Fahmy, T.M. An artificial antigen-presenting cell with paracrine delivery of IL-2 impacts the magnitude and direction of the T cell response. *J. Biol. Chem.* 2011;286(40):34883-92.
 108. Butler, M.O. Hirano, N. Human cell-based artificial antigen-presenting cells for cancer immunotherapy. *Immunol. Rev.* 2014;257(1):191-209.
 109. Butler, M.O., Ansén, S., Tanaka, M., Imataki, O., Berezovskaya, A., Mooney, M.M., Metzler, G., Milstein, M.I., Nadler, L.M. Hirano, N. A panel of human cell-based artificial APC enables the expansion of long-lived antigen-specific CD4⁺ T cells restricted by prevalent HLA-DR alleles. *Int. Immunol.* 2010;22(11):863-73.
 110. Maus, M.V., Thomas, A.K., Leonard, D.G., Allman, D., Addya, K., Schlienger, K., Riley, J.L. June, C.H. Ex vivo expansion of polyclonal and antigen-specific cytotoxic T lymphocytes by artificial APCs expressing ligands for the T-cell receptor, CD28 and 4-1BB. *Nat. Biotechnol.* 2002;20(2):143.
 111. Torikai, H., Reik, A., Liu, P.-Q., Zhou, Y., Zhang, L., Maiti, S., Huls, H., Miller, J.C., Kebriaei, P. Rabinovitch, B. A foundation for universal T-cell based immunotherapy: T cells engineered to express a CD19-specific chimeric-antigen-receptor and eliminate expression of endogenous TCR. *Blood* 2012;119(24):5697-705.
 112. Imai, C., Iwamoto, S. Campana, D. Genetic modification of primary natural killer cells overcomes inhibitory signals and induces specific killing of leukemic cells. *Blood* 2005;106(1):376-83.
 113. Sun, S., Cai, Z., Langlade-Demoyen, P., Kosaka, H., Brunmark, A., Jackson, M.R., Peterson, P.A. Sprent, J. Dual function of Drosophila cells as APCs for naive CD8⁺ T cells: implications for tumor immunotherapy. *Immunity* 1996;4(6):555-64.
 114. Latouche, J.-B. Sadelain, M. Induction of human cytotoxic T lymphocytes by artificial antigen-presenting cells. *Nat. Biotechnol.* 2000;18(4):405.
 115. Steenblock, E.R., Wrzesinski, S.H., Flavell, R.A. Fahmy, T.M. Antigen presentation on artificial acellular substrates: modular systems for flexible, adaptable immunotherapy. *Expert Opin. Biol. Th.* 2009;9(4):451-64.
 116. Turtle, C.J. Riddell, S.R. Artificial antigen presenting cells for use in adoptive immunotherapy. *Cancer J.* 2010;16(4):374.
 117. Tham, E.L., Jensen, P.L. Mescher, M.F. Activation of antigen-specific T cells by artificial cell constructs having immobilized multimeric peptide–class I complexes and recombinant B7–Fc proteins. *J. Immunol. Methods* 2001;249(1-2):111-9.
 118. Shalaby, W.S., Yeh, H., Woo, E., Corbett, J.T., Gray, H., June, C.H. Shalaby, S.W. Absorbable microparticulate cation exchanger for immunotherapeutic delivery. *J. Biomed. Mater. Res. Part B* 2004;69(2):173-82.
 119. Engelhard, V.H., Strominger, J.L., Mescher, M. Burakoff, S. Induction of secondary cytotoxic T lymphocytes by purified HLA-A and HLA-B antigens reconstituted into phospholipid vesicles. *Proc. Natl. Acad. of Sci. U. S. A.* 1978;75(11):5688-91.

120. Zappasodi, R., Di Nicola, M., Carlo-Stella, C., Mortarini, R., Molla, A., Vegetti, C., Albani, S., Anichini, A. Gianni, A.M. The effect of artificial antigen-presenting cells with preclustered anti-CD28/-CD3/-LFA-1 monoclonal antibodies on the induction of ex vivo expansion of functional human antitumor T cells. *Haematologica* 2008;93(10):1523-34.
121. Oelke, M., Maus, M.V., Didiano, D., June, C.H., Mackensen, A. Schneck, J.P. Ex vivo induction and expansion of antigen-specific cytotoxic T cells by HLA-Ig-coated artificial antigen-presenting cells. *Nat. Med.* 2003;9(5):619.
122. Perica, K., Tu, A., Richter, A., Bieler, J.G., Edidin, M. Schneck, J.P. Magnetic Field-Induced T Cell Receptor Clustering by Nanoparticles Enhances T Cell Activation and Stimulates Antitumor Activity. *ACS Nano* 2014;8(3):2252-60.
123. Fadel, T.R., Steenblock, E.R., Stern, E., Li, N., Wang, X., Haller, G.L., Pfefferle, L.D. Fahmy, T.M. Enhanced cellular activation with single walled carbon nanotube bundles presenting antibody stimuli. *Nano Lett.* 2008;8(7):2070-6.
124. Perica, K., Medero, A.D.L., Durai, M., Chiu, Y.L., Bieler, J.G., Sibener, L., Niemöller, M., Assenmacher, M., Richter, A. Edidin, M. Nanoscale artificial antigen presenting cells for T cell immunotherapy. *Nanomedicine* 2014;10(1):119-29.
125. Lu, X., Jiang, X., Liu, R., Zhao, H. Liang, Z. Adoptive transfer of pTRP2-specific CTLs expanding by bead-based artificial antigen-presenting cells mediates anti-melanoma response. *Cancer Lett.* 2008;271(1):129-39.
126. Butler, M.O., Lee, J.-S., Ansén, S., Neubergh, D., Hodi, F.S., Murray, A.P., Drury, L., Berezovskaya, A., Mulligan, R.C. Nadler, L.M. Long-lived antitumor CD8⁺ lymphocytes for adoptive therapy generated using an artificial antigen-presenting cell. *Clin. Cancer Res.* 2007;13(6):1857-67.
127. Walter, E.A., Greenberg, P.D., Gilbert, M.J., Finch, R.J., Watanabe, K.S., Thomas, E.D. Riddell, S.R. Reconstitution of cellular immunity against cytomegalovirus in recipients of allogeneic bone marrow by transfer of T-cell clones from the donor. *New Engl. J. Med.* 1995;333(16):1038-44.
128. Papanicolaou, G.A., Latouche, J.-B., Tan, C., Dupont, J., Stiles, J., Pamer, E.G. Sadelain, M. Rapid expansion of cytomegalovirus-specific cytotoxic T lymphocytes by artificial antigen-presenting cells expressing a single HLA allele. *Blood* 2003;102(7):2498-505.
129. Lu, X.-L., Liang, Z.-H., Zhang, C.-E., Lu, S.-J., Weng, X.-F. Wu, X.-W. Induction of the Epstein-Barr virus latent membrane protein 2 antigen-specific cytotoxic T lymphocytes using human leukocyte antigen tetramer-based artificial antigen-presenting cells. *Acta Biochim. Biophys. Sin.* 2006;38(3):157-63.
130. Brodie, S.J., Lewinsohn, D.A., Patterson, B.K., Jiyamapa, D., Krieger, J., Corey, L., Greenberg, P.D. Riddell, S.R. In vivo migration and function of transferred HIV-1-specific cytotoxic T cells. *Nat. Med.* 1999;5(1):34.
131. Schütz, C., Oelke, M., Schneck, J.P., Mackensen, A. Fleck, M. Killer artificial antigen-presenting cells: the synthetic embodiment of a 'guided missile'. *Immunotherapy* 2010;2(4):539-50.
132. Schutz, C., Fleck, M., Mackensen, A., Zoso, A., Halbritter, D., Schneck, J.P. Oelke, M. Killer-artificial-antigen-presenting-cells (KaAPC): a novel strategy to delete specific T cells. *Blood* 2007;

133. Lai, S.K., O'Hanlon, D.E., Harrold, S., Man, S.T., Wang, Y.Y., Cone, R. Hanes, J. Rapid transport of large polymeric nanoparticles in fresh undiluted human mucus. *Proc. Natl. Acad. Sci. U. S. A.* 2007;104(5):1482-7.
134. Gref, R., Luck, M., Quellec, P., Marchand, M., Dellacherie, E., Harnisch, S., Blunk, T. Muller, R.H. 'Stealth' corona-core nanoparticles surface modified by polyethylene glycol (PEG): influences of the corona (PEG chain length and surface density) and of the core composition on phagocytic uptake and plasma protein adsorption. *Colloid. Surf. B* 2000;18(3-4):301-13.
135. Rodriguez, P.L., Harada, T., Christian, D.A., Pantano, D.A., Tsai, R.K. Discher, D.E. Minimal "Self" peptides that inhibit phagocytic clearance and enhance delivery of nanoparticles. *Science* 2013;339(6122):971-5.
136. Sengupta, S., Eavarone, D., Capila, I., Zhao, G., Watson, N., Kiziltepe, T. Sasisekharan, R. Temporal targeting of tumour cells and neovasculature with a nanoscale delivery system. *Nature* 2005;436(7050):568-72.
137. Tanaka, M. Sackmann, E. Polymer-supported membranes as models of the cell surface. *Nature* 2005;437(7059):656-63.
138. Roder, F., Wilmes, S., Richter, C.P. Piehler, J. Rapid transfer of transmembrane proteins for single molecule dimerization assays in polymer-supported membranes. *ACS Chem. Biol.* 2014;9(11):2479-84.
139. Roder, F., Birkholz, O., Beutel, O., Paterok, D. Piehler, J. Spatial organization of lipid phases in micropatterned polymer-supported membranes. *J. Am. Chem. Soc.* 2013;135(4):1189-92.
140. Waichman, S., Roder, F., Richter, C.P., Birkholz, O. Piehler, J. Diffusion and interaction dynamics of individual membrane protein complexes confined in micropatterned polymer-supported membranes. *Small* 2013;9(4):570-7.
141. Roder, F., Waichman, S., Paterok, D., Schubert, R., Richter, C., Liedberg, B. Piehler, J. Reconstitution of membrane proteins into polymer-supported membranes for probing diffusion and interactions by single molecule techniques. *Anal. Chem.* 2011;83(17):6792-9.
142. Grakoui, A., Bromley, S.K., Sumen, C., Davis, M.M., Shaw, A.S., Allen, P.M. Dustin, M.L. The immunological synapse: A molecular machine controlling T cell activation. *Science* 1999;285(5425):221-7.
143. Chan, P.Y., Lawrence, M.B., Dustin, M.L., Ferguson, L.M., Golan, D.E. Springer, T.A. Influence of Receptor Lateral Mobility on Adhesion Strengthening between Membranes Containing Lfa-3 and Cd2. *J. Cell. Biol.* 1991;115(1):245-55.
144. Groves, J.T. Dustin, M.L. Supported planar bilayers in studies on immune cell adhesion and communication. *J. Immunol. Methods* 2003;278(1-2):19-32.
145. Sackmann, E. Supported membranes: Scientific and practical applications. *Science* 1996;271(5245):43-8.
146. LoidlStahlhofen, A., Kaufmann, S., Braunschweig, T. Bayerl, T.M. The thermodynamic control of protein binding to lipid bilayers for protein chromatography. *Nat. Biotechnol.* 1996;14(8):999-1002.
147. Galneder, R., Kahl, V., Arbuzova, A., Rebecchi, M., Radler, J.O. McLaughlin, S. Microelectrophoresis of a bilayer-coated silica bead in an optical trap: Application to enzymology. *Biophys. J.* 2001;80(5):2298-309.

148. Jacobson, B.S. Branton, D. Plasma-Membrane - Rapid Isolation and Exposure of Cytoplasmic Surface by Use of Positively Charged Beads. *Science* 1977;195(4275):302-4.
149. Cohen, C.M., Kalish, D.I., Jacobson, B.S. Branton, D. Membrane Isolation on Polylysine-Coated Beads - Plasma-Membrane from Hela-Cells. *J. Cell Biol.* 1977;75(1):119-34.
150. Kaufmann, S. Tanaka, M. Cell adhesion onto highly curved surfaces: One-step immobilization of human erythrocyte membranes on silica beads. *Chem. Phys. Chem.* 2003;4(7):699-704.
151. Liu, J., Jiang, X., Ashley, C. Brinker, C.J. Electrostatically mediated liposome fusion and lipid exchange with a nanoparticle-supported bilayer for control of surface charge, drug containment, and delivery. *J. Am. Chem. Soc.* 2009;131(22):7567-9.
152. Liu, J., Stace-Naughton, A. Brinker, C.J. Silica nanoparticle supported lipid bilayers for gene delivery. *Chem. Comm.* 2009;34):5100-2.
153. Liu, J., Stace-Naughton, A., Jiang, X. Brinker, C.J. Porous nanoparticle supported lipid bilayers (protocells) as delivery vehicles. *J. Am. Chem. Soc.* 2009;131(4):1354-5.
154. Ashley, C.E., Carnes, E.C., Phillips, G.K., Padilla, D., Durfee, P.N., Brown, P.A., Hanna, T.N., Liu, J., Phillips, B. Carter, M.B. The targeted delivery of multicomponent cargos to cancer cells by nanoporous particle-supported lipid bilayers. *Nat. Mater.* 2011;10(5):389.
155. Patel, P.D., Dand, N., Hirlekar, R.S. Kadam, V.J. Drug loaded erythrocytes: as novel drug delivery system. *Curr. Pharm. Des.* 2008;14(1):63-70.
156. Zarrin, A., Foroozesh, M. Hamidi, M. Carrier erythrocytes: recent advances, present status, current trends and future horizons. *Expert Opin. Drug Del.* 2014;11(3):433-47.
157. Muzykantov, V.R. Drug delivery by red blood cells: vascular carriers designed by mother nature. *Expert Opin. Drug Del.* 2010;7(4):403-27.
158. Hu, C.M., Zhang, L., Aryal, S., Cheung, C. Fang, R.H. Erythrocyte membrane-camouflaged polymeric nanoparticles as a biomimetic delivery platform. *Proc. Natl. Acad. Sci. U. S. A.* 2011;108(27):10980-5.
159. Hu, C.M., Fang, R.H., Luk, B.T., Chen, K.N., Carpenter, C., Gao, W., Zhang, K. Zhang, L. 'Marker-of-self' functionalization of nanoscale particles through a top-down cellular membrane coating approach. *Nanoscale* 2013;5(7):2664-8.
160. Hu, C.M., Fang, R.H., Copp, J., Luk, B.T. Zhang, L. A biomimetic nanosponge that absorbs pore-forming toxins. *Nat. Nanotechnol.* 2013;8(5):336-40.
161. Hu, C.M., Fang, R.H., Luk, B.T. Zhang, L. Nanoparticle-detained toxins for safe and effective vaccination. *Nat. Nanotechnol.* 2013;8(12):933-8.
162. Parodi, A., Quattrocchi, N., van de Ven, A.L., Chiappini, C., Evangelopoulos, M., Martinez, J.O., Brown, B.S., Khaled, S.Z., Yazdi, I.K., Enzo, M.V., Isenhardt, L., Ferrari, M. Tasciotti, E. Synthetic nanoparticles functionalized with biomimetic leukocyte membranes possess cell-like functions. *Nat. Nanotechnol.* 2013;8(1):61-8.
163. Menter, D.G., Steinert, B.W., Sloane, B.F., Gundlach, N., Ogara, C.Y., Marnett, L.J., Diglio, C., Walz, D., Taylor, J.D. Honn, K.V. Role of Platelet Membrane in

- Enhancement of Tumor-Cell Adhesion to Endothelial-Cell Extracellular-Matrix. *Cancer Res.* 1987;47(24):6751-62.
164. Furman, N.E.T., Lupu-Haber, Y., Bronshtein, T., Kaneti, L., Letko, N., Weinstein, E., Baruch, L. Machluf, M. Reconstructed Stem Cell Nanoghosts: A Natural Tumor Targeting Platform. *Nano Lett.* 2013;13(7):3248-55.
 165. Fang, R.H., Hu, C.M., Luk, B.T., Gao, W., Copp, J.A., Tai, Y., O'Connor, D.E. Zhang, L. Cancer cell membrane-coated nanoparticles for anticancer vaccination and drug delivery. *Nano Lett.* 2014;14(4):2181-8.
 166. Perica, K., Kosmides, A.K. Schneck, J.P. Linking form to function: biophysical aspects of artificial antigen presenting cell design. *BBA-Mol. Cell Res.* 2015;1853(4):781-90.
 167. Falconnet, D., Csucs, G., Grandin, H.M. Textor, M. Surface engineering approaches to micropattern surfaces for cell-based assays. *Biomaterials* 2006;27(16):3044-63.
 168. Doh, J. Irvine, D.J. Immunological synapse arrays: patterned protein surfaces that modulate immunological synapse structure formation in T cells. *Proc. Natl. Acad. Sci. U. S. A.* 2006;103(15):5700-5.
 169. Mossman, K.D., Campi, G., Groves, J.T. Dustin, M.L. Altered TCR signaling from geometrically repatterned immunological synapses. *Science* 2005;310(5751):1191-3.
 170. Chen, H.H., Ho, Y.-P., Jiang, X., Mao, H.-Q., Wang, T.-H. Leong, K.W. Quantitative comparison of intracellular unpacking kinetics of polyplexes by a model constructed from quantum dot-FRET. *Mol. Ther.* 2008;16(2):324-32.
 171. Hsu, C.-J., Hsieh, W.-T., Waldman, A., Clarke, F., Huseby, E.S., Burkhardt, J.K. Baumgart, T. Ligand Mobility Modulates Immunological Synapse Formation and T Cell Activation. *PLoS ONE* 2012;7(2):e32398.
 172. Giannoni, F., Barnett, J., Bi, K., Samodal, R., Lanza, P., Marchese, P., Billetta, R., Vita, R., Klein, M.R., Prakken, B., Kwok, W.W., Sercarz, E., Altman, A. Albani, S. Clustering of T Cell Ligands on Artificial APC Membranes Influences T Cell Activation and Protein Kinase C θ Translocation to the T Cell Plasma Membrane. *J. of Immunol.* 2005;174(6):3204-11.
 173. Prakken, B., Wauben, M., Genini, D., Samodal, R., Barnett, J., Mendivil, A., Leoni, L. Albani, S. Artificial antigen-presenting cells as a tool to exploit the immunesynapse'. *Nat. Med.* 2000;6(12):1406.
 174. Anderson, H.A., Hiltbold, E.M. Roche, P.A. Concentration of MHC class II molecules in lipid rafts facilitates antigen presentation. *Nat. Immunol.* 2000;1(2):156-62.
 175. Mandal, B., Bhattacharjee, H., Mittal, N., Sah, H., Balabathula, P., Thoma, L.A. Wood, G.C. Core-shell-type lipid-polymer hybrid nanoparticles as a drug delivery platform. *Nanomedicine* 2013;9(4):474-91.
 176. Mandal, S., Hammink, R., Tel, J., Eksteen-Akeroyd, Z.H., Rowan, A.E., Blank, K. Figdor, C.G. Polymer-Based Synthetic Dendritic Cells for Tailoring Robust and Multifunctional T Cell Responses. *ACS Chem. Biol.* 2015;10(2):485-92.
 177. Perica, K., Bieler, J.G., Sch tz, C., Varela, J.C., Douglass, J., Skora, A., Chiu, Y.L., Oelke, M., Kinzler, K. Zhou, S. Enrichment and expansion with nanoscale

- artificial antigen presenting cells for adoptive immunotherapy. *ACS Nano* 2015;9(7):6861-71.
178. Batista, F.D., Iber, D. Neuberger, M.S. B cells acquire antigen from target cells after synapse formation. *Nature* 2001;411(6836):489-94.
 179. Carrasco, Y.R., Fleire, S.J., Cameron, T., Dustin, M.L. Batista, F.D. LFA-1/ICAM-1 Interaction Lowers the Threshold of B Cell Activation by Facilitating B Cell Adhesion and Synapse Formation. *Immunity* 2004;20(5):589-99.
 180. Ketchum, C., Miller, H., Song, W. Upadhyaya, A. Ligand mobility regulates B cell receptor clustering and signaling activation. *Biophys. J.* 2014;106(1):26-36.
 181. Fleire, S.J., Goldman, J.P., Carrasco, Y.R., Weber, M., Bray, D. Batista, F.D. B Cell Ligand Discrimination Through a Spreading and Contraction Response. *Science* 2006;312(5774):738-41.
 182. Depoil, D., Fleire, S., Treanor, B.L., Weber, M., Harwood, N.E., Marchbank, K.L., Tybulewicz, V.L.J. Batista, F.D. CD19 is essential for B cell activation by promoting B cell receptor-antigen microcluster formation in response to membrane-bound ligand. *Nat. Immunol.* 2008;9(1):63-72.
 183. Arana, E., Vehlow, A., Harwood, N.E., Vigorito, E., Henderson, R., Turner, M., Tybulewicz, Victor L.J. Batista, F.D. Activation of the Small GTPase Rac2 via the B Cell Receptor Regulates B Cell Adhesion and Immunological-Synapse Formation. *Immunity* 2008;28(1):88-99.
 184. Lin, K.B.L., Freeman, S.A., Zabetian, S., Brugger, H., Weber, M., Lei, V., Dang-Lawson, M., Tse, K.W.K., Santamaria, R., Batista, F.D. Gold, M.R. The Rap GTPases Regulate B Cell Morphology, Immune-Synapse Formation, and Signaling by Particulate B Cell Receptor Ligands. *Immunity* 2008;28(1):75-87.
 185. Decuzzi, P., Godin, B., Tanaka, T., Lee, S.-Y., Chiappini, C., Liu, X. Ferrari, M. Size and shape effects in the biodistribution of intravascularly injected particles. *J. Control. Release* 2010;141(3):320-7.
 186. Xu, L., Auzins, A., Sun, X., Xu, Y., Harnischfeger, F., Lu, Y., Li, Z., Chen, Y.-H., Zheng, W. Liu, W. The synaptic recruitment of lipid rafts is dependent on CD19-PI3K module and cytoskeleton remodeling molecules. *J. Leukocyte Biol.* 2015;98(2):223-34.
 187. Wang, J., Tang, S., Wan, Z., Gao, Y., Cao, Y., Yi, J., Si, Y., Zhang, H., Liu, L. Liu, W. Utilization of a photoactivatable antigen system to examine B-cell probing termination and the B-cell receptor sorting mechanisms during B-cell activation. *Proc. Natl. Acad. Sci. U. S. A.* 2016;113(5):E558-E67.
 188. Zhang, S., Xu, L., Zhao, X., Chen, X., Fan, Y., Wan, Z., Xu, Y. Liu, W. A new and robust method of tethering IgG surrogate antigens on lipid bilayer membranes to facilitate the TIRFM based live cell and single molecule imaging experiments. *PLoS ONE* 2013;8(5):e63735.
 189. Tolar, P., Hanna, J., Krueger, P.D. Pierce, S.K. The Constant Region of the Membrane Immunoglobulin Mediates B Cell-Receptor Clustering and Signaling in Response to Membrane Antigens. *Immunity* 2009;30(1):44-55.
 190. Davey, A., Liu, W., Sohn, H.W., Brzostowski, J. Pierce, S.K. Understanding the initiation of B cell signaling through live cell imaging. *Method. Enzymol.* 2012;506(265-90).

191. Wang, C., Cen, L., Yin, S., Liu, Q., Liu, W., Cao, Y. Cui, L. A small diameter elastic blood vessel wall prepared under pulsatile conditions from polyglycolic acid mesh and smooth muscle cells differentiated from adipose-derived stem cells. *Biomaterials* 2010;31(4):621-30.
192. Wan, Z. Liu, W. The growth of B cell receptor microcluster is a universal response of B cells encountering antigens with different motion features. *Protein Cell* 2012;3(7):545-58.
193. Liu, W., Won Sohn, H., Tolar, P., Meckel, T. Pierce, S.K. Antigen-Induced Oligomerization of the B Cell Receptor Is an Early Target of FcγRIIB Inhibition. *J. Immunol.* 2010;184(4):1977-89.
194. Pihlgren, M., Silva, A.B., Madani, R., Giriens, V., Waeckerle-Men, Y., Fettelschoss, A., Hickman, D.T., López-Deber, M.P., Ndao, D.M., Vukicevic, M., Buccarello, A.L., Gafner, V., Chuard, N., Reis, P., Piorkowska, K., Pfeifer, A., Kündig, T.M., Muhs, A. Johansen, P. TLR4- and TRIF-dependent stimulation of B lymphocytes by peptide liposomes enables T cell-independent isotype switch in mice. *Blood* 2013;121(1):85-94.
195. Macauley, M.S., Pfrengle, F., Rademacher, C., Nycholat, C.M., Gale, A.J., von Drygalski, A. Paulson, J.C. Antigenic liposomes displaying CD22 ligands induce antigen-specific B cell apoptosis. *J. Clin. Invest.* 123(7):3074-83.
196. Wang, C., Liu, P., Zhuang, Y., Li, P., Jiang, B., Pan, H., Liu, L., Cai, L. Ma, Y. Lymphatic-targeted cationic liposomes: a robust vaccine adjuvant for promoting long-term immunological memory. *Vaccine* 2014;32(42):5475-83.
197. Yang, C., DelRio, F.W., Ma, H., Killaars, A.R., Basta, L.P., Kyburz, K.A. Anseth, K.S. Spatially patterned matrix elasticity directs stem cell fate. *Proc. Natl. Acad. Sci. U. S. A.* 2016;113(31):E4439-E45.
198. Engler, A.J., Sen, S., Sweeney, H.L. Discher, D.E. Matrix Elasticity Directs Stem Cell Lineage Specification. *Cell* 2006;126(4):677-89.
199. Li, Z., Gong, Y., Sun, S., Du, Y., Lü, D., Liu, X. Long, M. Differential regulation of stiffness, topography, and dimension of substrates in rat mesenchymal stem cells. *Biomaterials* 2013;34(31):7616-25.
200. Wong, S.T., Teo, S.-K., Park, S., Chiam, K.-H. Yim, E.K.F. Anisotropic rigidity sensing on grating topography directs human mesenchymal stem cell elongation. *Biomech. Model. Mechan.* 2014;13(1):27-39.
201. Onken, M.D., Mooren, O.L., Mukherjee, S., Shahan, S.T., Li, J. Cooper, J.A. Endothelial monolayers and transendothelial migration depend on mechanical properties of the substrate. *Cytoskeleton* 2014;71(12):695-706.
202. Chang, H., Zhang, H., Hu, M., Chen, J.-y., Li, B.-c., Ren, K.-f., Martins, M.C.L., Barbosa, M.A. Ji, J. Stiffness of polyelectrolyte multilayer film influences endothelial function of endothelial cell monolayer. *Colloids. Surf. B* 2017;149(379-87).
203. Chang, H., Liu, X.-q., Hu, M., Zhang, H., Li, B.-c., Ren, K.-f., Boudou, T., Albiges-Rizo, C., Picart, C. Ji, J. Substrate Stiffness Combined with Hepatocyte Growth Factor Modulates Endothelial Cell Behavior. *Biomacromolecules* 2016;17(9):2767-76.

204. Bashour, K.T., Gondarenko, A., Chen, H., Shen, K., Liu, X., Huse, M., Hone, J.C. Kam, L.C. CD28 and CD3 have complementary roles in T-cell traction forces. *Proc. Natl. Acad. Sci. U. S. A.* 2014;111(6):2241-6.
205. Hui, K.L., Balagopalan, L., Samelson, L.E. Upadhyaya, A. Cytoskeletal forces during signaling activation in Jurkat T-cells. *Mol. Biol. Cell* 2015;26(4):685-95.
206. O'Connor, R.S., Hao, X., Shen, K., Bashour, K., Akimova, T., Hancock, W.W., Kam, L.C. Milone, M.C. Substrate rigidity regulates human T cell activation and proliferation. *J. Immunol.* 2012;189(3):1330-9.
207. Judokusumo, E., Tabdanov, E., Kumari, S., Dustin, Michael L. Kam, Lance C. Mechanosensing in T Lymphocyte Activation. *Biophys. J.* 2012;102(2):L5-L7.
208. Wan, Z., Zhang, S., Fan, Y., Liu, K., Du, F., Davey, A.M., Zhang, H., Han, W., Xiong, C. Liu, W. B Cell Activation Is Regulated by the Stiffness Properties of the Substrate Presenting the Antigens. *J. Immunol.* 2013;190(9):4661-75.
209. Zeng, Y., Yi, J., Wan, Z., Liu, K., Song, P., Chau, A., Wang, F., Chang, Z., Han, W., Zheng, W., Chen, Y.-H., Xiong, C. Liu, W. Substrate stiffness regulates B-cell activation, proliferation, class switch, and T-cell-independent antibody responses in vivo. *Eur. J. Immunol.* 2015;45(6):1621-34.
210. Li, Y.-C., Chen, B.-M., Wu, P.-C., Cheng, T.-L., Kao, L.-S., Tao, M.-H., Lieber, A. Roffler, S.R. Cutting Edge: Mechanical Forces Acting on T Cells Immobilized via the TCR Complex Can Trigger TCR Signaling. *J. Immunol.* 2010;184(11):5959-63.
211. Kim, S.T., Takeuchi, K., Sun, Z.-Y.J., Touma, M., Castro, C.E., Fahmy, A., Lang, M.J., Wagner, G. Reinherz, E.L. The $\alpha\beta$ T Cell Receptor Is an Anisotropic Mechanosensor. *J. Biol. Chem.* 2009;284(45):31028-37.
212. Rivas, F.V., O'Keefe, J.P., Alegre, M.-L. Gajewski, T.F. Actin Cytoskeleton Regulates Calcium Dynamics and NFAT Nuclear Duration. *Mol. Cell. Biol.* 2004;24(4):1628-39.
213. Ilani, T., Vasiliver-Shamis, G., Vardhana, S., Bretscher, A. Dustin, M.L. T cell antigen receptor signaling and immunological synapse stability require myosin IIA. *Nat. Immunol.* 2009;10(5):531-9.
214. Bufi, N., Saitakis, M., Dogniaux, S., Buschinger, O., Bohineust, A., Richert, A., Maurin, M., Hivroz, C. Asnacios, A. Human primary immune cells exhibit distinct mechanical properties that are modified by inflammation. *Biophys. J.* 2015;108(9):2181-90.
215. Meyer, R.A., Sunshine, J.C., Perica, K., Kosmides, A.K., Aje, K., Schneck, J.P. Green, J.J. Biodegradable Nanoellipsoidal Artificial Antigen Presenting Cells for Antigen Specific T-Cell Activation. *Small* 2014;
216. Ingale, J., Stano, A., Guenaga, J., Sharma, S.K., Nemazee, D., Zwick, M.B. Wyatt, R.T. High-density array of well-ordered HIV-1 spikes on synthetic liposomal nanoparticles efficiently activate B cells. *Cell Rep.* 2016;15(9):1986-99.
217. Bennett, N.R., Zwick, D.B., Courtney, A.H. Kiessling, L.L. Multivalent antigens for promoting B and T cell activation. *ACS Chem. Biol.* 2015;10(8):1817-24.
218. Shook, D.R. Campana, D. Natural killer cell engineering for cellular therapy of cancer. *Tissue Antigens* 2011;78(6):409-15.

219. Denman, C.J., Senyukov, V.V., Somanchi, S.S., Phatarpekar, P.V., Kopp, L.M., Johnson, J.L., Singh, H., Hurton, L., Maiti, S.N. Huls, M.H. Membrane-bound IL-21 promotes sustained ex vivo proliferation of human natural killer cells. *PloS ONE* 2012;7(1):e30264.

Chapter 3: An Automated Multidimensional Thin Film Stretching

Device for the Generation of Anisotropic Polymer Micro- and Nanoparticles

3.1 Introduction

Shape and anisotropy are gaining increasing importance as design parameters in the construction of micro- and nanoparticles composed of various biomaterials. Although research in this area of biomaterials science has traditionally focused on spherical, isotropic particle formulation methods, non-spherical particles have been shown to enable superior biological performance compared to the spherical particle.¹ One of the properties of non-spherical particles that makes them an attractive candidate for various biomedical applications is their ability to avoid non-specific cellular uptake.² Particles of a wide size range from 500 nm³ to 5 μm⁴ have been shown to avoid clearance by macrophages, the primary cells responsible for elimination of particle based therapeutics. In addition, it has been shown that prolate ellipsoidal polymeric particles can avoid non-specific uptake by HeLa Cells and mesenchymal stem cells.⁵ Another unique property of non-spherical particles is their enhanced binding and targeted cellular internalization that has been exhibited when compared to isotropic particles.⁶ In addition to *in vitro* studies of specific particle binding and internalization, recently it has been shown that targeted

This chapter contains material modified from the following articles previously published as: Meyer RA, Meyer RS, Green JJ. An automated multidimensional thin film stretching device for the generation of anisotropic polymer micro- and nanoparticles. *J Biomed Mater Res: Part A*. 2015;103(8):2747-57. Ben-Akiva E, Rhodes KR, Meyer RA, Green JJ. Fabrication of anisotropic polymeric artificial antigen presenting cells for CD8+ T cell activation. *JoVE*. 2018. In press.

prolate and oblate ellipsoids localize to targets superiorly to equivalent spherical particles.^{7,8}

Taken together, the reduced non-specific cellular uptake and enhanced targeted cellular uptake make the anisotropic particle an attractive candidate for various biomedical applications. Most notably in the literature, these utilizations of non-spherical particles have been centered on drug delivery. Genetic therapeutics have successfully been delivered by anisotropic nanoparticles including RNA^{9,10} and DNA.^{11,12} In instances where spherical shape was compared to rod shape, the rod shaped particles exhibited enhanced biodistribution and were more effective at *in vivo* delivery of therapeutics.¹² In addition to genes, chemotherapeutic agents also have been delivered utilizing anisotropic particles. Micellar rods of high aspect ratio exhibited an increased capability to deliver different anti-tumor drugs to cancer cells.^{13,14} PLGA particles of anisotropic shape have been shown to be capable of delivering chemotherapeutic agents in an environmentally triggered manner.^{15,16} In addition to drug delivery, the field of immunoengineering has recently benefited from the use of non-spherical particles. RNA replicon vaccines have been successfully delivered to Vero cells utilizing a cylindrical shaped particle.¹⁰ Artificial antigen presenting cells for cancer immunotherapy have been constructed from ellipsoidal microparticles and have shown superior antigen specific activation of T-Cells compared to spherical microparticles.¹⁷

Given the unique properties and successful application of anisotropic particles as biomaterials in biomedical scenarios, there has been recent interest in novel methods of fabrication for these non-spherical particles. Significant research has been devoted to various microfluidic¹⁸⁻²⁰ and bottom-up approaches^{11,21-23} for the design of anisotropic

polymeric particles. One particularly well characterized method for fabrication of non-spherical particles in a highly controlled top-down scheme is the particle replication in non-wetting template or PRINT.²⁴ With the capability to fabricate any shape as specified by a photolithographic mask, this method has allowed for highly scalable top-down fabrication of anisotropic particles.^{25,26} Despite the strong control over the particle anisotropy, the PRINT method involves the use of expensive machinery for processes such as e-beam lithography to write the photomasks required to make nanoparticles. The most accessible method that has been developed to date for the fabrication of anisotropic polymeric particles is the thin-film stretching method. Originally pioneered by Ho et. al., this method consists of immobilizing polymeric particles in a thin plastic film, heating the film above the glass transition temperature of the polymer, and then stretching to deform the particles.²⁷ This method was originally used to produce polystyrene rods of defined aspect ratio, but has recently been expanded for the production of a wide variety of shapes including disk, rods, barrels, UFO's, and other shapes.^{28,29} In addition, by destabilizing the core of a polymeric particle, this method has been shown to be capable of producing red blood cell (RBC) shaped particles.³⁰ This process has gained popularity in recent years for the generation of anisotropic polymeric microparticles due to its simplicity of implementation and its capability to fabricate diverse shapes from different biomaterials.

Despite the simplicity of this method, there exist some difficulties in the thin film stretching protocol as it is described in the literature. The devices designed to stretch the thin film that have been utilized have relied on manual control of the applied machine force to stretch the film.^{27,28} In our experience, manual control has led to several

inconsistencies and faults in the method including the film tearing due to uneven application of strain, particles failing to stretch with the film due to exposure to ambient conditions during manual stretching resulting in subsequent cooling of the film, and excessive time consumption of the user to monitor the film and slowly stretch it to full deformation. To overcome these limitations, we have developed a thin film stretcher with an alternative design based on stepper motor automation to circumvent these difficulties. The original stretching protocol was used in conjunction with an automated tension application device to yield an automated thin film stretching procedure. This device was then utilized to fabricate anisotropic particles composed of various biomaterials. In this study we describe the device we have designed to use with this protocol and demonstrate the wide versatility of the method as it can be applied to make anisotropic particles of different size, shape, internal morphology, and biomaterial consistency. Continued development of the automated stretching procedure will allow for streamlining and scaling up of anisotropic particle production and expanded investigation into biomaterials for further biomedical applications.

3.2 Materials and Methods

3.2.1 Overview of Automated Stretcher Design

The automated stretcher was inspired by a design presented in Ho et. al.,²⁷ describing the original application of thin film stretching. The machine consists of two sets of mechanical grips mounted onto aluminum guide rails, designed to control the path of the film during stretching. To enable simultaneous 2D stretching of the thin film, we fixed the aluminum grips onto a custom designed composite lead screw, consisting of two

individual, opposing lead screws, threaded in opposite directions of each other (Roton Products; Kirkwood, MO). Upon turning either conjoined lead screw, the two grips holding the film will pull apart from the center point, allowing for controlled, efficient stretching of the thin film (**Figure 3.1A,C**).

Although the machine can be operated by manual turning of the lead screw, we opted to automate it to facilitate the thin film stretching process and have greater control over the strain rates applied to the viscoelastic films. To automate the machine, two 400 oz-in unipolar stepper motors (Probotix; Peoria, IL) were mounted and coupled to either axis. The wires running from the motors were also soldered to heat resistant 8-pin Amphenol connectors (Mouser Electronics; Mansfield, TX) and mounted to the machine board, to enable quick connect and disconnect whenever the stretching apparatus was moved in and out of the oven.

To control the stepper motors from any conventional computer and enable the sensitive electronics utilized in stepper motor control to remain out of the oven during a stretching procedure, we designed an external driver console to relay the USB control signal to the stepper motor. A 40 VDC, 10 A power supply (Probotix; Peoria, IL) was fused and wired to two unipolar stepper motor drivers (Probotix; Peoria, IL) as well as a microcontroller (Probotix; Peoria, IL) following the manufacturer's schematic. Each of the drivers were then linked to a 12.5 foot cable consisting of individual 22-gauge PTFE, heat resistant wires (Power Werx; Yorba Linda, CA), shielded in ¼ in PTFE tubing (Grainger; Lake Forest, IL). The cables were terminated in heat resistant Amphenol connectors (Mouser Electronics; Mansfield, TX), capable of quick connecting to the mounted sockets (**Figure 3.1B,D**).

Given that the stepper motor drivers emit a considerable amount of heat during operation, we installed an aluminum heat sink to the controlling integrated circuit following the manufacturer's suggestion. To permit convective cooling of the heat sink, we installed a 12 V computer fan (Radio Shack; Fort Worth, TX) and powered it using an AC power tap on the power supply, wired to a bridge rectifier and subsequently to a voltage regulator to bring the voltage to 12 V (Radio Shack; Fort Worth, TX). Finally, given the primary operation of the machine in a high temperature environment, we installed an external power switch for the main 40 V power supply. Therefore, the power source and stepper motors were not operational constitutively, but rather intermittently to minimize heat generation.

The microcontroller was chosen to be USB compatible and the controller software used was CNC-USB (Planet CNC). Standard G-Code was utilized to program the machine and instruct the stepper motors to move to a specified location at a user defined rate. Machine program settings were adjusted following the manufacturer's protocol.

3.2.2 Microparticle and Polymer Synthesis

All particles synthesized for this study were fabricated into microspheres by a single emulsion technique for organic polymeric particles. 100 mg of a chosen polymer or polymer blend was dissolved in 5 mL of dichloromethane. To generate labeled particles which could be visible across multiple fluorescence channels, 7-amino-4-methyl coumarin, (Sigma Aldrich; St. Louis, MO), coumarin-6 (Sigma Aldrich; St. Louis, MO), and Nile Red (Life Technologies; Grand Island, NY) dyes were added to the DCM each at a 1% w/w ratio to the polymer. The polymer-DCM solution was homogenized into 50 mL of a 1% PVA solution for one minute at either a low speed of 5,000 rpm, medium

speed of 10,000 rpm, high speed of 15,000 rpm, or for nanoparticle synthesis, sonication at 12W for 120 seconds, to generate the particles used in this study. The homogenizer low speed of 5,000 rpm was selected as the standard formulation condition for the standard sized particles utilized most often in this study. The initial emulsion was then poured into 100 mL of a 0.5% PVA solution and the DCM was allowed to evaporate over the course of 4 hours to permit for the formation of particles. The sample was then washed three times with water to yield the final product which was frozen and lyophilized prior to use in thin film stretching studies.

Most polymeric biomaterials utilized in this study were purchased commercially including the PLGA 50:50 lactic acid to glycolic acid content, MW 38,000-54,000 Da (Sigma-Aldrich; St. Louis, MO) and the PCL (MW 80,000 Da) (Sigma Aldrich; St. Louis, MO). The poly(beta-amino ester)s (PBAE)s utilized in this study were synthesized from commercially available monomers as described previously with modifications.³¹ Briefly 1, 4 butanediol diacrylate (Alfa Aesar; Ward Hill, MA) and 4, 4'-trimethylenedipiperidine (Sigma Aldrich; St. Louis, MO) were dissolved together in a 1.05:1 molar ratio in 5 mL of dichloromethane and heated at 90 °C for 24 hrs. The resulting polymer was then reacted and end-capped at room temperature for one hour with 1-(3-aminopropyl)-4-methylpiperazine (Alfa Aesar; Ward Hill, MA) in a 10-fold molar excess. The final polymer was then purified by addition of hexane, and the precipitated polymer was dried under a vacuum for 2 days. The polymer was then resuspended in dichloromethane at 100 mg/mL and stored in a dry environment at -20 °C until use.

3.2.3 Thin Film Stretching Method

The thin film stretching method adapted for this study was originally developed by Ho et. al.²⁷ and recently expanded by Champion et. al.²⁸ to produce particles of anisotropic shape. The lyophilized particles were suspended in 1 mL of water and then mixed with 19 mL of a 10% w/w PVA and 2% w/w glycerol solution by trituration. The resulting particle solution was then cast into films in 5 mL aliquots onto 5 cm x 7 cm rectangular petri dishes (VWR International; Radnor, PA) for 1D stretching or in 10 mL aliquots onto 10 cm x 10 cm (Thermo Fisher; Rockville, MD) square petri dishes for 2D stretching. The films were allowed to dry overnight and were then removed from the petri dish. The film was cut to size and then mounted on the aluminum blocks and heated to 70 °C (unless otherwise noted) to bring the polymeric microparticles above their glass transition temperatures. After 10 min of heating, the program was loaded to the microcontroller and the stepper motors were instructed to pull apart the film at a strain rate of 0.2 min⁻¹ (unless otherwise noted). The film was then allowed to rest for 1 min and then removed from the oven and allowed to cool for 20 min. After cooling, the film was cut from the grips and dissolved in 25 mL of water. The resulting particle suspension was then washed 3 times and lyophilized prior to use.

3.2.4 SEM Imaging and Image Analysis

All imaging was conducted with a Leo FESEM scanning electron microscope. To prepare samples for analysis, lyophilized particles were spread onto carbon tape (Nisshin EM Co.; Tokyo, Japan) adhered to aluminum tacks (Electron Microscopy Services; Hatfield, PA). The excess particles were removed and the particles then were sputter coated with a 20 nm thick layer of gold-palladium. The samples were then loaded into

the microscope and imaged. All images were processed in ImageJ to obtain relevant measurements (size, aspect ratio, etc.).

3.3 Results and Discussion

3.3.1 Particle Size Distribution

We were first interested to investigate the capability to control the size in the initial microparticle synthesis as a means to synthesize ellipsoidal microparticles with various sizes utilizing the automated stretching process. By controlling the type of agitation (sonication vs. homogenization) we were able to control whether or not our synthesized constructs were nanoparticles (**Figure 3.2A**) or microparticles (**Figure 3.2B-D**). In addition, by varying the homogenization speed, we were able to control the size distribution of the microparticles (**Figure 3.2E-H**). The emulsion made by sonication yielded nanoparticles with an average size of 224 nm. The particles generated at the low, middle, and high homogenization speeds were 3.02 μm , 1.77 μm , and 1.13 μm respectively.

Each particle formulation was then stretched 2-fold in PVA film to generate ellipsoidal particles. SEM (**Figure 3.2J-L**) and TEM (**Figure 3.2I**) images reveal the automated stretching process can be used to generate anisotropic, ellipsoidal particles of each formulation. In order to quantify anisotropy further, we analyzed the aspect ratio of the low homogenization speed microparticles in their spherical and non-spherical forms (**Figure 3.2M**). The aspect ratio of the spherical microparticles was distributed tightly around 1, whereas the aspect ratios of the ellipsoidal particles were distributed across a

variety of values with an average value of 3.3 (**Figure 3.2M**). This is near the predicted value for a two-fold stretched particle which was computed previously to be ~ 3 .¹⁷

3.3.2 2-Dimensional Particle Stretching

Upon successful 1-dimensional stretching of various particle sizes to form prolate ellipsoidal particles, we were next interested in generating disk shaped (oblate ellipsoidal) particles from stretching films in 2 dimensions. As the automated stretcher allows for constant strain rates to be applied to a film in both directions, we wanted to see the effect of stretching the films in 2 dimensions to different extents. Starting with a spherical particle (**Figure 3.3A**) we stretched the film in 2 dimensions at 1.25 x 1.25 fold (**Figure 3.3B**), 1.25 x 1.5 fold (**Figure 3.3C**), 1.5 x 1.5 fold (**Figure 3.3D**) and 1.75 x 1.75 fold (**Figure 3.3E**). The film stretching was limited to 1.75 fold due to the integrity of the film during the stretching procedure. As shown in the SEM images of these particles, the 2D stretching was successful at creating disk particles with various radii of curvature on both of their axes.

To determine whether or not the stretching was evenly applied across both dimensions, we conducted an aspect ratio analysis of the spherical particles compared to the 1.5 fold x 1.5 fold stretched particles to determine the amount of stretch fold applied to the particles. Although the aspect ratio analysis was more challenging due to the fact that not all of the disk shaped (oblate ellipsoidal) particles were positioned flat against the surface for imaging, we were able to determine that the spherical particles and the oblate ellipsoidal particles were similar in aspect ratio, which was expected due to equal stretch in two different dimensions, as opposed to the spherical vs. prolate ellipsoid comparison, where the one dimensional stretched prolate ellipsoids had significantly higher aspect

ratio (compare **Figure 3.3F** to **Figure 3.2M**). In addition, the distribution of aspect ratios of the oblate ellipsoids was narrower than that of the prolate ellipsoids, thus indicating successful automated stretching of the particles in 2 dimensions.

Next, we wanted to examine the effect of the temperature at which we stretched the particles as another variable which can be controlled precisely utilizing an automated process. Although our stretching protocol was successful at the temperature initially tested (70 °C), we wanted to see the effect of raising the temperature on particle stretching in 2 dimensions. We stretched the particles 1.5 fold x 1.5 fold at 70 °C (**Figure 3.4A**), 80 °C (**Figure 3.4B**), 90 °C (**Figure 3.4C**), and 100 °C (**Figure 3.4D**). All stretching conditions produced disk like particles similar to the ones we expected from the earlier studies (**Figure 3.3D**). However, one striking difference across the temperatures we tested was the emergence of a dimple at higher temperatures to produce red blood cell shaped particles (compare **Figure 3.4C** and **Figure 3.4D** to **Figure 3.4A** and **Figure 3.4B**). The dimple appeared to become more prevalent at 90 °C and 100 °C, and less prevalent or absent at 80 °C and 70 °C respectively. Due to precise control of the temperature during stretching afforded by the automated process, we have enabled control over the formation of dimpled vs. non-dimpled particles. The control of dimple formation may be an important aspect for the fabrication of biomaterials into cell-like biomimetic shapes and as a parameter to tune drug release from the center of a particle.

3.3.3 Stretching Strain Rate

Another parameter that can be precisely tuned by the automated version of the thin film stretching process is the strain rate. Although the maximal strain rate possible is determined by the material properties of the film (strain rate to failure) and not the

automated stretcher itself, we were interested to determine if there was any effect on the particle aspect ratio as a result of strain applied at different rates during the stretching procedure. Starting with a spherical microparticle, we stretched the film 2 fold at 0.2 min^{-1} (**Figure 3.5A**), 0.4 min^{-1} (**Figure 3.5B**), 0.8 min^{-1} (**Figure 3.5C**), 1.6 min^{-1} (**Figure 3.5D**), and 3.2 min^{-1} (**Figure 3.5E**). All strain rates produced ellipsoidal particles as expected. Aspect ratio analysis of the particles stretched at different strain rates demonstrated that there was no effect of the strain rate on the shape of the particles produced, and that all strain rates were capable of producing high aspect ratio particles (**Figure 3.5F**). Although this was hypothesized due to the successful manual film stretching procedures in the past, we have now proven that strain rate has minimal effect on particle production and can be tuned based on the needs of the user and the material properties of the PVA film.

3.3.4 Stretching of Different Biomaterials

One of the advantages of the thin film stretching method is that, due to its top-down nature, it can be applied to a wide variety of biomaterials. This versatility is limited by the ability to attain the glass transition temperature of the material to stretch, but for many biomaterials currently utilized for drug delivery applications, it is appropriate for the generation of anisotropic particles.

Among the numerous benefits of particle synthesis by emulsion is the ability to encapsulate drugs and imaging contrast agents. To that end, we first wanted to prove the versatility of the automated thin film stretching method by generating ellipsoidal particles of biodegradable PLGA with different fluorophores encapsulated in them. The fluorophores that were tested were 7-amino-4-methyl coumarin (fluorescence on the blue

DAPI channel) (**Figure 3.6A**), coumarin 6 (fluorescence on the green GFP channel) (**Figure 3.6B**), and Nile Red (**Figure 3.6C**) (fluorescence on the Red channel). As shown, all fluorophores can be encapsulated in the PLGA thus conferring different modes of fluorescence to the particles. Upon thin film stretching of each of these formulations, we were able to generate anisotropic microparticles with these different fluorescent properties conferred by 7-AMC (**Figure 3.6D**), coumarin-6 (**Figure 3.6E**), and Nile Red (**Figure 3.6F**). Encapsulation of these fluorophores did not affect our ability to stretch the particles or influence their final aspect ratios.

In addition to small molecule encapsulation, we were interested to apply the thin film stretching material to other materials aside from PLGA, including PCL and a PLGA/PBAE hybrid particle. We synthesized PCL (**Figure 3.7A**) and the PLGA/PBAE (**Figure 3.7B**) hybrid by single emulsion. Upon deforming each spherical polymeric particle by the automated thin film stretching procedure, we determined that we could synthesize anisotropic ellipsoidal particles from PCL (**Figure 3.7C**) and PLGA/PBAE (**Figure 3.7D**). Thus, the automated thin film stretching method was demonstrated to be robust and applicable to a variety of biomaterials.

3.3.5 Discussion

The study of anisotropic polymeric micro and nanoparticles is becoming increasingly important in the biomaterials community. Owing in part to their capability to resist non-specific cellular uptake² while simultaneously increasing *in vitro*⁶ and *in vivo*⁷ targeted specific cell interactions, the non-spherical particle is becoming a promising candidate for biomedical applications such as drug delivery. Although traditional particle fabrication methods have been shown to generate spherical

biodegradable particles of different sizes,³² different procedures have been and continue to be developed to synthesize non-spherical particles. Among these, the most popular and approachable method is the thin-film stretching method. Despite the simplicity of its design, there can be difficulty in implementing this method manually due to the imprecise nature of a human operator at applying strain to the films in different dimensions in order to fabricate particles with varied shapes. As such, we have developed and described here an automated film stretcher for the generation of oblate and prolate ellipsoidal particles.

One of the main advantages of the thin film stretching method is that it is a post-synthesis modification of a spherical particle. As such, it is compatible with a wide variety of particle fabrication techniques, including emulsion, which was specifically highlighted in this study. Particle synthesis by emulsion offers the capability to accurately and reproducibly control size distribution of synthesized particles. These particles can then be deformed to anisotropic shapes utilizing the thin film stretching methods while containing various encapsulated cargos as we have demonstrated. We have shown here that the automated thin film stretching method is capable of producing polymeric, ellipsoidal nanoparticles and microparticles of different sizes and shapes, with certain advantages compared to manual fabrication.²⁸ Particle size and shape have been determined to be very important parameters for biologic therapeutics impacting the biodistribution upon administration^{7,8,33} and elimination from the body.³⁴ In addition, particle size and shape have determined the potency of interaction of biomaterial surfaces with biological cells such as in immune stimulation by artificial antigen presenting cells.^{17,35} The capability of simultaneously controlling size and shape of a particle is a definitive advantage of this automated process.

We have shown in this study that it is possible to control the type of shape generated by an automated thin film stretching process. Although this method is limited to tuning particle shapes by axial deformations, the degree of deformation can specify the aspect ratio and class of the synthesized ellipsoid and multiple stretching steps in varied directions could also be performed. This has been naturally integrated into the automated process through the use of stepper motors for precise control over thin film grip positioning and rate of separation. We have shown here that prolate ellipsoids can be synthesized with a predictable average aspect ratio as previously specified by parametric modeling of spheroid deformation.¹⁷ In addition, we have generated oblate ellipsoidal particles of various aspect ratios and radii of curvature. The ability to control these parameters can be critical given cellular capability to respond to spatial cues and biomaterial surfaces in the environment.³⁶⁻³⁸ As a result, the capability to generate particles of various shapes by the automated thin film stretching method is another advantage of the process.

In addition to determining the effect of stretching distance of the deformation of the polymeric particle, we have explored the effect of stretching temperature and rate. The stretching temperature was determined to be a critical parameter for the generation of disk-like oblate ellipsoidal microparticles. At lower temperatures, the particles deformed as expected into oblate ellipsoids. By raising the temperature, the particles deformed instead into dimpled oblate ellipsoids similar in 3D shape to a red blood cell. Similarly shaped particles have been previously produced by the manual film stretching method through a chemical based destabilization of the core of a particle. Here we show for the first time that biomaterials can be fabricated into biomimetic red blood cell-shaped

particles, without the addition of destabilizing chemicals, through a film-stretching method at particular temperatures (higher than simply above the polymer glass transition temperature). The capability to mimic red blood cells (RBC) surface membranes^{39,40} and physiology^{41,42} has been investigated in the literature. The application of polymeric particles that have been deformed to RBC shape by the high temperature automated stretching procedure is an interesting future direction motivated by this work.

Strain rate was also investigated with respect to anisotropic particle synthesis by thin film stretching. At all strain rates tested, the generated ellipsoids had similar aspect ratios indicating strain rate independence. This has important implications for the scaled up production of these anisotropic particles which would ultimately be needed for potential manufacturing and clinical use. The automated process coupled with the ellipsoid particle insensitivity to strain rate makes this fabrication procedure scalable for rapid production of large quantities of anisotropic particles. Further investigation into the impact of strain rate on the generation of different polymeric particles will be of interest as their biomedical application expands.

A final advantage of using the thin film stretching method as a post synthesis modification of spherical microparticles is the ability to specify the material to deform including the polymer and any encapsulated bioactive small molecules. Biodegradable polymers have found vast application in drug delivery⁴³ and tissue scaffold engineering.⁴⁴ We have shown that the automated thin film stretching method is amenable to small molecule encapsulation as evidenced by the use of three fluorophores for visualization. In addition, we have shown in this study that PCL and PLGA/PBAE hybrid particles can also be deformed into ellipsoids utilizing the thin film stretching method. PCL is of

interest due to its use in various biomedical scenarios⁴⁵ and shape memory properties.⁴⁶ PBAEs have been investigated extensively for their genetic material delivery capabilities^{31,47,48} and the PLGA/PBAE hybrid particle has been utilized for intracellular delivery of vaccination agents⁴⁹ and genetic material.⁵⁰ Investigating the impact of shape in the context of these different biomaterials is a valuable pursuit in the study of anisotropic polymeric particles.

3.4 Conclusions

In conclusion, we have demonstrated in this work the construction of an automated device for the fabrication of polymeric biomaterials into anisotropic micro- and nanoparticles. The process can be applied uniformly to particles of different sizes and can be utilized to form ellipsoids with different aspect ratios and radii of curvature. In addition, we have described the scale up capability of this method by demonstrating an insensitivity to thin film strain rate and compatibility of the thin film process with automated stepper motor control. We have also shown the utility of this approach in generating biomimetic red blood cell-shaped particles. Finally, we have exhibited the versatility of this automated method by applying it to polymeric particles synthesized with different biomaterials and encapsulating various fluorescent small molecules. Application of this automated thin film stretcher to the generation of non-spherical polymeric particles can be of great utility in the study of anisotropy in biomedical materials applications.

3.5 Figures

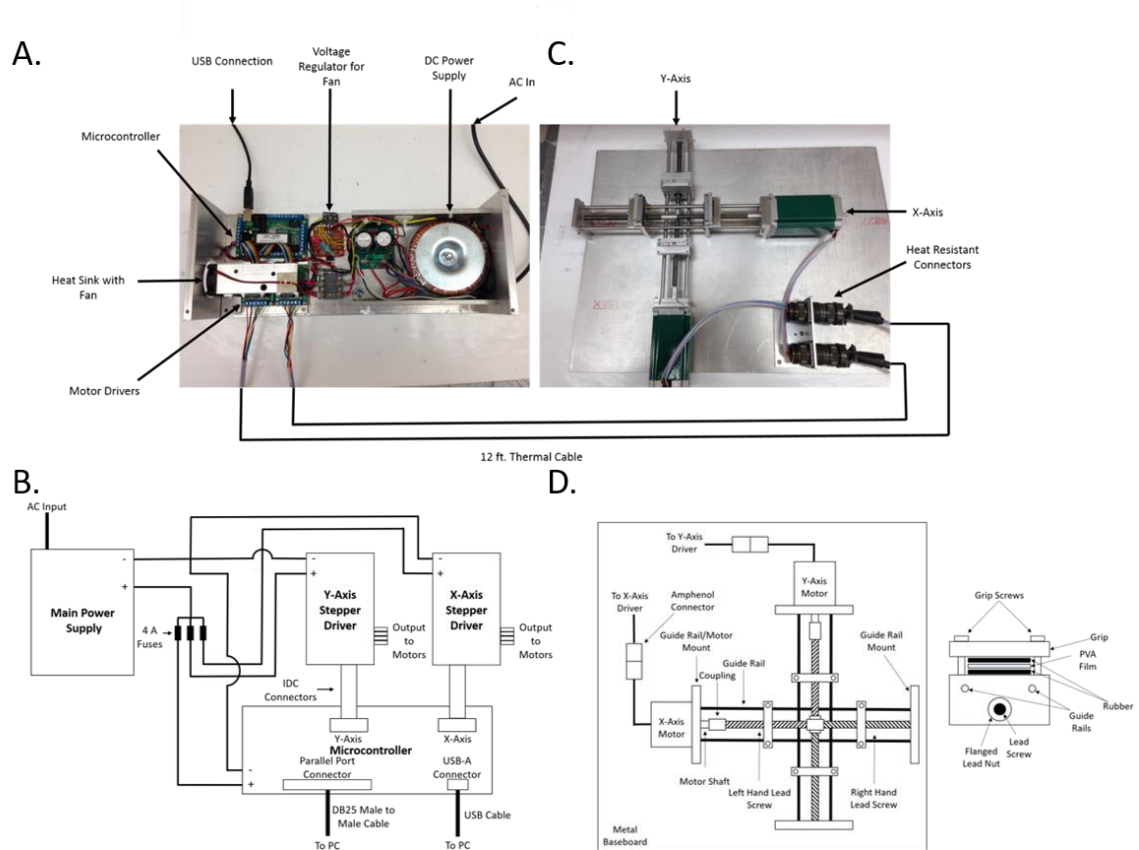


Figure 3.1: Image and schematic of the automated thin film stretcher utilized in this study. (A,C) A USB linked microcontroller is linked to two stepper motor drivers which relay signals to two unipolar stepper motors through thermally protected wire. (B,D) The stepper motors are mounted to the axes. Each axis is composed of opposing direction lead screws to drive apart two aluminum mounts which grip and stretch the film.

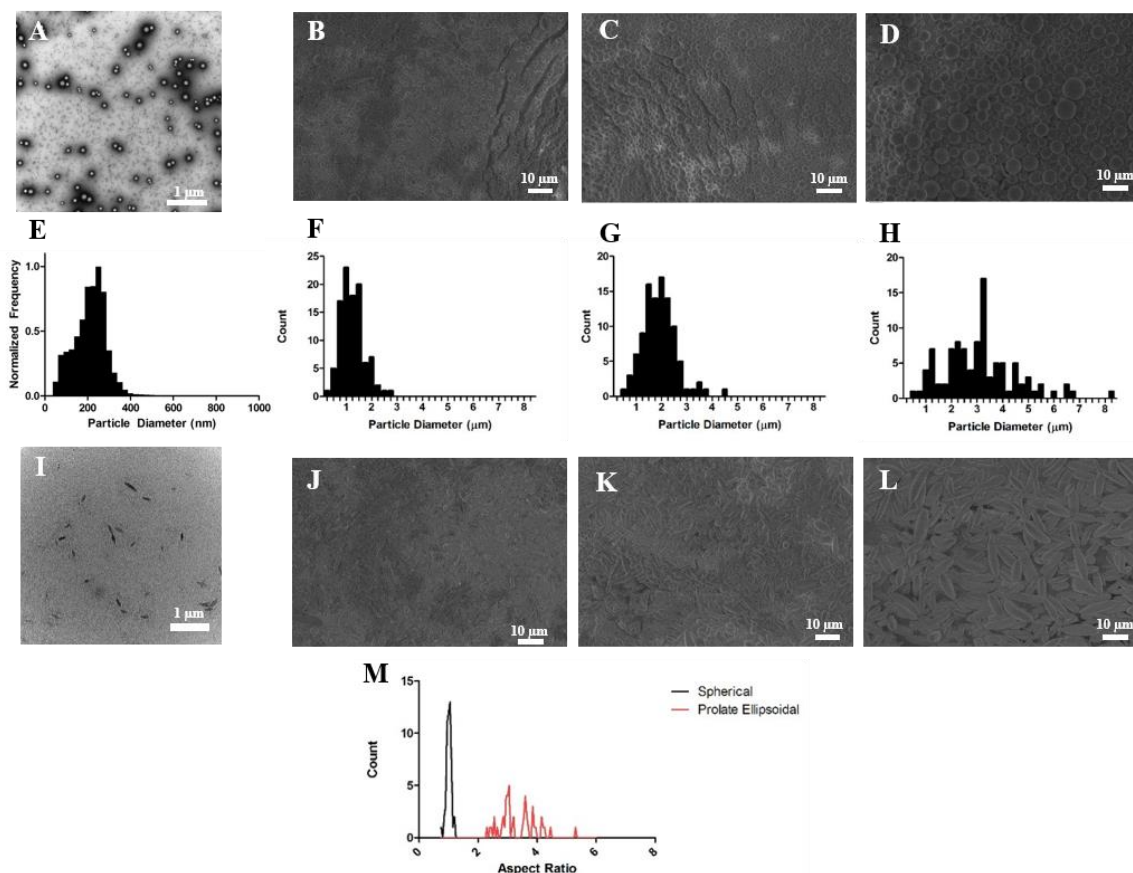


Figure 3.2: The automated thin film stretching method can be applied to a variety of different particle sizes. SEM micrographs of PLGA particles fabricated under (A) sonication, (B) high rpm, (C) medium rpm, and (D) low rpm homogenization. All particles demonstrated a spherical morphology (E, F, G, H). Particle size histograms of the fabricated particles in (A, B, C, D) respectively. SEM micrographs of 2-fold stretched particles under (I) sonication, (J) high rpm, (K) medium rpm, and (L) low rpm homogenization. (M) Aspect ratio analysis of SEM images reveals non-spherical ellipsoidal microparticles can be generated from the thin film stretching procedure.

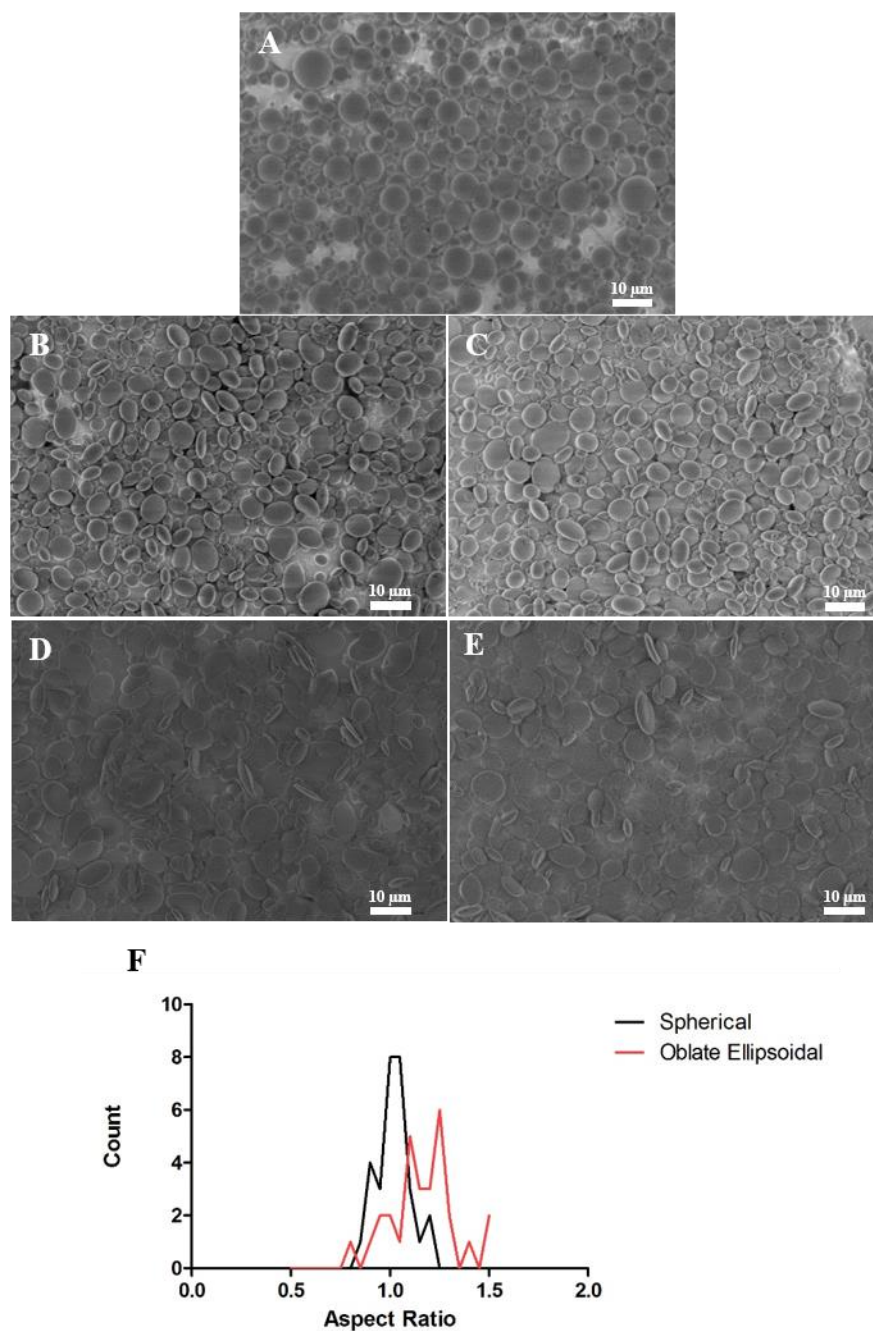


Figure 3.3: Non-spherical particles of various shapes can be synthesized with the two-dimensional automated thin film stretching method. (A) Spherical microparticles can be stretched (B) 1.25x by 1.25x, (C) 1.25x by 1.5x, (D) 1.5x by 1.5 x, (E) 1.75x by 1.75x to create particles of various flattened oblate ellipsoidal shape. (F) Aspect ratio analysis of 1.5x by 1.5x stretched particles reveals that the aspect ratio of one is roughly maintained through the 2D stretching procedure.

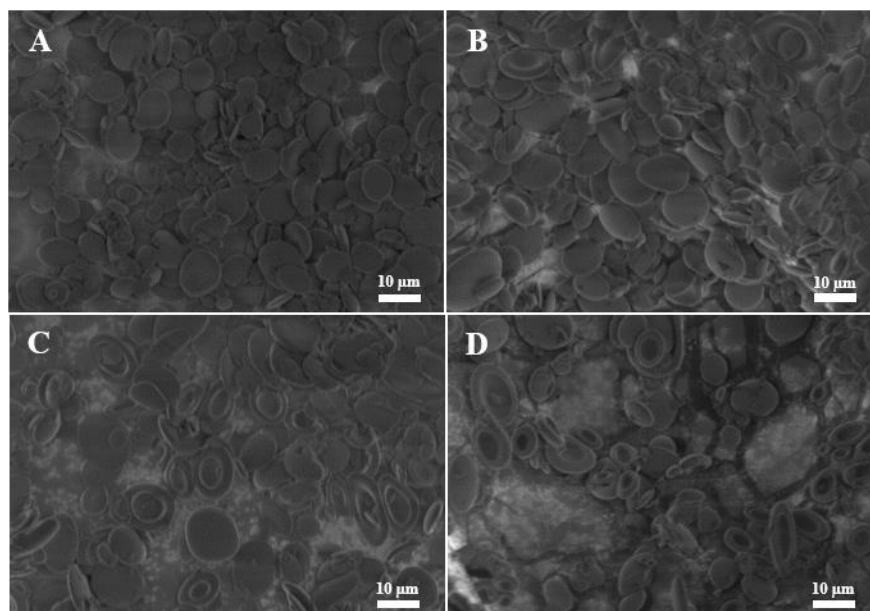


Figure 3.4: The shape of the particle depends on the temperature at which it was stretched. Spherical micro particles were stretched at (A) 70 °C, (B) 80 °C, (C) 90 °C, and (D) 100 °C in 2 dimensions at a fold of 1.5x by 1.5x. As the temperature increases the frequency of dimpled particles increases.

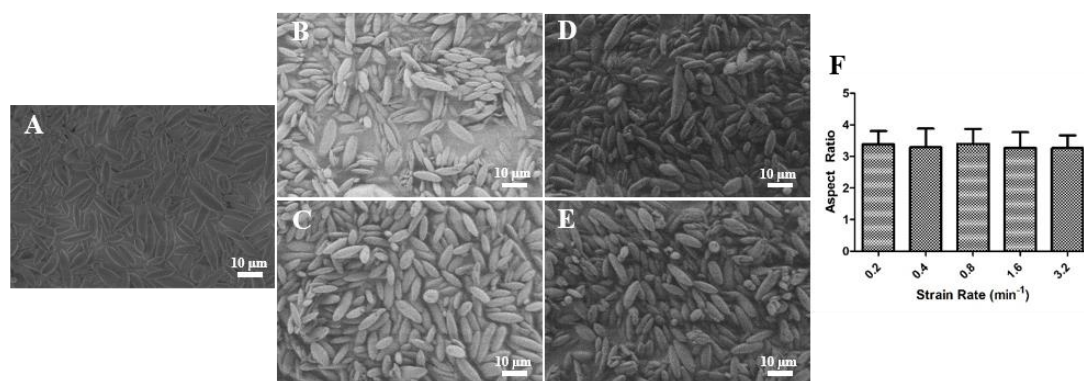


Figure 3.5: The strain rate at which the film is stretched does not have an effect on the final particle shape. Spherical microparticles were stretched at 70 °C to a 2 fold length in one dimension at a strain rate of (A) 0.2/min (B) 0.4/min, (C) 0.8/min, (D) 1.6/min, and (E) 3.2/min (F) Aspect ratio analysis reveals there was not an effect of the strain rate.

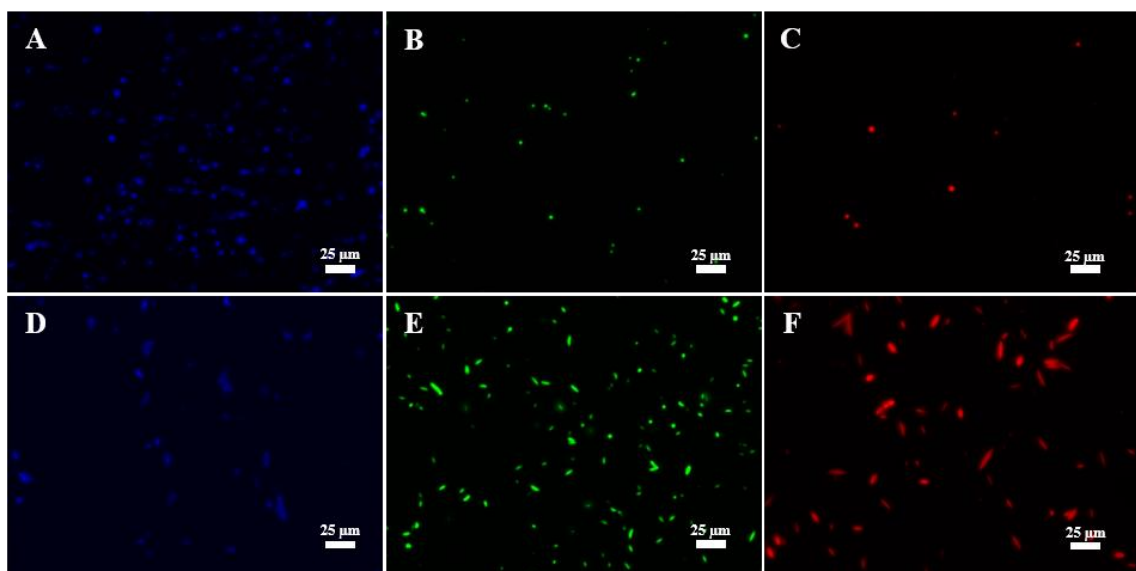


Figure 3.6: Fluorescence microscopy images of (A, B, C) spherical and (D, E, F) stretched microparticles encapsulating three fluorophores. Each of the fluorophores could be imaged on a separate channel including (A, C) blue DAPI channel for 7-AMC, (B, E) green GFP channel for coumarin-6, and (C, F) red channel for Nile Red.

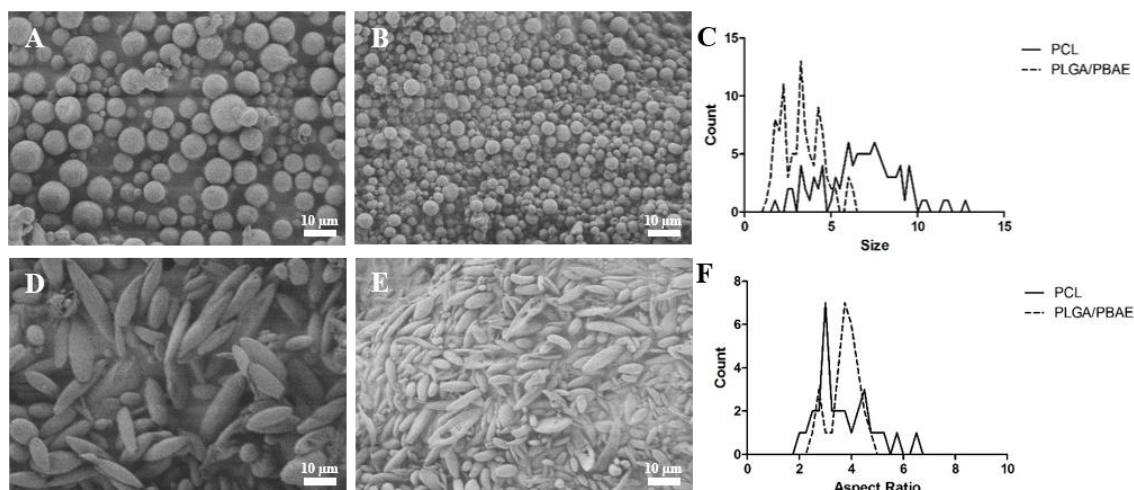


Figure 3.7: Different biomaterials can be made into ellipsoidal microparticles utilizing the automated thin film stretching procedure. In addition to PLGA as shown in Figure 1D and Figure 1L, (A, D) PCL, and (B, E) PLGA/PBAE blend can all be fabricated into ellipsoidal shapes by the automated stretching method. (C) Particle size distribution demonstrates that PCL microparticles have larger size than PLGA/PBAE microparticles. (F) Aspect ratio analysis of each sample shows that despite size differences, similar aspect ratios can be attained for each particle.

3.6 References

1. Tao L, Hu W, Liu Y, Huang G, Sumer BD, Gao J. Shape-specific polymeric nanomedicine: emerging opportunities and challenges. *Exp. Biol. Med. (Maywood)* 2011;236(1):20-9.
2. Toy R, Peiris PM, Ghaghada KB, Karathanasis E. Shaping cancer nanomedicine: the effect of particle shape on the in vivo journey of nanoparticles. *Nanomedicine* 2013;9(1):121-134.
3. Sharma G, Valenta DT, Altman Y, Harvey S, Xie H, Mitragotri S, Smith JW. Polymer particle shape independently influences binding and internalization by macrophages. *J Control. Release* 2010;147(3):408-12.
4. Yoo JW, Mitragotri S. Polymer particles that switch shape in response to a stimulus. *Proc. Natl. Acad. Sci. U. S. A.* 2010;107(25):11205-10.
5. Florez L, Herrmann C, Cramer JM, Hauser CP, Koynov K, Landfester K, Crespy D, Mailander V. How shape influences uptake: interactions of anisotropic polymer nanoparticles and human mesenchymal stem cells. *Small* 2012;8(14):2222-30.
6. Barua S, Yoo J-W, Kolhar P, Wakankar A, Gokarn YR, Mitragotri S. Particle shape enhances specificity of antibody-displaying nanoparticles. *Proc. Natl. Acad. Sci. U. S. A.* 2013;110(9):3270-3275.
7. Kolhar P, Anselmo AC, Gupta V, Pant K, Prabhakarapandian B, Ruoslahti E, Mitragotri S. Using shape effects to target antibody-coated nanoparticles to lung and brain endothelium. *Proc. Natl. Acad. Sci. U. S. A.* 2013;110(26):10753-8.
8. Adriani G, de Tullio MD, Ferrari M, Hussain F, Pascazio G, Liu X, Decuzzi P. The preferential targeting of the diseased microvasculature by disk-like particles. *Biomaterials* 2012;33(22):5504-13.
9. Hasan W, Chu K, Gullapalli A, Dunn SS, Enlow EM, Luft JC, Tian S, Napier ME, Pohlhaus PD, Rolland JP and others. Delivery of multiple siRNAs using lipid-coated PLGA nanoparticles for treatment of prostate cancer. *Nano Lett.* 2012;12(1):287-92.
10. Xu J, Luft JC, Yi X, Tian S, Owens G, Wang J, Johnson A, Berglund P, Smith J, Napier ME and others. RNA replicon delivery via lipid-complexed PRINT protein particles. *Mol. Pharm.* 2013;10(9):3366-74.
11. Jiang X, Leong D, Ren Y, Li Z, Torbenson MS, Mao HQ. String-like micellar nanoparticles formed by complexation of PEG-B-PPA and plasmid DNA and their transfection efficiency. *Pharm. Res.* 2011;28(6):1317-27.
12. Jiang X, Qu W, Pan D, Ren Y, Williford JM, Cui H, Luijten E, Mao HQ. Plasmid-templated shape control of condensed DNA-block copolymer nanoparticles. *Adv. Mater.* 2013;25(2):227-32.
13. Geng Y, Dalhaimer P, Cai S, Tsai R, Tewari M, Minko T, Discher DE. Shape effects of filaments versus spherical particles in flow and drug delivery. *Nat. Nanotechnol.* 2007;2(4):249-55.
14. Karagoz B, Esser L, Duong HT, Basuki JS, Boyer C, Davis TP. Polymerization-Induced Self-Assembly (PISA) – control over the morphology of nanoparticles for drug delivery applications. *Polym. Chem.* 2014;5(2):350.
15. Chu KS, Hasan W, Rawal S, Walsh MD, Enlow EM, Luft JC, Bridges AS, Kuijter JL, Napier ME, Zamboni WC, et. al. Plasma, tumor and tissue pharmacokinetics

- of Docetaxel delivered via nanoparticles of different sizes and shapes in mice bearing SKOV-3 human ovarian carcinoma xenograft. *Nanomedicine* 2013;9(5):686-93.
16. Chu KS, Finnis MC, Schorzman AN, Kuijter JL, Luft JC, Bowerman CJ, Napier ME, Haroon ZA, Zamboni WC, DeSimone JM. Particle replication in nonwetting templates nanoparticles with tumor selective alkyl silyl ether docetaxel prodrug reduces toxicity. *Nano Lett.* 2014;14(3):1472-6.
 17. Sunshine JC, Perica K, Schneck JP, Green JJ. Particle shape dependence of CD8+ T cell activation by artificial antigen presenting cells. *Biomaterials* 2014;35(1):269-77.
 18. Shum HC, Abate AR, Lee D, Studart AR, Wang B, Chen CH, Thiele J, Shah RK, Krummel A, Weitz DA. Droplet microfluidics for fabrication of non-spherical particles. *Macromol. Rapid Commun.* 2010;31(2):108-18.
 19. Luo G, Du L, Wang Y, Lu Y, Xu J. Controllable preparation of particles with microfluidics. *Particuology* 2011;9(6):545-558.
 20. Yang S, Guo F, Kiraly B, Mao X, Lu M, Leong KW, Huang TJ. Microfluidic synthesis of multifunctional Janus particles for biomedical applications. *Lab Chip* 2012;12(12):2097-102.
 21. Jang SG, Audus DJ, Klinger D, Krogstad DV, Kim BJ, Cameron A, Kim SW, Delaney KT, Hur SM, Killips KL and others. Striped, ellipsoidal particles by controlled assembly of diblock copolymers. *J. Am. Chem. Soc.* 2013;135(17):6649-57.
 22. Zhou Z, Anselmo AC, Mitragotri S. Synthesis of protein-based, rod-shaped particles from spherical templates using layer-by-layer assembly. *Adv. Mater.* 2013;25(19):2723-7.
 23. Petzetakis N, Dove AP, O'Reilly RK. Cylindrical micelles from the living crystallization-driven self-assembly of poly(lactide)-containing block copolymers. *Chem. Sci.* 2011;2(5):955.
 24. Rolland JP, Maynor BW, Euliss LE, Exner AE, Denison GM, DeSimone JM. Direct fabrication and harvesting of monodisperse, shape-specific nanobiomaterials. *J. Am. Chem. Soc.* 2005;127(28):10096-10100.
 25. Wang Y, Merkel TJ, Chen K, Fromen CA, Betts DE, DeSimone JM. Generation of a library of particles having controlled sizes and shapes via the mechanical elongation of master templates. *Langmuir* 2011;27(2):524-8.
 26. Morton SW, Herlihy KP, Shopsowitz KE, Deng ZJ, Chu KS, Bowerman CJ, Desimone JM, Hammond PT. Scalable manufacture of built-to-order nanomedicine: spray-assisted layer-by-layer functionalization of PRINT nanoparticles. *Adv. Mater.* 2013;25(34):4707-13.
 27. Ho C, Keller A, Odell J, Ottewill R. Preparation of monodisperse ellipsoidal polystyrene particles. *Colloid Polym. Sci.* 1993;271(5):469-479.
 28. Champion JA, Katare YK, Mitragotri S. Making polymeric micro- and nanoparticles of complex shapes. *Proc. Natl. Acad. Sci. U. S. A.* 2007;104(29):11901-4.
 29. Champion JA, Mitragotri S. Role of target geometry in phagocytosis. *Proc. Natl. Acad. Sci. U. S. A.* 2006;103(13):4930-4.

30. Doshi N, Zahr AS, Bhaskar S, Lahann J, Mitragotri S. Red blood cell-mimicking synthetic biomaterial particles. *Proc. Natl. Acad. Sci. U. S. A.* 2009;106(51):21495-9.
31. Tzeng SY, Guerrero-Cázares H, Martinez EE, Sunshine JC, Quiñones-Hinojosa A, Green JJ. Non-viral gene delivery nanoparticles based on poly (β -amino esters) for treatment of glioblastoma. *Biomaterials* 2011;32(23):5402-5410.
32. Rao JP, Geckeler KE. Polymer nanoparticles: preparation techniques and size-control parameters. *Prog. Polym. Sci.* 2011;36(7):887-913.
33. Decuzzi P, Godin B, Tanaka T, Lee S-Y, Chiappini C, Liu X, Ferrari M. Size and shape effects in the biodistribution of intravascularly injected particles. *J Control. Release* 2010;141(3):320-327.
34. Chou LY, Zagorovsky K, Chan WC. DNA assembly of nanoparticle superstructures for controlled biological delivery and elimination. *Nat. Nanotechnol.* 2014.
35. Steenblock ER, Fahmy TM. A comprehensive platform for ex vivo T-cell expansion based on biodegradable polymeric artificial antigen-presenting cells. *Mol. Ther.* 2008;16(4):765-772.
36. Barreto-Ortiz SF, Zhang SM, Davenport M, Fradkin J, Ginn B, Mao HQ, Gerecht S. A Novel In Vitro Model for Microvasculature Reveals Regulation of Circumferential ECM Organization by Curvature. *PloS ONE* 2013;8(11):14.
37. Fletcher DA, Mullins RD. Cell mechanics and the cytoskeleton. *Nature* 2010;463(7280):485-92.
38. Kim HN, Jiao A, Hwang NS, Kim MS, Kang DH, Kim D-H, Suh K-Y. Nanotopography-guided tissue engineering and regenerative medicine. *Adv. Drug Deliver. Rev.* 2013;65(4):536-558.
39. Hu C-MJ, Fang RH, Copp J, Luk BT, Zhang L. A biomimetic nanosponge that absorbs pore-forming toxins. *Nat. Nanotechnol.* 2013;8(5):336-340.
40. Aryal S, Hu C-MJ, Fang RH, Dehaini D, Carpenter C, Zhang D-E, Zhang L. Erythrocyte membrane-cloaked polymeric nanoparticles for controlled drug loading and release. *Nanomedicine* 2013;8(8):1271-1280.
41. Merkel TJ, Jones SW, Herlihy KP, Kersey FR, Shields AR, Napier M, Luft JC, Wu H, Zamboni WC, Wang AZ and others. Using mechanobiological mimicry of red blood cells to extend circulation times of hydrogel microparticles. *Proc. Natl. Acad. Sci. U. S. A.* 2011;108(2):586-91.
42. Chen K, Merkel TJ, Pandya A, Napier ME, Luft JC, Daniel W, Sheiko S, DeSimone JM. Low modulus biomimetic microgel particles with high loading of hemoglobin. *Biomacromolecules* 2012;13(9):2748-59.
43. Kumari A, Yadav SK, Yadav SC. Biodegradable polymeric nanoparticles based drug delivery systems. *Colloid. Surface. B* 2010;75(1):1-18.
44. Guo B, Ma PX. Synthetic biodegradable functional polymers for tissue engineering: a brief review. *Sci. China Ser. B* 2014;57(4):490-500.
45. Dash TK, Konkimalla VB. Poly- ϵ -caprolactone based formulations for drug delivery and tissue engineering: A review. *J. Control. Release* 2012;158(1):15-33.
46. Ping P, Wang W, Chen X, Jing X. Poly (ϵ -caprolactone) polyurethane and its shape-memory property. *Biomacromolecules* 2005;6(2):587-592.

47. Kozielski KL, Tzeng SY, Green JJ. A bio reducible linear poly (β -amino ester) for siRNA delivery. *Chem. Comm.* 2013;49(46):5319-5321.
48. Green JJ, Langer R, Anderson DG. A combinatorial polymer library approach yields insight into nonviral gene delivery. *Accounts Chem. Res.* 2008;41(6):749-759.
49. Little SR, Lynn DM, Ge Q, Anderson DG, Puram SV, Chen J, Eisen HN, Langer R. Poly- β amino ester-containing microparticles enhance the activity of nonviral genetic vaccines. *Proc. Natl. Acad. Sci. U. S. A.* 2004;101(26):9534-9539.
50. Fields RJ, Cheng CJ, Quijano E, Weller C, Kristofik N, Duong N, Hoimes C, Egan ME, Saltzman WM. Surface modified poly (β amino ester)-containing nanoparticles for plasmid DNA delivery. *J. Control. Release* 2012;164(1):41-48.

Chapter 4: Biodegradable Artificial Antigen Presenting Cells with Anti PD-1 Immunotherapy to Treat Melanoma

4.1 Introduction

Biomimetic materials that target the immune system hold promise for cancer immunotherapy.¹ Synthetic immunotherapies can be designed with defined characteristics and therefore often outperform their cell-based counterparts. These platforms can be engineered in terms of biodegradability,² controlled release of immunomodulators,³ and physical parameters including shape and size.⁴ Biomimetic materials can be customized to incorporate combination therapies in an all-in-one therapeutic and are therefore an exciting platform for the future of cancer immunotherapy. Despite their potential, current development of combinatorial immunotherapies utilizing biomaterials has been limited as their interaction with other existing therapeutics must first be understood.

Synthetic artificial antigen presenting cells (aAPC), a biomaterial-based immunotherapy, have shown success in generating an anti-tumor immune response *in vitro* and *in vivo*.⁵⁻⁸ aAPC are three-dimensional platforms that minimally express the two signals required for T cell activation – a signal 1, peptide-MHC (pMHC) to provide T cell receptor (TCR) specificity, and a signal 2, such as anti-CD28 monoclonal antibody (mAb) to provide the co-stimulatory “go” signal. aAPC can be functionalized with tumor-specific pMHC to activate a patient’s immune system against cancer antigens and

This chapter contains material modified from the following article previously published as: Kosmides AK, Meyer RA, Hickey JW, Aje K, Cheung KN, Green JJ, Schneck JP. Biomimetic biodegradable artificial antigen presenting cells synergize with PD-1 blockade to treat melanoma. *Biomaterials*. 2017;118:16-26.

mediate tumor rejection.⁹⁻¹¹ They can be utilized in adoptive cell transfer (ACT) of *ex vivo* activated autologous T cells^{9, 12, 13} or directly administered intravenously (IV) for *in vivo* anti-tumor T cell activation.^{14, 15} Synthetic aAPC platforms have distinct advantages over cellular systems in terms of long-term storage and the ability to optimize T cell activation and biocompatibility.¹⁶ Unlike biological antigen presenting cells used as cellular therapy, biomaterial-based aAPC have the advantage of being able to maintain an “always on” state that cannot be down-regulated by the microenvironment as well as flexibility for manufacturing as an acellular product. Compared to PLGA-based drug delivery particles for cancer therapy, the anti-cancer drugs must reach and destroy every cancer cell to ultimately be effective. In contrast, PLGA-based aAPC particles for immunotherapy need only reach tumor specific T cells that can recognize the tumor antigen for the aAPC to then be able to direct a robust systemic immunotherapy response against the cancer cells. Biomimetic modifications of PLGA-based aAPC materials that greatly enhance their effector capacity, including controlling the shape of the aAPC^{4, 17} or slowly releasing pro-inflammatory cytokines from their core,^{18, 19} have demonstrated the benefit of bringing novel materials engineering concepts to the development of immunotherapeutics.

In addition to amplifying positive regulators of the immune system, inhibiting negative regulators has also shown success in generating anti-tumor immune responses. Checkpoint molecules, including programmed death 1 (PD-1) and CTLA-4, are negative regulators of T cell function. These molecules are upregulated on tumor infiltrating lymphocytes and on activated T cells expanded during ACT, being described as a rheostat of the immune system.²⁰ PD-1 signaling inhibits CD8⁺ T cell effector function

upon ligation with its ligand, programmed death ligand 1 (PD-L1), and is one of the methods by which tumors escape immune surveillance. Checkpoint blockade with monoclonal antibodies against PD-1 and PD-L1 delay tumor growth in murine tumor models,^{21, 22} and FDA approved monoclonal anti-PD-1 and anti-CTLA-4 antibodies have shown significant overall response rates and long-term survival benefits. However, clinical responses only reach approximately 30%²³⁻²⁶ indicating that there is a necessity for improvement.

Single-targeted approaches have limited efficacy because cancerous cells utilize multiple mechanisms to avoid immune surveillance and the immune system internally suppresses prolonged strong activation.²⁷ The combination of checkpoint inhibitors with other immunotherapies that boost T cell effector functions or promote cancer cell recognition by the immune system have potential to increase anti-tumor effectiveness. Checkpoint blockade in conjunction with T cell costimulatory antibodies resulted in tumor regression in multiple murine tumor models²⁸⁻³⁰ and increased effector functions of exhausted CD8+ T cells by forcing them out of quiescence.³¹ These studies suggest that checkpoint blockade can boost the effects of other immune-stimulatory approaches, although their interaction with biomaterial-based antigen-specific T cell stimulation has not been studied.

Here, we investigate the synergy between a biomimetic material, biodegradable PLGA-based aAPC, and anti-PD-1 monoclonal antibody treatment for the activation of tumor-specific CD8+ T cells. Combinatorial treatment enhances CD8+ T cell effector functions *in vitro* and significantly delays tumor growth *in vivo*. These results demonstrate the effectiveness of PLGA-based aAPC in combination immunotherapy, and

identify a molecule that could potentially be incorporated and released from polymeric aAPC for increased effectiveness.

4.2 Materials and Methods

4.2.1 Artificial antigen presenting cell synthesis and characterization

Artificial antigen presenting cells were synthesized in a two-step core particle formation and functionalization. Particles cores were synthesized from poly (lactic-co-glycolic acid) (PLGA 50:50 lactic acid to glycolic acid ratio, MW 34,000-58,000 Da) that was purchased commercially (Sigma Aldrich; St. Louis, MO). For a typical microparticle synthesis, 100 mg of PLGA was dissolved in 5 mL dichloromethane and homogenized into a 50 mL, 1% poly vinyl alcohol (PVA) solution by an T-25 digital ULTRA-TURRAX IKA tissue homogenizer at a speed of 5,000 rpm (IKA Works; Wilmington, NC). The resulting microparticle emulsification was then added to 100 mL of 0.5% PVA solution. The dichloromethane was then allowed to evaporate over the course of 4 hrs. After particle hardening, the particles were washed three times in water through centrifugation at 3000 g for 5 min. The washed microparticle solution was flash frozen in liquid nitrogen and lyophilized for 1 day prior to characterization and use.

Functionalization was achieved through EDC/NHS chemistry to conjugate carboxylic acid terminated PLGA to amines on the proteins of interest. Lyophilized particles were dissolved in 0.1 M MES buffer at pH 6.0 at a concentration of 2 mg/mL. 100 μ L of EDC/NHS (Sigma Aldrich; St. Louis, MO) stock solution at 40 mg/mL and 48 mg/mL respectively were added to each sample and the particles were activated for 30 min. The resulting surface activated particles were washed in PBS through centrifugation at 5,000 g for 5 min. The particles were resuspended in PBS at 2 mg/mL. 8 μ g MHC

IgG dimer loaded with the antigen of choice and 10 µg anti-CD28 monoclonal antibody (mAb) (BD Biosciences; San Jose, CA) was added to each sample and the particles were allowed to react with the proteins overnight at 4 °C. The resulting aAPC were washed 3x in PBS through centrifugation at 5,000 g and then dissolved in 400 µL of 100 mg/mL endotoxin free sucrose. The resulting suspension was then lyophilized overnight.

Particle imaging was conducted with a Leo FESEM scanning electron microscope. To prepare samples for analysis, lyophilized particles were mounted onto carbon tape (Nisshin EM Co.; Tokyo, Japan) and placed upon aluminum tacks (Electron Microscopy Services; Hatfield, PA). The excess particles were removed by blowing air across the surface of the tack and the sample was then sputter coated with a 20 nm thick layer of gold-palladium. The samples were then loaded into the microscope and imaged. The images were processed in ImageJ to obtain size information.

To determine the amount of protein on the surface, conjugated aAPC microparticles were stained with Alexa Fluor 647 goat anti-mouse IgG for the dimer and Alexa Fluor 546 goat anti-hamster IgG for the anti-CD28 (Life Technologies; Grand Island, NY) for 1 hour at 4 °C. The particles were subsequently washed with PBS three times and fluorescence readings of particles were evaluated for fluorescence with a BioTek Synergy 2 plate reader (Biotek; Winooski, VT). The mass of protein on the particle was calculated to evaluate conjugation efficiency. Conjugation efficiency was calculated as $(\text{Protein Calculated on Particles})/(\text{Protein Added to Conjugation Media}) * 100\%$.

4.2.2 Anti-PD1 monoclonal antibody synthesis

Anti-PD-1 mAb clone G4 was grown from the G4 hybridoma cell line. Hybridoma cells were grown in hybridoma serum free media supplemented with L-glutamine. After one week, the supernatant was harvested and run over a HiTrap protein G column (GE Healthcare, Little Chalfont, Buckinghamshire, UK), then eluted according to the manufacturer's protocol. G4 mAb was concentrated by membrane ultrafiltration with a Vivaspin 20 50 kDa MWCO (GE Healthcare) and concentration was measured by Nanodrop ND-1000 Spectrophotometer.

4.2.3 *In vitro* artificial antigen presenting cell T cell stimulation

To determine the effectiveness of the aAPC at stimulating antigen specific T cells, we used primary CD8⁺ T cells isolated from PMEL or 2C mouse splenocytes. All mice were maintained according to Johns Hopkins University's Institutional Review Board. The mice were sacrificed and then the spleen was dissected out and homogenized through a cell strainer. The CD8⁺ T cells were then isolated using the Miltenyi CD8a⁺ Isolation Kit (Miltenyi; Auburn, CA). The cells were then stained with Vybrant Cell Tracker carboxyfluorescein succinyl ester (CFSE) (Life Technologies; Grand Island, NY) dye following the manufacturer's protocol. CFSE stained cells were incubated with the particle bearing the antigen of choice at a concentration of 1 mg, 0.1 mg, or 0.01 mg aAPC (polymer weight)/100,000 CD8⁺ T cells in RPMI supplemented with L-glutamine, non-essential amino acids, vitamin solution, sodium pyruvate, β -mercaptoethanol, 10% FBS, ciproflaxin, and a cocktail of T cell growth factors. CFSE dilution was then assessed after three days of incubation through flow cytometry analysis on a BD FACSCalibur. Each generation is defined as a distinct peak of the flow cytometry CFSE histogram, as the CFSE dye is diluted in half with each cell division. Generational

analysis was assessed using the built in function in FlowJo (TreeStar). Total proliferation after seven days was assessed by cell counting on a hemocytometer and using a trypan blue exclusion test to exclude dead cells.

4.2.4 *In vitro* anti-PD-1 mAb functionality assay

To evaluate the functional effectiveness of the synthesized anti-PD-1 mAb, we utilized an *in vitro* assay of repeated CD8⁺ T cell stimulation to upregulate PD-1 expression, as PD-1 expression is low on naïve CD8⁺ T cells. On day 0, primary splenocytes were isolated from naïve 2C transgenic mouse (Jackson Labs; Bar Harbor, ME) spleens through cell straining. Cells were treated with 4 mL of ACK lysis buffer for 1 minute to lyse red blood cells. CD8⁺ T cells were isolated by negative selection with the Miltenyi CD8a⁺ Isolation Kit following the manufacturer's protocol (Miltenyi; Auburn, CA). Micro anti-CD3 (145.2C11)/anti-CD28 (37.51) aAPC were synthesized on 4.5µm M-450 Epoxy Dynabeads (Life Technologies; Grand Island, NY) at a 1:1 protein ratio, following manufacturer's protocol. Anti-CD3 and anti-CD28 antibodies were purchased from BioXCell (West Lebanon, NH). 2C CD8⁺ T cells were mixed with micro aAPC at a 1:1 ratio and cultured in RPMI supplemented with L-glutamine, non-essential amino acids, vitamin solution, sodium pyruvate, β-mercaptoethanol, 10% FBS, ciproflaxin, and a cocktail of T cell growth factors. On day 4, additional T cell growth factors and anti-CD3/anti-CD28 beads were added at a 2:1 bead:cell ratio. On day 6, B16-SIY and B16-F10 cells were cultured in RPMI supplemented with L-glutamine, non-essential amino acids, vitamin solution, sodium pyruvate, β-mercaptoethanol, 10% FBS, ciproflaxin, and 20 ng/ml recombinant murine IFN-γ (R&D Systems, Minneapolis, MN) to upregulate PD-L1 expression.

On day 8, B16-F10 and B16-SIY were harvested and washed three times to remove all IFN- γ , as confirmed by ELISA. CD8⁺ T cells were also harvested, washed three times, and aAPC were removed with a magnet. PD-1 and PD-L1 expression was confirmed on CD8 and B16 cells by flow cytometry using fluorescently labeled anti-PD-1 and anti-PD-L1 antibodies (Biolegend). CD8⁺ T cells and B16-SIY or B16-F10 cells were mixed at a 1:1 effector target ratio in the presence of 10 μ g/ml anti-PD-1 mAb or Armenian hamster IgG isotype control antibody. The cells were co-incubated for 18 hours at 37 °C, then supernatants were collected. IFN- γ was measured by ELISA using the ebioscience murine IFN- γ Ready-SET-Go! Kit (San Diego, CA).

4.2.5 *In vitro* anti-PD-1 mAb and aAPC assay

To evaluate the synergistic effect of aAPC and anti-PD-1 mAb treatment, we utilized an *in vitro* T cell and tumor cell co-incubation assay. CD8⁺ T cells were stimulated at a single earlier time-point prior to the start of the assay to allow for resting time before the secondary stimulation. On day -5, primary splenocytes were isolated from naïve 2C transgenic mouse (Jackson Labs; Bar Harbor, ME) spleens through cell straining, and incubated with a 1:1 ratio of anti-CD3/anti-CD28 microbeads as above. Additional T cell growth factors and media were added on day -2. On day -2, B16-SIY and B16-F10 cells were cultured in the presence of 20 ng/ml IFN- γ , as above. On day 0, B16-F10 and B16-SIY were harvested and washed three times to remove all IFN- γ , as confirmed by ELISA. 2C cells were also harvested, washed three times, and aAPC were removed with a magnet. Cells were stained with PE anti-PD-1, PE anti-PD-L1, PE anti-PD-L2, and isotype control antibody (Biolegend) and read on a BD FACS Calibur to confirm expression. CD8⁺ T cells and B16-SIY or B16-F10 cells were mixed at a 1:1

effector target ratio, and anti-PD-1 mAb and PLGA aAPC were added into culture at titrating amounts. The cells were incubated for 18 hours at 37°, then supernatants were collected. IFN- γ was measured by ELISA using the ebioscience murine IFN- γ Ready-SET-Go! Kit (San Diego, CA).

4.2.6 *In vivo* particle and cell biodistribution study

To evaluate the influence of the combination of adoptively transferred cells on the biodistribution of our aAPC, we used near infrared (IR) fluorescence to track the aAPC upon intravenous administration. The particles and aAPC were synthesized as previously described except that 1 mg of a custom synthesized hydrophobic dye from LI-COR biotechnologies (LICOR Biosciences; Lincoln, NE) was added to the dichloromethane mixture to be encapsulated into the particles. Labeled aAPC were split up into two different treatment groups. For group 1, Thy 1.2+ C57BL/6 mice (Jackson Laboratories; Bar Harbor, ME) received intravenously 2 mg of the IR labeled aAPC alone. For group 2, Thy 1.2+ C57BL/6 mice received intravenously 2 mg of IR labeled aAPC with 1×10^6 Thy1.1+ PMEL CD8+ T cells that had been pre-incubated for 1 hour at 4 °C. Blood was collected retroorbitally at 10, 20, 30, and 40 min post injection to monitor elimination from the bloodstream and was imaged in the LI-COR Pearl Impulse. At 24 hours, mice were sacrificed and the liver, kidney, spleen, heart, and lung were dissected out and imaged in the LI-COR Pearl Impulse (LICOR Biosciences; Lincoln, NE) to determine biodistribution of the particles over 24 hrs. All fluorescence was quantified by ImageJ for normalized measurements of particle concentration. For retroorbital bleeds, the data for each mouse was normalized to the fluorescence value of the initial time point collected. This data was then fit to a single exponential decay curve using the GraphPad

non-linear regression analysis module (GraphPad Software; La Jolla, CA). For organ distribution, the fluorescence readings were normalized to the sum of the fluorescence values across all organs to get a percent distribution across the organs analyzed.

4.2.7 *In vivo* tumor treatment study

To evaluate the efficacy of dual treatment *in vivo* we utilized an adoptive immunotherapy murine melanoma treatment model. Power calculations were performed to determine the necessary group size using assumptions based on previous experience with subcutaneous B16-F10 tumor models. For a two-sided t-test at power level 0.8 and significance level 0.05, at least 6 mice are needed for each group to see statistically significant data in tumor burden differences.

Thy 1.2+ C57BL/6 mice (Jackson Laboratories; Bar Harbor, ME) were inoculated subcutaneously on the right flank with 3×10^5 B16-F10 melanoma cells four days prior to treatment. One day prior to treatment, the mice were irradiated with a central dose of 500 cGy, a sublethal dose to induce transient lymphopenia as per standard approaches to adoptive immunotherapy.³² On the day of treatment, when tumors were palpable, mice were subdivided into four groups randomly by cage: 1) no treatment, 2) CD8+ adoptive transfer + anti-PD-1 mAb, 3) CD8+ adoptive transfer + aAPC, or 4) CD8+ T cell adoptive transfer + anti-PD-1 mAb + aAPC. All injection volumes were 100 μ L. All injections were completed intravenously, and group 1 received mock injections of PBS, labeled as no treatment control. Group 2 received an injection of 1×10^6 Thy 1.1+ PMEL CD8+ T cells and 200 μ g of anti-PD-1 antibody intraperitoneally. Group 3 received an injection of 1×10^6 Thy 1.1+ PMEL CD8+ T cells that had been pre-incubated with 2 mg of PLGA aAPC particles for one hour at 4°C. Group 4 received an injection of 1×10^6

Thy 1.1+ PMEL CD8+ T cells that had been pre-incubated with 2 mg of PLGA aAPC particles as well as 200 µg of anti-PD-1 antibody intraperitoneally. One day post treatment, Groups 2 and 4 received an additional 100 µg of anti-PD-1 antibody intraperitoneally. PD-1 expression on PMEL cells stimulated with 1 mg/ml aAPC was confirmed by staining with an APC-anti-CD8 and PE-anti-PD-1 or isotype antibody (Biolegend) and reading them by flow cytometry after 7 and 24 hours.

At six, ten, and thirteen days post treatment, the mice were bled retroorbitally to analyze peripheral blood. Red blood cells were lysed with 4 min of treatment in ACK lysis buffer and then the remaining white blood cells were stained with anti-CD8a-APC (BD Biosciences; San Jose, CA) and anti-Thy1.1-Alexa Fluor 488 (BioLegend). The cells were then analyzed by flow cytometry on a BD FACSCalibur to evaluate the percentage of antigen specific Thy1.1+ CD8+ T cells in the periphery at the indicated time points. Beginning seven days after treatment, all tumor areas were measured by multiplying the length of the longest dimension by the length of the perpendicular dimension. The mice were sacrificed once tumor size progressed past 200 mm². The *in vivo* experiment was repeated two independent times and results were pooled.

4.2.8 *In vivo* CD8+ T cell harvest and analysis

To further probe the effect of treatment on CD8+ T cells, we used the same *in vivo* set up as used in Section 2.7. However, at day 11 post treatment, tumor size was measured, mice were sacrificed, and spleen and tumors were harvested and homogenized through a cell strainer. Tumor infiltrating lymphocytes (TILs) were isolated by a density separation technique, using Lympholyte-M (Cedarlane; Burlington, Ontario, Canada) according to the manufacturer's protocol. Splenocytes were treated with 4 mL of ACK

lysis buffer for 1 minute to lyse red blood cells. Total immune cells were measured from the spleen and TILs with manual counting on a hemocytometer and a Trypan blue exclusion test to exclude dead cells. Immune cells were stained with surface staining antibodies anti-PD-1-PE/Cy7, anti-Thy1.1-APC, anti-CD8-APC/Cy7(Biolegend); Live/Dead-FITC (Life Technologies; Carlsbad, CA) for 30 minutes at 4 °C. No more than 200,000 cells were used for any given condition. One sample per treatment group per organ was stained with anti-PD-1 mAb isotype antibody anti-RIgG2a-PE/Cy7. All samples were then washed and analyzed by flow cytometry on a BD FACSCalibur.

To look at the stimulatory potential of CD8⁺ T cells isolated from tumor-bearing animals of this *in vivo* experiment, we stimulated splenocytes isolated with micro-aAPC. Techniques previously described in 4.2.3. *In Vitro Artificial Antigen Presenting Cell T-Cell Stimulation* were followed with minor modifications. Briefly, micro Db-GP100/anti-CD28 mAb (37.51) aAPC on 4.5µm M-450 Epoxy Dynabeads (Life Technologies) were made at a 1:1 protein ratio, following manufacturer's protocol. Anti-CD28 monoclonal antibody was purchased from BioXCell (West Lebanon, NH). Splenocytes were stained with CFSE and Db-GP100/anti-CD28 mAb micro aAPC were added to isolated splenocytes at a 1:1 ratio. Total dilution was assessed after three days of incubation by flow cytometry. Percent of diluted CD8⁺ T cells was measured by comparing flow cytometry histograms to non-stimulated controls for each condition studied.

4.3 Results and Discussion

4.3.1 PLGA-based aAPC synthesis and characterization

PLGA-based aAPC were made as recently described.⁴ Briefly, the core PLGA particle was synthesized by a single emulsion technique. The particles were subsequently functionalized by EDC/NHS chemistry with two proteins to mimic the surface of the natural APC which relays two critical signals to CD8+ T cells.⁴ We used a soluble major histocompatibility complex (MHC) Class I-Ig fusion protein to mimic signal 1 in the aAPC/CD8+ T cell interaction, and an agonistic monoclonal anti-CD28 antibody to serve as a costimulatory molecule to mimic signal 2.¹⁷ In this way, the aAPC are designed to activate only a particular cognate CD8+ T cell that recognizes the specific MHC with loaded melanoma antigen peptide as signal 1, which differs from common aAPC synthesis that have anti-CD3 antibody to the surface that could interact with T cells without antigen specificity.

Initially we evaluated the physical and chemical properties of the PLGA-based aAPC by imaging lyophilized particles by scanning electron microscopy (SEM) to determine particle morphology and size (**Figure 4.1A**). SEM images revealed that the conjugated particles were spherical in nature. Image analysis determined an average particle size of 4.42 μm with a standard deviation of 1.45 μm (**Figure 4.1B**). We designed the aAPC to be approximately 4-5 μm in size as this is large enough to mimic the length scale of biological antigen presenting cells and also small enough to avoid pulmonary embolism following systemic injection.

We further looked to optimize protein conjugation and biodegradable particle stability by analyzing the surface protein content over various reaction times. To evaluate the surface protein content, we stained the particles with fluorescent monoclonal antibodies for the conjugated proteins, and measured the effect of incubation time of

activated particle and protein on conjugation efficiency over a 48 hour period (**Figure 4.1C**). There is a clear increase in both pMHC and anti-CD28 mAb content at longer incubation times, maximally approximately 10% and 3% at 48 hours, respectively. This is an important finding for future manufacturing of biodegradable aAPCs; thus, we synthesized all subsequent particles for this study by incubating for 48 hours with protein.

4.3.2 aAPC stimulate peptide-specific CD8⁺ T cells

Biologically, one of the most important properties of an aAPC is the capability to specifically stimulate T cells of interest. This is important because non-specific activation would be problematic as it could lead to off-target inflammation and autoimmunity events. To that end we evaluated the ability of our aAPC to specifically stimulate CD8⁺ T cells from two primary transgenic mice (PMEL or 2C) whose CD8⁺ T cells are all specific for the same peptide-MHC. The particles were functionalized with either Db-GP100 (cognate to PMEL CD8⁺ T cells) or Kb-SIY (cognate to 2C CD8⁺ T cells) peptide-MHC and an anti-CD28 co-stimulatory monoclonal antibody. CD8⁺ T cell activation was quantified by two measurements of cell proliferation – CFSE dilution and day 7 cell counts.

Each particle type was separately incubated with CFSE-labeled 2C or PMEL CD8⁺ T cells, and CFSE dilution was analyzed by flow cytometry after three days. In this assay, if the CD8⁺ T cells are stimulated by the aAPC, they rapidly divide, diluting the CFSE dye between daughter cells following each division. Effective stimulation of CD8⁺ T cells occurred only in the case of a cognate antigen/CD8⁺ T cell match as seen by CFSE dilution (**Figure 4.1D**).

Besides antigen-specificity, we also studied the antigen-specific dosing of aAPC to help guide *in vitro* and *in vivo* studies with checkpoint therapy. Nearly all CD8⁺ T cells divided one or more times at the highest 1 mg dose of aAPC. CD8⁺ T cell expansion was dose dependent as evidenced by CD8⁺ T cell generation analysis of CFSE data (**Figure 4.1D-E**). Nearly 80% of PMEL CD8⁺ T cells divided 4 or more times at a 1 mg particle dose as compared to only 15% at a 0.01 mg dose. For 2C CD8⁺ T cells, which have a lower activation threshold, robust proliferation was seen across all doses studied (**Figure 4.1D-E**).

Cell counts after 7 days of stimulation confirmed the dose-dependence of aAPC-based activation in both transgenic systems (**Figure 4.1F**). At the highest aAPC particle dose of 1 mg, PMEL CD8⁺ T cells reached approximately 30-fold expansion and 2C CD8⁺ T cells reached approximately 20-fold expansion which is similar to our previously reported proliferation levels for spherical PLGA aAPCs.⁴

4.3.3 Anti-PD-1 mAb and aAPC activate cognate CD8⁺ T cells *in vitro*

We hypothesized that simultaneous PD-1 blockade would further enhance activation of cognate cells for adoptive cell transfer. To investigate this, we first developed an *in vitro* system to mimic some of the major immunosuppressive characteristics of the tumor microenvironment. We utilized PD-L1^{hi} target tumor cells and pre-activated CD8⁺ T cells that express PD-1 (schematic, **Figure 4.2A**).

To establish the *in vitro* system, 2C CD8⁺ T cells were stimulated with cognate aAPC on days 0 and 4 to upregulate PD-1 expression. This resulted in elevated PD-1 expression by day 8 compared to naïve cells (**Figure 4.2B**). B16-SIY murine melanoma cells which express the cognate Kb-SIY pMHC, and noncognate B16-F10 murine

melanoma cells, were treated with IFN- γ for 48 hours to upregulate PD-L1 expression (**Figure 4.2C**). All IFN- γ was removed from B16-SIY cells from prior treatment, as confirmed by undetectable levels of the cytokine from B16-SIY cells alone (**Figure 4.2D**).

To validate that the resultant cell phenotypes can model the effect of PD-1 blockade *in vitro*, we first assessed IFN- γ release from CD8⁺ T cells in response to anti-PD-1 mAb alone. 8-day activated PD-1^{hi} 2C CD8⁺ T cells and 48 hour treated PD-L1^{hi} B16-SIY cells were co-incubated at a 1:1 ratio in the presence or absence of 10 μ g/ml anti-PD-1 mAb or isotype control antibody. IFN- γ secretion, a marker of T cell activation, was 2.5-fold higher in the presence of anti-PD-1 mAb (**Figure 4.2D**). Importantly, anti-PD-1 mAb did not stimulate CD8⁺ T cells in the absence of a cognate Signal 1, indicated by co-incubation with noncognate B16-F10 cells. These results demonstrate that this model can assess synergy between anti-PD-1 mAb and aAPC-based CD8⁺ T cell activation *in vitro*.

Next, we sought to investigate the combinatorial power of aAPC and anti-PD-1 mAb treatment *in vitro*. We hypothesized that this two-hit approach would disrupt the inhibitory PD-1/PD-L1 pathway which is upregulated during stimulation and therefore lead to greater CD8⁺ T cell activation by aAPC. 2C CD8⁺ T cells were stimulated for five days with cognate aAPC and B16-SIY cells were primed with IFN- γ as previously described. CD8⁺ T cells and B16 cells were co-incubated at a 1:1 ratio in the presence of titrating amounts of cognate PLGA aAPC and anti-PD-1 mAb alone or in combination, and response was quantified by IFN- γ release (schematic, **Figure 4.2A**). While CD8⁺ T cells secreted minimal levels of IFN- γ with no aAPC or anti-PD-1 mAb treatment, and

either treatment alone increased activation in a dose-responsive manner (**Figure 4.2E**), the combination of aAPC and anti-PD-1 mAb resulted in the greatest activation – over 3.5-fold more IFN- γ secretion over no treatment. No further increase in IFN- γ release was seen with higher anti-PD-1 mAb doses.

4.3.4 PLGA aAPC biodistribution

We next sought to demonstrate the biodistribution of aAPC with and without adoptively transferred CD8⁺ T cells. PLGA aAPC particles encapsulating a near infrared dye were injected intravenously into C57BL/6 mice. Particles were injected either alone or after a co-incubation with cognate CD8⁺ T cells to assess their impact on particle distribution. We serially collected blood and imaged the samples to track fluorescence of the particles (Figure 3a). There was a noticeably faster elimination of the particles in the presence of cells compared to particles alone. A single exponential decay curve was fit to each data set, and it was determined that the effective half-life of the aAPC alone was 11.6 min and aAPC in the presence of cells was 2.8 min. Thus, by 40 min, multiple half-lives occurred, sufficient for the majority of the particles to clear the blood and sufficient to calculate the respective half-lives. At 30 and 40 minutes post injection, there were significantly more aAPC particles still in circulation when particles were injected alone as compared to particles co-injected with cells (**Figure 4.3A**). The particles were not designed to have long circulation in the blood and we anticipated that they would be readily cleared within 40 min from the blood to these organs of interest.

24 hours post administration, the animals were sacrificed and the spleen, liver, kidney, heart, and lung were harvested for fluorescence quantification (**Figure 4.3B**). In both the aAPC alone and the aAPC with cells groups the major organs for accumulation

were the spleen and the liver. The aAPC in the presence of cells potentially had 60.1% greater accumulation in the spleen than the aAPC alone. With regard to the lung ($p<0.05$) and heart ($p<0.01$) it was concluded that there were fewer aAPC particles trapped in these tissues when the aAPC were in the presence of cells compared to aAPC alone. Thus, it was concluded that aAPC and CD8⁺ T cells should be co-injected for optimal localization to lymphoid organs.

This biodistribution study also demonstrated that systemic injection of the aAPC particles with or without cells did not cause an acute safety risk such as embolism. Systemic injection of these micron-scale biomimetic aAPC is a new administration route as we have previously used similar aAPC particles only subcutaneously.⁴ We found the intravenous injections to be well tolerated in all animals. This approach used for the biodistribution studies also highlights another potential advantage of these particular PLGA aAPC biomaterials as it validates that they are capable of co-encapsulating imaging or other agents internally, while orthogonally allowing presentation of biomolecules from their surfaces.

Our studies also suggest a trend that the aAPCs + CD8⁺ T cells resisted the first pass off-target clearance tissue (lung) to accumulate more at the on target immune tissue (spleen). This observed biodistribution to the spleen may help explain the therapeutic outcome. By investigating the interaction and biodistribution of the aAPC biomaterial *in vivo* for the first time, we observed that co-administration with T cells does make a difference. This is a novel approach to T cell immunotherapy as T cells are commonly activated *ex vivo* and then separated from their agonists prior to *in vivo* administration.

4.3.5 Anti-PD-1 mAb synergizes with biodegradable aAPC *in vivo* to delay tumor growth and extend survival

To evaluate the therapeutic potential of combination biodegradable aAPC and anti-PD-1 mAb therapies, we assessed their efficacy alone or in combination in an adoptive immunotherapy melanoma tumor treatment model. Thy1.2+ C5BL/6 mice were inoculated subcutaneously in the right flank with B16-F10 murine melanoma cells (schematic, **Figure 4.4A**). Three days later, all mice were irradiated with a sub-lethal dose of radiation to induce transient lymphopenia. On the following day, naïve cognate Thy1.1+ PMEL CD8+ T cells alone or co-incubated with PLGA aAPC were injected intravenously into treated mice. Anti-PD-1 mAb was given intraperitoneally on the same day and the day after aAPC and CD8+ T cell treatment, as per standard anti-PD-1 mAb treatment.³³ Likewise, PD-1 expression was shown to be upregulated by the CD8+ T cells within 7-24 hours of aAPC activation, and early anti-PD-1 mAb treatment ensured an effect on the stimulated cells. Peripheral blood samples were taken from the mice to evaluate antigen specific CD8+ T cell proliferation of the adoptively transferred cells, and tumor size was measured every other day (see Materials and Methods, 4.2.7).

Analysis of the circulating CD8+ T cell population revealed a proliferative advantage of the adoptively transferred cells in the dual treatment group (**Figure 4.4B**). Significantly higher percentages of Thy1.1+ antigen specific CD8+ T cells were seen in the periphery of mice treated with the combined aAPC and anti-PD-1 mAb treatment as opposed to aAPC or anti-PD-1 mAb alone ($p < 0.001$ on days 10 and 13). There was on average a 4-fold increase in proliferation of CD8+ T cells in the combination treatment

group over the anti-PD-1 mAb alone group and a 2-fold proliferative advantage of the combination treatment group over the aAPC alone group.

A therapeutic benefit of the combination treatment was also seen as determined by inhibition of tumor growth and prolonged survival (**Figure 4.4C-E**). There was a statistically significant reduction in tumor burden for the combination treatment group compared to all other groups past day 15 (**Figure 4.4C**). No single treatment significantly delayed tumor growth. By day 15, the combination treatment group had an average tumor size of 140 mm² – over a 30% reduction in tumor size from the no treatment and single treatment groups with all p values being less than 0.05. Additionally, the survival of the animals was extended only in the combination treatment group (p<0.05) (**Figure 4.4D**). No mice in the non-treated and single treatment groups survived past day 20, whereas 45% of mice in the dual treatment group survived past this time point. This survival advantage was statistically significant compared to all other groups.

4.3.6 Dual anti-PD-1 mAb and aAPC treatment results in superior tumor-specific CD8+ T cells *in vivo*

To understand mechanistically how the combination of aAPC and anti-PD-1 mAb treatment affects tumor-specific CD8+ T cells *in vivo*, we analyzed phenotypic and functional changes in adoptively transferred CD8+ T cells in the various treatment groups. Thy1.2+ C5BL/6 mice were inoculated subcutaneously in the right flank with B16-F10 murine melanoma cells and sublethally irradiated after three days. Mice received either Thy1.1+ PMEL CD8+ T cells alone or co-incubated with aAPC, and were treated with anti-PD-1 mAb as described above. Eleven days after treatment, tumor

infiltrating lymphocytes (TILs) and splenocytes were harvested and adoptively transferred cells were identified by the presence of Thy1.1+ on the cell surface (see Materials and Methods, 4.2.8).

Thy1.1+ CD8+ adoptively transferred PMEL T cells in the TILs expressed significantly higher levels of the immunosuppressive PD-1 molecule in the absence of anti-PD-1 treatment (**Figure 4.5A**). A similar trend was evident in the spleen, where adoptively transferred cells expressed higher PD-1 levels in the absence of any additional treatment (**Figure 4.5B**). PD-1 expression was decreased to a greater extent within TILs as compared to the spleen, approximately 2-fold and 6-fold, respectively, likely because these cells are more immunosuppressed and thus express higher levels of PD-1 in the absence of treatment. Additionally, there was about half the percentage of Thy1.1+ CD8+ T cells in the spleen of mice lacking aAPC treatment as compared to dual treated mice (**Figure 4.5C**).

To investigate the functional capacity of the tumor-specific cells, we studied their ability to expand in response to re-stimulation. Isolated splenocytes from each mouse were stained with a CFSE dye and re-stimulated *in vitro* with aAPC expressing cognate Db-GP100 pMHC and anti-CD28 mAb to expand only tumor-specific cells. After three days, CFSE dilution was assessed by flow cytometry and expanded cells identified. CD8+ T cells from dual treated mice expanded about 2-3 fold more in response to antigen-specific re-stimulation than compared to non-treated and anti-PD-1 mAb only treated mice (**Figure 4.5D**). Together, this data shows that dual aAPC and anti-PD-1 mAb treatment leads to a change in expression of checkpoint molecules and increases the proliferative capacity of CD8+ T cells both within the tumor microenvironment and

secondary lymphoid tissue. PD-1 blockade reduces CD8⁺ T cell PD-1 expression and aAPC treatment increases tumor-specific CD8⁺ T cell expansion and re-activation potential. Thus, combination therapy leads to a superior CD8⁺ T cell population by facilitating both lower expression of the immunosuppressive PD-1 molecule and increased proliferative and functional capacity.

4.3.7 Discussion

Stimulating a tumor-specific cytotoxic CD8⁺ T cell response is a promising approach in cancer immunotherapy, although several hurdles still exist in generating a population of cells that is both optimally effective and persistent. Often, very large numbers of activated T cells, up to $10^{11,12}$ are necessary for an objective response. Advancements in biomimetic and biodegradable aAPC have made robust activation for clinical therapy possible, although strong activation upregulates immunosuppressive surface molecules on the CD8⁺ T cells such as PD-1. As progress is made in the field of biomaterials for robust T cell activation, it is likewise necessary to understand their interaction with other conventional immunotherapeutics, including new clinical standards of care, to counterbalance the resultant inhibitory phenotype.

Here, we have characterized the synergistic interaction between biodegradable PLGA aAPC and PD-1 checkpoint blockade for murine tumor control in an adoptive transfer model. PLGA-based aAPC were chosen as they are effective T cell stimulators, and, due to well-known experience with PLGA particles in the body, offer translational potential for tumor-specific CD8⁺ T cell expansion *in vivo*. We showed antigen-specific stimulation of CD8⁺ T cells in response to PLGA aAPC conjugated with two different

peptide-MHC complexes. The aAPC are able to induce robust expansion in each of the tested cell types.

However, the immune system has developed ways to self-regulate itself by upregulating immunosuppressive molecules in response to activation. In this nature, activated CD8⁺ T cells express high levels of PD-1 which is important biologically to control autoimmunity, but detrimental in cancer immunotherapy where a strong anti-tumor response is desired. Tumors take advantage of this biological process and express the ligand for PD-1, PD-L1, to inhibit an anti-tumor CD8⁺ T cell response. Our *in vitro* model of PD-1^{hi} CD8⁺ T cells and PD-L1^{hi} tumor cells, mimicking those that would be found within the tumor microenvironment of a patient, showed increased CD8⁺ T cell activation in response to the combination of aAPC stimulation and PD-1 blockade. While both therapeutics alone increased activation, the combination was able to stimulate CD8⁺ T cells while turning off their “rheostat” and led to a further enhanced antigen-specific response.

Finally, we sought to study the effectiveness of combination treatment *in vivo* since the dynamics of the tumor microenvironment can play a significant role in the response. The aAPC were first demonstrated to circulate systemically, both with and without a co-injection of cognate CD8⁺ T cells. When aAPC were co-injected with CD8⁺ T cells, they spent less time in circulation and accumulated less in off-target sites such as the lung and heart. This comparison is both interesting and important, as the intrinsic honing capabilities of CD8⁺ T cells may cause accumulation of aAPC in immune-dense sites. Indeed, we did see a trend towards higher aAPC accumulation in secondary lymphoid tissue - the spleen. While this >50% change in distribution was not

significant under the conditions studied, it may help to explain the statistically shorter circulation half-life of particles co-injected with cells along with the greater accumulation of tumor-specific CD8⁺ T cells in the spleens of mice treated with particles and cells *in vivo*.

Combination of aAPC expressing tumor antigens and anti-PD-1 mAb treatment resulted in delayed tumor growth and extended survival *in vivo* in an adoptive transfer model of naïve tumor specific cells. While many adoptive immunotherapy approaches begin with pre-activated CD8⁺ T cells, our approach demonstrates significant anti-tumor activity in the absence of prior stimulation and thus reduces the time, cost, and technical hurdles associated with *ex vivo* cell culture. Importantly, this is the first time this PLGA aAPC-based therapeutic was effective in a therapeutic rather than prophylactic tumor model as well as the first time that it has been evaluated following systemic administration.⁴ The therapeutic effect was shown to be due to increased proliferation of the adoptively transferred tumor-specific cells both in the peripheral blood and spleen in response to aAPC transfer, as well as decreased PD-1 expression by these cells in the spleen and tumor in response to anti-PD-1 mAb treatment. Despite only two anti-PD-1 mAb treatments on days 0 and 1, there was still a significant nearly 6-fold decrease in CD8⁺ T cell PD-1 expression 10 days after the last anti-PD-1 administration. Importantly, this strong stimulation of the tumor-specific CD8⁺ T cells did not lead to unresponsiveness—CD8⁺ T cells from the spleen of the dual treatment group also expanded the greatest amount upon re-stimulation *ex vivo*.

In summary, anti-PD-1 immunotherapy unleashes more of the aAPC-activated CD8⁺ T cells to perform effector function whereas without anti-PD-1 mAb therapy more

aAPC-activated CD8⁺ T cells were ineffective due to the immunosuppressive tumor cells expressing PD-L1. Furthermore, aAPC activate and increase the number of CD8⁺ T cells that anti-PD1 therapy can target and affect. CD8⁺ T cells not activated by aAPC do not proliferate as much or upregulate PD1, thus decreasing the total effect of the checkpoint blockade immunotherapy. Therefore, both therapies complement and synergize to provide a more potent tumor immunotherapy.

4.4 Conclusions

Here we have developed a biomaterial-based combinatorial cancer immunotherapy. This therapeutic simultaneously activates cytotoxic CD8⁺ T cells while reducing the immune dampening effects of the tumor microenvironment. We have developed a biomimetic PLGA-based aAPC that can, in an antigen specific fashion, stimulate cancer-targeting CD8⁺ T cells and synergize with PD-1 checkpoint blockade. The aAPC particles generate a cytotoxic response against melanoma cells *in vitro* and, for the first time, these aAPC have been shown effective in an *in vivo* tumor treatment model following a single intravenous injection. The combined therapy was able to mediate a reduction in tumor burden and increase median survival time. As the aAPC are composed of PLGA, a biodegradable material that has a track-record of safe use in the clinic with related technologies, these advanced immunostimulatory materials may be promising for combination treatment in the clinical application of cancer immunotherapy.

4.5 Figures

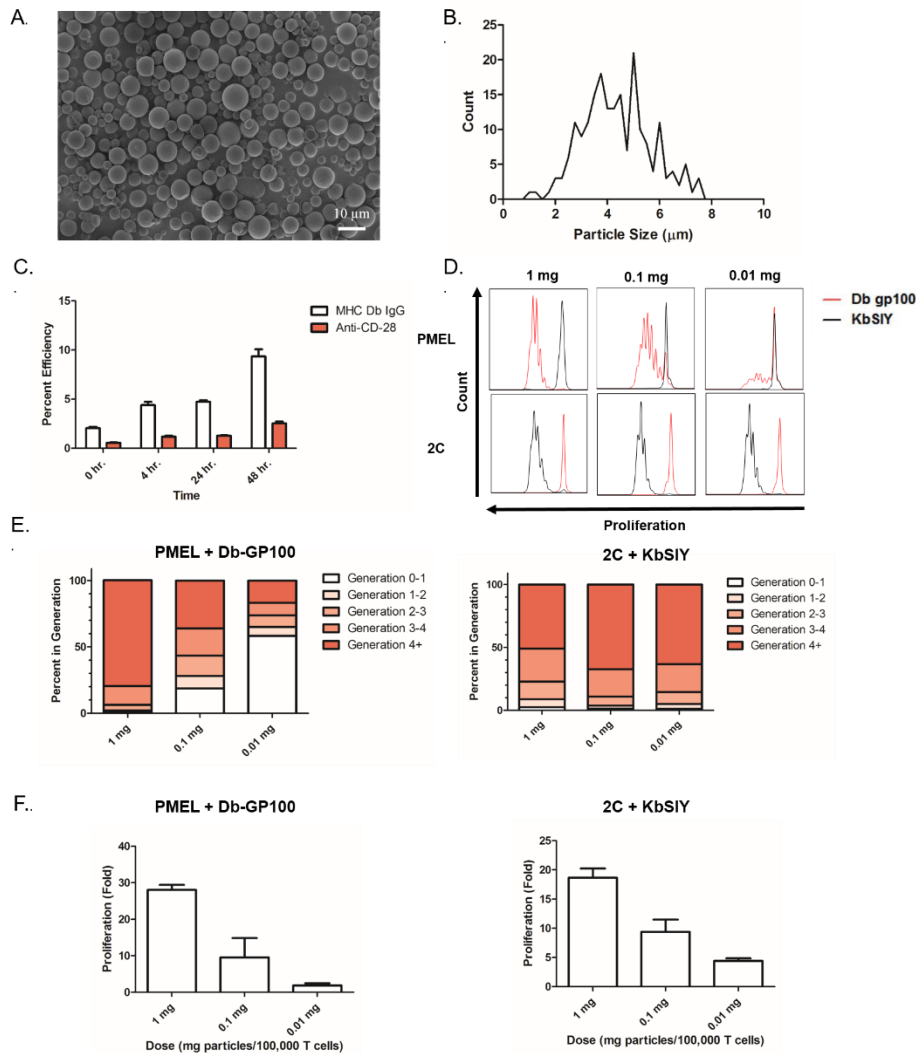


Figure 4.1: aAPC characterization and functional assessment. (a) SEM micrographs of conjugated aAPC microparticles. (b) Particle size distribution of conjugated aAPC microparticles as evaluated by image analysis of SEM micrographs. (c) Particle protein content on aAPC microparticles as evaluated by fluorescent antibody staining of the particles and measured by a fluorescent plate reader. Conjugation efficiency is defined in Materials and Methods. (d) Antigen specific CD8⁺ T cell stimulation capabilities of aAPC microparticles. CFSE dilution of CD8⁺ T cells from either PMEL or 2C TCR transgenic mice incubated for 3 days with indicated dose of particles (1 mg, 0.1 mg, 0.01 mg) functionalized with the indicated antigen, GP100 or SIY peptide. (e) Generation analysis of CFSE dilution data in (d) indicates antigen specific proliferation of PMEL and 2C CD8⁺ T cells in response to stimulation by Db-GP100 (left) or Kb-SIY (right) aAPC microparticles. (f) Fold proliferation calculated by day 7 cell counts after stimulation with the Db-GP100 (left) or Kb-SIY (right) aAPC microparticles indicates antigen specific proliferation of CD8⁺ T cells. Error bars are SEM of n=3 replicates.

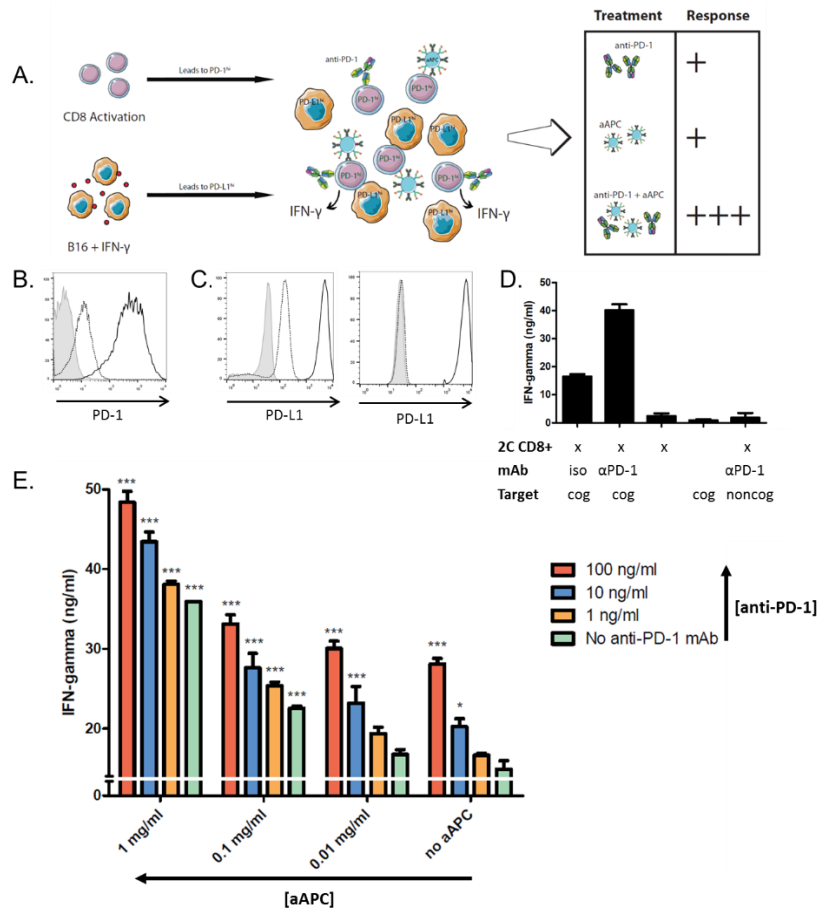


Figure 4.2: aAPC and anti-PD-1 mAb show greater CD8+ T cell activation in combination. (a) Schematic of *in vitro* tumor microenvironment model system. 2C CD8+ T cells were isolated and stimulated with a 1:1 cell:aAPC ratio and B16-SIY and B16-F10 cells were incubated with 20 ng/ml IFN-γ. Activated 2C CD8+ T cells and B16 cells were purified from aAPC and IFN-γ, respectively, and combined at a 1:1 effector to target ratio with additional aAPC in the presence or absence of anti-PD-1 mAb. IFN-γ release was measured by ELISA after 18 hours. (b) CD8+ T cells are PD-1^{hi} after dual aAPC activation (black), compared to expression on naive cells (dotted) and isotype (grey). (c) B16-SIY (left) and B16-F10 (right) are PD-L1^{hi} after IFN-γ treatment (black) as compared to untreated cells (dotted) and isotype (grey). (d) PD-1^{hi} 2C CD8+ T cells and target PD-L1^{hi} B16-SIY (cognate; cog) or B16-F10 (noncognate; noncog) were co-incubated at a 1:1 ratio in the presence of 10 ug/ml anti-PD1 mAb or isotype control (iso). Anti-PD-1 mAb increased CD8+ T cell IFN-γ release as compared to isotype. No IFN-γ release was measured in response to CD8+ T cells and noncognate B16-F10 cells incubated with anti-PD-1 mAb. Significance was measured by one-way ANOVA with Dunnett's post-test. (e) CD8+ T cells secrete more IFN-γ in response to increasing doses of both aAPC and anti-PD-1 mAb. Error bars represent SEM, and significance compared to no treatment (i.e. no aAPC, anti-PD-1) is shown (* = p<0.05, ** = p<0.01, *** = p<0.001). Both aAPC and anti-PD-1 significantly affect IFN-γ (p<0.001; F_{3,40}=226.4 and F_{3,40}=88.32, respectively) by two-way ANOVA.

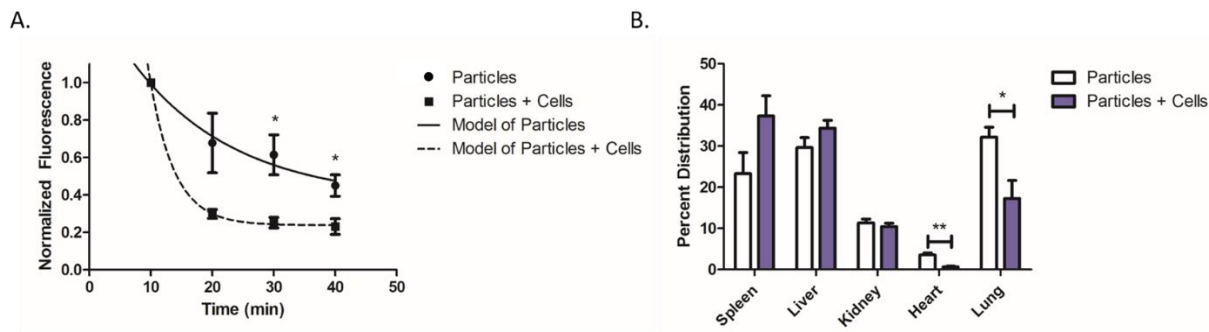


Figure 4.3: Co-administration of aAPC with CD8⁺ T cells impacts aAPC biodistribution. (a) Blood was collected retroorbitally following intravenous administration of IR fluorescence labeled particles alone or incubated with cells. Blood was imaged and fluorescence was quantified and normalized to the first time point collected. Asterisk indicates time points at which normalized data was significantly different between the two groups. Lines through the points denote first order exponential decay curves fit to the data. In the presence of cells, the aAPC particles are eliminated faster than without cells. (b) At 24 hrs post-aAPC administration, the organs were dissected out, imaged, and quantified for fluorescence. In the presence of cells, the aAPC particles resist getting trapped in the lungs ($p < 0.05$) or the heart ($p < 0.01$), and trend towards accumulating more in the spleen ($p = 0.1$). Error bars are SEM of $n = 3$ replicates. (*= $p < 0.05$, **= $p < 0.01$)

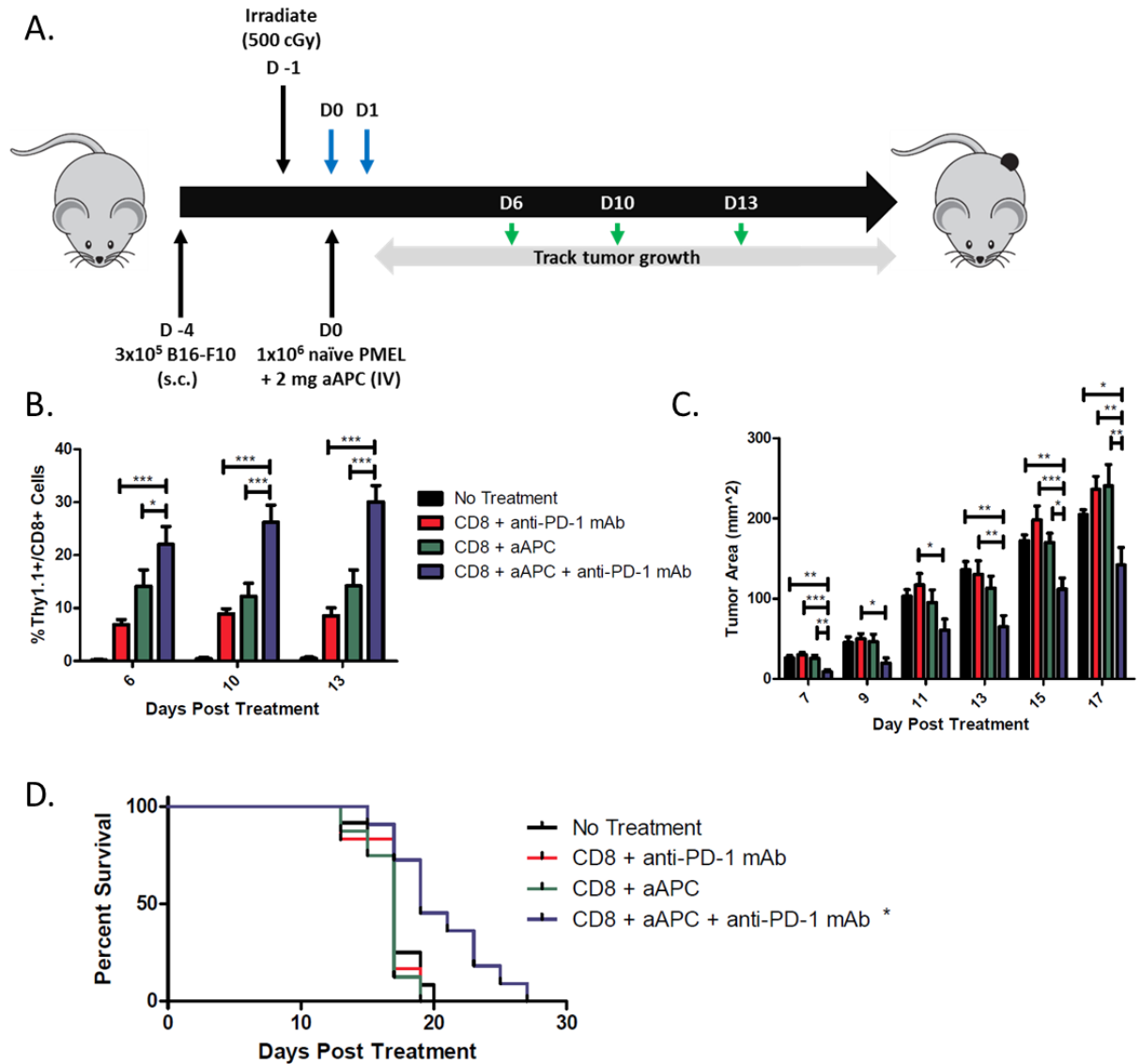


Figure 4.4: Anti-PD1 mAb and aAPC synergize to mediate anti-tumor activity *in vivo*. (a) Schematic of the adoptive transfer experiment. Blue arrows indicate anti-PD-1 mAb treatment, green arrows indicate blood sampling days. (b) Percent of CD8⁺ T cells in peripheral blood that are Thy1.1⁺. Anti-PD1 mAb and aAPC dual therapy mediated the best proliferation of antigen-specific CD8⁺ T cells *in vivo*. Significance evaluated with one-way ANOVA with Tukey's post-test. All treatment groups were significantly different from no treatment at all time points. (c) Tumor measurements indicate an anti-tumor response was mediated by the dual therapy group. Significance measured by one-way ANOVA with Tukey's post-test. (d) Kaplan-Meier survival plots indicate that dual therapy mediates the best survival. Only combination treatment resulted in significantly extended survival compared to no treatment by log-rank test ($p < 0.05$). Error bars represent the standard error of $n = 8-12$ mice/group. Results from two independent experiments are pooled. (* $p < 0.05$, ** $p < 0.01$, *** $p < 0.001$)

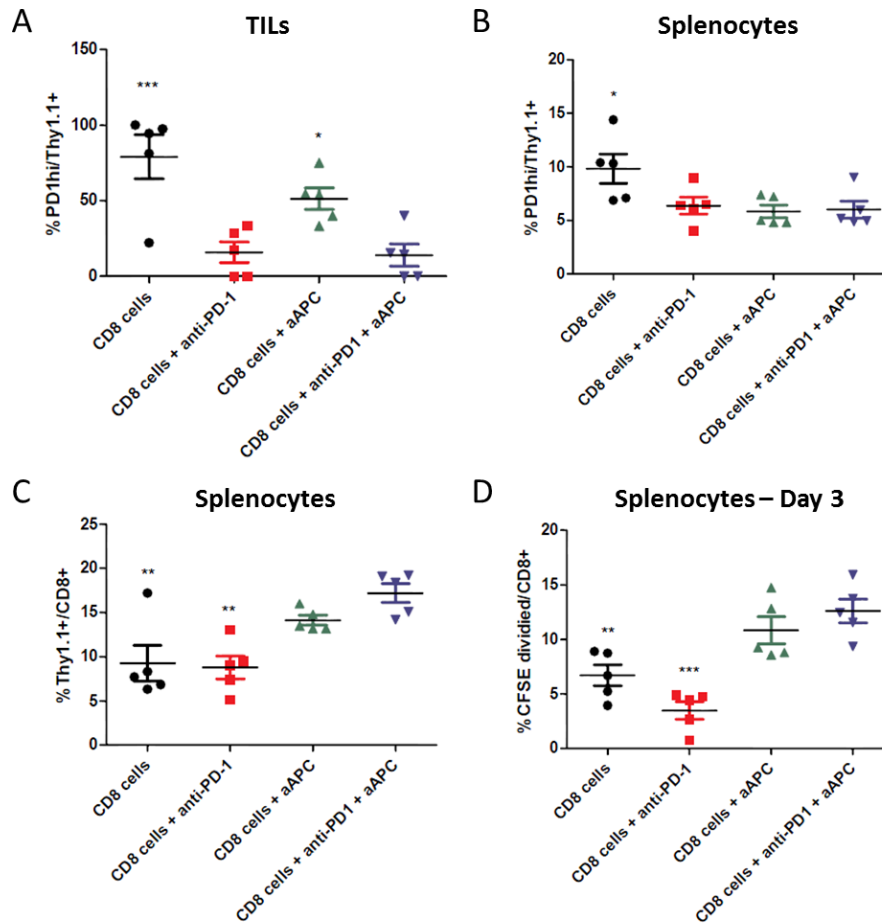


Figure 4.5: Anti-PD-1 mAb and aAPC combination therapy decreases PD-1 expression and increases expansion of tumor-specific CD8+ T cells. C57BL/6 mice were inoculated with B16-F10 tumors on day -4 and sublethally irradiated on day -1. On day 0, mice received an IV injection of PMEL Thy1.1+ CD8+ T cells either alone or co-incubated with cognate aAPC. Two of the groups also received an IP injection of anti-PD-1 mAb on days 0 and 1. Splenocytes and TILs were harvested on day 11. (a) Thy1.1+ TILs of mice not treated with anti-PD-1 mAb had significantly elevated PD-1 expression as compared to dual treated mice. (b) Thy1.1+ cells in the spleen of non-treated mice also had significantly elevated PD-1 expression as compared to dual treatment. (c) CD8+ T cells within the spleen of mice not treated with aAPC had a significantly lower percentage of Thy1.1+ tumor-specific cells as compared to dual treatment. (d) Splenocytes were CFSE stained and re-stimulated with Db-GP100/anti-CD28 mAb aAPC, and CFSE dilution was assessed after 3 days. There was significantly less expansion of tumor-specific CD8+ T cells in mice not treated with aAPC. Significance measured by one-way ANOVA with Dunnett's post-test comparing all groups to dual treatment. (* $p < 0.05$, ** $p < 0.01$, *** $p < 0.001$)

4.6 References

1. Purwada A, Roy K, Singh A. Engineering vaccines and niches for immune modulation. *Acta. Biomater.* 2014;10(4):1728-40.
2. Danhier F, Ansorena E, Silva JM, Coco R, Le Breton A, Préat V. PLGA-based nanoparticles: An overview of biomedical applications. *J. Control Release.* 2012;161(2):505–22.
3. Jhunjhunwala S, Raimondi G, Glowacki AJ, Hall SJ, Maskarinec D, Thorne SH, Thomson AW, Little SR. Bioinspired controlled release of CCL22 recruits regulatory T cells in vivo. *Adv. Mater.* 2012;24(35):4735-38.
4. Sunshine JC, Perica K, Schneck JP, Green JJ. Particle shape dependence of CD8+ T cell activation by artificial antigen presenting cells. *Biomaterials.* 2014;35(1):269–77.
5. Oelke M, Schneck JP. Overview of a HLA-Ig based “Lego-like system” for T cell monitoring, modulation and expansion. *Immunol. Res.* 2010;47(1-3):248–56.
6. Durai M, Krueger C, Ye Z, Cheng L, Mackensen A, Oelke M, Schneck JP. In vivo functional efficacy of tumor-specific T cells expanded using HLA-Ig based artificial antigen presenting cells (aAPC). *Cancer Immunol. Immunother.* 2009;58(2):209–20.
7. Sasawatari S, Tadaki T, Isogai M, Takahara M, Nieda M, Kakimi K. Efficient priming and expansion of antigen-specific CD8+ T cells by a novel cell-based artificial APC. *Immunol. Cell Biol.* 2006;84(6):512–21.
8. Latouche JB, Sadelain M. Induction of human cytotoxic T lymphocytes by artificial antigen-presenting cells. *Nat. Biotechnol.* 2000;18(4):405–9.
9. Ye Q, Loisiou M, Levine BL, Suhoski MM, Riley JL, June CH, Coukos G, Powell DJ Jr. Engineered artificial antigen presenting cells facilitate direct and efficient expansion of tumor infiltrating lymphocytes. *J. Transl. Med.* 2011;9(1):131.
10. Gong W, Ji M, Cao Z, Wang L, Qian Y, Hu M, Qian L, Pan X. Establishment and characterization of a cell based artificial antigen-presenting cell for expansion and activation of CD8+ T cells ex vivo. *Cell Mol. Immunol.* 2008;5(1):47–53.
11. Maus M V, Thomas AK, Leonard DGB, Allman D, Addya K, Schlienger K, Riley JL, June CH. Ex vivo expansion of polyclonal and antigen-specific cytotoxic T lymphocytes by artificial APCs expressing ligands for the T-cell receptor, CD28 and 4-1BB. *Nat. Biotechnol.* 2002;20(2):143–8.
12. Rosenberg SA, Restifo NP. Adoptive cell transfer as personalized immunotherapy for human cancer. *Science.* 2015;348(6230):62–8.
13. Butler MO, Lee J-S, Ansén S, Neuberg D, Hodi FS, Murray AP, Drury L, Berezovskaya A, Mulligan RC, Nadler LM, Hirano N. Long-lived antitumor CD8+ lymphocytes for adoptive therapy generated using an artificial antigen-presenting cell. *Clin. Cancer Res.* 2007;13(6):1857–67.
14. Ugel S, Zoso A, De Santo C, Li Y, Marigo I, Zanovello P, Scarselli E, Cipriani B, Oelke M, Schneck JP, Brote V. In vivo administration of artificial antigen-presenting cells activates low-avidity T cells for treatment of cancer. *Cancer Res.* 2009;69(24):9376–84.
15. Shen C, Cheng K, Miao S, Wang W, He Y, Meng F, Zhang J. Latex bead-based artificial antigen-presenting cells induce tumor-specific CTL responses in the

- native T-cell repertoires and inhibit tumor growth. *Immunol. Lett.* 2013;150(1-2):1–11.
16. Sunshine JC, Green JJ. Nanoengineering approaches to the design of artificial antigen-presenting cells. *Nanomedicine.* 2013;8(7):1173–89.
 17. Meyer RA, Sunshine JC, Perica K, Kosmides AK, Aje K, Schneck JP, Green JJ. Biodegradable Nanoellipsoidal Artificial Antigen Presenting Cells for Antigen Specific T-Cell Activation. *Small.* 2014:1–7.
 18. Steenblock ER, Fadel T, Labowsky M, Pober JS, Fahmy TM. An artificial antigen-presenting cell with paracrine delivery of IL-2 impacts the magnitude and direction of the T cell response. *J Biol Chem.* 2011;286(40):34883–92.
 19. Steenblock ER, Fahmy TM. A comprehensive platform for ex vivo T-cell expansion based on biodegradable polymeric artificial antigen-presenting cells. *Mol. Ther.* 2008;16(4):765–72.
 20. Okazaki T, Chikuma S, Iwai Y, Fagarasan S, Honjo T. A rheostat for immune responses: the unique properties of PD-1 and their advantages for clinical application. *Nat. Immunol.* 2013;14(12):1212–18.
 21. Iwai Y, Ishida M, Tanaka Y, Okazaki T, Honjo T, Minato N. Involvement of PD-L1 on tumor cells in the escape from host immune system and tumor immunotherapy by PD-L1 blockade. *Proc. Natl. Acad. Sci. U. S. A.* 2002;99(19):12293–7.
 22. Pilon-Thomas S, Mackay A, Vohra N, Mulé JJ. Blockade of programmed death ligand 1 enhances the therapeutic efficacy of combination immunotherapy against melanoma. *J. Immunol.* 2010;184(7):3442–9.
 23. Callahan MK, Wolchok JD. At the bedside: CTLA-4- and PD-1-blocking antibodies in cancer immunotherapy. *J. Leukoc. Biol.* 2013;94(1):1–13.
 24. Ascierto P a., Marincola FM. 2015: The Year of Anti-PD-1/PD-L1s Against Melanoma and Beyond. *EBioMedicine.* 2015;2(2):92–3.
 25. Robert C, Long G V., Brady B, et al. Nivolumab in previously untreated melanoma without BRAF mutation. *New Engl. J. Med.* 2015;372(4):320–30.
 26. Robert C, Ribas A, Wolchok JD, et al. Anti-programmed-death-receptor-1 treatment with pembrolizumab in ipilimumab-refractory advanced melanoma: a randomised dose-comparison cohort of a phase 1 trial. *Lancet.* 2014;384(9948):1109–17.
 27. Chen DS, Mellman I. Oncology Meets Immunology: The Cancer-Immunity Cycle. *Immunity.* 2013;39(1):1–10.
 28. Vilgelm AE, Johnson DB, Richmond A. Combinatorial approach to cancer immunotherapy: strength in numbers. *J. Leukoc. Biol.* 2016;100:149–60.
 29. Shindo Y, Yoshimura K, Kuramasu A, Watanabe Y, Ito H, Kondo T, Oga A, Ito H, Yoshino S, Hazama S, Tamada K, Yagita H, Oka M. Combination Immunotherapy with 4-1BB Activation and PD-1 Blockade Enhances Antitumor Efficacy in a Mouse Model of Subcutaneous Tumor. *Anticancer Res.* 2015;136:129–36.
 30. Chen S, Lee L-F, Fisher TS, et al. Combination of 4-1BB Agonist and PD-1 Antagonist Promotes Antitumor Effector/Memory CD8 T Cells in a Poorly Immunogenic Tumor Model. *Cancer Immunol Res.* 2014;3(2):149–60.

31. Buchan SL, Manzo T, Flutter B, et al. OX40- and CD27-mediated costimulation synergizes with anti-PD-L1 blockade by forcing exhausted CD8⁺ T cells to exit quiescence. *J. Immunol.* 2015;194(1):125–33.
32. Wrzesinski C, Paulos CM, Kaiser A, et al. Increased intensity lymphodepletion enhances tumor treatment efficacy of adoptively transferred tumor-specific T cells. *J. Immunother.* 2010;33(1):1-7.
33. Li B, Vanroey M, Wang C, Chen THT, Korman A, Jooss K. Anti-programmed death-1 synergizes with granulocyte macrophage colony-stimulating factor-secreting tumor cell immunotherapy providing therapeutic benefit to mice with established tumors. *Clin. Cancer Res.* 2009;15(5):1623-34.

Chapter 5: Biodegradable Nanoellipsoidal Artificial Antigen Presenting

Cells for Antigen Specific T-Cell Activation

5.1 Introduction

Biomimetic artificial antigen presenting cells (aAPCs) have shown substantial promise as a platform for immune system activation and modulation. Antigen specific aAPCs reconstitute the critical T-Cell recognition (“signal 1”) and activation (“signal 2”) signals presented at the surface of APCs by presenting peptide-in-MHC and positive costimulatory molecules such as anti-CD28 antibody on the surface of the particle. Classically, aAPCs are cell sized (2-10 μm), spherical particles, and have been made using a variety of materials, from liposomes^{1,2} to magnetic beads,³⁻⁷ to non-degradable⁸ and degradable polymeric microparticles.⁹⁻¹¹ Despite the extensive *in vitro* data supporting the efficacy of these particles *in vitro*, *in vivo* translation has been limited due to the poor bioavailability and activity of spherical micron sized particles. Nanoparticle systems offer an attractive alternative to micron sized particles as drug delivery vehicles for the aAPC platform. Recently, nanoparticles have been utilized for various therapeutic and diagnostic applications, such as tumor targeting and imaging.¹²⁻¹⁶ Biodistribution of these drug carriers has been of special interest in the past few years, as efforts have been made to engineer nanoparticles that simultaneously target the region of interest and can be eliminated efficiently to avoid toxicity.¹⁷⁻²⁰

This chapter contains material modified from the following article previously published as: Meyer RA, Sunshine JC, Perica K, Kosmides AK, Aje K, Schneck JP, Green JJ.. Biodegradable nanoellipsoidal artificial antigen presenting cells for antigen specific T-Cell activation. *Small*. 2015;11(13):1519-25.

One major issue with attempting to translate the aAPC technology onto the nanoscale is that the literature strongly supports the concept that receptor occupancy over a large surface area of contact is a critical determinant for activation; for aAPCs, 4-5 μm particles were found to be superior to 1 μm particles, and the difference could not be made up simply by increasing the particle dose.⁸ However, these systems use spherical particles as the core of the construct which, for a given volume, provide the minimum surface area of contact between a T-Cell and aAPC.

Non-spherical, anisotropic nanoparticles have recently gained increasing attention within the biomaterials community for a numerous reasons. A wide variety of shapes have been synthesized by bottom-up and top-down approaches.^{21,22} Nanoparticles with altered shape offer potential improvements in intracellular particle delivery and *in vivo* circulation time by aligning with blood flow and reducing phagocytosis,^{23,24} enhanced targeting of diseased microvasculature,²⁵ reduction of non-specific particle uptake,²⁶ and improved specific particle uptake and cancer cell killing.²⁷ In particular, prolate ellipsoids (semi-axes: $a > b = c$) showed the most efficient particle attachment with lowest *in vitro* internalization rates when compared to oblate ellipsoids (semi-axes: $a = b > c$) or spherical particles.²⁸ Non-spherical prolate nanoellipsoids have shown enhanced tissue targeting of brain and lung endothelium.²⁹ With regard to immune stimulation, we have recently shown that non-spherical microparticles were much more successful at functioning as aAPCs compared to spherical microparticle aAPCs, inducing stronger, and more efficient, antigen specific T-Cell responses.³⁰

For nanoscale aAPCs (naAPCs), altering the particle shape could allow for an interfacial geometry (at the interface between the aAPC and the T-Cell) that is more

similar to successful microparticulate systems, including a microscale radius of curvature for the long axis. In addition, non-spherical naAPCs have the potential for improved *in vivo* biodistribution as compared to microparticles due to easy access to draining lymph nodes and suitability for intravenous injection. Non-spherical naAPCs can also take advantage of a shape-dependent reduction in non-specific uptake and improved circulation time through avoidance of the RES system. Based upon these proposed benefits, we elected to study how shape might affect naAPC function and *in vivo* biodistribution. In addition, while aAPCs are often constructed of nondegradable materials for *ex vivo* use, we wished to construct effective biodegradable nanoscale aAPCs for the first time to make them more amenable for *in vivo* therapeutic use.

5.2 Materials and Methods

5.2.1 Nanoparticle preparation

Acid terminated poly (lactic-co-glycolic acid) (PLGA 50:50 lactic acid to glycolic acid ratio, MW 34,000-58,000 Da) was purchased commercially (Sigma Aldrich; St. Louis, MO). 200 mg of PLGA was dissolved in 5 mL dichloromethane and sonicated into 50 mL 1% poly vinyl alcohol (PVA) solution by Misonix S-4000 probe sonicator operating at 12 W of power (Qsonica; Newtown, CT). The resulting emulsification was then added to 100 mL of 0.5% PVA solution. The solution was agitated by magnetic stirbar and the dichloromethane was allowed to evaporate over the course of 4 hrs. The solution was then centrifuged at 3000 g for 5 min to pellet out any non nanodimensional materials. The supernatant was removed and ultracentrifuged three times at 17,000 g for 15 min to wash away the PVA. The resulting nanoparticle solution was flash frozen in liquid nitrogen and lyophilized for 2 days prior to characterization and use.

5.2.2 Thin film stretching and nonspherical particle preparation

Lyophilized PLGA nano particles were dissolved in a 10% PVA and 2% glycerol solution at a concentration of 5 mg/mL and 5 mL of this solution was deposited into 5 cm x 7 cm rectangular petri dishes (VWR; Radnor, PA) to dry overnight. The resulting film was cut to size and loaded in between two aluminum mounts and heated up to 90 °C. The film length was measured and the film was stretched slowly to produce the desired fold of stretch (e.g. 2 fold stretched ellipsoidal particles). The film was then allowed to cool down to room temperature and was removed from the aluminum blocks. The PVA film was dissolved in water and the resulting particle suspension was washed 3x by ultracentrifugation at 40,000g. The particles were lyophilized prior to use.

5.2.3 Protein conjugation and naAPC formation

Lyophilized spherical or non-spherical particles were dissolved in 0.1 M MES buffer at pH 6.0 at a concentration of 2 mg/mL 100 µL of EDC/NHS (Sigma Aldrich; St. Louis, MO) stock solution at 40 mg/mL and 48 mg/mL respectively were added to each sample and the particles were activated for 30 min. The resulting surface activated particles were washed by centrifugation at 16,000 g. The particles were resuspended in 1x PBS at 2 mg/mL. 8 µg MHC IgG Db dimer loaded with gp100 and 10 µg biotin anti-CD28 (BD Biosciences; San Jose, CA) was added to each sample and the particles were allowed to react with the proteins overnight at 4 °C. The resulting naAPCs were washed 3x by centrifugation at 16,000 g and then dissolved in 400 µL of 100 mg/mL endotoxin free sucrose. The resulting suspension was then lyophilized overnight.

5.2.4 Characterization of the naAPC

To confirm the formation of non-spherical particles, we imaged the samples under a Hitachi 7600 TEM (Hitachi High-Tech; Tokyo, Japan). The particle samples to be imaged were transferred to a parlodion grid for 5 min and then stained in 1% uranyl acetate for 1 min. The grids were dried and imaged under the TEM. To determine particle size we utilized a NanoSight NS500 (Malvern Instruments; Westborough, MA) for nano tracking analysis (NTA) following the manufacturer's protocols. Protein surface quantification was accomplished through the use of AlexaFluor 488 labeled dimers and APC conjugated anti CD28. The proteins were conjugated by EDC/NHS chemistry under the conditions described above, and then fluorescence readings were taken utilizing a BioTek Synergy 2 plate reader (Biotek; Winooski, VT). The resulting fluorescent signal was correlated back to a mass of protein by a standard curve to derive conjugation efficiency. To track particle surface release, we suspended particles conjugated to fluorescently labeled dimers and anti-CD28 in PBS at 37 °C. The resulting suspension was spun down at the indicated time points and the supernatant was removed to analyze fluorescence. The amount of fluorescence was correlated to the amount of protein released from the surface of the particles by standard curve.

5.2.5 *In Vitro* T-Cell Stimulation

To evaluate aAPC immune induction potential we utilized an *in vitro* T-Cell stimulation assay. Particles were prepared as described above at different stretch folds. Primary splenocytes were isolated from fresh PMEL mouse (Jackson Labs; Bar Harbor, ME) spleens through cell straining. The splenocytes were treated with 4 mL of ACK lysis buffer for 1 minute to lyse the red blood cells. CD8⁺ T-Cells were isolated from the splenocyte mixture utilizing the Miltenyi CD8a⁺ Cell Isolation Kit IIa following the

manufacturer's protocol (Miltenyi; Auburn, CA). The CD8⁺ cells were then stained with Vybrant carboxyfluorescein succinyl ester (CFSE) (Life Technologies; Grand Island, NY) for 15 min followed by washing and a 1 hr. incubation time. 100,000 labeled CD8⁺ T-Cells were then mixed with either 1 mg, 0.1 mg, or 0.01 mg of the appropriate naAPC sample and then cultured in RPMI supplemented with L-glutamine, non essential amino acids, vitamin solution, sodium pyruvate, β -mercaptoethanol, 10% FBS, ciprofloxacin, and a cocktail of T-Cell growth factors. Three days post stimulation, half of the CD8⁺ T-Cells were pooled and analyzed by flow cytometry for CFSE dilution. Seven days post stimulation, the cells were stained with trypan blue and manually counted (excluding stained cells) to determine proliferation fold over the initial input of cells.

5.2.6 Nanoparticle Cell Uptake

Nanoparticles were fabricated as described above except the initial DCM solution contained 2 mg of TAMRA in addition to the PLGA. The resulting labeled particles were stretched as described above and lyophilized prior to use. As a model of non-specific endothelial cell uptake, we utilized human umbilical vein endothelial cells (HUVECs). HUVECs were cultured in EGM-2 media with the added bullet kit of supplements (Lonza; Basel, Switzerland). As a model of phagocytic particle clearance, we utilized RAW 264.7 murine macrophages. RAW 264.7 macrophages were cultured in Dulbecco's Modified Eagle Medium (Life Technologies; Grand Island, NY) supplemented with 10% FBS and penicillin/streptomycin. Cells were seeded at a density of 15,000 cells per well on a 96 well plate. For dosing experiments, the media was withdrawn, and media containing the noted amount of particles was added and the cells were incubated for 24 hrs. For time course experiments, 0.1 mg of particles was added in

media to each sample and incubated for the times noted. At the end of the incubation, the cells were washed 3x with PBS and either trypsinized off (HUVECs) or triturated off (RAW 264.7 macrophages). The cells were then analyzed by flow cytometry on an Accuri C6 Flow Cytometer (BD Biosciences; San Jose, CA) for particle uptake. Confocal micrographs were obtained by fixing the cells, staining with AlexaFluor 488 phalloidin (Life Technologies; Grand Island, NY) and DAPI, and imaging under a Zeiss 710 LSM (Carl Zeiss Microscopy; Jena, Germany).

5.2.7 *In Vivo* Biodistribution Experiments

Spherical and non-spherical naAPCs were fabricated as described above except 1 mg of a custom synthesized near IR 800 nm hydrophobic fluorophore (LICOR Biosciences; Lincoln, NE) was added to the DCM mixture to label the particles for *in vivo* imaging. In addition, stretching was conducted at 75 °C as the dye was determined to be heat sensitive. For animal studies, nude SCID mice supplied by Jackson Labs (Jackson Laboratories; Bar Harbor, ME) were utilized. Prior to intravenous injection of the aAPCs, the particles were suspended in PBS and analyzed under the plate reader (Biotek; Winooski, VA) to determine the near IR fluorescence and the injectate per mouse was adjusted to 100,000 fluorescent units. After intravenous tail vein injection, blood was collected retroorbitally at 10 min, 20 min, 30 min, and 40 min post injection utilizing Micro-Hematocrit Capillary Tubes (Fisherbrand; Pittsburgh, PA). The whole animal was imaged at 1 hr., 2 hr., and 4 hr. timepoints utilizing a LICOR Pearl Impulse Imaging system (LICOR Biosciences; Lincoln, NE). Blood was also imaged upon collection in order to quantify fluorescence from the particles. To quantify the dispersion of the naAPC, we quantified the fluorescence in the regions of the image corresponding

to the liver and spleen ($F_{\text{liver+spleen}}$) as well as the entire animal ($F_{\text{entire animal}}$) and computed the dispersion fraction as:

$$DF = 1 - \frac{F_{\text{liver and spleen}}}{F_{\text{whole animal}}}$$

At the end of the 4 hr. timepoint, the animals were sacrificed and the organs were dissected out and imaged. The fluorescence was quantified to determine the distribution of the naAPC across the spleen, liver, kidney, and lung.

5.2.8 *In Vivo* T-Cell Stimulation Experiment

IV injected particles were assessed for their ability to stimulate adoptively transferred T cells *in vivo*. Spherical and non-spherical particles were fabricated as above. One day prior to adoptive transfer, transient lymphopenia was induced in C57BL/6 mice (Jackson Labs; Bar Harbor, ME) by sublethal irradiation (500 cGy) using an MSD Nordion Gammacell with dual Cs137 source (Johns Hopkins Molecular Imaging Center). The following day, CD8⁺ T-cells were isolated from Thy1.1⁺ PMEL mouse spleens, as described above. CD8 T-cells were washed and resuspended in PBS. T cells were then co-incubated with spherical, non-spherical, or no particles (2 mg per 10⁶ cells) for 1 hour at 4 °C. Recipient Thy1.2⁺ C57/BL6 mice tail veins were intravenously injected with 1 x 10⁶ PMEL T cells with or without particles (n=3-5 per group). Percent Thy1.1⁺ CD8 cells in peripheral blood was measured on days 6, 8, and 10 post IV injection. Blood was collected retroorbitally as described above, and red blood cells were lysed with ACK lysis buffer for 1 minute. Cells were stained with anti-Thy1.1-Alexa Fluor 488 (BioLegend) and anti-CD8a-APC (BD Biosciences; San Jose, CA) for 30 minutes and analyzed using a BD FACS Calibur. On day 10, spleens and inguinal, cervical, and axillary lymph nodes were harvested and were broken up to a single cell suspension.

Spleens were treated with ACK lysing buffer for 1 minute to lyse red blood cells. Spleen and lymph node samples were then stained with anti-Thy1.1-Alexa Fluor 488 (BioLegend; San Diego, CA) and anti-CD8a-APC (BD Biosciences; San Jose, CA) for 30 minutes and analyzed using a BD FACS Calibur and FlowJo software.

5.2.9 *In Vivo* Tumor Treatment Experiment

In order to analyze the tumor treatment efficacy we utilized the model that was developed in Chapter 4 for the evaluation of aAPC activity in the context of the immune checkpoint blockade anti PD-1. Briefly, 3×10^5 B16-F10 melanoma cells were injected into the right flank of Black 6 mice. 3 days following tumor implantation, the mice were irradiated with a sublethal dose of 500 cGy to induce transient lymphopenia. The following day, the mice were given one of the following treatments: 1×10^6 PMEL T-Cells i.v., 1×10^6 PMEL T-Cells i.v. with 200 μ g i.p. anti PD-1, 1×10^6 PMEL T-Cells i.v. with 200 μ g anti PD-1 i.p. and 2 mg of spherical nano aAPC i.v., or 1×10^6 PMEL T-Cells i.v. with 200 μ g anti PD-1 i.p. and 2 mg of ellipsoidal nano aAPC i.v. The following day the mice that received the 200 μ g dose of anti PD-1 received a follow up dose of 100 μ g of anti PD-1. Seven days following the initial treatment the tumor areas were measured and recorded every other day until the areas reached 200 mm² at which point the mouse was sacrificed.

5.2.10 Image Analysis and Statistics

All image analyses and quantifications were done utilizing ImageJ software. Statistics for T-Cell proliferation results and *in vivo* T-Cell stimulation were computed in GraphPad Prism (GraphPad Software; La Jolla, CA) as one way ANOVA with Dunnett's posttest comparing to the indicated control. Statistics for nanoparticle uptake and

biodistribution were computed as a one tailed unpaired t-test assuming unequal variances comparing spherical to ellipsoidal. Statistical significance was assumed if $p < 0.05$ for all tests conducted.

5.3 Results and Discussion

5.3.1 Characterization of non-spherical nano aAPCs

To study the utility of non-spherical naAPCs for antigen-specific T-cell activation, we adapted a film stretching technique originally developed by Ho et. al.³¹ and more recently adapted to generate polymeric micro- and nanoparticles of varied shape.³² To ensure biodegradability of the naAPCs, we synthesized PLGA nanoparticles using a single-emulsion with sonication method (see supplemental methods for details). We then cast them in a thin PVA film, and either stretched the film at 90°C or not (to fabricate ellipsoid or spheroid particles respectively), and then removed the nanoparticles by dissolution (**Figure 5.1A**). We applied different amounts of stretch extent to the film to generate a range of nanoparticle aspect ratios. Generation of prolate ellipsoids from spherical nanoparticles yields high aspect ratio and large radius of curvature particles with minimal change to overall particle surface area (see **Table 5.1** for more details). For example, a 2-fold stretch of a 200 nm spherical particle produces a prolate ellipsoid with an aspect ratio of 2.8, a radius of curvature along the long axis of 1.14 μm , and a modest surface area gain of 16%. Thus with an ellipsoidal aAPC, we can mimic the more effective microparticle based aAPC radius of curvature. We then fabricated the spherical and ellipsoidal nanoparticles into aAPCs by adding peptide loaded MHC-IgG dimers (pMHC-dimers) and anti-CD28 mAb to their surface via EDC/NHS chemistry to conjugate to the acid terminated PLGA polymer (**Figure 5.1A**).

The generated PLGA nanoparticles were 225 nm in diameter with a slightly net negative charge (-2.9 ± 0.8 mV in PBS); stretching the particles resulted in ellipsoidal nanoparticles with the same volume that were also similarly slightly negatively charged (-2.2 ± 0.2 mV in PBS). Stretching was confirmed by TEM analysis utilizing a negative stain of 1% uranyl acetate (**Figure 5.1B-E**). We conjugated fluorophore-labeled MHC-IgG dimer (labeled with Alexa 488) and labeled anti-CD28 mAb (labeled with APC) to the surface of spherical and ellipsoidal nanoparticles and quantified the total fluorescence on the particles by plate reader. Spherical and ellipsoidal nanoparticles showed similar levels of MHC-IgG dimer and anti-CD28 mAb conjugation. In addition, increasing amounts of MHC-IgG dimer and anti-CD28 in synthesis lead to an increased amount of protein conjugated to the particle surface, indicating that aAPC synthesis was concentration dependent over the range tested (**Figure 5.1F-G**). We also examined particle stability by conjugating fluorescently-labeled MHC-IgG dimer and anti-CD28 to the surface of the particles, incubating the particles in physiological conditions (1x PBS at 37 °C), and analyzing particle stability at various points in time. As shown, the spherical particles and ellipsoidal particles exhibited similar stability *in vitro* and more than 50% of the proteins were still conjugated to particles after incubation for 7 days (**Figure 5.2**).

5.3.2 Evaluation of immune stimulatory capacity of non-spherical nano aAPCs

To examine whether these functionalized naAPCs could generate antigen specific CD8⁺ T-Cell responses, we coupled gp100-loaded MHC-Ig dimer (or non-cognate peptide loaded dimer) and anti-CD28 monoclonal antibody (mAb) to the surface of spherical and ellipsoidal nanoparticles. Since optimal particle dosing was unknown, and

particle/antigen dose has been previously shown to be a critical parameter in activation of T-Cells by other aAPC systems, we performed a dose titration. T-Cells were exposed *in vitro* to 1 mg, 0.1 mg, and 0.01 mg PLGA naAPC / 100,000 cells, and antigen specific T-Cell expansion was evaluated via CFSE dilution (3 days post stimulation) and total T-Cell proliferation (7 days post stimulation).

CFSE dilution analysis of the non-spherical 2-fold stretched naAPCs vs. the spherical naAPCs revealed a clear shape dependency on initial proliferation rates (**Figure 5.3A-B**). This effect was noted to be most profound at the middle dose of 0.1 mg/100,000 T-Cells (**Figure 5.3B**). The lowest dose of 0.01 mg/100,000 cells appeared to have little effect on T-Cell proliferation for either spherical or nonspherical aAPC (**Figure 5.3A**). At the highest dose of 1 mg /100,000 cells both spherical and non-spherical naAPCs were effective at stimulating T-Cells (**Figure 5.3C**). Based on these results we decided to probe the effect of shape further by analyzing the effect of different degrees of stretch (1.5, 2, 2.5, 3, 3.5-fold) on the naAPC activation of CD8⁺ T-Cells. Generation analysis of CFSE data revealed that naAPCs were not effective at the low dose of 0.01 mg/100,000 T-Cells (**Figure 5.3D**). In addition, all naAPC formulations were able to generate > 10-fold antigen-specific T-Cell proliferation at a saturating dose of 1 mg/100,000 T-Cells (**Figure 5.3F**). However, at the mid-range dose of 0.1 mg / 100,000 cells, there was a marked difference at aAPC stimulation of the spherical and non-spherical naAPCs (**Figure 5.3E**).

T-Cell proliferation counts reflected the trends demonstrated in the CFSE generation data. At the lowest dose of naAPC stimulation (**Figure 5.3G**), there was little stimulation of all particle shapes tested except for 2.5-fold stretched naAPC, which

demonstrated a significant ($p < 0.05$) increase in proliferation (3-fold) compared to spherical naAPC (1-fold). The clearest shape dependency was demonstrated at the mid-range dose (**Figure 5.3H**). All ellipsoidal naAPC significantly outperformed the spherical naAPC ($p < 0.05$). As an example, the 2-fold stretched naAPC induced a 15-fold expansion of the T-Cells compared to the spherical particles which induced a 3-fold expansion. The benefit of the non-spherical shape was apparent at the high dose (**Figure 5.3I**), and significant ($p < 0.05$) for the 2.5-fold and 3.5-fold stretched naAPC. To simplify experimental comparison, all subsequent studies in this work were conducted with the spherical and the 2-fold stretched ellipsoidal particles.

5.3.3 Evaluation of cellular uptake of non-spherical nano aAPC

In addition to offering a functional benefit to T-Cell stimulation, another potential advantage of ellipsoidal naAPC is that they may offer improved *in vivo* drug delivery properties, such as a reduction in non-specific cell uptake.²⁸ To that end, we investigated whether nanoparticle uptake was shape dependent. By loading PLGA nanoparticles with a fluorescent dye (TAMRA), we were able to examine the impact of particle shape on uptake by confocal microscopy and flow cytometry. We modeled two different modes of uptake. For phagocytic cells present in the reticuloendothelial system (RES), RAW 264.7 macrophages were used as a model. Confocal analysis of the macrophages treated with 0.1 mg of particles / 15,000 cells demonstrated a clear preference for spherical particles (**Figure 5.4A**) vs. non-spherical particles (**Figure 5.4B**). Flow cytometry analysis reflected this difference across a variety of doses (**Figure 5.4C**) and incubation times (**Figure 5.4E**). Maximal dose-dependent uptake was determined to be 78% for the spherical particles and 14% for the ellipsoidal particles. Over the course of 72 hours, the

uptake percentages equilibrated between the spherical and ellipsoidal groups demonstrating the capability of the ellipsoidal particles to resist uptake.

As a model of non-specific uptake by endocytosis in vascular cells, we looked at particle uptake in primary human umbilical vein endothelial (HUVEC) cells *in vitro*. Spherical particles were taken up by up to 10% of the HUVEC cells during a 24 hour incubation period, with increasing frequency given an increased particle concentration (**Figure 5.4D**). In addition, the amount of particles taken up by the cells was noted to increase over longer incubation times (**Figure 5.4F**). We saw no significant ellipsoidal particle uptake at any particle dose or at any time point in the HUVECs. Representative gated flow cytometry plots show spherical particle uptake for the HUVECs and macrophages (**Figure 5.5**). Viability of RAW macrophages was similar between the spherical and nonspherical particle groups at all doses (**Figure 5.6**).

5.3.4 *In vivo* biodistribution of non-spherical nano aAPC

Next, we sought to validate the *in vitro* shape dependent uptake seen with HUVECs and macrophages *in vivo* by performing a biodistribution experiment to evaluate the circulation half-life and overall distribution characteristics of the ellipsoidal naAPCs compared to the spherical naAPCs. Biodistribution of spherical and ellipsoidal naAPCs were examined in nude SCID mice over a four-hour period. naAPCs for biodistribution were synthesized encapsulating a custom made hydrophobic 800nm near IR dye (LI-COR Bioservices) in the interior of the naAPCs and conjugating MHC-IgG dimer and mouse anti-CD28 mAb to the naAPC surface. Two groups of nude mice received 100,000 fluorescent units of spherical or ellipsoidal naAPC via tail vein injections. Retroorbital bleeding was conducted at 10, 20, 30 and 40 minute intervals

after injections of naAPC to determine blood clearance. Mice were then imaged with a LI-COR Pearl Impulse at 1, 2 and 4 hours post injection to evaluate biodistribution. After the 4 hour time point of imaging, mice were sacrificed to image spleen, liver, kidney and lung.

Ellipsoidal naAPCs demonstrated superior pharmacokinetic profiles compared to the spherical naAPCs. Live whole animal imaging analysis revealed that the ellipsoidal naAPCs remained in the periphery for longer periods of time, as evidenced by the greater signal distributed throughout the animal (compare **Figure 5.7A** and **5.7B**). Images of the blood collected were analyzed by Image J to quantitatively examine the elimination from the blood over the first hour of the experiment. Results indicate that ellipsoidal naAPCs maintained a higher concentration in the bloodstream than spherical naAPCs, sustained over 40 min (**Figure 5.7C**). By fitting a first-order exponential decay curve we extracted the time constants for blood elimination and calculated the half-life. Ellipsoidal naAPCs exhibited a significantly ($p < 0.05$) longer half-life at 34.8 min \pm 0.8 min than the spherical naAPCs at 25.2 min \pm 2.8 min (**Figure 5.7D**). In order to further characterize resistance to uptake by the RES, we quantified the signal obtained from the regions corresponding to the liver and spleen and subtracted it from the signal obtained from the entire animal. This value was then normalized to the signal measured over the entire region of the animal to obtain a parameter termed the dispersion fraction. The higher nanoellipsoidal circulation concentration was reflected in the dispersion fraction at the 1 hour time point (**Figure 5.7E**), further validating the finding that the ellipsoidal naAPCs could resist RES uptake compared to spherical naAPCs. No significant difference was noted at the longer 2 hour and 4 hour timepoints, which was expected due to the particle

half-lives. Spleen and liver accumulation of the naAPC was similar based on image analysis of the 1 hour, 2 hour, and 4 hour timepoints (**Figure 5.8**). Organ distribution analysis demonstrated similar endpoint distributions for the spherical and non-spherical naAPC (**Figure 5.9**).

5.3.5 *In vivo* T-Cell stimulation capacity of non-spherical nano aAPCs

Given the advantages of the ellipsoidal aAPC compared to the spherical aAPC seen *in vitro*, including superior T-Cell stimulation, reduced non-specific cell uptake, and better half-life/distribution upon systemic injection, we were interested to evaluate the *in vivo* T-Cell stimulatory capabilities of the ellipsoidal naAPC versus the spherical naAPC. To this end, we utilized an adoptive immunotherapy murine model. We irradiated Thy 1.2+ C57BL/6 mice with a sublethal dose of radiation and then administered the antigen specific aAPC and Thy 1.1+ PMEL T-cells simultaneously via intravenous tail vein injection. Mice received either the 2-fold stretched ellipsoidal aAPC with T-Cells, the spherical aAPC with T-Cells, or T-Cells alone. On days 6, 8, and 10 post injection, the mice were bled retroorbitally and the blood was analyzed for PMEL T-Cell expansion through the use of labeled anti-CD8 and anti-Thy 1.1 antibodies and flow cytometry. At the end of 10 days, the mice were sacrificed, and the spleen and lymph nodes were dissected and analyzed for PMEL T-Cell expansion.

Ellipsoidal naAPCs mediated significantly higher PMEL CD8+ T-Cell expansion *in vivo* compared to spherical naAPCs over the course of the experiment as evidenced by blood analysis of PMEL T-Cell content (**Figure 5.10A**). On both day 6 and day 8, there was a statistically significant increase in ellipsoidal aAPC mediated T-Cell expansion compared to both spherical mediated T-Cell expansion and no aAPC treatment. On day

10, there was a statistically significant increase of the ellipsoidal aAPC mediated expansion of PMEL T-Cells compared to control. However, the spherical naAPC could not mediate a statistically significant increase in T-Cell proliferation compared to the control groups on any of the days measured. The ellipsoidal aAPC induced nearly a 3-fold greater expansion over the no treatment group and a 2-fold greater expansion over the spherical aAPC group. Analysis of the dissected spleen (**Figure 5.10B**) and lymph nodes (**Figure 5.10C**) supported the observations seen in the blood with an overall greater increase in PMEL T-Cell content of the ellipsoidal aAPC compared to the spherical aAPC and the no treatment groups. This difference was statistically significant between the ellipsoidal and no treatment groups only.

5.3.6 *In vivo* tumor treatment mediated by non-spherical nano aAPCs

Finally, in order to evaluate the potential cancer immunotherapy applications of the non-spherical nano aAPC compared to the spherical nano aAPC, we utilized a murine melanoma model developed in Chapter 4 to evaluate the efficacy of aAPC in the context of immune checkpoint blockade. As expected, the anti PD-1 in the context of cognate T-Cells could not mediate any substantial reduction in tumor burden compared to the control of cognate T-Cell administration alone. The addition of spherical nano aAPC also could not mediate a significant effect vs. the controls. However, the inclusion of the ellipsoidal nano aAPC resulted in a stark effect on tumor measurements that was statistically significant compared to all other groups almost every day the measurements were taken. For example, 15 days post treatment all groups, including the spherical nano aAPC group were measured in the range of 150 mm². The ellipsoidal nano aAPC group, however, had a tumor burden in the range of only 50 mm², a 66% reduction compared to

controls (**Figure 5.11A**). The decreased tumor burden translated to an increased survival benefit in the ellipsoidal nano aAPC group only (**Figure 5.11B**). The median survival was increased from 17 days post-treatment (observed for all other groups including spherical nano aAPCs) to 24 days post-treatment. Taken together, this data demonstrates the ellipsoidal nano aAPC is significantly more effective at mediating an immunological anti-tumor effect *in vivo*, thus validating it as an important improvement over traditional spherical aAPC technology.

5.4 Conclusions

Nanoellipsoidal aAPCs offer multiple advantages over traditional spherical aAPCs. We demonstrated that, under the same synthesis conditions and particle surface protein content, non-spherical naAPCs are more effective at antigen specific induction of CTLs than spherical naAPCs. In addition, these non-spherical naAPCs demonstrated stronger *in vivo* stimulation of immune cells and enhanced pharmacokinetic properties. Previous studies of nano aAPCs focused on the use of quantum dots, spherical PLGA particles, and magnetic iron dextran particles.^{7,10,33} We showed for the first time that the efficacy of biodegradable nanoscale aAPCs can be enhanced by modulating shape in synthesis. By utilizing a non-spherical biodegradable nanoparticle, ellipsoidal naAPCs achieved T-Cell activation and proliferation comparable to previously reported nano aAPCs at a reduced overall protein dose.⁷ In addition to offering an efficiency advantage, ellipsoidal nanoparticles offer reduced cellular uptake by macrophages and endothelial cells *in vitro* and resist hepatic and splenic elimination *in vivo*. Finally, the ellipsoidal nano aAPC demonstrated enhanced capacity to stimulate cognate T-Cells *in vivo*, as well as mediate an anti-tumor effect in a melanoma immunotherapy model. Taken together,

the enhanced immune stimulatory capabilities and systemic biodistribution of ellipsoidal naAPCs make them a promising platform for “off the shelf” immunotherapy and nanomedicine.

5.5 Tables

Table 5.1: Nanoparticle parameters altered by the thin film stretching procedure. Stretch = Fold stretch for the film in the stretching procedure. AR = Calculated aspect ratio. Rel. SA = Normalized surface area to the spherical particle. Eq R_a = Equivalent radius of curvature along the short axis of the prolate ellipsoid for a stretched 200 nm particle. EqR_b = Equivalent radius of curvature along the long axis for a stretched 200 nm particle. Calculations were completed following the model presented in Ref 1.

Stretch	AR	Rel SA	EqR _a (nm)	EqR _b (nm)
Sphere	1	1	200	200
1.5	1.84	1.06	88	560
2	2.83	1.16	50	1140
2.5	3.95	1.27	32	1980
3	5.20	1.38	22	3200
3.5	6.55	1.48	16	4600

5.6 Figures

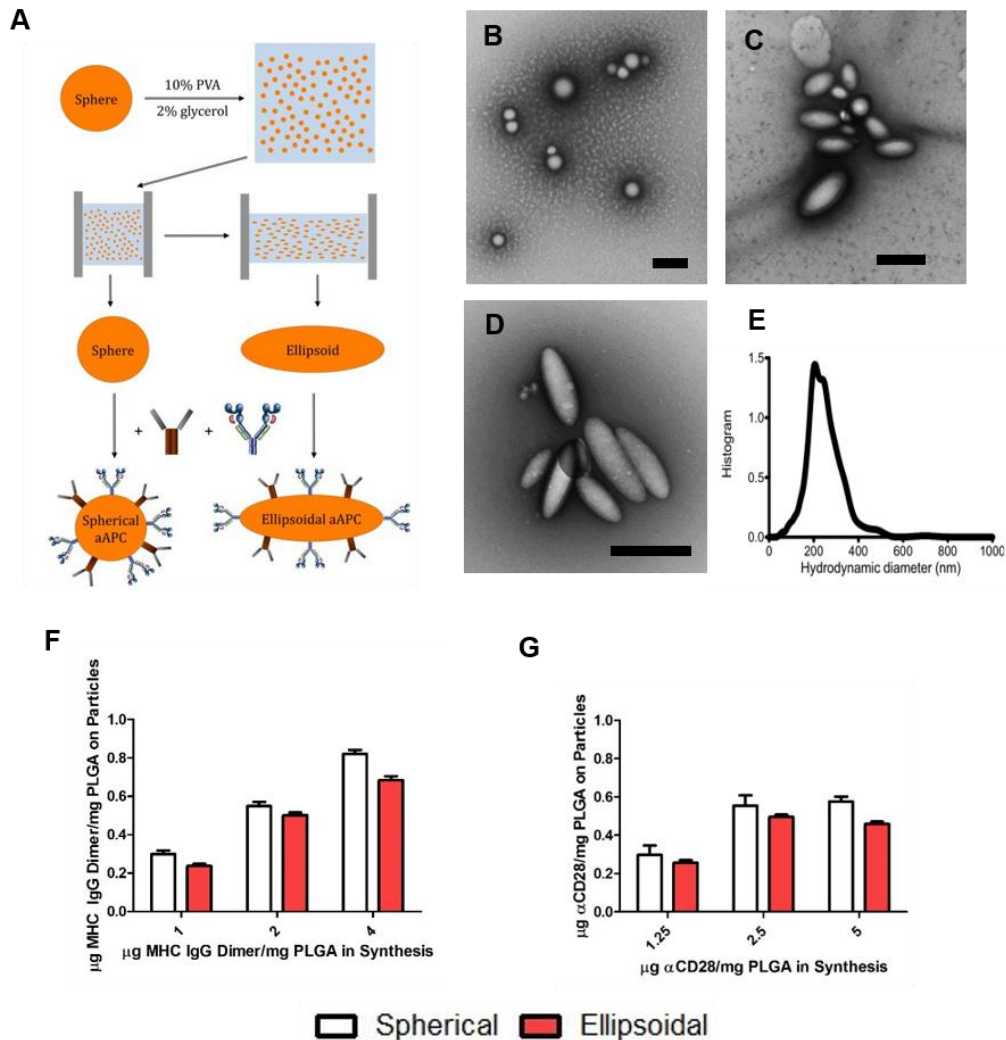


Figure 5.1: Non-spherical and spherical nanodimensional artificial antigen presenting cell (naAPC) characterization. (a) PLGA nanoparticles were synthesized by single emulsion and elongated utilizing the film stretching method. Conjugation of MHC Db Ig Dimer and anti CD-28 mediated by EDC/NHS chemistry resulted in naAPCs. (b,c,d) TEM images of (b) non-stretched spherical particles (c) 2-fold stretched particles, and (d) 3-fold stretched particles. Scale bars are 500 nm. (e) Particles were sized by Nanoparticle Tracking Analysis and determined to be 224 nm in size. The particle protein conjugation efficiency on spherical and 2-fold stretched ellipsoids for (f) MHC Db Ig dimer and (g) anti CD-28 was analyzed by conjugation of fluorescent protein. Conjugation results demonstrate similar amounts of protein bound to each particle shape. Error bars represent standard errors of >3 trials.

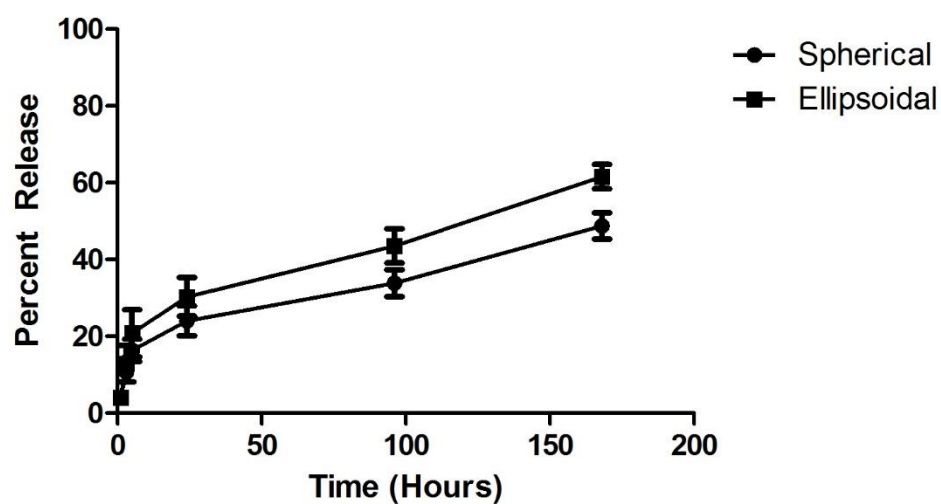


Figure 5.2: 2-fold stretched ellipsoidal and spherical nano aAPC exhibit similar stabilities in aqueous media. Particles were conjugated to fluorescently labeled gp100 MHC Db Ig dimer and were incubated at physiological conditions (37 °C in PBS). At indicated time points, the particles were centrifuged out of solution and the supernatant was analyzed for fluorescent protein content. Error bars represent standard errors of 3 replicates.

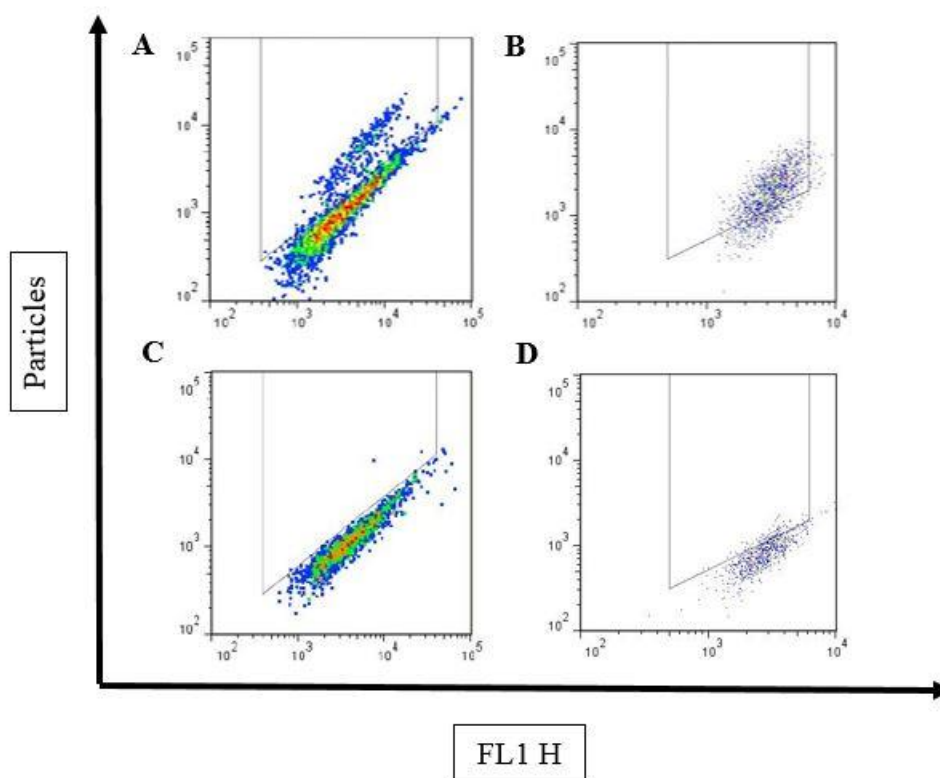


Figure 5.3: Representative flow cytometry gating for nanoparticle uptake experiments. (a,c) HUVECs or (b,d) RAW macrophages were incubated with 0.1 mg (a,b) spherical nanoparticles or (c,d) 2-fold stretched non spherical nanoparticles per 15,000 cells. Cells incubated for 24 hours and then washed 3x with PBS prior to flow cytometry analysis.

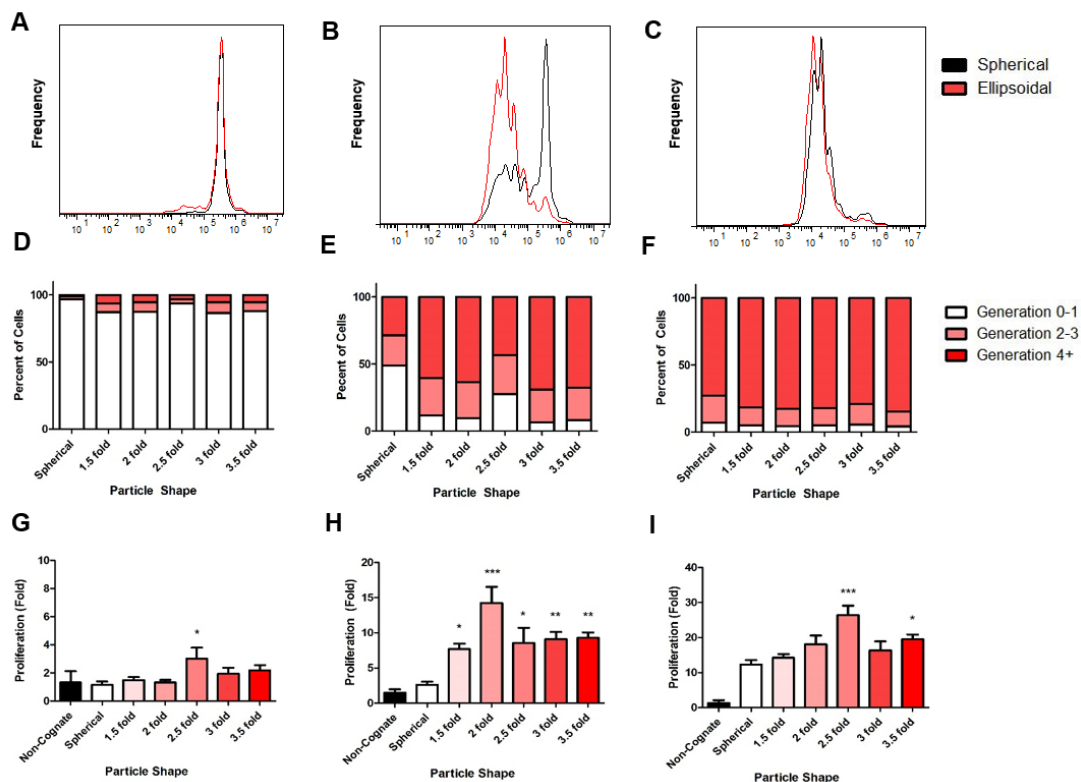


Figure 5.4: Non-spherical naAPCs stimulate T-Cells more effectively than spherical naAPCs *in vitro*. PMEL transgenic CD8⁺ T-Cells were incubated with (a,d,g) 0.01 mg, (b,e,h) 0.1 mg, (c,f,g) 1 mg of spherical (black/white) and 2-fold stretched, ellipsoidal (red) naAPCs of various aspect ratios. Cells were stained with CFSE and evaluated by flow cytometry for proliferation after 3 days of incubation with aAPCs (a-c). Generation analysis of CFSE flow cytometry data demonstrates increased proliferation of cells in non-spherical aAPC groups (d-f). Cells were also evaluated after 7 days of incubation by manual counting and normalizing cell titers to an untreated condition (g-i). Results indicate ellipsoidal nanoparticles of higher aspect ratios stimulate CD8⁺ T-Cells more effectively than their spherical counterparts (* = $p < 0.05$, ** = $p < 0.01$, *** = $p < 0.001$ compared to spherical). Error bars represent standard errors > 3 replicates.

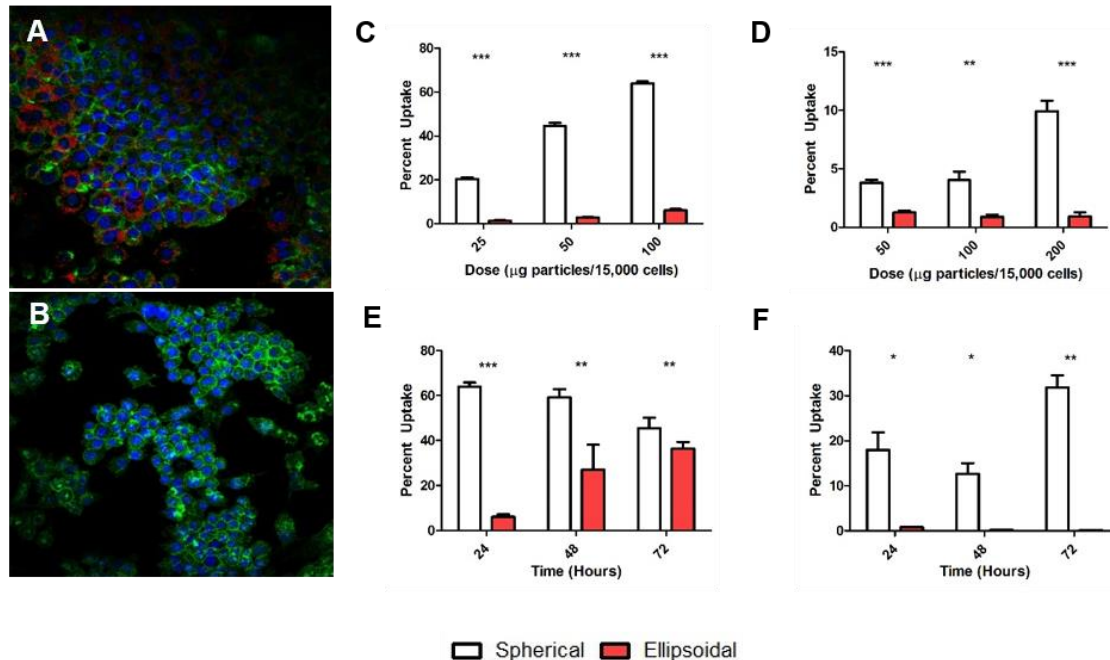


Figure 5.5: Nanoparticle uptake is shape dependent. RAW macrophages were incubated with 0.5 mg (a) nanospherical and (b) 2-fold stretched nanoellipsoidal particles encapsulating TAMRA per 15,000 cells for 24 hours. Confocal micrographs show clear uptake of spherical particles compared to ellipsoidal aAPCs (Blue = DAPI, Green = Actin, Red = Particles). RAW macrophages were incubated with nanospherical and 2-fold stretched nanoellipsoidal particles at varying (c) doses or (e) times. Macrophages showed clear preference for spherical nanoparticle uptake which was maintained through 2 days and up to 200 $\mu\text{g}/15,000$ cells. Similar experiments were repeated with HUVECs with varying (d) dose and (f) time. Results indicate that HUVECs had near complete preference for spherical nanoparticles over 2-fold stretched ellipsoidal nanoparticles. Error bars represent standard error of the mean with $n > 3$ for all experiments.

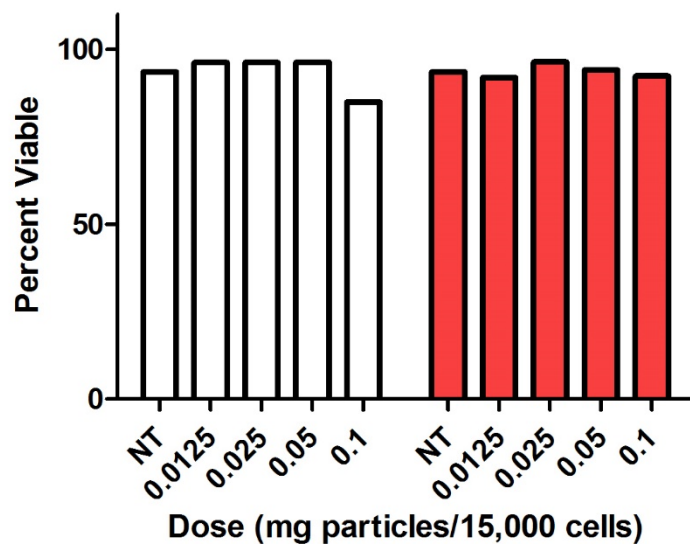


Figure 5.6: Viability of RAW macrophages is not affected at high doses of PLGA nanoparticles. Live and dead cells were distinguished by 7-AAD staining and flow cytometry analysis. White = Spherical nanoparticles, Red = 2-fold stretched ellipsoidal nanoparticles.

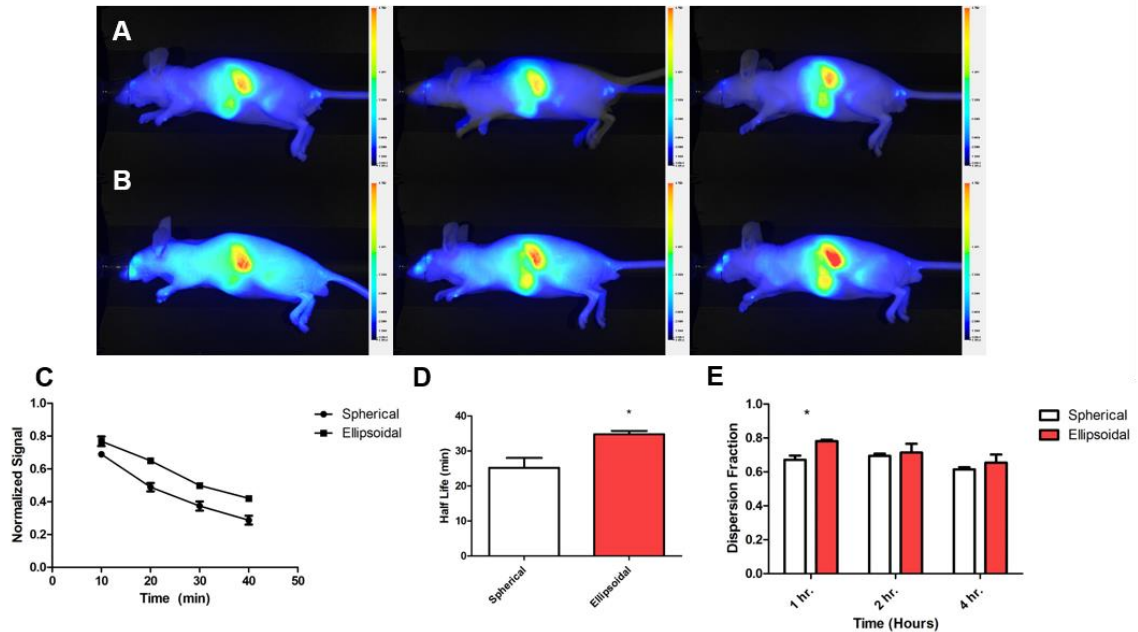


Figure 5.7: Non-spherical nanoellipsoidal aAPCs have superior pharmacokinetics over nanospherical aAPCs. Conjugated (a) spherical and (b) 2-fold stretched ellipsoidal naAPC particles encapsulating a near IR fluorophore were injected intravenously into nude mice. Animals were imaged at 1 hour (left), 2 hours (middle), and 4 hours (right). (c) Blood collected retroorbitally at 10 min intervals was imaged and quantified for fluorescence over the first hour post injection. Results show the nanoellipsoidal aAPCs circulate at higher concentrations over the time periods examined, and (d) have a longer half-life (* = $p < 0.05$). (e) Two regions of interest from (a) and (b) were quantified: The entire animal, and the entire animal minus the region of the spleen and liver. The ratio of these values was computed to give the distribution throughout the animal. Nanoellipsoidal aAPCs demonstrated greater dispersion throughout the animal at the 1 hour time point (* = $p < 0.05$). Error bars represent standard error of the mean with $n = 3$ for all experiments.

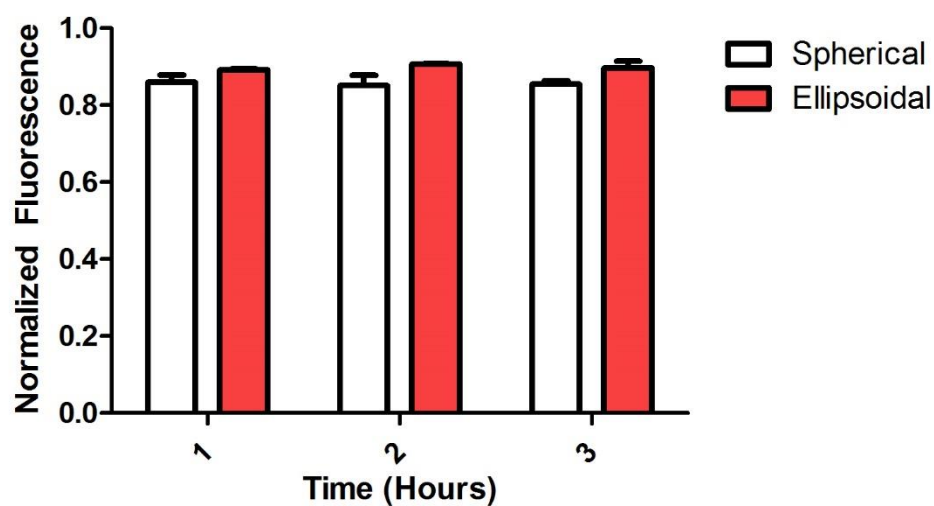


Figure 5.8: Spleen and liver signals from dispersion fraction analysis are similar between spherical and 2-fold stretched ellipsoidal nano aAPCs. Mice were imaged at 1, 2, and 4 hr. post injection with near IR labeled naAPCs. The animals were then imaged from the left side and the fluorescence from the region of interest corresponding to the spleen and liver were quantified and compared across the different timepoints.

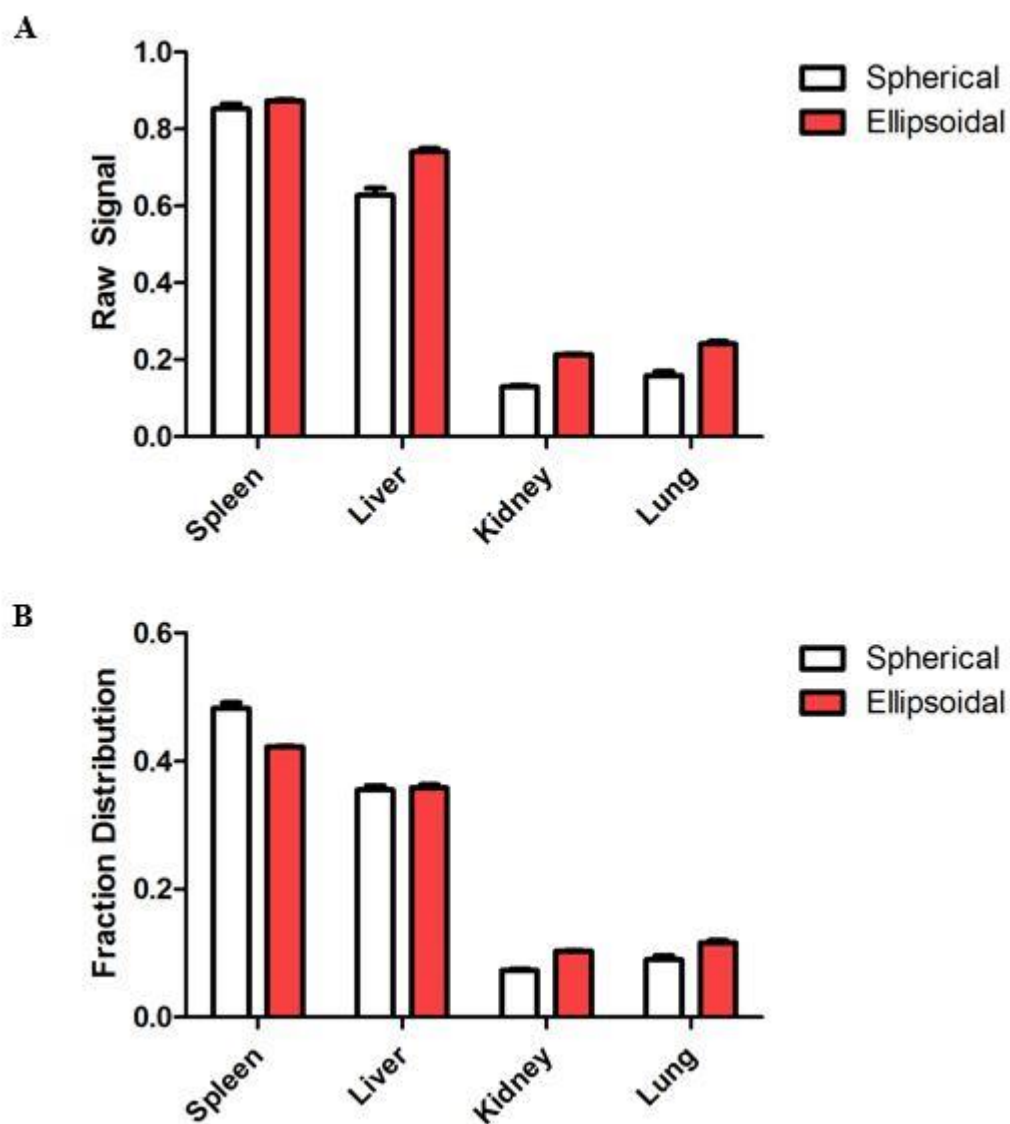


Figure 5.9: Organ distribution is similar for 2-fold stretched and spherical nano aAPCs. Organs were dissected at the 4 hours post intravenous injection of near IR labeled nano aAPCs. Organs were then imaged and fluorescence intensity analyzed by Image J to give a raw signal quantification for each organ (a). Subsequent normalization to the total signal analyzed from the set of organs in each group gave the percent distribution within the spleen, liver, kidney, and lung. Analysis reveals spleen and liver to be major centers of nanoparticle accumulation for both ellipsoidal and spherical nano aAPCs.

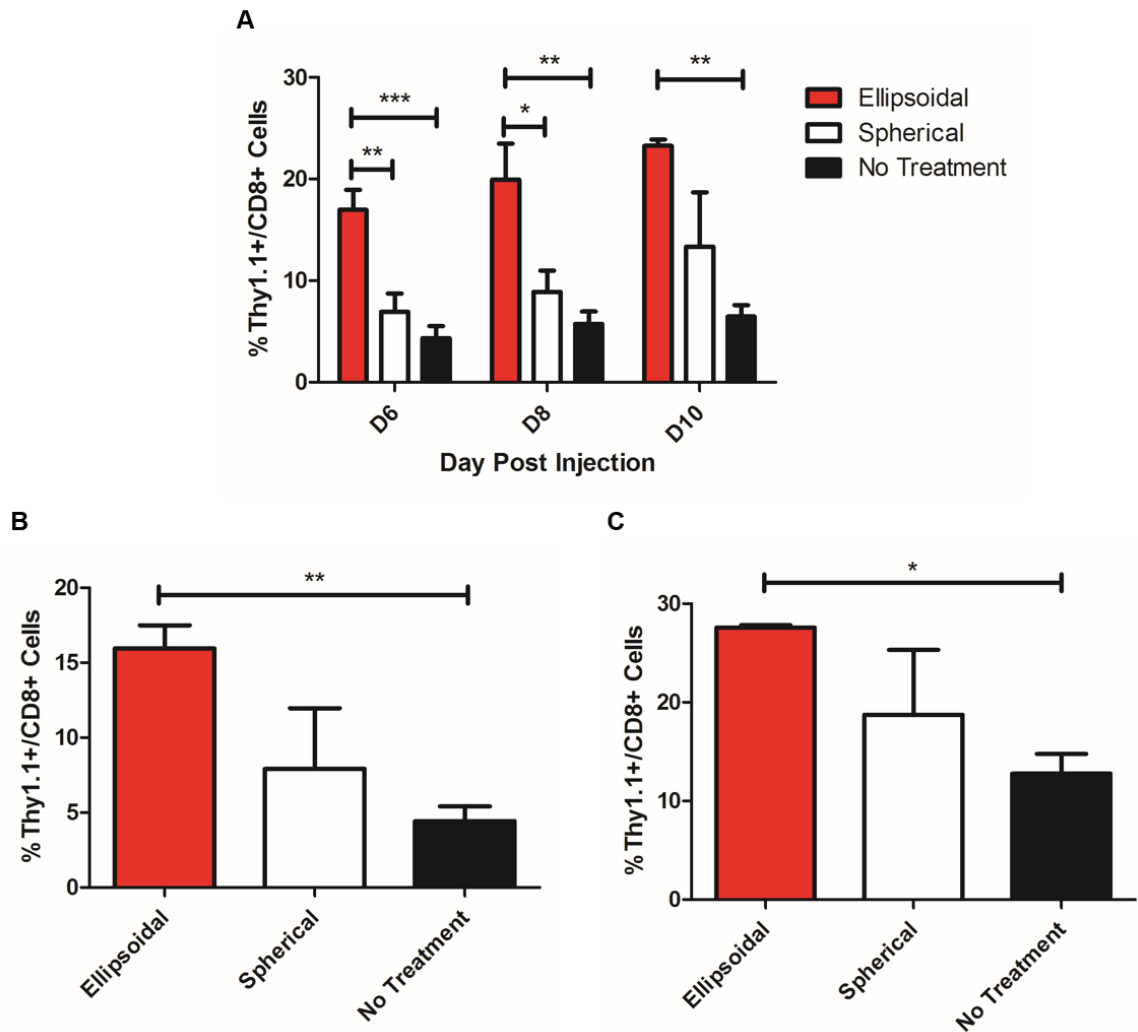


Figure 5.10: 2-fold stretched ellipsoidal nano aAPCs stimulate T-Cells superiorly to spherical nano aAPCs. Ellipsoidal and spherical aAPCs were injected intravenously into irradiated mice accompanied by 10^6 antigen specific CD8+ T-Cells bearing the marker Thy 1.1. “No treatment” groups received T-Cells only. (a) Blood was collected retroorbitally on day 6, 8, and 10 post injection and analyzed for the percent of CD8+ cells that were also Thy 1.1 positive. Results indicate a statistically significant increase in the percentage of antigen specific T-Cells stimulated *in vivo* by ellipsoidal aAPCs compared to spherical aAPCs on day 6 and 8 post injection and no aAPC control groups on all days analyzed. The mice were killed on day 10 post injection and the spleen and lymph nodes were dissected and analyzed for percent CD8+ cells that were also Thy 1.1 positive. Results show that for both (b) spleens and (c) lymph nodes, there was an increase in the Thy 1.1 positive cells in the ellipsoidal groups compared to spherical, and statistically significant increase of ellipsoidal over no-treatment. Error bars indicate the SEM of $n = 3$ to 5 mice per group. (* = $p < 0.05$, ** = $p < 0.01$, *** = $p < 0.001$).

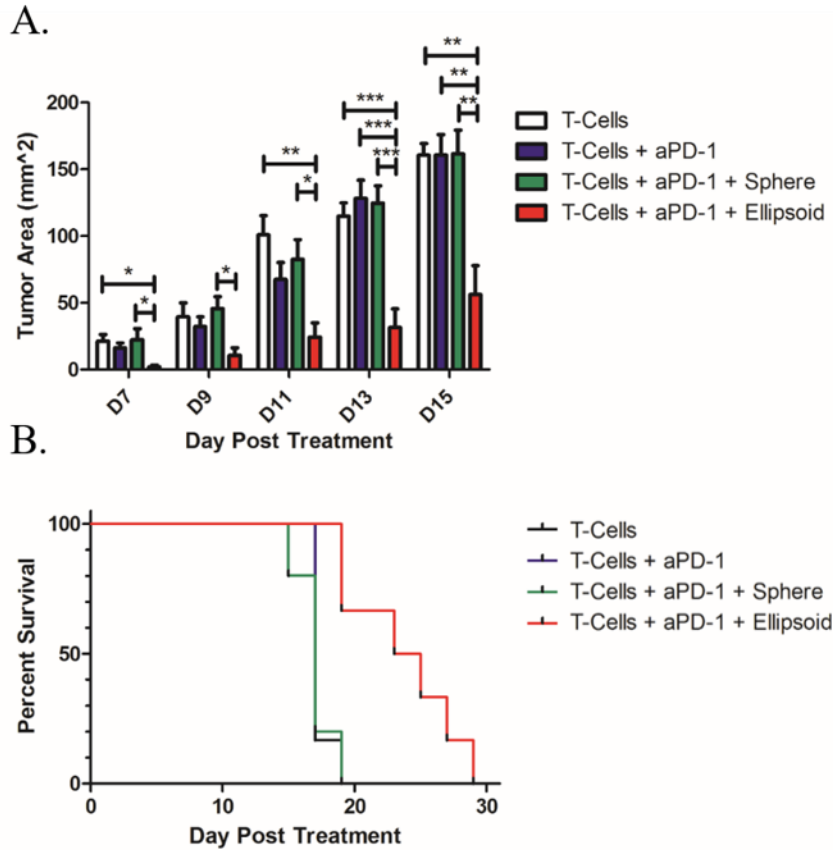


Figure 5.11: Non-spherical nano aAPC mediate a superior anti-tumor effect in an *in vivo* tumor treatment model. (A) Tumor area measurements indicate that the ellipsoidal nano-aAPC mediate a reduced tumor burden compared to all controls and the spherical nano aAPC (*= $p < 0.05$, **= $p < 0.01$, ***= $p < 0.001$ by daily one way ANOVA followed by Tukey's post test). (B) Decreased tumor burden resulted in increased survival of tumor bearing mice. The median survival increased from 17 days to 24 days for the Str2 (ellipsoidal) nano aAPC group. Survival effect was significant based on a log-rank test with $p < 0.01$ for ellipsoidal vs. all controls and the spherical nano aAPC group.

5.7 References

1. Engelhard, V.H., Strominger, J.L., Mescher, M. Burakoff, S. Induction of secondary cytotoxic T lymphocytes by purified HLA-A and HLA-B antigens reconstituted into phospholipid vesicles. *Proc. Natl. Acad. Sci. U. S. A.* 1978;75(11):5688-91.
2. Giannoni, F., Barnett, J., Bi, K., Samodal, R., Lanza, P., Marchese, P., Billetta, R., Vita, R., Klein, M.R. Prakken, B. Clustering of T cell ligands on artificial APC membranes influences T cell activation and protein kinase C θ translocation to the T cell plasma membrane. *J. Immunol.* 2005;174(6):3204-11.
3. Ugel, S., Zoso, A., De Santo, C., Li, Y., Marigo, I., Zanovello, P., Scarselli, E., Cipriani, B., Oelke, M. Schneck, J.P. In vivo administration of artificial antigen-presenting cells activates low-avidity T cells for treatment of cancer. *Cancer Res.* 2009;69(24):9376-84.
4. Oelke, M., Maus, M.V., Didiano, D., June, C.H., Mackensen, A. Schneck, J.P. Ex vivo induction and expansion of antigen-specific cytotoxic T cells by HLA-Ig-coated artificial antigen-presenting cells. *Nat. Med.* 2003;9(5):619.
5. Levine, B.L., Bernstein, W.B., Connors, M., Craighead, N., Lindsten, T., Thompson, C.B. June, C.H. Effects of CD28 costimulation on long-term proliferation of CD4⁺ T cells in the absence of exogenous feeder cells. *J. Immunol.* 1997;159(12):5921-30.
6. Maus, M.V., Riley, J.L., Kwok, W.W., Nepom, G.T. June, C.H. HLA tetramer-based artificial antigen-presenting cells for stimulation of CD4⁺ T cells. *Clin. Immunol.* 2003;106(1):16-22.
7. Perica, K., Medero, A.D.L., Durai, M., Chiu, Y.L., Bieler, J.G., Sibener, L., Niemöller, M., Assenmacher, M., Richter, A. Edidin, M. Nanoscale artificial antigen presenting cells for T cell immunotherapy. *Nanomed. Nanotechnol.*, 2014;10(1):119-29.
8. Mescher, M. Surface contact requirements for activation of cytotoxic T lymphocytes. *J. Immunol.* 1992;149(7):2402-5.
9. Han, H., Peng, J.-R., Chen, P.-C., Gong, L., Qiao, S.-S., Wang, W.-Z., Cui, Z.-Q., Yu, X., Wei, Y.-H. Leng, X.-S. A novel system of artificial antigen-presenting cells efficiently stimulates Flu peptide-specific cytotoxic T cells in vitro. *Biochem. Biophys.* 2011;411(3):530-5.
10. Steenblock, E.R. Fahmy, T.M. A comprehensive platform for ex vivo T-cell expansion based on biodegradable polymeric artificial antigen-presenting cells. *Mol. Ther.* 2008;16(4):765-72.
11. Steenblock, E.R., Fadel, T., Labowsky, M., Pober, J.S. Fahmy, T.M. An artificial antigen-presenting cell with paracrine delivery of IL-2 impacts the magnitude and direction of the T cell response. *J. Biol. Chem.* 2011;286(40):34883-92.
12. Tao, Z., Hong, G., Shinji, C., Chen, C., Diao, S., Antaris, A.L., Zhang, B., Zou, Y. Dai, H. Biological imaging using nanoparticles of small organic molecules with fluorescence emission at wavelengths longer than 1000 nm. *Angew. Chem. Int. Ed.* 2013;125(49):13240-4.
13. Gao, X., Cui, Y., Levenson, R.M., Chung, L.W. Nie, S. In vivo cancer targeting and imaging with semiconductor quantum dots. *Nat. Biotechnol.* 2004;22(8):969.

14. Bhavna, Md, S., Ali, M., Baboota, S., Sahni, J.K., Bhatnagar, A. Ali, J. Preparation, characterization, in vivo biodistribution and pharmacokinetic studies of donepezil-loaded PLGA nanoparticles for brain targeting. *Drug Dev. Ind. Pharm.* 2014;40(2):278-87.
15. Choi, H.S., Liu, W., Liu, F., Nasr, K., Misra, P., Bawendi, M.G. Frangioni, J.V. Design considerations for tumour-targeted nanoparticles. *Nat. Nanotechnol.* 2010;5(1):42.
16. Ye, F., Barrefelt, Å., Asem, H., Abedi-Valugerdi, M., El-Serafi, I., Saghafian, M., Abu-Salah, K., Alrokayan, S., Muhammed, M. Hassan, M. Biodegradable polymeric vesicles containing magnetic nanoparticles, quantum dots and anticancer drugs for drug delivery and imaging. *Biomaterials* 2014;35(12):3885-94.
17. Toita, R., Nakao, K., Mahara, A., Yamaoka, T. Akashi, M. Biodistribution of vaccines comprised of hydrophobically-modified poly (γ -glutamic acid) nanoparticles and antigen proteins using fluorescence imaging. *Bioorgan. Med. Chem.* 2013;21(21):6608-15.
18. Liu, J., Yu, M., Zhou, C. Zheng, J. Renal clearable inorganic nanoparticles: a new frontier of bionanotechnology. *Mater. Today* 2013;16(12):477-86.
19. Kulkarni, S.A. Feng, S.-S. Effects of particle size and surface modification on cellular uptake and biodistribution of polymeric nanoparticles for drug delivery. *Pharm. Res.* 2013;30(10):2512-22.
20. Chou, L.Y., Zagorovsky, K. Chan, W.C. DNA assembly of nanoparticle superstructures for controlled biological delivery and elimination. *Nat. Nanotechnol.* 2014;9(2):148-55.
21. Merkel, T.J., Herlihy, K.P., Nunes, J., Orgel, R.M., Rolland, J.P. DeSimone, J.M. Scalable, shape-specific, top-down fabrication methods for the synthesis of engineered colloidal particles. *Langmuir* 2009;26(16):13086-96.
22. Glotzer, S.C. Solomon, M.J. Anisotropy of building blocks and their assembly into complex structures. *Nat. Mater.* 2007;6(8):557.
23. Geng, Y., Dalhaimer, P., Cai, S., Tsai, R., Tewari, M., Minko, T. Discher, D.E. Shape effects of filaments versus spherical particles in flow and drug delivery. *Nat. Nanotechnol.* 2007;2(4):249.
24. Muro, S., Garnacho, C., Champion, J.A., Leferovich, J., Gajewski, C., Schuchman, E.H., Mitragotri, S. Muzykantov, V.R. Control of endothelial targeting and intracellular delivery of therapeutic enzymes by modulating the size and shape of ICAM-1-targeted carriers. *Mol. Ther.* 2008;16(8):1450-8.
25. Adriani, G., de Tullio, M.D., Ferrari, M., Hussain, F., Pascazio, G., Liu, X. Decuzzi, P. The preferential targeting of the diseased microvasculature by disk-like particles. *Biomaterials* 2012;33(22):5504-13.
26. Florez, L., Herrmann, C., Cramer, J.M., Hauser, C.P., Koynov, K., Landfester, K., Crespy, D. Mailänder, V. How shape influences uptake: interactions of anisotropic polymer nanoparticles and human mesenchymal stem cells. *Small* 2012;8(14):2222-30.
27. Barua, S., Yoo, J.-W., Kolhar, P., Wakankar, A., Gokarn, Y.R. Mitragotri, S. Particle shape enhances specificity of antibody-displaying nanoparticles. *Proc. Natl. Acad. Sci. U. S. A.* 2013;110(9):3270-5.

28. Sharma, G., Valenta, D.T., Altman, Y., Harvey, S., Xie, H., Mitragotri, S. Smith, J.W. Polymer particle shape independently influences binding and internalization by macrophages. *J. Control. Release* 2010;147(3):408-12.
29. Kolhar, P., Anselmo, A.C., Gupta, V., Pant, K., Prabhakarandian, B., Ruoslahti, E. Mitragotri, S. Using shape effects to target antibody-coated nanoparticles to lung and brain endothelium. *Proc. Natl. Acad. Sci. U. S. A.* 2013;110(26):10753-8.
30. Sunshine, J.C., Perica, K., Schneck, J.P. Green, J.J. Particle shape dependence of CD8+ T cell activation by artificial antigen presenting cells. *Biomaterials* 2014;35(1):269-77.
31. Ho, C., Keller, A., Odell, J. Ottewill, R. Preparation of monodisperse ellipsoidal polystyrene particles. *Colloid Polym. Sci.* 1993;271(5):469-79.
32. Champion, J.A., Katare, Y.K. Mitragotri, S. Making polymeric micro-and nanoparticles of complex shapes. *Proc. Natl. Acad. Sci. U. S. A.* 2007;104(29):11901-4.
33. Perica, K., Tu, A., Richter, A., Bieler, J.G., Edidin, M. Schneck, J.P. Magnetic field-induced T cell receptor clustering by nanoparticles enhances T cell activation and stimulates antitumor activity. *ACS Nano* 2014;8(3):2252-60.

Chapter 6: Biodegradable Cationic Polymer Blends for Fabrication of Enhanced Artificial Antigen Presenting Cells and Acellular “Off-The-Shelf” Cancer Immunotherapy

6.1 Introduction

Biotechnologies to harness and modulate the immune system have increasingly been shown promise in diseases ranging from cancer¹ and infectious diseases² to transplantation³ and autoimmune diseases.⁴ Biomimicry is a fascinating area of materials research where bio-inspired forms enable new functionality for maintaining health and treating disease.⁵ A particularly promising approach in immune engineering is the use of biodegradable particulate systems, ranging from the size of a virus to the size of a cell, and mimicking the surfaces of the natural biologic materials, as agents of cellular programming. Such therapeutic agents have the potential to be used “off-the-shelf” as biological, but non-cellular, therapies with greatly reduced costs, manufacturing challenges, and regulatory hurdles compared to cellular therapies.

In particular, biomimetic artificial antigen presenting cells (aAPC) have shown increasing promise to serve as a cancer immunotherapy.⁶ From a minimalist standpoint, the aAPC technology consists of three components: a biocompatible core material, a protein to serve as “Signal 1” or antigen recognition signal, and a protein to serve as “Signal 2” or effector direction signal.⁷ The two proteins must be conjugated to the surface of the particle in such a way that a T-Cell can interact with the particle as it would a normal antigen presenting cell. In the past decade, there have been great strides in the advancement of aAPC technology and engineering surfaces for T-Cell activation.⁸ Multiple platforms have been developed to enhance this stimulation including controlled

release of a “Signal 3” protein to direct the T-Cell response,^{9,10} incorporation of magnetite to enable magnetic isolation of aAPC from T-Cells to for therapeutic use,¹¹ use of magnetite as the core material to enable magnetic clustering of T-Cell receptors,¹²⁻¹⁴ and modulation of the surface area available for T-Cell activation through modification of particle shape¹⁵ or surface roughness.¹⁶ Many of these innovations have significantly increased aAPC efficacy. However, the promise of aAPC translation to the clinic has been hampered by the requirement of *ex vivo* manipulation of antigen specific T-Cells to achieve an effect. Although *ex vivo* manipulation of cells for cell based therapies is possible from a translational and commercial standpoint,¹⁷ in many cases translation to the clinic is prohibitively expensive. An “off-the-shelf” enhanced aAPC (eaAPC) therapy could circumvent these difficulties but has thus far been difficult to implement as a standalone therapeutic. **(Figure 6.1)**

One promising area of research that has been recently investigated is the use of different biodegradable polymers for the plastic core of the aAPC. Primarily, these aAPC particles cores have been composed of poly(lactic-co-glycolic acid) (PLGA),^{9,10,15,18} a hydrolytically biodegradable polymer that has also been used in the construction of multiple FDA-approved devices.¹⁹ Although PLGA has been well characterized for various applications, other biodegradable materials may possess beneficial properties for the construction of aAPCs. For example, it has been shown that the elastic modulus of a polymeric substrate for T-Cell activation can have a significant effect on T-Cell activation and subsequent phenotype.²⁰ In addition, lateral rigidity of the surface proteins has been shown to impact the magnitude and direction of an artificially directed T-Cell response.²¹ In both cases, softer, more pliable materials have been found to be more

beneficial than PLGA. In conjunction with the type of material, the surface density of signal proteins has been found to be an important parameter governing T-Cell activation.¹⁵ Ligand spacing has been found to be optimal when they are spaced closely together as opposed to farther apart.²²

In addition to specific mechanisms of increasing T-Cell stimulation, materials can have a non-specific adjuvant effect during a biomaterials/immune cell interaction. One study utilized a blend of PLGA and poly(β -amino ester) microparticles for intracellular delivery of nucleic acid vaccines to immune cells.²³ The PLGA/PBAE particle simultaneously provided structural support for the encapsulation of the vaccine material and imparted intracellular drug delivery function to the particle. Furthermore, encapsulation of small immunostimulatory molecules within PBAE nanoparticles can enhance their intracellular delivery and anti-cancer activity.²⁴ PBAEs particles have also been shown to be able to act directly as immunostimulatory, although this effect is attenuated as the material breaks down into lower molecular weight and free polymer.²⁵ Finally, by incorporating cationic polymer into aAPC particles there is the potential to increase protein binding to the surface of the particles, increasing ligand density for interactions with T-cells. Thus, a blend of PLGA/PBAE as a core material for next generation aAPCs could potentially have enhanced biological efficacy.

In this study, we have developed a hybrid PLGA/PBAE based aAPC for cancer immunotherapy. We have found that the particles made from this dual polymeric blend offer significantly superior immune stimulation *in vitro* and *in vivo* compared to traditional PLGA. This extra immune stimulatory capacity is correlated to an increase in signal protein density on the surface of the particle compared to the PLGA particle. The

enhanced *in vitro* activity also translated to a tumor treatment effect in a murine melanoma model, in the absence of adoptively transferred or *ex vivo* manipulated T-Cells. Taken together, these results highlight the potential to use PLGA/PBAE aAPC as a standalone therapy for melanoma and other forms of untreatable cancer.

6.2 Materials and Methods

6.2.1 PBAE Synthesis

Poly (lactic-co-glycolic acid) (MW = 38-54 kDa, L:G = 50:50, acid-terminated) (PLGA) was purchased commercially (Sigma Aldrich; St. Louis, MO). Poly (β -amino ester) (PBAE) was synthesized from commercially available monomers using a previously established protocol²⁶ (**Figure 6.2**). Briefly 1,4 butanediol diacrylate (Alfa Aesar; Ward Hill, MA) and 4, 4' trimethylenedipiperidine (Sigma Aldrich; St. Louis, MO) were heated to 90 °C for 30 min to melt the reagents. The two were then mixed in a 1.2:1 molar ratio (diacrylate:amine) in 5 g aliquots. A stirbar was added to ensure homogenous distribution of the monomers. The mixture was maintained at 90 °C for 24 hr. At the end of the reaction, the polymer was cooled to room temperature and dissolved in 20 mL of dichloromethane. 1-(3-Aminopropyl)-4-methylpiperazine (Alfa Aesar; Ward Hill, MA) was then added in a 10 fold molar excess (assuming 2 end groups per polymer and a molecular weight of 10 kDa). The endcapping reaction then proceeded for 1 hr. and at the end of the reaction, the polymer was purified via the addition of hexane to the reaction mixture in a 4:1 hexane:DCM ratio. The purification procedure was repeated twice. After purification and decantation of the organic solvent, the polymer was dried for 24 hr. on a desiccator and then stored at -20 °C under a nitrogen seal.

6.2.2 Microparticle and aAPC Synthesis

To synthesize the microparticles used in this study, an emulsification procedure was utilized similar to the procedure given in Chapter 3 (**Figure 6.3**). The PLGA was dissolved by itself in DCM at a concentration of 20 mg/mL for PLGA microparticles and the PLGA/PBAE was dissolved in dichloromethane at a 75:25 ratio with a final polymer concentration of 20 mg/mL. 5 mL of the polymer solution was then emulsified into 50 mL of 1% PVA solution for 1 min using an IKA T-25 homogenizer set to 1500 rpm. The 50 mL emulsification was then poured into 100 mL of a 0.5% PVA solution, agitated by a stir bar, and the particles were allowed to harden overnight. After hardening, the particles were washed with deionized water three times through centrifugation of particles at 1000 g and subsequent decantation of the supernatant. The particles were then frozen and lyophilized for future use.

For size and morphology analysis, the particles were imaged with a Leo FESEM. To prepare the samples for analysis, the particle powder was mounted onto carbon tape (Nisshin EM Co.; Tokyo, Japan) and placed upon aluminum tacks (Electron Microscopy Services; Hatfield, PA). The particles were then sputter coated with 20 nm of a gold-palladium alloy and imaged at a 1000x magnification. Size was determined through ImageJ analysis of the particles in the pictures.

In order to synthesize aAPC from the PLGA or PLGA/PBAE microparticles, protein was conjugated to the surface similar to the procedure given in Chapter 4. The lyophilized particles were reconstituted in 0.1 M MES buffer titrated to a pH of 6.0 at a concentration of 2 mg/mL. 100 μ L of EDC/NHS (Sigma Aldrich; St. Louis, MO) freshly prepared stock solution at 40 mg/mL and 48 mg/mL respectively were added to 1 mL of each particle sample and the particles were activated for 30 min. using these reagents.

The particles were then washed by centrifugation (5000 g for 5 min) and then resuspended in 1 mL of PBS. 8 µg of the MHC Class 1 IgG dimer loaded with gp100 of SIY and 10 µg of anti-CD28 monoclonal antibody (BD Biosciences; San Jose, CA) were then added to each particle sample and the particles were able to conjugate to the protein overnight. For evaluation of conjugation efficacy, fluorescent analogues of the proteins were utilized in conjugation as described in Chapter 4. After conjugation, the particles were washed three times with PBS and then resuspended in 200 µL of 100 µg/mL endotoxin-free sucrose. The particles were then frozen and lyophilized.

6.2.3 *In Vitro* Evaluation of Functional Efficacy

In order to compare the efficacy of the PLGA/PBAE eaAPC with the standard PLGA aAPC, we used a similar *in vitro* functional efficacy assay as was given in Chapter 4. 2C CD8⁺ T-Cells were isolated from mouse spleens using a Miltenyi CD8a⁺ Isolation Kit (Miltenyi; Auburn, CA). The cells were stained with Vybrant Cell Tracker carboxyfluorescein succinyl ester (CFSE) dye (Life Technologies; Grand Island, NY) following the manufacturers protocol. CFSE stained cells were then incubated with various doses of aAPC in RPMI based growth media supplemented as described in Chapter 4. CFSE dilution as an indicator of proliferation was then assessed 3 days after stimulation using a BD FACScalibur flow cytometer. Total proliferation was assessed through manual counting of the cell sample 7 days after stimulation using trypan blue to visually isolate viable cells.

6.2.4 *In Vitro* Evaluation of T-Cell Binding

To assess the interaction of the PLGA and PLGA/PBAE aAPC with T-Cells, we used a confocal imaging assay similar to previously described work with non-spherical

aAPC.¹⁵ The aAPC were synthesized as described in section 6.2.1 except Nile Red was added to the polymer solution at a concentration of 20 µg/mL in order to visualize the particles under confocal microscopy. 2C or PMEL T-Cells were isolated from mouse spleens using the Miltenyi CD8a+ T-Cell Isolation Kit and the cells were stained with CFSE as described in section 6.2.2. The cells and the particles were then incubated at 37 °C for 1 hr. at a ratio of 1 mg of particles to 500,000 T-Cells in a volume of 100 µL. The mixture was then imaged under confocal microscopy and the images were analyzed by ImageJ to determine qualitatively assess binding events. To quantitatively assess binding events the samples were then run on a BD FACScalibur and double-positive fluorescent events were considered as a positive binding event.

6.2.5 *In Vivo* aAPC Functional Efficacy

In order to assess enhanced aAPC activity as a potential standalone cancer immunotherapy, we utilized a modified version of the melanoma tumor treatment model as described in Chapter 4. Black 6 mice were inoculated with 3×10^5 B16-F10 melanoma cells subcutaneously on the right flank. Four days after tumor inoculation, the eaAPC were administered intravenously in half of the mice, and the other half received no treatment. Anti-PD1 clone RMP-14 (BioXCell; West Lebanon, NH) was administered intraperitoneally at 200 µg on the day of particle treatment and 100 µg on the day following. Eleven days after tumor inoculation, tumor size was assessed with digital calipers every other day until the tumor size reached 200 mm². After the tumor reach this size, the mice were sacrificed by CO₂ asphyxiation and cervical dislocation.

6.3 Results and Discussion

6.3.1 Characterization of aAPC Size and Conjugation Efficiency

PLGA and PLGA/PBAE particles were synthesized by single emulsion using identical chemical and physical parameters. The resultant particles from a size and morphology standpoint were nearly identical as determined by SEM imaging and subsequent Image J analysis. The morphology of the PLGA and PLGA/PBAE particles was spherical and was similar between the two samples (**Figure 6.4A-B**). Upon sizing by ImageJ, it was found that the PLGA particles $1.1\ \mu\text{m} \pm 0.3\ \mu\text{m}$ and the PLGA/PBAE particles were $1.3\ \mu\text{m} \pm 0.3\ \mu\text{m}$ thus confirming the particle sizes were within 1 standard deviation of each other. This size was determined to be sufficient for T-Cell activation based on previous results with aAPC technology.^{27,28} In addition, based on our previous work it was found that the particles would be safe to administer intravenously as larger particles were determined to be safe from a pharmacokinetic standpoint.¹⁸ Regardless it will be necessary to thoroughly compare the pharmacokinetic profile of both the PLGA/PBAE particles and the PLGA particle prior to therapeutic use.

Despite the relatively similar physical properties, from a surface chemistry standpoint the PLGA/PBAE particles were found to have a dramatic improvement on protein conjugation efficiency. It was found that the PLGA/PBAE particles conjugated protein 10-20 times more efficiently than the PLGA particles (**Figure 6.5**). The protein efficiency was characterized for the Signal 1 protein as representative as we have previously found that the Signal 2 anti-CD28 and Signal 1 dimer follow similar dose based trends in conjugation efficiency studies.^{15,29} From an aAPC efficacy standpoint, this increased conjugation efficiency can be critical to aAPC activity. It has previously been found that the surface density of proteins on the surface of aAPCs is a critical parameter in T-Cell activation and must be optimized.²² Further conjugation

optimization of PLGA/PBAE particles to increase ligand surface density may further improve biological activity.

Based on observational analysis of the particles during the washing steps, it was determined that the PLGA/PBAE particles were more difficult to resuspend than the PLGA particles, suggesting an increase in the non-specific hydrophobic interactions between the particles. The PLGA/PBAE particles were able to conjugate significant levels of protein without the EDC/NHS conjugation reagents and with higher efficiency than the PLGA particles with the EDC/NHS conjugation (**Figure 6.5**). It has previously been shown that proteins can conjugate to the surface of hydrophobic polystyrene particles in the absence of any other chemically active reagent.³⁰ The increase in protein efficiency could be attributed to a more hydrophobic and/or cationic surface mediated by the incorporation of the PBAE into the particle formulation.

6.3.2 *In Vitro* Functional T-Cell Stimulation

Upon analysis of the T-Cell stimulation results it was found that the PLGA/PBAE aAPC dramatically outperformed the PLGA based aAPC (**Figure 6.6**). It was found by CFSE dilution analysis that there was near complete activation of the T-Cells by the PLGA/PBAE at a dose of 1 µg per 100,000 T-Cells compared to 100 µg per 100,000 T-Cells for PLGA. Furthermore, the limiting dose of activation was found to be 0.01 µg for PLGA/PBAE compared to 1 µg for PLGA. The manual proliferation counts reinforced this result with similar parameters for activation and dose-limiting stimulation. The PLGA aAPC stimulation of the T-Cells was similar in potency to our previously reported results.^{15,18} The PLGA/PBAE aAPC, however was just as effective as the PLGA aAPC at a 100-fold lower dose. There was also no adverse effect on the viability based on

trypan blue analysis. These results suggest that the PLGA/PBAE aAPC are significantly stronger than the PLGA aAPC for immune stimulation and could be used as an enhanced aAPC for standalone immunotherapy.

6.3.3 *In Vitro* T-Cell Binding Analysis

In order to characterize further the potential mechanism of the PLGA/PBAE enhanced efficacy, we conducted an analysis of aAPC binding to the T-Cells by confocal microscopy and flow cytometry. The confocal imaging analysis of T-Cell particle binding revealed results that reinforced the idea that the PLGA/PBAE particles have enhanced interaction with T-Cells (**Figure 6.7A-D**). For the non-cognate condition, both the PLGA and PLGA/PBAE particles had minimal interaction with the T-Cells as evidenced by few to no binding events determined by ImageJ analysis. This suggests that both particles have minimal interaction with non-cognate T-Cells thus directing the antigen specificity of the immune stimulation, an important factor in aAPC technology.^{7,31} The cognate aAPC for both the PLGA and PLGA/PBAE aAPC exhibited increased interaction with the T-Cells compared to the non-cognate aAPC, and the PLGA/PBAE had significantly more interaction with cognate T-Cells than the PLGA particles. This trend was reinforced by quantitative flow cytometry results (**Figure 6.7E**). The PLGA cognate aAPC exhibited minimal increase in double positive events suggesting a weak targeted interaction of the biomaterial and the particle. However, the PLGA/PBAE aAPC exhibited near 100-fold increase in double positive events compared to the non-cognate control suggesting an enhanced interaction of the aAPC with the T-Cells as supported by the confocal imaging results. This directed targeted interaction has been found to be correlated with increased aAPC activity and enhanced particle

binding.^{15,32} Furthermore, it has been found that increased density of targeting protein correlates to increased binding and subsequently increased immune stimulation.³³

Therefore these results are promising as a correlative indicator to explain the increased T-Cell activation by the PLGA/PBAE particles.

6.3.4 *In Vivo* Tumor Treatment Efficacy

An ideal aAPC technology would be capable of standalone , acellular therapy that could be mass produced and stably stored over a long periods of time. This is in contrast to cell-based therapies which, though promising, are expensive to manufacture and have limited availability due to costs and the personalized nature of the therapeutic.³⁴

Therefore, we wanted to improve the efficacy of PLGA-based aAPCs beyond previous capacities that required adoptive transfer.¹⁸ We hypothesized that by reformulating the aAPC particle core material with PBAE and also combining the aAPCs with a background of anti-PD1 antibody, biological activity could be enhanced and PLGA/PBAE aAPCs could stimulate endogenous anti-tumor T-Cells. Therefore, we utilized the model developed in Chapter 4 for evaluation of aAPC efficacy except without the adoptive transfer component (**Figure 6.8A**). We compared the PLGA/PBAE aAPC to a sham PBS treatment to evaluate the capability of the new eaAPC to mediate anti-tumor treatment. Throughout the experiment, the tumor in the PLGA/PBAE treated case was smaller than the untreated case. This effect was statistically significant 13 days after the particle treatment (**Figure 6.8B**) and the tumors were 33% smaller 13 days after the particle treatment compared to the no treatment control. This translated into an increase in median survival of the mice from 13 days post treatment to 17 days post treatment, and this difference was statistically significant (**Figure 6.8C**). This result is significant for

the development aAPC technology as it has never been shown that this biodegradable particle, cell-free therapy can be used as a stand-alone *in vivo* treatment for melanoma. Additionally, the B16-F10 melanoma model is very immunosuppressive and it typically requires multiple particle injections³⁵ or requires multiple biologically engineered therapies to treat effectively.³⁶ Here, we have shown that a single injection of the PLGA/PBAE particles in context of an immune checkpoint blockade can significantly increase the survival in a murine melanoma model, thus validating the PLGA/PBAE particle as an enhanced aAPC for “off-the-shelf” immunotherapy.

6.4 Conclusions

In this study, we have developed a novel biomaterials platform for an enhanced aAPC for standalone cancer immunotherapy. The new PLGA/PBAE aAPC particles have similar physical properties to the PLGA aAPC particles from the standpoint of size and morphology. However, the PLGA/PBAE particles have a more hydrophobic and cationic surface that is much more efficient at conjugating the required signal proteins for aAPC efficacy. This resulted in significantly higher binding efficiency of the PLGA/PBAE particles to T-cells compared to the PLGA particles. This in turn was led to a significant increase in PLGA/PBAE particle immune stimulation efficacy as evidenced by T-Cell proliferation *in vitro* and *in vivo*. This was especially significant as the new PLGA/PBAE biomaterial could be used as a new platform for the enhanced effect of targeted drug delivery therapeutics. We have shown the promise of the PLGA/PBAE aAPC to serve as a standalone melanoma immunotherapy through a murine tumor treatment model. These new eaAPC could enable the aAPC technology to become cost-efficient and more readily available for translation to the clinic and accessible to a

broader patient population. Subsequently this could fulfill the goal of aAPC technology and allow for truly “off-the-shelf” aAPC immunotherapy.

6.5 Figures

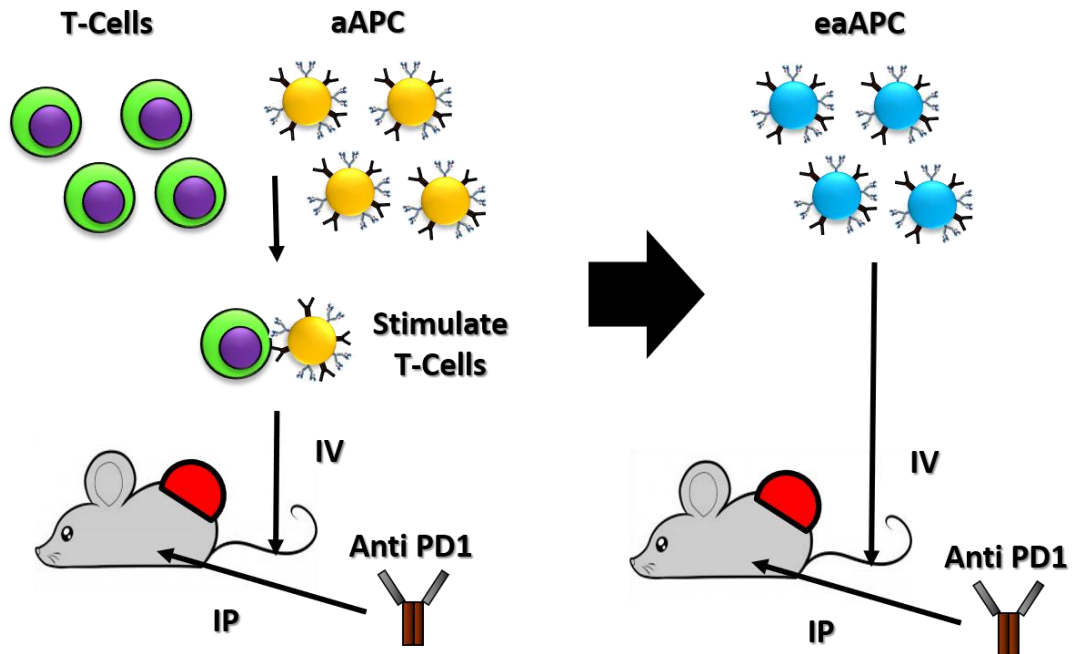
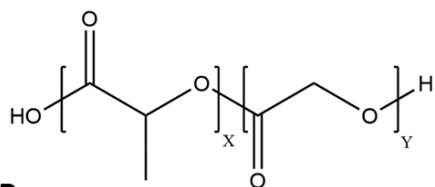


Figure 6.1: Schematic of the principle of augmented aAPC activity. The left diagram demonstrates the current standard for aAPC treatment within the context of adoptive immunotherapy in which the T-Cells must be stimulated *ex vivo* in the context of aAPC. The right diagram demonstrates the goal of the study in which an enhanced aAPC (eaAPC) is administered without T-Cells as a standalone immunotherapy.

A.



B.

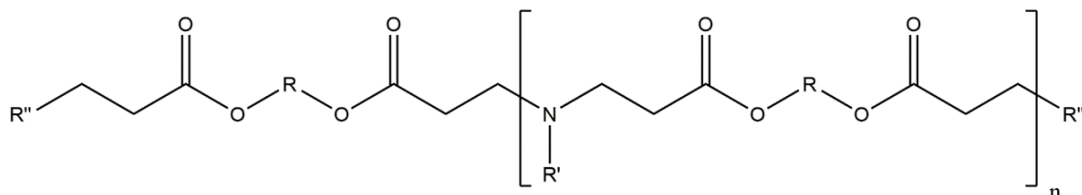


Figure 6.2: Chemical drawings of the two materials used to synthesize the eaAPC. (a) Poly (lactic-co-glycolic acid) is used as the core material and (b) poly (β-amino ester) is used as a material to enhance aAPC activity. The two are blended in a 75:25 ratio for the synthesis of the eaAPC.

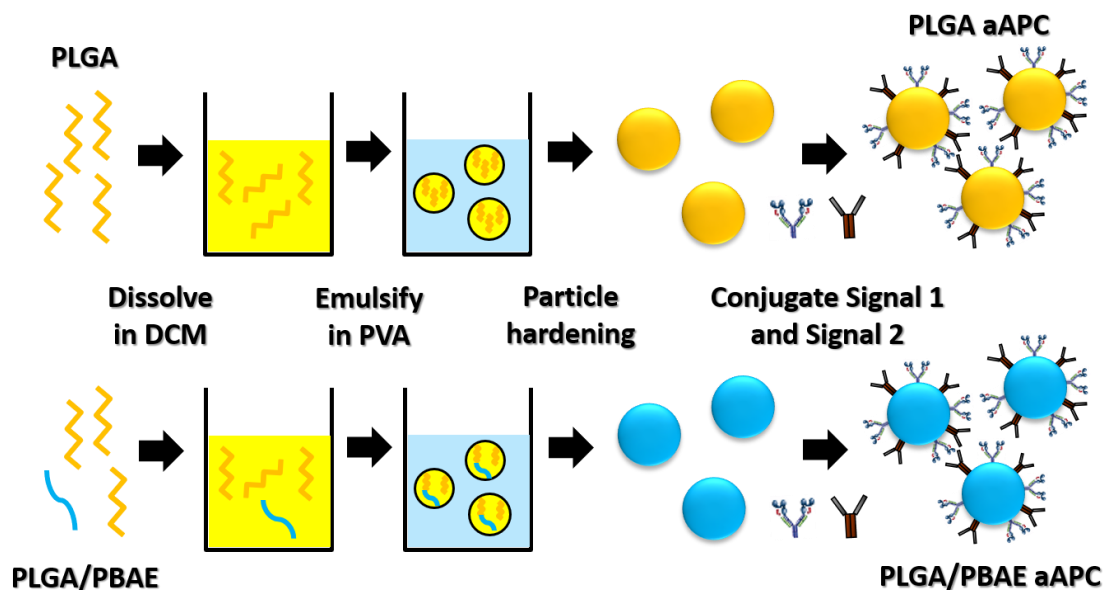


Figure 6.3: Schematic of the synthesis strategy for PLGA and PLGA/PBAE aAPC. PLGA or PLGA/PBAE blend (75:25) were dissolved in dichloromethane and emulsified into a PVA solution. The dichloromethane evaporated leaving hardened PLGA or PLGA/PBAE hybrid polymer particles. The Signal 1 and Signal 2 proteins were then conjugated to the surface of the particles to make PLGA based aAPC and PLGA/PBAE based eaAPC.

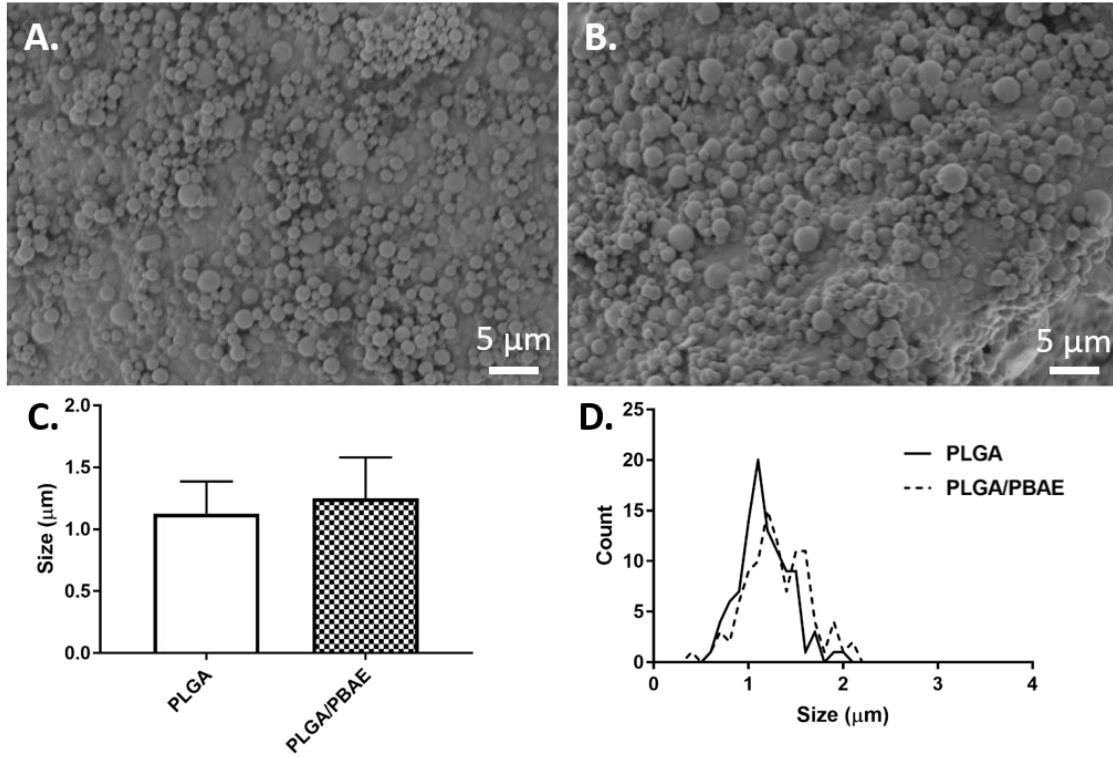


Figure 6.4: Size and morphology of PLGA and PLGA/PBAE particles. SEM images of (a) PLGA and (b) PLGA/PBAE particles. The particles were then sized manually by Image J to yield (c) average particle sizes (error bars are SD of 100 particle replicates) and (d) particle size distributions.

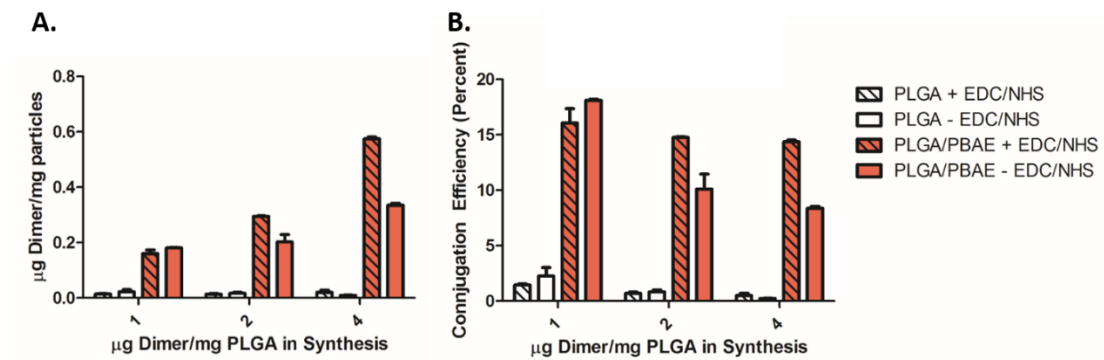


Figure 6.5: Protein conjugation efficiency of PLGA and PLGA/PBAE particles to make enhanced aAPC. (a) Total amount of Signal 1 protein on the surface and (b) percent conjugation efficiency of both types of particles with and without conjugation reagents. The PLGA/PBAE particles bound significantly more protein than the PLGA particles with and without the conjugation reagents (error bars are SEM of three replicates).

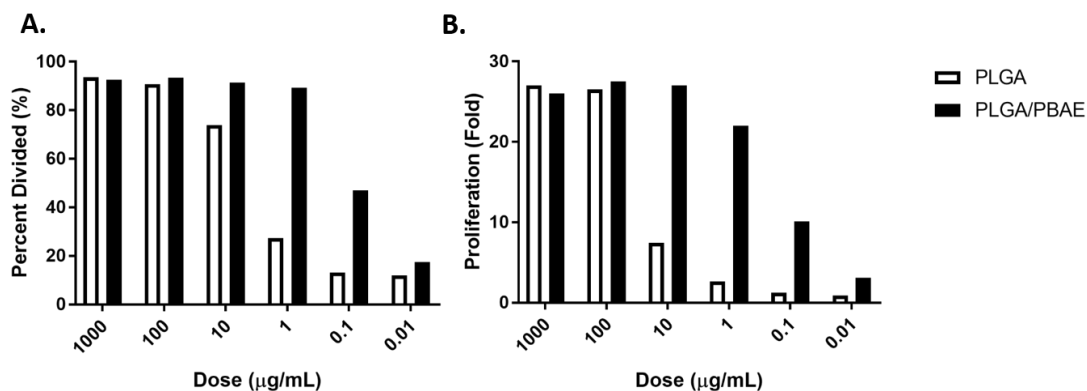


Figure 6.6: *In vitro* T-Cell activation efficacy of aAPC and eaAPC. CFSE dilution analysis of cognate T-Cells yielded (a) percent divided of the initial T-Cell population three days after the initial stimulation. (b) Manual proliferation counts seven days after the initial stimulation to discover fold stimulation. In both assays the PLGA/PBAE based eaAPC significantly outperformed the PLGA based aAPC.

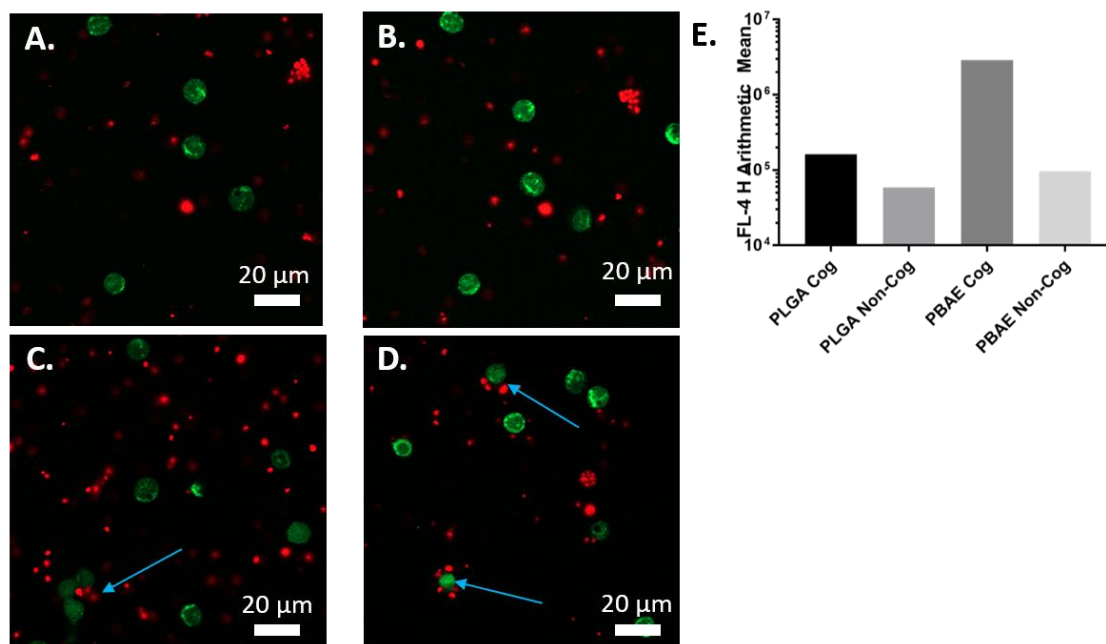


Figure 6.7: *In vitro* analysis of T-Cell/eaAPC interaction. Confocal imaging was completed of T-Cells (green) interacting with (a) non-cognate PLGA, (b) non-cognate PLGA/PBAE, (c) cognate PLGA, and (d) cognate PLGA/PBAE based aAPC following 1 hr. of incubation. The images illustrate a greater frequency of binding between the T-Cells and the particles in the cognate PLGA/PBAE case compared to all others (illustrated by the blue arrows). (e) Flow cytometry analysis of samples from (a-d) indicates significantly higher levels of binding in the PLGA cognate case compared to all others.

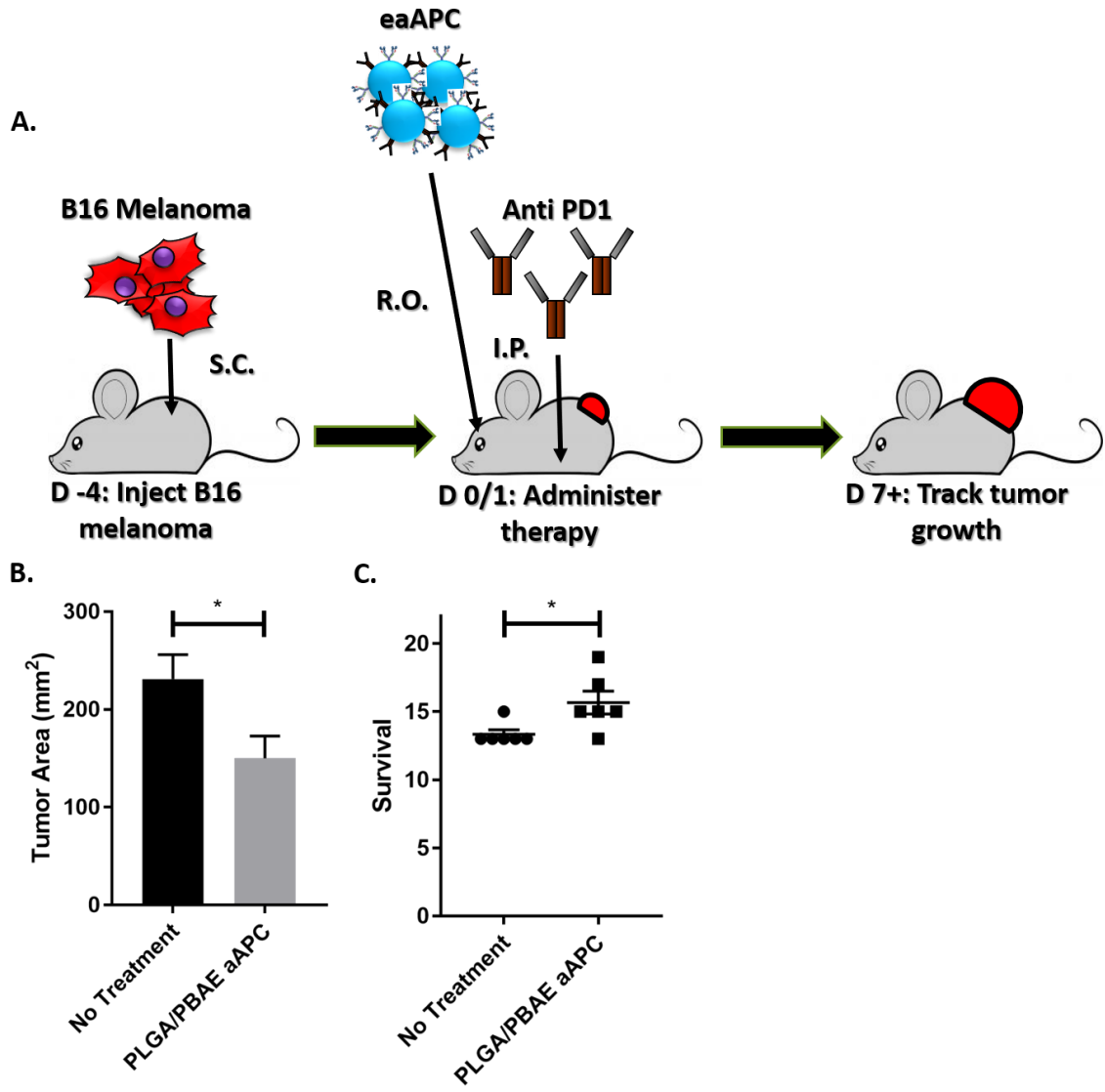


Figure 6.8: *In vivo* functional efficacy of the eaAPC. (a) Schematic of the *in vivo* tumor treatment experiment. Mice were inoculated with B16-F10 melanoma and upon the establishment of tumors, they were administered the aAPC or no treatment along with anti-PD1. The mice were then evaluated for tumor burden starting seven days after treatment. (b) On D13 the tumor burden in the PLGA/PBAE group was significantly lower than that in the no treatment group. (*= $p < 0.05$ by t-test) (c) This translated into an increased survival benefit for the mice with PLGA/PBAE aAPC treatment (*= $p < 0.05$ by log-rank test).

6.6 References

1. Mahoney, K.M., Rennert, P.D. Freeman, G.J. Combination cancer immunotherapy and new immunomodulatory targets. *Nat. Rev. Drug Discover.* 2015;14(8):561.
2. Moldawer, L.L. Hotchkiss, R. Immunotherapy: It is not just for cancer anymore. *J. Leukocyte Biol.* 2018;103(1):9-11.
3. Vaikunthanathan, T., Safinia, N., Boardman, D., Lechler, R. Lombardi, G. Regulatory T cells: tolerance induction in solid organ transplantation. *Clin. Exp. Immunol.* 2017;189(2):197-210.
4. Pishesha, N., Bilate, A.M., Wibowo, M.C., Huang, N.-J., Li, Z., Dhesycka, R., Bousbaine, D., Li, H., Patterson, H.C. Dougan, S.K. Engineered erythrocytes covalently linked to antigenic peptides can protect against autoimmune disease. *Proc. Natl. Acad. Sci. U. S. A.* 2017;201701746.
5. Green, J.J. Elisseeff, J.H. Mimicking biological functionality with polymers for biomedical applications. *Nature* 2016;540(7633):386.
6. Oelke, M., Krueger, C., Giuntoli II, R.L. Schneck, J.P. Artificial antigen-presenting cells: artificial solutions for real diseases. *Trend. Mol. Med.* 2005;11(9):412-20.
7. Meyer, R.A. Green, J.J. Artificial Antigen-Presenting Cells: Biomimetic Strategies for Directing the Immune Response. in *Biomaterials in Regenerative Medicine and the Immune System* 257-77 (Springer, 2015).
8. Ben-Akiva, E., Meyer, R.A., Wilson, D.R. Green, J.J. Surface engineering for lymphocyte programming. *Adv. Drug Deliver. Rev.* 2017;114:102-15.
9. Steenblock, E.R. Fahmy, T.M. A comprehensive platform for ex vivo T-cell expansion based on biodegradable polymeric artificial antigen-presenting cells. *Mol. Ther.* 2008;16(4):765-72.
10. Steenblock, E.R., Fadel, T., Labowsky, M., Pober, J.S. Fahmy, T.M. An artificial antigen-presenting cell with paracrine delivery of IL-2 impacts the magnitude and direction of the T cell response. *J. Biol. Chem.* 2011;286(40):34883-92.
11. Fadel, T.R., Sharp, F.A., Vudattu, N., Ragheb, R., Garyu, J., Kim, D., Hong, E., Li, N., Haller, G.L. Pfefferle, L.D. A carbon nanotube–polymer composite for T-cell therapy. *Nat. Nanotechnol.* 2014;9(8):639-47.
12. Perica, K., Medero, A.D.L., Durai, M., Chiu, Y.L., Bieler, J.G., Sibener, L., Niemöller, M., Assenmacher, M., Richter, A. Edidin, M. Nanoscale artificial antigen presenting cells for T cell immunotherapy. *Nanomedicine* 2014;10(1):119-29.
13. Perica, K., Bieler, J.G., Sch tz, C., Varela, J.C., Douglass, J., Skora, A., Chiu, Y.L., Oelke, M., Kinzler, K. Zhou, S. Enrichment and expansion with nanoscale artificial antigen presenting cells for adoptive immunotherapy. *ACS Nano* 2015;9(7):6861-71.
14. Perica, K., Tu, A., Richter, A., Bieler, J.G., Edidin, M. Schneck, J.P. Magnetic field-induced T cell receptor clustering by nanoparticles enhances T cell activation and stimulates antitumor activity. *ACS Nano* 2014;8(3):2252-60.

15. Sunshine, J.C., Perica, K., Schneck, J.P. Green, J.J. Particle shape dependence of CD8+ T cell activation by artificial antigen presenting cells. *Biomaterials* 2014;35(1):269-77.
16. Fadel, T.R. Fahmy, T.M. Immunotherapy applications of carbon nanotubes: from design to safe applications. *Trend. Biotechnol.* 2014;32(4):198-209.
17. Cheever, M.A. Higano, C.S. PROVENGE (Sipuleucel-T) in prostate cancer: the first FDA-approved therapeutic cancer vaccine. *Clin. Cancer Res.* 2011;17(11):3520-6.
18. Kosmides, A., Meyer, R., Hickey, J., Aje, K., Cheung, K., Green, J. Schneck, J. Biomimetic biodegradable artificial antigen presenting cells synergize with PD-1 blockade to treat melanoma. *Biomaterials* 2017;118:16-26.
19. Bobo, D., Robinson, K.J., Islam, J., Thurecht, K.J. Corrie, S.R. Nanoparticle-based medicines: a review of FDA-approved materials and clinical trials to date. *Pharm. Res.* 2016;33(10):2373-87.
20. O'Connor, R.S., Hao, X., Shen, K., Bashour, K., Akimova, T., Hancock, W.W., Kam, L.C. Milone, M.C. Substrate rigidity regulates human T cell activation and proliferation. *J. Immunol.* 2012;189(3):1330-9.
21. Hsu, C.-J., Hsieh, W.-T., Waldman, A., Clarke, F., Huseby, E.S., Burkhardt, J.K. Baumgart, T. Ligand mobility modulates immunological synapse formation and T cell activation. *PloS ONE* 2012;7(2):e32398.
22. Delcassian, D., Depoil, D., Rudnicka, D., Liu, M., Davis, D.M., Dustin, M.L. Dunlop, I.E. Nanoscale ligand spacing influences receptor triggering in T cells and NK cells. *Nano Lett.* 2013;13(11):5608-14.
23. Little, S.R., Lynn, D.M., Ge, Q., Anderson, D.G., Puram, S.V., Chen, J., Eisen, H.N. Langer, R. Poly- β amino ester-containing microparticles enhance the activity of nonviral genetic vaccines. *Proc. Natl. Acad. Sci. U. S. A.* 2004;101(26):9534-9.
24. Wilson, D.R., Sen, R., Sunshine, J.C., Pardoll, D.M., Green, J.J. Kim, Y.J. Biodegradable STING agonist nanoparticles for enhanced cancer immunotherapy. *Nanomedicine* 2018;14(2):237-46.
25. Andorko, J.I., Hess, K.L., Pineault, K.G. Jewell, C.M. Intrinsic immunogenicity of rapidly-degradable polymers evolves during degradation. *Acta Biomater.* 2016;32:24-34.
26. Tzeng, S.Y., Guerrero-Cázares, H., Martinez, E.E., Sunshine, J.C., Quiñones-Hinojosa, A. Green, J.J. Non-viral gene delivery nanoparticles based on poly (β -amino esters) for treatment of glioblastoma. *Biomaterials* 2011;32(23):5402-10.
27. Hickey, J.W., Vicente, F.P., Howard, G.P., Mao, H.-Q. Schneck, J.P. Biologically Inspired Design of Nanoparticle Artificial Antigen-Presenting Cells for Immunomodulation. *Nano Lett.* 2017;17(11):7045-54.
28. Mescher, M. Surface contact requirements for activation of cytotoxic T lymphocytes. *J. Immunol.* 1992;149(7):2402-5.
29. Meyer, R.A., Sunshine, J.C., Perica, K., Kosmides, A.K., Aje, K., Schneck, J.P. Green, J.J. Biodegradable nanoellipsoidal artificial antigen presenting cells for antigen specific T-cell activation. *Small* 2015;11(13):1519-25.
30. Champion, J.A. Mitragotri, S. Role of target geometry in phagocytosis. *Proc. Natl. Acad. Sci. U. S. A.* 2006;103(13):4930-4.

31. Oelke, M. Schneck, J.P. Overview of a HLA-Ig based “Lego-like system” for T cell monitoring, modulation and expansion. *Immunol. Res.* 2010;47(1-3):248-56.
32. Meyer, R.A., Mathew, M.P., Ben-Akiva, E., Sunshine, J.C., Shmueli, R.B., Ren, Q., Yarema, K.J. Green, J.J. Anisotropic biodegradable lipid coated particles for spatially dynamic protein presentation. *Acta Biomater.* 2018;72:228-38.
33. Cheung, A.S., Zhang, D.K., Koshy, S.T. Mooney, D.J. Scaffolds that mimic antigen-presenting cells enable ex vivo expansion of primary T cells. *Nature Biotechnol.* 2018;
34. Silva, F.d.S., Almeida, P.N., Rettore, J.V.P., Maranduba, C.P., Souza, C.M.d., Souza, G.T.d., Zanette, R.d.S.S., Miyagi, S.P.H., Santos, M.d.O. Marques, M.M. Toward personalized cell therapies by using stem cells: seven relevant topics for safety and success in stem cell therapy. *Biomed. Res. Int.* 2012;2012.
35. Kosmides, A.K., Sidhom, J.-W., Fraser, A., Bessell, C.A. Schneck, J.P. Dual targeting nanoparticle stimulates the immune system to inhibit tumor growth. *ACS Nano* 2017;11(6):5417-29.
36. Moynihan, K.D., Opel, C.F., Szeto, G.L., Tzeng, A., Zhu, E.F., Engreitz, J.M., Williams, R.T., Rakhra, K., Zhang, M.H. Rothschilds, A.M. Eradication of large established tumors in mice by combination immunotherapy that engages innate and adaptive immune responses. *Nat. Med.* 2016;22(12):1402.

Chapter 7: Anisotropic Biodegradable Lipid Coated Particles for Spatially Dynamic Protein Presentation⁵

7.1 Introduction

Lipid polymer hybrid particles, that combine the biomimetic cellular surface features of a liposome with the structural support and stability of a polymeric particle, have been of great interest to the biomaterials community in recent years. Generally, these constructs are of core-shell design with the polymer encapsulating various therapeutics in the core, and naturally or synthetically derived lipids forming a shell. By fusing a preformed lipid vesicle to a polymeric particle¹ or taking advantage of self-assembling lipid bilayers during particle synthesis,² these particles can be fabricated with a variety of different strategies depending on the desired application.

The lipid polymer hybrid particle technology holds tremendous promise and has already been demonstrated in several applications³ including drug delivery,⁴ diagnostic imaging,⁵ and gene delivery.^{6,7} Furthermore, this lipid coating strategy has been extended to the synthesis of polymeric nanoparticles containing membranes derived from red blood cells,⁸ platelets,⁹ and cancer cells.¹⁰ Polymeric particles with naturally derived membranes have been shown to be useful for many other applications including adsorption of hemolytic toxins,¹¹ pathogen binding,⁹ and cancer cell antigen delivery for vaccines.¹⁰

This chapter contains material modified from the following article previously published as: Meyer RA, Mathew MP, Ben-Akiva E, Sunshine JC, Shmueli RB, Ren Q, Yarema KJ, Green JJ. Anisotropic biodegradable lipid coated particles for spatially dynamic protein presentation. *Acta Biomaterialia*. 2018;72:228-38.

One particle design limitation of this approach, however, has been that, up to now, almost all lipid coated particles have been of isotropic, spherical shape. Yet, emerging evidence suggests that non-spherical micro- and nanoparticles possess several key advantages over traditional spherical particles which include inhibited non-specific cellular uptake¹² and simultaneously potential enhanced target-specific binding and cell uptake.¹³ As a result, anisotropic particles have been appropriated for several recent biological applications such as anti-cancer drug delivery,^{14,15} gene delivery *in vitro* and *in vivo*,^{6,16,17} and immunoengineering to stimulate T-Cells against tumor associated antigens.^{18,19} In all of these applications, the non-spherical anisotropic particle has been shown to be superior to the isotropic spherical particle.

To investigate the feasibility of combining these previously separate particle technologies—the use of anisotropic shapes in particle core design and the hybridization of lipids on polymeric particles for dynamic surfaces—we developed a procedure to reproducibly generate non-spherical, ellipsoidal lipid coated particles with a biodegradable polymer support. The process includes generating non-spherical particles, which can be manufactured from both top-down¹³ and bottom-up methods.²⁰ In the current work, we utilized (as outlined in **Figure 7.1**) a thin film stretching method developed by Ho et. al.²¹ that we recently automated²² with an electromechanical stretching device to robustly generate ellipsoidal anisotropic microparticles to serve as the support for the lipids. Next, the ellipsoidal lipid coated particles were generated by fusing 200 nm liposomes to these particles under sonication. Subsequently, the lipid surfaces were functionalized in a flexible manner through the use of biotinylated biomolecules as outlined in **Figure 7.2**. These new biomaterials, anisotropic

biodegradable particles that exhibit resistance to non-specific cellular internalization and enable spatially dynamic protein presentation from their surfaces, are promising as biotechnology devices for delivery and diagnostic applications.

7.2 Materials and Methods

7.2.1 Particle preparation and characterization

Acid terminated poly(lactic-co-glycolic acid) (PLGA- 85:15 L:G ratio, MW 45,000 Da – 55,000 Da) (Akina Inc.; West Lafayette, IN) was dissolved in 5 mL of dichloromethane (DCM) at a concentration of 20 mg/mL. In order to visualize particles under fluorescence microscopy, 7-amino-4-methyl coumarin (7-AMC- Sigma-Aldrich; St. Louis, MO) or Nile Red (Life Technologies; Grand Island, NY) were added to the DCM solution at a 1% w/w ratio to the polymer. The resulting solution was homogenized by a T-25 digital ULTRA-TURRAX IKA tissue homogenizer at 5,000 rpm for 1 min in 50 mL of 1% poly(vinyl alcohol) (PVA) solution (IKA Works; Wilmington, NC). The subsequent emulsion was then transferred to 100 mL of 0.5% PVA solution agitated by magnetic stir bar and the DCM was allowed to evaporate over the course of 4 h. The suspended particles were centrifuged out of solution at 3000g for 5 min and washed 3 times with water. The resulting particles were flash frozen in liquid nitrogen and lyophilized prior to use.

To synthesize non-spherical ellipsoidal particles, we utilized the thin film stretching method developed by Ho et. al.²¹ Spherical particles synthesized by emulsion were suspended into a solution of 10% PVA and 2% glycerol at a concentration of 5 mg/mL and 10 mL of this solution was deposited into a rectangular petri dish. The film was allowed to dry overnight, and the next day the film was cut to size and mounted onto

an automated thin film stretching device.²² The entire apparatus was heated up to 90 °C and the film was stretched 2-fold in one direction to produce ellipsoidal particles with a major axis roughly 2 times the original particle diameter and a minor axis roughly 0.7 times the original particle diameter. After stretching, the film was allowed to cool back down to room temperature and then was dissolved in water. Particles were washed and subsequently lyophilized prior to use and characterization.

Particle characterization was conducted using scanning electron microscopy (Leo FESEM). Lyophilized particles were mounted onto an aluminum tack (Electron Microscopy Services; Hatfield, PA) using carbon tape (Nisshin EM Co.; Tokyo, Japan). The particles were then sputter coated with 30 nm of gold-palladium alloy. After sputter coating, the particles were imaged by SEM. Particle size and aspect ratio data were obtained by ImageJ analysis of the subsequent SEM images.

7.2.2 Lipid coated particle preparation and imaging

Non-spherical lipid coated particles were prepared utilizing a two-step method similar in concept to what has previously described for spherical particles.²³ 1,2-dioleoyl-sn-glycero-3-phosphocholine (DOPC) and cholesterol (Avanti Polar Lipids; Alabaster, AL) were mixed into a 70:30 w/w ratio. For fluorescent lipid imaging studies, rhodamine conjugated DOPC (Avanti Polar Lipids; Alabaster, AL) was mixed with DOPC, and cholesterol in a 1:69:30 w/w ratio. For surface functionalization, 1,2-dioleoyl-sn-glycero-3-phosphoethanolamine-N-[4-(p-maleimidomethyl)cyclohexanecarboxamide] (MCC-DOPC) (Avanti Polar Lipids; Alabaster, AL), DOPC, and cholesterol were mixed in a 35:35:30 w/w ratio. A total of 1 mg of the lipids was aliquoted and left to dry into a thin film overnight under a vacuum. The lipids were then

hydrated in 1 mL of water. The lipids were heated to 60 °C and extruded through a 200 nm filter (Avanti Polar Lipids; Alabaster, AL). Liposome formation was verified with sizing at 200 nm using dynamic light scattering (Malvern Instruments; Westborough, MA). The liposomes were then mixed with spherical or non-spherical particles (in a 33.4 µg liposome to 1 mg particle ratio) and sonicated for 30 s at 2 W power in a 1.5 mL Eppendorf tube. Temperature was maintained at 4 °C with an aluminum cooling block (Light Labs; Dallas, TX). The subsequent lipid coated particles were purified from solution through centrifugation at 4 °C for 5 min at 300g. After three washes, the lipid coated particles were stored at 4 °C until further use.

To analyze the formation of lipid constructs on the particle surface, confocal imaging of PLGA particles encapsulating 7-AMC were coated with rhodamine lipid containing liposomes. Confocal image acquisition was completed with a Zeiss 780 FCS Confocal Microscope. To derive profile information, we used the ImageJ profile measurement tool and drew a line through the particle to determine relative fluorescence information.

7.2.3 Cellular uptake studies

RAW 264.7 (ATCC) macrophages were cultured in T-175 flasks in Dulbecco's Minimal Essential Media (Life Technologies; Grand Island, NY) supplemented with 10% fetal bovine serum and penicillin/streptomycin. For flow cytometry studies, cells were harvested through the gentle use of a cell scraper (to prevent excessive cell damage) and seeded into 96-well plates at a density of 30,000 cells/well. After cell adherence, the cells were stained with Vybrant CFDA-SE Cell Tracer Kit following the manufacturer's protocol (Life Technologies; Grand Island, NY) as a counterstain to identify live cells in

flow cytometry. The cell media was removed and replaced with 500 μ L of cell media containing either spherical or ellipsoidal particles encapsulating 5(6)-carboxy-tetramethyl-rhodamine (Merck KGaA; Darmstadt, GE) in a 2-fold dilution series starting at 0.5 mg particles/mL. The cells were then incubated for 4 hr at 37 °C for uptake studies and 4 °C for binding studies and washed 3x with PBS to remove free particles. The cells were dissociated from the plate by vigorous trituration prior to analysis by flow cytometry. Cell viability was evaluated after 24 and 48 hr in separate but identical experimental setups incubation using a cell titer kit (Promega; Madison, WI) following the manufacturer's protocol. The cells were incubated with the cell titer reagent for 1 hr and assessment of viability was conducted via relative absorbance measurements.

For confocal imaging, cells were seeded at the same concentration and incubated with 0.125 mg particles/mL of fluorescently labeled particles (corresponding roughly to 10 particles/cell), except the incubation was conducted in LabTek Chamber slides (Fisher Scientific; Pittsburgh, PA). The cells were washed 3x with PBS and then fixed in 10% formalin stabilized with methanol for 15 min (Sigma-Aldrich; St. Louis, MO). After fixing, actin was stained with Alexa 488 Phalloidin (Life Technologies; Grand Island, NY) and the nucleus was visualized with DAPI stain (BioChemica; Darmstadt, Germany), both following the manufacturer's protocol. The cells were then visualized using confocal microscopy on a Zeiss 780 FCS.

7.2.4 Surface protein conjugation and characterization

In order to functionalize the lipid coated particles to be receptive to protein conjugation, we first functionalized the surface with thiolated avidin (Protein Mods; Madison, WI). We first were interested in whether or not the avidin could conjugate to

the surface of the maleimide activated particle. We pre-conjugated biotinylated fluorescein (Sigma- Aldrich; St. Louis, MO) with the avidin and then dialyzed overnight with a 10 kDa MWCO dialysis bag (Life Technologies; Grand Island, NY). The particles were then reacted overnight with various amounts of fluorescent avidin and washed three times. Fluorescence intensity was measured under a plate reader and correlated to the amount of fluorescent avidin on the surface of the particle.

To evaluate our capabilities to conjugate a target biotinylated protein to the surface of our lipid coated particles, we formed the lipid coated particles of ellipsoidal and spherical shape and conjugated them to the thiolated avidin overnight at 4 °C at a 4 µg avidin/mg PLGA ratio. We then conjugated Cy5-biotin (Click Chemistry Tools; Scottsdale, AZ) at a concentration of 4 µg Cy5-biotin/mg PLGA ratio for 1 h at room temperature. After washing 3 times at 4 °C, we evaluated the conjugation through confocal imaging of the particles.

To confirm that this method would work for a bioactive protein, we utilized biotinylated anti-CD28 as a model protein for particle surface capture. Avidin functionalized lipid coated particles were prepared as previously, but instead of a fluorophore, we added the protein at various concentrations to test reaction efficiency. To quantitate the amount of protein bound to the surface, we washed the particles 3 times, collected the supernatants, and analyzed them for a reduction in protein content utilizing an Octet Red system (Forte Bio; Menlo Park, CA). Reduction in protein content in the supernatant was then converted to protein immobilized on the surface through subtraction from the total amount of protein added into the system.

7.2.5 Targeted anisotropic lipid coated particle binding

In order to evaluate the capability of anisotropic lipid coated particles to mediate enhanced targeted cell binding compared to spherical lipid coated particles, we prepared TAMRA loaded spherical and prolate ellipsoidal microparticles coated with MCC-lipids were synthesized as described in Section 2.1 and 2.2. Particles were then conjugated to anti-CD3 (OKT3 clone) as described in Section 2.4. Jurkat T-Cells were labeled with Vybrant CFDA SE Cell Tracer Kit (CFSE) (Life Technologies; Grand Island, NY) following the manufacturer's protocol. The particles were then incubated at a concentration of 0.1 mg/mL with 100,000 Jurkat T-Cells in 100 uL of T-Cell culture media formulated as described previously¹⁸ for 1 hr. To evaluate binding the samples were then imaged by confocal microscopy on a Zeiss 800 FCS Confocal Microscope. A total of 10 images were taken per sample and analyzed for binding frequency and area of contact between particles and cells using Image J.

7.2.6 FRAP Analysis

In order to confirm the fluidic character of the spherical and ellipsoidal lipid coated particles, diffusivity was evaluated utilizing the fluorescence recovery after photobleaching technique (FRAP). The fluorescent signal was supplied by the Cy5 immobilized to the lipid coated particles. Particles were suspended in 1x PBS and incubated at 37 °C for the duration of the FRAP experiments. Using a Zeiss 780 FCS Confocal Microscope rectangular regions of interest were selected on a number of particles, these regions were bleached, following which the fluorescent recovery in the selected regions was tracked over time. The fluorescent intensity measured at each time point ($I(t)$) was then converted to a normalized fluorescent intensity ($NFI(t)$) using the following equation:

$$NFI(t) = \frac{I(t) - I_{post\ bleach}}{I_{pre\ bleach} * I_{post\ recovery}}$$

The NFI was then plotted against time and fit to a one phase exponential association curve using GraphPad Prism 7 (GraphPad Software, Inc.; La Jolla, CA). From the fit of the curves, time constants for half recovery were derived ($t_{0.5}$). In order to determine diffusion constants, we assumed a circular bleaching region in the spherical particles with a radius determined from ImageJ analysis the 2D images of post bleached particles (r_{bleach}). To account for the differences in surface area bleached in the spherical vs. ellipsoidal particles, we assumed the area bleached in the ellipsoidal particles was an ellipse as opposed to a circle. The characteristic length was then taken to be the minor axis of the ellipse which was computed from measuring the major axis of the bleaching area by ImageJ in the 2D images and using an aspect ratio of 2.8 for the 2-fold stretched particles.¹⁸ These values were then applied to the model set forth by Kang et al.²⁴ for derivation of lipid diffusion constants from FRAP:

$$D_{lipid} = \frac{r_{bleach}^2}{4 * t_{0.5}}$$

Diffusion constants for 10 particles for both shapes were computed with this model and compared.

7.2.7 Statistical analysis

All statistics were completed using statistical analysis software modules in GraphPad Prism 7 (GraphPad Software, Inc.; La Jolla, CA). For cellular uptake studies, the percent uptake positive and percent binding positive replicates were compared between shapes at each individual dose using a t-test. Significance was assumed if the p value of this test was less than 0.05. For avidin immobilization on particles and protein bound to the

particles, a two-way ANOVA test was performed considering dose and shape as variables with interactions considered to be significant if the p value of the test was less than 0.05. Bonferroni's post-test was performed to analyze differences between shapes at the various doses and the difference was considered significant with a p value less than 0.05. For cellular binding studies, the percent bound replicates were compared across the spherical and non-spherical shapes with and without anti-CD3 functionalization using a one way ANOVA with Tukey's post test to compare across groups. Significance was taken if the p value of this test was less than 0.05. The length of contact was compared between anti-CD3 functionalized and non-functionalized particles by a t-test and significance was assumed if the p value of the test was less than 0.05. Lateral diffusion coefficients extracted from FRAP recovery curves were compared between particle shapes using a t-test and significance was assumed if the p value of the test was less than 0.05.

7.3 Results and Discussion

7.3.1 Lipid coated particle preparation and characterization

Spherical microparticles were generated (by homogenization of a PLGA in dichloromethane solution into a solution of 1% poly(vinyl alcohol)) and their size was measured by Image J analysis of scanning electron microscopy (SEM) micrographs (**Figure 7.3A-B**) and determined to be $3.2\ \mu\text{m} \pm 1.2\ \mu\text{m}$ in diameter (**Figure 7.3C**). We confirmed the maintenance of particle shape during the fabrication process by aspect ratio analysis of SEM micrographs of non-spherical particles coated with lipids (**Figure 7.3D**). The aspect ratio of the ellipsoidal particles was measured to be 3.3 ± 0.6 (**Figure 7.3D**). Confocal imaging of a representative batch of lipids on particles revealed that the 7-AMC fluorescence was confined to the interior of the particles for both spherical (**Figure 7.4A**)

and ellipsoidal (**Figure 7.4B**) lipid coated particles, whereas the lipid-rhodamine signal was localized to the exterior of the particles in both cases. Profile analysis of each sample revealed that for both the spherical (**Figure 7.4C**) and the ellipsoidal particles (**Figure 7.4D**) that the maximum signal from the lipid-rhodamine conjugate was localized to the exterior of the particle utilizing the 7-AMC signal as a reference point.

7.3.2 Macrophage uptake of lipid coated particles

Particles, which were formulated encapsulating a fluorescent dye, were coated with lipids and conjugated to avidin via thiol/maleimide chemistry. The lipid coated particles were incubated with macrophages for four hours to permit phagocytosis to occur. Viability of the macrophages was unaltered during this incubation, as evidenced by a cell titer assay of both the spherical and ellipsoidal lipid coated particles at the end of 24 and 48 hrs. (**Figure 7.5**). At the conclusion of four hours, the macrophages were either fixed and stained for confocal imaging or removed from the plate by trituration for flow cytometry analysis.

Confocal imaging analysis yielded a qualitative comparison of spherical vs ellipsoidal lipid coated particle phagocytosis (**Figure 7.6A** vs. **Figure 7.6B**). In all cases examined by microscopy, spherical particles were phagocytosed at a higher rate and in greater number compared to the ellipsoidal particles. Quantitative flow cytometry analysis of the cells after four hours of particle treatment at 37 °C showed statistically significant inhibition of particle uptake with ellipsoidal shape compared to spherical shape at doses ranging from 7.8 µg particles per well (9.7% vs. 17.7% uptake) to 500 µg particles per well (43.1% vs. 61.2% uptake) in 96-well plates (**Figure 7.6C**). For cells

incubated at 4 °C, there was a significant reduction in observed binding for the spherical particles compared to the ellipsoidal particles at the 500 µg and 250 µg dose.

7.3.3 Functionalization of lipid coated particles

To establish interchangeable functionalization of these particles, we employed a two-step coupling strategy. We first utilized a maleimide based conjugation to attach thiolated avidin to the surfaces of the particles followed by capture of biotinylated target biomolecules through the biotin-avidin interaction. In this manner, there is flexibility to attach any molecule to the surface that can be biotinylated, such as proteins or imaging agents. As proof of principle, we first functionalized the particles with biotinylated dye, biotinylated-Cy5. We independently confirmed that the avidin thiol was binding to the surface of the particles through incubating the particles with pre-fluorophore labeled avidin and assessing avidin content on the particles through fluorescence (**Figure 7.7**). As shown in the confocal micrographs of these spherical (**Figure 7.8A**) and ellipsoidal (**Figure 7.8B**) particles, the Cy5 signal was localized to the exterior of the particles using 7-AMC as a reference to denote the interior of the particles. We confirmed that the coupling of the biotinylated molecule is avidin specific by incubating particles with Cy-5 biotin but no avidin thiol. Confocal images demonstrate that the particles did not conjugate Cy5-biotin (**Figure 7.9**). Stability of the lipid coated particle to lyophilization (**Figure 7.10**) and extended exposure to 25 °C or 37 °C temperatures over a 7 day period (**Figure 7.11**) were evaluated and the particles experienced no measurable degradation in either case, demonstrating robustness of the fabrication of the anisotropic particles and their surface modification.

After verifying the reproducible capture of a biotinylated fluorophore by avidin conjugated to the surface of the lipid coated particles, we next evaluated the capture of a biotinylated antibody for murine CD28, an important costimulatory surface protein in the activation of lymphocytes. Through analysis of protein content in the supernatant of the wash steps, it was determined that the biotinylated antibody was captured on the surface of the particle and the conjugation procedure was dose dependent (**Figure 7.8C**). In addition, the efficiency of conjugation was evaluated to be 50-70%, across the doses of protein in synthesis (**Figure 7.8D**). These experiments demonstrate the flexibility and efficiency of incorporating target biomolecules onto the surfaces of these anisotropic particles by simple mixing at room temperature.

7.3.4 Cellular binding of lipid coated particles

To determine the capability of ellipsoidal microparticles to bind to cells in a targeted manner, we incubated the anti-CD3 conjugated microparticles loaded with TAMRA with Jurkat T-Cells labeled with CFSE. Confocal imaging of the particle samples revealed the presence of conjugates between the particles and cells only in the presence of anti-CD3 (**Figure 7.12A-D**). Moreover the ellipsoidal particles visually appeared to interact with cells along the long axis of the ellipsoidal particles (**Figure 7.12D**). Multiple confocal images were taken of the samples and using ImageJ, the number of conjugates per number of cells was determined for all four samples. This percentage was found to be significantly higher in the ellipsoidal lipid coated particle with anti-CD3 compared to the spherical with anti-CD3 and both shapes not coated with antibody (**Figure 7.12E**). Furthermore, using ImageJ to measure the length of contact between the particle and the cell, it was found that the ellipsoidal lipid coated particles

with anti-CD3 had a significantly higher length of contact with the cells than the spherical particles with anti-CD3 (**Figure 7.12F**).

7.3.5 Lateral membrane fluidity of particle supported lipids

To assess particle surface fluidity, we utilized fluorescence recovery after photobleaching (FRAP). Briefly, a particle was first located under confocal microscopy and a small circular region of the lipid layer approximately 1 μm in diameter was identified and bleached as described in the Methods section. The resulting bleached region was monitored over time and the recovery of the fluorescence signal was measured as labeled lipids diffused into the photobleached zone. Both spherical (**Figure 7.13A**) and ellipsoidal (**Figure 7.13B**) particles showed close to complete recovery of fluorescence within 150 s, using this data. Diffusion constants were determined by a normalization and fit of the signal recovery data (**Figure 7.13C**). Both spherical and ellipsoidal particles had statistically similar diffusion constants that were also on the same order of magnitude ($10^{-10} \text{ cm}^2\text{s}^{-1}$) as those observed for proteins on natural, biological membranes.²⁵ This value of surface diffusivity is important for applications where mimicry of biological membranes is desired, such as to emulate the diffusion and clustering of receptors found on natural cellular surfaces.

7.3.5 Discussion

Validation of our ability to generate ellipsoidal and spherical lipid coated particles utilizing poly(lactic-co-glycolic) acid (PLGA) for polymeric structural support is provided in **Figure 7.3**. As determined by aspect ratio analysis, our average aspect ratio was 3.3 for the stretched particles. This is near the predicted value of 2.8 as computed for a spherical particle that is stretched two-fold in a thin film.¹⁸ To confirm the fabrication of lipid coated particles, and the ability to encapsulate cargo within the particles as well

as coupled to the lipid surface, PLGA microparticles encapsulating 7-amino-4-methyl coumarin (7-AMC) were first made to visualize the core of the lipid polymer hybrid particle. After thin film stretching, the particles were coated with fluorescent liposomes containing rhodamine and imaged using confocal microscopy. We could visualize an enrichment of rhodamine signal around the outside of the particle. Furthermore, the encapsulated dye was also visible and determined to be localized to the center. This demonstrates that our spherical or ellipsoidal lipid coated particle platform has the ability to be used in the delivery of small hydrophobic drugs or contrast agents as has been demonstrated previously in other biodegradable particle platforms.^{26,27}

The biomimetic properties of lipid coated non-spheroidal particles may have precluded a hypothesized advantage of the ellipsoidal lipid coated particle constructs, namely their capability to reduce non-specific uptake compared to spherical particles of the same volume and mass. Therefore, upon validation of non-spheroidal lipid coated particle synthesis, the next goal was to investigate non-specific uptake of the ellipsoidal lipid coated particles. As demonstrated with confocal imaging, both spherical and ellipsoidal particles were capable of being internalized. However, there was a noted difference between the spherical and ellipsoidal samples. Across multiple doses of particles administered to the cells, there was a statistically significant decrease in internalization rate of ellipsoidal lipid coated particles compared to spherical lipid coated particles. Furthermore, the binding of particles was significantly reduced in the spherical compared to the ellipsoidal lipid coated particles suggesting this observed uptake difference was from differences in quantities of internalized particles, not non-specific adherence of the particles to the cell membranes. This trend, which has previously been

described in the literature for non-lipid coated polymeric particles with varied shape¹² confirms that our newly developed ellipsoidal lipid coated particles maintain the advantageous biological properties of non-spherical anisotropic particles.²⁸ Viability of the macrophages was unaltered during this incubation, as evidenced by a cell titer assay of both the spherical and ellipsoidal lipid coated particles, indicating that these lipid coated particles do not exhibit non-specific cytotoxic effects.

Upon confirmation that the lipid coating did not negate the key advantage of reduced non-specific uptake, we next demonstrated that our technique was compatible with a flexible conjugation strategy of attaching biomolecules such as protein to the surface of the anisotropic lipid coated particles under gentle conditions. For many applications, such as cell type-specific targeting, this approach involves the conjugation of antibodies that recognize tumor-associated antigens (TAAs) to the supported lipids. In other cases, fluorescent moieties are conjugated to the particle to assist in the visualization and imaging of the particle or to study the fluidic properties of the lipid coating. To achieve a robust and versatile platform for the presentation of any target protein or small molecule for applications such as drug delivery, gene delivery, and immunoengineering, we utilized maleimide functionalized lipids during the liposome synthesis and then conjugated thiolated avidin (that had been pre-bound to biotinylated fluorescein) to the surface of the lipid coated particles. Once lipids are functionalized with avidin, they become a versatile platform for conjugation of any biotinylated moiety, which we demonstrated using biotinylated Cy5 fluorophore and a biotinylated immunologically relevant antibody (anti-CD28). We did not note a plateau in the amount

of protein immobilized on the surface, however the amount that could be conjugated is significantly high enough to elicit a physiological response from T-Cells.¹⁸

One of the key advantages of ellipsoidal micro and nanoparticles compared to their spherical equivalents is the ability to bind more efficiently in a targeted fashion. This has been attributed to the higher radius of curvature of ellipsoidal particles compared to spherical particles and subsequently more surface area available for interaction with the cell.²⁹ This has been shown both *in vitro* and *in vivo* to enhance the accumulation of ellipsoidal particles at targeted binding sites compared to spherical particles.³⁰ We have demonstrated in this study that this highly advantageous shape mediated targeting property is preserved with the anisotropic lipid coated particle system. We utilized anti-CD3, an immunostimulatory ligand, to target the binding of the spherical and ellipsoidal lipid coated particles to T-Cells. Both the amount of cells bound to particles and the length of contact between particles and cells were enhanced with the ellipsoidal lipid coated particles compared to the spherical lipid coated particles. This trend has been reported in the literature with similar sized particles and was found to be correlated with a significant increase in antigen specific immune stimulation.¹⁸

An important biomimetic feature of the supported lipids is their membrane fluidity. One instance where this has been determined to be important is in the presentation of immunostimulatory ligands by artificial antigen presenting cells. Natural antigen presenting cells undergo dynamic rearrangement of their surface receptors upon engagement with a cognate T-Cell, and the lateral fluidity of these T-Cells has been deemed important for T-Cell activation.⁵ To that end we were interested in evaluating the fluidity of the new spherical and ellipsoidal lipid coated particles utilizing an established

fluorescence recovery after photobleaching technique (FRAP).² Both spherical and ellipsoidal particles had statistically similar diffusion constants that were also on the same order of magnitude ($10^{-10} \text{ cm}^2\text{s}^{-1}$) as those observed for proteins on natural, biological membranes.²⁵ For a supported lipid bilayer on glass, this diffusion constant is significantly lower than the average of $10^{-8} \text{ cm}^2\text{s}^{-1}$. However, it is worth noting that diffusion constants for supported lipid bilayers on non-glass substrates are typically lower than this number. For example, Sterling et. al. demonstrated that lipids deposited on actin coated glass slides had diffusion coefficients 50% lower than lipids on uncoated glass.³¹ Furthermore, Scomparin et. al. compared lipids deposited on glass and mica and noted an order of magnitude drop in the diffusion constant for lipids coated on mica compared to glass.³² Some of these reported diffusion constants were also in the range of our finding of $10^{-10} \text{ cm}^2\text{s}^{-1}$. This is significant as through these studies, these new anisotropic, synthetic biodegradable particles, are now demonstrated to mimic natural biological cells in four important ways: 1) Biological micron length-scale size, 2) Anisotropic shape and (via the automated stretching device) tunable radius of curvature, 3) Fluid lipid surface (with biomimetic diffusivity), and 4) facile incorporation/presentation of protein from the lipid surface. These artificial biomimetic particles as a biomaterial may be useful for varied biomedical applications.

7.4 Conclusions

In conclusion, we have successfully developed a procedure to synthesize biomimetic anisotropic lipid coated particles. By combining fabrication procedures for biodegradable particle synthesis, thin film stretching, lipid coating, and flexible biomolecular conjugation, we have enabled the capability for modular surface

presentation of biologically relevant proteins on a fluidic synthetic lipid membrane of defined anisotropic geometry. Critically, we have verified that this platform maintains the advantageous aspects of the non-spherical particle, specifically the capability to resist macrophage phagocytosis. In addition, this protein presentation reproduces the dynamic membrane properties of living cells and can be supported by particles of different shapes and tunable radius of curvature. This biotechnology can allow for more accurate mimicry of natural cells through the presentation of laterally mobile proteins on the surface of anisotropic biodegradable particles, while enabling independent control of the geometry of the particle, and enabling encapsulation of biological cargos. Therefore, this biomaterial platform may be of great benefit for varied applications including imaging and therapy.

7.5 Figures

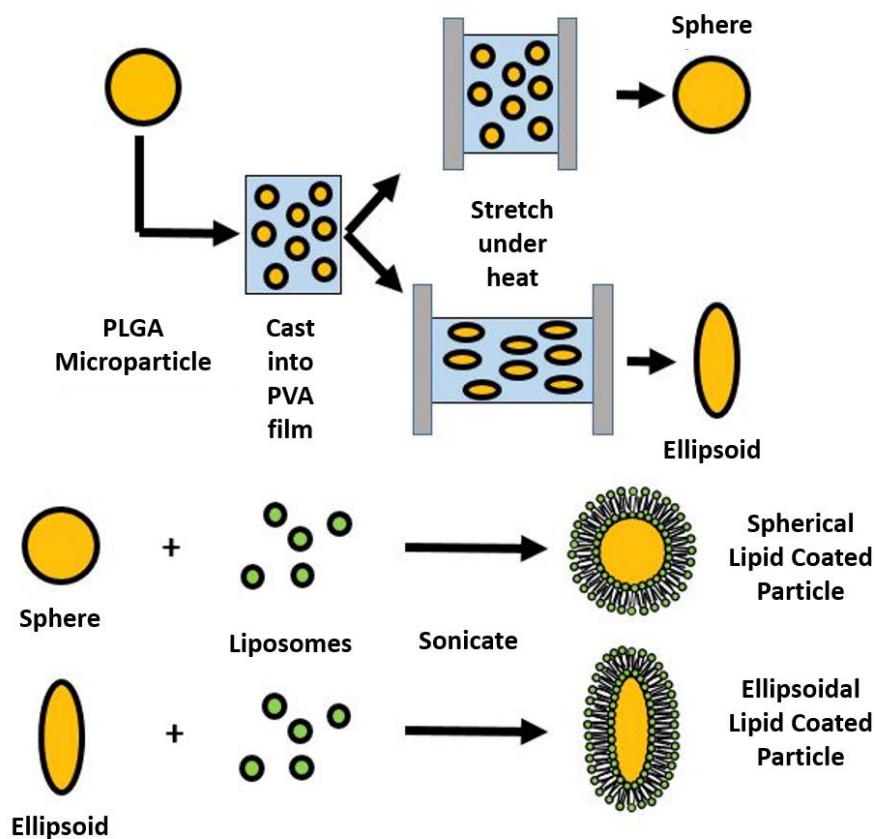


Figure 7.1: Schematic representation of ellipsoidal and spherical lipid coated particle synthesis. (a) Ellipsoidal microparticles were prepared utilizing a thin film stretching method starting from spherical PLGA microparticles prepared by single emulsion. (b) Liposomes that ~200 nm in size were prepared by extrusion and then sonicated in the presence of microparticles to yield lipid coated particles with shape specified by the initial particle template.

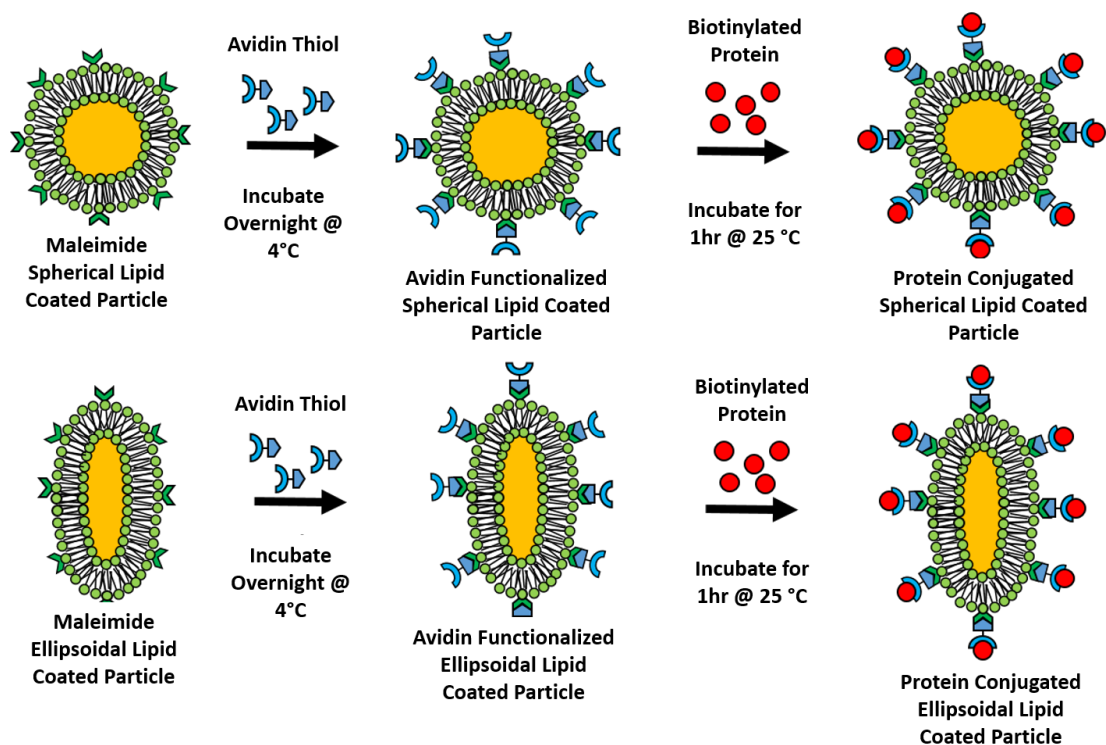


Figure 7.2: Functionalization strategy for lipid coated particles. (a) Lipid coated particles were synthesized on both spherical and ellipsoidal microparticles containing maleimide activated lipids. These maleimide lipids were reacted overnight at 4 °C with thiolated avidin to produce (b) lipid coated particles with avidin on the surface. These avidin functionalized lipids were then reacted with biotinylated molecules (either a fluorophore or protein) to produce (c) the final functional product.

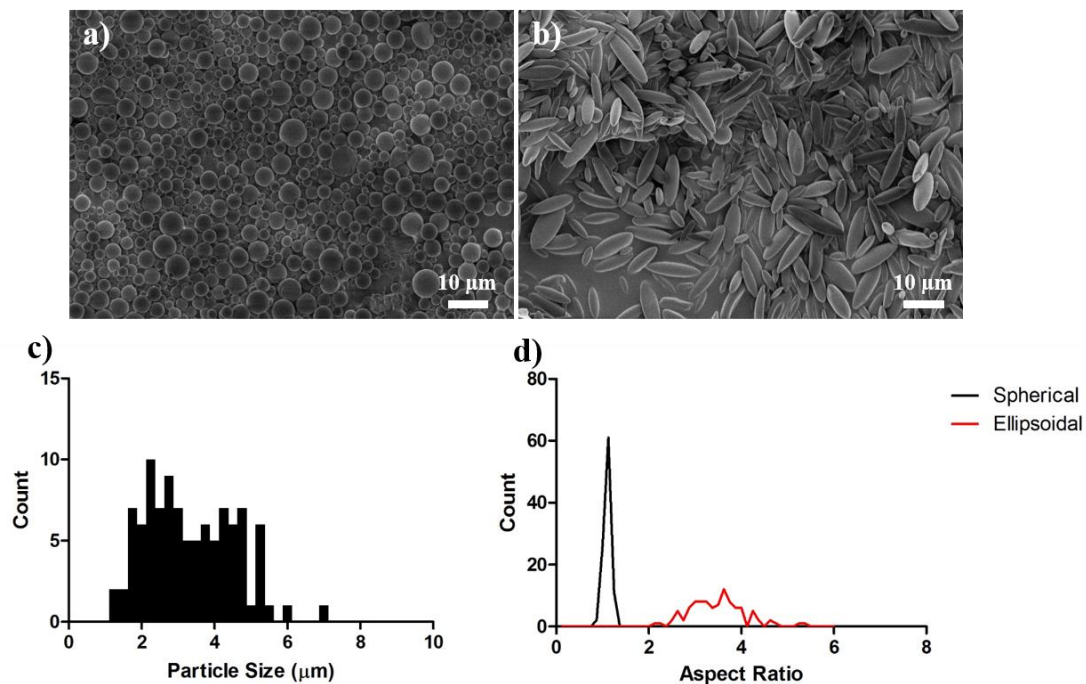


Figure 7.3: Spherical and non-spherical particles utilized for the synthesis of lipid coated particles. SEM images of (a) spherical and (b) ellipsoidal microparticles utilized as templates for the support of the lipids. (c) Size of spherical particles and (d) measured aspect ratio of spherical and ellipsoidal particles.

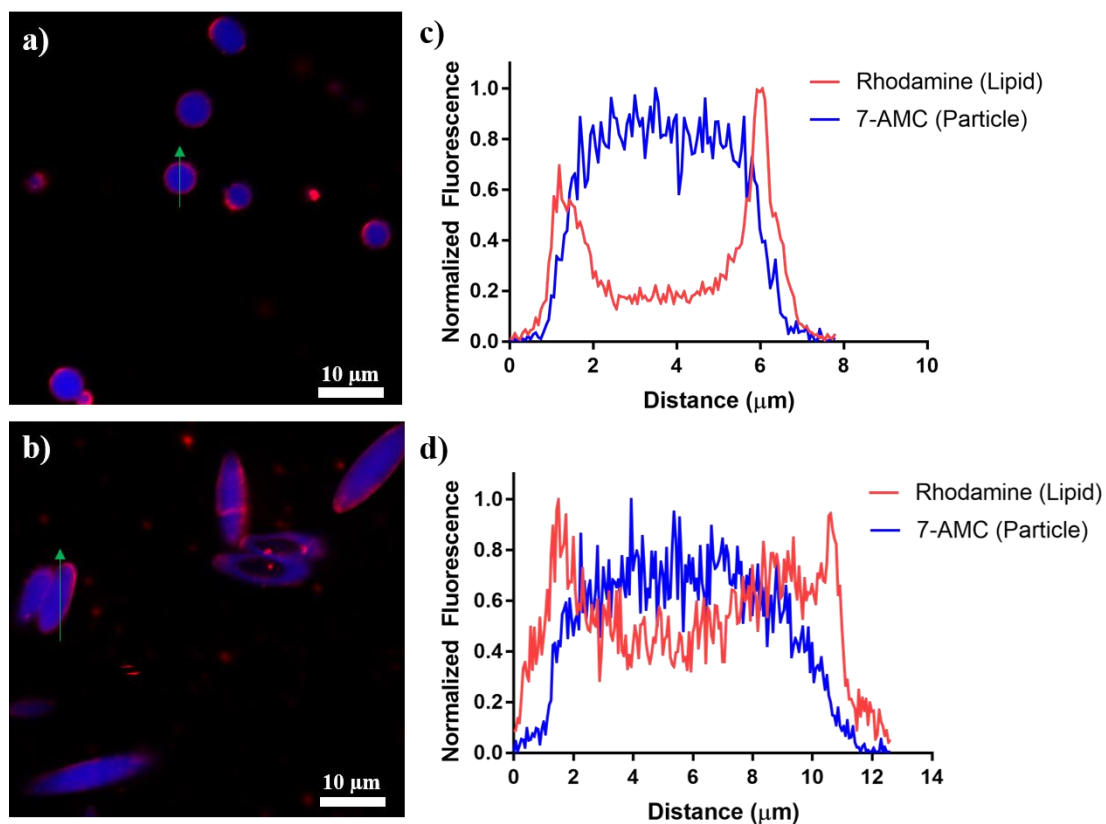


Figure 7.4: Ellipsoidal and spherical lipid coated particles can be synthesized utilizing a pre-formed particle template. Confocal micrographs of (a) spherical and (b) ellipsoidal particles encapsulating 7-AMC (blue) coated with a fluorescent lipids (red). Representative profile of the two fluorescence channels across the (c) center of the sphere and the (d) long axis of the ellipsoid. Green arrows on (a) and (b) denote where the profile was taken.

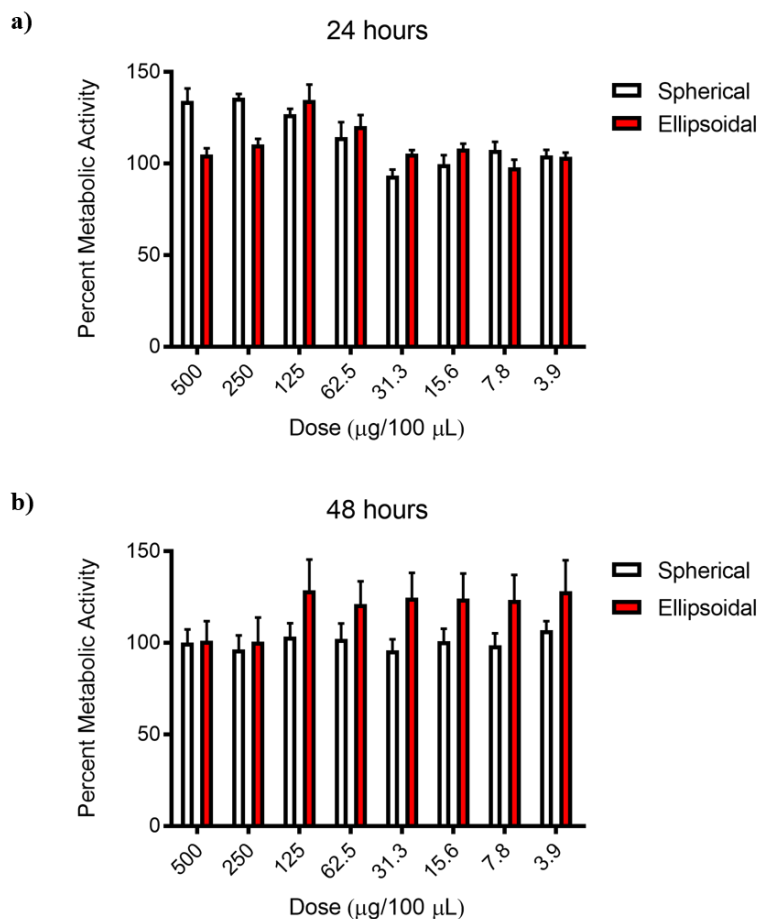


Figure 7.5: Viability of macrophages during cell uptake experiments is not statistically reduced by the presence of lipid coated particles. Macrophages were incubated for (a) 24 hrs. or (b) 48 hrs. with the indicated concentration of particles and viability was established by cell titer assay and normalization to the untreated control. Error bars represent standard deviation of four replicates.

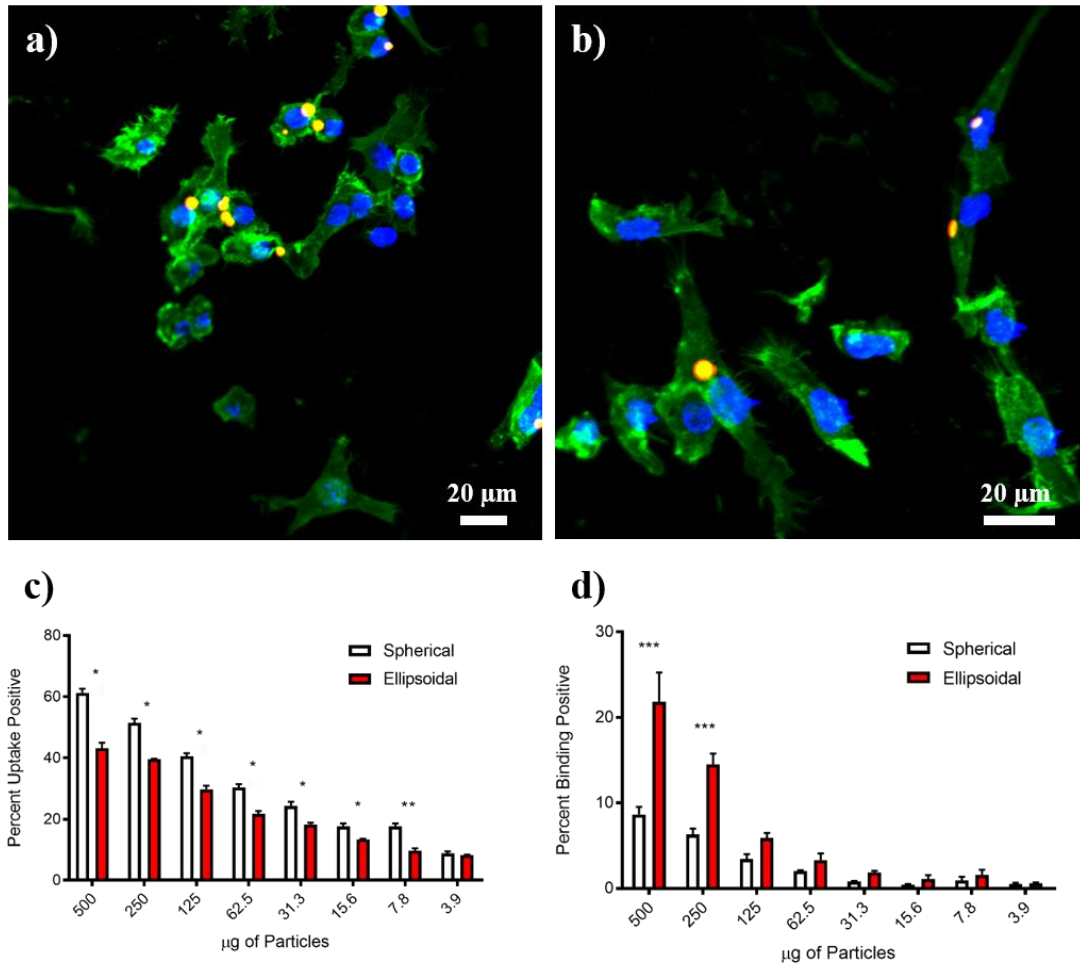


Figure 7.6: Macrophage uptake is shape dependent for spherical and ellipsoidal lipid coated particles. Confocal micrographs of non-specific uptake of (a) spherical and (b) ellipsoidal lipid coated particles (red) by macrophages (green = actin, blue = DAPI) demonstrates that ellipsoids resist non-specific cell uptake. Flow cytometry of macrophages treated with lipid coated particles at (c) 37 °C and (d) 4 °C of spherical and ellipsoidal shape reinforce the conclusion that ellipsoidal lipid coated particles resist cellular uptake. (* = $p < 0.05$, ** = $p < 0.01$, *** = $p < 0.001$, **** = $p < 0.0001$)

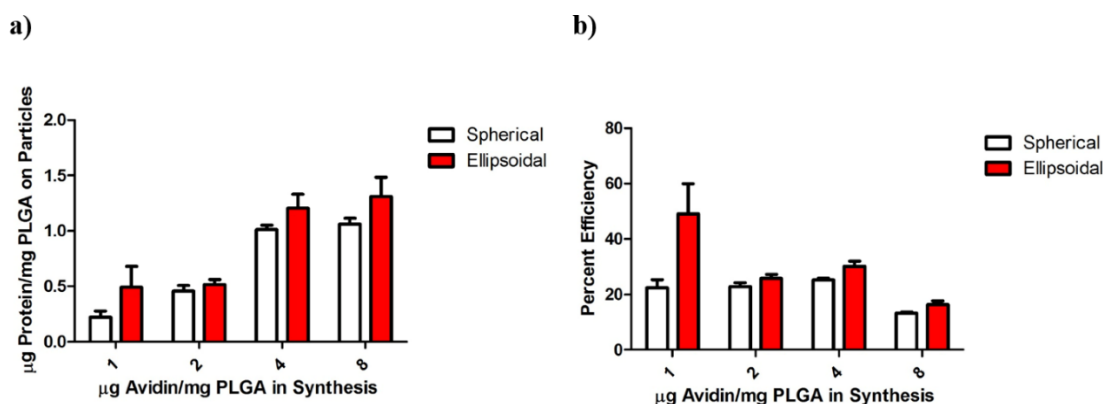


Figure 7.7: (a) Total protein conjugation amount of fluorescent avidin to spherical and ellipsoidal supported lipid bilayers. (b) Efficiency of conjugation for various ratios of avidin to mass of particles in synthesis. A two way ANOVA was performed to analyze statistical differences in the efficiency data set: $p = 0.0303$ for shape/dose interaction, $p = 0.0057$ for shape impact on results, and $p = 0.0013$ for dose impact on results. There was no significant difference between shapes at any dose tested as evaluated by Bonferroni's post test ($p > 0.05$) except for at 1 µg avidin/mg PLGA ($p < 0.01$).

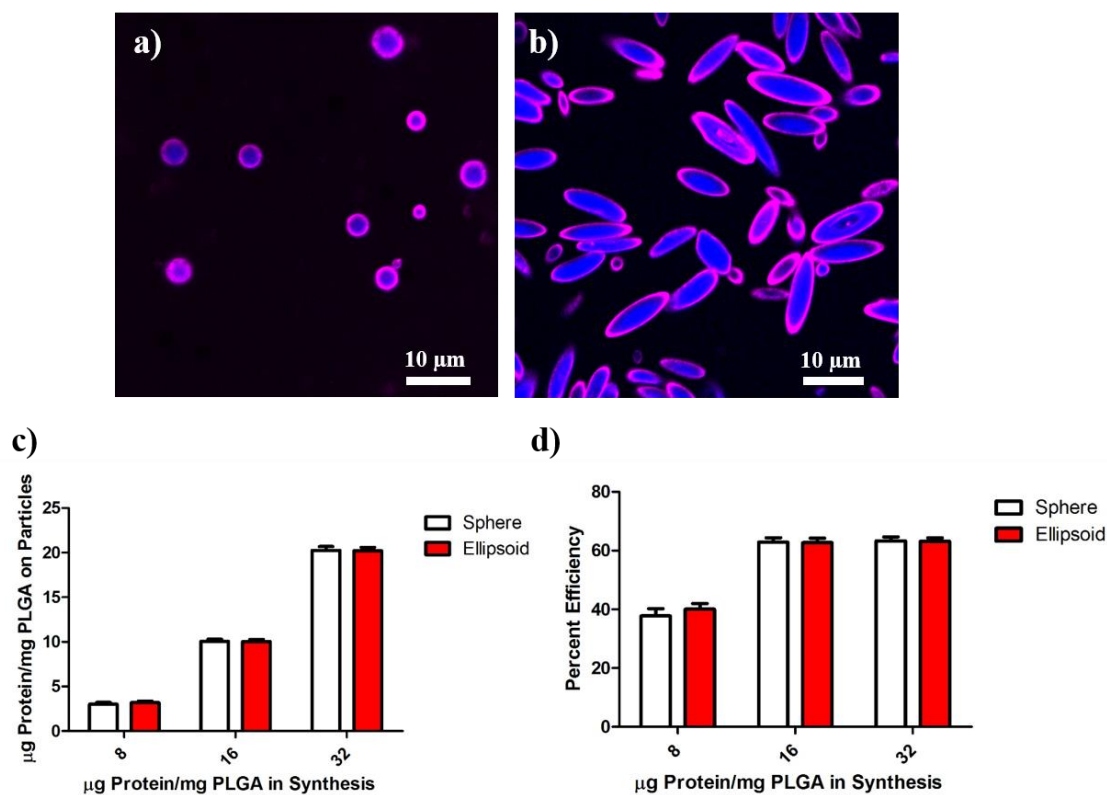


Figure 7.8: Interchangeable protein surface conjugation to spherical and non-spherical lipid coated particles. (a) Spherical and (b) ellipsoidal lipid coated particles encapsulating 7-AMC (blue) conjugated to avidin-biotin-fluorophore (magenta) conjugated on the surface. (c) Total protein captured by particles exhibits dependency on the amount of protein dosed in synthesis. (d) Efficiency of conjugation between spherical and non-spherical lipid coated particles at various doses is similar. Error bars represent SEM of 3 replicates.

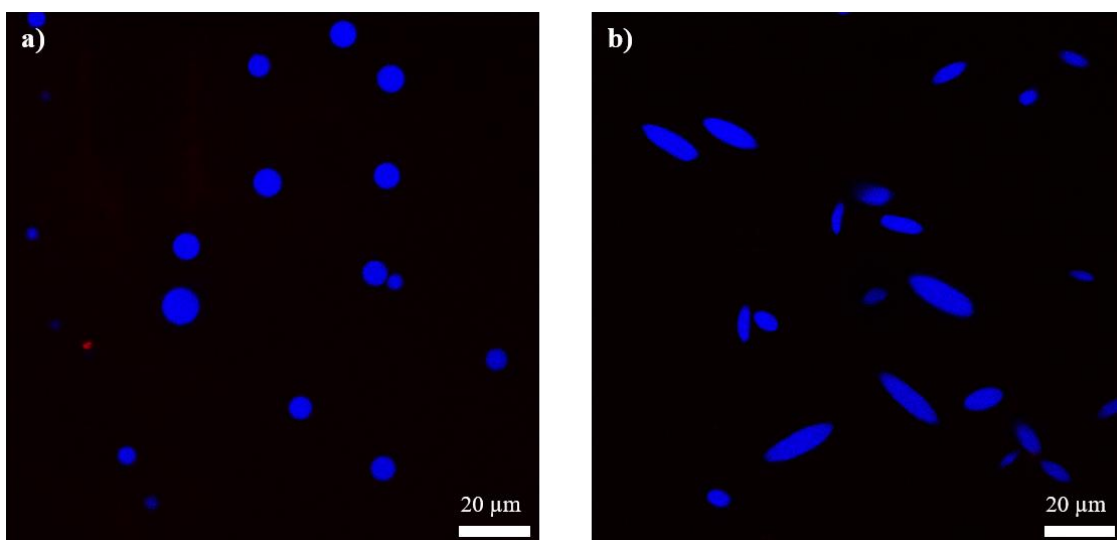


Figure 7.9: Biotinylated molecules do not adhere to the lipid coated particles without avidin intermediate protein. (a) Spherical and (b) ellipsoidal lipid coated particles were prepared in the absence of avidin thiol and then incubated with Cy5-biotin. Particles (blue) and Cy5-biotin (red) were then imaged using confocal microscopy.

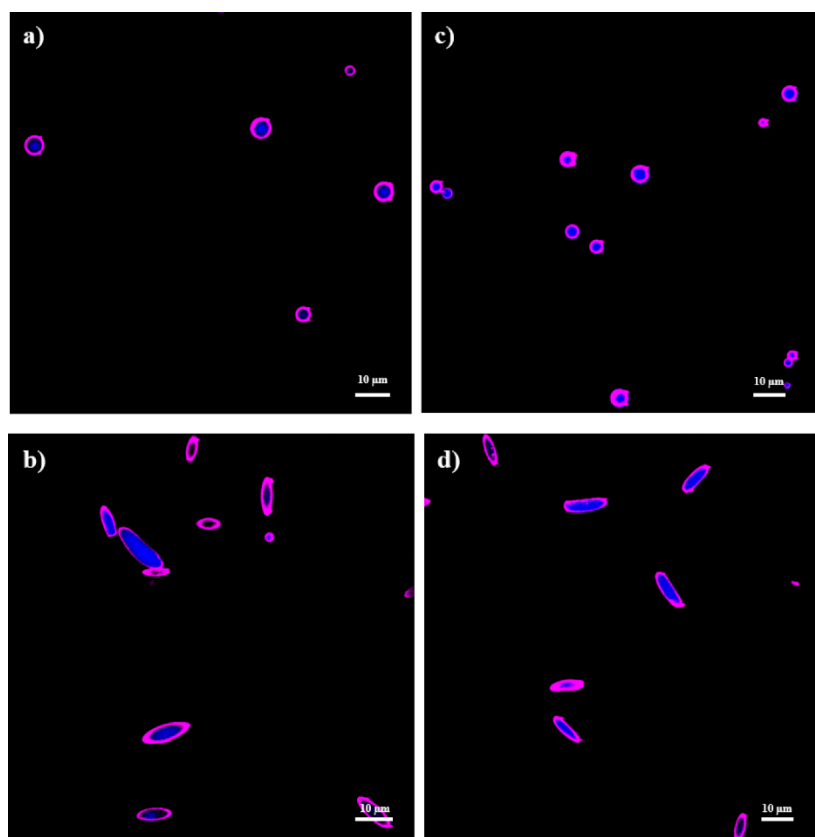


Figure 7.10: (a)/(c) Spherical and (b)/(d) ellipsoidal protein conjugated lipid bilayers are stable (a)/(b) before and (c)/(d) after lyophilization.

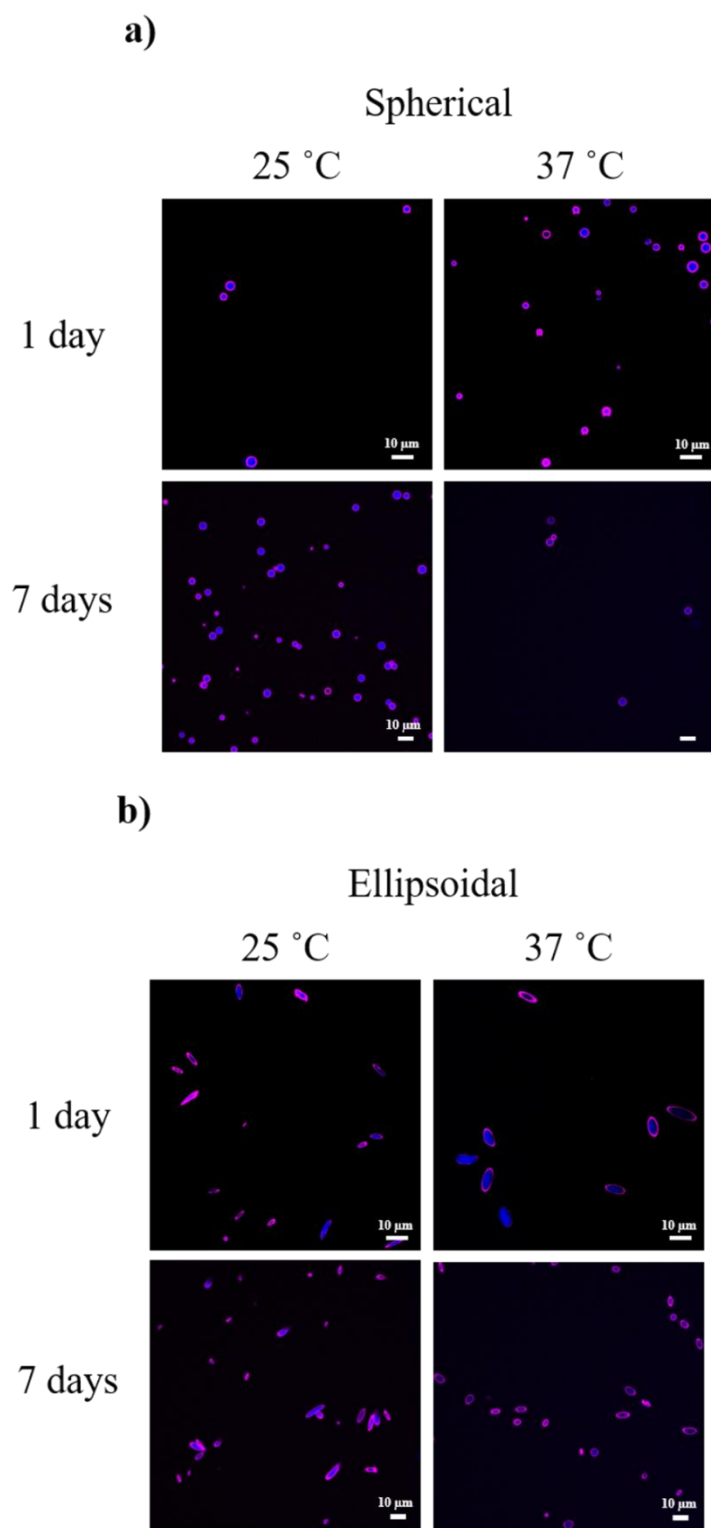


Figure 7.11: (a) Spherical and (b) ellipsoidal SLBs with Cy5 biotin conjugated to the surface were incubated at the indicated temperature for the indicated amount of time to assess stability of lipid coats. Confocal image analysis demonstrates stable presentation of surface ligands over all time points and conditions tested.

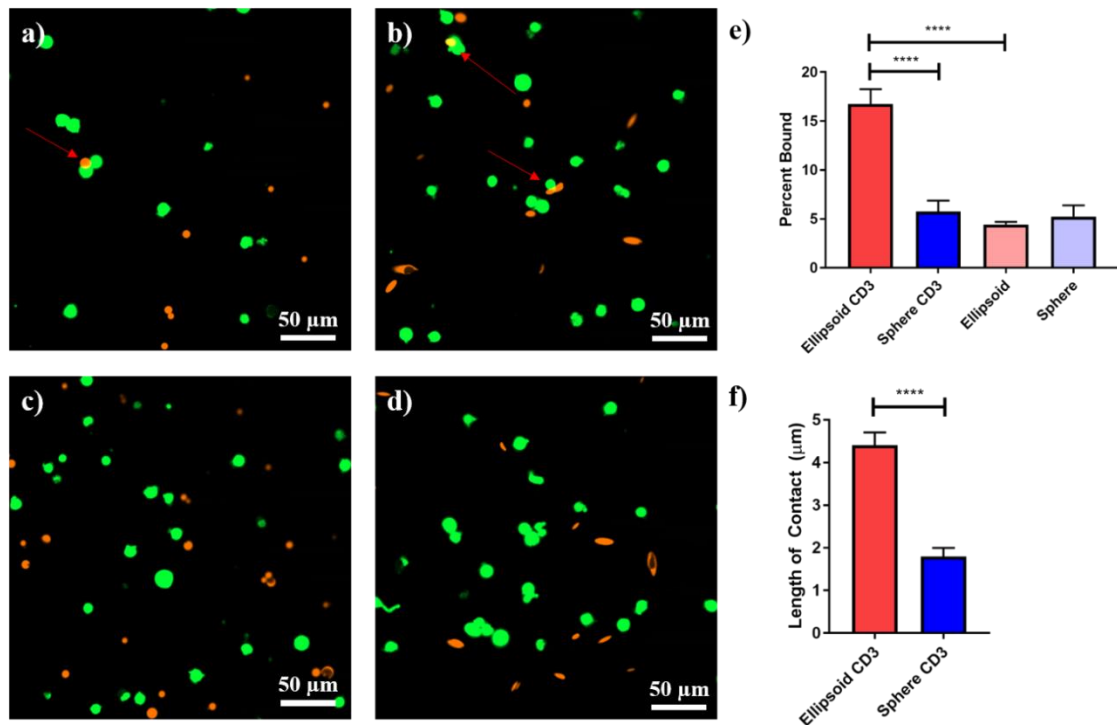


Figure 7.12: Targeted cell binding is shape dependent for lipid coated particles. Jurkat T-Cells were incubated with spherical or ellipsoidal anti-CD3 conjugated lipid coated particles or unconjugated lipid coated particles. Confocal images of (a) anti-CD3 spherical, (b) anti-CD3 ellipsoidal, (c) blank spherical, and (d) blank ellipsoidal particles demonstrate enhanced binding of ellipsoidal anti-CD3 lipid coated microparticles (red arrows denote instances of binding). Images were quantified by ImageJ for (e) frequency of cells bound to particles and (f) length of contact between particles and cells. Ellipsoidal anti-CD3 outperformed other conditions in both of these analyses. Error bars represent SEM of 10 image analyses. (**** = $p < 0.0001$)

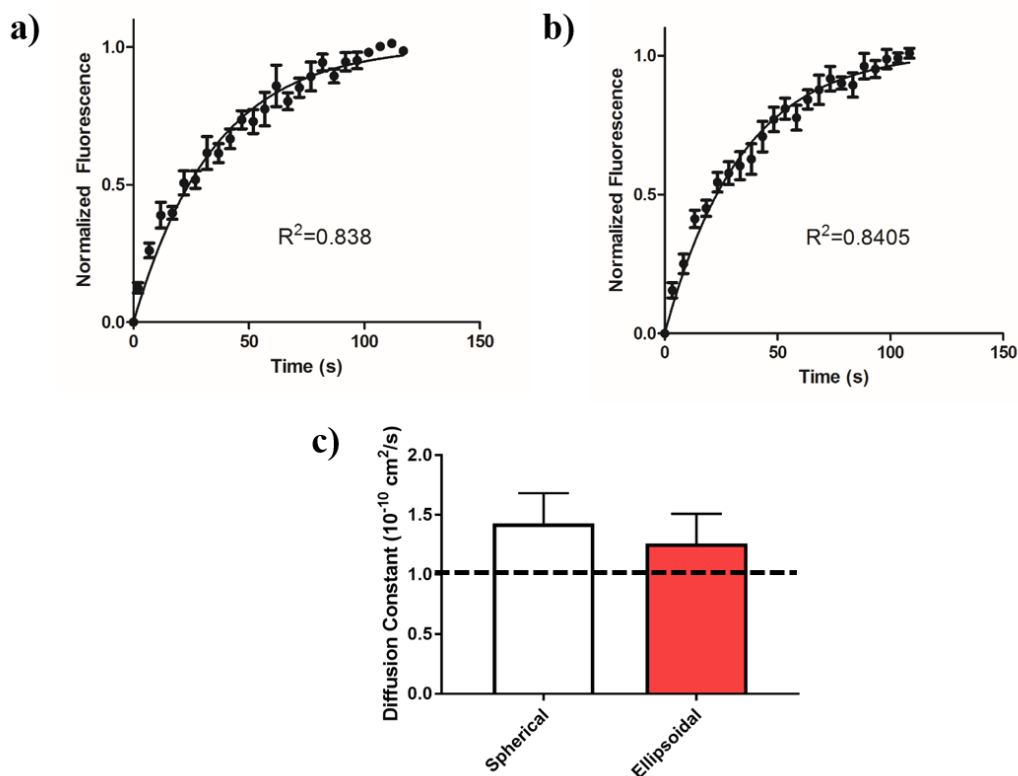


Figure 7.13: Lipid coated particles bearing conjugated molecules demonstrate fluidity. (a) Spherical lipid coated particles and (b) ellipsoidal lipid coated particles were subjected to region specific bleaching under confocal microscopy and subsequently imaged to measure recovery of fluorescence. From an exponential fit of the recovery of the lipid signal, (c) lateral diffusion constants were derived for the spherical and ellipsoidal lipid coated particles and were determined to be equivalent. The dotted line represents a reported lateral diffusion coefficient value for membrane bound proteins in a natural cell.

7.6 References

1. Wang, H., Zhao, P., Su, W., Wang, S., Liao, Z., Niu, R. Chang, J. PLGA/polymeric liposome for targeted drug and gene co-delivery. *Biomaterials* 2010;31(33):8741-8.
2. Bershteyn, A., Chaparro, J., Yau, R., Kim, M., Reinherz, E., Ferreira-Moita, L. Irvine, D.J. Polymer-supported lipid shells, onions, and flowers. *Soft Matter* 2008;4(9):1787-91.
3. Hadinoto, K., Sundaresan, A. Cheow, W.S. Lipid-polymer hybrid nanoparticles as a new generation therapeutic delivery platform: a review. *Eur. J. Pharm. Biopharm.* 2013;85(3):427-43.
4. Cheow, W.S. Hadinoto, K. Factors affecting drug encapsulation and stability of lipid-polymer hybrid nanoparticles. *Colloid. Surface. B.* 2011;85(2):214-20.
5. Mieszawska, A.J., Gianella, A., Cormode, D.P., Zhao, Y., Meijerink, A., Langer, R., Farokhzad, O.C., Fayad, Z.A. Mulder, W.J. Engineering of lipid-coated PLGA nanoparticles with a tunable payload of diagnostically active nanocrystals for medical imaging. *Chem. Comm.* 2012;48(47):5835-7.
6. Xu, J., Luft, J.C., Yi, X., Tian, S., Owens, G., Wang, J., Johnson, A., Berglund, P., Smith, J. Napier, M.E. RNA replicon delivery via lipid-complexed PRINT protein particles. *Mol. Pharm.* 2013;10(9):3366-74.
7. Hasan, W., Chu, K., Gullapalli, A., Dunn, S.S., Enlow, E.M., Luft, J.C., Tian, S., Napier, M.E., Pohlhaus, P.D. Rolland, J.P. Delivery of multiple siRNAs using lipid-coated PLGA nanoparticles for treatment of prostate cancer. *Nano Lett.* 2011;12(1):287-92.
8. Hu, C.-M.J., Zhang, L., Aryal, S., Cheung, C., Fang, R.H. Zhang, L. Erythrocyte membrane-camouflaged polymeric nanoparticles as a biomimetic delivery platform. *Proc. Natl. Acad. Sci. U. S. A.* 2011;108(27):10980-5.
9. Hu, C.-M.J., Fang, R.H., Wang, K.-C., Luk, B.T., Thamphiwatana, S., Dehaini, D., Nguyen, P., Angsantikul, P., Wen, C.H. Kroll, A.V. Nanoparticle biointerfacing by platelet membrane cloaking. *Nature* 2015;526(7571):118.
10. Fang, R.H., Hu, C.-M.J., Luk, B.T., Gao, W., Copp, J.A., Tai, Y., O'Connor, D.E. Zhang, L. Cancer cell membrane-coated nanoparticles for anticancer vaccination and drug delivery. *Nano Lett.* 2014;14(4):2181-8.
11. Hu, C.-M.J., Fang, R.H., Copp, J., Luk, B.T. Zhang, L. A biomimetic nanosponge that absorbs pore-forming toxins. *Nat. Nanotechnol.* 2013;8(5):336.
12. Sharma, G., Valenta, D.T., Altman, Y., Harvey, S., Xie, H., Mitragotri, S. Smith, J.W. Polymer particle shape independently influences binding and internalization by macrophages. *J. Control. Release* 2010;147(3):408-12.
13. Canelas, D.A., Herlihy, K.P. DeSimone, J.M. Top-down particle fabrication: control of size and shape for diagnostic imaging and drug delivery. *WIREs: Nanomed. Nanobiotechnol.* 2009;1(4):391-404.
14. Karagoz, B., Esser, L., Duong, H.T., Basuki, J.S., Boyer, C. Davis, T.P. Polymerization-Induced Self-Assembly (PISA)-control over the morphology of nanoparticles for drug delivery applications. *Polym. Chem.* 2014;5(2):350-5.
15. Chu, K.S., Finnis, M.C., Schorzman, A.N., Kuijter, J.L., Luft, J.C., Bowerman, C.J., Napier, M.E., Haroon, Z.A., Zamboni, W.C. DeSimone, J.M. Particle

- replication in nonwetting templates nanoparticles with tumor selective alkyl silyl ether docetaxel prodrug reduces toxicity. *Nano Lett.* 2014;14(3):1472-6.
16. Jiang, X., Leong, D., Ren, Y., Li, Z., Torbenson, M.S. Mao, H.-Q. String-like micellar nanoparticles formed by complexation of PEG-b-PPA and plasmid DNA and their transfection efficiency. *Pharm. Res.* 2011;28(6):1317-27.
 17. Jiang, X., Qu, W., Pan, D., Ren, Y., Williford, J.M., Cui, H., Luijten, E. Mao, H.Q. Plasmid-templated shape control of condensed DNA–block copolymer nanoparticles. *Adv. Mater.* 2013;25(2):227-32.
 18. Sunshine, J.C., Perica, K., Schneck, J.P. Green, J.J. Particle shape dependence of CD8+ T cell activation by artificial antigen presenting cells. *Biomaterials* 2014;35(1):269-77.
 19. Meyer, R.A., Sunshine, J.C., Perica, K., Kosmides, A.K., Aje, K., Schneck, J.P. Green, J.J. Biodegradable nanoellipsoidal artificial antigen presenting cells for antigen specific T-cell activation. *Small* 2015;11(13):1519-25.
 20. Champion, J.A., Katare, Y.K. Mitragotri, S. Particle shape: a new design parameter for micro-and nanoscale drug delivery carriers. *J. Control. Release* 2007;121(1-2):3-9.
 21. Ho, C., Keller, A., Odell, J. Ottewill, R. Preparation of monodisperse ellipsoidal polystyrene particles. *Colloid Polym. Sci.* 1993;271(5):469-79.
 22. Meyer, R.A., Meyer, R.S. Green, J.J. An automated multidimensional thin film stretching device for the generation of anisotropic polymeric micro-and nanoparticles. *J. Biomed. Mater. Res. Part A* 2015;103(8):2747-57.
 23. Ashley, C.E., Carnes, E.C., Phillips, G.K., Padilla, D., Durfee, P.N., Brown, P.A., Hanna, T.N., Liu, J., Phillips, B. Carter, M.B. The targeted delivery of multicomponent cargos to cancer cells by nanoporous particle-supported lipid bilayers. *Nat. Mater.* 2011;10(5):389.
 24. Kang, M., Day, C.A., Kenworthy, A.K. DiBenedetto, E. Simplified equation to extract diffusion coefficients from confocal FRAP data. *Traffic* 2012;13(12):1589-600.
 25. Lenaz, G. Lipid fluidity and membrane protein dynamics. *Bioscience Rep.* 1987;7(11):823-37.
 26. Sun, T., Zhang, Y.S., Pang, B., Hyun, D.C., Yang, M. Xia, Y. Engineered nanoparticles for drug delivery in cancer therapy. *Angew. Chem. Int. Edit.* 2014;53(46):12320-64.
 27. Mariano, R.N.s., Alberti, D., Cutrin, J.C., Geninatti Crich, S. Aime, S. Design of PLGA based nanoparticles for imaging guided applications. *Mol. Pharm.* 2014;11(11):4100-6.
 28. Meyer, R.A. Green, J.J. Shaping the future of nanomedicine: anisotropy in polymeric nanoparticle design. *WIREs: Nanomed. Nanobiotechnol.* 2016;8(2):191-207.
 29. Toy, R., Peiris, P.M., Ghaghada, K.B. Karathanasis, E. Shaping cancer nanomedicine: the effect of particle shape on the in vivo journey of nanoparticles. *Nanomed.* 2014;9(1):121-34.
 30. Kolhar, P., Anselmo, A.C., Gupta, V., Pant, K., Prabhakarpanthian, B., Ruoslahti, E. Mitragotri, S. Using shape effects to target antibody-coated nanoparticles to

- lung and brain endothelium. *Proc. Natl. Acad. Sci. U. S. A.* 2013;110(26):10753-8.
31. Sterling, S.M., Dawes, R., Allgeyer, E.S., Ashworth, S.L. Neivandt, D.J. Comparison of actin-and glass-Supported phospholipid bilayer diffusion coefficients. *Biophys. J.* 2015;108(8):1946-53.
 32. Scomparin, C., Lecuyer, S., Ferreira, M., Charitat, T. Tinland, B. Diffusion in supported lipid bilayers: Influence of substrate and preparation technique on the internal dynamics. *Eur. Phys. J.* 2009;28(2):211-20.

Chapter 8: Anisotropic Biodegradable Particles Coated with Naturally Derived Red Blood Cell Membranes for Enhanced Drug Delivery⁶

8.1 Introduction

In recent years, there has been growing interest in pioneering bio-inspired engineering criteria for biomaterials based therapeutics.¹ Biomimetic strategies for the design of micro- and nanotherapeutics have been successfully leveraged to achieve enhanced effects in drug delivery,² tissue engineering,³ and immunoengineering applications.⁴ Some of the most successful platforms to date rely on biomimicry of physical and chemical properties of cells to achieved their desired goals. Examples of this include modulation of particle mechanic characteristics,⁵ surface chemistry,⁶ geometry,⁷ and response to stimuli.⁸ Two specifically promising engineering approaches to the biomimetic augmentation of particle efficacy include biointerfacing through coating with naturally derived cell membranes and deformation of particle shape to mimic the complex cell membrane structure⁹ and overall cell morphology¹⁰ respectively.

Nanoparticle coating with naturally derived cell membranes has recently been employed to confer novel properties to these constructs for therapeutic applications. Although many platforms have been engineered with synthetic components to mimic certain aspects of the cell membrane,^{11,12} it is very difficult to encompass every conceivable property of the cell membrane in a bioengineered design. Incorporation of naturally derived cell membranes have successfully circumvented this difficulty as a top-down design approach and confer a desired function. For example, red blood cell

⁶ This chapter contains material that is intended for publication in the following article: Ben-Akiva E, Meyer RA, and Green JJ, Anisotropic Biodegradable Particles Coated with Naturally Derived Red Blood Cell Membranes for Enhanced Drug Delivery. In preparation.

membranes have been coated onto polymeric nanoparticles¹³ to achieve enhanced pharmacokinetic properties and to engineer detoxifying nanosponges for sepsis treatment.¹⁴ In addition, platelet membranes have been utilized to enable enhanced targeting of diseased and inflamed tissue such as the site of an infection or a tumor.¹⁵ Leukocyte membranes have also been used to recapitulate various functions of these cells including avoiding elimination by the immune system and artificial diapedesis.¹⁶ Cancer cell membranes have also been employed to mediate enhanced delivery of antigenic material to antigen presenting cells for cancer immunotherapy.¹⁷ Nanoghosts derived from mesenchymal stem cells have been found to enhance tumor targeting capabilities and allow for more effective drug delivery.¹⁸ The application of naturally derived membranes for particle bio-interfacing have indeed been numerous and varied. Yet, in many of these cases mimicry has been restricted to the surface modulation thus limiting potential enhancement of the particle therapeutic.

One important parameter which could synergize well with these biomimetic naturally derived membrane coatings is particle shape. Anisotropic particles have been determined to be superior to spherical particles with respect to two features that could make them attractive candidates for a combination strategy. The first property is the resistance to non-specific cellular elimination upon systemic administration.¹⁹ This has been found to be due in part to the impact of angle of approach to the cell membrane, which is only applicable to a particle of anisotropic shape.²⁰ This would theoretically synergize well with the stealth nature of particle coated with a naturally derived membrane in avoidance of immune clearance. The second advantageous characteristic of an anisotropic particle is that it is able to have enhanced targeted interactions with

biological cells for drug delivery²¹ and immunoengineering applications.⁷ This has been found to be due to the higher surface area to volume ratio that is afforded by anisotropic shape. Theoretically, this would also synergize well with the targeting capabilities that are conferred by a naturally derived cell membrane coat that would be augmented by the higher surface area of contact with the target of the particle therapeutic. Furthermore, there exist a variety of methods for the simple and controllable synthesis of anisotropic polymeric particles that are completely amenable to protocols for coating spherical particles with naturally derived cell membranes due to the preservation of core material properties in the deformation process.²²

In this study, we have developed anisotropic polymeric micro- and nanoparticles coated with red blood cell membranes which have a biomimetic shape and surface composition. We synthesized spherical, prolate ellipsoidal, and oblate ellipsoidal micro- and nanoparticles and coated them with red blood cell membranes using previously established protocols for spherical particles.¹³ We demonstrate that these particles have biomimetic surface features such as lateral lipid fluidity and membrane bound ligand presentation. Furthermore, we determined that these anisotropic shape and membrane coating are able to synergize with respect to *in vitro* resistance to cellular uptake and *in vivo* reduction of clearance rate upon systemic administration. Finally, we have demonstrated the drug delivery utility of these novel constructs through the augmentation of nanosponge activity in a sepsis detoxification model. Continued investigation into the combinations of biomimetic paradigms such as surface chemistry and morphology will undoubtedly yield optimal particle formulations for enhanced biomedical therapeutics.

8.2 Materials and Methods

8.2.1 Anisotropic Micro- and Nanoparticle Synthesis

Polymeric microparticles and nanoparticles were synthesized using single emulsion techniques as we have previously described.^{23,24} Poly (lactic-co-glycolic acid) acid terminated (38-54 kDa, 50:50 L:G ratio) (PLGA, Sigma Aldrich; St. Louis, MO) was used as the core material for particle synthesis. In order to visualize the microparticles under confocal microscopy, the particles were loaded with 7-amino-4-methyl coumarin (7-AMC, Sigma Aldrich; St. Louis, MO) or 1,1'-dioctadecyl-3,3,3',3'-tetramethylindodicarbocyanine perchlorate (DiD, Thermo Fisher; Waltham, MA) were encapsulated at a 1% wt/wt ratio and a 0.1% wt/wt ratio, respectively, to the polymer. The PLGA was dissolved at 20 mg/mL in dichloromethane (DCM) and 5 mL of the polymer solution was emulsified in 50 mL of 1% PVA solution using an IKA T-25 homogenizer (IKA Works; Wilmington, NC) set to 5000 rpm or a VCX 750 sonicator (Sonics & Materials Inc.; Newtown, CT) set to 60% amplitude. The resulting emulsification was poured into 100 mL of a 0.5% PVA solution and the particles were allowed to harden for 4 hrs. Afterward, the particles were washed three times (@3000 g for 5 min for microparticles or 40000 g for 15 min for nanoparticles), frozen and lyophilized.

Lyophilized micro- or nanoparticles were deformed into prolate or oblate ellipsoidal particles using the thin film stretching methods as has been previously reported.²⁵ Particles were dissolved at a concentration of 2.5 mg/mL in a 10% PVA and 2% glycerol solution. The dissolved particles were then deposited into rectangular or square petri dishes to deform the particle in 1D or 2D to make prolate ellipsoidal or oblate ellipsoidal particles respectively. The films were then loaded onto an automated

thin film stretcher that has previously been designed²⁶ and the films were stretched in one direction at 90 °C for prolate ellipsoidal particles or in two directions for biconcave discoid red-blood cell shaped particles. The films were then cooled at room temperature, and the films were removed from the stretcher. The films were then dissolved in water via vortexing and the anisotropic particles were washed three times with water and lyophilized prior to use.

Anisotropic microparticles were analyzed by scanning electron microscopy for size and morphology analysis (Leo FESEM). Lyophilized particles were mounted on the aluminum tack (Electron Microscopy Services; Hatfield, PA) coated with carbon tape (Nisshin EM Co.; Tokyo, Japan). Particle images were analyzed by ImageJ to determine size and aspect ratio of the anisotropic particles.

8.2.2 RBC Coating of Anisotropic Particles

Anisotropic micro- and nanoparticles were coated with red blood cell membranes using a combination of previously developed protocols.^{6,13} Pathogen-free whole CD1 (*in vitro* characterization) or B6 (*in vivo* characterization) mouse blood was purchased from Innovative Research (Innovative Research; Novi, MI). 1 mL of whole blood was centrifuged twice at 800g to separate the packed RBCs from the serum and the white blood cells. The RBCs were then suspended in 1 mL of a hypotonic lysis buffer of 0.25x PBS and chilled to 4 °C. The lysis proceeded for 20 min, and then the resultant RBC ghosts were centrifuged twice at 17,000g for five min and resuspended in 1x PBS. In order to visualize the RBC membrane, we fused the RBC ghosts with rhodamine labeled liposomes. The rhodamine liposomes were formed by mixing 50 µg of a rhodamine labeled DSPE lipid and 50 µg of a PEGylated DSPE lipid (Avanti Polar Lipids;

Alabaster, AL) in a glass vial and the organic solvent was removed under a vacuum and the lipids were then hydrated in 1x PBS. The liposome mixture was then mixed with the RBCs and incubated for 1 hr. at 37 °C. After this incubation, the ghosts were washed 3x in 1x PBS at 1000g. The RBC ghosts were then sonicated in a VCX 750 sonicator with a cup attachment in a glass vial at 50% amplitude for 2 min. to prepare vesicles that were sub-200 nm in size. The vesicles were then mixed with 2 mg of micro- or nanoparticles and sonicated again at 50% amplitude for 2 min. The particles were then centrifuged at 1000g for microparticles and 17,000g for nanoparticles and washed three times and resuspended via vortexing and trituration for nanoparticles to prevent dissociation of the RBC coat from the particle. The resultant RBC coated particles were then imaged or used for functional assessment.

8.2.3 Confocal Imaging and Evaluation of Lateral Fluidity

To evaluate the physical properties of the membrane coating on the particle, we used a Zeiss 780 FCS microscope to image and characterize the labeled RBC lipid membrane on the surface of the particle. Images were acquired with a 40x objective in a 37 °C incubation chamber to attain a biomimetic temperature for membrane characterization.

For evaluation of lateral membrane fluidity, we used a similar fluorescence recovery after photobleaching (FRAP) technique as was given in Chapter 7 for the evaluation of synthetic membrane fluidity. A region of interest was identified under the microscope and the fluorescence of the membrane was bleached using the highest power setting of the laser. The region of interest was tracked over time for the recovery of fluorescent signal and a second region of interest on another particle in the image was

tracked to control for bleaching during imaging. The raw fluorescence $I(t)$ values were then normalized to $NFI(t)$ using the following equation:

$$NFI(t) = \frac{I(t) - I_{post\ bleach}}{I_{pre\ bleach} * I_{post\ recovery}}$$

The normalized fluorescence intensity vs. time was then fit to a single exponential recovery curve as a model for FRAP signal recovery using GraphPad Prism 7 (GraphPad Software, Inc.; La Jolla, CA). The time constants of half recovery were extracted ($t_{0.5}$) from the model and the characteristic length (r_{bleach}) of the recovery region was determined by ImageJ analysis of the confocal images during the recovery. These two values were then used to compute the lateral diffusion constants of the lipids in the RBC membranes using the following model set forth by Kang et. al.²⁷:

$$D_{lipid} = \frac{r_{bleach}^2}{4 * t_{0.5}}$$

8.2.4 Characterization of RBC Coated Anisotropic Nanoparticles

Nanoparticles coated with RBC membranes were characterized by transmission electron microscopy FEI Tecnai 12 TWIN TEM. The membrane coated nanoparticles were stained in 1% uranyl formate as a negative stain in order to visualize the particle morphology and membrane structure on the surface of the particle. The particles were also characterized by dynamic light scattering using a Malvern ZetaSizer (Malvern Instruments; Westborough, MA). The particles were suspended at a concentration of 0.1 mg/mL and sized in a low volume disposable cuvette using recommended machine settings. The z-average size of the coated and uncoated nanoparticles were then compared for evidence of increased size due to membrane coating. In order to evaluate the presence of CD47 on the surface of the particle, we used an APC labeled anti-CD47

(BioLegend; San Diego, CA).. Coated and uncoated particles were incubated with a 1:100 dilution of the antibody for 1 hr. at 4 °C in PBS. Following incubation, the particles were washed three times in 1x PBS and were read on a BioTek Synergy 2 (Biotek; Winooski, VT) plate reader. The coated particle fluorescence readings were then normalized to the uncoated fluorescence readings to determine the fold increase in antibody staining to demonstrate the presence of CD47 on the surface of the particles.

8.2.5 Evaluation of *In Vitro* Macrophage Uptake

To assess potential synergy of the RBC membrane and the anisotropic shape for drug delivery applications, we modeled the elimination of the nanoparticles from body with an *in vitro* macrophage uptake experiment. We used RAW 264.7 (ATCC) murine macrophages as a model cell for phagocytic elimination. The cells were cultured in Dulbecco's Minimal Essential Media (Life Technologies; Grand Island, NY) supplemented with 10% fetal bovine serum and penicillin/streptomycin. Uptake was evaluated qualitatively with confocal imaging and quantitatively with flow cytometry. For flow cytometry studies, macrophages were seeded at a density of 30,000 cells/well. Particles of different shapes and membrane coatings were added to the macrophages and the cells incubated with the particles labeled with DiD dye. After the incubation, the cells were washed gently 3x with PBS. The cells and particles were then fixed in 10% formalin stabilized with methanol (Sigma Aldrich; St. Louis, MO) for 15 min. The cells were then washed three times with PBS and were stained with Alexa 488 Phalloidin (Life Technologies; Grand Island, NY) for actin in the cytosol and DAPI for the nucleus (BioChemica; Darmstadt, Germany) following the manufacturer's protocol. The fixed samples were then visualized using confocal microscopy using a Zeiss 780 FCS.

8.2.6 Evaluation of *In Vivo* Pharmacokinetics of RBC Coated Particles

To assess the potential pharmacokinetic benefits the union of anisotropic particles and biomimetic membrane coatings could realize, we evaluated the biodistribution of the coated and uncoated spherical, prolate ellipsoidal, and oblate ellipsoidal nanoparticles (n = 3 mice/group). To visualize the particles *in vivo* we encapsulated a custom synthesized hydrophobic dye with a 770ex/800em fluorescence profile. (LICOR Biosciences; Lincoln, NE). 2 mg of the nanoparticle solution suspended in 100 μ L of sterile PBS was injected retroorbitally into the right eye. Blood samples were then collected retroorbitally at 15 min, 30 min, 45 min, 2 hr, 4 hr, and 24 hr following particle administration from the left eye. The blood samples were then read on the BioTek Synergy 2 plate reader and the sample fluorescence was normalized to the initial 15 min time point to control for variability in the injection. The fluorescence readings were then normalized to a single phase exponential decay curve in GraphPad 7 Prism and half-lives were derived from the best fit equations. At 72 hr post administration, the animals were sacrificed and the liver, spleen, kidney, heart, and lung were dissected out and imaged on a LICOR Pearl Impulse Imager. A region of interest was drawn around the area of the organ in the image and the mean gray value was evaluated in Image J. These values were then normalized to the total sum of fluorescence signal from all animals combined to derive percent distribution information at 72 hr post particle administration.

8.2.7 Evaluation of *In Vivo* Activity of the Anisotropic Nanosponge

As a proof of principle of the drug delivery capabilities of anisotropic red blood cell membrane coated nanoparticles, we used an *in vitro* and *in vivo* alpha toxin neutralization assay developed by Hu et. al.¹⁴ In this model, the RBC membrane itself

serves as the drug to be delivered as it acts as a decoy nanosponge to absorb the hemolytic alpha toxin and spare the host's red blood cells.

For *in vitro* evaluation of nanoparticle activity, we mixed 1.5 μg of alpha toxin (Sigma Aldrich; St. Louis, MO) with 100 μL of the RBC membrane coated spherical, prolate ellipsoidal, or oblate ellipsoidal nanoparticles at 2 mg/mL for 30 min. Mouse RBCs were centrifuged at 800 g and resuspended in 1x PBS to remove hemoglobin from the RBC suspension. Following this incubation, 900 μL of 5% mouse RBCs were added to the particle/toxin mixture and the mixture was incubated for an additional 30 min. Following the 30 min, the particles were centrifuged at 17000 g for 5 min. The absorbance of the supernatant at 540 nm was read by plate reader to assess the hemolysis present in the sample. The absorbance readings were normalized to a sample that did not have particles to neutralize the toxin.

For *in vivo* evaluation of anisotropic nanosponge activity, we administered a lethal dose of alpha toxin systemically through retroorbital injection (2.5 $\mu\text{g}/\text{mouse}$). The treatments were administered 2 min later and consisted of either no treatment, uncoated nanoparticles, coated spherical nanoparticles, coated prolate ellipsoidal nanoparticles, and coated oblate ellipsoidal nanoparticles ($n = 6$ mice/group, 3 mg/particle injection). The animals were monitored for survival every 30 min for 8 hours following particle injection and every 24 hrs. thereafter. Animals that survived past 24 hrs. were taken to be long-term survivors and were found to be healthy 1 week following the start of the experiment.

8.3 Results and Discussion

8.3.1 Characterization of RBC Coated Microparticles

For the purposes of initial membrane coating experiments and lipid fluidity measurements, we opted to use microparticles as a model system prior to nanoparticles. The general overview of the coating procedure that was used for microparticle and nanoparticle coating is given in **Figure 8.1**. Spherical particles were synthesized by single emulsion and then stretched using the thin film stretching protocol that our lab has recently optimized.²⁶ Following retrieval of the particles from the thin films, the particles were fused with processed nanovesicles from fresh RBC membranes to yield a biomimetic lipid membrane on the surface of the particle that is derived from a natural cell plasma membrane. This core-shell particle design offers the advantages of being able to encapsulate a therapeutic cargo in the polymeric core, along with a biomimetic surface that could be used in stealth applications for avoidance of reticuloendothelial system (RES) clearance.²⁸

We initially characterized the anisotropic particle surface using SEM imaging of the particle samples followed by subsequent analysis of the particle sample with Image J (**Figure 8.2A-C**). The size of the microparticles used in this study was determined to be approximately 5 μm in size with a standard deviation of approximately 2 μm (**Figure 8.2D**). Although used as a model system, this size would be acceptable for systemic administration based on our previous work.²³ Upon stretching, the prolate ellipsoidal particles are predicted to have an aspect ratio of 2.8 for the 2-fold stretching method used in this study.⁷ The oblate ellipsoidal particles would be predicted to maintain an aspect ratio of 1 while lying on their flat surface as the particles were stretched 1.5 fold in each direction. These predicted aspect ratios were close to the measured values at an average near 3 for the prolate ellipsoidal particles and an average near 1 for the oblate ellipsoidal

particles (**Figure 8.2E**). There was a distribution of the aspect ratios in the ellipsoidal particles, however this could potentially be partially attributed to the particles not laying perfectly flat during SEM imaging. Aspect ratio control such as this is important for the manifestation of anisotropic properties, as the aspect ratio has been shown to impact cell uptake,^{29,30} intracellular drug delivery,^{31,32} and biodistribution.³³

Upon coating the particles with RBC membranes, the samples were then imaged under confocal microscopy to determine the localization of the membrane fluorescent signal with respect to the particle fluorescent signal. Imaging revealed a halo of RBC membrane fluorescence around the spherical particles that coated the entire particle (**Figure 8.3A**). Upon drawing a line through the center of the particle and analyzing the fluorescence intensity through the particle core, we found localization of the membrane signal on the exterior of the particle (**Figure 8.3B**). Regardless of where the line was drawn through the particle, the same result was achieved. The prolate ellipsoidal particle images revealed similar fluorescent signal localizations (**Figure 8.3C-D**) indicating successful coating of 1-D stretched particles. The oblate biconcave discoid particles also exhibited similar patterns of fluorescence including within the dimple of the particle as indicating complete coverage (**Figure 8.3E-F**). This coverage with fluorescent membranes is similar to our previous work with synthetic lipids⁶ as well as previously reported work investigating surface membrane functionalization of PLGA microparticles with lipid membranes.³⁴

To assess the stability of the microparticles, we subjected coated samples to lyophilization and incubation at 37 °C. Particles that had been lyophilized demonstrated similar levels of membrane coverage to pre and post lyophilization (compare **Figure 8.3**

to **Figure 8.4**). This confirms that the membrane coating is stable during freeze-drying and that the particles could be stably stored at room temperature for long periods of time as had been demonstrated with similar biomaterials for drug delivery.³⁵ Incubation of the particles revealed that all shapes coated with fluorescent red blood cell membranes were stable at 37 °C for 1 day and 7 days indicating that the particles could be therapeutically active on the time scale of progression of many diseases such as sepsis.³⁶

One important property of the RBC coated microparticles that was also assessed was the lateral membrane fluidity of the lipids coating the particles. We and other groups have previously shown that therapeutically relevant biomaterials coated with these membranes maintain this important biomimetic property.^{26,37} FRAP recovery curves demonstrate that this membrane fluidity remains intact for all particle samples that were coated with RBC derived membrane vesicles (**Figure 8.6A-C**). In addition, the membrane fluidity recovery curves were successfully fit to a single exponential recovery model. Using the model set forth by Kang et. al.²⁷ we found that the lateral diffusion coefficients for all particle samples tested was on the order of 10^{-10} cm²/s (**Figure 8.6D**). This estimated lateral diffusion constant was similar across all particle shapes tested. Furthermore, this lateral diffusion constant is within the range of diffusion constants for lipids in natural cell membranes³⁸ indicating successful biomimicry of this parameter on the surface of the polymeric particles. Such a characteristic would be important for many applications such as recapitulation of the immunological synapse on artificial antigen presenting cell technology.³⁹ Upon engagement of an antigen presenting cell with its target, there is a dynamic spatial rearrangement of signaling receptors on the cell surface.⁴⁰ This IS has been successfully recapitulated by supported lipid bilayers⁴¹ and it

has been found that membrane fluidity is an important parameter governing immune cell activation.

8.3.2 Characterization of RBC Coated Nanoparticles

Although a significant amount of work has been completed investigating microparticles as a potential platform for biomimetic membrane coating,⁴² nanoparticles offer distinct advantages for drug delivery, particularly from a pharmacokinetic standpoint. Nanoparticles typically have superior biodistribution compared to their microparticle counterparts⁴³ and this would theoretically translate to more effective drug delivery for the anisotropic RBC membrane coated nanoparticles. Therefore, we elected to apply the coating procedure to anisotropic PLGA nanoparticles. Upon coating of the particles with the RBC membrane, we imaged the samples under TEM to determine morphologically the structure of the coating on the surface of the particle (**Figure 8.7A-C**). We found that the particles were successfully deformed into non-spherical shapes as has been previously shown in our work and that the synthesized particles were approximately 220 nm in size.²⁴ However, we noticed that the nanoparticles had a halo around the surface of the particle that approximately matched the thickness of a cellular membrane at 10 nm.¹³ Comparing the images of coated nanoparticles to equivalent non-coated nanoparticles we found that the membrane halo was not present on the non-coated samples (**Figure 8.7D-F**). This is similar to the results reported which demonstrated the presence of a membrane halo around the surface of the particle upon RBC membrane coating.¹³

To further confirm the presence of an RBC membrane coat on the anisotropic nanoparticles we sized the spherical nanoparticles before and after coating by DLS

(**Figure 8.7G**). We noted that the coated nanoparticles exhibited an increase in size of approximately 20 nm, which is consistent with what would be expected for a ~10 nm membrane coat on both sides of the particle. We were also interested in confirming the presence of CD47 on the surface of the particle for assessment of functional potential. CD47 has recently been referred to as the “don’t eat me” signal on the surface of RBCs that allows them to escape elimination by macrophages in the RES.⁴⁴ Furthermore, synthetic CD47 based peptides have been found to enhance biodistribution of systemically administered biomaterials by inhibiting phagocytosis.⁴⁵ We stained the particles with a fluorescent antibody against CD47 and found that relative to uncoated controls, there was a 6-fold increase in CD47 antibody signal (**Figure 8.7H**). Taken together, this evidence indicates that we were successfully able to coat the spherical and non-spherical nanoparticles with biomimetic RBC derived membranes.

8.3.3 *In Vitro* Macrophage Uptake of Anisotropic RBC Coated Nanoparticles

An important characteristic of systemically administered biomaterials is the capability to avoid immediate clearance from the bloodstream and persist for longer periods of time in circulation. Typically this is achieved through a biocompatible material on the surface of the particle that can enable it to stealthily avoid the host’s immune system such as poly ethylene glycol.⁴⁶ It has also been shown that non-spherical particles can successfully evade elimination, contributing to longer circulation times and enhanced therapeutic efficacy.²⁴ We hypothesized based on these previous studies that the anisotropic shaped nanoparticle could synergize with the biomimetic RBC membrane coating to achieve a more favorable pharmacokinetic profile. As an *in vitro* model of RES clearance, we evaluated phagocytic uptake of the coated and uncoated nanoparticles

by murine macrophages (RAW 264.7). We evaluated nanoparticle uptake qualitatively by confocal microscopy and quantitatively by flow cytometry. We found that altering the nanoparticle shape and imparting a biomimetic RBC membrane surface to the particle both reduced cellular uptake by macrophages (**Figure 8.8A** compare magenta signal across different shapes and coatings). This apparent difference in cellular uptake was confirmed by flow cytometry analysis of macrophages that had been incubated with the particles. We found that the membrane coating resulted in a 30-50% reduction in cellular uptake compared to uncoated particles (**Figure 8.8B**). In addition, we found that there was an additional 30-40% reduction in cellular uptake attributed to the anisotropic shape of the nanoparticle. Combined, these two parameters resulted in a 50-60% reduction in cellular uptake of anisotropic coated nanoparticles, compared to isotropic uncoated nanoparticles. Furthermore, this trend of both parameters working together to achieve cell uptake reduction was apparent across multiple doses of particles tested with the macrophages. It has been previously found that both shape⁴⁷ and membrane coating¹⁵ can reduce cellular uptake individually, however we have shown in this experiment that the two can synergize to achieve a superior resistance to macrophage elimination that either characteristic can mediate on its own.

8.3.4 *In Vivo* Pharmacokinetic Analysis of RBC Coated Anisotropic Nanoparticles

Next, we wanted to evaluate *in vivo* the potential for more favorable biodistribution of anisotropic nanoparticles coated with a biomimetic RBC membrane. Following the *in vitro* finding of reduced non-specific cellular elimination of anisotropic coated particles, we expected that this result could translate *in vivo* and that both the non-

spherical shape and the biomimetic RBC membrane coating could contribute to enhancement of nanoparticle pharmacokinetics.

We synthesized particles of spherical, prolate ellipsoidal, and oblate ellipsoidal shape and encapsulated a hydrophobic near IR fluorophore in the core for fluorescence analysis of nanoparticles in the bloodstream. The particles, with or without a biomimetic RBC coat, were injected intravenously and blood was sampled 15 min, 30 min, 45 min, 2 hr, 4 hr, and 24 hr post particle administration to evaluate systemic nanoparticle concentration. We found that all particle concentrations decayed over time exponentially as expected (**Figure 8.9A**). However, we found that for all particle shapes, incorporation of the RBC membrane resulted in a slower exponential decay compared to respective uncoated controls (**Figure 8.9A** compare light colors to respective dark colors). We fit the experimental data to a single-phase exponential decay curve in order to derive systemic half-life information for the particle samples. We found that the half-life of the coated nanoparticles significantly exceeded that of the uncoated particles (**Figure 8.9B**). For example, the uncoated spherical nanoparticles had an average half-life of 24.6 min whereas the coated spherical nanoparticles had an average half-life of 64.8 min, a 163% increase. Furthermore, we noted that the prolate ellipsoidal shape resulted in a superior half-life compared to both the spherical and oblate ellipsoidal shapes with coated prolate ellipsoidal nanoparticles having a half-life of 171.6 min compared to 82.0 min for coated oblate ellipsoidal particles and 64.8 min for coated spherical particles. Taken together, this data suggests that combination of anisotropic prolate ellipsoidal shape and coating could result in a near 6-fold increase in half-life with both parameters synergizing. With respect to the oblate ellipsoidal particles, although *in vitro* results were favorable with

respect to resistance to cellular elimination, the *in vivo* effect was not as dramatic as expected. This could partially be attributed to the fact that prolate ellipsoidal particles are more hydrodynamically efficient than the spherical or oblate ellipsoidal particles. This effect has been demonstrated in a microfluidic system as of recently⁴⁸ and would be expected to be translated to the dynamic system of fluid flow in the bloodstream.

At 24 hr. post administration, we dissected out the major non-bowel organs (spleen, kidney, liver, lung, and heart) to analyze fluorescent content and determine the ultimate distribution of the particles following systemic administration. We found that the major centers of accumulation of the particles were the spleen and liver (**Figure 8.10**), as expected based of previous trials with particle distribution experiments.²⁴ Moreover, there was no noted statistical difference in the organ distribution at 24 hr post administration indicating that despite the apparent difference in particle half-life, there is no difference in the ultimate destination. This was also expected based on previous results using non-spherically shaped nanoparticles conjugated to targeting antibodies which showed minimal changes in the biodistribution for non-targeted particles.⁴⁸ Based on previous results demonstrating that it is possible to incorporate a targeting moiety into the naturally derived membrane²⁸, it would be possible to leverage the slower systemic elimination to target the nanoparticles to a desired site, such as a tumor for cancer drug delivery.

8.3.5 *In Vitro* and *In Vivo* Anisotropic Nanosponge Activity

Finally, we were interested in the potential enhancement of drug delivery that the combination of anisotropic shape and RBC mimetic coating could achieve. As a proof of principle we opted to use the RBC membrane itself as the drug to be delivered in a

bacterial alpha toxin absorption assay (**Figure 8.11A**). In this system, the membrane coated nanoparticles function as a decoy to absorb the hemolytic toxin from the systemic circulation before it can cause irreversible damage to the host's RBCs. This model had previously been used as a biomimetic nanosponge of spherical nanoparticles¹⁴ and we were interested to assess how the anisotropic particle shape could influence alpha toxin absorption capabilities.

In order to assess the impact of shape alone (without the complicating factor of *in vivo* pharmacokinetics) we utilized an *in vitro* model of alpha toxin absorption. Particles and toxin were coincubated for 30 min, and fresh RBCs were then added to determine the toxicity of the mixture by absorption based measurements of hemolysis. We found there was a significantly lower rate of hemolysis in the coated anisotropic particle samples compared to the spherical nanoparticles (85% for spherical particles compared to 20-30% for anisotropic particles) (**Figure 8.11B**). This could be partly due to the fact that during the stretching process, the particles attain a higher surface area to volume ratio.⁷ With greater surface area, there would be more available RBC membrane to serve as a decoy to absorb the alpha toxin. Therefore, there would be insufficient alpha toxin to mediate a large amount of hemolysis that could be detected *in vitro*.

Following these favorable *in vitro* results, and considering the enhanced pharmacokinetic profile of the anisotropic, coated nanoparticles compared to the spherical, coated nanoparticles, we were interested to evaluate the detoxification potential of the anisotropic nanoparticles *in vivo*. In order to accomplish this, we systemically administered a lethal dose of alpha toxin to mice. After a delay, we then administered coated nanoparticles of spherical, prolate ellipsoidal, or oblate ellipsoidal shape, as well

as an uncoated spherical particle control or no particle treatment ($n = 6$ mice/group). We then tracked survival over the course of 24 hours to determine detoxification capabilities of the nanoparticles. We found that the mice in the control group had a median survival of 2.75 hr and that there was no statistical improvement of the particles alone or the spherical coated particles (**Figure 8.11C**). However, there was a dramatic and statistically significant improvement in survival with administration of the anisotropic nanoparticles, both oblate and prolate ellipsoidal. In addition, approximately 50% of the prolate ellipsoidal treated and 33% of the oblate ellipsoidal treated mice were found to be healthy at the end of 1 week post particle administration. This result aligns with our *in vitro* test for alpha toxin absorption which could have potentially been enhanced by the reduced systemic elimination of the anisotropic, coated nanoparticles. Thus, the anisotropic RBC membrane coated nanoparticle has been validated as a potentially stronger treatment than equivalent spherical coated nanoparticles for detoxification of sepsis patients⁴⁹ and also useful for drug delivery in general.

8.4 Conclusions

In this study, we have successfully demonstrated the utility of biomimetic anisotropic nanoparticles coated with naturally derived RBC membranes. Through mimicry of both the shape and the surface membrane of blood cells, we have determined that combination of these two features achieves an enhancement of drug delivery efficacy that neither parameter can successfully attain on its own. The anisotropic nanoparticles coated with red blood cell membranes are able to superiorly evade elimination by macrophages compared to their spherical, uncoated counterparts. Furthermore, prolate ellipsoidal, coated nanoparticles exhibit reduced rates of systemic elimination upon

intravenous administration compared to other particle shapes tested in this study. Finally, the enhanced pharmacokinetic properties of the anisotropic, coated particle, in conjunction with the increased surface area due to anisotropic shape, resulted in a stronger capability to mediate detoxification of systemically administered bacterial toxin. These studies also revealed that changes to morphology can be a double-edged sword as the oblate, 2-D stretched particles had higher surface area good for clearing toxin, but inferior biodistribution properties compared to prolate, 1-D stretched particles. The prolate particles proved superior *in vivo* even though they were not clearly superior from *in vitro* testing, highlighting the importance of *in vivo* properties when designing particle shape. Further investigations into the utility of biointerfacing through biomimetic particle engineering will allow for the realization of next generation drug delivery vehicles and the implementation of novel, robust biomedical technologies in modern medicine.

8.5 Figures

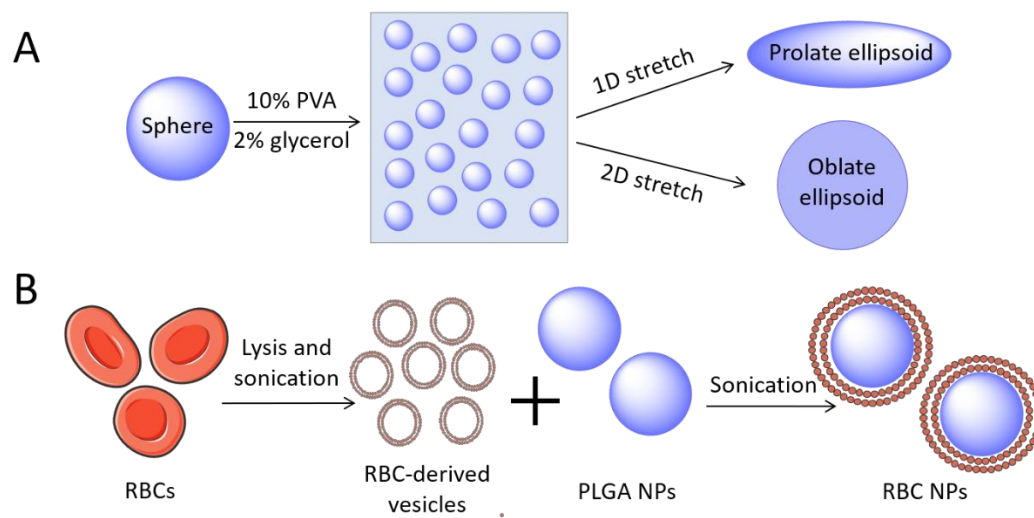


Figure 8.1: Schematic of the red blood cell coating procedure. (a) Particles were deformed into prolate and oblate ellipsoidal polymeric particles using the thin film stretching method. (b) Red blood cells were processed into 200 nm vesicles using hypotonic lysis and sonication based disruption of the RBC ghost membranes. The vesicles were then sonicated in the presence of the anisotropic particles to coat them with the RBC derived membranes.

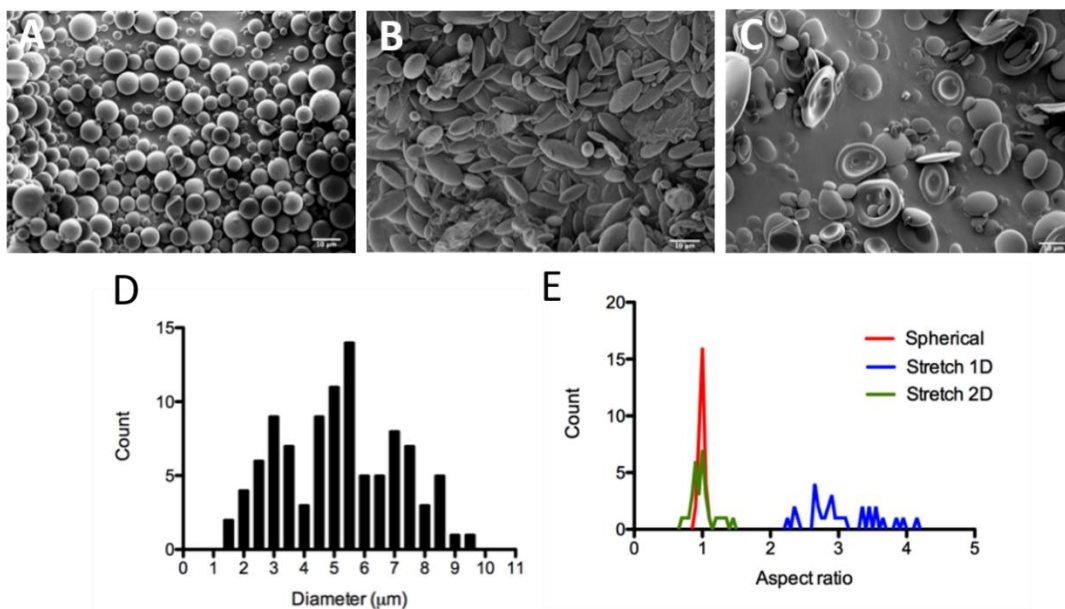


Figure 8.2: Physical characterization of the anisotropic microparticles. (a) Spherical, (b) prolate ellipsoidal, and (c) oblate ellipsoidal microparticles were imaged by SEM. Scale bars are 10 μm (d) The spherical particles were sized by ImageJ and the size distribution was determined. (e) Aspect ratio distribution was measured for each particle type using Image J.

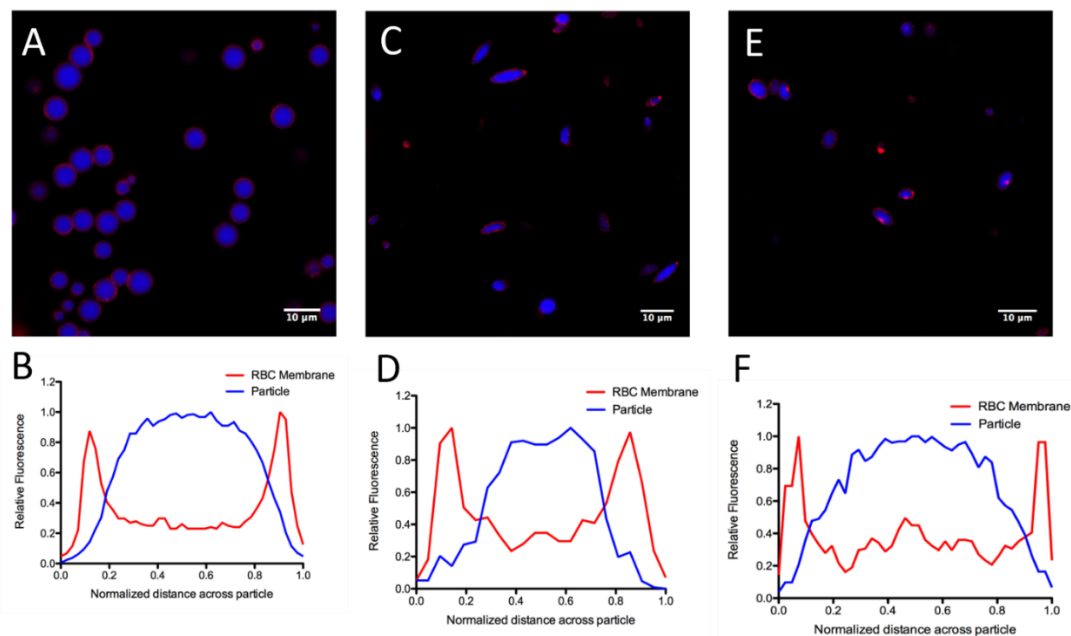


Figure 8.3: Confocal analysis of red blood cell membrane coated microparticles. (a) Spherical, (c) prolate ellipsoidal, (e) oblate ellipsoidal microparticles loaded with 7-AMC (blue) were coated with RBC membranes (red) and imaged under confocal to determine localization of the two signals. Linear fluorescent profile analysis through the center of the particle of (b) spherical, (d) prolate ellipsoidal, and (e) oblate ellipsoidal particles demonstrated localization of the RBC membrane signal on the exterior of the particle using the encapsulated 7-AMC dye as a reference point.

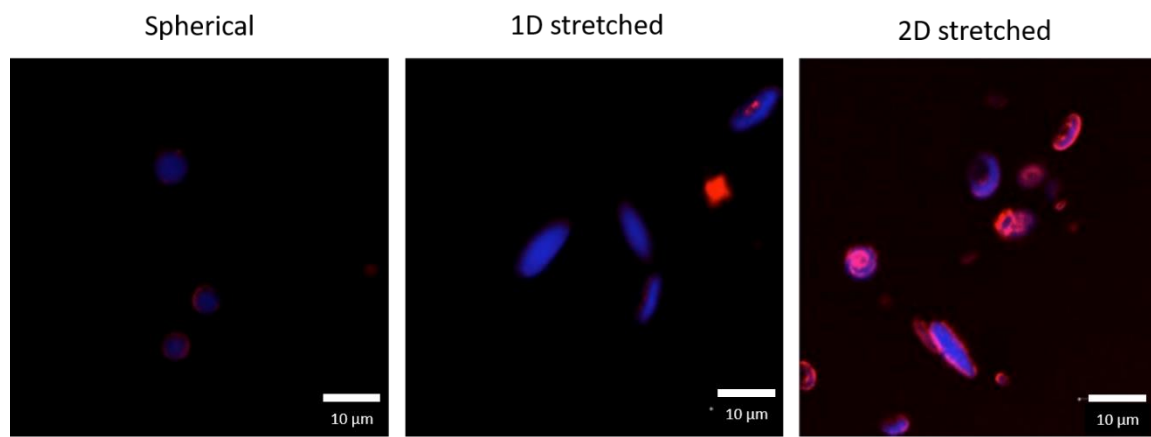


Figure 8.4: Stability of the particles after lyophilization. Particles samples from **Figure 8.3** were lyophilized in 10% endotoxin free sucrose. Following reconstitution, they were imaged using confocal microscopy. Membrane coatings were of similar quality to pre-lyophilized samples.

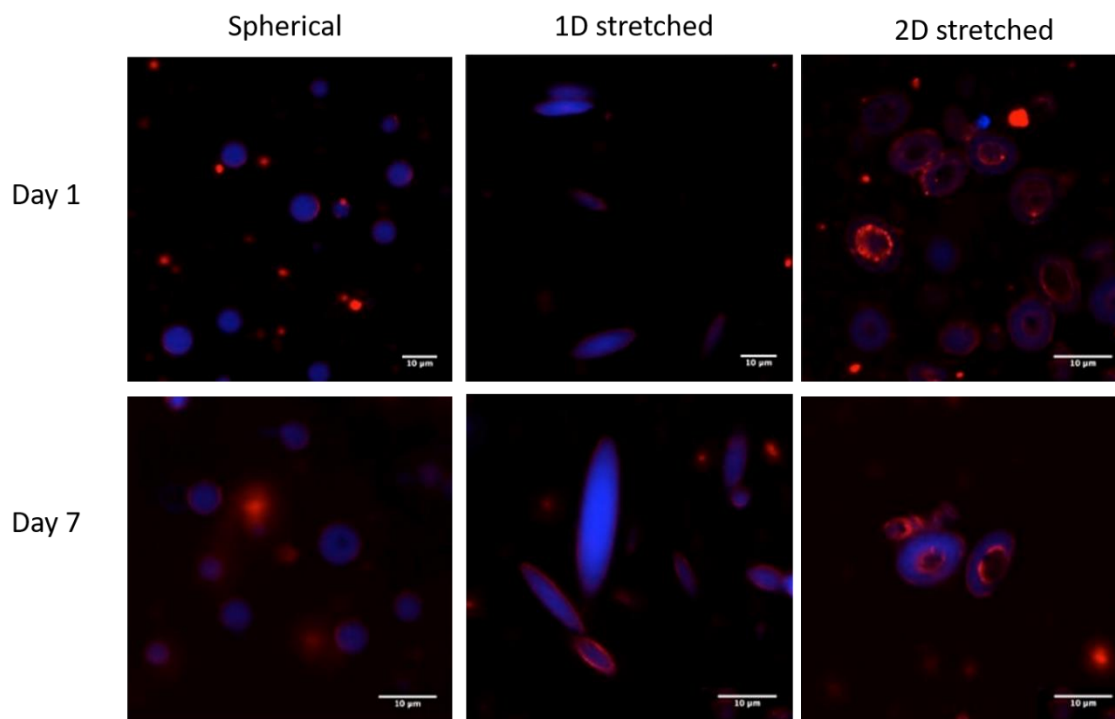


Figure 8.5: Non-spherical particles were coated as in **Figure 8.3** and then incubated at 37 °C for the indicated amount of time on the left of the image set. For the duration of the incubation for all particle types, the membrane coating remained stable on the surface.

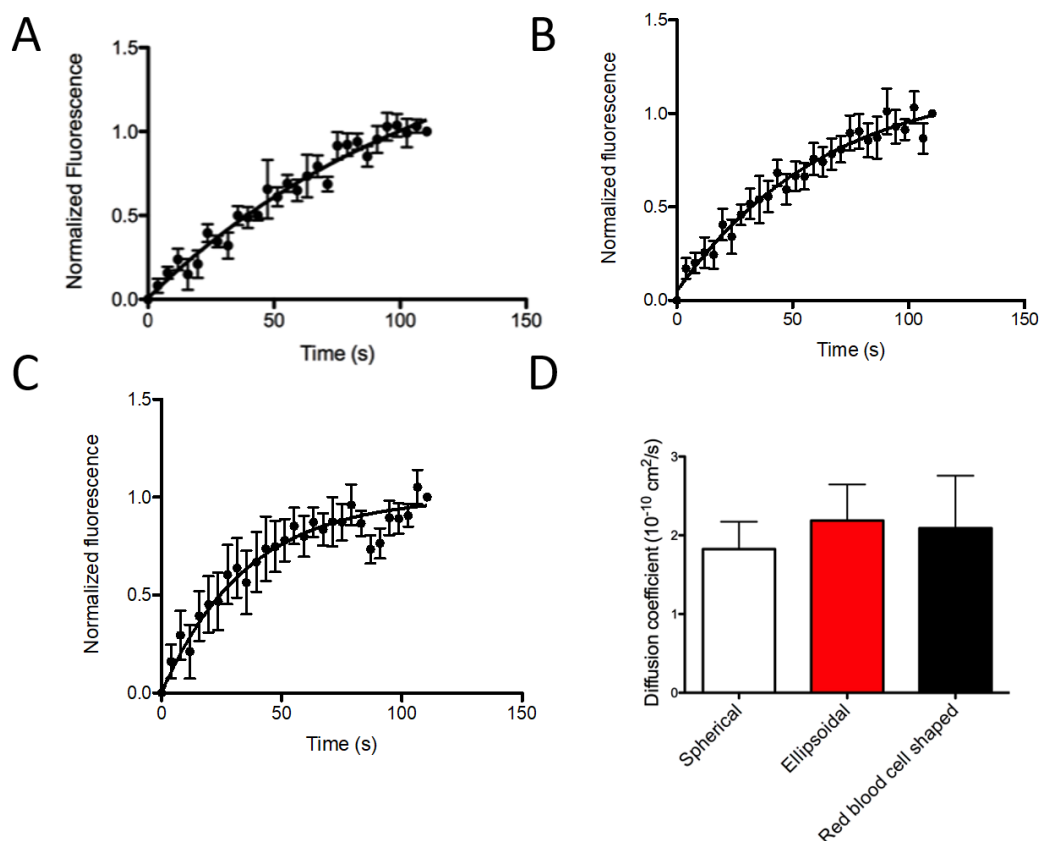


Figure 8.6: Determination of lateral rigidity of membrane coating by fluorescence recovery after photobleaching. (a) Spherical, (b) Prolate ellipsoidal, and (c) Oblate ellipsoidal microparticles were analyzed by FRAP for fluorescence recovery over time (dots) and fit to a one-exponential recovery model (lines). (d) From the FRAP recovery curves, lateral diffusion coefficients were derived and found to be on the order of lipid lateral diffusion coefficients in naturally derived membranes for all particle types. Error bars represent the SEM of 10 individual particle replicates.

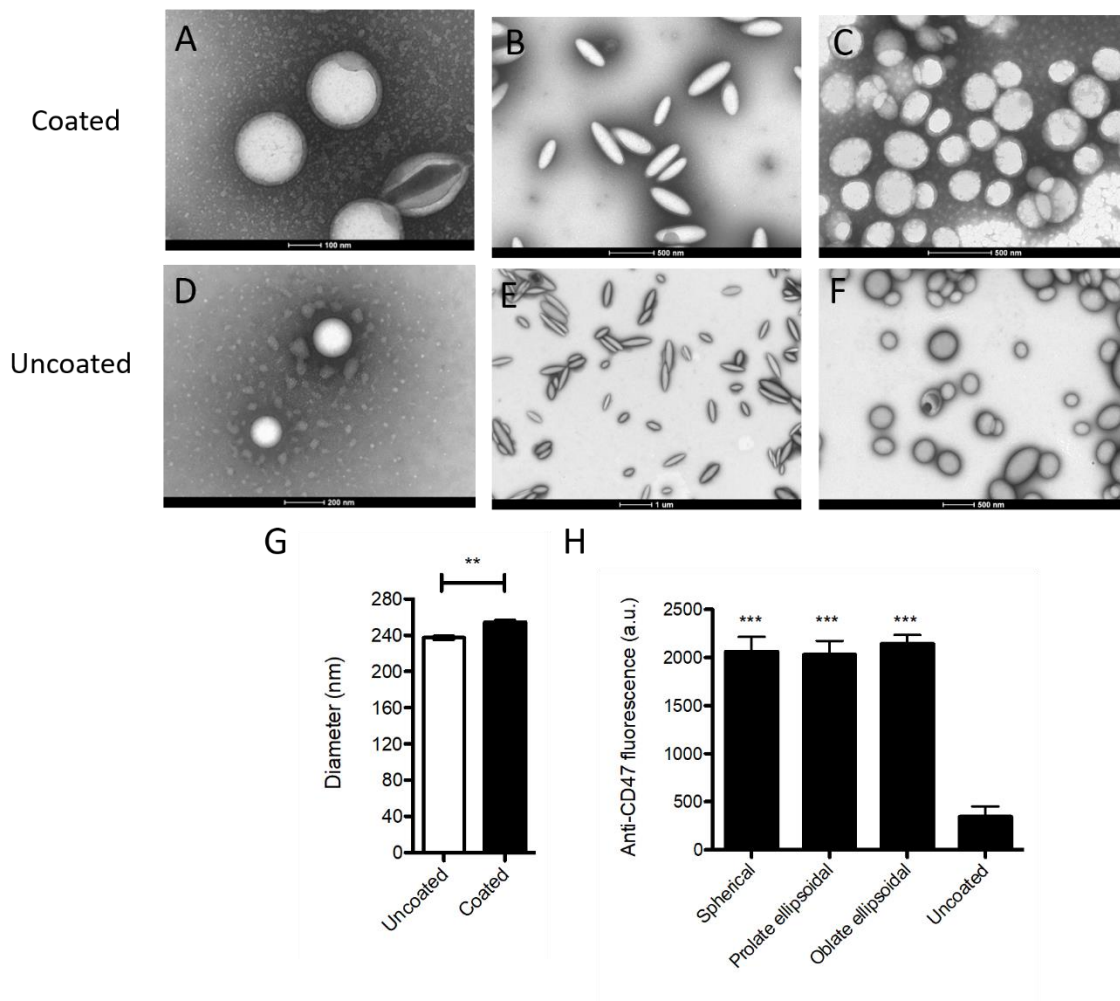


Figure 8.7: Physical and chemical characterization of RBC membrane coated anisotropic nanoparticles. TEM images of coated (a) spherical, (b) prolate ellipsoidal, (c) and oblate ellipsoidal nanoparticles reveal a 10 nm coating on the surface that is not present on the surface of the uncoated (d) spherical, (e) prolate ellipsoidal, and (f) oblate ellipsoidal nanoparticles. (g) DLS analysis of coated vs. uncoated nanoparticles indicates a slight increase in size of coated nanoparticles on the order of what would be expected for a membrane coating. (h) Fluorescent antibody stain for CD47 on the surface of RBC membrane coated particles demonstrates functional potential of the RBC coated nanoparticles. Error bars represent the SEM of 3 individual staining replicates.

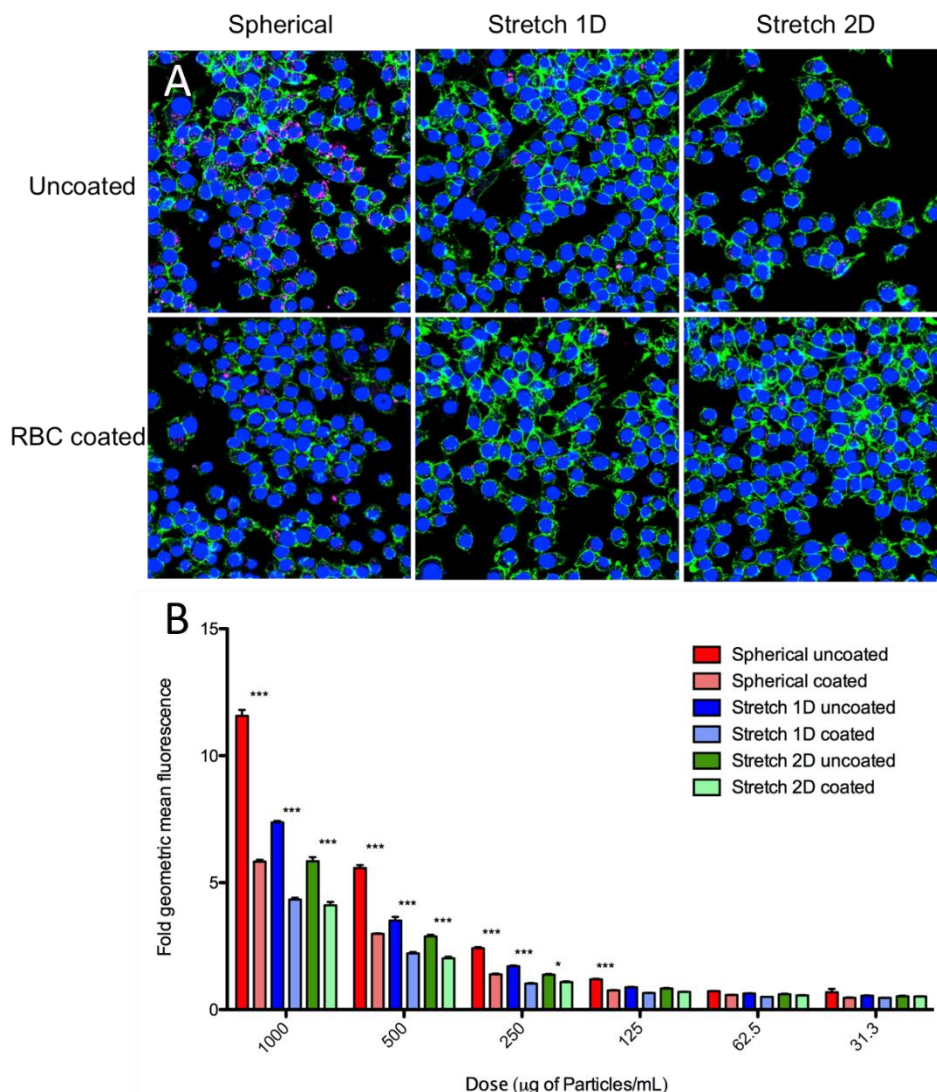


Figure 8.8: *In vitro* model of coated nanoparticle elimination by macrophages. Nanoparticles encapsulating DiD dye were incubated with macrophages for 4 hr. and uptake was analyzed by confocal microscopy (green = actin, blue = DAPI, magenta = particles) and flow cytometry. (a) Confocal images reveal that both the coating of the nanoparticles, and the deformed shape reduced nanoparticle uptake by macrophages as evidenced by reduced incidence of the magenta signal. (b) Flow cytometry analysis of cell fluorescence reveals quantitatively the reduction in nanoparticle uptake by macrophages. Error bars represent the SEM of three experimental replicates. (*= $p < 0.05$, ***= $p < 0.001$ by one way ANOVA with Tukey's post-test)

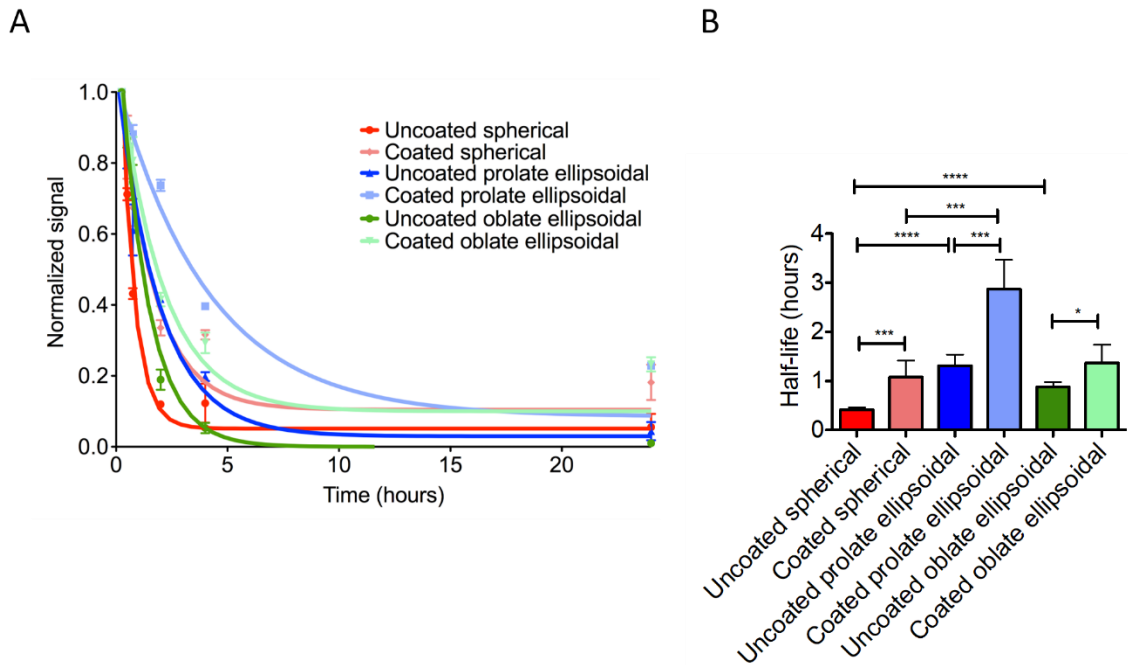


Figure 8.9: *In vivo* pharmacokinetics of red blood cell membrane coated nanoparticles. (a) Blood elimination of nanoparticles following intravenous administration as assessed by fluorescence readings of the blood sample (dots) and fit to a single exponential decay model (lines). (b) Particle bloodstream half-life was derived from the exponential fit of blood decay curves and found to be augmented in the presence of the particle coating as well as if the particle was deformed into a prolate ellipsoidal shape. Error bars represent the SEM of 3 individual mouse replicates. (*= $p < 0.05$, ***= $p < 0.001$ by one-way ANOVA with Tukey's post-test).

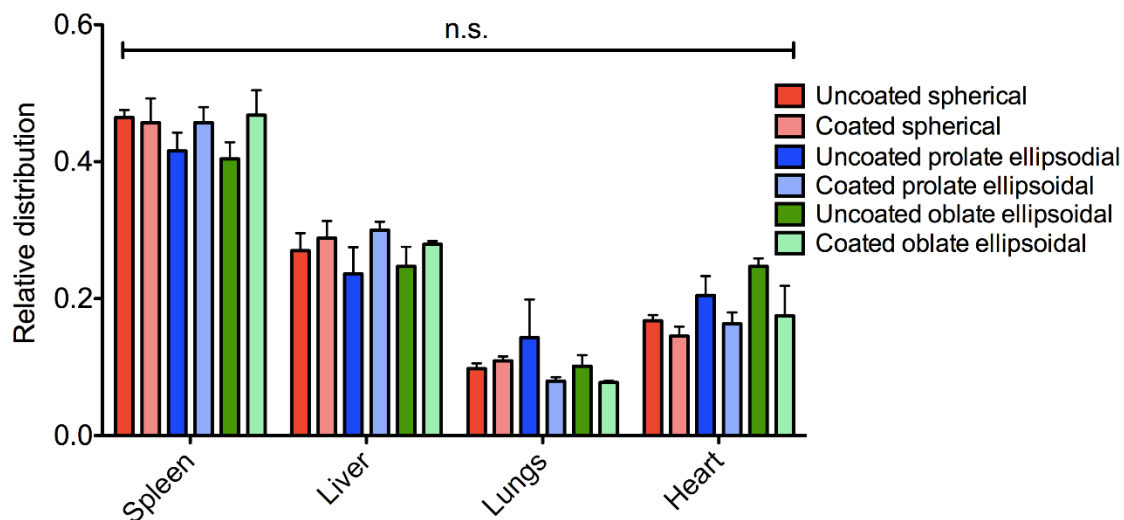


Figure 8.10: Organ distribution at 24 hr. of RBC coated anisotropic nanoparticles is similar across the different shapes with no significant statistical comparisons by one-way ANOVA with Tukey's post-test.

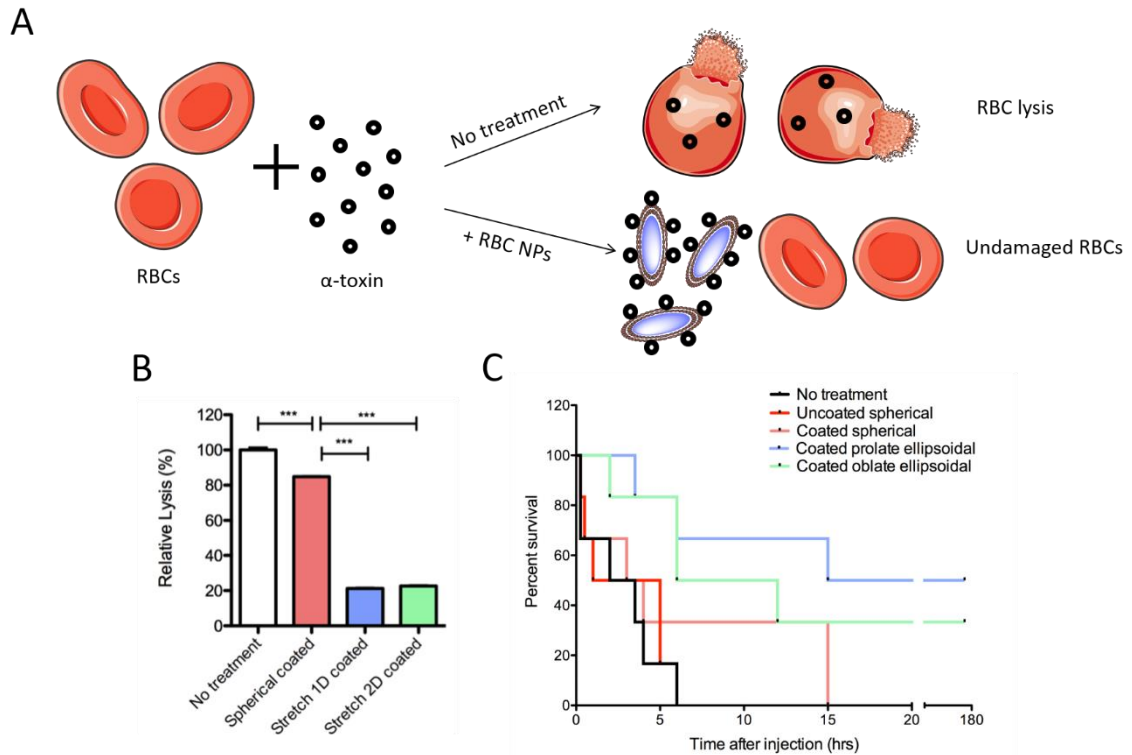


Figure 8.11: *In vivo* anisotropic biomimetic toxin nanosponge absorption capabilities. (a) Schematic of the principle of nanosponge principle. With no treatment, RBCs would absorb the lytic toxin and be detrimental to the host. With the administration of RBC coated nanoparticles, the particles would serve as a decoy, absorbing the toxin and leaving the RBCs unharmed. (b) *In vitro* evaluation of hemolytic toxin absorption by the anisotropic nanosponge. The anisotropic nanosponges were able to absorb significantly more alpha toxin as evidenced by reduction in relative lysis. Error bars represent the SEM of 3 experimental replicates. (***)= $p < 0.001$ by one-way ANOVA with Tukey's post-test) (c) Survival following intravenous alpha toxin administration followed by nanosponge administration. Mice receiving anisotropic nanosponges had a significant long-term survival benefit compared to spherical nanosponges or uncoated particles ($n = 5$).

8.6 References

1. Yoo, J.-W., Irvine, D.J., Discher, D.E. Mitragotri, S. Bio-inspired, bioengineered and biomimetic drug delivery carriers. *Nat. Rev. Drug Discov.* 2011;10(7):521.
2. Balmert, S.C. Little, S.R. Biomimetic Delivery with Micro-and Nanoparticles. *Adv. Mater.* 2012;24(28):3757-78.
3. Torres-Rendon, J.G., Femmer, T., De Laporte, L., Tigges, T., Rahimi, K., Gremse, F., Zafarnia, S., Lederle, W., Ifuku, S. Wessling, M. Bioactive gyroid scaffolds formed by sacrificial templating of nanocellulose and nanochitin hydrogels as instructive platforms for biomimetic tissue engineering. *Adv. Mater.* 2015;27(19):2989-95.
4. Sunshine, J.C. Green, J.J. Nanoengineering approaches to the design of artificial antigen-presenting cells. *Nanomedicine: NBM* 2013;8(7):1173-89.
5. Merkel, T.J., Chen, K., Jones, S.W., Pandya, A.A., Tian, S., Napier, M.E., Zamboni, W.E. DeSimone, J.M. The effect of particle size on the biodistribution of low-modulus hydrogel PRINT particles. *J. Control. Rel.* 2012;162(1):37-44.
6. Meyer, R.A., Mathew, M.P., Ben-Akiva, E., Sunshine, J.C., Shmueli, R.B., Ren, Q., Yarema, K.J. Green, J.J. Anisotropic biodegradable lipid coated particles for spatially dynamic protein presentation. *Acta Biomater.* 2018;72:228-38.
7. Sunshine, J.C., Perica, K., Schneck, J.P. Green, J.J. Particle shape dependence of CD8+ T cell activation by artificial antigen presenting cells. *Biomaterials* 2014;35(1):269-77.
8. Stuart, M.A.C., Huck, W.T., Genzer, J., Müller, M., Ober, C., Stamm, M., Sukhorukov, G.B., Szleifer, I., Tsukruk, V.V. Urban, M. Emerging applications of stimuli-responsive polymer materials. *Nat. Mater.* 2010;9(2):101.
9. Nicolson, G.L. The Fluid—Mosaic Model of Membrane Structure: Still relevant to understanding the structure, function and dynamics of biological membranes after more than 40years. *BBA-Biomembranes* 2014;1838(6):1451-66.
10. Fletcher, D.A. Mullins, R.D. Cell mechanics and the cytoskeleton. *Nature* 2010;463(7280):485.
11. Lashof-Sullivan, M.M., Shoffstall, E., Atkins, K.T., Keane, N., Bir, C., VandeVord, P. Lavik, E.B. Intravenously administered nanoparticles increase survival following blast trauma. *Proc. Natl. Acad. Sci. U. S. A.* 2014;111(28):10293-8.
12. Doshi, N., Zahr, A.S., Bhaskar, S., Lahann, J. Mitragotri, S. Red blood cell-mimicking synthetic biomaterial particles. *Proc. Natl. Acad. Sci. U. S. A.* 2009;106(51):21495-9.
13. Hu, C.-M.J., Zhang, L., Aryal, S., Cheung, C., Fang, R.H. Zhang, L. Erythrocyte membrane-camouflaged polymeric nanoparticles as a biomimetic delivery platform. *Proc. Natl. Acad. Sci. U. S. A.* 2011;108(27):10980-5.
14. Hu, C.-M.J., Fang, R.H., Copp, J., Luk, B.T. Zhang, L. A biomimetic nanosponge that absorbs pore-forming toxins. *Nat. Nanotechnol.* 2013;8(5):336.
15. Hu, C.-M.J., Fang, R.H., Wang, K.-C., Luk, B.T., Thamphiwatana, S., Dehaini, D., Nguyen, P., Angsantikul, P., Wen, C.H. Kroll, A.V. Nanoparticle biointerfacing by platelet membrane cloaking. *Nature* 2015;526(7571):118.
16. Parodi, A., Quattrocchi, N., Van De Ven, A.L., Chiappini, C., Evangelopoulos, M., Martinez, J.O., Brown, B.S., Khaled, S.Z., Yazdi, I.K. Enzo, M.V. Synthetic

- nanoparticles functionalized with biomimetic leukocyte membranes possess cell-like functions. *Nat. Nanotechnol.* 2013;8(1):61.
17. Fang, R.H., Hu, C.-M.J., Luk, B.T., Gao, W., Copp, J.A., Tai, Y., O'Connor, D.E. Zhang, L. Cancer cell membrane-coated nanoparticles for anticancer vaccination and drug delivery. *Nano Lett.* 2014;14(4):2181-8.
 18. Kaneti, L., Bronshtein, T., Malkah Dayan, N., Kovregina, I., Letko Khait, N., Lupu-Haber, Y., Fliman, M., Schoen, B.W., Kaneti, G. Machluf, M. Nanoghosts as a novel natural nonviral gene delivery platform safely targeting multiple cancers. *Nano Lett.* 2016;16(3):1574-82.
 19. Toy, R., Peiris, P.M., Ghaghada, K.B. Karathanasis, E. Shaping cancer nanomedicine: the effect of particle shape on the in vivo journey of nanoparticles. *Nanomedicine: NBM* 2014;9(1):121-34.
 20. Champion, J.A. Mitragotri, S. Role of target geometry in phagocytosis. *Proc. Natl. Acad. Sci. U. S. A.* 2006;103(13):4930-4.
 21. Barua, S., Yoo, J.-W., Kolhar, P., Wakankar, A., Gokarn, Y.R. Mitragotri, S. Particle shape enhances specificity of antibody-displaying nanoparticles. *Proc. Natl. Acad. Sci. U. S. A.* 2013;110(9):3270-5.
 22. Meyer, R.A. Green, J.J. Shaping the future of nanomedicine: anisotropy in polymeric nanoparticle design. *WIREs: Nanomed. Nanobiotechnol.* 2016;8(2):191-207.
 23. Kosmides, A., Meyer, R., Hickey, J., Aje, K., Cheung, K., Green, J. Schneck, J. Biomimetic biodegradable artificial antigen presenting cells synergize with PD-1 blockade to treat melanoma. *Biomaterials* 2017;118:16-26.
 24. Meyer, R.A., Sunshine, J.C., Perica, K., Kosmides, A.K., Aje, K., Schneck, J.P. Green, J.J. Biodegradable nanoellipsoidal artificial antigen presenting cells for antigen specific T-cell activation. *Small* 2015;11(13):1519-25.
 25. Champion, J.A., Katare, Y.K. Mitragotri, S. Making polymeric micro-and nanoparticles of complex shapes. *Proc. Natl. Acad. Sci.* 2007;104(29):11901-4.
 26. Meyer, R.A., Meyer, R.S. Green, J.J. An automated multidimensional thin film stretching device for the generation of anisotropic polymeric micro-and nanoparticles. *J. Biomed. Mater. Res. A* 2015;103(8):2747-57.
 27. Kang, M., Day, C.A., Kenworthy, A.K. DiBenedetto, E. Simplified equation to extract diffusion coefficients from confocal FRAP data. *Traffic* 2012;13(12):1589-600.
 28. Hu, C.M.J., Fang, R.H. Zhang, L. Erythrocyte-Inspired Delivery Systems. *Adv. Healthc. Mater.* 2012;1(5):537-47.
 29. Florez, L., Herrmann, C., Cramer, J.M., Hauser, C.P., Koynov, K., Landfester, K., Crespy, D. Mailänder, V. How shape influences uptake: interactions of anisotropic polymer nanoparticles and human mesenchymal stem cells. *Small* 2012;8(14):2222-30.
 30. Dasgupta, S., Auth, T. Gompper, G. Shape and orientation matter for the cellular uptake of nonspherical particles. *Nano Lett.* 2014;14(2):687-93.
 31. Jiang, X., Leong, D., Ren, Y., Li, Z., Torbenson, M.S. Mao, H.-Q. String-like micellar nanoparticles formed by complexation of PEG-b-PPA and plasmid DNA and their transfection efficiency. *Pharm. Res.* 2011;28(6):1317-27.

32. Jiang, X., Qu, W., Pan, D., Ren, Y., Williford, J.M., Cui, H., Luijten, E. Mao, H.Q. Plasmid-templated shape control of condensed DNA–block copolymer nanoparticles. *Adv. Mater.* 2013;25(2):227-32.
33. Geng, Y., Dalhaimer, P., Cai, S., Tsai, R., Tewari, M., Minko, T. Discher, D.E. Shape effects of filaments versus spherical particles in flow and drug delivery. *Nat. Nanotechnol.* 2007;2(4):249.
34. Bershteyn, A., Chaparro, J., Yau, R., Kim, M., Reinherz, E., Ferreira-Moita, L. Irvine, D.J. Polymer-supported lipid shells, onions, and flowers. *Soft Matter* 2008;4(9):1787-91.
35. Tzeng, S.Y., Guerrero-Cázares, H., Martinez, E.E., Sunshine, J.C., Quiñones-Hinojosa, A. Green, J.J. Non-viral gene delivery nanoparticles based on poly (β -amino esters) for treatment of glioblastoma. *Biomaterials* 2011;32(23):5402-10.
36. Alberti, C., Brun-Buisson, C., Chevret, S., Antonelli, M., Goodman, S.V., Martin, C., Moreno, R., Ochagavia, A.R., Palazzo, M. Werdan, K. Systemic inflammatory response and progression to severe sepsis in critically ill infected patients. *Am. J. Resp. Crit. Care* 2005;171(5):461-8.
37. Cheung, A.S., Zhang, D.K., Koshy, S.T. Mooney, D.J. Scaffolds that mimic antigen-presenting cells enable ex vivo expansion of primary T cells. *Nat. Biotechnol.* 2018;
38. Lenaz, G. Lipid fluidity and membrane protein dynamics. *Bioscience Rep.* 1987;7(11):823-37.
39. Meyer, R.A. Green, J.J. Artificial Antigen-Presenting Cells: Biomimetic Strategies for Directing the Immune Response. in *Biomaterials in Regenerative Medicine and the Immune System* 257-77 (Springer, 2015).
40. Alarcón, B., Mestre, D. Martínez-Martín, N. The immunological synapse: a cause or consequence of T-cell receptor triggering? *Immunology* 2011;133(4):420-5.
41. Hsu, C.-J., Hsieh, W.-T., Waldman, A., Clarke, F., Huseby, E.S., Burkhardt, J.K. Baumgart, T. Ligand mobility modulates immunological synapse formation and T cell activation. *PloS One* 2012;7(2):e32398.
42. Ashley, C.E., Carnes, E.C., Phillips, G.K., Padilla, D., Durfee, P.N., Brown, P.A., Hanna, T.N., Liu, J., Phillips, B. Carter, M.B. The targeted delivery of multicomponent cargos to cancer cells by nanoporous particle-supported lipid bilayers. *Nat. Mater.* 2011;10(5):389.
43. Perica, K., Medero, A.D.L., Durai, M., Chiu, Y.L., Bieler, J.G., Sibener, L., Niemöller, M., Assenmacher, M., Richter, A. Edidin, M. Nanoscale artificial antigen presenting cells for T cell immunotherapy. *Nanomedicine: NBM* 2014;10(1):119-29.
44. McCracken, M.N., Cha, A.C. Weissman, I.L. Molecular pathways: activating T cells after cancer cell phagocytosis from blockade of CD47 “Don't Eat Me” signals. *Clin. Cancer Res.* 2015;21(16):3597-601.
45. Rodriguez, P.L., Harada, T., Christian, D.A., Pantano, D.A., Tsai, R.K. Discher, D.E. Minimal "self" peptides that inhibit phagocytic clearance and enhance delivery of nanoparticles. *Science* 2013;339(6122):971-5.
46. Butcher, N.J., Mortimer, G.M. Minchin, R.F. Drug delivery: unravelling the stealth effect. *Nature Nanotechnol.* 2016;11(4):310.

47. Sharma, G., Valenta, D.T., Altman, Y., Harvey, S., Xie, H., Mitragotri, S. Smith, J.W. Polymer particle shape independently influences binding and internalization by macrophages. *J. Control. Release* 2010;147(3):408-12.
48. Kolhar, P., Anselmo, A.C., Gupta, V., Pant, K., Prabhakarandian, B., Ruoslahti, E. Mitragotri, S. Using shape effects to target antibody-coated nanoparticles to lung and brain endothelium. *Proc. Natl. Acad. Sci. U. S. A.* 2013;110(26):10753-8.
49. Appen, K., Weber, C., Losert, U., Schima, H., Gurland, H.J. Falkenhagen, D. Microspheres based detoxification system: a new method in convective blood purification. *Artif. Organs* 1996;20(6):420-5.

Chapter 9: Entanglement-Based Thermoplastic Shape Memory

Particles with Photothermal Actuation for Biomedical Applications

9.1 Introduction

Entropy elasticity has been widely applied to empower polymers with shape-memory functionality for various applications such as actuators, sensors and biomedical devices.¹⁻³ Shape memory polymers (SMPs) can exhibit an entropy-driven shape memory effect (SME) through recovering from a temporary, deformed shape at a low entropy state to a permanent, equilibrium shape at an entropically more favorable state by an external stimulus.⁴ The application of SMPs for therapeutic purposes, however, has been dampened by the lack of controllability of SME under restrictive clinical requirements. Most SMPs can be thermally induced to undergo SME through an external application of heat or other actuation methods such as light, microwave or magnetic field.⁵⁻⁷ Generally these materials are deformed under a mechanical stress and then triggered to revert back to their original form through bulk heating past the transition temperature (T_t) of the material.⁸ Clinical hyperthermia treatments are performed at a maximum of 45 °C for less than 30 min to prevent thermal injury and significant cell death.⁹ Maintaining SMP shapes at 37 °C but only triggering SME at a narrow temperature range ($37\text{ °C} < T < 45\text{ °C}$) with a proper speed for clinical applications has been extremely challenging. Although SMPs with transition temperatures near body temperature have been reported, no systems presented controllability under clinical

This chapter contains material modified from the following article previously published as:
Guo Q, Bishop CJ, Meyer RA, Wilson DR, Olasov L, Schlesinger DE, Mather PT, Spicer JB, Elisseeff JH, Green JJ. Entanglement-based thermoplastic shape memory polymeric particles with photothermal actuation for biomedical application. *ACS Applied Materials and Interfaces*. 2018;10(16):13333-41.

hyperthermia conditions at a suitable speed.¹⁰⁻¹⁴ As a result, the development of an SMP platform with a T_t in the optimal biocompatible range and the ability to be rapidly controlled in shapes is highly desirable to analyze the potential application of SME in biomedical therapeutics.

The development of shape memory polymeric systems down to micron/submicron scales had been challenging until a film-stretching method recently enabled the facile programming of shape-memory functionality at such small scales.¹⁵⁻²⁰ Most often SMPs of small sizes require either chemical crosslinks²¹ or an additional set of polymer domains serving as physical netpoints²² that determine the permanent shape of the material. Polymer entanglements, a universal property of polymers with sufficient molecular weight, can also act as efficient physical netpoints.^{5,23} On the macroscale, entanglement-based shape memory has been well-recognized and used industrially to produce shrink films. The use of polymer entanglements can potentially open a door for a broader selection of thermoplastic polymers in shape memory systems for a variety of applications such as biomedical applications with restrictive requirements in chemistry or materials modification.²⁴ Yet no study to date has successfully implemented such a strategy in miniature shape memory systems probably due to processing and handling difficulties.

One therapeutic application that could benefit from small-scale SMPs is the use of micro- and nanoparticles for drug delivery. Recently, there has been great interest in the use of non-spherical micro-/nanoparticles for drug delivery applications.^{25,26} This is due to two beneficial properties exhibited by non-spherical shaped compared to spherical shaped particles. The first is reduced non-specific cellular uptake. This has been found

to be linked to the interaction of the particle with the cell membrane, namely the angle of approach.¹⁵ It has been repeatedly demonstrated that non-spherical ellipsoidal micro- and nanoparticles can avoid cellular uptake and phagocytosis compared to their spherical counterparts.^{16,27} The second advantageous property is the feature of increased targeted binding. This is mediated by the increased surface area and radius of curvature available for interaction with biological surfaces.²⁸ This feature was exploited to direct the targeted accumulation of nanoparticles in the lung and brain endothelium compared to spherical particles.¹⁸ Furthermore, it has been found that the increased targeted binding of non-spherical artificial antigen presenting cells to T-Cells enhances the activity of the particles for immunomodulation.²⁹ Reversion of an ellipsoidal to a spherical microparticle has been shown to increase the phagocytic rate by macrophages, but this particular material took hours to undergo a surface-tension driven shape switch instead of entropy-driven shape memory response with controls in the shapes at specific temperatures.¹⁷

There is a need for new biomedical systems that can exhibit externally triggered changes to their physical and biological properties in a spatiotemporally controlled manner. One strategy to enable spatiotemporal control over SME is through the use of a photothermal converter such as gold nanoparticles (AuNPs).³⁰ AuNPs have been utilized in a wide variety of applications including image contrast,³¹ gene therapy (for co-delivery of DNA/siRNA³² and to assert control over expression kinetics³³), and photothermal treatment of tumors.³⁴ Typically, the photothermal heating process happens when free electrons of AuNPs are photo-excited via surface plasmon resonance and release their energy first through electron-phonon interactions to the gold lattice inside the AuNPs and

then through phonon-phonon interactions to the surrounding medium.³⁵⁻³⁷ Zhao et al.^{30,37,38} and other groups^{22,39,40} have recently reported that, although gold does not exhibit SME, it could be distributed in colloidal form throughout an SMP for photothermal conversion, to couple the spatiotemporally precise application of laser energy to trigger SME. Nevertheless, it was unclear if such a AuNP-based photothermal trigger could be applied to SMP in small scales.

In this study, we hypothesized that the AuNPs embedded in shape memory particles could be plasmonically heated under continuous wave laser irradiation and then transfer their thermal energy to their surrounding PDLLA matrix, which could subsequently result in a shape memory response of the particles when the temperature of the PDLLA matrix increased beyond T_t . The main objective of this study was to develop a micron-scale biocompatible shape memory system with both an optimal T_t within the human body-tolerable temperature range and a spatiotemporally controlled trigger for induction of SME for biomedical applications.

9.2 Materials and Methods

9.2.1 Hydrophobic Gold Nanoparticle Synthesis

A modified version of Chatterjee et al.⁹ was used to synthesize hydrophobic gold nanoparticles. More specifically, lyophilized 1,2-dioleoyl-sn-glycero-3-phosphocholine (Avanti Polar Lipids; DOPC) was reconstituted at 25 mg/mL in chloroform and mixed with toluene, forming a 250 μ g/mL solution (33 mL) which was vortexed for about 10 seconds. 5 mL of this solution put into 6 different 20 mL scintillation vials (underlying metal cap insert was extracted and discarded out of each cap to not reduce Au^{3+}). Tetrachloroauric acid trihydrate (HAuCl_4) was reconstituted in ultrapure distilled water to

100 mg/mL and served as a stock. 250 μ L of the stock HAuCl₄ solution was mixed with 24.75 mL of ultra-pure distilled water forming a 1 mg/mL solution of HAuCl₄. 2 mL of this 1 mg/mL solution was added to each of the 6 20 mL scintillation vials already containing 5 mL of the 250 μ g/mL DOPC solution in toluene. Each vial also contained a VWR magnetic stir bar. Prior to placing the scintillation vials on a multi-position stir plate, each vial was vortexed to produce a non-transparent, and to the extent possible, a homogenous mixture of the aqueous and organic phases prior to adding 1 mL of sodium citrate tribasic dihydrate at 10 mg/mL drop-wise. The stirring was continued for approximately 18 hours. Once completed, the organic and aqueous phases were allowed to sufficiently separate over a few minutes and the organic toluene phases were extracted, mixed, and placed into a new scintillation vial. All aqueous solvent was again taken out of the organic phase if phase separation occurred.

To encapsulate the lipid-coated gold nanoparticles into the PDLLA microparticles, the gold nanoparticles (1 mL of gold nanoparticles in toluene in 1.5 mL tubes; total of 5 mL) were centrifuged at 16,000g. All but the pellets were aspirated (975 μ L) and replaced with an equal volume of dichloromethane (DCM). The gold nanoparticles were sonicated (Misonix) to become a homogenous mixture in the DCM. The 5 mL of gold nanoparticles in DCM were used directly in the single-emulsion encapsulation during PDLLA microparticle formation.

9.2.2 PDLLA Anisotropic Microparticle Synthesis and Characterization

PDLLA with ester endcap (M_n = 70.2 kDa, PDI = 1.95) was purchased from PolySciTech (Akina Inc.). A larger molecular weight polydispersity is helpful to better entangle polymer chains and contribute to the shape memory effect. Two solutions of

polyvinyl alcohol were made (PVA1 = 1% PVA; PVA0.5 = 0.5% PVA) in deionized MilliQ water. 200 mL of PVA0.5 was dispensed into a beaker with a VWR stir bar (spinning at 450 RPM). 100 mg of PDLLA was dissolved in 5 mL of DCM containing gold nanoparticles and poured into 50 mL of PVA1 while being homogenized (5000 rpm). For fluorescent visualization of the particles, 1 mg of Nile Red or 7-amino-4-methyl coumarin was added to the DCM mixture. The microparticle solution encapsulating gold nanoparticles was poured into the stirring PVA0.5 and stirred for an additional 4 hours to evaporate the organic solvent. Subsequently, we washed the microparticles 3x by centrifugation at 4 °C (3000 g; 5 minutes) to remove PVA. After the 3rd wash, the microparticles were resuspended in 1 mL of deionized water, triturated to avoid clumping, snap frozen in liquid nitrogen, lyophilized, and then stored dry at 4 °C or below until further use.

The particles were deformed into anisotropic shapes by an automated thin film stretching procedure as described in Meyer et. al.²⁰ Briefly, the particles were lyophilized, suspended in a solution containing 10% w/w PVA and 2% w/w glycerol, and then cast into a PVA film. The film was allowed to dry overnight and mounted on customized aluminum blocks. After 10 min of heating at a predetermined temperature, the film was loaded for 1-D stretching with stepper motors set at a strain rate of 0.2 min⁻¹. The stretched film was immediately cooled at room temperature for one hour, cut from the grips, and dissolved in water. The resulting particle suspension was then washed 3 times and lyophilized prior to use.

To characterize the microparticle size and shape, scanning electron microscopy was utilized. Lyophilized particle samples were spread onto carbon tape mounted to

aluminum tacks. The particles were then sputter coated with 30 nm of a gold-chromium alloy and imaged with a LeoFESEM. Size was determined by ImageJ analysis of the resulting SEM micrographs. Aspect ratio throughout all of the studies was determined through analysis of the particles and taking the ratio of the longer axis to the shorter axis. For the fluorescent particle image analysis, confocal imaging was completed using a Zeiss 780 FCS confocal microscope.

Differential scanning calorimetry (DSC) was carried out using a DSC 8000 (Perkin Elmer, Waltham, MA) to determine the glass transition of PDLLA particles. The particles incubated in water was sealed in an aluminum pan. The DSC tests were performed by heating-cooling-heating between 10 °C and 90 °C at 10 °C/min. The second heating trace was analyzed by Pyris Series software (Perkin Elmer) to determine the glass transition temperature and glass transition breadth.

Polarized light optical microscopy (POM) was utilized to monitor polymer alignment in stretched microparticles. POM studies were performed in an Olympus BX51 microscope equipped with 90° crossed polarizers, a HCS402 hot stage (Instec Inc.) and a CCD camera (QImaging). Images were acquired using QCapture Pro software (QImaging) at various angles of the sample stage (i.e. 0°, 45°, 90°, 135°, 180°, 225°, 270° and 315°). Shape recovery of 65 °C stretched microparticles was monitored in the hot stage set at 45 °C.

9.2.3 Characterization of Gold Nanoparticles in PDLLA Microparticles

In order to quantify the number of AuNPs within the microparticles, a standard curve was created; the AuNPs' stock concentration was assessed using Beer-Lambert's law⁴¹ using an extinction coefficient of $3.189 \times 10^{10} \text{ M}^{-1}\text{cm}^{-1}$. A standard curve was

created using various dilutions of the AuNPs in toluene (1 mL) with 5 mg of pure PDLLA microparticles solvated in 400 μ L of dimethyl sulfoxide (DMSO); 1 μ L of the total volume of 1400 μ L was used to assess the absorbance via NanoDrop (Thermo Scientific). When quantifying how many AuNPs there were per mg of particle, 5 mg of 4 unknown samples were solvated in 1 mL of toluene and 400 μ L of DMSO. The number of AuNPs/ μ L of sample was interpolated with the standard curve and multiplied by 1400 (total volume in μ L) and divided by 5 mg.

9.2.4 Laser Triggering of Shape Memory Effect

For analysis of the temporal control of the shape memory effect, the particles were irradiated with a 532 nm laser at a power of 2 W distributed across a 5 mm diameter circular spot. The particles were irradiated at a concentration of 4×10^7 particles/mL in a glass cuvette. Temperature was assessed with a Fluke thermocoupling device. After irradiation for the indicated period of time in the experiment, the particles were collected and imaged under SEM for evaluation of aspect ratio. The measured aspect ratio (AR_m) was then normalized to the initial aspect ratio (AR_o) to give percent shape reversion according to the following formula:

$$\frac{(AR_m - AR_o)}{1 - AR_o} \times 100\%$$

Characterization of the spatial selectivity of the shape memory effect was achieved through immobilization of the particles in a PEG hydrogel at a concentration of 2×10^5 particles/mL PEG gel. The hydrogel was then mounted to the laser and irradiated at a single circular spot approximately 5 mm in diameter for 5 minutes. Heating of PEG hydrogel was tracked by imaging with an FL-IR camera. After laser irradiation, the gel was imaged under confocal microscopy and individual images 200 μ m in width were

generated and stitched together for the length of the hydrogel. Aspect ratio was then quantified across the image to analyze the spatial dependence of the shape memory effect on the laser spot size.

9.2.5 Cell Uptake Experiments

Cell uptake of the particles triggered to undergo the shape memory effect was assessed using RAW 264.7 macrophages. Cell uptake was evaluated using flow cytometry and confocal microscopy. For flow cytometry, the cells were seeded onto a 96-well plate at a density of 30,000 cells/well two days prior to the start of the experiment. On the day of the experiment, the medium was aspirated, and medium containing the particles at the indicated dose was added. Following an incubation of 4 hours at 37 °C the cells were washed 3 times with 1x PBS and prepared for flow cytometry or confocal microscopy. For distinction of particles from cells, cells were then stained with carboxyfluorescein succinyl ester (CFSE) according to the manufacturer's protocol. CFSE stained cells were then removed from the plate with vigorous trituration and were analyzed by flow cytometry. Flow cytometry was performed using a BD Accuri C6 (BD Biosciences, San Jose, CA) flow cytometer with two lasers (488 and 633 nm) with four channels corresponding to green, yellow, red and far-red fluorescence (FL1 at 530±15 nm, FL2 at 565±10 nm, FL3 at 610±10 nm, and FL4 at 675±12.5 nm respectively) in combination with a Hypercyt autosampler (Intellicyt, Albuquerque, NM).

For confocal microscopy, the cells were cultured on a LabTek chamber slide at a density of 30,000 cells per well. After 4 hours incubation time with the particles, the excess particles were washed away with 3 washes of 1x PBS and then the cells were fixed with 10% formalin for 15 minutes at room temperature. Following fixation and

washing, the cells were stained with Alexa 647 phalloidin for actin visualization and DAPI for nuclear visualization following manufacturer protocols. The cells were then imaged using a Zeiss FCS 780 confocal microscope. Cell viability was evaluated using an MTS Celltiter 96 Aqueous One (Promega, Madison, WI) cell proliferation assay following the manufacturer's protocol.

9.3 Results and Discussion

9.3.1 Fabrication and Characterizations of Shape Memory Microparticles

We developed a shape memory micro-system based on high molecular weight purely amorphous polymer, i.e. poly(D,L-lactic acid) (PDLLA), which was expected to only have polymer entanglements serving as physical netpoints for shape memory actuation. Recently, Petisco-Ferrero et al. systematically tested the rheological properties of PDLLA of multiple molecular weights and observed the rubbery plateau of the material that confirms the entanglements of the polymer with an entanglement molecular weight of 5200 g/mol.⁴² We purposely applied this widely used biocompatible polymer without any chemical modifications in our shape memory system because of its having already been proved safety to human body for clinical translation.²⁴ This shape memory system encapsulated a hydrophobically stabilized AuNP formulation as a photothermal trigger.

Through stretching at low temperatures (e.g. 65 °C) we expected the physical crosslinks to remain intact and drive the SME upon heating past the transition temperature. On the other hand, we hypothesized that stretching at high temperatures (e.g. 90 °C) would erase this polymer entanglement and thus the SME. To confirm the presence of polymer alignment and the entropy driven mechanism of the SME,

microparticles stretched at either 65 °C or 90 °C were analyzed by polarized light optical microscopy (POM) (**Figure 9.1B**). As shown in the images, the particles stretched at 65 °C showed strong birefringence under crossed polarizers, indicating polymer alignment inside the particles. In contrast, the particles stretched at 90 °C only exhibited light reflection from the particle surface, suggesting random orientation of polymer chains. This confirmed our theory that low temperatures would preserve the polymer entanglements of the particles whereas high temperatures would erase them.

As part of the characterization process we evaluated the properties of the colloidal gold immobilized in the polymer matrix. UV-Vis spectroscopy indicated that the AuNPs maintained their absorption peak at 530 nm even after encapsulation (**Figure 9.4A**). We calculated the concentration of nanoparticles through analysis of absorbance and were able to derive a standard curve of gold nanoparticle concentration vs. absorbance (**Figure 9.4B**). Using this standard we determined the concentration of the gold in the microparticles to be 1.63×10^{10} AuNPs per mg of loaded PDLLA microparticles. We further characterized the gold content of the microparticles through transmission electron microscopy (TEM) (**Figure 9.5**). There were approximately 0.58 ng of AuNPs per mg of PDLLA. Each AuNP and PDLLA microparticle had a mass of approximately 25 attograms ($\times 10^{-18}$) and 98 pg, respectively, constituting approximately 0.041% of AuNPs by mass. Each PDLLA microparticle contained approximately 1.6×10^3 AuNPs. The lower magnification images (**Figure 9.6A-B**) were unable to distinguish AuNP encapsulation compared to PDLLA microparticles without AuNPs (**Figure 9.7**) which were used to prepare the UV-Vis standard curve (**Figure 9.4B**). However, the higher magnification images made it possible to identify individual AuNPs in the microparticles

(**Figure 9.6C-D**, red arrows). As expected, the diameters of the encapsulated AuNPs within the PDLLA microparticles were not as apparent and difficult to distinguish in comparison to **Figure 9.5** which lead to a slight increase in the calculated diameters from 14 ± 6 nm (**Figure 9.5**) to 15 ± 3 nm (**Figure 9.6A-B**) via ImageJ (Fiji). These experiments confirmed that we could successfully encapsulate absorptive colloidal gold at high concentrations in our particles without significant aggregation.

9.3.2 Direct Thermal Actuation of Shape Memory Microparticles

Upon successful synthesis and characterization of the shape memory materials, we next turned to analyze the entropy-driven SME property of the particles. We first assessed the SME through bulk heating of the media to determine the window of trigger temperatures before the surface tension effects drive the particles back to spheres. As illustrated by aspect ratio analysis vs. time (**Figure 9.8**) for different bulk heating temperatures, the low temperature stretched particles maintained their shapes at 37 °C over 24 h and completely recovered their shapes at all temperatures tested above 37 °C (i.e. 40 °C, 45 °C, and 50 °C) within 30 min. Therefore, these particles could rapidly undergo SME even at a temperature slightly below T_g (i.e. 41.3 °C). This can be explained by the small-sized shape memory system in micron scale and the shape recovery temperature still above the initiation temperature of glass transition (i.e. 39 °C). Furthermore, we observed that the birefringence of these particles gradually decreased with time during shape recovery process, which confirms our hypothesis of polymer alignment as the driving force for SME. However, the high temperature stretched particles did not begin to revert until longer incubations at 45 °C and 50 °C. This provided us with an optimal transition temperature range for entropy-driven shape

memory that is within the biocompatible temperature range. Of note, while the high temperature stretched particles not showing a shape memory effect could naturally deform back to spheres over longer time scales of days due to surface tension, the shape memory effect remarkably increased the shape recovery rate at a relevant switch-like speed within the body-compatible temperature range. This shape change to the thermodynamically favored sphere obviates challenges with fixity and recovery that are typically present in macroscopic shape memory systems.

9.3.3 Photothermal Actuation of Shape Memory Microparticles

With verification of the predicted SME in a bulk heating scenario, we then evaluated the capability for the laser to trigger the shape memory effect through photothermal heating of the gold laden microparticles in bulk media. In order to verify entropy driven SME, we compared the 65 °C low temperature stretched and the 90 °C high temperature stretched microparticles for analysis of SME by photothermal heating. We irradiated the particles for 1-5 min using the 532 nm laser at 2 W focused on a circular spot, 5 mm in diameter (**Figure 9.9A-H**). As shown in the SEM images of the irradiated particles, the low temperature stretched particles underwent visibly significant SME within 3 min of the start of laser irradiation (**Figure 9.9A-D**). However, there was almost no shape change or SME observed in the high temperature stretched particles for that same time period as well as throughout the entire 5 min experiment (**Figure 9.9E-H**). We further characterized this SME through aspect ratio analysis of the irradiated particles. As shown in **Figure 9.9I**, the low temperature stretched particles showed near complete reversion to an aspect ratio of 1 (spherical), whereas the high temperature stretched particles maintained a high aspect ratio (>3) throughout the duration of the

heating. Following a percent reversion normalization equation we determined that the low temperature particles reverted nearly 100% back to their spherical form whereas the high temperature stretched particles showed approximately 10-20% reversion over the duration of the experiment (**Figure 9.9J**). In order to verify this difference was not due to differential photothermal heating of the particles stretched at different temperatures, we tracked the bulk media temperature during the experiment and found the temperatures for the two particle sets to be identical with respect to time of irradiation (**Figure 9.9K**).

9.3.4 Spatiotemporal Control of Shape Memory Recovery

Upon verification that SME could be triggered by photothermal heating, we then sought to characterize the spatial resolution of the SME with respect to the laser irradiation spot. To accomplish this goal, we formulated the gold laden microparticles with a fluorophore, stretched them at a low temperature, and immobilized them in an artificial extracellular matrix made of a poly(ethylene glycol) (PEG) hydrogel. The gel was subsequently irradiated and determined to undergo successful heating based on IR imaging of the matrix (**Figure 9.10A**). After irradiation for 5 min, we imaged the gel under confocal microscopy to analyze the aspect ratio of the particles with respect to the spatial dimension. We found that the region of the gel directly irradiated with the laser successfully exhibited SME as evidenced by reversion back to spherical form (**Figure 9.10B**). Immediately outside of the irradiation region, there was partial SME observed in a 1 mm region on either side, however the reversion to spherical form was not complete most likely suggesting this was the result of the thermal conductivity of the matrix. Outside of this small 1 mm region, there was little or no SME observed suggesting the laser spot size specifies the spatial resolution of the SME. This is also illustrated in

Figure 3c. As shown in these confocal micrographs, there was a clear visual transition from the region that was not irradiated (yielding only high aspect ratio particles) and the region that was irradiated (yielding only spherical particles). This confirms that not only is the SME able to be triggered by a laser in the biocompatible temperature range, but also the SME is restricted (with 1 mm resolution) to the irradiated area of the laser.

9.3.5 Shape Memory Response Impacts Macrophage Phagocytosis

One of the advantageous properties of an anisotropic over a spherical equivalent is that due to the entropic interaction of the particle with the cell membrane, there is less non-specific endocytosis and phagocytosis of ellipsoidal particles compared to spherical particles and hence, slower elimination from the body.²⁷ This was recently exploited in shape-switching particles that are triggered to revert back to spherical form to enable more rapid phagocytosis of the particles.¹⁷ We wanted to determine if the thermally triggered SME in the gold laden microparticles could render the particles more susceptible to phagocytosis by macrophages. To confirm that SME could be observed in the fluorophore loaded particles, we did confocal imaging of bulk heated particles stretched at either low or high temperatures to confirm SME. As shown in **Figure 9.11A-B**, the low temperature stretched particles exhibited complete reversion to spherical form whereas the high temperature stretched particles had no reversion (for full time course, see **Figure 9.12**). Upon addition of the particles to the macrophages, we triggered the SME through short term (15 min) bulk heating of the cells to 45 °C. As shown in the confocal micrographs of cells with low temperature stretched particles, this heating resulted in spherical particles that could be more readily phagocytosed than the ellipsoidal high temperature stretched particles (**Figure 9.11C-D**). This was

quantitatively assessed using flow cytometry to determine the percent uptake of the particles (**Figure 9.11E**) and the geometric fluorescent signal mean for comparison of how many particles were taken up per cell (**Figure 9.11F**). As shown, there was statistically significant reduction in both the percent uptake positive and geometric mean for high temperature stretched, ellipsoidal microparticles compared to the SME triggered low temperature stretched particles. Both bulk heated and laser triggered shape memory microparticles demonstrated similar effect in controlling macrophage response. This observed trend was significant for a variety of doses ranging from 3.75 - 25 μg particles/30,000 cells. We also assessed the viability of the macrophages to determine if the particles exerted any toxicity on the cells. As shown in **Figure 9.13**, the viability was unaltered over a wide range of doses compared to a no treatment control.

9.4 Conclusions

In this study, we have developed a novel shape memory system with entropy-driven SME that can be triggered at biocompatible temperatures in a spatiotemporally controlled manner. To our knowledge, this is the first instance of a material bearing all of these properties and this biotechnology could enable applications ranging from precise triggered drug delivery to switchable biomedical microdevices. We have verified that these particles possess physical polymeric alignment, driving the entropy based SME. The particles can be triggered to change shape upon irradiation and photothermal heating of encapsulated AuNPs. This triggering is both specific to the spot of irradiation, and the time of irradiation thus establishing spatiotemporal control over the SME. Furthermore, this material exhibits SME when the bulk media temperature is 40 °C. This is significantly below temperatures at which thermal injury occurs, rendering these particles

fully biocompatible. This technology and related platforms can enable the once elusive union of shape memory materials and biomedical applications.

9.5 Figures

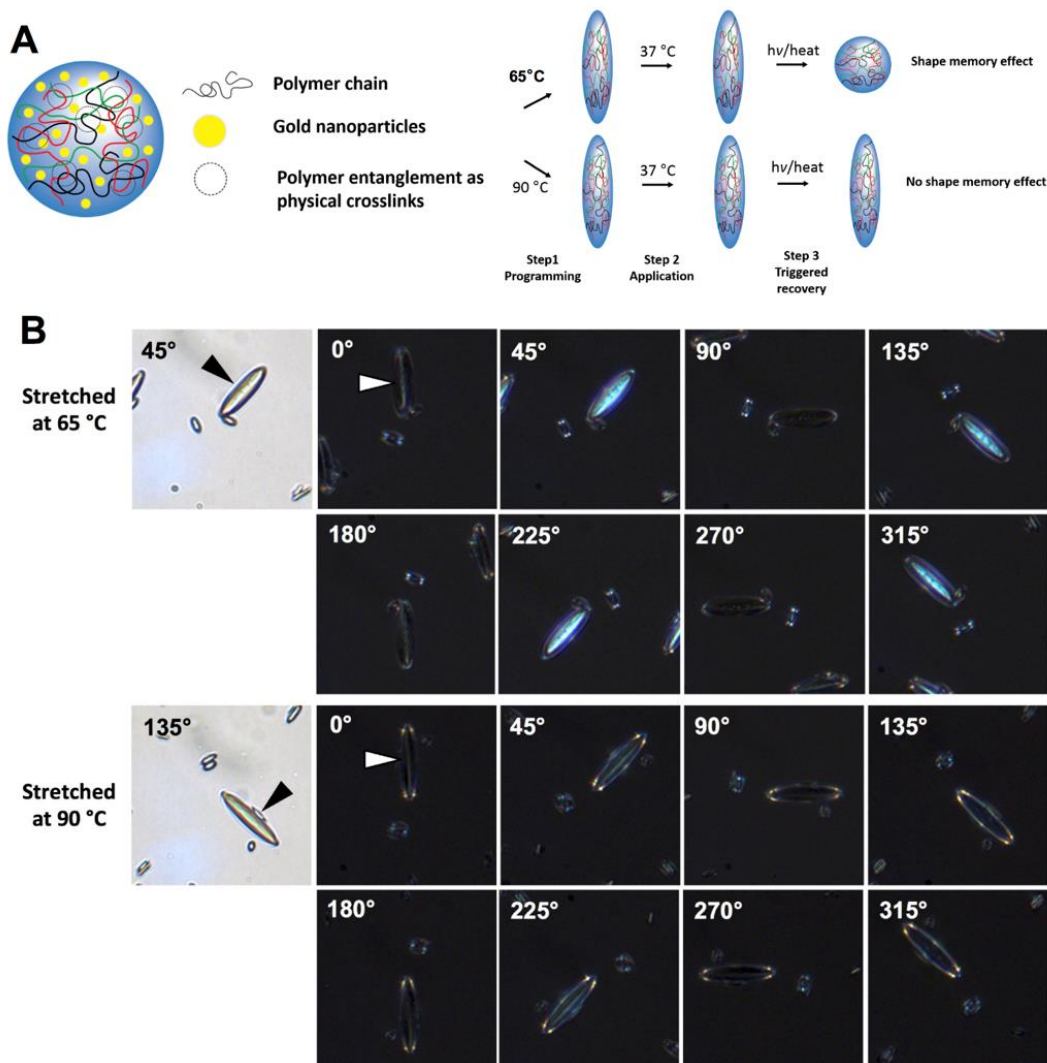


Figure 9.1: Polymeric particle entropy-driven shape memory effect. (A) Poly (D,L lactic acid) particles were fabricated encapsulating hydrophobic lipid stabilized gold nanoparticles. Due to high molecular weight of the polymer in use, physical crosslinks of the polymer were present in the sample. Polymeric particles are stretched to anisotropic shapes under low or high temperatures and then the entropy driven shape memory effect was triggered by thermal means. Low temperature stretched particles assumed their original shape whereas high temperature stretched particles did not. (B) Polymer alignment was observed in POM images of 65 °C stretched particles to a higher degree as opposed to 90 °C stretched particles. This indicates that polymer orientation between polymer entanglements maintained in the low-temperature stretched particles, which can serve as driving force to trigger shape memory effect, while disentanglement of polymers happened and polymer orientation were lost in the high-temperature stretched particles.

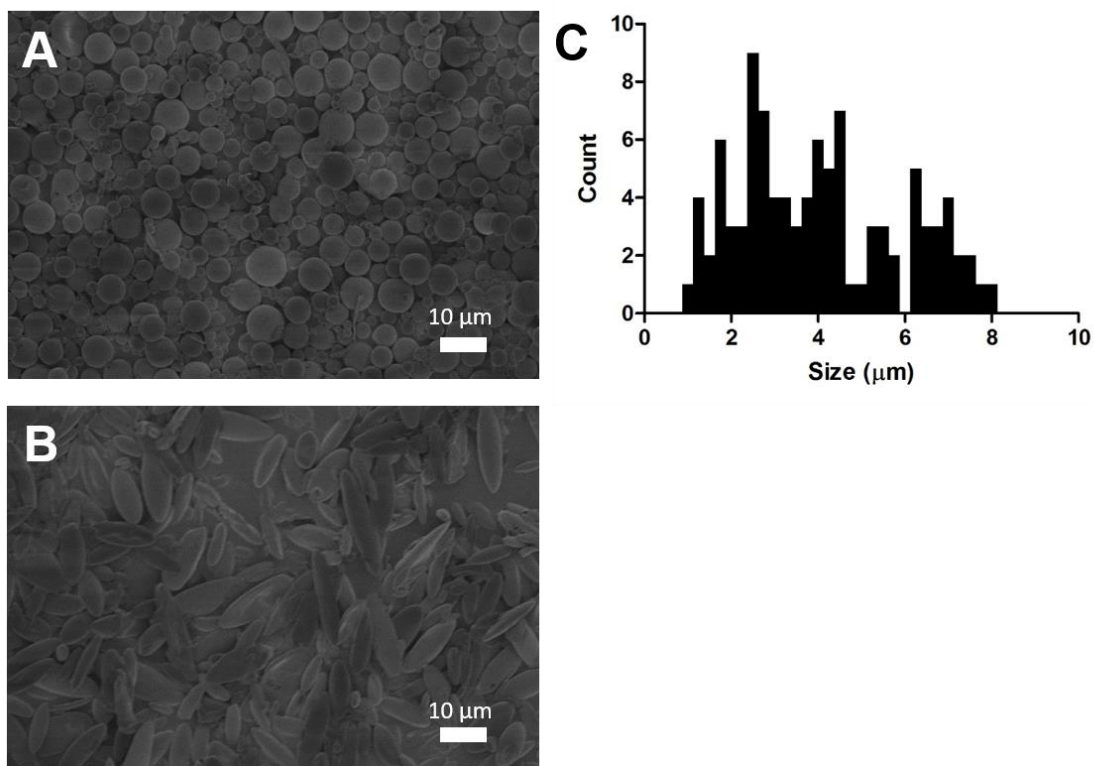


Figure 9.2: SEM characterization of (A) Spherical and (B) Non-spherical particles. (C) Size characterization of the spherical particles demonstrates a mean size of approximately 5 μm .

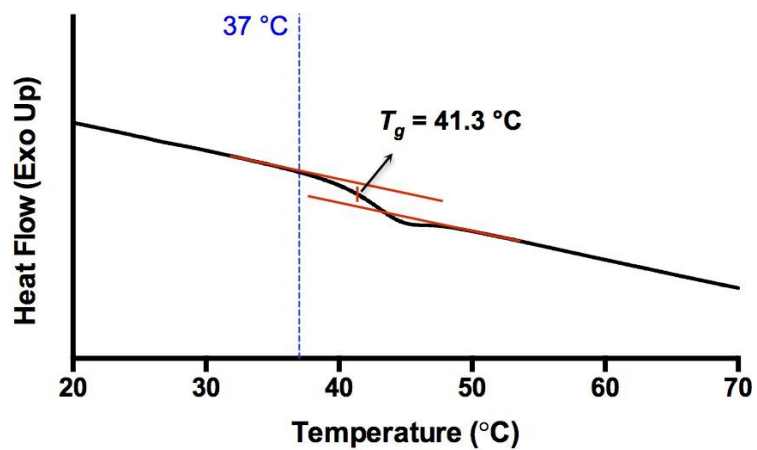


Figure 9.3: DSC second heating curve of PDLLA particles incubated in water.

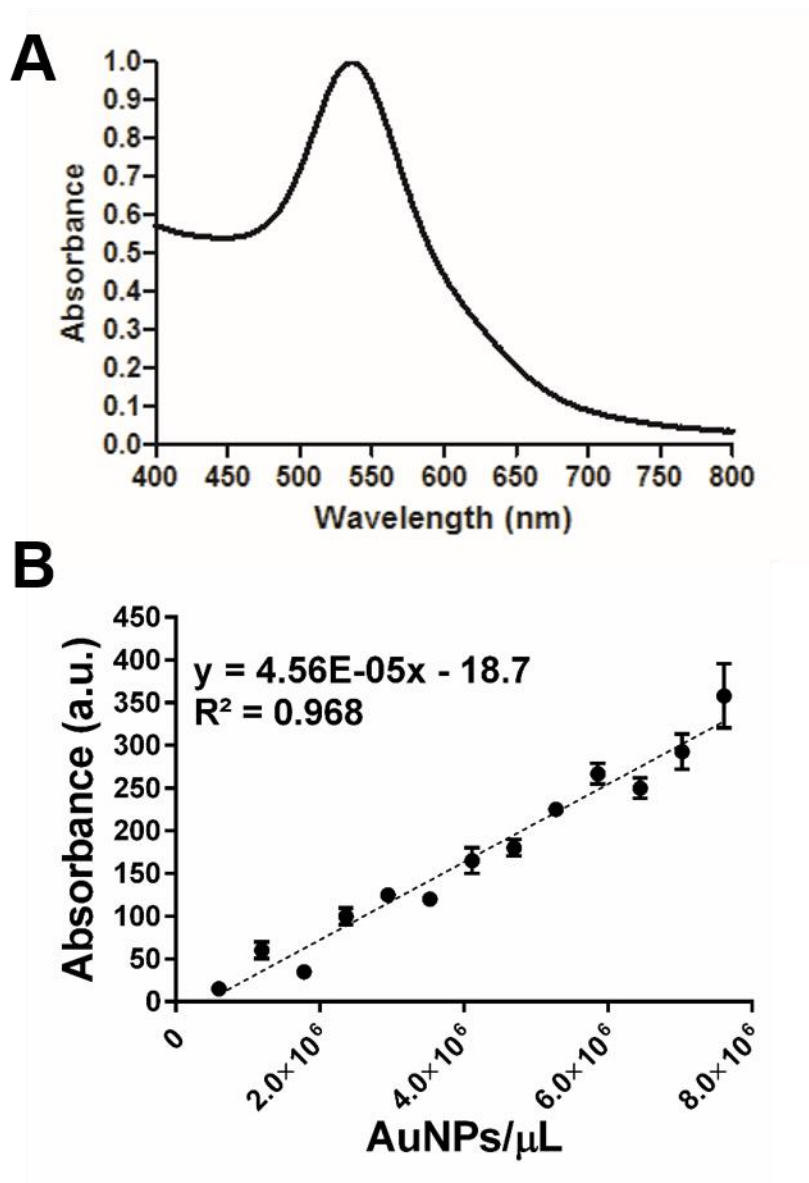


Figure 9.4: (A) Absorbance spectrum and (B) standard curve of AuNPs (various concentrations in 1 mL of toluene) in the presence of pure PDLLA microparticles (5 mg in 400 μL of DMSO). The gold nanoparticles were present at 1.63×10^{10} particles/mg of PDLLA microparticles (including the mass of AuNPs loaded) and the absorbance peak was 530 nm.

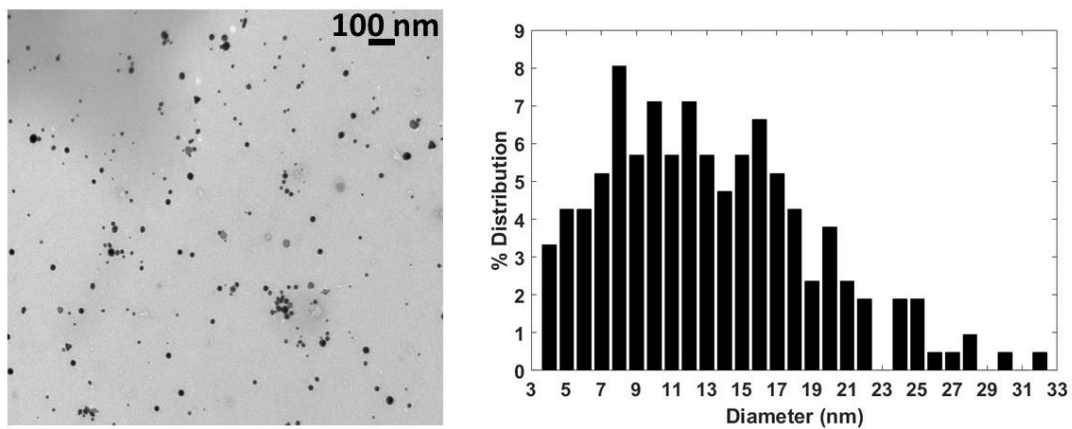


Figure 9.5: TEM characterization of DOPC AuNPs (left) and histogram (right) of diameters observed (14 ± 6 nm).

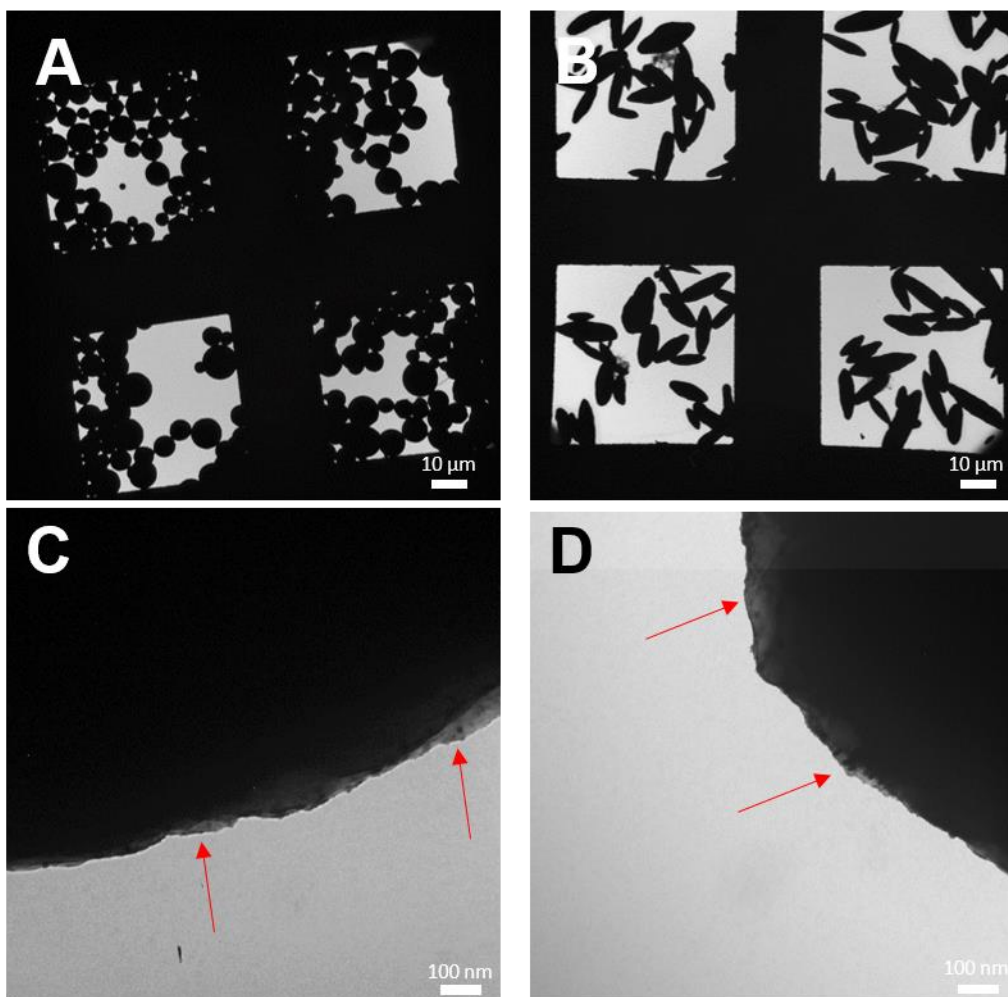


Figure 9.6: (A) Spherical and (B) non-spherical PDLLA microparticles encapsulating gold nanoparticles were imaged under TEM to analyze the presence of gold nanoparticles. Zoomed in pictures of the edges (area of minimal polymer TEM image interference) of (C) Spherical and (D) Stretched microparticles demonstrate the presence of gold nanoparticles (red arrows) encapsulated within the polymeric microparticles.

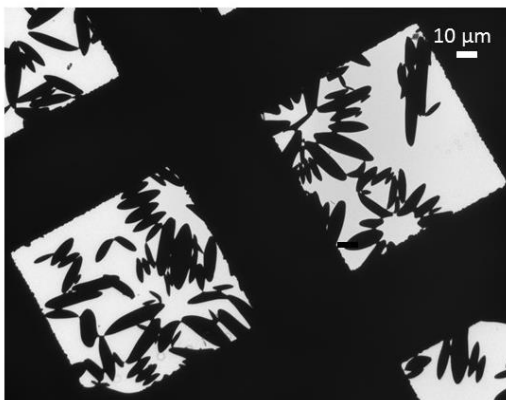


Figure 9.7: PDLLA microparticles without encapsulated AuNPs used for the background in the calibration curve.

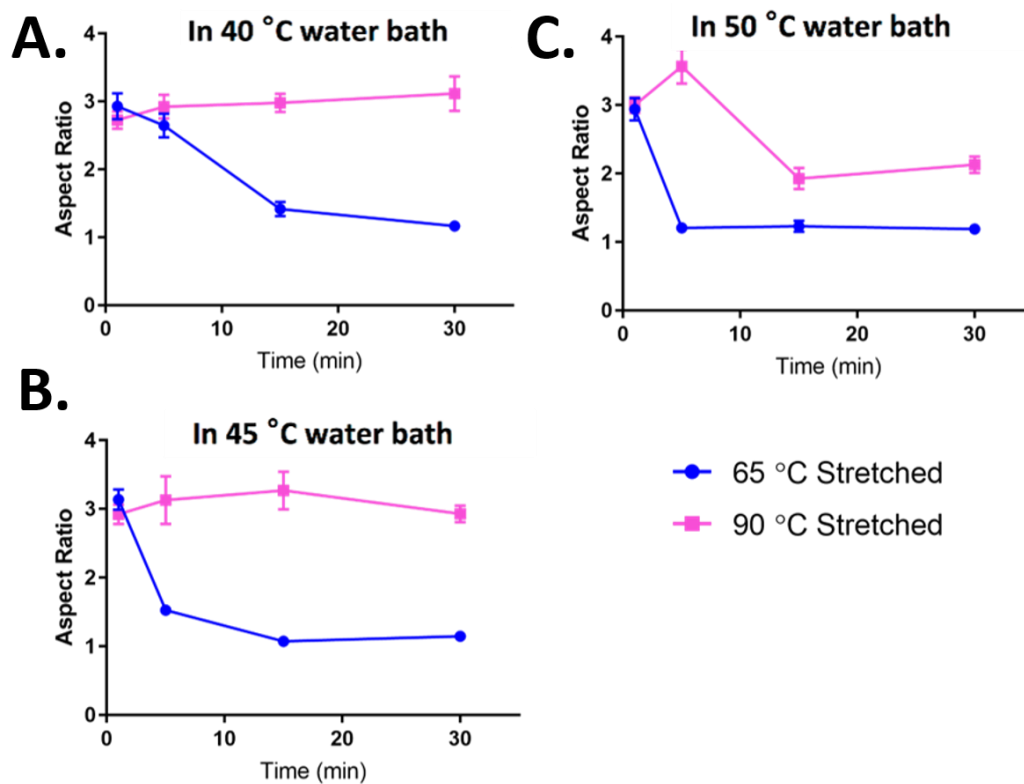


Figure 9.8: Aspect ratio analysis from SEM of particles stretched at 65 °C or 90 °C heated at (A) 40 °C, (B) 45 °C or (C) 50 °C for the indicated time points demonstrates preferential reversion back to spherical form by the particles stretched at a lower temperature. Error bars are the standard error of 20 particle replicates.

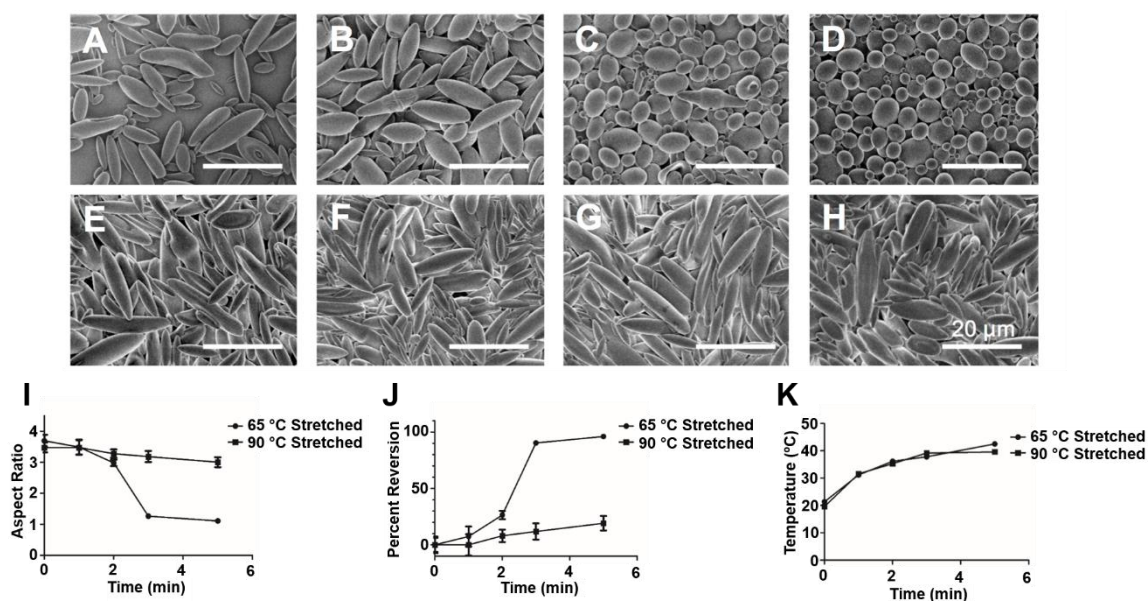


Figure 9.9: Thermoplastic shape memory effect can be thermally triggered by light in a temporally controlled fashion. Particles were loaded with hydrophobic gold nanoparticles and stretched at either (A-D) 65 °C or (E-H) 90 °C to generate ellipsoidal microparticles. The particles were then triggered using laser light at 532 nm for (A, E) 1 min, (B, F) 2 min, (C, G) 3 min, or (D, H) 5 min. The particles deformed at 65 °C exhibited full shape reversion to spherical forms whereas the particles stretched at 90 °C did not. (I) Aspect ratio analysis and (J) percent reversion of SEM images demonstrate quantitatively the shape memory effect observed only in particles stretched at 65 °C. (K) The temperature for both 65 °C and 90 °C stretched particle media during laser heating was identical. Error bars represent the standard error of 20 individual particle replicates.

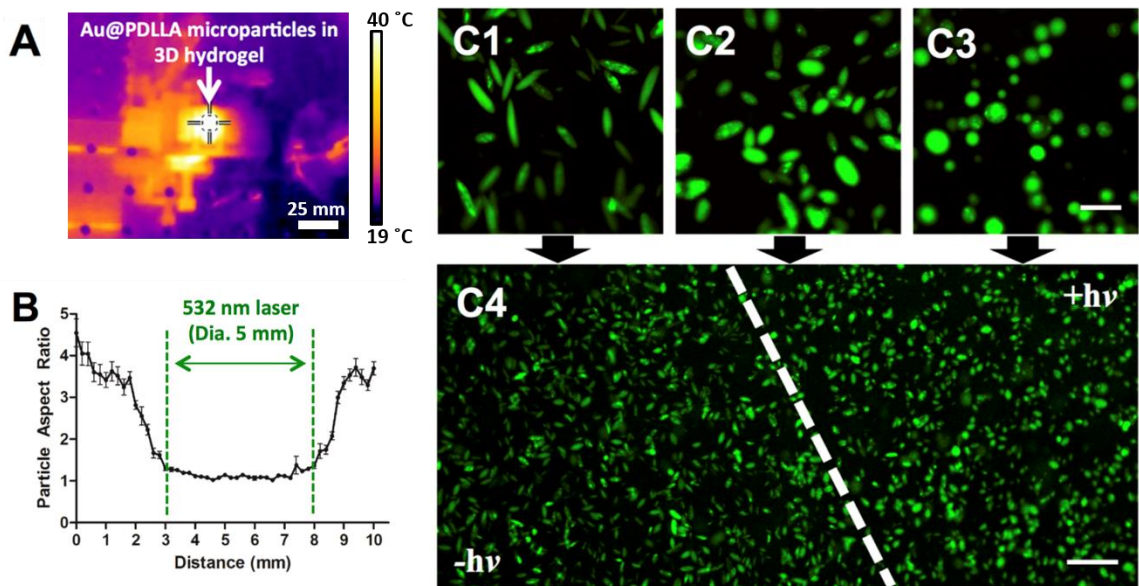


Figure 9.10: Shape memory is spatiotemporally controlled by laser irradiation. Ellipsoidal microparticles encapsulating gold nanoparticles were immobilized in a PEG hydrogel and irradiated with a laser at 532 nm. (A) The PEG hydrogel exhibited heating during the laser irradiation process as evidenced by IR imaging. The temperature measured at the center of the crosshairs was 40 °C. (B) Particles were subsequently imaged by confocal microscopy and aspect ratio analysis was conducted across the width of the laser irradiation spot. Aspect ratio reversion was detected only within the 5 mm diameter of the laser spot with a 1 mm transition zone on either side. (C) Confocal images of (1) particles not irradiated, (2) particles in transition zone, (3) particles in irradiation zone, (4) zoomed out transition zone illustrate qualitatively the phenomenon illustrated in (B). Error bars represent the standard error of 20 individual particle replicates. Scale bars are 20 μm for images (C1-C3) and 100 μm for image (C4).

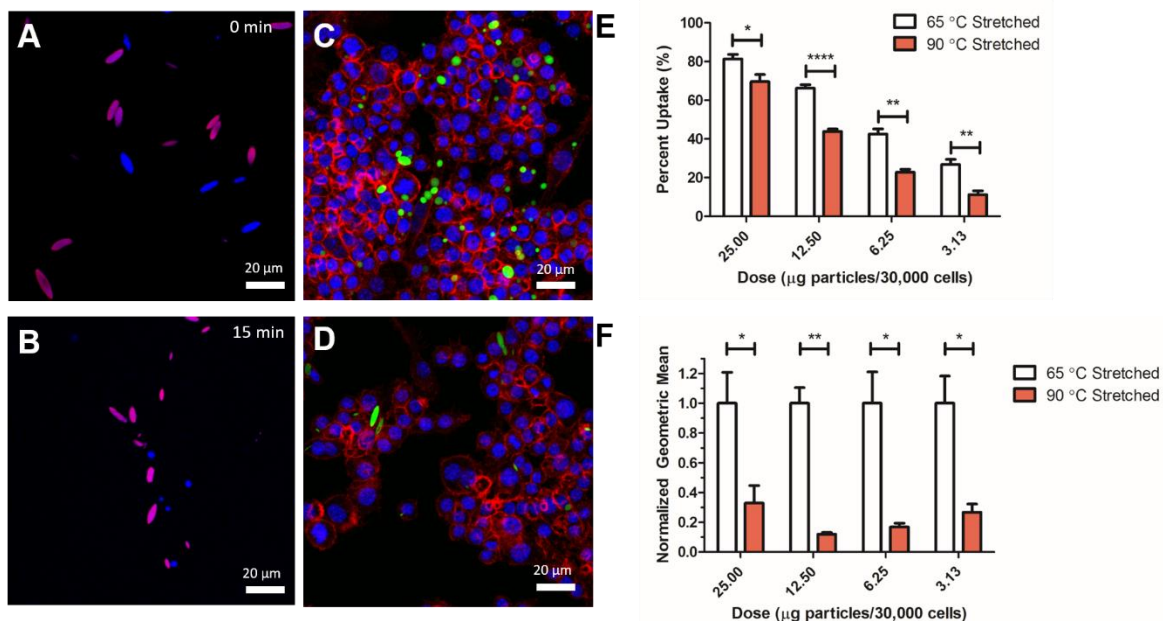


Figure 9.11: Phagocytic cells demonstrate different responses to differentially stretched particles that are triggered by the laser. Confocal images of a mixed population of bulk microparticles heated at 45 °C for (A) 0 min and (B) 15 min. For full time course, see Figure S8. 65 °C stretched particles (blue) demonstrate full reversion over the heating whereas 90 °C stretched particles (magenta) demonstrate no reversion to their spherical form. (C) 65 °C stretched and (D) 90 °C stretched particles were cultured with macrophages first heated at 42 °C for 15 min to trigger SME and then incubated at 37 °C for 4 hours. Confocal imaging demonstrates that there is a preference of macrophages to phagocytically take up spherical particles in high quantities compared to non-spherical particles. Blue = DAPI, Red = Actin, Green = Particles. (E) Percent positive uptake and (F) particle fluorescence geometric mean as analyzed by flow cytometry demonstrates that the 65 °C stretched laser triggered shape memory particles were taken up at a higher percentage of the course of 4 hours. Error bars are standard error of $n = 4$ replicates.

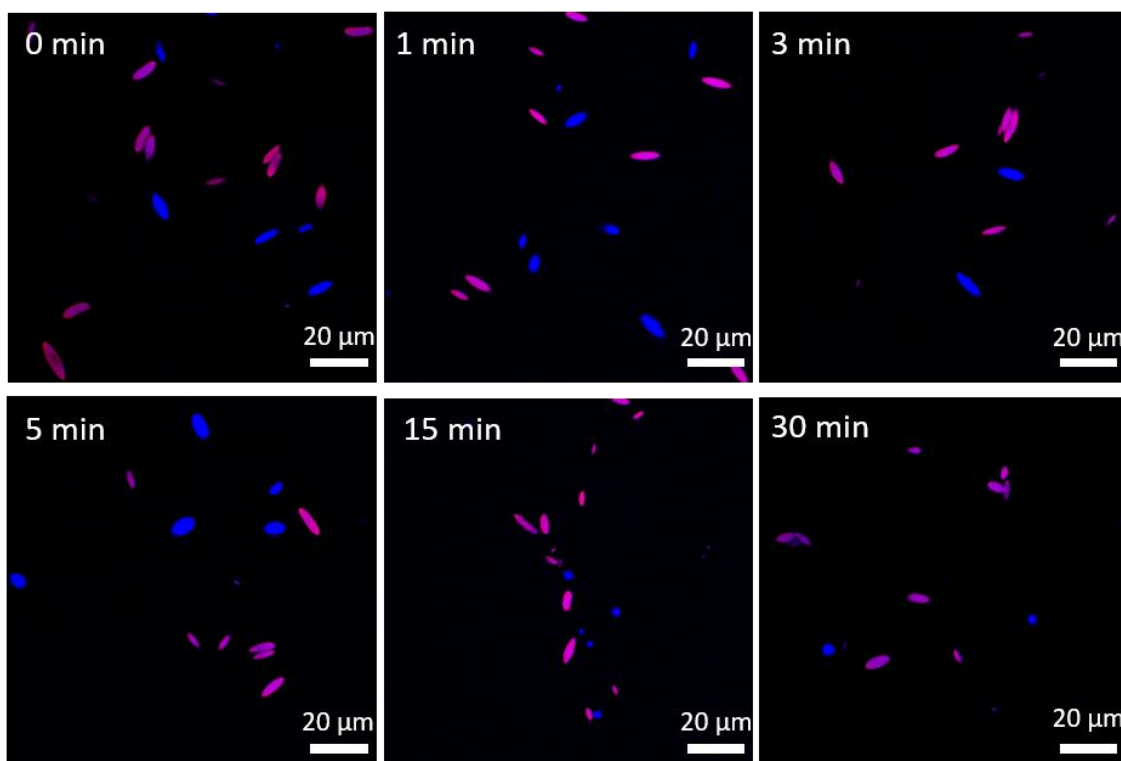


Figure 9.12: Time course images taken of mixed particles heated at 45 °C for the indicated times. Blue particles were stretched at 65 °C and magenta particles were stretched at 90 °C. Images show complete reversion to spherical form over the 30 min period of heating for the 65 °C stretched particles, and no reversion of shape for the 90 °C stretched particles.

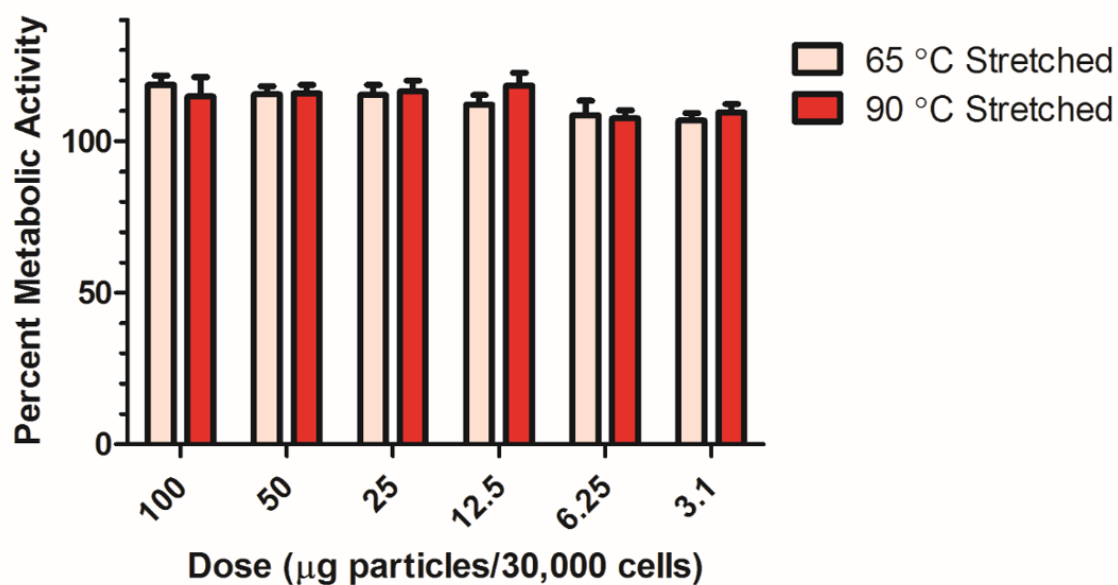


Figure 9.13: Cell viability is not altered by exposure of the cell to various doses. Cell metabolic rate was assessed after 4 hr. of exposure to the particles by MTS assay. The rates were then normalized to untreated cells to give percent metabolic activity. No significant reduction was noted. Error bars are standard error of $n = 4$ replicates.

9.6 References

1. Behl, M., Razzaq, M.Y. Lendlein, A. Multifunctional Shape-Memory Polymers. *Adv. Mater.* 2010;22(31):3388-410.
2. Hager, M.D., Bode, S., Weber, C. Schubert, U.S. Shape memory polymers: past, present and future developments. *Prog. Polym. Sci.* 2015;49:3-33.
3. Chan, B.Q.Y., Low, Z.W.K., Heng, S.J.W., Chan, S.Y., Owh, C. Loh, X.J. Recent advances in shape memory soft materials for biomedical applications. *ACS Appl. Mater. Interfaces* 2016;8(16):10070-87.
4. Lendlein, A. Kelch, S. Shape-memory polymers. *Angew. Chem. Int. Ed.* 2002;41(12):2034-57.
5. Zhao, Q., Qi, H.J. Xie, T. Recent progress in shape memory polymer: New behavior, enabling materials, and mechanistic understanding. *Prog. Polym. Sci.* 2015;49:79-120.
6. Wischke, C., Neffe, A.T., Steuer, S. Lendlein, A. Evaluation of a degradable shape-memory polymer network as matrix for controlled drug release. *J Control. Release* 2009;138(3):243-50.
7. Wang, W., Liu, Y. Leng, J. Recent developments in shape memory polymer nanocomposites: Actuation methods and mechanisms. *Coordin. Chem. Rev.* 2016;320:38-52.
8. Mather, P.T., Luo, X. Rousseau, I.A. Shape memory polymer research. *Annu. Rev. Mater. Res.* 2009;39(445-71).
9. Chatterjee, D.K., Diagaradjane, P. Krishnan, S. Nanoparticle-mediated hyperthermia in cancer therapy. *Ther. Deliv.* 2011;2(8):1001-14.
10. Le, D.M., Kulangara, K., Adler, A.F., Leong, K.W. Ashby, V.S. Dynamic Topographical Control of Mesenchymal Stem Cells by Culture on Responsive Poly (ϵ -caprolactone) Surfaces. *Adv. Mater.* 2011;23(29):3278-83.
11. Davis, K.A., Burke, K.A., Mather, P.T. Henderson, J.H. Dynamic cell behavior on shape memory polymer substrates. *Biomaterials* 2011;32(9):2285-93.
12. Hearon, K., Wierzbicki, M.A., Nash, L.D., Landsman, T.L., Laramy, C., Lonneck, A.T., Gibbons, M.C., Ur, S., Cardinal, K.O. Wilson, T.S. A processable shape memory polymer system for biomedical applications. *Adv. Healthcare Mater.* 2015;4(9):1386-98.
13. Baker, R.M., Tseng, L.-F., Iannolo, M.T., Oest, M.E. Henderson, J.H. Self-deploying shape memory polymer scaffolds for grafting and stabilizing complex bone defects: A mouse femoral segmental defect study. *Biomaterials* 2016;76:388-98.
14. Zhang, Y., Gao, H., Wang, H., Xu, Z., Chen, X., Liu, B., Shi, Y., Lu, Y., Wen, L. Li, Y. Radiopaque Highly Stiff and Tough Shape Memory Hydrogel Microcoils for Permanent Embolization of Arteries. *Adv. Funct. Mater.* 2018;
15. Champion, J.A. Mitragotri, S. Role of target geometry in phagocytosis. *Proc. Natl. Acad. Sci. U. S. A.* 2006;103(13):4930-4.
16. Sharma, G., Valenta, D.T., Altman, Y., Harvey, S., Xie, H., Mitragotri, S. Smith, J.W. Polymer particle shape independently influences binding and internalization by macrophages. *J. Control. Release* 2010;147(3):408-12.
17. Yoo, J.-W. Mitragotri, S. Polymer particles that switch shape in response to a stimulus. *Proc. Natl. Acad. Sci. U. S. A.* 2010;107(25):11205-10.

18. Kolhar, P., Anselmo, A.C., Gupta, V., Pant, K., Prabhakarpanthian, B., Ruoslahti, E. Mitragotri, S. Using shape effects to target antibody-coated nanoparticles to lung and brain endothelium. *Proc. Natl. Acad. Sci. U. S. A.* 2013;110(26):10753-8.
19. Ho, C., Keller, A., Odell, J. Ottewill, R. Preparation of monodisperse ellipsoidal polystyrene particles. *Colloid Polym. Sci.* 1993;271(5):469-79.
20. Meyer, R.A., Meyer, R.S. Green, J.J. An automated multidimensional thin film stretching device for the generation of anisotropic polymeric micro-and nanoparticles. *J. Biomed. Mater. Res. A* 2015;103(8):2747-57.
21. Brosnan, S.M., Jackson, A.M.S., Wang, Y. Ashby, V.S. Shape memory particles capable of controlled geometric and chemical asymmetry made from aliphatic polyesters. *Macromol. Rapid Comm.* 2014;35(19):1653-60.
22. Xiao, Z., Wu, Q., Luo, S., Zhang, C., Baur, J., Justice, R. Liu, T. Shape matters: a gold nanoparticle enabled shape memory polymer triggered by laser irradiation. *Part. Part. Syst. Char.* 2013;30(4):338-45.
23. Gu, X. Mather, P.T. Entanglement-based shape memory polyurethanes: Synthesis and characterization. *Polymer* 2012;53(25):5924-34.
24. Doppalapudi, S., Jain, A., Khan, W. Domb, A.J. Biodegradable polymers—an overview. *Polym. Adv. Technol.* 2014;25(5):427-35.
25. Meyer, R.A. Green, J.J. Shaping the future of nanomedicine: anisotropy in polymeric nanoparticle design. *WIREs: Nanomed. Nanobiotechnol.* 2016;8(2):191-207.
26. Meyer, R.A., Sunshine, J.C. Green, J.J. Biomimetic particles as therapeutics. *Trends Biotechnol.* 2015;33(9):514-24.
27. Meyer, R.A., Sunshine, J.C., Perica, K., Kosmides, A.K., Aje, K., Schneck, J.P. Green, J.J. Biodegradable nanoellipsoidal artificial antigen presenting cells for antigen specific T-cell activation. *Small* 2015;11(13):1519-25.
28. Toy, R., Peiris, P.M., Ghaghada, K.B. Karathanasis, E. Shaping cancer nanomedicine: the effect of particle shape on the in vivo journey of nanoparticles. *Nanomedicine* 2014;9(1):121-34.
29. Sunshine, J.C., Perica, K., Schneck, J.P. Green, J.J. Particle shape dependence of CD8+ T cell activation by artificial antigen presenting cells. *Biomaterials* 2014;35(1):269-77.
30. Zhang, H. Zhao, Y. Polymers with dual light-triggered functions of shape memory and healing using gold nanoparticles. *ACS Appl. Mater. Interfaces* 2013;5(24):13069-75.
31. Mieszawska, A.J., Mulder, W.J., Fayad, Z.A. Cormode, D.P. Multifunctional gold nanoparticles for diagnosis and therapy of disease. *Mol. Pharm.* 2013;10(3):831-47.
32. Bishop, C.J., Tzeng, S.Y. Green, J.J. Degradable polymer-coated gold nanoparticles for co-delivery of DNA and siRNA. *Acta Biomater.* 2015;11(393-403).
33. Bishop, C.J., Liu, A.L., Lee, D.S., Murdock, R.J. Green, J.J. Layer-by-layer inorganic/polymeric nanoparticles for kinetically controlled multigene delivery. *J. Biomed. Mater. Res. A* 2016;104(3):707-13.

34. Terentyuk, G., Panfilova, E., Khanadeev, V., Chumakov, D., Genina, E., Bashkatov, A., Tuchin, V., Bucharskaya, A., Maslyakova, G. Khlebtsov, N. Gold nanorods with a hematoporphyrin-loaded silica shell for dual-modality photodynamic and photothermal treatment of tumors in vivo. *Nano Res.* 2014;7(3):325-37.
35. Huang, X., Jain, P.K., El-Sayed, I.H. El-Sayed, M.A. Plasmonic photothermal therapy (PPTT) using gold nanoparticles. *Laser. Med. Sci.* 2008;23(3):217.
36. Abadeer, N.S. Murphy, C.J. Recent progress in cancer thermal therapy using gold nanoparticles. *J. Phys. Chem. C* 2016;120(9):4691-716.
37. Zhang, H., Xia, H. Zhao, Y. Optically triggered and spatially controllable shape-memory polymer–gold nanoparticle composite materials. *J. Mater. Chem.* 2012;22(3):845-9.
38. Zhang, H., Zhang, J., Tong, X., Ma, D. Zhao, Y. Light Polarization-Controlled Shape-Memory Polymer/Gold Nanorod Composite. *Macromol. Rapid Comm.* 2013;34(19):1575-9.
39. Leonardi, A., Puig, J., Antonacci, J., Arenas, G., Zucchi, I., Hoppe, C., Reven, L., Zhu, L., Toader, V. Williams, R. Remote activation by green-light irradiation of shape memory epoxies containing gold nanoparticles. *Eur. Polym. J.* 2015;71:451-60.
40. Zheng, Y., Li, J., Lee, E. Yang, S. Light-induced shape recovery of deformed shape memory polymer micropillar arrays with gold nanorods. *RSC Adv.* 2015;5(39):30495-9.
41. Liu, X., Atwater, M., Wang, J. Huo, Q. Extinction coefficient of gold nanoparticles with different sizes and different capping ligands. *Colloids Surf. B: Biointerfaces* 2007;58(1):3-7.
42. Petisco-Ferrero, S., Fernandez, J., San Martín, M.F., Ibarburu, P.S. Oiz, J.S. The relevance of molecular weight in the design of amorphous biodegradable polymers with optimized shape memory effect. *J. Mech. Behav. Biomed. Mater.* 2016;61:541-53.

Chapter 10: Noninvasive Targeted Transcranial Neuromodulation via Focused Ultrasound Gated Drug Release from Nanoemulsions

10.1 Introduction

A long sought after goal of both clinical and basic neuroscience is the ability to focally modulate the activity of a spatially-delimited region of the brain, noninvasively, and in a safe and reversible manner.¹ Recent advances in MR-guided focused ultrasound (MRgFUS) suggest that this modality could meet this challenge and enable clinically translatable neuromodulation.²⁻⁵ However, the mechanism by which focused ultrasound (FUS) may directly induce changes in neural activity is unknown and is a matter of debate.⁵ Additionally, different studies describe divergent effects of FUS on neural activity with some describing net stimulatory effects³ and others describing net inhibitory effects.^{2,4} Despite the excellent robustness and reliability of focused ultrasound techniques it is unclear how FUS alone impacts neural activity.

We propose an alternate strategy for FUS-mediated neuromodulation via FUS-gated drug delivery to the brain. This would combine the predictability of the FUS-induced pressure field with the robustness of pharmacology. Recent application of FUS for central nervous system (CNS) drug delivery has enabled advances in the local delivery of nanoparticle-based therapeutics for varied applications including glioma treatment,⁶ neurological disorders,⁷ and neuroregeneration.⁸ Although promising, all of these prior nanoparticle-based strategies depend on the transient physical opening of the

This chapter contains material modified from the following article previously published as: Airan RD, Meyer RA, Ellens NPK, Rhodes KR, Farahani K, Pomper MG, Kadam SD, Green JJ. Noninvasive targeted transcranial neuromodulation via focused ultrasound gated drug release from nanoemulsions. *Nano Lett.* 2017;17(2);652-9.

blood-brain barrier (BBB) via ultrasound-induced cavitation of microbubbles.

Additionally, a recent set of studies has tried to enable robust pharmacological neuromodulation via FUS-mediated BBB opening.⁷ The BBB is a crucial component of the CNS as it maintains the optimal microenvironment for neuronal activity and protects the neurons from many endogenous and exogenous neurotoxins that are commonly found in circulation.⁹⁻¹¹

We therefore focus on delivery of agents that may readily cross the blood-brain barrier, and propose to use focused ultrasound-mediated drug uncaging from nanoparticle carriers, with the ultrasound focusing providing a limit on the spatial extent of the drug-based neuromodulation. We then rely upon metabolism and redistribution of the drug to limit the temporal extent of this activity. While this limits us to small molecule lipophilic agents that are known to cross the blood brain barrier passively without the need for disruption,¹¹ many if not most drugs of neurological and psychiatric interest fall under this umbrella. In practice, after an intravenous infusion of the nanoparticles inertly labels the blood pool of the subject, FUS application releases the drug in the vascular bed of the tissue of interest, in a region that is spatially limited by the size of the ultrasound focus. The drug would then cross the intact blood-brain barrier and act upon the brain parenchyma during a first-pass of perfusion. Given the availability of FDA-approved clinical MRgFUS systems that allow noninvasive transcranial focal sonication of millimeter sized regions of the brain,^{12,13} this strategy could potentially allow focal, noninvasive, and safe neuromodulation with an immediate path towards clinical translation.

We have generated ultrasound-gated nanoparticle carriers of the small molecule anesthetic propofol. These particles are modified forms of prior described ultrasound-gated “phase-change” particles that were originally designed for chemotherapeutic delivery.¹⁴ These particles are made of a biodegradable, biocompatible polyethylene glycol-*b*-polycaprolactone block copolymer matrix encapsulating a liquid perfluorocarbon core and the drug of interest. Under sonication, the perfluorocarbon core undergoes a liquid to gas phase transition, thereby releasing the drug cargo (**Figure 10.1**). Perfluoropentane was chosen for the perfluorocarbon core given its relatively high boiling point while encapsulated that would prevent spontaneous phase change.¹⁵ This amphiphilic polyester block co-polymer was chosen for the emulsifying agent as polymer perfluorocarbon nanoemulsions have been demonstrated to be more stable in general than analogous lipid nanoemulsions.¹⁶ We have established the efficacy of drug release from these particles *in vitro*, as well as the *in vivo* biodistribution and clearance kinetics of the nanoparticles. As a proof-of-principle, we have further demonstrated the potency of the nanoparticles to modulate neural activity *in vivo* by using them to inducibly silence seizure activity in an acute rat seizure model. We have then demonstrated the safety of this technique by observing no appreciable injury nor BBB opening within the sonicated brain. As the components of these particles have been regarded as safe when utilized in other clinical applications,¹⁷ these particles may be able to be readily combined with existent clinical transcranial MRgFUS systems^{12,13} to enable clinical translation. Overall, this strategy provides a neuromodulation approach that has an immediate pathway to clinical translation; has a well-defined mechanism of action via the drug being delivered; does not rely upon invasive neurosurgery, gene therapy, or a deleterious action upon the

brain; and is generalizable for neuromodulation via any drug that these particles could encapsulate. Indeed, this approach provides a pathway for clinical neuromodulation that is noninvasive, image-guided, and targeted to spatially compact regions of the brain, with the patient otherwise able to participate in a neuropsychological assessment.

10.2 Materials and Methods

10.2.1 Nanoparticle formulation and characterization

Adapting methods of prior reports of phase change nanoparticles,^{14,18} micelles of polymer (50 mg; polyethylene glycol-b-polycaprolactone, PEG-PCL; MW 2000:2000 Da) and propofol (5 mg) were made by dissolving each into 1 mL of anhydrous tetrahydrofuran (THF), then adding 1 mL of PBS, mixing, and then vacuum evaporation of the THF overnight. Micelles were then diluted 3:10 in PBS and perfluoropentane (PFP) was added to a net 1:4 polymer:PFP (w/v) ratio. To emulsify the PFP, the mixture was sonicated in 1 mL volumes with an immersion micro-tip sonicator operating at 20 kHz center frequency (Model VCX500, Sonics and Materials Inc.; Newton, CT) operated at 30% maximum amplitude for 30 sec. Free polymer and propofol were then removed via centrifugation at 5,000 rcf for 5 min, then removal of the supernatant, and then resuspension in fresh PBS. Centrifugation/resuspension was completed twice with the final resuspension at 700 μ L. Then mixture was then mixed with an equivalent volume of hexane to extract residual free propofol, and 650 μ L of the aqueous phase was collected and diluted with an additional 350 μ L PBS. Particle size was determined with nanoparticle tracking analysis via NanoSight (Malvern Instruments, Worcestershire, UK). For in vivo animal experiments, the above process was completed using sterile technique in cell culture hoods, with sterile reagents. For biodistribution experiments, 1 mg of a

custom hydrophobic infrared fluorescent dye (IR800, LICOR Biosciences, Lincoln, NE) was included in the original micelle mixture (50:1 polymer:dye ratio w/w). To evaluate the drug content in the nanoparticles, 100 μ L of the nanoparticles were added to 900 μ L of dimethyl sulfoxide (DMSO) to dissolve the polymer, PFP, and drug. The sample was then evaluated for fluorescence at 280 ex/310 em on a BioTek Synergy 2 plate reader (BioTek; Winooski, VT), and quantified for propofol using a standard curve of propofol in DMSO. This concentration of drug/mL of nanoparticles was then normalized to the amount of drug initially added to the PFP/micelle mixture to derive the percent encapsulation efficiency.

To test particle release efficacy *in vitro*, the particles were sonicated by loading into a custom designed chamber and sonicated using a focused ultrasound transducer (1 MHz center frequency; RK-300, FUS Instruments, Toronto, CA) with 10, 50, 100, or 150 ms bursts at 0.5 Hz burst frequency for 2 min (60 bursts) at either 0.5, 1.0, or 1.5 MPa estimated peak *in situ* pressure. Samples were loaded as 200 μ L with a layer of 100 μ L of hexane placed on top of the aqueous phase to simulate the lipophilic sink of the brain parenchyma. Following FUS, 50 μ L of the hexane phase was removed without disturbing the aqueous layer, and this was diluted by 100 μ L hexane. The propofol concentration was quantified by UV fluorescence at 280 ex/310 em and compared to a standard curve of propofol in hexane.

10.2.2 Animals

All procedures included in this study were approved by the Johns Hopkins IACUC. Male Fischer 344 rats (150-200 gm weight; Charles River Laboratories, Wilmington, MA) were used throughout these experiments.

10.2.3 Biodistribution

For biodistribution experiments, propofol-loaded particles doped with an infrared fluorescent dye with maximum excitation of 770 nm and emission at 800 nm (LICOR Biosciences; Lincoln, NE) were prepared as described above under sterile conditions. These particles were administered intravenously via a 24 g tail vein catheter to rats (N=4) in a total volume of 1 ml.

Timed retro-orbital blood samples were acquired in capillary tubes at 10 min, 20 min, 30 min, 40 min, 2 hr, 4 hr, and 8 hr. and split into two volumes. Whole blood sample fluorescence was assessed using a LICOR Pearl Impulse Imager (LICOR Biosciences; Lincoln, NE) and quantification was completed using regions of interest of the same size across samples, drawn to be within the capillary tube. As second volume of each sample was centrifuged in a microcentrifuge for a total of 10 min. The serum fraction from these samples were then collected and their fluorescence was quantified similar to the whole-blood samples. After the 24 h blood sample timepoint, animals were euthanized while under isoflurane anesthesia via cervical dislocation, and the major non-bowel organs were harvested. Organ fluorescence was also assessed via the LICOR Pearl Impulse Imager and quantified using regions of interest of the same size drawn to be within the image of each organ.

10.2.4 Seizure model, EEG acquisition and analysis

Rats were weighed and administered ketamine/xylazine (85/13 mg/kg) intraperitoneally (IP) for anesthesia. A 24 g tail vein cannula was placed. The dorsal fur was removed via electrical clipper and then a chemical depilatory (Veet, RB Inc, purchased through Amazon). This skin was then washed with saline and isopropanol.

Three subdermal silver EEG electrodes (1 recording, 1 reference, and 1 ground) were placed overlying the parietal cortex with bregma as a reference. The silver electrodes (IVES EEG; Model # SWE-L25 – MA, USA) were implanted and subdermally fixed with minimal adhesive.

The animal was placed supine on the bed of a focused ultrasound transducer (1 MHz center frequency; RK300, FUS Instruments, Toronto, CA), with ultrasound gel used to couple the dorsal scalp to a Kapton membrane pad containing degassed water, which was itself coupled to the ultrasound transducer with degassed water. The head orientation and position was fixed with a vendor provided bite bar and nose cone integrated with the transducer bed, via which supplemental oxygen was provided at 2 L/min. The subdermal electrodes were then connected to a tethered preamplifier and commutator. The lead wires were placed to ensure that they did not cross the central dorsal scalp to allow for ultrasound transmission. EEG recordings and synchronous video data were acquired using Sirenia Acquisition software (Pinnacle Technology Inc. Kansas, USA) according to previously established protocols.^{19,20} EEG files were recorded in the EDF format. Data were sampled at 400 Hz with pre-amplifier gain of 100 and bandpass filtered filters between 1-60 Hz to remove ambient noise.

Following acquisition of an EEG baseline of 5-10 min, animals were administered the chemoconvulsant pentylenetetrazole (PTZ) 45 mg/kg IP.²¹ Animals were monitored via real-time EEG and visual inspection for evidence of convulsive and seizure activity. Repeat administration of 45 mg/kg IP doses of PTZ were administered until clear seizure activity was noted by both visual inspection (clear tonic-clonic limb twitching) and real-time EEG, within 5 min of the last PTZ dose. Animals required 2-4 doses of 45mg/kg

PTZ to achieve this state in this study. Animals were then administered the indicated sterile particles in 1 mL total volume intravenously as a slow bolus with a 100 μ L sterile saline flush. After several minutes to allow for stabilization of the EEG trace following any handling-related seizure activity and post-ictal depression, at least 5 min of a new EEG baseline was acquired. Focused ultrasound was then applied with 1.0 MPa estimated peak in situ pressure (estimated as in O'Reilly et al.²²) in 50 ms bursts delivered every 1 sec for a total of 1 min (60 bursts) delivered to each of two points 2.5 mm to the left and right of midline, 15 mm caudal to the eyes, which translates to approximately 5 mm caudal to bregma. 10 min of EEG traces were then acquired. Then, if convulsive/seizure activity persisted, FUS was applied as above except with 1.5 MPa of estimated peak in situ pressure. Two animals that received propofol particles did not have appreciable seizure activity after the first FUS application at 1.0 MPa and did not receive FUS at 1.5 MPa peak in situ pressure. After 10 min more of EEG trace acquisition, an adequate depth of anesthesia was confirmed and the animal was euthanized via perfusion fixation or cervical dislocation. Perfused animal brains were then harvested. Throughout this procedure, ketamine/xylazine anesthesia depth was confirmed via toe pinch, and if a visible toe pinch response was present then a repeat dose of the same amount of ketamine/xylazine was given. However, if seizure induction with PTZ had been completed, and the animal was evidently waking from anesthesia, the animal was excluded from further experimentation. An electrical artifact from unshielded components of the FUS system precluded EEG analysis during FUS applications.

For EEG analysis, using Sirenia Sleep software (Pinnacle Technology Inc. Kansas, USA), automated spectral analysis was completed with total and theta band (6-12 Hz) EEG power calculated in 10 s bins of the raw EEG trace. Power values greater than 10 S.D. beyond the mean trace values were considered artefactual outliers and removed from subsequent analysis. Each power time course was normalized by its average power within the three minutes prior to FUS application. Raw, not normalized total baseline power prior to FUS administration was $586.8 \pm 174.4 \mu\text{V}^2/\text{s}$ (mean \pm s.e.m.) for propofol and $495.3 \pm 141.0 \mu\text{V}^2/\text{s}$ for blank animals, with no statistical significance for this comparison. Normalized total power values over a 5-minute period prior to FUS application were 1.037 ± 0.054 for propofol and 1.014 ± 0.061 for blank animals, with no statistical significance for this comparison.

10.2.5 Ex vivo MRI

Fixed brains harvested following EEG/FUS experiments were scanned while submerged in fixative on a 17.6 T MRI (Bruker 750 MHz; Billerica, MA) in axial and coronal planes covering the whole brain using flip angle = 180, effective TE/TR=12.8/5000 ms, RARE factor=4, matrix = 128 x 128, FOV = 20 x 20 mm, slice thickness = 1 mm. All MRI studies were reviewed by a board certified radiologist for evidence of parenchymal damage.

10.2.6 Histology

Following ex vivo MRI, fixed brains were transferred to a 15% sucrose solution for 3 days, then a 30% sucrose solution for 2 days and then flash frozen with dry ice and stored at -80 °C. Brains were then sectioned in the coronal plane at 40 μm thickness using a cryotome (Leica, Buffalo Grove, IL) over a 2 mm span centered at the expected

FUS sonication site. Fixed frozen sections were mounted on Super Frost Plus glass slides (VWR, Radnor, PA). Slides were stained with Cresyl Violet and imaged under bright field and fluorescence on a MCID 7.0 Elite (InterFocus Imaging, Ltd., Cambridge, UK) at coordinates matching the in vivo FUS targets. All acquired sections were reviewed for evidence of damage within the parenchyma that would suggest FUS or particle mediated injury.

10.2.7 In vivo MRI and Serum Propofol Quantification

In a separate cohort, a tail vein catheter was placed, ketamine/xylazine anesthesia was induced, supplemental oxygen was provided, and propofol-loaded particles were administered intravenously. Using a 11.7T MRI (Bruker, N Billerica, MA), T2-weighted and T1-weighted scans were completed. Parameters for T2 scans were flip angle = 90, effective TE/TR=30/2500 ms, RARE factor=8, matrix = 128 x 128, FOV = 35 x 35 mm, slice thickness = 1 mm. Parameters for T1 scans were flip angle = 90, effective TE/TR=5.5/1500 ms, RARE factor=4, matrix = 256 x 256, FOV = 35 x 35 mm, slice thickness = 1 mm. Then sonication was delivered to the same targets as the EEG experiments using 1.0 MPa estimated in situ pressure, delivered in 50 ms bursts, 1 burst per focus at 1 Hz burst frequency for 60 sec. Magnevist (0.2 µl/gm; Bayer, Whippany, NJ) was administered intravenously. The T1-weighted MRI was repeated post contrast administration to assess for BBB opening. All MRI images were reviewed by a board-certified radiologist for evidence of parenchymal damage.

To quantify residual propofol in the bloodstream of the rats after particle and FUS administration, timed retro-orbital blood samples were collected from rats into heparinized tubes 1 minute after particle injection, 1 minute after sonication, and 10

minutes after sonication. Blood was centrifuged at 5,000 rcf for 5 minutes to separate out the serum. Propofol concentration in serum was then quantified following the method reported in Cussonneau et. al. with some modification.²³ Serum samples were mixed with an equal volume of a 600mg/L solution of thymol in acetonitrile and centrifuged at 2,000 rcf for 10 minutes. 100 μ L of the supernatants were taken for HPLC. Separation and propofol quantification was performed using a Waters 600 HPLC System (Waters; Milford, MA). The stationary phase consisted of an HC-C18(2) (250 mm \times 4.6 mm, 5 μ m) column (Agilent Technologies; Santa Clara, CA), and the mobile phase utilized a ratio of 65:35 (v/v) acetonitrile to water. Thymol was used as an internal standard. A 10 μ L injection volume, 1 mL/min flow rate, and 25 minute separation time were used for sample separation.

Propofol standards were prepared by diluting propofol in serum and mixing with an equal volume of 600 mg/L thymol in acetonitrile. The standard curve was generated by plotting the peak area ratio of propofol to thymol as a function of propofol concentration at an absorbance wavelength of 270 nm. The propofol concentration in the bloodstream at the time points was quantified using the standard curve.

10.3 Results and Discussion

10.3.1 *In Vitro* Characterization of Nanoemulsion Properties

Particles that encapsulated propofol with a liquid perfluorocarbon core and a biodegradable, biocompatible polymer coating were produced (**Figure 10.1**) and sized via nanoparticle tracking analysis (**Figure 10.2C**). There was a single nano-scale peak of 320 \pm 150 nm (mean \pm S.D). Encapsulation efficiency of the propofol was 11.8% \pm 1.2% (mean \pm S.D) yielding an encapsulated 177 μ g \pm 19 μ g propofol per mL of

particles. *In vitro* particle release efficacy was assessed by focused ultrasound applied at 1 MHz center frequency in short continuous bursts with 0.5 Hz burst frequency for a total of 2 min, with varying peak *in situ* pressure and the individual burst length – the short amount of time that sonication is applied continuously. The amount of released propofol was assessed by extraction into a hexane sink (**Figure 10.2A**) and quantified via UV fluorescence. There was a dose response evident for propofol release with peak *in situ* pressures past a threshold of 0.5 MPa. For burst length, a release threshold of 10 ms was present, with saturation of a dose response between 50-100 ms (**Figure 10.2B**). Particles kept in storage and *in vivo*-like conditions for two hours followed by sonication at room temperature showed intact release ability, although release efficacy was reduced after two hours of incubation at room and *in vivo* temperatures (**Figure 10.2D**), possibly due to diffusion of the perfluoropentane (PFP) from the core of the particles with higher temperature incubation.

10.3.2 *In Vivo* Pharmacokinetics of the Nanoemulsions

To evaluate the *in vivo* biodistribution and intra-vascular residence time of the nanoparticles, the particles were initially doped with a custom synthesized hydrophobic dye. Following intravenous administration of these doped nanoparticles, timed blood samples demonstrated that the whole-blood fluorescence has a decay profile that is faithfully characterized with a double exponential decay model (**Figure 10.3A**). The initial phase decay half-life was 8.8 min and the second phase decay half-life was 270 min. Notably, the whole blood samples were expected to contain both intact particles and free and micelle-bound portions of the dye. The serum of these samples, which would contain free dye or potentially PEG-PCL micelle-bound dye after high-speed

centrifugation pellets the cellular and nanoparticle constituents, showed a markedly lower fluorescence and cleared more rapidly than the whole-blood fluorescence signal, with no appreciable serum fluorescence by 2 hours. The serum sample fluorescence decayed with a monoexponential profile with a half-life calculated as 8 min – notably similar to the short half-life component of the whole blood samples. After 24 hours from particle administration, there was no remnant intra-vascular signal above background. End organ fluorescence demonstrated no evidence of nonspecific particle binding to the brain (**Figure 10.3B-C**). Instead, the nanoparticles were principally taken up by the liver, spleen, and to a lesser extent the lungs, with minimal amounts in the kidney and heart.

10.3.3 *In Vivo* Functional Efficacy of the Nanoemulsions

To demonstrate and assess the functional potency of particle release *in vivo*, an acute pentylenetetrazol (PTZ)-induced status epilepticus protocol²¹ was developed for adult male Fischer 344 rats (**Figure 10.4A-B**). We specifically chose this protocol and preparation as prior groups have used this system to assess the degree to which FUS may directly modulate neural activity.²⁴ Following seizure induction and particle administration, there was no significant difference in baseline EEG power between animals receiving propofol-loaded particles and particles generated with no drug ('Blank'; see Materials and Methods). Importantly, following FUS administration first at 1.0 MPa estimated peak *in situ* pressure, and then at 1.5 MPa, immediate statistically significant declines of total and theta band EEG power were seen in the animals receiving propofol-loaded particles, but not in the animals receiving blank particles (**Figure 10.4C-F**).

10.3.4 *Ex Vivo* Safety Profile of the Nanoemulsions

Ex vivo 17.6 T MRI, *in vivo* 11.7 T MRI, and histology confirmed that no deleterious effect of FUS and particle administration was visible (**Figure 10.5**). In particular, given the high susceptibility dependence of the MRI protocol used here (note the blooming artifact from microscopic air bubbles along the brain periphery in **Figure 10.5A**), the lack of any noted susceptibility artifact or brain parenchymal signal change within the sonicated region confirms the lack of petechial hemorrhage or other cavitation induced damage to the brain parenchyma. Notably, the 17.6 T MRI evaluation covered the entire brain in both axial and coronal planes, without inter-slice gaps, ensuring that a complete evaluation of the parenchyma was completed for each brain. All MRI images were reviewed by a board-certified neuroradiologist. *In vivo* MRI also confirmed no damage to the brain parenchyma of particle administration and sonication, and no evidence of blood-brain barrier opening with this technique (**Figure 10.5B**). Whole-brain histological sections, and more focused evaluation of the sonicated dorsal dentate gyrus in comparison with the non-sonicated ventral dentate gyrus showed no evidence of parenchymal damage, and certainly no damage that could be attributed to sonication (**Figure 10.5C**).

10.3.5 Discussion

We have therefore described nanoparticles that allow focused ultrasound-induced uncaging of the small molecule anesthetic agent propofol (**Figure 10.1**), and demonstrated the *in vitro* and *in vivo* efficacy of the nanoparticles as a proof-of-principle. Given that these particles have a hydrodynamic diameter of approximately 320 nm, and that similar perfluorocarbon-based phase-change particles have been shown to increase diameter up to 5-6x during sonication^{14,18} the maximal diameter of these particles after

activation would be $<2\ \mu\text{m}$, suggesting no substantial risk of embolization of capillaries with these nanoparticles and their use. These particles release their drug cargo with dose responses with both peak *in situ* pressure and with sonication burst length (**Figure 10.2**). The threshold peak *in situ* pressure of 0.5 MPa and the maximal pressure of 1.5 MPa that were used here are both achievable by current clinical transcranial MRgFUS systems.^{12,13} Additionally, the dynamic range of the burst length dose response between 10 ms and 50-100 ms is also achievable with these clinical transcranial MRgFUS systems. These burst lengths and duty cycles are unlikely to induce substantial heating of the brain parenchyma, especially given heat dissipation by cerebral perfusion.

We were able to use particles doped with an IR fluorescent dye as a surrogate marker of particle intravascular residence and distribution (**Figure 10.3**). The serum fluorescence, which would contain the unbound free dye fraction, showed a much more rapid clearance from the blood pool than the whole-blood samples that represent both the particle-bound and unbound fractions. The whole-blood fluorescence particle elimination profile showed two phases: an initial rapid (9 min half-life) phase that likely corresponds to the unbound dye fraction of the sample, and a slower (270 min half-life) phase that more represents the particle decay profile itself (**Figure 10.3A**). This half-life would allow enough time for a clinically relevant intervention with these particles, but not so long of a particle vascular residence time that it would preclude repeat particle administration or would suggest a potential toxicity of extended particle residence in the body. The lack of particle uptake in the brain (**Figure 10.3B-C**) confirms that our results are unlikely to be due to particle crossing of the blood brain barrier, particle binding to the brain, or some other nonspecific action of the particles upon the brain. The finding

that the liver and spleen primarily take up these particles is expected as the reticuloendothelial system generally sequesters nano-scale material.²⁵

The ability of focused ultrasound to activate the intravascular propofol-loaded particles and yield silencing of seizure activity *in vivo* (**Figure 10.4**) indicates that these particles indeed can enable a potent neuromodulatory effect upon focused ultrasound application. Crucially, given that there was no significant effect of sonication in rats receiving the blank particles, and seeing as the blank particles were otherwise constructed exactly the same as the propofol-loaded particles, the effects seen here are specifically related to the release of propofol in this system, and not a nonspecific effect of ultrasound or particle interaction with neural tissue, or of the individual polymer or perfluorocarbon particle constituents. Given that our total encapsulation efficiency of 177 $\mu\text{g/ml}$ translates to ~ 1 mg/kg in these experiments, and that a normal loading dose for anesthetic effect in rats is an order of magnitude higher at 10 mg/kg , it is unlikely that our results are due to a nonspecific leak of the propofol from the particles. Indeed, serum propofol concentrations taken immediately and 10 min after sonication showed no appreciable propofol above the background (**Figure 10.4F**), indicating that this propofol release was likely limited to the brain, without nonspecific systemic delivery. The detectable serum propofol seen immediately following particle administration likely reflects a small amount of free propofol in the particle batch given our method of production – although this level of ~ 0.6 $\mu\text{g/ml}$ is an order of magnitude less than the typical serum concentrations of propofol thought to be necessary for an anesthetic effect. Taken together, these results suggest that these particles indeed yield a higher local drug concentration in the brain following FUS application than might be suggested by the raw

total amount of drug delivered in the bolus intravenous dose. Additionally, given the fast, 2-3 min distribution half-life of propofol from the blood-pool,²⁶ that we waited 5-10 min from particle administration to FUS application, and that we did not see significant differences in the baseline EEG power between propofol and blank treated rats, it is unlikely that free or loosely bound propofol in the particle solution could have substantially contributed to our results. Notably, the EEG power was seen to decrease immediately following FUS application suggesting that the kinetics of this neuromodulatory effect are rapid (**Figure 10.4D**). Additionally, we did not observe any deleterious consequence to the brains with *ex vivo* MRI, *in vivo* MRI, or post hoc histology (**Figure 10.5**), suggesting that these effects are not due a nonspecific damage of the brain parenchyma. Indeed, the lack of blood-brain barrier opening with this technique (**Figure 10.5B**) confirms the safety of this technique and the distinction of this technique to other proposed methods of FUS-mediated neuromodulation.^{24,27}

In this study, we have not directly visualized the particle activation *in vivo* to assess the effective spatial resolution of this technique. Additionally, the volume conduction effect of EEG signals, particularly for subdermal EEG, and the nature of the generalized status epilepticus model used for this study limits our ability to spatially resolve this signal in this *in vivo* preparation. Similarly, given the acute nature of PTZ-induced seizures that may not recur substantially once they are aborted, this study protocol is limited in ability to determine over what time interval the action of the gated propofol persists. Those limitations said, the *in situ* ultrasound focus induced by the particular ultrasound transducer used in this study is known to have a FWHM of ~1.5 mm transaxially and ~5 mm longitudinally at 1 MHz (personal communication with the

vendor, FUS Instruments, Toronto, CA), providing an effective initial spatial extent for the action of the particles in this preparation. Additionally, we saw no substantial systemic propofol load with sonication (**Figure 10.4F**), confirming that the propofol release was likely limited to the brain. While groups have shown that activated perfluorocarbon particles may induce further activation of unsonicated particles in static solutions,¹⁴ we would expect cerebral perfusion to rapidly clear the activated particles from the sonication field, especially given the lack of particle binding to the brain (**Figure 10.3**), thereby limiting this potential confound. Additionally, the temporal residence of propofol in the brain and its time of action is known to be rapid on the order of minutes or even tens of seconds²⁸ and similar to the time-scales used in this experiment. This time of action would be clinically practical for neuropsychological assessment, as evidenced by the current protocol of the Wada test,²⁹ which is used for clinical mapping of the laterality of brain functions. Given the size of the rat cerebrum (~15 x 15 x 10 mm) and the technical limitations of signal volume conduction in subdermal EEG, further characterization of the spatial and temporal resolution of this technique will necessitate experiments that assess baseline non-seizure neural activity, likely in larger animal models, and potentially with a different measure of neural activity, such as fMRI or PET. Nonetheless, our results provide a proof-of-principle that these nanoparticles yield potent inducible neuromodulation using noninvasive focused ultrasound and that this approach has the potential to enable precise spatial (mm) and temporal (min) control of brain activity, with a pathway to clinical translation.

10.4 Conclusions

In this study we have successfully designed nanoemulsions loaded with propofol and demonstrated they could be used for transcranial focused ultrasound mediated suppression of neural activity. With regard to clinical translation, each component of these particles has been previously approved for clinical use in different contexts.¹⁷ Additionally, the sonication pressures and burst lengths used in this study are well achievable by FDA-approved transcranial MRgFUS systems that are currently in clinical use.¹² Taken together, this provides a pathway towards clinical translation that is otherwise unavailable to other targeted molecular neuromodulation strategies. Further, the chemistry that enables these particles to encapsulate a given drug relies mainly upon the lipophilicity of the drug in question, so that it may bind the hydrophobic domains of the encapsulating block copolymer and the hydrophobic polymer-perfluorocarbon interface. Given that most molecules that passively cross the blood-brain barrier are highly lipophilic, this suggests that the nanotechnology strategy presented here could be adapted for focal and targeted delivery of most any small molecule that naturally crosses the blood-brain barrier, including imaging agents as well as compounds that act directly upon the adrenergic, serotonergic, or dopaminergic systems – in addition to the excitation/inhibition axis that propofol modulates. This opens the door to a wide variety of potential nanotechnological tools for targeted clinical modulation of brain activity.

10.5 Figures

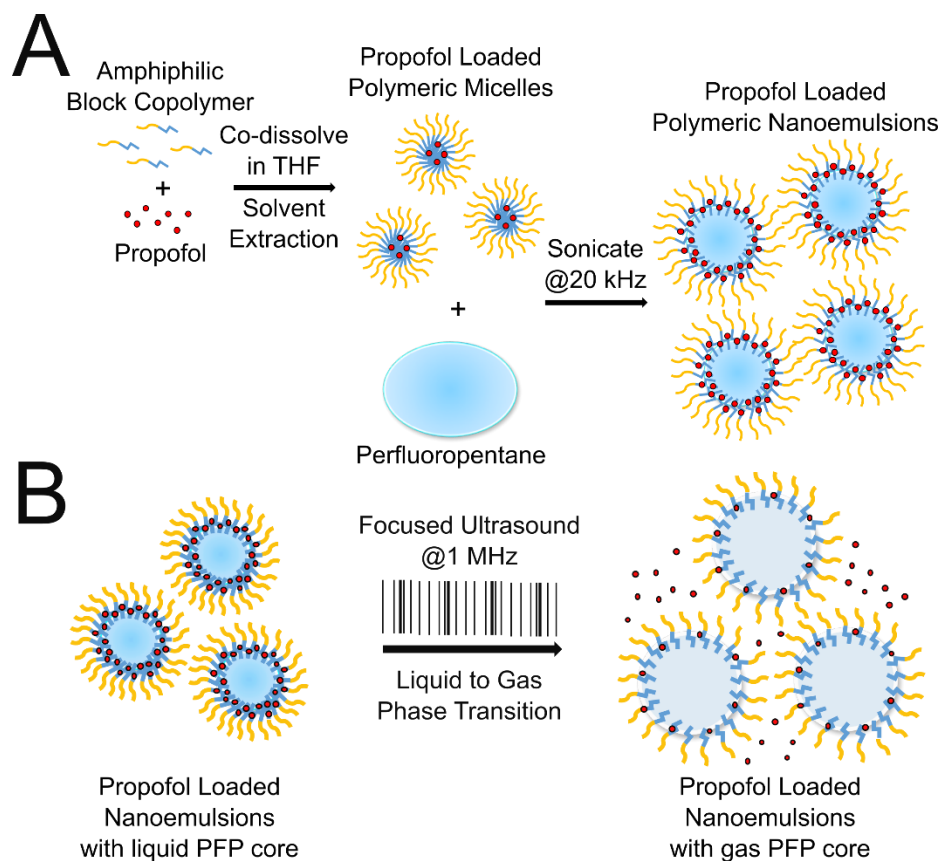


Figure 10.1: Schematic of focused ultrasound-gated drug delivery nanoparticles preparation and use. (A) To produce the propofol loaded nanoemulsions, first the block co-polymer (yellow and blue lines) and drug (red circles) are dissolved into THF, which is followed by a solvent extraction into PBS to produce propofol-loaded polymeric micelles. These micelles then emulsify liquid perfluoropentane (PFP; light blue) through sonication at 20 kHz. (B) In use, the propofol loaded nanoemulsions with a liquid PFP core are sonicated at a higher frequency such as 1 MHz in these experiments. That sonication induces a liquid to gas phase transition of the PFP which thins the encasing drug-loaded polymer shell, inducing drug release.

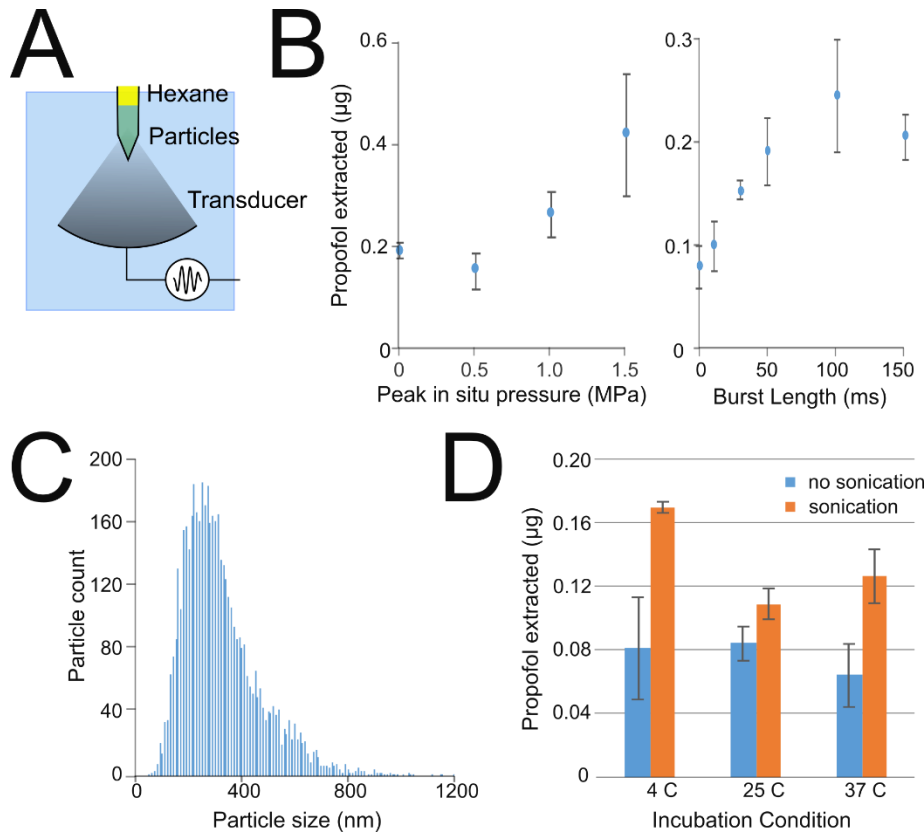


Figure 10.2: Schematic and *in vitro* characterization of nanoparticles enabling ultrasound-gated release of propofol for targeted neuromodulation (A) Schematic of *in vitro* testing apparatus. A PCR tube containing the aqueous particle sample (green) was held at the focal spot of the FUS transducer. A layer of hexane was applied on top of the sample (yellow) to serve as a chemical sink for the released propofol. (B) Sonication induces release of propofol from particles into the medium with a dose response after a threshold peak *in situ* pressure of 0.5 MPa (left); and after a threshold burst length of 10 ms (middle). The response to burst length saturates at 50-100 ms. N=3-4 samples/group (C) Histogram of particle sizes assessed by direct particle tracking demonstrates a single nano-scale peak centered at 317.6 +/- 148.2 nm (mean +/- S.D). (D) After two hours of incubation, particles were tested for release with 1.5 MPa peak *in situ* pressure and 50 ms burst lengths (N=4 samples/group). There was intact release ability after incubation, although release efficacy is relatively reduced at room (25 °C) and *in vivo* (37 °C) temperatures.

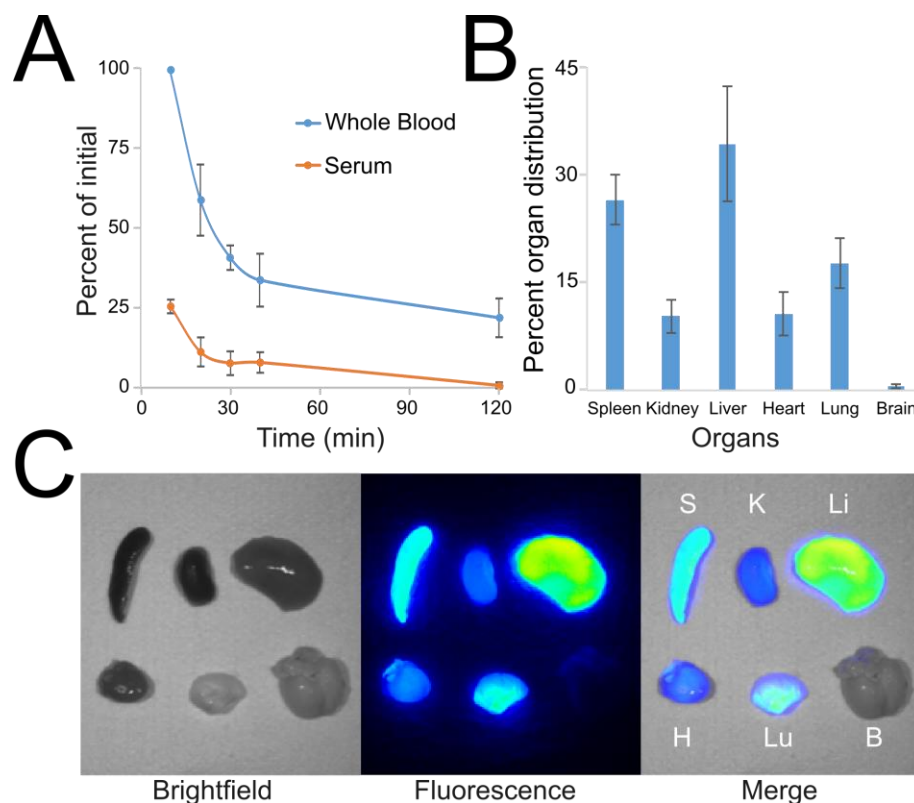


Figure 10.3: Biodistribution and clearance *in vivo* of the propofol-loaded nanoparticles. (A) Time course of the amount of an initial bolus of particles found in the intravascular space, as assessed by fluorescence of timed whole-blood samples after administration of propofol-loaded particles doped with an infrared fluorescent dye, compared to assessment of the serum fluorescence to determine the unbound dye kinetics. Presented are mean \pm S.D., normalized by the initial whole-blood sample fluorescence (N = 4 rats). (B) Organ distribution of particle uptake at 24 hours (mean \pm S.D. for 4 rats) show that particles are sequestered in expected organs such as liver, spleen, and lung, with minimal amounts seen in kidney and heart that may represent blood pool activity. No significant uptake is seen in the brain. Values are presented as their percentage of the total fluorescence across the harvested organs. (C) Sample bright field (left), fluorescence (middle), and bright field/fluorescence merged (right) images for the spleen (S), kidney (K), liver (Li), heart (H), lung (Lu), and brain (B) after harvest from a single rat.

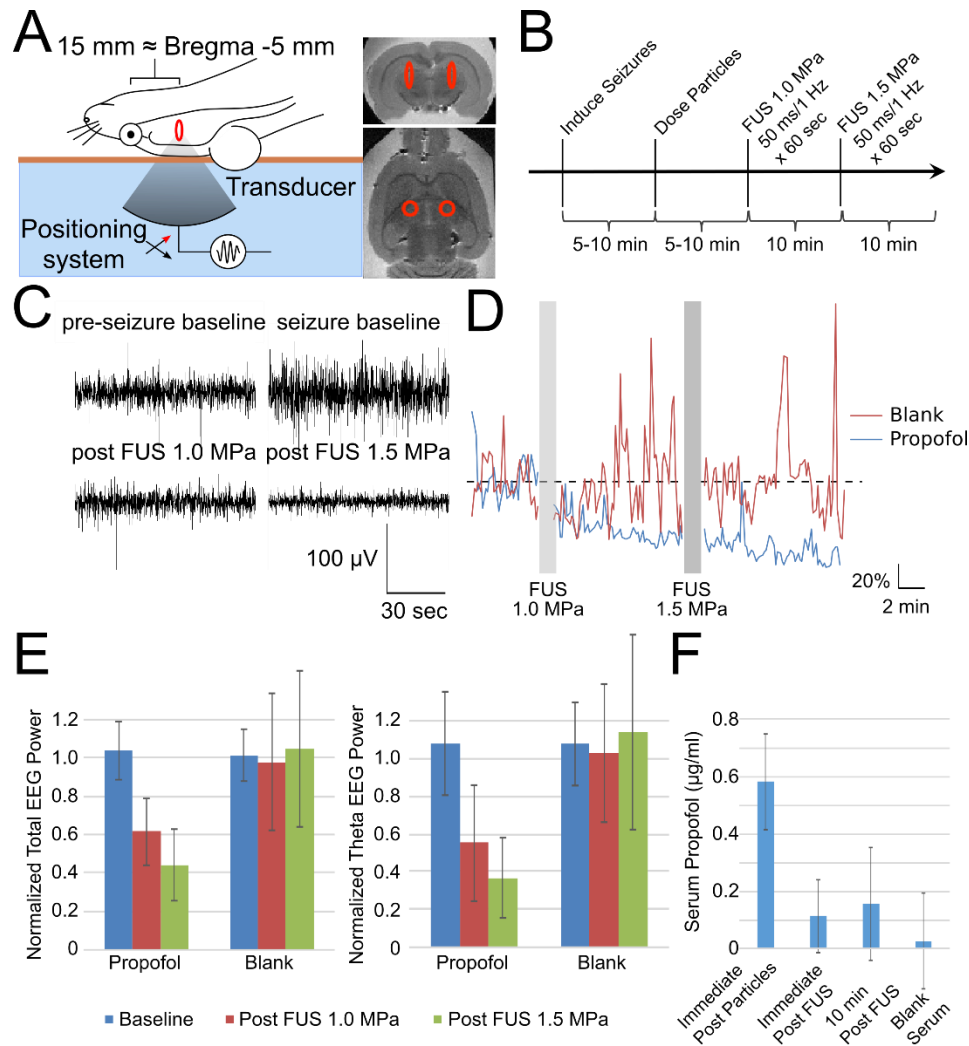


Figure 10.4: Focused ultrasound-gated propofol release is potent enough to silence seizure activity. (A) Schematic of rat positioning for this demonstration of *in vivo* efficacy. After removal of the dorsal scalp fur, rats were placed supine on the bed of a focused ultrasound transducer, coupled to the transducer via degassed water (light blue), a Kapton membrane filled with degassed water (orange-brown), and ultrasound gel (not pictured). Rats underwent seizure induction using the chemoconvulsant pentylenetetrazol (PTZ). A sonication focus (red ellipse) was developed at one target within each hemisphere, 2.5 mm lateral to midline, and 15 mm caudal to the eye center, which equals \sim 5 mm caudal to bregma. Expected location of the two sonication foci are overlaid onto *ex vivo* MRI images, with the red ellipse indicating the FWHM of the sonication focus. (B) Schematic of experiment timing for seizure induction, particle administration, and FUS application. (C) Sample traces of EEG voltage from one rat receiving propofol-loaded particles before and after seizure-induction and focused ultrasound application at the indicated pressures. (D) Total EEG power normalized by baseline averaged across rats receiving particles loaded with either propofol (blue) or no drug (Blank, red) across experiment time (N = 7 propofol, 5 blank). Gray bars indicate time of focused ultrasound (FUS) application at the indicated estimated *in situ* peak pressures, in 50 ms bursts

applied every 1 sec for 60 sec. An electrical artifact precluded EEG analysis during FUS applications. (E) Mean \pm S.D. of normalized total (left) and theta band (right) EEG power in the indicated time period across rats receiving propofol-loaded particles or blank particles (N = 7 propofol, 5 blank). Two-way ANOVA across animals receiving both FUS treatments demonstrates significant differences with FUS application ($p < 0.01$) and with particle content ($p < 0.05$). Post-hoc multiple comparison corrected tests show significant ($p < 0.01$) differences of EEG power between baseline and each of the post FUS application periods for the propofol particle treated rats only. (F) Mean \pm S.D. of the HPLC-quantified serum propofol concentration of samples from N=4 rats taken immediately after propofol-loaded particle administration, immediately after sonication, and 10 min post sonication, compared to a blank serum sample. There was no appreciable serum propofol peak for the post sonication samples.

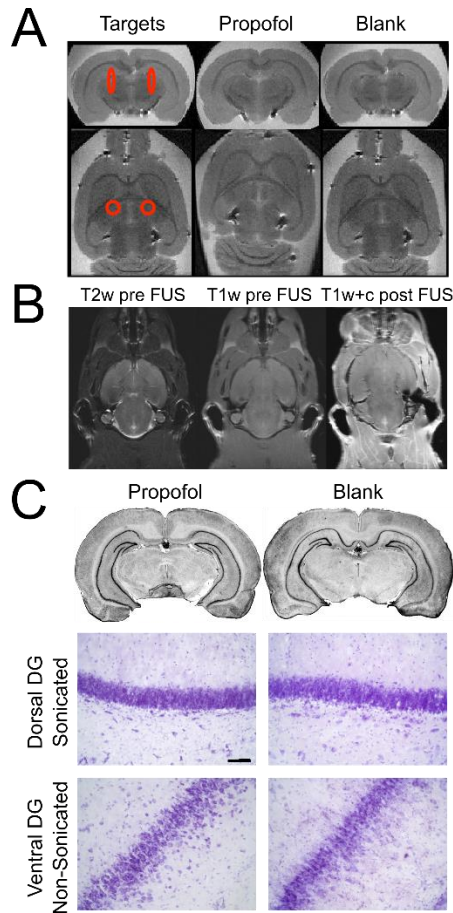


Figure 10.5: MRI and histological evaluation of brains following focused-ultrasound gated propofol release. (A) Sample whole-brain *ex vivo* 17.6 T MRI of rats treated with either propofol loaded particles or blank particles, and which underwent the seizure model and FUS application of Figure 4. Red ellipses in the left images indicate the expected location and FWHM of the sonication foci, overlaid onto the ‘Blank’ images. Black spots at the periphery of the brain on the MRI images are microscopic air bubbles that show a susceptibility related blooming artifact. Notably no such findings are present near the expected sonication field to indicate tissue damage due to either particle administration or sonication. (B) 11.7T *in vivo* MRI images taken pre-sonication (T2 and T1-weighted images left and center) and post-particle administration, post-sonication, and post-contrast administration (right) show no evidence of parenchymal damage or blood-brain barrier opening due to particle administration and sonication. (C) Cresyl violet histology shows no evidence of parenchymal damage on either wide-field views (top, 4x) or magnified views (bottom, scale bar 40 μ m) for either propofol-loaded or blank particle treated animals that received the full sonication protocol of Figure 4. The more medial dorsal dentate gyrus (DG) was within the sonication trajectory. The more lateral ventral dentate gyrus was not within the sonication trajectory and serves as a negative control for assessment of damage.

10.6 References

1. Jorgenson, L.A., Newsome, W.T., Anderson, D.J., Bargmann, C.I., Brown, E.N., Deisseroth, K., Donoghue, J.P., Hudson, K.L., Ling, G.S. MacLeish, P.R. The BRAIN Initiative: developing technology to catalyse neuroscience discovery. *Phil. Trans. R. Soc. B* 2015;370(1668):20140164.
2. Kim, H., Park, M.Y., Lee, S.D., Lee, W., Chiu, A. Yoo, S.-S. Suppression of EEG visual-evoked potentials in rats via neuromodulatory focused ultrasound. *Neuroreport* 2015;26(4):211.
3. King, R.L., Brown, J.R. Pauly, K.B. Localization of ultrasound-induced in vivo neurostimulation in the mouse model. *Ultrasound Med. Biol.* 2014;40(7):1512-22.
4. Legon, W., Sato, T.F., Opitz, A., Mueller, J., Barbour, A., Williams, A. Tyler, W.J. Transcranial focused ultrasound modulates the activity of primary somatosensory cortex in humans. *Nat. Neurosci.* 2014;17(2):322.
5. Sassaroli, E. Vykhodtseva, N. Acoustic neuromodulation from a basic science prospective. *J. Ther. Ultrasound* 2016;4(1):17.
6. Oberoi, R.K., Parrish, K.E., Sio, T.T., Mittapalli, R.K., Elmquist, W.F. Sarkaria, J.N. Strategies to improve delivery of anticancer drugs across the blood–brain barrier to treat glioblastoma. *Neuro-oncology* 2015;18(1):27-36.
7. Lin, C.-Y., Hsieh, H.-Y., Chen, C.-M., Wu, S.-R., Tsai, C.-H., Huang, C.-Y., Hua, M.-Y., Wei, K.-C., Yeh, C.-K. Liu, H.-L. Non-invasive, neuron-specific gene therapy by focused ultrasound-induced blood-brain barrier opening in Parkinson's disease mouse model. *J. Control. Release* 2016;235:72-81.
8. Samiotaki, G., Acosta, C., Wang, S. Konofagou, E.E. Enhanced Delivery and Bioactivity of the Neurturin Neurotrophic Factor through Focused Ultrasound—Mediated Blood—Brain Barrier Opening in vivo. *J. Cerebr. Blood Flow Met.* 2015;35(4):611-22.
9. Abbott, N.J., Patabendige, A.A., Dolman, D.E., Yusof, S.R. Begley, D.J. Structure and function of the blood–brain barrier. *Neurobiol. Dis.* 2010;37(1):13-25.
10. Persidsky, Y., Ramirez, S.H., Haorah, J. Kanmogne, G.D. Blood–brain barrier: structural components and function under physiologic and pathologic conditions. *J. Neuroimmune Pharm.* 2006;1(3):223-36.
11. Sharma, G., Lakkadwala, S., Modgil, A. Singh, J. The role of cell-penetrating peptide and transferrin on enhanced delivery of drug to brain. *Int. J. Mol. Sci.* 2016;17(6):806.
12. Ghanouni, P., Pauly, K.B., Elias, W.J., Henderson, J., Sheehan, J., Monteith, S. Wintermark, M. Transcranial MRI-guided focused ultrasound: a review of the technologic and neurologic applications. *Am. J. Roentgenol.* 2015;205(1):150-9.
13. McDannold, N., Clement, G.T., Black, P., Jolesz, F. Hynynen, K. Transcranial magnetic resonance imaging–guided focused ultrasound surgery of brain tumors: initial findings in 3 patients. *Neurosurgery* 2010;66(2):323-32.
14. Rapoport, N. Phase-shift, stimuli-responsive perfluorocarbon nanodroplets for drug delivery to cancer. *WIREs: Nanomed. Nanobiotechnol.* 2012;4(5):492-510.
15. Sheeran, P.S. Dayton, P.A. Phase-change contrast agents for imaging and therapy. *Curr. Pharm. Design* 2012;18(15):2152-65.

16. Rapoport, N. Drug-loaded perfluorocarbon nanodroplets for ultrasound-mediated drug delivery. *Adv. Exp. Med. Biol.* 221-41 (Springer, 2016).
17. Kamaly, N., Xiao, Z., Valencia, P.M., Radovic-Moreno, A.F. Farokhzad, O.C. Targeted polymeric therapeutic nanoparticles: design, development and clinical translation. *Chem. Soc. Rev.* 2012;41(7):2971-3010.
18. Gao, Z., Kennedy, A.M., Christensen, D.A. Rapoport, N.Y. Drug-loaded nano/microbubbles for combining ultrasonography and targeted chemotherapy. *Ultrasonics* 2008;48(4):260-70.
19. Kang, S., Johnston, M.V. Kadam, S. Acute TrkB inhibition rescues phenobarbital-resistant seizures in a mouse model of neonatal ischemia. *Eur. J. Neurosci.* 2015;42(10):2792-804.
20. Kang, S.K., Markowitz, G.J., Kim, S.T., Johnston, M.V. Kadam, S.D. Age- and sex-dependent susceptibility to phenobarbital-resistant neonatal seizures: role of chloride co-transporters. *Front. Cell. Neurosci.* 2015;9:173.
21. Lüttjohann, A., Fabene, P.F. van Luijckelaar, G. A revised Racine's scale for PTZ-induced seizures in rats. *Physiol. Behav.* 2009;98(5):579-86.
22. O'Reilly, M.A., Muller, A. Hynynen, K. Ultrasound insertion loss of rat parietal bone appears to be proportional to animal mass at submegahertz frequencies. *Ultrasound Med. Biol.* 2011;37(11):1930-7.
23. Cussonneau, X., De Smet, E., Lantsoght, K., Salvi, J.-P., Bolon-Larger, M. Boulieu, R. A rapid and simple HPLC method for the analysis of propofol in biological fluids. *J. Pharm. Biomed. Anal.* 2007;44(3):680-2.
24. Min, B.-K., Bystritsky, A., Jung, K.-I., Fischer, K., Zhang, Y., Maeng, L.-S., Park, S.I., Chung, Y.-A., Jolesz, F.A. Yoo, S.-S. Focused ultrasound-mediated suppression of chemically-induced acute epileptic EEG activity. *BMC Neurosci.* 2011;12(1):23.
25. Sadauskas, E., Wallin, H., Stoltenberg, M., Vogel, U., Doering, P., Larsen, A. Danscher, G. Kupffer cells are central in the removal of nanoparticles from the organism. *Part. Fibre Toxicol.* 2007;4(1):10.
26. Kanto, J. Gepts, E. Pharmacokinetic implications for the clinical use of propofol. *Clin. Pharmacokinet.* 1989;17(5):308-26.
27. McDannold, N., Zhang, Y., Power, C., Arvanitis, C.D., Vykhodtseva, N. Livingstone, M. Targeted, noninvasive blockade of cortical neuronal activity. *Sci. Rep.* 2015;5:16253.
28. Upton, R.N. Ludbrook, G.L. A physiological model of induction of anaesthesia with propofol in sheep. 1. Structure and estimation of variables. *Brit. J. Anaesth.* 1997;79(4):497-504.
29. Baxendale, S. The wada test. *Curr. Opin. Neurol.* 2009;22(2):185-9.

Chapter 11: Future Directions

11.1 Introduction

Throughout this thesis micro- and nanoparticle systems that possess biomimetic traits have been successfully developed. Within the three paradigms of particle shape, particle surface chemistry, and particle stimulus controlled drug release, multiple particle platforms have been developed for future therapeutic use. Despite the work completed as part of this thesis, these studies merely represent the tip of the iceberg with respect to unlocking the full potential that bio-inspired design has for biomedical therapeutics. In this chapter, we describe future directions for several of the projects detailed in the thesis, that will contribute to the development and implementation of biomimetic particles for biomedical therapeutics.

This chapter is broken up into four sections, based on the broad area of research covered in this thesis. The first section details the next steps for the development of anisotropic aAPC technology. We detail the state of the art, continuous microfluidic synthesis platform we have developed to allow for precise control over particle size. This platform was subsequently appropriated for the design of monodisperse anisotropic aAPC for cancer therapy. In addition, we summarize the potential for the use of oblate ellipsoidal aAPC for cancer immunotherapy. Oblate ellipsoids possess a significantly higher surface area than prolate ellipsoidal particles and thus could serve as a novel enhancement of aAPC technology.

This chapter contains material modified from the following article previously published as: Meyer RA, Green JJ. Biodegradable polymer iron oxide nanocomposites: the future of biocompatible magnetism. *Nanomed. Fut. Med.* 2015;10(23);3421-25.

The second section describes the potential for the use of PBAE polymers for new immunotherapeutic strategies. We describe how the PLGA/PBAE particle platform can be used not just to activate T-Cells for immunotherapy, but also to induce regulatory T-Cells for targeted immunosuppression as would be required for transplant tolerance and autoimmune disease. We also describe how the PLGA/PBAE particles can be used to induce and activate natural killer cells for a supplement to more traditional T-Cell based cancer immunotherapies. In both cases, the PLGA/PBAE particles significantly outperform their PBAE counterparts. Finally, we demonstrate how PBAEs can be used as a standalone gene therapy vector for the redirection of the cancer cell/immune cell interaction. Through transfection with immunostimulatory ligands, we successfully converted the tumor cell into a tumor-derived aAPC (taAPC) to enhance cancer immunotherapy.

The third section describes our recent efforts to enhance the surface mimicry of the anisotropic polymeric particle. Specifically, we detail the efforts to coat the particles with platelet derived membranes. Platelets exhibit interesting therapeutic properties, including tumor localization, inflammation localization, and binding to circulating tumor cells.¹ Furthermore, we describe the efforts to coat the particles with activated dendritic cell membranes to allow for the development of a truly biomimetic aAPC. This particle would possess all of the characteristics on the surface of a natural aAPC, without the potential for cell-based immune suppression. Finally, we describe the potential aspect of a functionalized supported lipid bilayer (SLB) nanoparticle designed to click to the surface of cancer cell overexpressing sialic acid analogues. Such a platform could

leverage the SLB technology to synthesize a lipid-polymer hybrid particle that could allow for effective, universal drug delivery platform for cancer.

The fourth and final section details the most recent advances in biomimetic technology for stimulus controlled drug release and therapeutic action. First we describe efforts to develop a photothermally controlled anisotropic microparticle system for precise controlled release of a therapeutic, specified by the firing of a laser. Next we detail the advances in focused ultrasound triggered drug release for the potential controlled release of anti-cancer therapeutics for retinoblastoma. Finally, we document the new polymeric particle platform that uses encapsulated magnetic nanoparticles to confer a superparamagnetic nature to the polymeric micro-and nanoparticles. Such a platform could be used as a diagnostic contrast tool in magnetic resonance imaging, or a therapeutic platform for magnetic hyperthermia based treatment of solid tumors. Continued work on these projects will allow for the next step in the realization of clinically translatable biomimetic particle technologies.

11.2 Future Directions for Anisotropic aAPC Particles

11.2.1 Synthesis of Anisotropic Monodisperse Particles

Anisotropic particles have been gaining popularity due to their useful properties in drug delivery applications.² Recently it has been shown that prolate ellipsoidal particles can serve as a platform for artificial antigen presenting cells (aAPCs).³ By conjugating a biomimetic Signal 1 protein and Signal 2 protein it has been shown that these prolate ellipsoidal aAPCs can more effectively stimulate T-Cells than spherical counterparts. Despite these studies, it has been difficult to fully evaluate this T-Cell/particle interaction owing to the polydisperse nature of synthesized particles as well

as the limited repertoire of shapes considered. The goal of this study was to develop a monodisperse, biodegradable, anisotropic particle synthesis platform for aAPC technology.

Monodisperse poly (lactic-co-glycolic acid) (PLGA) microparticles were synthesized utilizing a flow-focusing microfluidic device adapted from a previous study.⁴ Poly vinyl alcohol was appropriated as the continuous phase and PLGA dissolved in dichloromethane was the focused dispersed phase. The subsequent monodisperse particles were converted to oblate ellipsoidal, prolate ellipsoidal, or biconvave discoid particles using a thin film stretching method described previously.⁵

Monodisperse spherical PLGA microparticles were successfully synthesized using a microfluidic flow focusing device (**Figure 11.1A**). Particles were imaged by brightfield microscopy (**Figure 11.1B**) and SEM (**Figure 11.1C**) The average size of the microparticles synthesized using the method described above was 14.36 μm (**Figure 11.1D**). The polydispersity index of the microparticles was 1.05 indicating a nearly uniform population which was significantly more monodisperse than particles synthesized by bulk emulsion (**Figure 11.1D**). The monodisperse spherical particles were loaded with a fluorophore (**Figure 11.1E**) and successfully stretched into prolate ellipsoidal particles (**Figure 11.1F**).

We have developed a platform for the synthesis of monodisperse, anisotropic, biodegradable artificial antigen presenting cells. Using flow focusing technology, we have reproducibly produced anisotropic particles of defined size and shape in a process that is amenable to scaling up for translational applications. Investigation into the role of

particle shape in the development of aAPCs will be beneficial for therapeutic application of these constructs in immune system modulation.

11.2.2 Oblate Ellipsoidal aAPC for Cancer Immunotherapy

Biomimetic aAPC hold promise to serve as a “off-the-shelf” immunotherapy to treat cancer and infectious disease.⁶ Although effective *in vitro* as a standalone immunostimulatory platform, the efficacy *in vivo* has been less than sufficient to act in the absence of adoptively transferred T-Cells. Therefore, new strategies are required to augment aAPC activity to enable their use as an “off-the shelf” therapeutic. One potential aAPC parameter that has been shown to enhance T-Cell activity is particle shape. We have previously shown that the prolate ellipsoidal aAPC can induce T-cell activation significantly more effectively than the spherical particle.³ In this study, we studied the utility of oblate ellipsoidal and biconcave discoid particles as the core particle material for enhanced aAPC activity.

Anisotropic polymeric microparticles of spherical, prolate ellipsoidal, oblate ellipsoidal, and biconcave discoid shape were synthesized by single emulsion and thin film stretching as described in Chapter 3. The particles were conjugated to the MHC Class 1 IgG dimer as Signal 1 and an agonistic antibody for Signal 2 as described previously.⁷ Primary PMEL CD8⁺ T-Cells were isolated from mouse spleens and labeled with CFSE for proliferation analysis. The particles were then incubated with the T-Cells to evaluate immune stimulation. After three days of incubation, the T-Cells were analyzed by flow cytometry to evaluate proliferation and after seven days the cells were manually counted to determine proliferation fold.

Oblate ellipsoidal aAPC demonstrated significantly enhanced T-Cell stimulation compared to prolate ellipsoidal and biconcave discoids, which in turn were superior to spherical microparticles. As evaluated by CFSE dilution, there was a significant increase in the magnitude of the proliferation peaks of the oblate ellipsoidal, compared to the other shapes (**Figure 11.2A**). Furthermore, the manual proliferation counts supported this trend. At limiting doses of 0.01 mg aAPC/100,000 T-Cells and 0.005 mg aAPC/100,000 T-Cells, there was a higher amount of T-Cells counted at both doses for the oblate ellipsoidal particles compared to other shapes. The prolate ellipsoidal particles and spherical particles exhibited stronger proliferation than the spherical particles, but this was not shown to be higher than that of the oblate ellipsoidal particles. (**Figure 11.2B**) Taken together, this suggests the oblate ellipsoidal aAPC are the superior platform for T-Cell activation.

In this study, we have developed aAPC of spherical, prolate ellipsoidal, oblate ellipsoidal, and biconcave discoidal shape and compared their relative influence on T-Cell activation. We found that the oblate ellipsoidal aAPC performs stronger than that of the other shapes, and that the prolate ellipsoidal and biconcave discoidal outperform the spherical. Taken together these results shed new light on the role of shape on aAPC design and shed light on potential enhancements to be made to enable aAPC to function as a standalone therapy.

11.3 Future Directions for PLGA/PBAE Cationic Polymer Blended Particles

11.3.1 PLGA/PBAE aAPC for Regulatory T-Cell Induction

Modulation of regulatory T-Cells hold promise to treat a variety of diseases where immunosuppression is the intended therapeutic outcome such as in the case of transplant tolerance⁸ and autoimmune disease.⁹ Although there has been significant research in the induction of regulatory T-Cells for this purpose,¹⁰ the promise of antigen-specific T-Reg induction *in vivo* remains elusive. Here we demonstrate the potential for the PLGA/PBAE aAPC to serve as a potential platform for “off-the-shelf” T-Reg induction. Such a construct would enable antigen targeted suppression of the immune systems in situations such as transplant tolerance and autoimmune disease.

PLGA/PBAE microparticles were synthesized by a single emulsion technique using a blend of custom synthesized PBAE and commercially purchase PLGA as described in Chapter 6. The particles were conjugated to anti-CD3 to serve as the Signal 1 and anti-CD28 to serve as the Signal 2. Naïve mouse helper T-Cells were isolated a selection protocol for CD4⁺ and against CD25⁺ cells as previously described.¹¹ PLGA/PBAE aAPC or PLGA aAPC were incubated with the naïve mouse T-Cells for five days in the presence of IL-2 and TGF- β to direct T-Cell phenotype towards the regulation. After five days, the cells were stained for CD4 and Foxp3 to evaluate regulatory T-Cell induction.

PLGA/PBAE aAPC were able to mediate a significant increase in percent induction of regulatory T-Cells compared to PLGA aAPC (**Figure 11.3**). The PLGA/PBAE particles and PLGA particles were tested at low, mid, and high doses of surface protein administered on various particle doses. At the low and mid-range protein dose, the PLGA/PBAE aAPC demonstrated significantly higher levels of T-Reg induction compared to PLGA aAPC at all particle doses tested (**Figure 11.3A-B**). At the

high dose, there was a significant increase in T-Reg induction, however the effect was not as significant, indicating a potential protein saturation effect observed for both particle types. (**Figure 11.3C**)

In this study, we have developed an enhanced aAPC for T-Reg induction. The PLGA/PBAE platform serves as a stronger core material for surface protein presentation compared to the PLGA particle. Future incorporation of an MHC Class II tetramer, loaded with the antigen of choice could lead to this novel particle based platform for antigen specific T-Reg induction. Such an advancement in aAPC technology would allow for new frontiers to be achieved in targeted immunosuppression for transplant tolerance and autoimmune disease.

11.3.2 PLGA/PBAE aAPC for Natural Killer Cell Activation

Natural killer (NK) cells' ability to selectively destroy tumor cells without requiring antigen specificity makes them a valuable weapon that can be harnessed for cancer immunotherapy. However, immunosuppressive cues in the tumor microenvironment decrease the activity of NK cells, limiting their ability to recognize and destroy cancerous cells.¹² This problem is being addressed with therapies that target NK cells and restore their cytotoxic abilities. Adoptive NK cell therapies have shown success in a variety of murine cancer models, but these therapies can be costly and limited in scalability. As an alternative strategy, we have developed a microparticle-based system with the ability to expand NK cell populations *in vitro*.

Microparticles were synthesized from poly (lactic-co-glycolic acid) (PLGA) or a blend of PLGA and poly (beta-amino ester) (PLGA/PBAE) using a single emulsion technique. The particles were functionalized with anti-CD134 (OX40), anti-CD137 (4-

1BB), or a combination of both (4-1BB+OX40) monoclonal antibodies through EDC/NHS chemistry. To evaluate the ability of different surface-conjugated proteins to stimulate NK cells *in vitro*, we isolated NK cells from B6 mice and incubated them with 4-1BB, OX40, or 4-1BB+OX40 microparticles in the presence of IL-2. After 7 days, NK cells were counted manually to assess proliferation. To investigate the effects of polymer type on the ability of particles to expand NK cell populations we isolated and cultured NK cells with PLGA and PLGA/PBAE microparticles conjugated with anti-4-1BB in the presence of various IL-2 concentrations. At the end of 3 days, NK cell proliferation was assessed.

Following synthesis, scanning electron microscopy was used to image PLGA (**Figure 11.4A**) and PLGA/PBAE (**Figure 11.4B**) microparticles and confirm their size and morphology. After seven days in culture, 4-1BB particles led to stronger NK cell proliferation in a dose-dependent manner compared to OX40 or 4-1BB+OX40 particles (**Figure 11.4C**). PLGA/PBAE microparticles conjugated with anti-4-1BB led to an approximately 50-fold increase in proliferation over PLGA particles (**Figure 11.4D**). Varying the concentration of soluble IL2 from 50 to 1000 U/mL did not significantly affect NK cell proliferation.

We have developed a novel particle-based method using 4-1BB-conjugated PLGA/PBAE microparticles to effectively expand NK cell populations *in vivo*. These particles show potential as a platform for natural killer cell-mediated cancer immunotherapy.

11.3.3 Redirection PBAE Transfection Nanoparticles for Cancer Immunotherapy

Advances in cancer immunotherapy have great potential for combatting tumors that are refractory to conventional treatments.¹³ T-cells can be primed to kill cancer cells

by antigen-presenting cells (APCs), which present three crucial signals: Signal 1, major histocompatibility complex (MHC) I with a tumor antigen (Ag) peptide; Signal 2, a co-stimulatory molecule; and Signal 3, secreted cytokines that promote T-cell recruitment, growth, and differentiation.^{14,15} Here, we use synthetic nanoparticles (NPs) to transfect melanoma cells with DNA encoding a Signal 2 co-stimulatory molecule and Signal 3 cytokine, effectively reprogramming these cells into tumor-derived APCs (tAPCs). *In vitro* assays show T-cell stimulation by melanoma tAPCs, and intratumoral injection of NPs into a murine B16-F10 melanoma shows significantly slowed tumor growth. This reprogramming approach represents a novel strategy for immunotherapy that could have potentially broad impact on many types of hard-to-treat cancer.

A poly(beta-amino ester) (PBAE) for non-viral gene delivery was synthesized by Michael addition and used to transfect B16-F10 melanoma cells *in vitro* as previously described, using red fluorescent protein (RFP) to optimize NP formulation.¹⁶ Cells were then transfected with 4-1BBL (Signal 2) and IL-2 (Signal 3) plasmids and co-cultured with antigen-specific CD8⁺ T-cells *in vitro*. T-cell activation was assessed by IFN- γ secretion. For *in vivo* efficacy, C57BL/6 mice with subcutaneous B16-F10 tumors were injected once intratumorally (i.t.) with PBAE/DNA NPs encoding either 4-1BBL or a control gene, and tumor size was assessed over time using calipers.

B16-F10 melanoma cells can be transfected with high (>90%) efficacy using PBAEs. Cells can also be co-transfected with signal 2 (4-1BBL) and 3 (IL-2). Surface 4-1BBL expression was measured by flow cytometry, and secreted IL-2 was measured by ELISA (**Figure 11.5A-B**). The relative expression of each can be tailored by the ratio of plasmids used in transfection. Transfected B16-F10 tAPCs induced significantly greater

($p < 0.05$) IFN- γ secretion by CD8⁺ T-cells after co-culture, indicating their ability to activate T-cells. Crucially, injection of PBAE/DNA NPs into a tumor resulted in substantially slowed tumor growth (**Figure 11.5C**) in an aggressive murine melanoma model that is generally known to have low immunogenicity.

PBAE NPs can transfect tumor cells with co-stimulatory molecules and immunostimulatory cytokines to reprogram them, leading to decreased tumor growth. Importantly, by hijacking the intrinsic expression of Signal 1 by tumor cells, this acellular, off-the-shelf immunotherapy is antigen-agnostic and has the potential to be broadly applicable to multiple types of hard-to-treat tumors across patients.

11.4 Future Directions for Biomimetic Particle Membrane Coating

11.4.1 Platelet Membrane Coated Anisotropic Microparticles

There is growing interest in engineering biomimetic particles that are coated with naturally derived cell membranes to extend half-life *in vivo* and mimic the functionality of different cell types. Particles have been coated with the cell membranes from red blood cells, platelets, leukocytes, cancer cells, etc. and have promising therapeutic potential.^{1,17} However, all previous work has used spherical particles. Particle shape is an important aspect of cellular biomimicry and has been shown to have a large impact on the drug delivery properties of particle therapeutics.¹⁷ Here, we have fused vesicles derived from platelets with anisotropic poly(lactic-co-glycolic acid) (PLGA) microparticles to enhance the stealth properties of these particles for drug delivery purposes and to develop a novel wound healing therapy.

Nonspherical platelet shaped (discoid shaped) and ellipsoidal microparticles that mimicked the size of platelets (approximately 1 μm in diameter) were synthesized by

emulsion methods followed by thin film stretching in two dimensions or one dimension, respectively.⁵ Particles were imaged using scanning electron microscopy (SEM) to confirm shape and size. Human platelets were activated using adenosine 5'-diphosphate (ADP) in the presence of ethylenediaminetetraacetic acid (EDTA) to prevent aggregation. Activated platelets were snap frozen and then thawed at room temperature. Platelets were then processed into 200 nm-sized vesicles through sonication, and vesicles were subsequently coated on PLGA particles under sonication. Vesicles were fused with a fluorescent lipid mediated by a PEGylated accessory lipid in order to visualize the membranes under confocal microscopy. Anisotropic nanoparticles were generated and coated with cell membranes using a similar protocol and stained with fluorescent anti-CD47 to verify coating.

We visualized the coated microparticles using confocal microscopy and found that there was a clear enrichment of the fluorescent membrane signal on the surface of the spherical, ellipsoidal, and platelet-shaped particles indicating successful coating with activated (**Figure 11.6**). We confirmed the presence of CD47 on coated spherical and anisotropic nanoparticles, verifying successful coating. CD47 prevents phagocytosis by macrophages. Thus, the presence of this protein on the particles may prevent uptake and clearance by the mononuclear phagocyte system, prolonging circulation in the blood. We are currently developing a microfluidic device vasculature model that will assess the functionality of the platelet-coated particles. The device is coated with factors, such as collagen and von Willebrand factor, that are typically found in the subendothelial space exposed in the formation of a wound. This device will be used with the platelet-coated

particles to determine their ability to bind these factors and aggregate with each other and the body's own platelets under physiological shear flow.

We have successfully engineered activated platelet coated particles with the potential to evade clearance *in vivo* by mimicking the shape, membrane content, and fluidity of natural cells. This platform could provide a modular and versatile technology for enhancing drug delivery that can be applied to many different cell types and functions. Additionally, we are investigating the potential for using the platelet-coated particles as biodegradable artificial platelets for wound healing applications.

11.4.2 Dendritic Membrane Coated Microparticles

Artificial antigen presenting cells that have been developed in the past are typically engineered from a minimalist standpoint with two proteins serving as a Signal 1 and Signal 2. Although effective for T-Cell stimulation, this strategy represents the bare minimum of signals to adequately direct and modulate T-Cell activity as is done *in vivo*.¹⁸ Therefore, we propose an alternative approach in which the antigen presenting cell membrane itself is directly immobilized onto the surface of the particle. This would allow for optimal presentation of all required surface ligands for T-Cell activation, without the potential for immunosuppression of the antigen presentation system. In this study, we have demonstrated that the polymeric microparticle can be successfully coated with dendritic cell membrane derived vesicles.

Dendritic cell membrane vesicles were prepared in a similar fashion to a procedure previously reported.¹⁹ Briefly a confluent T-175 flask of the dendritic cell line DC 2.4 was detached from a flask and washed 3 times with PBS. The cells were then suspended in 1 mL ACK lysis buffer and homogenized with a 2mL Dounce homogenizer

using a tight- fitting pistil. The cell lysate was spun at 3200 g for 5 min to remove intact cellular and nuclear material and the supernatant was reserved. Then the pellet was resuspended in 1 mL ACK lysis buffer and homogenized again. The second cell lysate was spun out again and the supernatant was pooled with the supernatant collected from the previous spin. The pooled supernatants were then spun out at 17000 g for 20 min to remove subcellular organelles. The supernatants of this spin were then collected and spun once more at 100,000g for 1 hr. to remove the membrane vesicle fraction. These vesicles were then resuspended in PBS and mixed with 1 mg of PLGA for the membrane coating.

To analyze the formation of supported biomimetic dendritic cell membranes, confocal imaging of PLGA particles encapsulating 7-AMC were coated with rhodamine containing membrane derived vesicles. Confocal image acquisition was completed with a Zeiss 780 FCS Confocal Microscope. Acquired images demonstrated a clear increase in fluorescence of the dendritic cell membrane derived vesicle, compared to the dye in the particle core (**Figure 11.7**). Furthermore, this fluorescence was localized to the outside of the particle as has been exhibited recently with lipid coated polymeric particles that were deemed functional by *in vitro* and *in vivo* functional assays (see Chapter 8).

In this study, we have shown that polymeric microparticles can successfully be coated with antigen presenting cell membranes for a truly biomimetic surface to enhance aAPC technology. The activity of the cell membrane itself in stimulating immune cells for cancer immunotherapy would not be altered by tumor derived suppression mechanisms. This result represents another step forward in the translation of highly biomimetic therapeutics for cancer immunotherapies.

11.4.3 Functionalized Membrane Coating for Sugar Analog Based Cancer

Therapeutics

Delivery of anti-cancer drugs through actively targeted nanoparticles has been a subject of great recent interest.²⁰ Through encapsulation of a therapeutic molecule and immobilization of targeting ligand, these platforms have had success in treating malignant tumors in various contexts.²¹ One challenge that is prevalent in these targeting ligand approaches is the heterogeneity of cancer cells. A more effective strategy would be one that exploits a universal feature of cancer for directed localization of drug loaded nanoparticles to target cell membranes. Taking advantage of the upregulation of sialic acid presentation on cancer cell membranes,²² unnatural azido sialic acid analogues can be employed to allow nanoparticle accumulation to a cancer cell membrane through copper-free click chemistry.²³ In this study, we developed a dibenzocyclooctyne (DBCO) functionalized lipid-polymer hybrid nanoparticle for directed delivery of anti-cancer therapeutics.

DBCO functionalized nanoparticles were synthesized via single emulsion of a mixture of poly(lactic-co-glycolic acid) 4% w/w lipids containing DBCO and rhodamine for imaging. The analogue used was 1,3,4 Bu₃ManNAz and synthesized as previously described.²⁴ To establish the general applicability of this therapeutic approach we evaluated nanoparticle accumulation on the SW1990 (pancreatic), PANC1 (pancreatic), BXPC3 (pancreatic), GB319 (brain), MDA MB 231 (breast) cancer cell lines and the non-cancerous MCF10A breast epithelial cell line. Cells were incubated with 50 μ M of sugar analogue for 72 hours and then with DBCO functionalized nanoparticles for 1 hour.

Cells were subsequently imaged by fluorescence microscopy for evaluation of nanoparticle accumulation.

Nanoparticles were successfully synthesized and determined to be approximately 200 nm in size. DBCO functionality was confirmed through the successful capture of an azide bearing fluorophore. The nanoparticles were shown to specifically accumulate at MDA MB 231 cell membranes following treatment with the sugar analogue and DBCO containing nanoparticles (**Figure 11.8A-C**). In addition, this accumulation was determined to be specific to cancer cell lines as the healthy cell line tested exhibited no significant accumulation of nanoparticles compared to a no-treatment control (**Figure 11.8D**). For various cancer cell lines, this accumulation was determined to be 3-8 fold over the no-treatment control.

In this study, we have successfully developed DBCO functionalized lipid/polymer hybrid nanoparticles to enable cancer targeted drug delivery. These nanoparticles were shown to specifically associate with a variety of cancer cells, while not associating with a healthy cell line. Further development of universal targeting strategies such as this one may have great potential for translational cancer therapies.

11.5 Future Directions for Stimulus Controlled Therapeutics

11.5.1 Photothermally Triggered Drug Release from Anisotropic Particles

There has been recent interest in the development of spatiotemporally controlled drug release systems for various biomedical applications, including for treating cancer.²⁵ One promising platform achieve this goal is through the use of photothermal conversion of light energy into thermal energy for hyperthermia and glass transition temperature controlled drug release through the use of thermoplastic polymers and gold

nanoparticles.²⁶ Although photothermal therapy is promising from a theoretical standpoint, the gold nanoparticles achieve extreme temperatures that could potentially be damaging to healthy tissues.²⁷ We propose to encapsulate hydrophobically stabilized gold nanorods in polymeric particles to enable a thermal diffusion controlled heat source for photothermal therapy. Moreover, the polymers can be loaded with anti-cancer therapeutics for the glass transition temperature controlled release of the drug during the photothermal hyperthermia therapy. Such a platform would allow for spatiotemporally controlled release of heat and drug for localized cancer therapy.

We synthesized hydrophilic gold nanorods using a seed growth process as previously described.²⁸ Through a capping ligand exchange process and a subsequent solvent exchange process, we generated stable gold nanorods that can be dispersed in an organic solvent for encapsulation in polymeric particles. The gold nanorods were then evaluated upon encapsulation to determine absorbance properties for photothermal therapy. In a separate experiment, we also evaluated thermally controlled drug release from two polymer candidates (PLGA and PDLLA) with glass transition temperatures in the acceptable range for photothermal hyperthermia.

Gold nanorods were successfully synthesized using a seed growth technique (**Figure 11.9A**). Through modulation of the silver content in the crystal growth media, we were able to synthesize nanorods with an aspect ratio to yield an absorbance peak of 800 nm (**Figure 11.9B**). This wavelength is in the near IR range to allow for sufficient penetration of biological tissue to achieve photothermal activation of the nanorods *in vivo*. Upon TEM analysis of the particles encapsulating gold nanorods, we found that the gold nanorods were intact and did not aggregate extensively (**Figure 11.9C-D**). The

thermally controlled drug release experiment determined that PLGA has a doxorubicin release in a switch-like response once the temperature exceeds that of the polymer glass-transition temperature ($\sim 45^\circ\text{C}$). Significant drug release was not observed with the PDLLA for the duration of the heating (4 hrs.).

In this study, we have successfully developed gold nanorod polymer composites that can be used for safe photothermal hyperthermia as well as thermally controlled drug release. The gold nanorods do not substantially aggregate during the encapsulation process and maintain their absorptive properties for photothermal conversion. Furthermore, the PLGA polymer used had a switch-like drug release response between 37°C and 60°C , suggesting this as a potential candidate for a combined platform for hyperthermia and chemotherapy of localized tumors. Continued development of this platform could allow for spatiotemporally controlled treatment of cancer through dual localized heat and drug therapy.

11.5.2 Focused Ultrasound Triggered Release of Doxorubicin for Retinoblastoma Therapy

Retinoblastoma is a major cause of cancer in young children of less than 3 years of age.²⁹ Although treatment is usually successful with radiation and chemotherapies, typically the patient loses vision in the eye or eyes that the tumor has manifested.³⁰ Therefore, there is a need to design more effective localized chemotherapies that can treat the tumor without adverse systemic toxic effects. Nanoparticulate controlled release platforms offer an alternative to systemic treatment and it has been found that these particles can maintain a therapeutic concentration of chemotherapies in the eye, without the adverse toxic events associated with systemic administration.³¹ We propose to use a

recently developed nanoemulsion system³² with focused ultrasound triggered release of a chemotherapeutic. In this manner, precise spatiotemporal control can be appropriated for the local treatment of the retinoblastoma, potentially sparing the patient's vision.

We developed a focused ultrasound triggered release platform for doxorubicin to treat retinoblastoma. The nanoemulsions are based on a formulation we described previously in Chapter 10 for focused ultrasound mediated delivery of propofol. Micelles of an amphiphilic block copolymer were formed, encapsulating doxorubicin using solvent extraction. The micelles were then used to emulsify perfluoropentane to form doxorubicin loaded polymeric nanoemulsions. The nanoemulsions were then evaluated for their release of doxorubicin through tip sonication at 20 kHz at various amplitudes and burst lengths followed by fluorescence analysis of the supernatant to evaluate drug release in response to the ultrasound.

Polymeric nanoemulsions encapsulating doxorubicin were successfully formed and had a size of approximately 400-500 nm. The nanoemulsions were evaluated for ultrasound triggered release of doxorubicin vs. spontaneous release over time to determine the control over the release effect (**Figure 11.10**). We found that the nanoemulsions released doxorubicin in proportion to the amplitude of the ultrasound and time of sonication thus indicating a dose response and control of the release rate. Furthermore, we found that the nanoemulsions released drug 600% faster when in the presence of the ultrasound thus demonstrating the ability for controlled acceleration of the drug release rate for localized administration in retinoblastoma patients.

In this study, we have developed a novel doxorubicin loaded perfluoropentane nanoemulsion for the focused ultrasound triggered release of chemotherapy for

retinoblastoma. Further optimizations into the particle design and stability of the nanoemulsions will allow for enhanced spatiotemporal control over the delivery of this therapeutic for ocular oncology applications.

11.5.3 Anisotropic Magnetic Particles for Enhanced Biomedical Therapeutics

Superparamagnetic iron oxide nanoparticles (SPIONs) have become increasingly popular for various biomedical applications. The superparamagnetic properties of these nanoparticles enable their magnetic manipulation of biological targets such as cells, proteins, and nucleic acids. In addition, SPIONs allow for magnetic resonance imaging (MRI) contrast for cells and tissues. Although generally nontoxic, these particles on their own are not sufficiently biocompatible due to their inorganic nature. One strategy to circumvent this compatibility issue is to coat the SPIONs with a biocompatible polymer. Although polymer coating is effective at mitigating potential complications at the SPION/biological interface, this only scratches the surface of the functionality that can be enabled by polymer-SPION nanocomposites. For example, polymeric nanostructures can have multifunctional drug delivery abilities, including control of the delivery of biological payloads in both space and time. An emerging strategy is to combine the advantages of inorganic SPIONs with the drug delivery capabilities of biodegradable polymeric particles to create multifunctional theranostic polymer-SPION nanocomposites. By treating the SPIONs as a cargo to be loaded into larger biodegradable polymeric nanostructures, new nanocomposites can be created to unite the beneficial features of paramagnetism and controlled drug release into one single nanoparticle. Biodegradable polymer iron oxide nanoparticles are promising for applications to many areas of medicine

Incorporation of SPIONs into a nanocomposite confers all of the superparamagnetic related properties of SPIONs to the entire nanocomposite. In addition, these biodegradable polymer SPION nanocomposites can be loaded with other entities as well such as drug payloads and quantum dots for functionality as therapeutics and multimodal imaging agents respectively.³³ These encapsulated SPIONs have been shown not to interfere with particle physical properties such as size and shape, while at the same time maintaining sufficient magnetic susceptibility to allow them to be used in varied biological applications.³⁴

Generally, these nanocomposites are synthesized via modified emulsion or precipitation methods that are commonplace in particle fabrication techniques. The surface character of the SPION dictates whether single emulsion or double emulsion is appropriate. For hydrophobic SPIONs, synthesized by thermal decomposition of organic iron precursors or co-precipitation followed by organic ligand capping, the iron oxide can be co-dissolved directly into the organic phase with any other hydrophobic drugs or molecules, and subsequently be emulsified to generate nanocomposites. Such procedures have shown to yield excellent SPION loading into poly(lactic-co-glycolic acid) (PLGA) nanoparticles.³⁵

We have successfully replicated this procedure to synthesize PLGA microparticles loaded with hydrophobic magnetic nanoparticles. The PLGA particles aggregate when brought in proximity to a magnet and subsequently disperse when they are removed from the magnet (**Figure 11.11A**). We also conducted a T2 weighted scan of the microparticles in an MRI (**Figure 11.11B**). We found that the magnetic PLGA microparticles can provide sufficient contrast at a limiting dose of 10 $\mu\text{g/mL}$ (**Figure**

11.11C). Furthermore, we found that the encapsulation of the magnetite did not interfere with the ability to deform the particles into anisotropic shapes using the thin film stretching method or the magnetic properties of the SPIONs.

In this study, we have successfully adapted a protocol to encapsulate hydrophobically labeled SPIONs in anisotropic polymeric microparticles. The microparticles encapsulating nanoparticles exhibit superparamagnetic properties and MRI contrast to a limiting dose. Combining the properties of superparamagnetism with the ability of anisotropic particles to resist non-specific elimination and enhance targeted binding, this approach could lead more effective magnetic field based therapies for tumor hyperthermia and diagnostic contrast.

11.6 Conclusions

In this chapter, we have summarized the relevant future directions for the biomimetic and bio-inspired micro- and nanoparticulate systems described in this thesis. For anisotropic aAPC cancer immunotherapy, synthesis of oblate ellipsoidal particle through a continuous, scaled microfluidic process may yield a translatable product that can be used as an “off-the-shelf” therapeutic. The use of PLGA/PBAE particles to modulate different functions of the immune system including T-Reg induction, natural killer cell activation, or tumor immunosuppression could expand the concept of aAPC technology to different therapeutic scenarios. Further research into bio-interfacing micro- and nanoparticles through the use of platelet or dendritic cell membranes, or through the use of sugar analogues for universal cancer therapy can accelerated their clinical translation for a variety of drug delivery applications. Finally, the use of stimulus controlled drug techniques such as photothermal conversion by gold nanorods, focused

ultrasound triggered vaporization of a volatile solvent, or magnetically activated and polymerically encapsulated SPIONs could allow for spatiotemporally controlled, local release of chemotherapeutics for various cancers or enhanced MRI based diagnostics. The potential of biomimetic particle technologies for biomedical applications is indeed being realized through these and many other projects using bio-inspired designs. With these criteria, the future of micro- and nanoparticle biological interfacing is now and the imminent translation of these materials will revolutionize biomedical therapeutics.

11.7 Figures

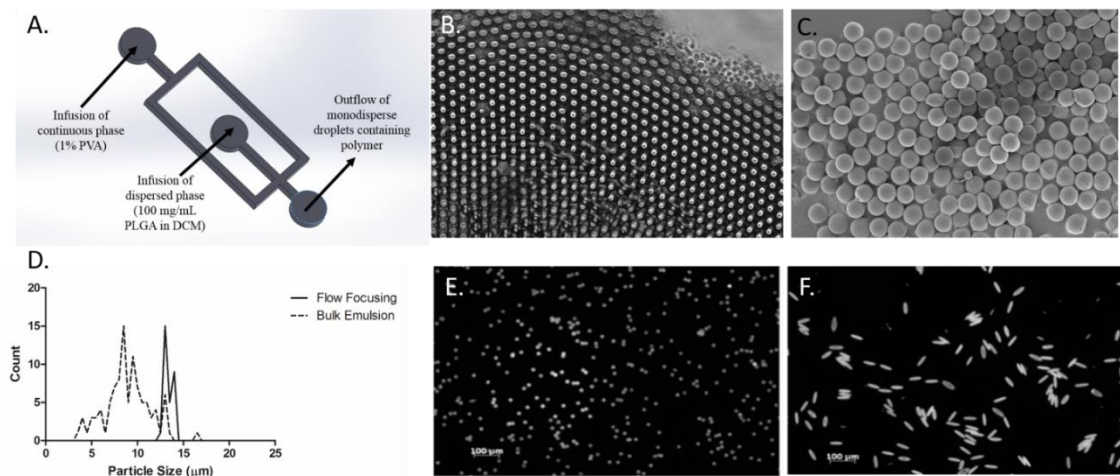


Figure 11.1: Synthesis of monodisperse anisotropic microparticles. (a) Schematic of the flow-focusing microfluidic device for the synthesis of monodisperse microparticles. The polymer solution forms the dispersed phase in the flow focusing device and the aqueous emulsifying solution forms the continuous phase. (a) Brightfield image of monodisperse particles demonstrates highly uniform crystalline like structure in aqueous solution. (c) SEM images of microparticles synthesized by microfluidic device that were used to derive particle size information. (d) Size distribution of monodisperse microparticles indicates significantly lower polydispersity than the particles synthesized by bulk emulsion. (e) Spherical particles encapsulating fluorophores were (f) Stretched by the thin film stretching method to generate monodisperse prolate ellipsoidal microparticles.

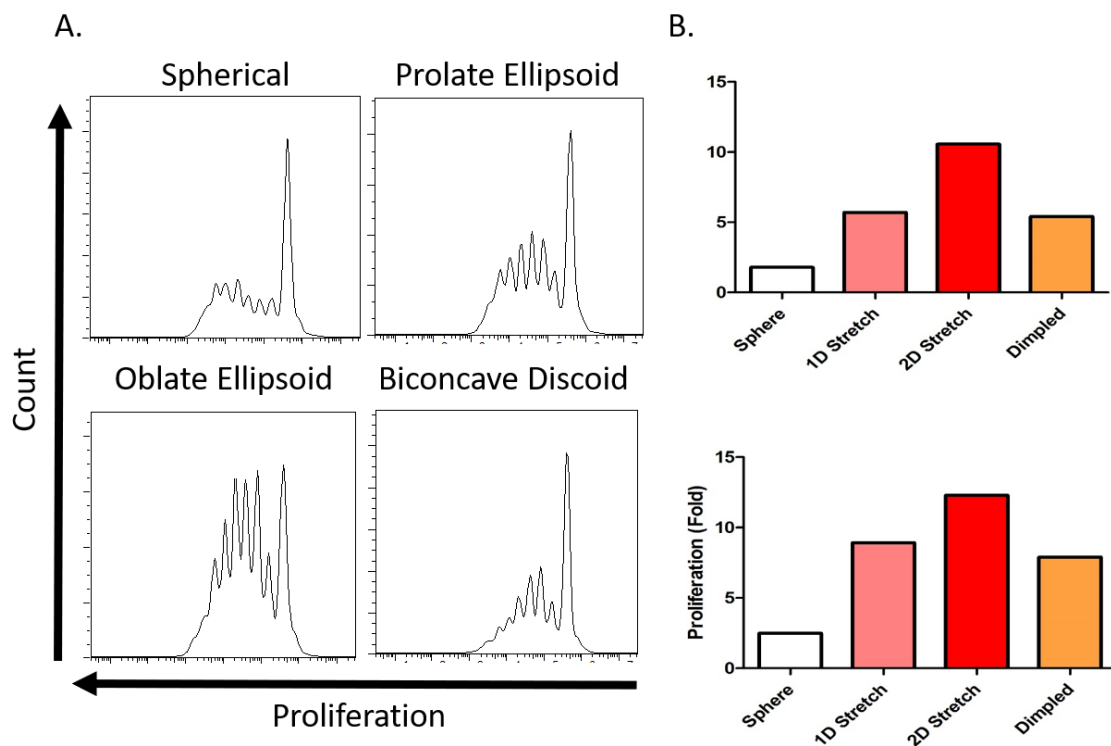


Figure 11.2: Oblate ellipsoidal microparticles outperform prolate ellipsoidal, biconcave discoid, and spherical particles in a T-Cell proliferation assay. (a) Oblate ellipsoidal particles resulted in more proliferating as evidenced by CFSE dilution analysis three days post stimulation. (b) Manual proliferation counts T-Cells stimulated with particles of different shapes reveals similar enhanced proliferation by the oblate ellipsoidal particles.

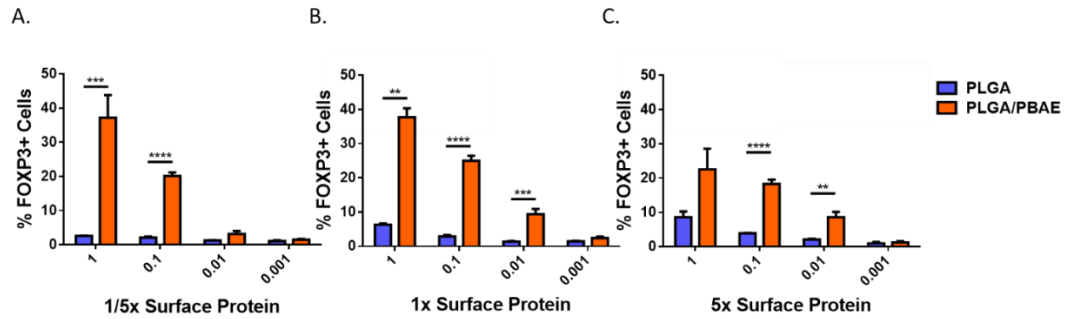


Figure 11.3: PLGA/PBAE aAPC successfully induce high levels of regulatory T-Cells. PLGA or PLGA/PBAE microparticles were synthesized with (a) low, (b) medium, and (c) high levels of signal proteins, and incubated with naïve T-Cells in the presence of TGF- β . Percent Foxp3+ T-Cells across multiple doses were higher for PLGA/PBAE vs PLGA alone. (** = $p < 0.01$, *** = $p < 0.001$, and **** = $p < 0.0001$ by two-way ANOVA with Bonferroni's post-test).

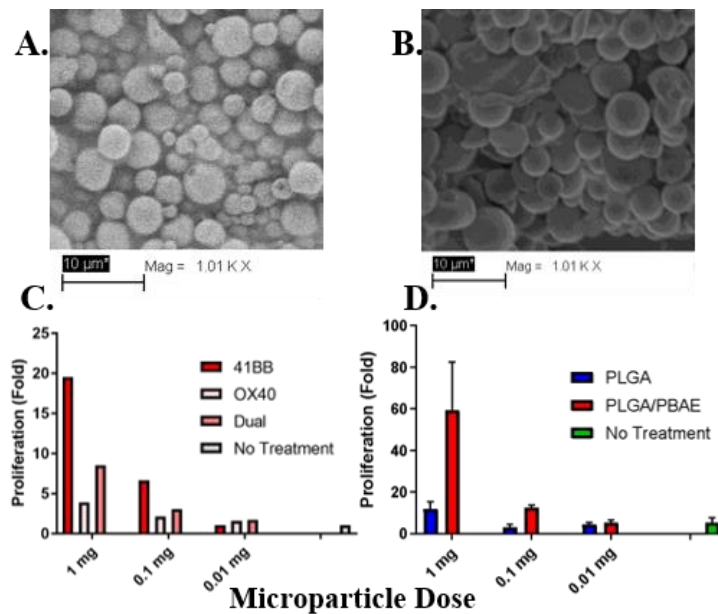


Figure 11.4: Natural killer cell activation is enhanced by the use of PLGA/PBAE particles. SEM images of (A) PLGA and (B) PLGA/PBAE microparticles. (C) *In vitro* NK cell proliferation mediated by 4-1BB particles is stronger than OX40 and 4-1BB+OX40 particles. (D) PLGA/PBAE microparticles lead to higher NK cell proliferation compared to PLGA microparticles.

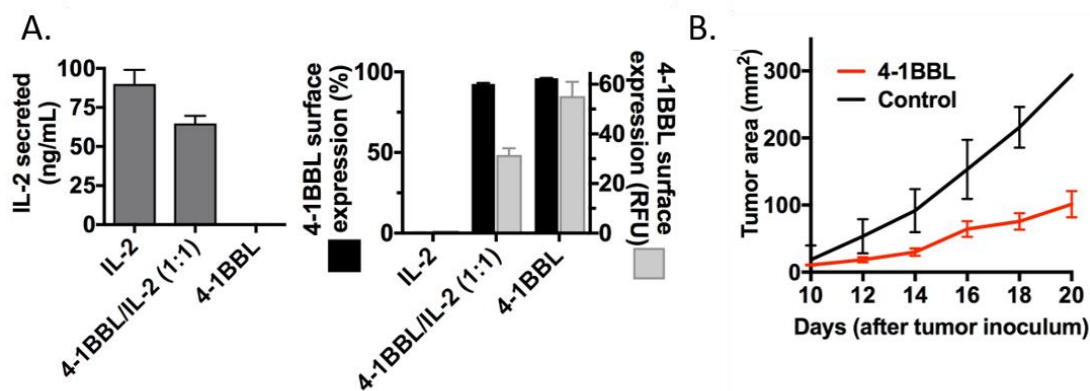


Figure 11.5: PBAE based transfection of immunostimulatory genes in B16 melanoma cells results in enhanced cancer immunotherapy. (a) B16 melanoma cells were transfected with a plasmid containing either 4-1BBL or IL-2. (left) Measured IL-2 secretion following melanoma cell transfection and (right) measured surface presented 4-1BBL. (b) Tumor bearing mice were injected intratumorally with transfection nanoparticles as well as intraperitoneally with an immune checkpoint blockade. The transfection with immunostimulatory ligands resulted in delayed tumor growth over time. Error bars represent the SEM of 5 animal replicates.

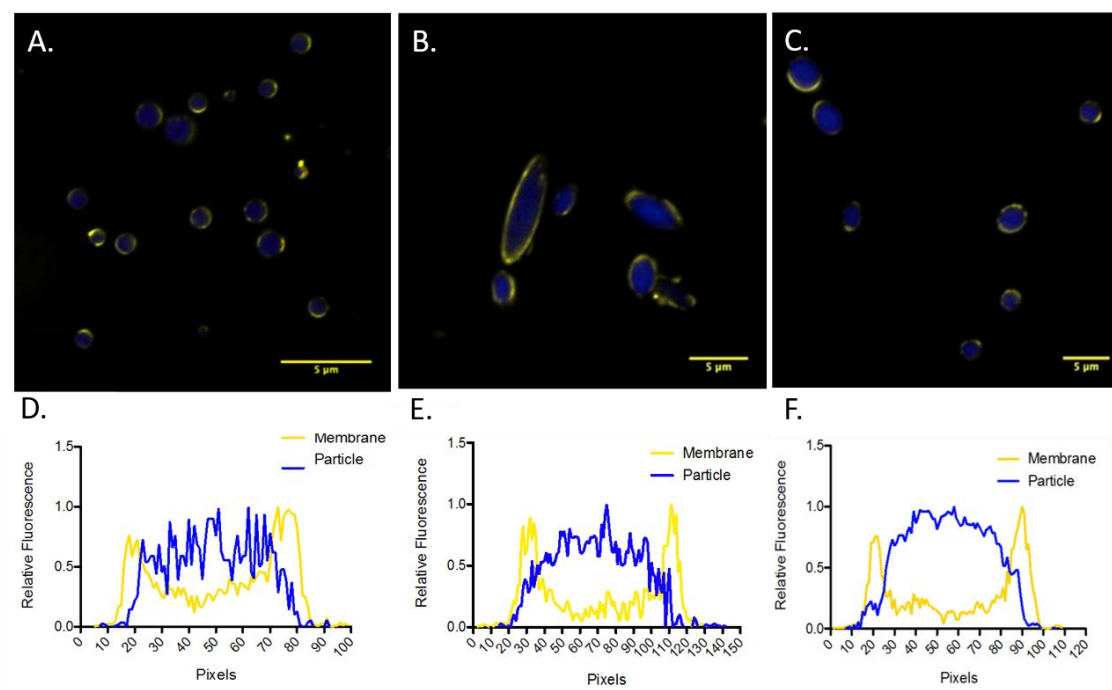


Figure 11.6: Anisotropic particles can be successfully coated with platelet membranes. (a) Spherical, (b) Prolate ellipsoidal, and (c) Oblate ellipsoidal microparticles were synthesized with a dye in the core (blue) and fluorophore labeled platelet membranes (yellow). Confocal imaging and fluorescence profile analysis of the particles through the center of the (d) Spherical, (e) prolate ellipsoidal, and (f) oblate ellipsoidal microparticles demonstrate successful membrane coating.

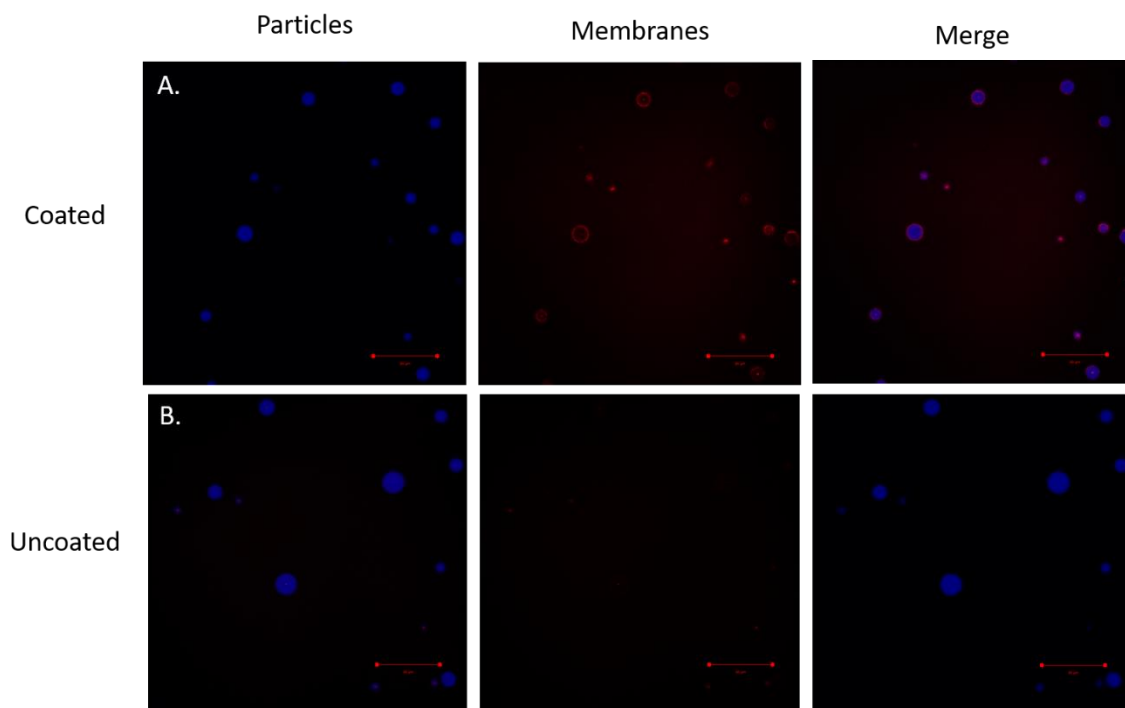


Figure 11.7: Dendritic cell membranes can be coated on the surface of spherical microparticles. (a) Coated and (b) uncoated particles with dendritic cell isolated membranes. Images show enrichment of dendritic cell membrane material on the surface of the coated particles only.

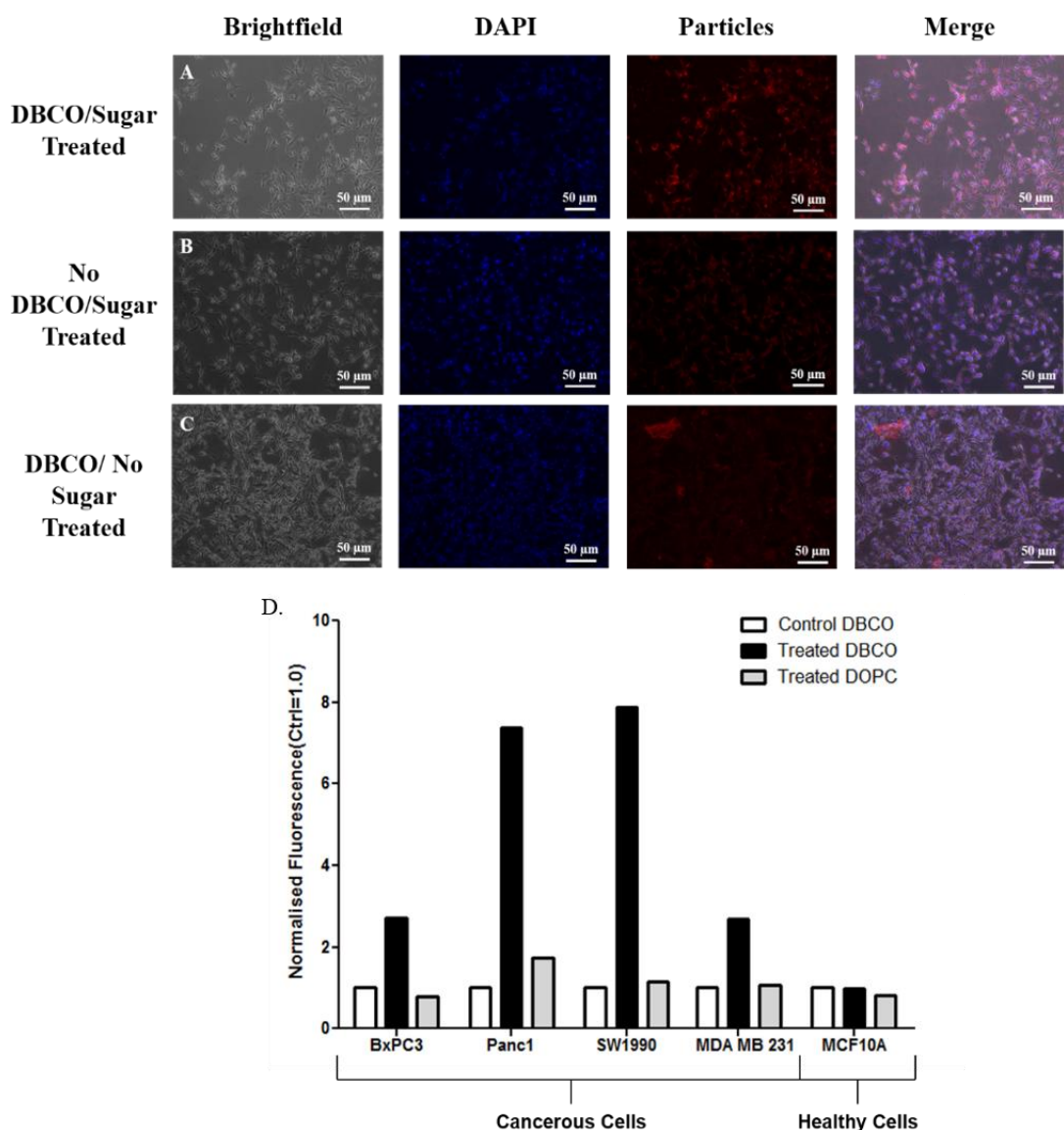


Figure 11.8: (a-c) DBCO functionalized nanoparticles accumulate at sialic acid overexpressing breast cancer cells (MDA MB 231). Cells receive the indicated treatment in the left column and were analyzed for fluorescence on the channel indicated on the top row. (d) DBCO functionalized nanoparticles accumulate on cancer cells. Particle channel fluorescence was quantified and normalized to a no nanoparticle treatment control. All analogue treated cancer cell lines had an increase in functional particle accumulation (Treated DBCO) compared to non-functional nanoparticles (Treated DOPC) and non-treated cells (Control DBCO). The healthy cell line did not exhibit this nanoparticle accumulation.

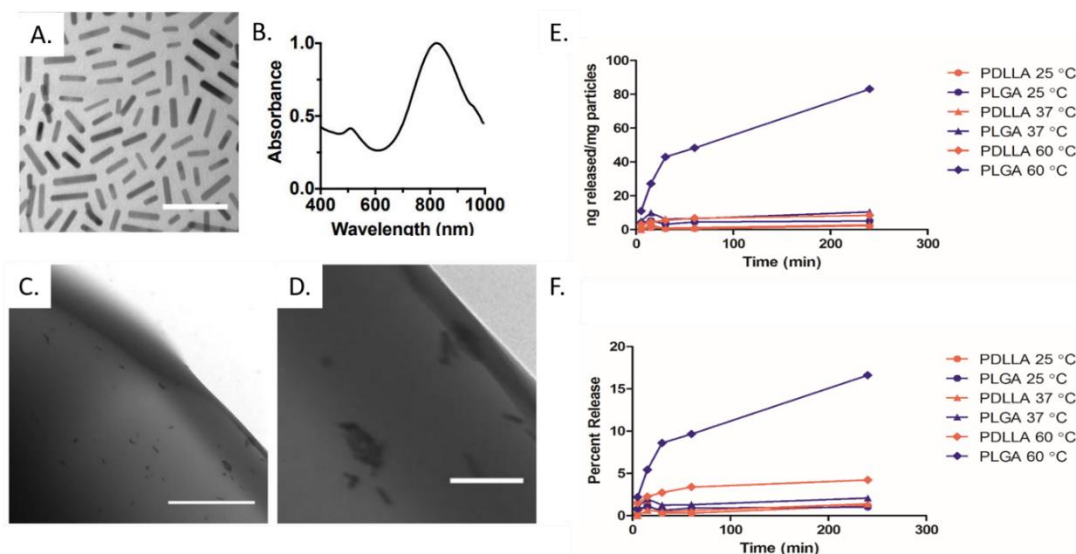


Figure 11.9: Polymeric microparticles can successfully encapsulated gold nanorods for photothermal drug release. (a) TEM images of gold nanorods that were hydrophobically functionalized and subsequently maintained their (b) absorbance peak at 810 nm. Gold nanorods encapsulated in polymeric microparticles can be visualized by TEM shows minimal aggregation of the rods during the encapsulation process (c) scale bar = 500 nm, (d) scale bar = 100 nm. (e) Thermally dependent release of doxorubicin from polymeric microparticles demonstrates minimal release below each material's glass transition temperature but significant release upon heating past it.

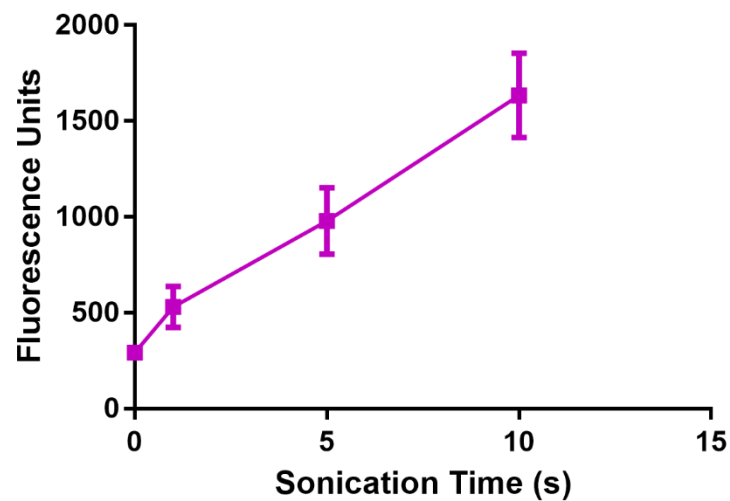


Figure 11.10: Doxorubicin release from ultrasound triggered nanoemulsions for cancer drug delivery. Doxorubicin release was analyzed by the fluorescence of the supernatant following sonication. Data demonstrates dose dependent release of doxorubicin based on sonication time. Error bars represent the SEM of 4 replicates.

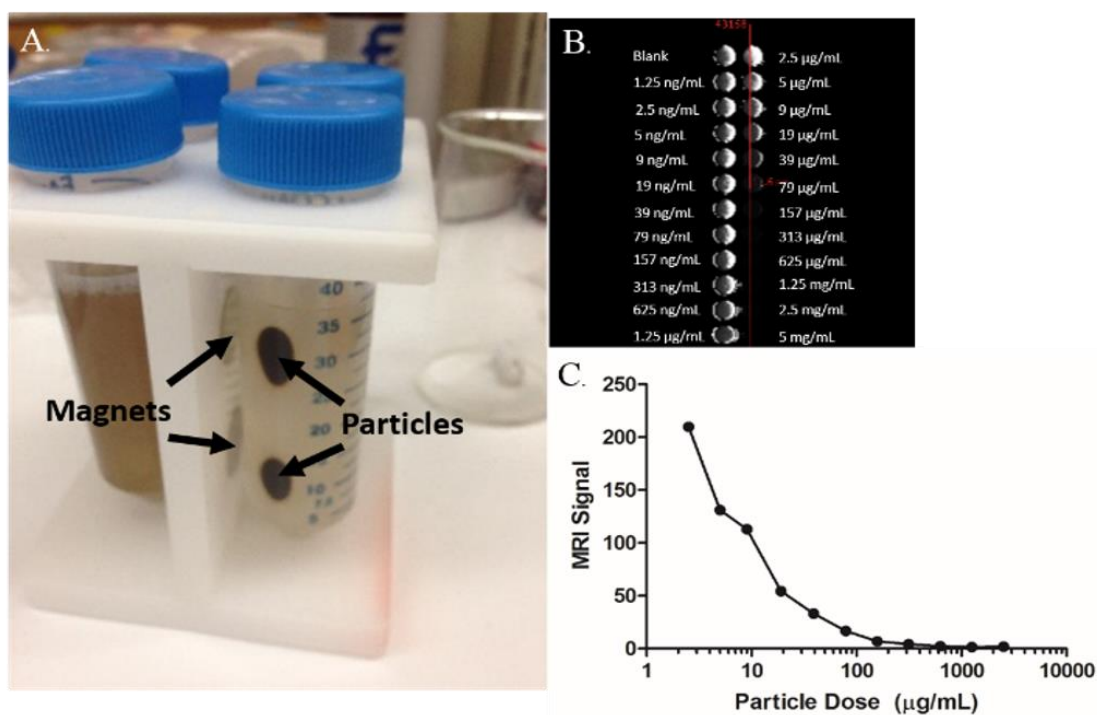


Figure 11.11: Polymeric microparticles can successfully encapsulate magnetic polymeric nanoparticles for conferment of superparamagnetic properties to anisotropic particles. (a) Polymeric microparticles accumulate under the influence of a magnet and disperse when the magnet is removed. (b) MRI image of microparticles encapsulating magnetite indicate the potential for magnetic contrast at as low as (c) 10 $\mu\text{g/mL}$ based on quantification of the signal from the MRI images.

11.8 References

1. Hu, C.-M.J., Fang, R.H., Wang, K.-C., Luk, B.T., Thamphiwatana, S., Dehaini, D., Nguyen, P., Angsantikul, P., Wen, C.H. Kroll, A.V. Nanoparticle biointerfacing by platelet membrane cloaking. *Nature* 2015;526(7571):118.
2. Meyer, R.A. Green, J.J. Artificial Antigen-Presenting Cells: Biomimetic Strategies for Directing the Immune Response. In *Biomaterials in Regenerative Medicine and the Immune System* 257-77 (Springer, 2015).
3. Sunshine, J.C., Perica, K., Schneck, J.P. Green, J.J. Particle shape dependence of CD8⁺ T cell activation by artificial antigen presenting cells. *Biomaterials* 2014;35(1):269-77.
4. Xu, Q., Hashimoto, M., Dang, T.T., Hoare, T., Kohane, D.S., Whitesides, G.M., Langer, R. Anderson, D.G. Preparation of monodisperse biodegradable polymer microparticles using a microfluidic flow-focusing device for controlled drug delivery. *Small* 2009;5(13):1575-81.
5. Meyer, R.A., Meyer, R.S. Green, J.J. An automated multidimensional thin film stretching device for the generation of anisotropic polymeric micro-and nanoparticles. *J. Biomed. Mater. Res. A* 2015;103(8):2747-57.
6. Oelke, M., Krueger, C., Giuntoli II, R.L. Schneck, J.P. Artificial antigen-presenting cells: artificial solutions for real diseases. *Trend. Mol. Med.* 2005;11(9):412-20.
7. Kosmides, A., Meyer, R., Hickey, J., Aje, K., Cheung, K., Green, J. Schneck, J. Biomimetic biodegradable artificial antigen presenting cells synergize with PD-1 blockade to treat melanoma. *Biomaterials* 2017;118:16-26.
8. Edozie, F.C., Nova-Lamperti, E.A., Povoleri, G.A., Scottà, C., John, S., Lombardi, G. Afzali, B. Regulatory T-cell therapy in the induction of transplant tolerance: the issue of subpopulations. *Transplantation* 2014;98(4):370-9.
9. LaMothe, R.A., Kolte, P.N., Vo, T., Ferrari, J.D., Gelsinger, T.C., Wong, J., Chan, V.T., Ahmed, S., Srinivasan, A. Deitemeyer, P. Tolerogenic Nanoparticles Induce Antigen-Specific Regulatory T Cells and Provide Therapeutic Efficacy and Transferrable Tolerance against Experimental Autoimmune Encephalomyelitis. *Front. Immunol.* 2018;9:281.
10. McHugh, M.D., Park, J., Uhrich, R., Gao, W., Horwitz, D.A. Fahmy, T.M. Paracrine co-delivery of TGF- β and IL-2 using CD4-targeted nanoparticles for induction and maintenance of regulatory T cells. *Biomaterials* 2015;59(172-81).
11. Xu, L., Kitani, A., Fuss, I. Strober, W. Cutting edge: regulatory T cells induce CD4⁺ CD25⁻ Foxp3⁻ T cells or are self-induced to become Th17 cells in the absence of exogenous TGF- β . *J. Immunol.* 2007;178(11):6725-9.
12. Vitale, M., Cantoni, C., Pietra, G., Mingari, M.C. Moretta, L. Effect of tumor cells and tumor microenvironment on NK-cell function. *Eur. J. Immunol.* 2014;44(6):1582-92.
13. Farkona, S., Diamandis, E.P. Blasutig, I.M. Cancer immunotherapy: the beginning of the end of cancer? *BMC Med.* 2016;14(1):73.
14. Ben-Akiva, E., Meyer, R.A., Wilson, D.R. Green, J.J. Surface engineering for lymphocyte programming. *Adv. Drug Deliver. Rev.* 2017;114(102-15).

15. Curtsinger, J.M., Schmidt, C.S., Mondino, A., Lins, D.C., Kedl, R.M., Jenkins, M.K. Mescher, M.F. Inflammatory cytokines provide a third signal for activation of naive CD4⁺ and CD8⁺ T cells. *J. Immunol.* 1999;162(6):3256-62.
16. Tzeng, S.Y., Higgins, L.J., Pomper, M.G. Green, J.J. Biomaterial-mediated cancer-specific DNA delivery to liver cell cultures using synthetic poly (beta-amino esters). *J. Biomed. Mater. Res. A* 2013;101(7):1837.
17. Meyer, R.A., Sunshine, J.C. Green, J.J. Biomimetic particles as therapeutics. *Trend. Biotechnol.* 2015;33(9):514-24.
18. Lutz, M.B. Schuler, G. Immature, semi-mature and fully mature dendritic cells: which signals induce tolerance or immunity? *Trend. Immunol.* 2002;23(9):445-9.
19. Fang, R.H., Hu, C.-M.J., Luk, B.T., Gao, W., Copp, J.A., Tai, Y., O'Connor, D.E. Zhang, L. Cancer cell membrane-coated nanoparticles for anticancer vaccination and drug delivery. *Nano Lett.* 2014;14(4):2181-8.
20. Cho, K., Wang, X., Nie, S. Shin, D.M. Therapeutic nanoparticles for drug delivery in cancer. *Clin. Cancer Res.* 2008;14(5):1310-6.
21. Cheng, Z., Al Zaki, A., Hui, J.Z., Muzykantov, V.R. Tsourkas, A. Multifunctional nanoparticles: cost versus benefit of adding targeting and imaging capabilities. *Science* 2012;338(6109):903-10.
22. Büll, C., Stoel, M.A., den Brok, M.H. Adema, G.J. Sialic acids sweeten a tumor's life. *Cancer Res.* 2014;74(12):3199-204.
23. Koo, H., Lee, S., Na, J.H., Kim, S.H., Hahn, S.K., Choi, K., Kwon, I.C., Jeong, S.Y. Kim, K. Bioorthogonal Copper-Free Click Chemistry In Vivo for Tumor-Targeted Delivery of Nanoparticles. *Angew. Chem. Int. Ed.* 2012;51(47):11836-40.
24. Almaraz, R.T., Aich, U., Khanna, H.S., Tan, E., Bhattacharya, R., Shah, S. Yarema, K.J. Metabolic oligosaccharide engineering with N-Acyl functionalized ManNAc analogs: Cytotoxicity, metabolic flux, and glycan-display considerations. *Biotechnol. Bioeng.* 2012;109(4):992-1006.
25. Chan, J.M., Zhang, L., Tong, R., Ghosh, D., Gao, W., Liao, G., Yuet, K.P., Gray, D., Rhee, J.-W. Cheng, J. Spatiotemporal controlled delivery of nanoparticles to injured vasculature. *Proc. Natl. Acad. Sci. U. S. A.* 2010;107(5):2213-8.
26. Alkilany, A.M., Thompson, L.B., Boulos, S.P., Sisco, P.N. Murphy, C.J. Gold nanorods: their potential for photothermal therapeutics and drug delivery, tempered by the complexity of their biological interactions. *Adv. Drug Deliver. Rev. U. S. A.* 2012;64(2):190-9.
27. Huff, T.B., Tong, L., Zhao, Y., Hansen, M.N., Cheng, J.-X. Wei, A. Hyperthermic effects of gold nanorods on tumor cells. *Nanomed. Fut. Med.* 2007;2(1):125-32.
28. Jana, N.R., Gearheart, L. Murphy, C.J. Seed-mediated growth approach for shape-controlled synthesis of spheroidal and rod-like gold nanoparticles using a surfactant template. *Adv. Mater.* 2001;13(18):1389.
29. Shields, J.A. Shields, C.L. Current management of retinoblastoma. in *Mayo Clin. Proc.*, Vol. 69 50-6 (Elsevier, 1994).
30. Kang, S.J., Durairaj, C., Kompella, U.B., O'Brien, J.M. Grossniklaus, H.E. Subconjunctival nanoparticle carboplatin in the treatment of murine retinoblastoma. *Arch. Ophthalmol. – Chic.* 2009;127(8):1043-7.

31. Shome, D., Poddar, N., Sharma, V., Sheorey, U., Maru, G.B., Ingle, A., Sarin, R., Banavali, S., Dikshit, R. Jain, V. Does a nanomolecule of carboplatin injected periocularly help in attaining higher intravitreal concentrations? *Invest. Ophthalm. Visual* 2009;50(12):5896-900.
32. Rapoport, N.Y., Nam, K.-H., Gao, Z. Kennedy, A. Application of ultrasound for targeted nanotherapy of malignant tumors. *Acoust. Phys.* 2009;55(4-5):594-601.
33. Ye, F., Barrefelt, Å., Asem, H., Abedi-Valugerdi, M., El-Serafi, I., Saghafian, M., Abu-Salah, K., Alrokayan, S., Muhammed, M. Hassan, M. Biodegradable polymeric vesicles containing magnetic nanoparticles, quantum dots and anticancer drugs for drug delivery and imaging. *Biomaterials* 2014;35(12):3885-94.
34. Solar, P., González, G., Vilos, C., Herrera, N., Juica, N., Moreno, M., Simon, F. Velásquez, L. Multifunctional polymeric nanoparticles doubly loaded with SPION and ceftiofur retain their physical and biological properties. *J. Nanobiotechnol.* 2015;13(1):14.
35. Liu, X., Kaminski, M.D., Chen, H., Torno, M., Taylor, L. Rosengart, A.J. Synthesis and characterization of highly-magnetic biodegradable poly (D, L-lactide-co-glycolide) nanospheres. *J. Control. Release* 2007;119(1):52-8.

Randall A. Meyer

Mailing Address: 2507 E Fairmount Ave.
Baltimore, MD 21224
(845)-625-3336
rmeyer16@jhmi.edu

Permanent Address: 4 Lawn Place
Wappingers Falls, NY 12590
(845)-625-3336
rmeyer16@jhmi.edu

Education

PhD. In Biomedical Engineering, Johns Hopkins School of Medicine, Baltimore, MD, GPA: 4.0	Expected 2018
B.S. in Biological Engineering (summa cum laude) with minor in Biomedical Engineering, Cornell University, Ithaca, NY, GPA: 4.18	2008-2012

Current Position

Graduate Research Assistant - Under the mentorship of Jordan Green, PhD. Independently conduct academic research in the general fields of immunoengineering, biomaterials, and drug delivery. Supervise a team of six undergraduate and graduate students in the completion of these research activities. Collaborate with pre-doctoral and post-doctoral peers. Prepare and revise peer reviewed manuscripts for publication. Assist in the preparation of various research grants (NIH and non-NIH affiliated). Johns Hopkins School of Medicine Baltimore, MD	2013-Present
---	--------------

Professional Experience

Graduate Research Assistant - Under the mentorship of Tza Hui Wang, PhD. Independently conduct academic research in collaboration with senior peers in the field of microfabrication and biomedical diagnostics. Johns Hopkins University School of Medicine Baltimore, MD	2012
Undergraduate Research Assistant - Under the mentorship of James Casey, PhD. Independently conduct academic research in the fields of virology and immunology. Investigated aquatic animal viral transmission with regards to pre- and post-mortem zebrafish subjects. Developed an assay to detect viral prevalence from environmentally derived fish tissues. Cornell University Ithaca, NY	2008-2012

Honors and Awards

JHU BME Student Seminar Competition First Place: Award given to an individual with the best seminar in an academic semester as determined by students and faculty in the audience.	2018
Siebel Scholar Class of 2018: Given to individuals pursuing degrees in various fields of graduate study in top universities throughout the world for scientific achievements and leadership potential.	2017
ASGCT Outstanding Poster Presentation Award: Given to individuals that demonstrated excellence in their conference poster presentations at the annual meeting of the American Society for Gene and Cell Therapy.	2017

Biomedical Engineering Society Graduate Student Design and Research Award: Awarded to graduate students for excellence in the design and execution of a research project	2016
NIH: National Research Service Award F31: Fellowship awarded to exceptional graduate students to support training in biomedical research.	2016-2018
Achievement Rewards for College Scientists Metro-Washington Chapter Jones Group Scholar: Graduate research scholarship awarded for outstanding academic achievement.	2016-2017
Cancer Nanotechnology Center Research Fellowship: Graduate research fellowship for the development of nanobiotechnology for use in the field of cancer research.	2012-2015
Merrill Presidential Scholar: Awarded to the top 1% of Cornell graduating seniors for potential to contribute to society.	2012
Degree Marshall for the College of Agriculture and Life Sciences: Awarded to the two individuals with the highest GPAs among graduating Cornell seniors.	2012
Award for Academic Achievement in Biological Engineering: Awarded to the individual in the graduating Cornell Class of 2012 Bioengineering with the highest GPA.	2012
Outstanding Biochemistry Teaching Assistant Award: Awarded to the individual with the highest level of performance of undergraduate student teaching performance as evaluated by student satisfaction and the professor's evaluation.	2011
Barry M. Goldwater Scholar: Awarded to undergraduate students with high achievement in STEM related academics and research.	2011
Rawlings Cornell Presidential Research Scholar: Award to conduct university supported undergraduate research under the direction of a faculty mentor.	2008-2012
Thomas J. Watson IBM Memorial Scholar: Award to high school/undergraduate students with high academic achievement and potential to contribute to society.	2008-2012

Publications

Peer Reviewed Publications:

1. Ben-Akiva E,* Rhodes K,* **Meyer RA**, and Green JJ. Fabrication of anisotropic polymeric artificial antigen presenting cells for CD8+ T-Cell activation. *Journal of Visualized Experiments*. 2018. e58332-e58332. 2018
2. **Meyer RA**,* Mathew MP,* Ben-Akiva E, Sunshine JC, Shmueli RS, Ren Q, Yarema KJ, and Green JJ. Anisotropic biodegradable particles coated with supported lipid bilayers for spatially dynamic protein presentation. *Acta Biomaterialia*. 72, 2018, 228-238. 2018
3. Guo Q,* Bishop CJ,* **Meyer RA**,* Wilson DR, Olasov L, Schlesinger DE, Mather PT, Spicer JB, Eliseeff JH, and Green JJ. Entanglement-Based Thermoplastic Shape Memory Polymeric Particles with Photothermal Actuation for Biomedical Applications, *ACS Applied Materials and Interfaces*, 10(16), 2018, 13333-13341. 2018
4. Kosmides AK,* **Meyer RA**,* Hickey JW, Aje K, Green JJ, and Schneck JP. Biodegradable artificial antigen presenting cells with anti PD-1 immunotherapy to treat melanoma. *Biomaterials*, 118, 2017, 16-26. 2017
5. Airan RD*, **Meyer RA***, Ellens NK, Rhodes KR, Ren Q, Deng C, Farahani K, Pomper MG, Kadam SD, Green JJ. Focused ultrasound mediated drug delivery from polymeric perfluorocarbon nanoemulsions for noninvasive neuromodulation, *Nano Letters*, 17(2), 2017, 652-659. 2017

6. Wilson DR, Mosenia A, Suprenant MP, Upadhyaya R, Routkevitch D, **Meyer RA**, Quinones-Hinojosa A, Green JJ. Continuous microfluidic assembly of biodegradable poly (beta-amino ester)/DNA nanoparticles for enhanced drug delivery. *Journal of Biomedical Materials Research Part A*, 105(6), 2017, 1813-1825. 2017
7. Ben-Akiva E,* **Meyer RA**,* Wilson DR,* and Green JJ. Surface engineering for lymphocyte programming. *Advanced Drug Delivery Reviews*. 114(2017), 2017, 102-115. 2017
8. **Meyer RA**, and Green JJ. Biodegradable Polymer Iron Oxide Nanocomposites: The Future of Biocompatible Magnetism. *Nanomedicine* 10(23), 2015, 3421-3425. 2015
9. **Meyer RA**,* Sunshine JC,* and Green JJ. Biomimetic Particles as Therapeutics. *Trends in Biotechnology* 33(9), 2015, 514-524. 2015
10. **Meyer RA** and Green JJ. Shaping the Future of Nanomedicine: Anisotropy in Polymeric Nanoparticle Design. *Wiley Interdisciplinary Reviews: Nanomedicine and Nanobiotechnology*, 8(2), 2016, 191-207. 2015
11. **Meyer RA**, Meyer RS, and Green JJ. An automated multidimensional thin film stretching device for the generation of anisotropic polymeric micro- and nanoparticles. *Journal of Biomedical Materials Research Part A* 103(8), 2015, 2747-2757. 2015
12. **Meyer RA**,* Sunshine JC,* Perica K, Kosmides AK, Aje K, Schneck JP, and Green JJ. Biodegradable Nanoellipsoidal Artificial Antigen Presenting Cells for Antigen Specific T-Cell Activation. *Small* 11(13), 2015, 1519-1525. (Featured on the Back Cover) 2015

Book Chapters/Editorials:

1. **Meyer RA** and Green JJ. Artificial Antigen Presenting Cells: Biomimetic Strategies for Directing the Immune Response. *Biomaterials in Regenerative Medicine and the Immune System*. Springer International Publishing, 2015, 257-277. 2015
2. Bishop CJ,* Kim J,* Kozielski KL,* **Meyer RA**,* and Green JJ. Highlights from the latest articles in nanomedicine. *Nanomedicine* 9(7), 2014, 945. 2014

* = Authors contributed equally

Abstracts and Presentations

Oral Presentations

National/International Meetings

1. **Meyer RA**, Hickey JW, Kosmides AK, Rhodes KR, Bartkowski A, Schneck JP, Green JJ. Biomimetic Biodegradable Artificial Antigen Presenting Cells for Enhanced "Off-The-Shelf" Melanoma Immunotherapy. *Biomedical Engineering Society*. 2017 2017
2. Rhodes KR, **Meyer RA**, Green JJ. An Acellular Polymeric Particle-Based Platform For The Highly Efficient Activation And Expansion Of Natural Killer Cells. *Biomedical Engineering Society*. 2017 2017
3. **Meyer RA**, Ben-Akiva E, Cheung Ka Ho, Green JJ. Biomimetic Anisotropic Polymeric Particles with Naturally Derived Cell Membranes for Enhanced Drug Delivery. *Tissue Engineering and Regenerative Medicine Society*. 2016 2016
4. **Meyer RA**, Airan RD, Ellens NK, Farahani K, Pomper MG, Kadam SD, Green JJ. Focused Ultrasound Mediated Drug Delivery from Polymeric Perfluorocarbon Nanoemulsions for Noninvasive Neuromodulation. *Biomedical Engineering Society*, 2016. 2016

5. Airan RD, **Meyer RA**, Ellens NK, Farahani K, Green JJ. Targeted Release of Anesthetic Agents with Focused Ultrasound. *American Society of Neuroradiology*, 2016.
6. **Meyer RA**, Sunshine JC, Schlesinger DE, Schneck JP, Green JJ. Biodegradable Monodisperse Oblate and Prolate Ellipsoidal Artificial Antigen Presenting Cells for Antigen Specific T-Cell Activation. *World Biomaterials Congress*, 2016.
7. **Meyer RA**, Kosmides AK, Aje K, Schneck JP, and Green JJ. Anti-PD1 and Biodegradable Artificial Antigen Presenting Cell Dual Therapy for Melanoma. *Biomedical Engineering Society Annual Meeting*, 2015.
8. Guo Q, Bishop CJ, **Meyer RA**, Olasov L, Schlesinger DE, Spicer JB, Elisseeff JH, Kumar A, and Green JJ. Development of Light Induced Shape Memory Microparticles for Biomedical Applications. *Biomedical Engineering Society Annual Meeting*, 2015.
9. **Meyer RA**, Sunshine JC, Kosmides AK, Perica K, Schneck JP, and Green JJ. Particle Shape as a Biointerface Parameter to Control the Behavior of Immune Cells. *Tissue Engineering and Regenerative Medicine International Society World Meeting*, 2015.
10. **Meyer RA**, Meyer RS, Sunshine JC, Perica K, Kosmides AK, Aje K, Schneck JP, and Green JJ. *Society for Biomaterials Annual Meeting*, 2015.
11. **Meyer RA**, Sunshine JC, Perica K, Aje K, Schneck JP, and Green JJ. Biodegradable Nanoellipsoidal Artificial Antigen Presenting Cells for Immune Modulation. *Tissue Engineering and Regenerative Medicine International Society-America Meeting*, 2014.
12. **Meyer RA**, Sunshine JC, Perica K, Aje K, Schneck JP, and Green JJ. Biodegradable Nanoellipsoidal Artificial Antigen Presenting Cells for Cancer Immunotherapy. *Biomedical Engineering Society Annual Meeting*, 2014.
13. **Meyer RA**, Hope KM, and Casey JW. Investigation of Viral Hemorrhagic Septicemia Virus Shedding and Transmission Utilizing a Zebrafish Model. *National Conference of Undergraduate Research*, 2011.

Local/Regional Meetings

1. **Meyer RA**. Biomimetic Materials for Drug Delivery and Immunotherapy. *JHU BME Graduate Speaker Series*. 2016 (Invited Talk).
2. **Meyer RA**, Sunshine JC, Perica K, Aje K, Schneck JP, and Green JJ. Biodegradable Anisotropic Artificial Antigen Presenting Cells for Cancer Immunotherapy. *Cornell Interuniversity Graduate Student Seminar Series*, 2014 (Invited Talk).
3. **Meyer RA**, Hope KM, and Casey JW. Investigation of Viral Hemorrhagic Septicemia Shedding Utilizing a Zebrafish Model. *Cornell Undergraduate Research Board Forum*, 2010.

Poster Presentations

National/International Meetings

1. Schlesinger DE, Guo Q, Bishop CJ, **Meyer RA**, Wilson DR, Olasov L, Spicer JB, Elisseeff JH, Green JJ. Entanglement-based thermoplastic shape memory polymeric particles with photothermal actuation for biomedical applications. *Tissue Engineering and Regenerative Medicine Society Annual Meeting*. 2017
2. **Meyer RA**, Mathew MP, Ren Q, Yarema KJ, and Green JJ. Cancer-specific nanoparticle binding by click chemistry to membrane bound sialic acid analogues, *Controlled Release Society Annual Meeting*, 2017

3. **Meyer RA**, Kosmides AK, Hickey JW, Aje K, Cheung Ka Ho, Schneck JP, Green JJ. 2017
Biomimetic Artificial Antigen Presenting Cells Synergize with Anti-PD1 in the Treatment of Melanoma. *American Society for Gene and Cell Therapy*. 2017
4. **Meyer RA**, Hickey JW, Kosmides AK, Rhodes KR, Sunshine JC, Perica K, Schneck JP, Green JJ. Enhanced Tumor Immunotherapy Mediated by Nanoellipsoidal Artificial Antigen Presenting Cells. *Society for Biomaterials*. 2017
5. **Meyer RA**, Meyer RS, Green JJ. An Automated Thin Film Stretching Device for the Generation of Anisotropic Polymeric Micro- and Nanoparticles. *NanoDDS*. 2016
6. Ren Q, **Meyer RA**, Mathew MP, Yarema KJ, and Green JJ. Lipid coated nanoparticles for targeted delivery to cancer cells using copper-free click chemistry, *Biomedical Engineering Society Annual Meeting*, 2015
7. **Meyer RA**, Mathew MP, Sunshine JC, Shmueli RB, Ren Q, Yarema KJ, and Green JJ. Anisotropic Supported Lipid Bilayers for Spatially Dynamic Surface Protein Presentation. *Society for Biomaterials Annual Meeting*, 2015.
8. Sunshine JC, Perica K, **Meyer RA**, Schneck JP, and Green JJ. Antigen-Specific CD8+ T-Cell Activation with Non-Spherical Micro- and Nano- Artificial Antigen Presenting Cells (aAPC). *US-Japan Symposium on Drug Delivery Systems*, 2013.

Local/Regional Meetings

1. **Meyer RA**, Airan RD, Ellens NK, Farahani K, Pomper MG, Green JJ. Focused Ultrasound Mediated Drug Delivery from Polymeric Perfluorocarbon Nanoemulsions for Noninvasive Neuromodulation. *Institute for Nanobiotechnology Spring Forum*, 2017
2. **Meyer RA**, Sunshine JC, Perica K, Aje K, Schneck JP, and Green JJ. Biodegradable Nanoellipsoidal Artificial Antigen Presenting Cells for Cancer Immunotherapy. *Institute for Nanobiotechnology Spring Forum*, 2016.
3. **Meyer RA**, Meyer RS, and Green JJ. An automated multidimensional thin film stretching device for the generation of anisotropic polymeric micro- and nanoparticles. *Institute for Nanobiotechnology Spring Forum*, 2015.
4. **Meyer RA**, Sunshine JC, Perica K, Aje K, Schneck JP, and Green JJ. Biodegradable Nanoellipsoidal Artificial Antigen Presenting Cells for Cancer Immunotherapy. *Institute for Nanobiotechnology Spring Forum*, 2014.
5. Sunshine JC, Perica K, **Meyer RA**, Schneck JP, and Green JJ. Antigen-Specific T-Cell Activation with Non-Spherical Micro- and Nano- Artificial Antigen Presenting Cells (aAPC). *Institute for Nanobiotechnology Spring Forum*, 2013
6. **Meyer RA**, Casey R, Emmeneger E, Bowser P, and Casey JW. Development of a qRT-PCR Assay for the Detection of Spring Viremia of Carp Virus and Application to a 2010 Great Lakes Survey. *Cornell Undergraduate Research Board Forum*, 2012.
7. **Meyer RA**, Hope KM, and Casey JW. Investigation of Viral Hemorrhagic Septicemia Virus Shedding and Transmission Utilizing a Zebrafish Model. *Cornell Undergraduate Research Board Forum*, 2011.

Patents and Technology Transfer

1. Green JJ, Schneck JP, **Meyer RA**, Kosmides AK, Rhodes KR, Hickey JW. 2017
Biodegradable Biomimetic Particles. Provisional Patent Filed on October 10, 2017
Application No. 62/570,249.

2. Airan RD, Green JJ, **Meyer RA**. 2016 Particulate Drug Delivery System to Enable Targeted Ultrasound-Gated Release of Neuromodulatory Agents, Provisional Patent Application filed on May 20, 2016. JHU Case #C13913. 2016
3. Green JJ, Ben-Akiva E, **Meyer RA**. Biomimetic Anisotropic Polymeric Particles with Naturally Derived Cell Membranes for Enhanced Drug Delivery. JHU Case #C13853. 2016
4. Green JJ, Semenza G, **Meyer RA**, Guo Q, Bishop C. Polymeric Nanoparticles Containing Inhibitors of Hypoxia-Inducible Factors." JHU Case #C13843. 2016
5. Bishop CJ, Green JJ, Guo Q, Kumar A, **Meyer RA**. 2015 Shape Memory Particles for Biomedical Uses, Provisional Patent Application filed on April 6, 2016 JHU Case #C13505. 2016
6. Green JJ, Mathew MP, **Meyer RA**, Shmueli RB, Sunshine JC, Yarema KJ. 2015 Biomimetic Artificial Cells: Anisotropic Supported Lipid Bilayers on Biodegradable Micro and Nanoparticles for Spatially Dynamic Surface Protein Presentation. Provisional Patent Application no. 62/138,707. JHU Case #C13425 2015

Leadership and Service Activities

- BME EDGE Director of Professional Development: Served as a member of the BME EDGE student committee. Tasked with promoting development of professional skills in the BME community as well as organizing professional development seminars for BME students, staff, and faculty. Co-led the planning of a professional headshot day for graduate students. 2016-2017
- Translational Tissue Engineering Center Student Representative: Served as a faculty-student liaison to for the Translational Tissue Engineering Center. Worked to plan social and professional events for the center. 2016-Present
- BME PhD. Council Co-President: Served as the leader of the BME PhD council, the student organization tasked with representing the BME PhD student community. Planned social events for students as well as led the planning of the BME new student recruitment initiative. Served as a liaison for the students and BME faculty and worked to plan the annual BME retreat. 2013-2014
- BME EDGE Director of Engagement: Served as a member of the BME EDGE student committee. Tasked with promoting faculty participation in EDGE activities and promoting EDGE internship opportunities to students. 2013-2014
- Ithaca Science Museum Student Volunteer: Acted as a student volunteer for individual science days at the museum. Partook in the planning and presentation of scientific demonstrations for local children. Taught concepts related to nanotechnology and materials science to museum visitors. 2010-2012
- Phi Sigma Pi Honor Fraternity: Served as the fundraising chair, tasked with raising sufficient funding on an annual basis to ensure self-sufficiency in the fraternity. Initiated novel fundraising events to bring in outside money and interest in the fraternity. 2010-2012
- Into the Streets Lead Member: Served as a student volunteer tasked with organizing an initiative to clean up trash in the local parks. Acted as a coordinator between the students and the event officials to plan the day-long cleaning. 2010

Educational Activities

- Graduate Student Course Instructor: Designed, implemented and taught a course during Intersession at Johns Hopkins University on the topic of immunoengineering. 2017
- Graduate Student Teaching Assistant for Systems Bioengineering Laboratory II: Conduct laboratory sessions, grade papers, and assist in course management 2016

Graduate Student Teaching Assistant for Cell Engineering: Conduct office hours/review sessions, grade papers, and assist in course management.	2014
Undergraduate Student Teaching Assistant for Fluid Mechanics: Graded testing materials and assignments for comprehensive course, designed new assignments.	2011
Undergraduate Student Teaching Assistant for Biochemistry: Conducted office hours and graded testing materials for comprehensive auto-tutorial course.	2011-2012
Undergraduate Student Teaching Assistant for Principles of Biological Engineering: Designed and evaluated new assignments for the upcoming semester.	2010
Undergraduate Student Teaching Assistant for Introduction to Computer Programming: Conducted lab sessions, held office hours, graded exams and student assignments.	2009

Mentored Individuals

Qiuyin Ren: Mentored student on various projects surrounding gene delivery, targeted drug delivery, and immunoengineering. The student was included on 2 professional abstracts as well as a peer reviewed publication for contributions to the laboratory. The student also attended the national BMES conference under the mentorship. In addition, the student won the Provost's Undergraduate Research Award from Johns Hopkins University under the mentorship.	2013-2017
Daphne Schlesinger: Mentored student on several projects surround biomaterials properties, microfabrication, and immunoengineering. The student was included on 2 professional abstracts as well as a peer-reviewed publication for contributions to the laboratory. The student also attended the national NanoDDS conference under the mentorship. In addition, the student won the Provost's Undergraduate Research Award from Johns Hopkins University under the mentorship.	2014-2018
Ka Ho Nicholas Cheung: Mentored student on various projects surrounding immunoengineering and controlled drug release. The student was included on 2 professional abstracts as well as a peer reviewed publication for contributions to the laboratory.	2014-2016
Callie Deng: Mentored the student on multiple projects including the fabrication of biodegradable, magnetic particles and the use of focused ultrasound for targeted drug release. The student was included on a professional abstract for contributions to the laboratory.	2014-2015
Alison Bartkowski: Mentored the student on the design of artificial antigen presenting cells for cancer immunotherapy. The student was included on a professional abstract for contributions to the laboratory.	2016-Present
Austin Petronak: Mentored the student on the development of biomimetic materials with naturally derived cell membrane coats and development of particles for use as artificial antigen presenting cells.	2016-2017
Jenna Ballard: Mentored the student on the use of various biomaterials for the design of artificial antigen presenting cells as well as investigation on the role of shape in the design of these particles.	2016-2017

Professional Memberships

Society for Biomaterials Student Member	2015-Present
---	--------------

Tissue Engineering and Regenerative Medicine International Society	2014-Present
Biomedical Engineering Society Student Member	2014- Present
Golden Key International Honor Society	2011-2012
Tau Beta Pi Honor Society	2010-2012
Alpha Epsilon: Food, Agriculture, and Biological Engineering Honors Fraternity	2010-2012